Niet-lineair gedrag van doorlopende betonliggers verstevigd met uitwendig gelijmde FRP wapening

Non-Linear Behaviour of Continuous Concrete Beams Strengthened with Externally Bonded FRP Reinforcement

Lander Vasseur

Promotoren: prof. dr. ir. S. Matthys, prof. dr. ir. L. Taerwe
Proefschrift ingediend tot het behalen van de graad van
Doctor in de Ingenieurswetenschappen: Bouwkunde

Vakgroep Bouwkundige Constructies
Voorzitter: prof. dr. ir. L. Taerwe
Faculteit Ingenieurswetenschappen
Academiejaar 2008 - 2009

UNIVERSITEIT
GENT

ISBN 978-90-8578-264-3
NUR 955
Wettelijk depot: D/2009/10.500/22

Promotoren – Supervisors
Prof. Dr. Ir. Stijn Matthys
Prof. Dr. Ir. L. Taerwe
Universiteit Gent, Vakgroep Bouwkundige Constructies

Prof. Dr. Ir. Stijn Matthys
Prof. Dr. Ir. L. Taerwe
Ghent University, Department of Structural Engineering

Onderzoeksinstelling – Research institute
Universiteit Gent, Vakgroep Bouwkundige Constructies
Laboratorium Magnel voor Betononderzoek
Technologiepark-Zwijnaarde 904
9052 Gent

Ghent University, Department of Structural Engineering
Magnel Laboratory for Concrete Research
Technologiepark-Zwijnaarde 904
B-9052 Ghent

Beursverlenende instantie – Research grant offered by
Fonds Wetenschappelijk Onderzoek – Vlaanderen (FWO)
Egmontstraat 5
1000 Brussel

Research foundation - Flanders (FWO)
Egmontsraat 5
B-1000 Brussels

Dankwoord

Nog enkel dit dankwoord en dan is het zover... Na 4,378 jaren zwoegen, zweten en collegiaal amusement is het eindelijk zover: mijn thesis, mijn boek, hij is af. Uiteraard ben ik er mij ten zeerste van bewust dat ikzelf niet als enige verantwoordelijk ben voor het welslagen van dit proefschrift. Velen anderen hebben immers, elk op hun manier, een steentje bijgedragen aan dit werk en verdienen dan ook een vermelding in dit dankwoord.

Op professioneel gebied zou ik graag in de eerste plaats mijn dank willen betuigen aan mijn beide promotoren, met name Prof. Stijn Matthys en Prof. Luc Taerwe. Dankzij hen heb ik de kans gekregen dit doctoraat te mogen starten. Tijdens mijn doctoraat kon ik altijd bij hen aankloppen in de zoektocht naar een antwoord op mijn vele vragen. In de slotfase van mijn doctoraat waren het ook zij die een onmetelijke tijd gespendeerd hebben aan het lezen, corrigeren en herlezen van de vele pagina's tekst, waarvoor mijn dank.

Vervolgens had ik ook graag de andere collega's van Labo Magnel willen bedanken met in het bijzonder volgende personen: Willem voor de, hoe zou ik het zeggen, alle bejuwel'de momenten in onze bureau. Hierbij wordt verwezen naar de serieuze momenten waarbij algemene kennis en Engelstalige taalvaardigheid het onderwerp van discussie waren alsook naar de minder serieuze momenten zoals de Anora- en vrijdagsmomenten (waarvoor ook dank aan Philip). Graag had ik ook Gert willen bedanken voor de interessante discussies betreffende statistiek, verbouwingen en belastingen die soms in het labo, soms in de buurtwinkel van Ledeberg of wel eens naast de Falcke gehouden werden. Of course it is not allowed to forget Aniello, who was responsible for the interesting discussions concerning FRP EBR and also who was responsible for the very amusing trips to Porto and Zürich. Dimitri had ik ook graag persoonlijk willen bedanken. Samen met Willem zijn wij drie op 1 september 2004 in het labo van start gegaan. Dimitri was ook de collega op wie je kan rekenen voor de feestelijkheden in het labo, dit tot in de late/vroege uurtjes. Verder dient ook nog een woordje van lof gericht te worden aan Anibal, Katrien, Veerle, Nicolas, Peter, Qiang, Geert, Dorleta, Ceren, Emmanuel, Robby, Elke, Marijke, Pieter, Geoffrey, Bart, Arnold, Anne-Mieke, Viviane, Mariette, Christel, Nele, Kim, Frederik, Peppa en Liu.

Bij de planning, de uitvoering en de verwerking van de vele proeven in het labo was de hulp van het technische personeel natuurlijk ook niet te onderschatten. Hierbij gaat speciale dank uit naar Stefan, Nathan, Peter, Tom, Dieter, Marc, Nicolas, Peter, Jan, Jan, Tommy, Bart en Sandra. Zij hebben mij ongelofelijk goed geholpen bij het bekisten, betonneren, opstellen, beproeven en opmeten van de balken.

De koolstoflaminaten alsook de verlijming van deze laminaten, die het specifieke onderwerp waren van dit onderzoek, zijn ons vrij ten dienste gesteld door de firma ECC, waarvoor mijn dank. Bijkomstig wil ik nogmaals de firma ECC bedanken voor de kans die ze mij geven mijn kennis die ik de laatste 4 jaar heb opgebouwd, in de praktijk te kunnen toepassen.

Op persoonlijk vlak had ik in de eerste plaats graag mijn ouders willen bedanken. Zij hebben mij immers alle kansen en mogelijkheden aangeboden mijn studies burgerlijk ingenieur tot een goed einde te brengen. Zonder hun steun zou ik niet staan waar ik nu sta. Ook Annelot en Hannelore had ik graag vermeld, voor er te zijn als kotgenoot, als kinderoppas, als kok of als verrasser tijdens de examens met lekkers.

Een woord van dank dient ook te gaan naar alle personen die instonden voor de ontspannende momenten, de momenten waar de batterijen opgeladen werden. Hierbij denk ik aan de Bollers, Sloefers, VTK'ers, F1-confraters, Kastaar'ers, Somi en Yannis.

Tot slot kan en mag ik mijn twee grootste schatten niet vergeten. Mijn schatten, mijn meisjes, mijn trots. Zij die vele eenzame avonden en weekends hebben moeten trotseren, terwijl ik weeral aan het schrijven/werken was. Zij die mij warmte gaven op momenten dat het heel koud was. Zij die mij een glimlach gaven, op momenten dat een traan de overhand kreeg, zij die mij altijd steunden. Rosy en Ella, mijn gezin, mijn alles. Jullie maken mij heel gelukkig!

Lander

30 maart 2009

Chapter 1: Introduction

Chapter 2: Non-linear behaviour of strengthened continuous beams: Moment redistribution

Chapter 3: Bond behaviour of externally bonded FRP to concrete in the case of continuous beams

Chapter 4: Plastic hinges and rotation capacity of externally strengthened sections

Chapter 5: Influence of externally bonded reinforcement on the crack spacing

Chapter 6: Design recommendations

Chapter 7: Conclusions

Appendix A: Analytical implementation of the non-linear theory for a two-span beam

Appendix B: Overview of 3-point-bending tests

Appendix C: Strengthening of both the span and the mid-support of a beam with internal reinforcement ratios different from the linear elastic distribution

Notations

Often used in the notations are the subscripts 'support' and 'span'. These subscripts are referring to the location of the critical cross-section (section where the acting bending moment is maximal) of the support and the span respectively.

Roman upper case letters

A_c	cross-sectional area of concrete
A_{eq}	cross-sectional area of equivalent reinforcement
A_f	cross-sectional area of FRP reinforcement
A_s	cross-sectional area of longitudinal steel reinforcement
A_{s1}	cross-sectional area of longitudinal tensile steel reinforcement
A_{s2}	cross-sectional area of longitudinal compressive steel reinforcement
E	modulus of elasticity
E_a	modulus of elasticity of adhesive
E_c	modulus of elasticity of concrete
E_{cm}	mean modulus of elasticity of concrete
E_f	modulus of elasticity of FRP
E_s	modulus of elasticity of steel
F	point load
F_{cr}	cracking load of a cross-section
F_{deb}	debonding load
$F_{deb,calc}$	calculated debonding load
$F_{deb,exp}$	experimental obtained debonding load
F_y	yielding load
$F_{str,exp}$	experimental obtained failure load of strengthened beam
F_u	load at ultimate
$F_{u,non\text{-}lin}$	load at ultimate according the non-linear theory
$F_{u,plast}$	load at ultimate according the plasticity theory
$F_{u,span}$	load at ultimate of the span
$F_{u,support}$	load at ultimate of the support
$F_{u,unstr}$	load at ultimate of unstrengthened beam
$F_{u,0.4\%}$	load at ultimate at which a strain of 0.4 % in the laminate is obtained
G_a	shear modulus of adhesive
I	moment of inertia
I_c	moment of inertia of transformed (cracked) section
K	flexural stiffness
K_0	flexural stiffness before cracking of the concrete cross-section
K_1	flexural stiffness after cracking of the concrete cross-section and before yielding of the internal steel reinforcement
K_2	flexural stiffness after yielding of the internal steel reinforcement
L	distance between support or point of contraflexure and end of FRP
L_b	bond length between FRP and concrete
M(x)	moment at distance x
M_{cr}	cracking moment

M_{curt}	bending moment which can be taken completely by the internal reinforcement
M_d	design value of moment
M_{el}	moment calculated following the linear elastic theory
M_k	characteristic value of moment
M_{LE-LR}	the bending moment according to the linear elastic theory with limited redistribution
M_{Rd}	resisting design moment
M_{red}	redistributed moment
M_{Sd}	acting design moment
M_{span}	moment at the span
$M_{support}$	moment at the mid-support
M_u	bending moment at ultimate
$M_{u,0.4\%}$	bending moment at ultimate at which a strain of 0.4 % in the laminate is obtained
M_y	moment at yielding of steel reinforcement
M_{yd}	design value of moment at which internal steel starts yielding
N_{cr}	cracking load
$N_{cr,m}$	$= (N_{cr,n}+N_y)/2$
$N_{cr,n}$	load beyond which concrete element is in stabilized cracking phase
N_f	force in FRP
N_{fa}	FRP force to be anchored
N_{fad}	design value of FRP force to be anchored
$N_{fa,max}$	maximum FRP force which can be anchored
$N_{fad,max}$	design value of maximum FRP force which can be anchorage
N_{fd}	acting design force in FRP
N_s	force in steel
N_{Sd}	longitudinal design force in the cross-section due to the loading configuration or prestressing
N_u	ultimate load
N_y	load after yielding of the internal steel reinforcement
$V(x)$	shear force at distance x
V_c	$= 0.5\ f_{ct}\ b\ d$
V_d	acting design shear force
V_R	resisting shear capacity
V_{Rbd}	resisting design shear force at which bond failure is initiated
V_{Rd}	resisting design shear capacity
V_{Rd1}	resisting design shear capacity of the concrete
V_{Rp}	resisting shear force at which shear crack peeling is initiated
V_{Rpd}	resisting design shear force at which peeling initiates
V_{Sd}	acting design shear force
V_w	resisting shear capacity of steel stirrups
V_{wd}	resisting design shear capacity of steel stirrups
V_1	shear force between the point load and the outer support
V_2	shear force between the point load and the mid-support
W_e	external work
W_i	internal work

Roman lower case letters

a	distance between the point-load and the outer support of a two span beam
a_L	fictitious shear span
a_u	length of the bond interface at ultimate taken by second decreasing branch of the bilinear τ-s model
b	width of concrete member or distance between point load and mid-support of a two span beam
b_w	minimum width of the section (width of the web)
c	equals the distance between the mid-support and the point where the bending moment equals 0
c_1, c_2, c_3, c_4	coefficient
d	effective depth of the concrete member
d_s	diameter of steel bar
f_c	concrete compressive strength
f_{cb}	bond shear strength of the concrete
f_{cbd}	design bond shear strength of the concrete
f_{cbk}	characteristic bond shear strength of the concrete
$f_{c,cub}$	concrete compressive strength measured on cubes
f_{cd}	design value of concrete compressive strength
f_{ck}	characteristic value of concrete compressive strength
f_{cm}	mean concrete compressive cylinder strength
f_{ct}	pure concrete tensile strength
f_{ctf}	flexural concrete tensile strength
f_{ctk}	characteristic value of concrete tensile strength
f_{ctm}	mean concrete tensile strength
f_f	FRP tensile strength
f_{fd}	design value of the FRP tensile strength
f_{fk}	characteristic value of the FRP tensile strength
f_s	steel tensile strength
f_{sd}	design value of the steel tensile strength
f_{sk}	characteristic value of the steel tensile strength
f_y	yield stress of the steel reinforcement
f_{yd}	design value of the yield stress of the steel reinforcement
f_{yk}	characteristic value of the yield stress of the steel reinforcement
h	total depth of the concrete member
k	bending stiffness ratio
k_b	geometrical factor
k_c	factor related to compaction of concrete
k_1, k_2 ,k_3, k_4	coefficients
l	distance
$l_{b,max}$	anchorage length related to maximum FRP force which can be anchored
$l_{cr,n}$	transfer length at stabilized cracking
l_f	transfer length of FRP reinforcement
l_{pl}	length of plastic hinge
l_{pl}^*	= 2d conventional plastic hinge length
l_s	transfer length of steel rebars

l_t	anchorage or transfer length
m	moment ratio
max $\Delta\sigma_{fd}$	maximum variation of the design tensile stress in the FRP laminate
m_{el}	moment ratio following the linear elastic theory
m_t	transition value of moment ratio
p	uniform load
p_u	uniform ultimate load
$p_{u,plast}$	uniform ultimate load obtained according to the plasticity theory
r	parameter
1/r	curvature
$1/r_{cr}$	curvature at cracking of the cross-section
$1/r_u$	curvature at ultimate
$1/r_y$	curvature at yielding
s(x)	slip at distance x
s_f	slip between FRP and concrete
s_{f0}	slip where debonding of the FRP laminate occurs according to the bilinear τ-s relation
s_{f1}	slip at maximum bond stress according to the bilinear τ-s relation
s_{rm}	mean crack spacing
s_{rmax}	maximum crack spacing
$s_{rm,exp}$	experimental obtained mean crack spacing
$s_{rm,lim}$	limit between short and long crack spacing
s_s	slip between steel reinforcement and concrete
t_a	thickness of adhesive layer
t_f	(total) thickness of FRP reinforcement
u	bond perimeter
u_f	bond perimeter of the FRP reinforcement
u_s	bond perimeter of the steel reinforcement
v	vertical crack displacement
w	horizontal crack displacement
w_f	width of FRP reinforcement
x_e	depth of the compression zone (linear elastic analysis)
z	lever arm between total tensile force and compression force
z_f	lever arm between FRP tensile force and compression force
z_s	lever arm between steel tensile force and compression force

Greek upper case letters

Δ	deflection at a critical cross-section
ΔF	variation of the point load
ΔM	variation of the moment
ΔN_f	variation of the FRP force
ΔN_{fd}	variation of the design value of the FRP force
Δx	small distance
$\Delta\sigma_f$	variation of the tensile stress in the FRP laminate
Ø	(mean) diameter

Greek lower case letters

α	reduction factor
α_f	$= E_f/E_c$
α_s	$= E_s/E_c$
χ	$= 1/r$ curvature
χ_{cr}	$= 1/r_{cr}$ curvature at cracking of the cross-section
χ_{da}	coefficient relating the dowel action to the axial stiffness of the reinforcement
χ_u	$= 1/r_u$ curvature at failure
$\chi_{u,anal}$	analytical obtained curvature at failure
$\chi_{u,exp}$	experimental obtained curvature at failure
$\chi_{u,str}$	curvature at failure of a strengthened cross-section
$\chi_{u,unstr}$	curvature at failure of an unstrengthened cross-section
χ_y	$= 1/r_y$ curvature at yielding
δ_G	distance from the compression face to the centroid of the compression force divided by the depth of the compression zone (stress block centroid coefficient)
δ	moment redistribution ratio
δ_{max}	maximum moment redistribution ratio
ε	strain
ε_c	concrete strain at the extreme compression fibre
ε_{cu}	ultimate concrete strain
ε_{cu2}	ultimate strain of the parabola-rectangle diagram for concrete under compression
ε_f	FRP reinforcement strain
ε_{fu}	ultimate FRP strain
ε_{fud}	design value of the ultimate FRP strain
ε_s	steel reinforcement strain
$\varepsilon_{soffit,max}$	maximum strain in the FRP laminate applied at the soffit of the beam
ε_{su}	ultimate strain of the steel reinforcement
ε_{sy}	yield strain of the steel reinforcement
$\varepsilon_{top,max}$	maximum strain in the FRP laminate applied at the top of the beam
ε_u	ultimate strain
ε_0	initial strain at the extreme tensile fibre before strengthening
ζ_f	boundary condition
γ_c	material safety factor for the concrete
γ_f	material safety factor for the FRP
γ_s	material safety factor for the steel
θ	plastic rotation at a critical cross-section
θ_d	acting plastic rotation
θ_{pl}	rotation capacity
$\theta_{pl,d}$	design rotation capacity
$\theta_{pl,exp}$	experimental obtained rotation capacity
$\theta_{pl,max}$	maximum rotation capacity
$\theta_{pl,mean}$	mean rotation capacity
$\theta_{pl,M}$	moment contribution to the rotation capacity
$\theta_{pl,V}$	shear force contribution to the rotation capacity
θ_u	ultimate plastic rotation at a critical cross-section

λ	= a/b ratio of distances
ξ	= x/d
ξ_b	bond parameter
$\xi_{e,s}$	= x_e/d
$\xi_{e,f}$	= x_e/h
ξ_u	= x_u/d at ultimate
ρ	reinforcement ratio
ρ_{eq}	equivalent reinforcement ratio
ρ_f	FRP reinforcement ratio
ρ_s	steel reinforcement ratio
σ	stress
σ_c	concrete stress
σ_{cp}	= N_{Sd}/A_c
σ_f	FRP stress
σ_{fd}	design value of FRP stress
σ_s	steel reinforcement stress
$\sigma_{soffit,max}$	maximum stress in the FRP laminate applied at the soffit of the beam
$\sigma_{top,max}$	maximum stress in the FRP laminate applied at the top of the beam
τ	shear stress
τ_b	bond shear stress
$\tau_{b.m}$	mean bond shear stress
$\tau_{b,max}$	maximum bond shear stress
τ_{cza}	shear stress transferred in the compression zone and the shear crack (aggregate interlocking)
τ_{fm}	mean constant bond stress between FRP and concrete over the transfer length
τ_{f1}	maximum bond stress of the bilinear τ-s relation
τ_m	mean shear stress
τ_{max}	maximum shear stress
τ_{sm}	mean constant bond stress between steel reinforcement and concrete over the transfer length
τ_{Rd}	design value of resisting shear stress of concrete
τ_{Rk}	characteristic shear stress of concrete
τ_{Rp}	resisting shear stress at initiation of peeling
τ_{Rpd}	design value of resisting shear stress at initiation of peeling
τ_{Rpk}	characteristic value of resisting shear stress at initiation of peeling
φ	ratio of the critical crack width at which no aggregate interlocking is noticed any more
ω	mechanical reinforcement ratio or constant

ABSTRACT

Structures may need to be strengthened for different reasons, among which a change in function, implementation of additional services or to repair damage. Different strengthening techniques exist. Often applied is externally bonded reinforcement (EBR), based on fibre reinforced polymer (FRP), the so-called FRP EBR. FRP EBR can be applied for the strengthening of existing structures, enhancing the flexural and shear capacity or to strengthen by means of confinement. The efficiency of the FRP EBR strengthening technique is often limited by the capability to transfer stresses in the bond interface. Hereby bond failure between the laminate and the concrete may occur, which implies the loss of composite action between the concrete and the FRP reinforcement. This type of failure is often very sudden and brittle. According to [1, 2] different bond failure aspects can be distinguished, among which:

- Debonding at flexural cracks
- Debonding at shear cracks
- Debonding by a limited anchorage length
- Debonding by end-shear failure

The structural behaviour of reinforced concrete beams strengthened in flexure with externally bonded FRP (Fibre Reinforced Polymer) reinforcement has been extensively investigated with respect to isostatic beams. However, limited information is available in literature on the behaviour of continuous beams (statically indeterminate structures), strengthened with composite reinforcement. By considering these continuous beams some remarkable differences can be noticed compared to the isostatic beams.

A first difference of a continuous beam compared to an isostatic beam is the non-linear behaviour. Depending on the bending stiffnesses along the length of the beam, especially when reinforcement ratios are used different from the linear elastic theory, a considerable moment redistribution can be obtained.

In FRP strengthened beams, despite of the use of a linear elastic material until failure, also a non-linear behaviour can be obtained. For the calculation of the non-linear behaviour of FRP EBR strengthened two-span beams, an analytical model is developed based on the analytical model considering unstrengthened two-span beams. In the framework of this thesis an experimental program is executed, by which 4 large scale two-span beams are tested. Resulting from these tests, the developed analytical model is verified, as the experimental results agree well with the analytical results.

The moment redistribution on his turn does influence also the debonding mechanisms. Due to the moment redistribution, both the acting shear force as well as some parameters which are necessary to check the debonding mechanism, e.g. the anchorage length and the distance between laminate end and point of contraflexure are influenced. This dependency can result in earlier or later debonding of the laminates compared to the linear elastic theory. As a result, it is of importance to check all different debonding mechanisms by taken into account the correct moment redistribution.

A second difference appearing in a continuous beam compared to an isostatic beam is the possibility to anchor the externally bonded laminates into a compression zone. A continuous beam possesses a moment line with opposite

signs. Herewith the bending moments at the mid-support are positive while the bending moments in the spans are negative. As a result, the compression zones in the spans are situated at top of the beam, at the support the compression zone is situated at the soffit of the beam. This allows, in contrast to isostatic beams, to anchor the CFRP laminates in the compression zones (except for the end supports). By extending a laminate into these compression zones, two out of the four different debonding mechanisms will be avoided: 'debonding by a limited anchorage length' and 'debonding by end shear failure' (concrete rip-off). This phenomenon also is verified by means of the experimental program on strengthened two-span beam.

Concerning the two other debonding mechanisms ('Debonding at flexural cracks' and 'Debonding at shear cracks') special attention is needed when a FRP laminate is applied at top of the mid-support. In this zone, a combination of high shear forces and high moments can be found which results in the appearance of flexural/shear cracks. From above mentioned experimental program (considering strengthened two-span beam) it seems that the best prediction of debonding at a flexural/shear crack of the laminate at top of the mid-support is approximated by the 'debonding at shear cracks' model. On the other hand, near to the two-span beam tests, five strengthened three-point-bending tests were executed. As in these tests also a combination of high shear forces and high moments can be found, these tests are simulating the intermediate support of a continuous beam. Resulting from these tests, it seems that the best prediction of debonding at flexural/shear cracks is given by the 'debonding at flexural cracks' model.

Related to the non-linear behaviour of continuous beams, plastic hinges are needed at different critical cross-sections along the length of the beam. This in order to obtain a sufficient redistribution of moments. For an unstrengthened cross-section, a large plastic rotation capacity is obtained due to the yielding capacity of the internal steel reinforcement. This rotation capacity results from the large horizontal third branch in the moment-curvature diagram. For a FRP-strengthened cross-section, the rotation capacity of the cross-section is considerably reduced due to the use of the linear elastic FRP-material, as the use of linear elastic FRP-material results in an increasing third branch of the moment-curvature diagram. Moreover, failure of a FRP-strengthened cross-section is also characterized by debonding of the externally bonded laminates. This reduces the third branch to an important degree, by which the rotation capacity is reduced to a further extent. These findings again are verified by means of the four two-span beam large scale tests and by the five three-point-bending tests. Given this restrained rotation in post-yielding stage of a FRP-strengthened cross-section and the related impact on the moment redistribution, FRP strengthening is not advisable in cross-sections where plastic rotations are required to invoke the required moment redistribution.

To conclude, certain strengthening strategies are recommended depending on the internal and external reinforcement ratios. If for example the internal reinforcement distribution is according to the linear elastic theory, possible strengthening strategies are:

- Strengthening of one zone (mid-support zone or span zone) in order to obtain a plastic hinge at the other zone (span zone or mid-support zone) and hence to consider moment redistribution

- Strengthening both zones (mid-support zone and span zone) according to the linear elastic theory in order to obtain a linear elastic moment distribution. In this case no redistribution (FRP strengthened hinges) is obtained.

If on the other hand the internal reinforcement is different from the linear elastic distribution, it is recommended to strengthening the zone with the lower internal reinforcement ratio compared to the linear elastic theory in order to obtain a plastic hinge at the zone with the high internal reinforcement ratio compared to the linear elastic theory, and a related moment redistribution.

[1] fib, *fib bulletin 14, Externally bonded FRP reinforcement for RC structures*. International federation for structural concrete, Lausanne. 2001: pp. 138.

[2] S. Matthys, *Structural behaviour and design of concrete members strengthened with externally bonded FRP reinforcement*. PhD thesis. Department of Structural Engineering, Ghent University. Ghent, Belgium. 2000. pp. 345.

ABSTRACT

Een betonnen structuur kan verstevigd worden ten gevolge van verschillende redenen. Zo kan de structuur een andere functie toegewezen krijgen, kunnen er andere belastingen aangrijpen of dient een herstelling uitgevoerd te worden. Voor het verstevigen/herstellen van een betonnen structuur bestaan er meerdere technieken, waarbij een vaak toegepaste techniek de uitwendig opgelijmde koolstofvezel wapening (FRP-wapening) is. Deze techniek kan worden toegepast teneinde de buigingscapaciteit te verhogen, de dwarskrachtcapaciteit te verhogen of voor het omwikkelen van een betonnen element. De efficiëntie van deze techniek is echter wel beperkt door de gelimiteerde overdracht van spanningen in het contactvlak tussen de koolstofwapening en het beton. Te hoge schuifspanningen resulteren namelijk in een plotse onthechting van de opgelijmde wapening. Volgens [1, 2] kan de oorzaak van onthechting onderverdeeld worden in vier verschillende mechanismen. Hierbij wordt een onderscheid gemaakt tussen:

- Onthechting bij buigingsscheuren
- Onthechting bij dwarskrachtscheuren
- Onthechting door onvoldoende verankeringslengte
- Onthechting ten gevolge van het mechanisme eindverankering-dwarskrachtbreuk

Het structurele gedrag van betonnen liggers verstevigde op buiging met uitwendig opgelijmde FRP-wapening is reeds uitgebreid beschreven in de literatuur. Echter worden de experimentele luiken van deze studies vooral gekenmerkt door het testen van isostatische liggers en slechts in beperkte mate door het testen van doorlopende liggers (statische onbepaalde liggers). Bij doorlopende liggers worden echter specifieke verschillen waargenomen in vergelijking met de isostatische liggers, die betrekking kunnen hebben op de toepassing van de opgelijmde wapening

Een eerste verschil is het niet-lineaire gedrag (momentenherverdeling) wat wel optreedt bij een doorlopende ligger maar niet bij een isostatische ligger. Afhankelijk van de optredende buigstijfheden langsheen de lengte van de ligger, vooral wanneer wapeningsverhoudingen gebruikt worden verschillend van de lineair elastische theorie, kan een momentenherverdeling optreden. Niettegenstaande er in FRP-versterkte liggers gebruik gemaakt wordt van een lineair elastisch FRP-materiaal, kan echter een niet-lineair gedrag optreden. Voor de berekening van dit niet-lineaire gedrag (momentenherverdeling), is in het kader van dit werk een analytisch model uitgewerkt. Dit analytische model beperkt zich in hoofdzaak tot een doorlopende ligger met twee overspanningen en twee puntlasten. Door middel van een experimenteel programma bestaande uit 4 proeven op doorlopende liggers telkens met twee overspanningen en twee puntlasten, werd dit analytische model geverifieerd.

Het optredende niet-lineaire gedrag zal op zijn buurt ook een invloed hebben op de eerder vermelde onthechtingsmechanismen. Door middel van de herverdeling van momenten zullen de aangrijpende dwarskrachten alsook meerdere parameters ter bepaling van de onthechtingsmechanismen beïnvloed worden. Deze invloeden kunnen resulteren in een vroegere of latere onthechting van de laminaten in vergelijking met berekening volgens de lineair elastische theorie.

Teneinde een zo correct mogelijke controle van de onthechtingsmechanismen te bekomen in een statisch onbepaalde ligger is het van belang een zo correct mogelijke momentenherverdeling in rekening te brengen.

Een tweede verschil bij een doorlopende ligger in vergelijking met een isostatische ligger is de mogelijkheid tot verankeren van de laminaten in een drukzone. Daar de momentenlijn van een doorlopende ligger bestaat uit zowel positieve als negatieve momenten, is er ter plaatse van de middensteunpunten een drukzone onderaan de balk en ter plaatse van de velden (overspanning) een drukzone bovenaan de balk terug te vinden. Verankering van de opgelijmde laminaten in deze drukzones resulteert in het vermijden van twee onthechtingsmechanismen: 'onthechting door onvoldoende verankeringslengte' en 'onthechting ten gevolge van het mechanisme eindverankering-dwarskrachtbreuk'. Dit fenomeen werd opnieuw geverifieerd door het experimentele programma op de doorlopende liggers.

Betreffende de twee overige onthechtingsmechanismen ('onthechting bij buigingsscheuren' en 'onthechting bij dwarskrachtscheuren') dient extra aandacht geschonken te worden als de FRP-wapening verlijmd is in de middensteunpunt zone. In deze zones treed er immers een combinatie op van hoge momenten en hoge dwarskrachten. Bijgevolg zijn de optredende scheuren in deze zone een combinatie van buiging- en dwarskrachtscheuren. Uit het experimentele programma op doorlopende liggers blijkt dat onthechting ter plaatse van een buiging/dwarskracht scheur het best voorspeld wordt door middel van het mechanisme 'onthechting bij dwarskrachtscheuren'. Bijkomstig werd een reeks drie-punt-buigproeven uitgevoerd. Daar deze configuratie een gelijkaardige combinatie vertoont van hoge momenten en hoge dwarskrachten kan deze configuratie vergeleken worden met de middensteunpuntszone van een doorlopende balk. Uit het experimentele programma met drie-punt-buigproeven blijkt echter dat onthechting ter plaatse van een buiging/dwarskracht scheur het best voorspeld wordt door middel van het mechanisme 'onthechting bij buigingsscheuren'.

Teneinde een vooropgestelde momentenherverdeling te bekomen bij doorlopende liggers, moeten er plastische scharnieren kunnen optreden. Bij niet-verstevigde secties is door middel van de vloeicapaciteit van de inwendige staalwapening, hiervoor een grote rotatie capaciteit voorhanden. Deze vloeicapaciteit resulteert immers in een lange horizontale derde tak van het momenten-kromming diagram. Bij een verstevigde sectie is echter een beperktere rotatie capaciteit aanwezig, daar er gebruik gemaakt wordt van een lineair elastisch FRP-materiaal. Dit resulteert in een stijgende derde tak van het momenten-kromming diagram. Daarenboven zal de typische vroege onthechting van het opgelijmde FRP materiaal resulteren in een afname van deze derde tak. Door middel van zowel het experimentele programma op doorlopende liggers als het experimentele programma op isostatische liggers werden deze bevindingen geverifieerd. Met de beperkte rotatiecapaciteit van een met FRP verstevigde doorsnede indachtig, wordt het ten stelligste afgeraden een FRP versteviging toe te passen in zones waar een plastische rotatie nodig is, teneinde de vooropgestelde momentenherverdeling te bekomen.

Finaal worden verschillende verstevigingstrategieën aanbevolen afhankelijk van de inwendige en uitwendige wapeningsverhoudingen. Is de inwendige wapening

overeenkomstig met de lineaire elastische theorie, dan worden volgende strategieën aanbevolen:

- Versteviging van één zone (midden-steunpunt of veld), teneinde een plastisch scharnier te bekomen in de andere zone (veld of midden-steunpunt).
- Versteviging van beide zones (midden-steunpunt en veld) volgens de lineaire elastische theorie, teneinde een lineair elastische momenten verdeling te bekomen. In dit geval treedt geen herverdeling van momenten op.

Is de inwendige wapening verschillend van de lineair elastische theorie, dan is het aanbevolen de zone met een lagere inwendige wapeningsverhouding in vergelijking met de lineair elastische theorie, te verstevigen. Hierbij worden plastische scharnieren bekomen in de zones met een hogere inwendige wapeningsverhouding in vergelijking met de lineair elastische theorie.

[1] fib, fib bulletin 14, Externally bonded FRP reinforcement for RC structures. International federation for structural concrete, Lausanne. 2001: pp. 138.

[2] S. Matthys, Structural behaviour and design of concrete members strengthened with externally bonded FRP reinforcement. PhD thesis. Department of Structural Engineering, Ghent University. Ghent, Belgium. 2000. pp. 345.

Chapter 1
INTRODUCTION

1 Fiber Reinforced Polymers (FRP) as structural reinforcement

FRP ('Fibre Reinforced Polymer' or 'Fibre Reinforced Plastic') is a composite material consisting of non-metallic fibres (with diameter between 5-20 μm) imbedded in a matrix (see Fig. 1.1). Generally a thermoset material such as polyester, vinyl ester or epoxy is used as matrix. The types of fibres mostly used for civil construction are: glass fibres (GFRP), aramid fibres (AFRP) and carbon fibres (CFRP) (see Fig. 1.2).

These fibre composite materials have several advantages as they combine the favourable properties of both the fibres and the matrix. Due to the high length/diameter ratio of the fibres, an effective transfer of the loads by means of the matrix to the fibres is obtained. A disadvantage of the fibrous structure is the anisotropic property of the composite. Therefore, the aim of the FRP material in each specific application needs to be investigated.

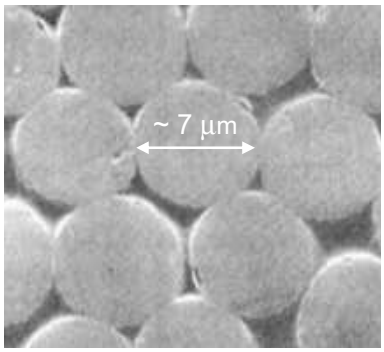

Fig. 1.1: Enlarged view of a CFRP element

Since the 1940's, fibre-composite-materials are applied in different sectors, such as the space and aircraft–industry. By means of the evolution in the different industries and the decreasing cost of the material, fibre-composite-materials have found other applications such as in the civil construction [1, 2]. In the late 70's commercial products became available.

A growing number of research projects has been performed on the application of FRP in structural or civil engineering since the 1980's. A breakthrough of FRP materials in civil construction occurred, when the use of synthetic glues for structural applications became more widely accepted [3]. This has promoted strongly the further development of externally bonded reinforcement in Belgium.

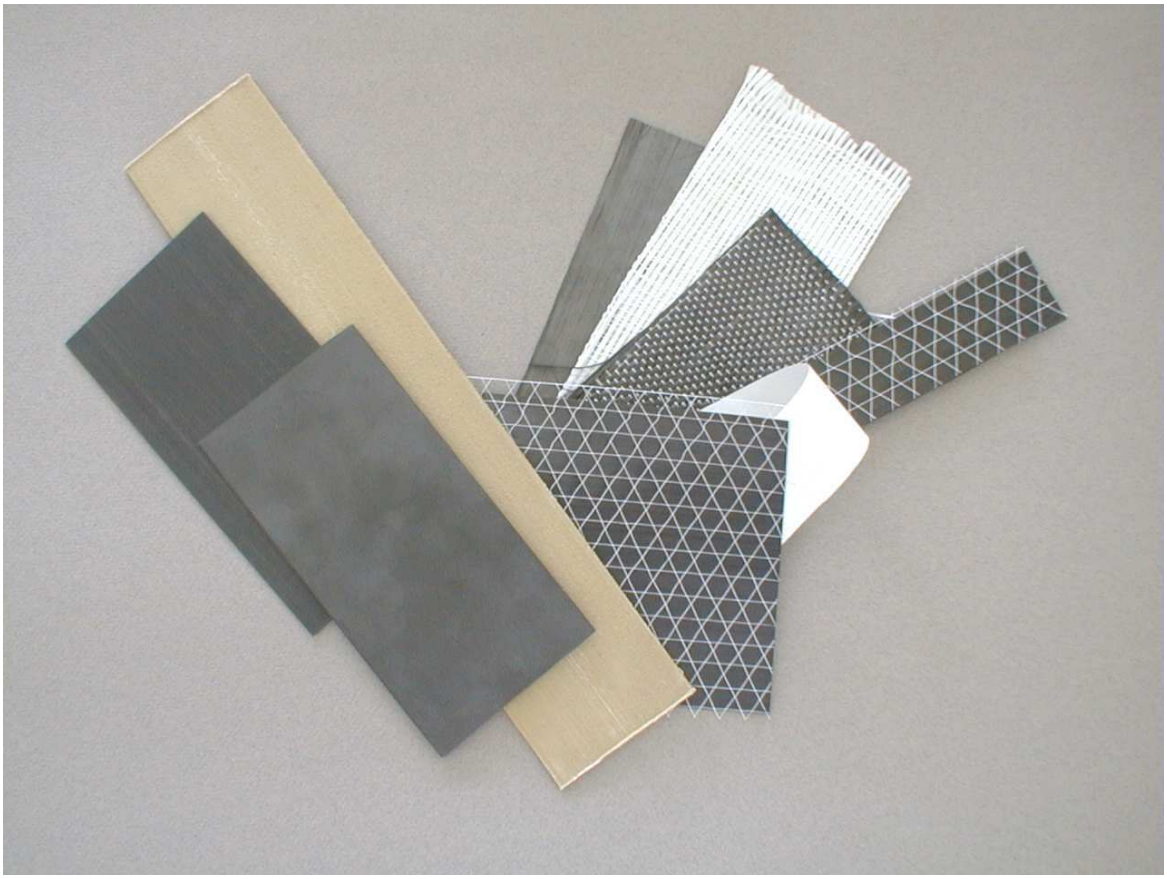

Fig. 1.2: Overview of different FRP materials for civil construction [4]

FRP as externally bonded reinforcement is often used for structural concrete (see Fig. 1.3). Nevertheless FRP EBR is also applicable to structures made out of masonry, wood, steel, etc. The FRP EBR technique is often applied for the maintenance, the rehabilitation and the strengthening of structural elements [4, 5]. With the FRP EBR technique a strengthening effect is obtained by enlarging the (tensile) reinforcement section of the structure. FRP EBR can be applied for the strengthening of existing structures, enhancing the flexural and shear capacity or to strengthen by means of confinement.

By applying this strengthening technique, the externally bonded FRP reinforcement is glued to an external face of the existing concrete structure by means of a structural epoxy. To obtain a good bonding between the FRP EBR and the substrate, specific preparations of both the strengthening material and the concrete surface are needed. The concrete surface needs to be roughened by means of gritblasting or grinding with special equipment. The surface of the FRP-material needs to be degreased before the application.

Different materials can be used in the EBR strengthening technique, among which steel plates [6] or FRP materials. The use of FRP material has the following benefits:

- The weight of the FRP materials is low, especially in comparison with steel plates. Due to this low weight, the dead weight of the structure is hardly increased and handling and application becomes more easily. Secondly, no

additional fixation of the FRP laminates is required during hardening of the structural epoxy.
- The FRP laminates generally have a very good resistance against most aggressive environments.
- FRP laminates can be manufactured with no limitations concerning the length. Hence no overlap between different strips is necessary if high lengths of the reinforcement are required.
- As the FRP EBR strengthening technique exists in applying laminates with a limited thickness (~ 1 mm), no loss of the free height under the structure is obtained.
- Due to the low weight and the flexibility of the material, it is easy to bring the materials on the locations which need to be strengthened.
- Under a dynamic loading combination, FRP materials and especially CFRP materials have a good behaviour, given the high fatigue resistance.

Fig. 1.3: Reinforced concrete structure strengthened with FRP EBR (ECC – Luchtbal/Antwerpen)

Some disadvantages related to the use of FRP EBR are as follows:
- In comparison with steel, the FRP material is quite expensive. Nevertheless, taking into account the more simple application methods and efficiency of use, the overall cost is often lower than the alternative techniques. Also reduced disrupt cost are often applicable, given the ease-of-application and related limited execution period.
- FRP laminates are characterized by a linear elastic behaviour until failure. Also the strain at failure is limited.
- The achieved stress level in the FRP materials in applications related to RC structures, is often relatively small in comparison to the available high strength of FRP materials.

2 Objectives

The structural behaviour of reinforced concrete beams strengthened in flexure with externally bonded FRP (Fibre Reinforced Polymer) reinforcement has been extensively investigated with respect to statically determined (isostatic) beams. However, limited information is available on the behaviour of continuous beams strengthened with composite reinforcement [7, 8], though continuous members often occur in practice. The aim of this study is to obtain a better insight in the behaviour of reinforced concrete structures strengthened in flexure in a multi-span situation.

The specific objectives of this thesis can be subdivided in four different points:

1/ Moment redistribution of reinforced concrete beams strengthened with FRP EBR:

In case of statically indeterminate structures, the question can be raised if moment redistribution is still possible when applying the FRP strengthening technique. As the FRP material is a linear elastic material until failure, the question can be raised to which degree the moment redistribution assumed in the design stage also equals the obtained moment redistribution. Related to this is the question which optimum strengthening configuration has to be used.

2/ Debonding mechanisms between the externally bonded reinforcement and the concrete in continuous beams:

Typically for the use of FRP EBR is the possible bond failure. This implies the loss of composite action between the concrete and the FRP reinforcement and is often very sudden and brittle. Different debonding mechanisms have been identified in the case of statically determined (isostatic) elements [4, 9]. The question can be raised to which extent these debonding mechanisms and related models can be applied to statically indeterminate elements.
An interesting difference between isostatic beams and continuous beams, for the debonding mechanisms, is the moment line with opposite signs (see Fig. 1.4). As a result, the compression zones in the spans are situated at the top of the beam, at the intermediate supports the compression zone is situated at the soffit of the beam (shaded zones in Fig. 1.5). In contrast to isostatic beams, this allows the anchoring of the CFRP laminates in the compression zones (except for the end supports) (see Fig. 1.5).

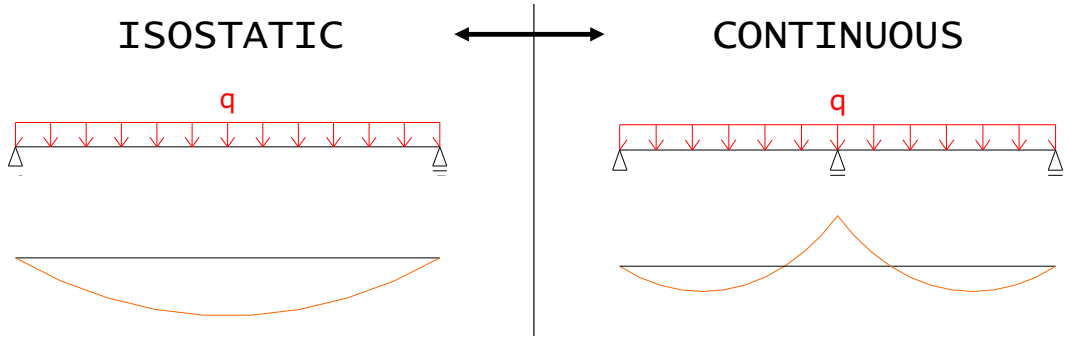

Fig. 1.4: Isostatic beam versus continuous beam

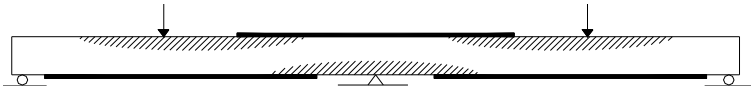

Fig. 1.5: Compression zones over the length of the continuous beam

3/ Plastic rotation capacity of a cross-section strengthened with FRP:

Due to the linear elastic material properties of an FRP material and the early debonding of the FRP material which is typical for FRP strengthened structures, only a limited plastic rotation capacity is obtained in a FRP strengthened cross-section. By delaying the debonding of the laminates, a more pseudo-ductile behaviour may be obtained. Hence a possible increase of the rotation capacity is obtained. This delay of debonding can be achieved by wrapping the cross-section with FRP textiles.

4/ Design considerations and strengthening strategy in case of flexural strengthening of continuous members:

For flexural strengthening of a continuous beam different techniques are available. The FRP can be applied above the intermediate supports and/or in the spans. Depending on the internal reinforcement ratios, the assumed moment redistribution and the location of the assumed plastic hinges, some strengthening configurations may give better results compared to others. Herewith recommendations are needed for FRP-strengthening of continuous beams.

3 Continuous beams – general considerations

3.1 Non-linear moment-curvature diagram, strengthened versus non-strengthened configuration

Performing an analysis of a structure according to the linear elastic theory, a linear relationship between the moment and the curvature is assumed, i.e.

$$\chi = \frac{1}{r} = \frac{M}{EI} \tag{1.1}$$

with 1/r the curvature, M the bending moment and EI = K the bending stiffness which is often assumed to be constant and therefore independent of the value of the bending moment. However, for the cross-section of a concrete beam the moment-curvature diagram is non-linear, which corresponds to a variable bending stiffness. This is illustrated in Fig. 1.6, where the non-linear behaviour is simplified by three straight lines. Fig. 1.6 compares the moment-curvature relationship of an unstrengthened and a FRP flexural strengthened RC cross-section. The bending stiffness K (found in Fig. 1.6) corresponds to the slope of the moment–curvature lines. Hereby K_0 represents the stiffness of the uncracked concrete section, K_1 of the section after cracking and K_2 of the cracked section after yielding of the internal steel reinforcement. In a cross–section with both steel and externally bonded FRP reinforcement, higher values for K are obtained in comparison with the same cross-section without FRP. Especially for the bending stiffness of the cross-section after yielding of the internal reinforcement (K_2 and K_2'), a remarkable difference can be noticed. For the unstrengthened cross-section the stiffness K_2 almost equals zero, while the strengthened cross-section still has the ability to take up an additional moment. This different behaviour will influence the moment redistribution of a continuous beam.

Remark that the M-χ relationship as presented in Fig. 1.6, assumes 3 linear branches, which is an approximation of the real behaviour. E.g. for the cracked situation ($M_{cr} < M < M_y$), in reality the M-χ relation is non-linear. In [10], where a similar approximation is used, still a good agreement is obtained between experimental and analytical results regarding the non-linear behaviour of continuous beams.

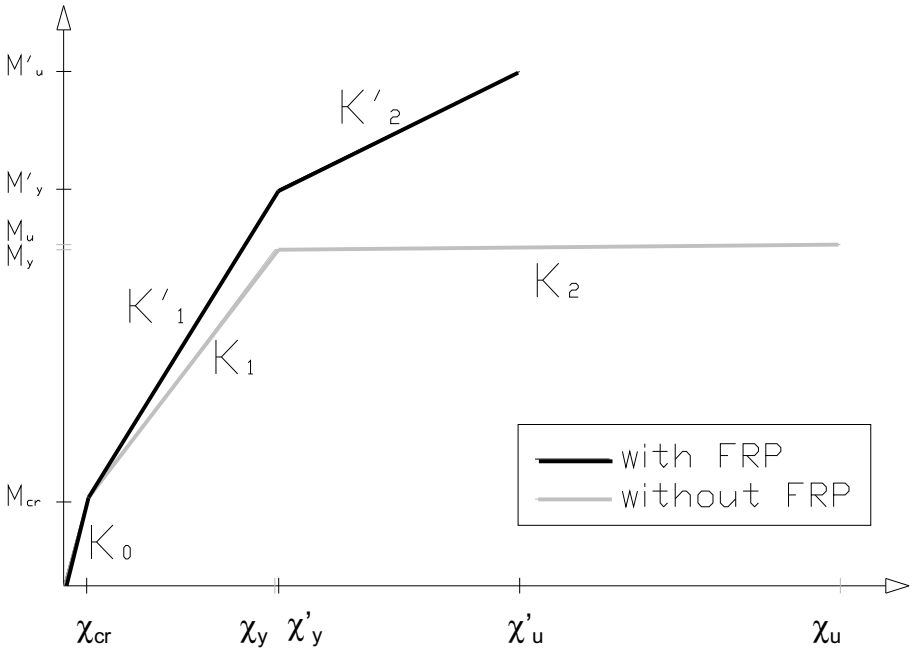

Fig. 1.6: Moment-curvature diagram

Let us consider a continuous beam under an increased load. Initially, the beam is uncracked along its full length which corresponds to the use of K_0 as bending stiffness. After cracking, the beam is characterized by cracked and uncracked zones, each with the corresponding value of bending stiffness. This change of stiffness causes a first redistribution of moments. At the yield load F_y, one or more cross-sections reach the yield moment (M_y). In yield zones without FRP EBR, the bending stiffness K_2 is so small that plastic deformations appear in the critical cross-section and in a restricted area near to it. This is the so called formation of a plastic hinge. The increasing load is mainly carried by the non plastic zones and the bending moment in the plastic hinge stays almost constant or is slowly increasing. In zones with FRP EBR, the value of the bending stiffness is higher ($K'_2 > K_2$). Plastic deformations appear, but in a constrained way. The yielding zone still carries a significant part of the increasing load and the formation of the plastic hinge is restricted.

Fig. 1.7 focuses on the yielding branch of the M-χ relationship. Different M-χ curves are considered, whereas each curve represents a different amount of FRP reinforcement (A_f) and a different amount of steel reinforcement (A_s). The reinforcement amounts A_f and A_s, applied in Fig. 1.7 are chosen in such a way, that the equivalent reinforcement amount (A_{eq}), and the equivalent reinforcement ratio (ρ_{eq}) remain constant. The equivalent reinforcement amount is based on the amounts of both the internal and external reinforcement, whereas the difference in modulus of elasticity of the FRP with respect to the steel is taken into account (as can be seen in equation 1.2).

$$A_{eq} = A_s + A_f \frac{E_f}{E_s} \tag{1.2}$$

$$\rho_{eq} = \frac{A_{eq}}{bd} \tag{1.3}$$

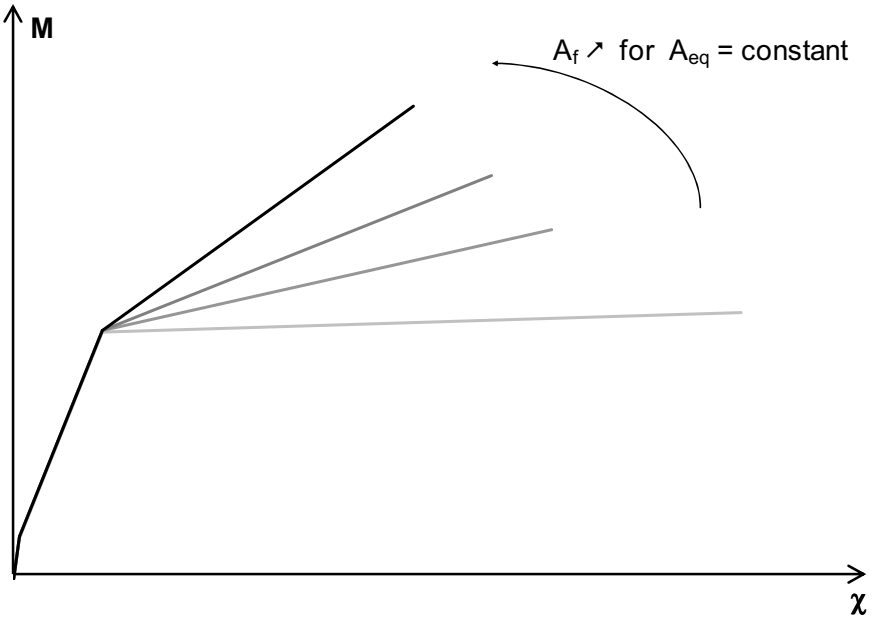

Fig. 1.7: Moment-curvature curves for different amounts of FRP (A_f), taken into account a constant equivalent steel reinforcement amount (A_{eq})

As can be seen in Fig. 1.7, all different configurations have the same bending stiffness both in the uncracked stage (K_0=K'_0) and in the cracked pre-yielding stage (K_1=K'_1). Once the internal moment exceeds the yielding moment M_y, different bending stiffnesses for the different configurations are obtained. Herewith a cross-section with a high amount of FRP maintains a high bending stiffness after yielding of the steel reinforcement, while the cross-sections with a low or no amount of FRP have lower bending stiffness. Remark that for simplicity reasons, the lever arm of the internal and external reinforcement is taken equal. As a result in Fig. 1.7, the bending stiffness K_1 is constant for ρ_{eq} constant (in reality small differences in K_1 will occur depending on the ratio A_f/A_s).

3.2 Analysis of two-span beams

The moment redistribution theories for strengthened continuous beams will be explained for the case of a symmetric two span beam. In each span a point load F is applied at a distance a of the end-supports and at a distance b of the mid-support. The total length of one span equals l (= a+b). In the following analytical studies, all equations are derived in function of the variables a, b, l and F. Unless indicated otherwise, graphical examples of the obtained equations are given for a beam with spans of 5 m, the distance a equals 2 m and the distance b equals 3 m.

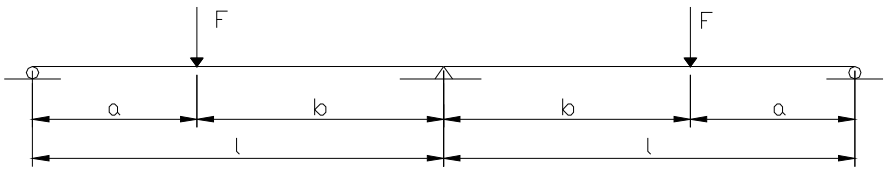

Fig. 1.8: Continuous beam with two spans

To analyze the moment redistribution and the effect of the formation of plastic hinges on the moment redistribution, three different cases are considered as illustrated in Fig. 1.9.

In case A, the moment distribution follows from the classic linear elastic theory. Herewith a constant bending stiffness is assumed over the entire length of the beam. By applying the linear elastic theory, the following values for the internal moments at the mid-support $M_{support,el}$ and span $M_{span,el}$ are obtained:

$$M_{support,el} = \frac{l+a}{2l^2}(ab)F \tag{1.4}$$

$$M_{span,el} = \left(\frac{ab}{l} - \frac{l+a}{2l^3}\left(a^2b\right)\right)F \tag{1.5}$$

In Fig. 1.9, the moment line is illustrated in two different ways. The left hand moment line is represented in the classical way, with the X-axis the zero moment line. In the right hand moment line the zero moment line is moved into a bilinear line (thick line in alternative graph). The X-axis, on its turn, represents at the mid-support the maximal internal moment and at the end-supports the internal moment which equals zero. The meaning of these graphs, is to give a better visual interpretation of the moment redistribution of a particular configuration and to compare the moment lines of different configurations.

In case B, a moment redistribution is occurring. Hereby the reinforcement ratios are such that the first plastic hinge is obtained at the mid-support. This is a consequence of different applied stiffnesses along the length of the beam. Hereby it can be observed that the internal moment at the mid-support is smaller in comparison with the linear elastic moment distribution, while the maximum span moment is larger in comparison with the linear elastic moment distribution. This is illustrated in the right part of Fig. 1.9.B, in which the zero moment line according the linear elastic theory is given (dashed grey line).

In case C, a moment redistribution is occurring, by which the reinforcement ratios are such that the first plastic hinges are obtained in the spans. This again is a consequence of different applied stiffnesses along the length of the beam. By the appearance of plastic hinges at the critical cross-sections (cross-section with maximum internal moment) in the spans, a maximum mid-support moment can be established which is larger than for the linear elastic theory. This is illustrated in the right of Fig. 1.9.C.

Remark that for all cases the absolute value of the distance between the maximum moment in the spans and the connection line between the maximum

moment at the mid-support and at the end-support retains a constant value, namely $\left(\frac{ab}{l}\right) F$.

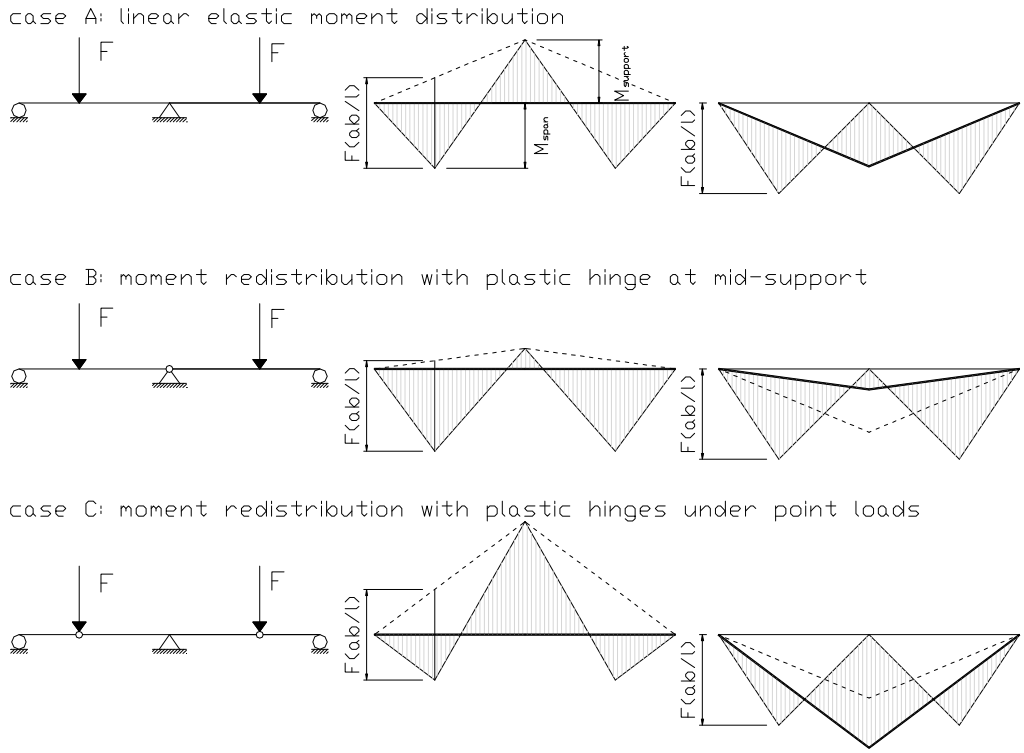

Fig. 1.9: Moment line of two span beam for three different cases

4 Outline of the thesis

In this thesis the flexural strengthening of multi-span reinforced concrete beams is investigated.

In the next chapter (Chapter 2) the non-linear behaviour (and related to this the moment redistribution) of strengthened continuous beams is studied by means of a model based on the non-linear theory. The non-linear behaviour is mainly caused by the different stiffnesses over the length of the beam and by the non-linear moment-curvature diagram of the critical cross-sections (see section 3.1). By means of an experimental research programme on 4 large scale beams (two-span beams, with span lengths equal to 5 m), the developed non-linear calculation model is verified.

Typically for the use of FRP EBR is the bond failure. An overview of these different debonding mechanisms is given in Chapter 3. Also the differences of debonding in continuous beams compared to the isostatic beams are discussed. Verification is executed by means of the above mentioned experimental 2-span beam programme. In addition, also 3-point-bending tests are conducted to investigate debonding of the laminates applied at intermediate supports.

Related to the non-linear behaviour of continuous beams (moment redistribution), plastic hinges are required in several critical cross-sections. In Chapter 4 an overview is given of the different parameters influencing the plastic rotation capacity of both strengthened and unstrengthened cross-sections. This rotation capacity is further verified by means of the experimental tests mentioned in Chapter 2 and 3.

In Chapter 5, the influence of externally bonded reinforcement (EBR) on the crack spacing is investigated by means of a microscopic study on cross-sections of the two-span beams. To complement the microscopic study, also measurements by means of Digital Image Correlation Technique (DICT) are executed. With these two techniques, the crack spacing is investigated in the zone just beneath the externally bonded FRP laminates.

Finally, in Chapter 6 different design recommendations are given for the use of FRP EBR in continuous beams. These recommendations are based on the specific findings from Chapter 2 until Chapter 4.

In Chapter 7 the main conclusions of the work are summarized and recommendations for future research are given.

References

[1] J.L. Clarke, *Alternative materials for the reinforcementand prestressing of concrete*. Chapman & Hall. London, U.K. 1993: pp. 204.

[2] A. Nanni, *Fibre-Reinforced-Plastic (FRP)reinforcement for concrete structures: properties and applications*. Developments in Civil Engineering 42. Amsterdam, The Netherlands. 1993: pp. 450.

[3] NBN-EN-1504-5, *Producten en systemen voor het beschermen en herstellen van betonconstructies - Definities, eisen, kwaliteitsborging en conformiteitsbeoordeling - Deel 5: Injecteren van beton = EN 1504-5:2004*. 2005.

[4] fib, *fib bulletin 14, Externally bonded FRP reinforcement for RC structures*. International federation for structural concrete, Lausanne. 2001: pp. 138.

[5] ACI, *ACI 440.2R-02, Guide for the Design and Construction of externally Bonded FRP Systems for strengthening Concrete Structures*. 2002.

[6] B. Täljsten, *Plate Bonding - Strengthening of Existing Concrete Structures with Epoxy Bonded Plates of Steel or Fibre Reinforced Plastics*. PhD thesis. Division of structural engineering, University of Technology. Lulea. 1994. pp. 281.

[7] S.A. El-Refaie, A.F. Ashour and S.W. Garrity, *Sagging and Hogging Strengthening of Continuous Reinforced Concrete Beams Using Carbon Fiber-Reinforced polymer Sheets.* ACI Structural Journal. 2003. Vol. 100: pp. 446-453.

[8] A.F. Ashour, S.A. El-Refaie and S.W. Garrity, *Flexural strengthening of RC continuous beams using CFRP laminates.* Cement and Concrete Composites. 2004. Vol. 26 (7): pp. 765-775.

[9] S. Matthys, *Structural behaviour and design of concrete members strengthened with externally bonded FRP reinforcement*. PhD thesis. Department of Structural Engineering, Ghent University. Ghent, Belgium. 2000. pp. 345.

[10] CUR-rapport-83, *Doorgaande balken van gewapend beton*. Stichting voor onderzoek, voorschriften en kwaliteitseisen op het gebied van beton. 1980. pp. 124.

Chapter 2

NON-LINEAR BEHAVIOUR OF STRENGTHENED CONTINUOUS BEAMS: MOMENT REDISTRIBUTION

1 Introduction

1.1 Outline

In this chapter the non-linear behaviour of continuous beams is investigated by means of the non-linear theory [1, 2]. This non-linear theory can be applied to a strengthened as well as to an unstrengthened continuous beam.

For unstrengthened continuous beams, a moment redistribution can be observed especially after yielding of one of the critical cross-sections. As a consequence a plastic hinge will be formed. The formation of these plastic hinges is clearly visible in the moment redistribution graphs.

For strengthened concrete beams, after reaching the yield moment, the FRP strengthened cross-section is still able to carry additional load and the formation of a plastic hinge will be restricted. In these cases the term 'restrained hinge' is used instead of the term 'plastic hinge'.

As the FRP EBR is a linear elastic material until failure, the moment redistribution of a continuous beam strengthened with FRP EBR is forced to follow the linear elastic moment distribution [3, 4]. As a consequence, the formation of the restrained hinges is not clearly visible any more in the moment redistribution graphs. In some cases it is even possible to move the location of the plastic hinge (from sagging zone to hogging zone or vice versa) by applying FRP EBR in a zone with low internal steel reinforcement. Some phenomenon's and outcomes, which are discussed further, can also be applied on frames and/or infinitely continuous beams.

In this chapter the non-linear investigation is mainly limited to prismatic two-span RC beams unstrengthened or strengthened with FRP EBR. As the study focuses on the investigation of the moment redistribution, it is assumed that shear failure is not governing the ultimate state and hence that the beams are over-designed for shear

In section 2 the non-linear theory for a strengthened two-span beam is investigated. In section 3, the experimental verification of this non-linear theory is given by means of tests on large-scale two span beams. The beam configuration used in this study is given in Fig. 2.1. The two-span beam is loaded with one point load in each span. The position of the point load is determined by the parameter $\lambda = a/b$, with a = 2 m; b = 3 m.

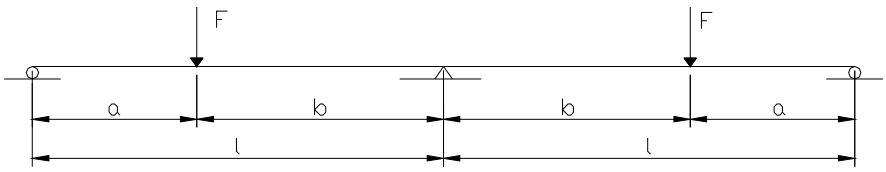

Fig. 2.1: Continuous beam with two spans

1.2 Moment redistribution graphs

Several methods are possible to present the moment redistribution of a continuous beam. In this work two different types of graphs will be presented.

The first type of graph is being explained by means of Fig. 2.2, which is a typical moment redistribution graph for an unstrengthened two-span beam. In this graph, both the maximal moment in the span M_{span} (sagging zone; negative values of M) and at the mid-support $M_{support}$ (hogging zone; positive values of M) are given in function of the acting point load F. In the graph a linear curve and a non-linear curve are given. The linear curve (grey line) is the moment distribution calculated by the classic linear theory. In this case, the relationship between the acting load and the moment is linear. The non-linear curve (black line) is the moment distribution calculated by the non-linear theory. Herewith, the formation of a plastic hinge in a critical cross-section can be noticed, by means of a (more) vertical line in the non-linear curve. This vertical line indicates that the considered critical cross-section (mid-support or span at the location of maximal moment) is yielding and hence is not able to take up additional load. As a result, the additional load is redistributed, as can be observed from the more horizontal appearance of the non-linear curve of the other critical cross-section. This behaviour, typical for an unstrengthened configuration, is obtained because the bending stiffness of the yielding cross-section is considerable smaller than the bending stiffness of the non-yielding cross-section. In the moment redistribution example illustrated in Fig. 2.2 the first plastic hinge appears at the critical cross section in the mid-support. This vertical line continues until the spans also starts to yield. At this point, both critical cross-sections obtain a low but similar bending stiffness, which results in moments taken up by both the span and mid-support. In fact, plastic hinges are present both at the mid-support and in the spans, which causes a mechanism. But due to the strain hardening behaviour of the internal steel reinforcement, this so-called mechanism is still able to take up some additional loads. This continues until one of the critical cross-sections fails by reaching the end of its rotation capacity.

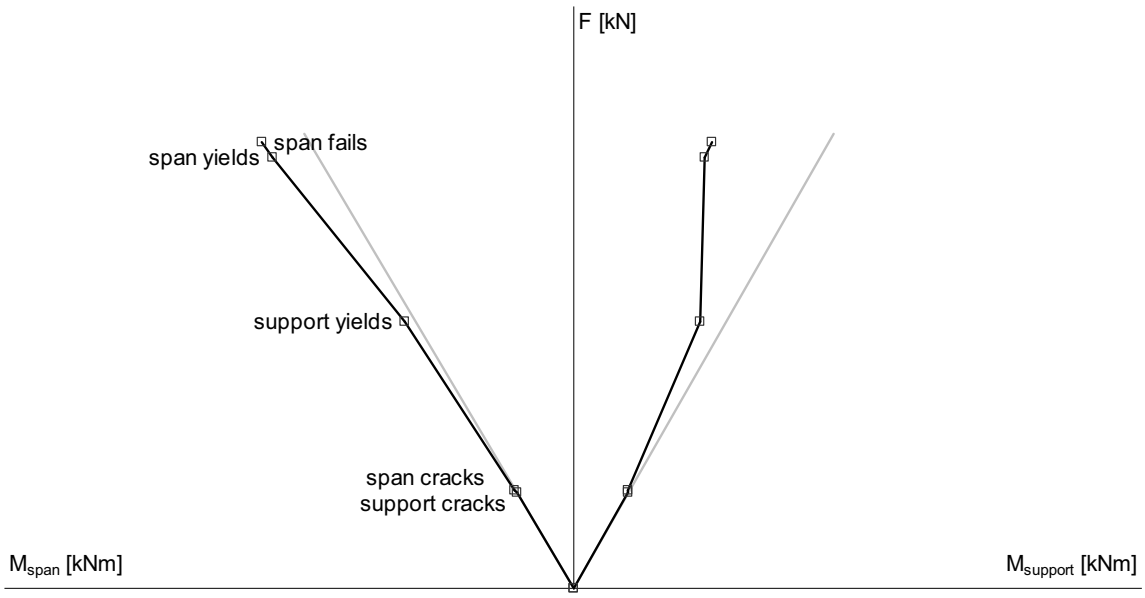

Fig. 2.2: Moment redistribution presented by $M_{support}$ and M_{span} in function of the applied load

In the second type of graph, illustrated in Fig. 2.3, the moment redistribution factor $\delta_{support}$ related to the moment redistribution at the mid-support is given (see Eq. 2.1).

$$\delta_{support} = \frac{M_{red,support}}{M_{el,support}} \tag{2.1}$$

with $M_{red,support}$ = moment at the mid-support after redistribution
$M_{el,support}$ = moment at the mid-support calculated according to the linear elastic theory

Similar to the previous graph, the moment ratio is shown in function of the applied load. Both a linear and a non-linear curve are given. The linear curve (vertical grey line) is the redistribution ratio calculated by the classic linear theory, which equals $\delta_{support} = 1$ for the entire loading range. The non-linear curve (black line) is based on the redistribution ratio at the mid-support calculated by the non-linear theory. The advantage of this graph is that the moment redistribution is indicated by a ratio which in several design calculations is limited to a certain maximum value.

Furthermore in Fig. 2.3 there can be noticed that the moment redistribution exists of an elastic part and a plastic part. The elastic part represents the redistribution until one critical cross-section is yielding, while the plastic part represents the redistribution from the first yielding of a critical cross-section until failure of the beam. Remark that in comparison with the plastic redistribution, the elastic redistribution also represents a considerable part of the total moment redistribution.

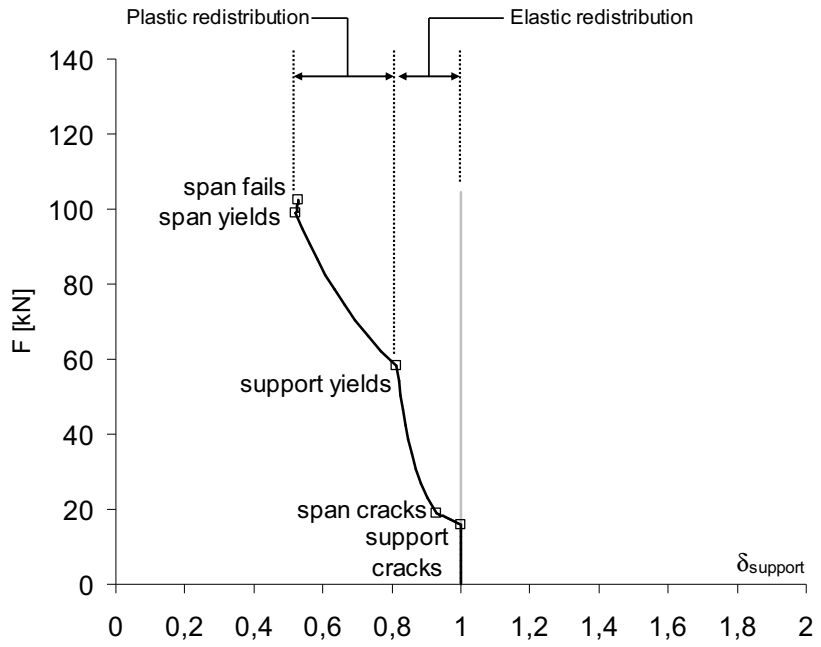

Fig. 2.3: Moment redistribution presented by redistribution factor $\delta_{support}$ in function of the applied load

In Fig. 2.3, only the redistribution ratio of the mid-support moment is visualized. The redistribution ratio of the maximum moment in the span can be obtained by the use of the static equilibrium equations of the two-span beam. In the following, a derivation is given to determine δ_{span} out of $\delta_{support}$, for different configurations.

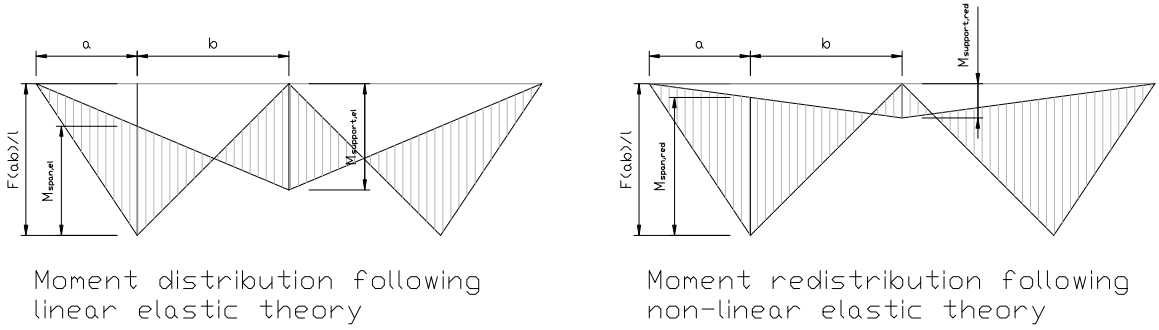

Fig. 2.4: Moment distribution according to linear elastic theory versus moment redistribution according to non-linear theory

For the two-span beam given in Fig. 2.1, the factor δ_{span} can be calculated as follows (see Fig. 2.4):

$$M_{span,red} = \frac{ab}{l}F - M_{support,red}\left(\frac{a}{l}\right) \qquad (2.2)$$

By dividing both sides of the equation with $M_{el,span}$, the following equation is obtained:

$$\delta_{span} = \frac{a}{l}\left(\frac{M_{support,el}}{M_{span,el}}\left(\frac{bF}{M_{support,el}} - \delta_{support}\right)\right) \quad (2.3)$$

In Chapter 1, the following equations for the maximum moments at the mid-support and in the span calculated according to the linear elastic theory, in function of the parameters a, b, l and F are obtained:

$$M_{support,el} = \frac{l+a}{2l^2}(ab)F \quad (2.4)$$

$$M_{span,el} = \left(\frac{ab}{l} - \frac{l+a}{2l^3}\left(a^2b\right)\right)F \quad (2.5)$$

Introducing Eq. 2.4 and 2.5 in Eq.2.3, δ_{span} can be rewritten as:

$$\delta_{span} = \frac{1}{\frac{2l^2}{(l+a)a} - 1}\left(\frac{2l^2}{(l+a)a} - \delta_{support}\right) \quad (2.6)$$

For a two-span beam with a span length of 5 meter (l = 5 meter) and the factor λ equal to 2/3 and 3/2 respectively, Eq. 2.6 reduces to:

$$\delta_{span} = 0.389\left(3.571 - \delta_{support}\right) \quad \text{for} \quad \lambda = 2/3 \quad (2.7)$$

$$\delta_{span} = 0.923\left(2.083 - \delta_{support}\right) \quad \text{for} \quad \lambda = 3/2 \quad (2.8)$$

Eq. 2.7 and 2.8 can be found in Fig. 2.5. Moreover, also the relationship between δ_{span} and $\delta_{support}$ is given for an infinitely long continuous beam, loaded by a uniform load q:

$$\delta_{span} = 2\left(\frac{2}{3} - \delta_{support}\right) \quad \text{for uniformly loaded, infinitely long continuous beam} \quad (2.9)$$

Notice in Fig. 2.5 the negative slope of all lines, which means that a small value of $\delta_{support}$ corresponds to a large value of δ_{span} and vice versa. Or, in other words, a decrease of $M_{support}$ relative to $M_{el,support}$ is related to an increase of M_{span} relative to $M_{el,span}$.

In Fig. 2.5, a considerable difference can be noticed between the different lines. All curves are crossing the point (1;1), because no redistribution occurs in this

case. Also notice that all curves in Fig. 2.5 are linear. From Fig. 2.5 the following can be noticed, e.g. for $\delta_{support}$ = 0.5:

- For a uniformly loaded infinitely long continuous beam (light grey curve) with a plastic hinge at the mid-support and $M_{red,support}$ = 50% $M_{el,support}$, a duplication of the moment in the spans is needed.
- For a two-span beam with λ = 3/2 (grey curve), it can be noticed that this linear relation almost coincides with a -45° line. Herewith, a reduction of $\delta_{support}$ with 50% results approximately in an increase of δ_{span} with 50%.
- For a two-span beam with λ = 2/3 (black curve), a steeper curve is observed in comparison with both other curves. In this configuration a reduction of the mid-support redistribution ratio results in a more restricted increase of the span redistribution ratio.

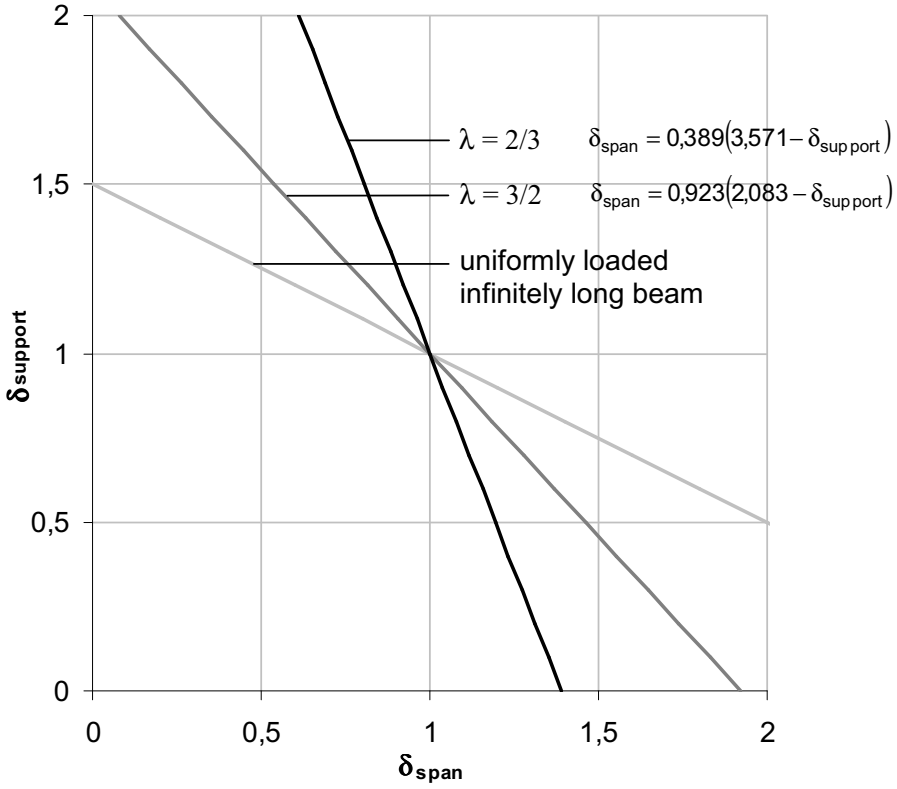

Fig. 2.5: δ_{span} in function of $\delta_{support}$

2 Non-linear theory of continuous beams – Theoretical analysis

2.1 Constitutive material models

The stress- strain models for the concrete and the steel reinforcement used in the analysis are given in Fig. 2.6 and Fig. 2.7. Both materials are represented by a bilinear stress-strain curve.

The intersection of the linear curves in Fig. 2.6 represents yielding of the steel reinforcement. The end point of the bi-linear curve represents the ultimate strain at ultimate stress. Values are resulting from a standard tensile test [5].

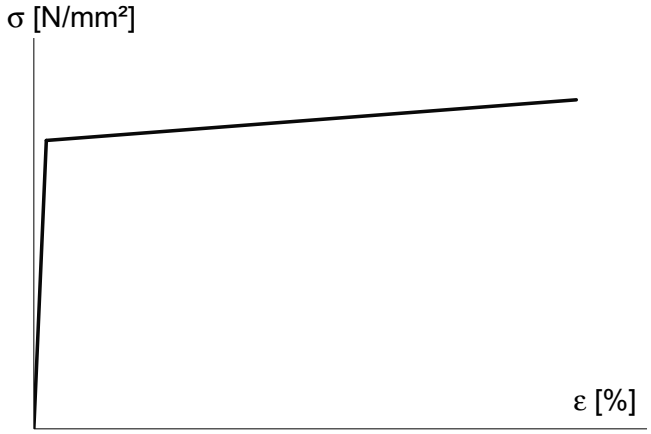

Fig. 2.6: Used stress-strain curve for internal reinforcement

The end point of the bi-linear curve corresponds to an ultimate strain of 3.5 ‰ [6].

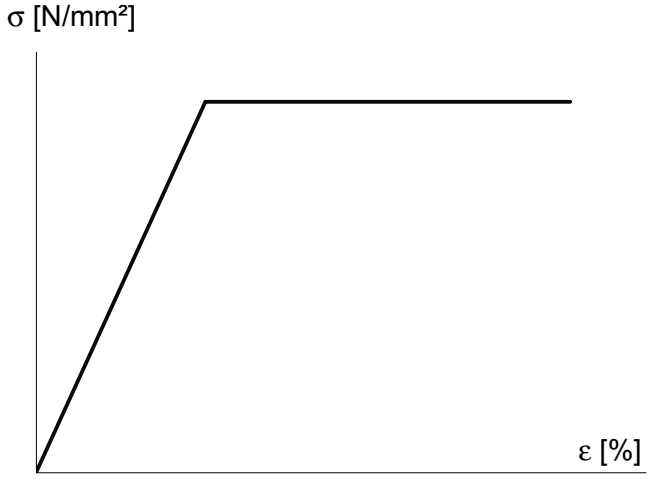

Fig. 2.7: Used stress-strain curve for concrete

The used stress-strain model for FRP is a linear curve as can be noticed in Fig. 2.8. This curve results from a standard tensile test [7].

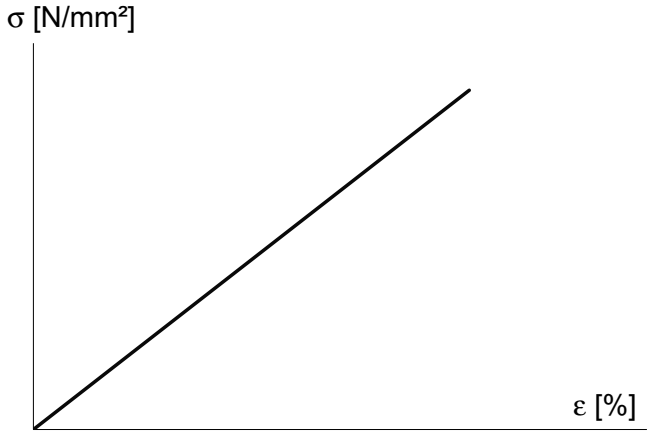

Fig. 2.8: Used stress-strain model of FRP

2.2 Determination of moment redistribution graph

2.2.1 Bending stiffness ratio versus moment distribution ratio

Considering a continuous beam with two identical spans and by two symmetric point loads (Fig. 2.1), two zones can be defined (see Fig. 2.9):

- one zone with positive moments (above mid-support, so called hogging zone)
- one zone with negative moments (in the span, so called sagging zone).

It is assumed that in each zone, the bending stiffness is constant [8-11]. So the mid-support zone and the span zone respectively have the stiffness $K_{support}$ and K_{span}. Given Fig. 2.9, the non-dimensional variables m (moment ratio), k (bending stiffness ratio) and λ (location of point load) are introduced (see equation 2.10).

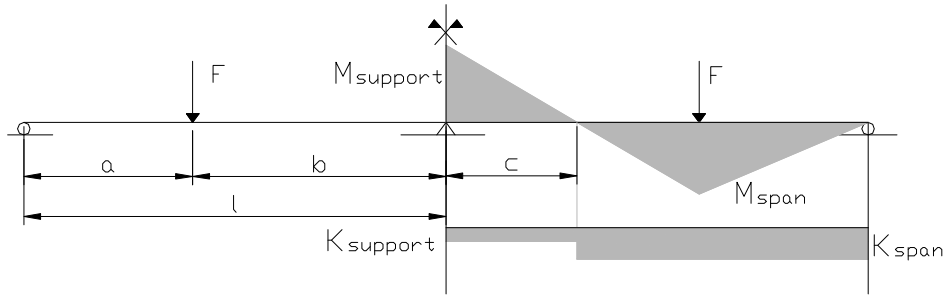

Fig. 2.9: Variable bending stiffness of 2-span beam

$$m = \frac{M_{support}}{M_{span}} \qquad k = \frac{K_{support}}{K_{span}} \qquad \lambda = \frac{a}{b} \tag{2.10}$$

Because the 2-span beam is statically indeterminate, one additional equation is required in addition to the traditional equations resulting from the horizontal, vertical and moment equilibrium. Given a certain bending stiffness ratio k, by expressing the angle of rotation above the mid-support equal to zero and applying Mohr's analogy, equation 2.11 is obtained [12]:

$$-\frac{M_{support}\,c}{2K_{support}}\left(l-\frac{c}{3}\right)\frac{1}{l}+\frac{M_{span}(l-c)}{2K_{span}}\frac{1}{3l}(2a+b-c)=0 \qquad (2.11)$$

where c equals the distance between the mid-support and the point where the bending moment equals 0, also known as the point of contraflexure (see Fig. 2.9). The distance c is given by following equation:

$$c=\frac{bM_{support}}{M_{support}+M_{span}} \qquad (2.12)$$

By combining equations 2.10 to 2.12, the following equation in function of the variables m, k and λ is obtained .

$$(2+3\lambda)m^3+(3+3\lambda-2k\lambda^2)m^2-k\lambda(3+4\lambda)m-(1+\lambda)(1+2\lambda)k=0 \qquad (2.13)$$

In the further theoretical analysis of the non-linear theory and in the experimental verifications, the distance between the point load and the end-supports (a) is taken equal to 2 m. The distance between the point load and the mid-support (b) is taken equal to 3 m. Hence, the parameter λ equals 2/3 and equation 2.13 can be rewritten as:

$$36m^3+(45-8k)m^2-34km-35k=0 \qquad (2.14)$$

To enlarge the theoretical analysis, the case of λ = 3/2 is also considered. For λ = 3/2, equation 2.13 becomes:

$$13m^3+(15-9k)m^2-27km-20k=0 \qquad (2.15)$$

In Fig. 2.10, equations 2.14 and 2.15 can be found in comparison to the line representing the k - m curve of an infinitely long continuous beam, loaded by a uniform load q (see Eq. 2.16).

$$(m-2)\sqrt{1+m}=2(k-1) \qquad (2.16)$$

Remark that the variables along the axes are transformed from k and m to respectively k/(1+k) and m/(1+m).

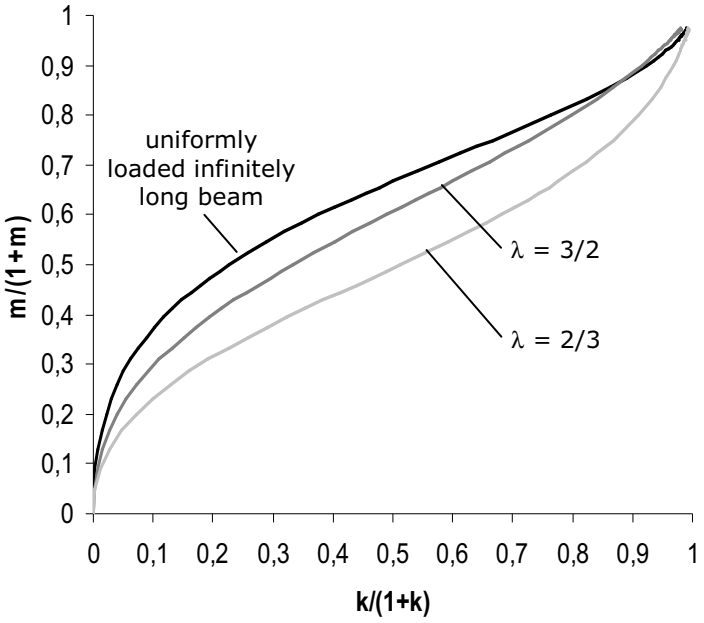

Fig. 2.10: Ratio of moments m in function of the ratio of bending stiffnesses k

Given the k – m relationship (Fig. 2.10) which is valid for the specific beam geometry and loading configuration, the bending moment ratio m can be derived as soon as the bending stiffness ratio k is known. The bending stiffness ratio k depends on the internal and the external reinforcement ratios and on the load level, as can be seen in Fig. 1.6.

2.2.2 Calculation of moment redistribution graphs

2.2.2.1 Stage k_1: $F \leq \min(F_{cr,span};F_{cr,support})$

The calculation of the moment redistribution graphs (illustrated in Fig. 2.2 and Fig. 2.3) is similar. To start, the moment distribution ratio m_1 is calculated, given the bending stiffness ratio k_1. Herewith k_1 corresponds with the uncracked stage over the entire length of the continuous beam, which results in a bending stiffness $K_{support,0}$ for the critical cross-section at the intermediate support and in a bending stiffness $K_{span,0}$ for the critical cross-section in the span. For the uncracked cross-section, the contribution of the tensile reinforcement to the overall moment of inertia is negligible, so that K_0 can be simplified (Eq. 2.18). Hereby $K_{support,0}$ equals $K_{span,0}$, which result in a bending stiffness ratio k equal to 1 (see Eq. 2.17). The stiffness over the entire length of the continuous beam is constant from which it follows that the moment ratio m_1 equals the linear elastic moment distribution ratio m_{el} (see also Eq. 2.17). This moment ratio m_1 ($=m_{el}$) can be obtained from Eq. 2.13 or Eq. 2.16 depending on the used loading configuration (see Fig. 2.10) and applies as long as no cracks appear in the beam, which implies that $M_{support} \leq M_{cr,support}$ and $M_{span} \leq M_{cr,span}$ (see Eq. 2.19)

$$k_1 = \frac{K_{support,0}}{K_{span,0}} = 1 \quad \text{and} \quad m_1 = m_{el} \tag{2.17}$$

$$\text{with:} \quad K_0 = E_{cm} I_c = E_{cm} \frac{bh^3}{12} \tag{2.18}$$

$$M_{cr} \approx M_{cr,support} \approx M_{cr,span} \approx f_{ctm} \frac{bh^2}{6} \tag{2.19}$$

2.2.2.2 Stage k_2: $\min(F_{cr,span};F_{cr,support}) \leq F \leq \max(F_{cr,span};F_{cr,support})$

The applied load is increased until the bending stiffness at one of the critical cross-sections changes, due to cracking. Hereby one of the critical cross-sections is characterized by the bending stiffness K_1 (see Fig. 1.6), which equals the bending stiffness of a fully cracked cross-section. This bending stiffness K_1 is obtained from the second branch of the M-χ diagram.

Depending on which critical section cracks first, the stiffness ratio k_2 is calculated as:

$$k_2 = \frac{K_{support,1}}{K_{span,0}} \quad \text{or} \quad k_2 = \frac{K_{support,0}}{K_{span,1}} \tag{2.20}$$

Once the bending stiffness ratio k_2 is obtained, the moment distribution ratio m_2 can be derived from Eq. 2.13 or Eq. 2.16 according to the used loading configuration (see Fig. 2.10).

2.2.2.3 Stage k_3: $\max(F_{cr,span};F_{cr,support}) \leq F \leq \min(F_{y,span};F_{y,support})$

In the third stage of the moment redistribution graph, both the critical cross-sections at the intermediate support and in the spans are cracked. In this case the following bending stiffness ratio k_3 is obtained:

$$k_3 = \frac{K_{support,1}}{K_{span,1}} \tag{2.21}$$

The bending stiffness K_1 for these cross-sections is obtained from the second branch of the M-χ diagram. Given k_3, the moment distribution ratio m_3 can be obtained from Eq. 2.13 or Eq. 2.16 according to the used loading configuration (see Fig. 2.10) and applies as long as both critical cross-sections do not change from bending stiffness. This is visualized in the particular example of both Fig. 2.2 and Fig. 2.3 by the branch between the moments corresponding to cracking and yielding of the span section.

2.2.2.4 Stage k_4: $\min(F_{y,span};F_{y,support}) \leq F \leq \max(F_{y,span};F_{y,support})$

The next bending stiffness ratio k_4 applies from the moment that one of the critical cross-sections starts to yield. Either the intermediate support or the span will reach the bending stiffness K_2 (see Eq. 2.22). Note that the bending stiffness K_2 can be obtained from the third branch of the M-χ diagram.

$$k_4 = \frac{K_{support,2}}{K_{span,1}} \quad \text{or} \quad k_4 = \frac{K_{support,1}}{K_{span,2}} \tag{2.22}$$

2.2.2.5 Stage k_5: $\max(F_{y,span};F_{y,support}) \leq F \leq \min(F_{u,span};F_{u,support})$

The last bending stiffness ratio to obtain the final part of the moment redistribution graph, is the ratio k_5 (see Eq. 2.23). This bending stiffness ratio is obtained, when both critical cross-sections are yielding. Herewith the bending stiffness in both cross-sections equals K_2. Given k_5, the moment distribution ratio m_5 is obtained from Eq. 2.13 or Eq. 2.16.

$$k_5 = \frac{K_{support,2}}{K_{span,2}} \tag{2.23}$$

2.2.2.6 Redistribution curve

Summarizing, the entire moment redistribution graph can be obtained by firstly calculating the bending stiffness ratios for every stage in the loading process, where a distinction is made between the uncracked, cracked and yielding stage both for the intermediate support zone and the span zone. In this analysis, the different bending stiffnesses are derived from the M-χ diagram of the critical cross-section concerned.

Once the bending stiffness ratios are known, the moment redistribution ratios can be calculated according to Fig. 2.10, or according to Eqs. 2.14 and 2.15 for a two-span beam (see Fig. 2.1) with $\lambda = 2/3$ and $\lambda = 3/2$ respectively or according to Eq. 2.13 for a uniformly loaded infinitely long continuous beam. To determine the redistribution curve, a distinction is made between the five stages (stage k_1 until stage k_5) discussed in the previous sections. The following stepwise procedure is applied (see also Fig. 2.11).

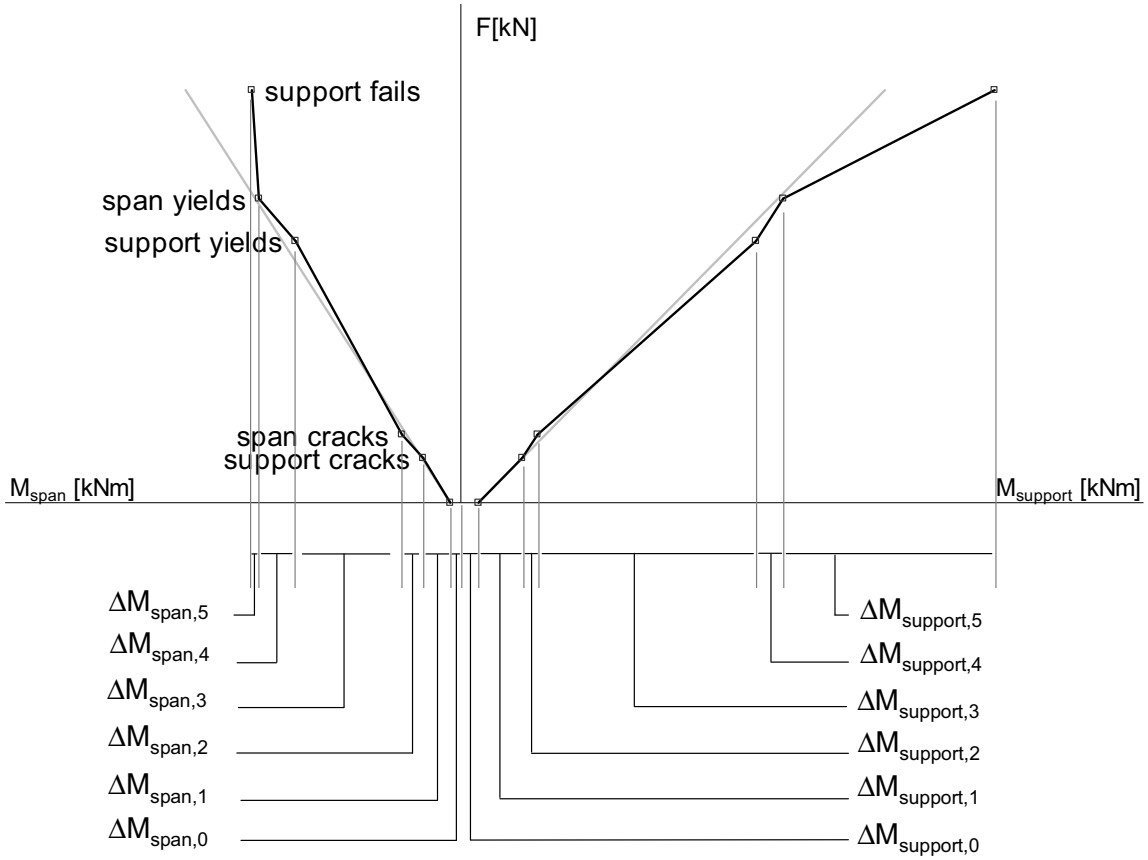

Fig. 2.11: Different subdivisions of the entire moment redistribution

- At the end of the first stage (stage k_1), the lowest of the two cracking loads ($F_{cr,span}$ or $F_{cr,support}$) is determined. The moment in the other critical cross-section at this situation is obtained by applying the moment redistribution ratio m_1 (see Eqs. 2.25 and 2.26).

$$m_1 = \frac{\Delta M_{support,1}}{\Delta M_{span,1}} = \frac{\left(M_{support,1} - M_{support,0}\right)}{\left(M_{span,1} - M_{span,0}\right)} \qquad (2.24)$$

with M_0 = the moment in a critical cross-section resulting from the dead mass situation
M_1 = the moment in a critical cross-section at the end of stage k_1
ΔM_1 = the increase of the moment during stage k_1

if $F_{cr,support} < F_{cr,span}$: $M_{support,1} = M_{cr,support}$

if $F_{cr,support} > F_{cr,span}$: $M_{span,1} = M_{cr,span}$

Hence:

$$m_1 = \frac{M_{cr,support} - M_{support,0}}{M_{span,1} - M_{span,0}} \qquad \text{if } F_{cr,support} < F_{cr,span} \tag{2.25}$$

$$m_1 = \frac{M_{support,1} - M_{support,0}}{M_{cr,span} - M_{span,0}} \qquad \text{if } F_{cr,support} > F_{cr,span} \tag{2.26}$$

The related load results from the vertical equilibrium and moment equilibrium at the end of stage k_1.

- At the end of stage k_2, the highest of the two cracking loads ($F_{cr,span}$ or $F_{cr,support}$) is reached. The increase of the moment in the other critical cross-section is than obtained by the moment redistribution ratio m_2 (see Eqs. 2.27).

$$m_2 = \frac{\Delta M_{support,2}}{\Delta M_{span,2}} = \frac{\left(M_{support,2} - M_{support,1}\right)}{\left(M_{span,2} - M_{span,1}\right)} \tag{2.27}$$

with M_1 = the moment in a critical cross-section at the end of stage k_1
M_2 = the moment in a critical cross-section at the end of stage k_2
ΔM_2 = the increase of the moment during stage k_2

if $F_{cr,support} < F_{cr,span}$: $M_{support,1} = M_{cr,support}$
$M_{span,2} = M_{cr,span}$

if $F_{cr,support} > F_{cr,span}$: $M_{support,2} = M_{cr,support}$
$M_{span,1} = M_{cr,span}$

The related increase of the load results from the vertical equilibrium and moment equilibrium at the end of stage k_2.

- At the end of stage k_3, the lowest of the two yielding loads ($F_{y,span}$ or $F_{y,support}$) is reached. The increase of the moment in the other critical cross-section is than obtained by the moment redistribution ratio m_3 (see Eqs. 2.28).

$$m_3 = \frac{\Delta M_{support,3}}{\Delta M_{span,3}} = \frac{\left(M_{support,3} - M_{support,2}\right)}{\left(M_{span,3} - M_{span,2}\right)} \tag{2.28}$$

with M_2 = the moment in a critical cross-section at the end of stage k_2
M_3 = the moment in a critical cross-section at the end of stage k_3
ΔM_3 = the increase of the moment during stage k_3

if $F_{y,support} < F_{y,span}$: $M_{support,3} = M_{y,support}$

if $F_{y,support} > F_{y,span}$: $M_{span,3} = M_{y,span}$

The related increase of the load results from the vertical equilibrium and moment equilibrium at the end of stage k_3.

- At the end of stage k_4, the highest of the two yielding loads ($F_{y,span}$ or $F_{y,support}$) is reached. The increase of the moment in the other critical cross-section is than obtained by the moment redistribution ratio m_4 (Eq.2.29).

$$m_4 = \frac{\Delta M_{support,4}}{\Delta M_{span,4}} = \frac{\left(M_{support,4} - M_{support,3}\right)}{\left(M_{span,4} - M_{span,3}\right)} \qquad (2.29)$$

with M_3 = the moment in a critical cross-section at the end of stage k_3
M_4 = the moment in a critical cross-section at the end of stage k_4
ΔM_4 = the increase of the moment during stage k_4

if $F_{y,support} < F_{y,span}$: $M_{span,4} = M_{y,span}$
$M_{support,3} = M_{y,support}$

if $F_{y,support} > F_{y,span}$: $M_{support,4} = M_{y,support}$
$M_{span,3} = M_{y,span}$

The related increase of the load results from the vertical equilibrium and moment equilibrium at the end of stage k_4.

- At the end of stage k_5, the lowest of the two ultimate loads ($F_{u,span}$ or $F_{u,support}$) is obtained. The increase of the moment in the other critical cross-section is than obtained by the moment redistribution ratio m_5 (Eq. 2.30).

$$m_5 = \frac{\Delta M_{support,5}}{\Delta M_{span,5}} = \frac{\left(M_{support,5} - M_{support,4}\right)}{\left(M_{span,5} - M_{span,4}\right)} \qquad (2.30)$$

with M_4 = the moment in a critical cross-section at the end of stage k_4
M_5 = the moment in a critical cross-section at the end of stage k_5
ΔM_5 = the increase of the moment during stage k_5

if $F_{u,support} < F_{u,span}$: $M_{support,5} = M_{u,support}$

if $F_{u,support} > F_{u,span}$: $M_{span,5} = M_{u,span}$

The related increase of the load results from the vertical equilibrium and moment equilibrium at the end of stage k_5.

Finally the full moment redistribution graph is obtained by connecting the above obtained critical points.

2.2.2.7 Simplified calculation of moment redistribution graph

As mentioned in both Fig. 1.6 and in previous sections, three different bending stiffnesses (K_0, K_1 and K_2) are considered to calculate the moment redistribution graph. This results in five different stages in the moment redistribution graph (stage k_1 till k_5), each characterized by a particular bending stiffness ratio and a moment redistribution ratio. At the other hand, to simplify the calculation of the moment redistribution graph, a bilinear moment-curvature diagram can be used (see Fig. 2.12), in which a constant stiffness is assumed until the cross-section yields (stiffness K_1'), in stead of the use of the stiffnesses K_0 and K_1.

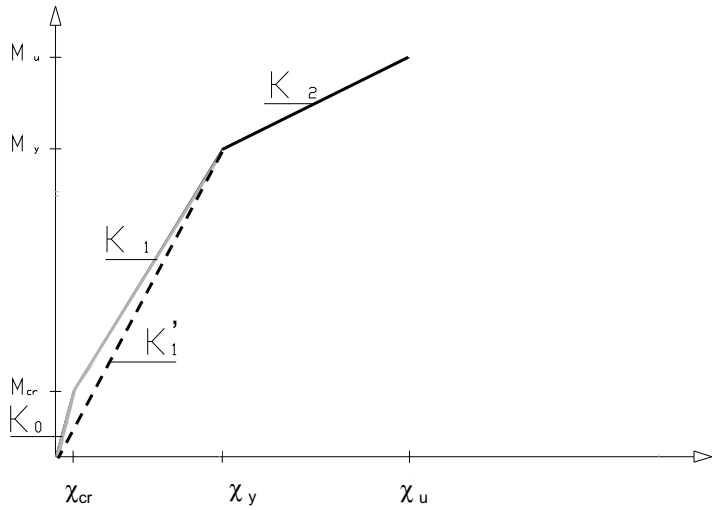

Fig. 2.12: Simplified moment-curvature diagram

For a single reinforced and FRP strengthened rectangular cross-section, the bending stiffness K_1' of the fully cracked cross-section can be calculated by Eq. 2.31.

$$K_1^{'} = A_s E_s d^2 \left(1-\xi_{e,s}\right)\left(1-\frac{\xi_{e,s}}{3}\right) + A_f E_f h^2 \left(1-\xi_{e,f}\right)\left(1-\frac{\xi_{e,f}}{3}\right) \qquad (2.31)$$

where $\xi_{e,s} = x_e/d$ and $\xi_{e,f} = x_e/h$. Hereby x_e equals the neutral axes depth before yielding of the cross-section and is calculated based on the longitudinal equilibrium of this cross-section.

By using this bilinear diagram only three different stages in stead of five are obtained. There is stage k_3' (see Eq. 2.32), stage k_4' (see Eq. 2.33) and stage k_5' (see Eq. 2.34). Remark that stage k_5' is equal to stage k_5 given in section 2.2.2.5.

stage k_3': $F \leq \min(F_{y,span}; F_{y,support})$

$$k_3^{'} = \frac{K_{support,1}^{'}}{K_{span,1}^{'}} \qquad (2.32)$$

stage k_4': $\min(F_{y,span};F_{y,support}) \le F \le \max(F_{y,span};F_{y,support})$

$$k_4 = \frac{K_{support,2}}{K'_{span,1}} \quad \text{or} \quad k_4 = \frac{K'_{support,1}}{K_{span,2}} \tag{2.33}$$

stage k_5': $\max(F_{y,span};F_{y,support}) \le F \le \min(F_{u,span};F_{u,support})$

$$k_5 = \frac{K_{support,2}}{K_{span,2}} \tag{2.34}$$

2.2.3 Remarkable values of the k-m curve

2.2.3.1 k = 1

A first remarkable value of the k – m curve is given by the value of m_{el}, corresponding to a bending stiffness ratio k = 1. This is the moment redistribution ratio according to the linear elastic theory and assumes a constant bending stiffness over the entire length of the beam. Values of m_{el} are given in Table 2.1. In Fig. 2.13 the values can be found on the intersection of the respective k – m curves with the k = 1 line (vertical black line).

Table 2.1: Moment distribution ratios related to k = 1

	bending stiffness ratio	moment distribution ratio
two-span beam (Fig. 2.1) with λ = 2/3	k=1	m_{el} = 0.9722
two-span beam (Fig. 2.1) with λ = 3/2	k=1	m_{el} = 1.5385
uniformly loaded infinitely long beam	k=1	m_{el} = 2.0000

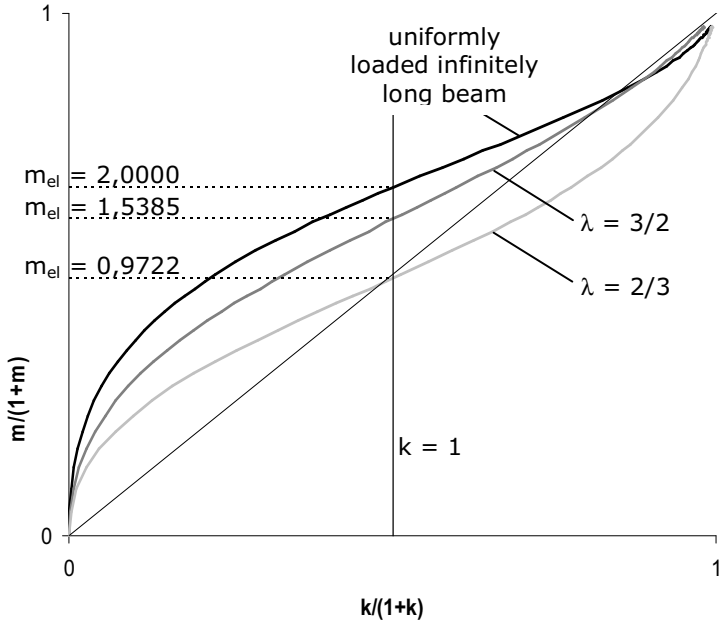

Fig. 2.13: Moment distribution ratios related to k = 1

In the calculation of the moment redistribution graph, the starting bending stiffness k_1 (see Eq. 2.17) equals 1. Hence, initially the moment distribution graph equals the linear elastic moment distribution line, as long as no critical cross-section of the continuous beam is cracked. In the further development of the moment redistribution graph, the moment redistribution basically depends on the reinforcement ratios. It is possible to use a combination of reinforcement ratios for which the bending stiffness ratio k_3 (see Eq. 2.21) of the two-span beam also equals 1. As outlined in section 2.2.2.3 k_3 equals the bending stiffness ratio of a continuous beam, for which all critical cross-sections are cracked (yet not yielded).

For $k_3 = 1$ and given the limited influence of k_2, the obtained moment redistribution equals the linear elastic moment distribution until one particular cross-section yields. Herewith, the acting moment distribution at service loads approximately corresponds to the linear elastic moment distribution. An example of the moment redistribution of a two span beam (Fig. 2.1) with span length 5 m and $\lambda = 3/2$, for the case $k_3 = 1$, is given in Fig. 2.14. The mechanical properties of the used reinforcing steel, FRP and concrete are given in Table 2.2. The applied reinforcement ratios can be found in Table 2.3.

Table 2.2: Mechanical properties

	C35/45		S500		CFRP	
Compressive strength	35	N/mm²				
Yield stress			500	N/mm²		
Tensile stress	3.5	N/mm²	550	N/mm²	2850	N/mm²
Failure strain	0.35	%	12.40	%	1.81	%
E-modulus	32000	N/mm²	200000	N/mm²	175000	N/mm²

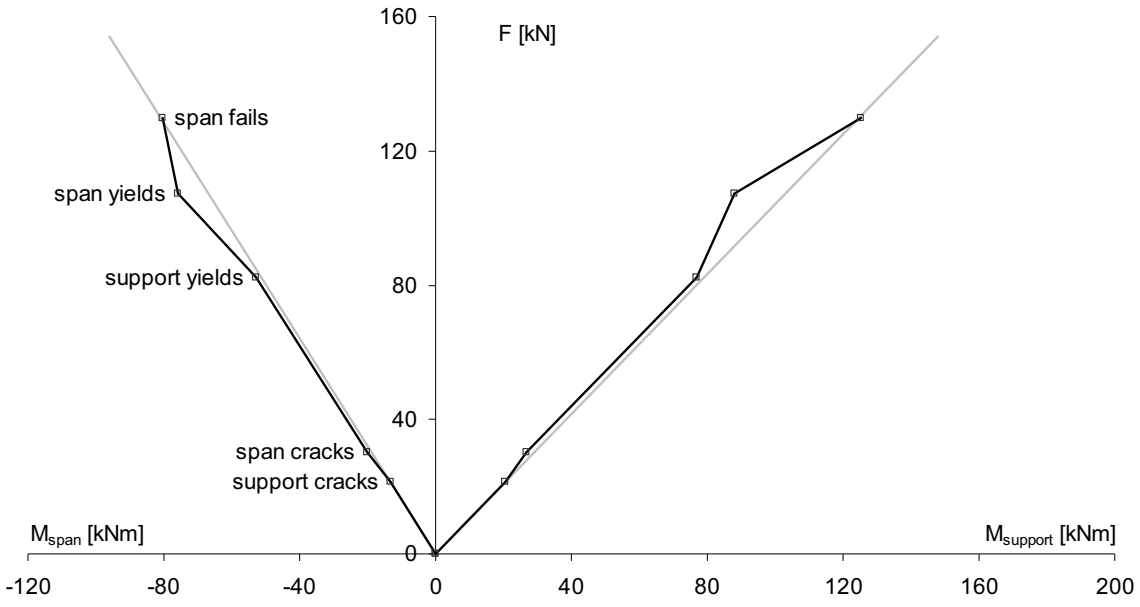

Fig. 2.14: Moment redistribution with k_3=1

Table 2.3: Reinforcement ratios (for $k_3 = 1$)

	Mid-support	Span
steel reinforcement ratio ρ_s	0.45 %	0.63 %
CFRP reinforcement ratio ρ_f	0.14 %	0.00 %

Given the limited influence of stage k_2 and for $k_3 = 1$, almost no redistribution is observed until one of the critical cross-sections yields. For this particular example no redistribution is observed until the mid-support yields. When the mid-support starts to yield, a significant moment redistribution is observed, as can be noticed in Fig. 2.14.

2.2.3.2 $k = m_{el}$

Another remarkable value in the k-m curve, is given by the intersection of the k-m curve with the vertical line of k_3 equal to m_{el}. The values k and m for this intersection are indicated in both Table 2.4 and Fig. 2.15. By assuming $k_3 = m_{el}$, it is assumed that a continuous beam is reinforced according to the linear elastic moment distribution. According to [13], it is concluded that a continuous beam, which is reinforced with only internal steel reinforcement according to the linear elastic moment distribution ratio, obtains an acting moment redistribution which is approximately equal to the linear elastic moment distribution.

Table 2.4: Moment distribution ratios related to $k = m_{el}$

	bending stiffness ratio	moment distribution ratio
two-span beam (Fig. 2.1) with $\lambda = 2/3$	k = 0.9722	m = 0.9571
two-span beam (Fig. 2.1) with $\lambda = 3/2$	k = 1.5385	m = 2.0427
uniformly loaded infinitely long beam	k = 2.0000	m = 3.0000

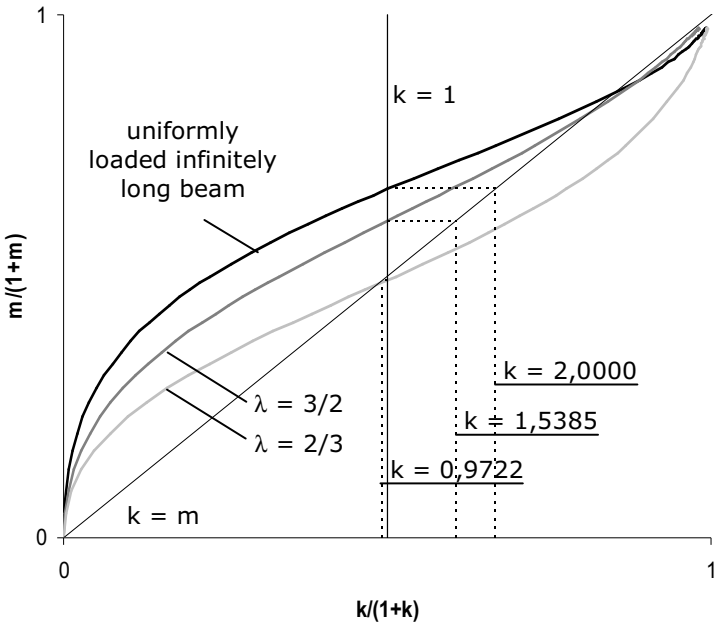

Fig. 2.15: Moment distribution ratios related to $k = m_{el}$

In contrast with the unstrengthened beams, the moment redistribution of the strengthened continuous beams for $k_3 = m_{el}$ is more complex and will be explained by means of five different examples, each with a certain internal steel and external steel reinforcement ratio (see case A until E mentioned below). Each case corresponds to a symmetric two span beam (Fig. 2.1) with span lengths equal to 5 m and $\lambda = 3/2$. We consider the following cases:

- Case A continuous unstrengthened beam (internal steel reinforcement ratios are calculated according to the linear elastic theory [13])
- Case B continuous beam only strengthened at the soffit of the spans
- Case C continuous beam only strengthened at the top of the mid-support
- Case D continuous beam with the same amount of strengthening at the soffit of the spans and at top of the mid-support
- Case E continuous beam with internal steel reinforcement ratios calculated according to the linear elastic theory and with additional externally bonded reinforcement ratios also dimensioned according to the linear elastic theory

The reinforcement and strengthening ratios, for each case are given in Table 2.5. Herewith, the amount of steel and FRP reinforcement was chosen such that the equivalent ratio ρ_{eq} is almost equal for the 5 cases. The mechanical properties of the applied reinforcements and concrete are those given in Table 2.2.

Table 2.5: Reinforcement ratios for the different cases

	Mid-support			Span		
	Steel reinf. ratio $\rho_{s,support}$	FRP reinf. ratio $\rho_{f,support}$	Eq. reinf. Ratio $\rho_{eq,support}$	Steel reinf. ratio $\rho_{s,span}$	FRP reinf. ratio $\rho_{f,span}$	Eq. reinf. Ratio $\rho_{eq,span}$
Case A	0.71 %	0.00 %	0.71 %	0.48 %	0.00 %	0.48 %
Case B	0.71 %	0.00 %	0.71 %	0.38 %	0.13 %	0.49 %
Case C	0.61 %	0.13 %	0.72 %	0.48 %	0.00 %	0.48 %
Case D	0.61 %	0.13 %	0.72 %	0.38 %	0.13 %	0.49 %
Case E	0.55 %	0.18 %	0.71 %	0.38 %	0.11 %	0.48 %

Table 2.6: Bending stiffness ratios k and related moment distribution ratios m for the different cases

	k_1	m_1 ($=m_{el}$)	k_3	m_3	k_5	m_5
Case A	1.034	1.572	1.539	2.043	1.668	2.158
Case B	1.013	1.551	1.538	2.043	0.039	0.242
Case C	1.054	1.592	1.539	2.043	41.362	30.378
Case D	1.033	1.571	1.539	2.043	0.978	1.516
Case E	1.034	1.572	1.538	2.043	1.485	1.994

In Fig. 2.16 till Fig. 2.20 the moment redistribution graphs are given for case A until case E. For the calculation of these curves full composite action is assumed between the concrete and the bonded FRP. Remarkable is that the moment redistribution until the first critical cross-section yields (yielding of mid-support in all cases) is similar for all cases. This is due to the fact that the equivalent reinforcement ratio ρ_{eq} is taken equal for all cases. As explained in Chapter 1, by keeping the equivalent ratio ρ_{eq} constant, the bending stiffness K_0 and K_1 for both the mid-support as the spans will not change. Hence from equations 2.17 and

2.21, it follows that the bending stiffness ratios k_1 and k_3 will not change and the moment distribution ratios m_1 and m_3 neither. This phenomenon can be observed in Table 2.6. As a consequence of this, the moment redistribution until the first critical cross-section yields will not change. Furthermore, for the first part of the moment redistribution curves (until the first critical cross-section yields) a good agreement is noticed for all graphs, between the real moment redistribution and the linear elastic moment distribution. This is due to the bending stiffness ratios k_3, which are taken similar for all cases to m_{el} (= m_1) (see Table 2.6).

The difference between the moment redistribution of the five cases is found in the upper parts of the graphs. For case A, which represents the continuous beam without strengthening, hardly any redistribution is observed. The acting moment redistribution curve follows the linear elastic moment distribution curve. This conclusion is also found in [13] as well as in Table 2.6, where it can be observed that $k_5 \approx m_{el}$.

Regarding cases B and C, which represent the continuous beam with strengthening at either the soffit of the spans or at the top of the mid-support, a considerable moment redistribution can be observed. This redistribution is noticed starting from the yielding of the last critical cross-section (yielding of span in all cases). After yielding of this last critical cross-section, the additional moments are taken up to a large extent by the strengthened cross-section only. In this case the bending stiffness ratio k_5 (see Table 2.6) differs from the linear elastic moment distribution ratio m_{el} and causes the noticed moment redistribution shown in Fig. 2.17 and Fig. 2.18.

Regarding case D, no moment redistribution is noticed after yielding of the last critical cross-section (yielding of span). The additional moments are taken both by the strengthened cross-section in the span and at the mid-support. Because $\rho_{f,support}$ equals $\rho_{f,span}$, the bending stiffness ratio $k_5 \approx 1$ (see Table 2.6). This results in a moment distribution ratio $m = m_{el}$, for which a perfectly linear elastic moment distribution is obtained (see Fig. 2.19).

Also in case E, hardly any moment redistribution is noticed after yielding of the last critical cross-section (yielding of span). This is due to the use of strengthening ratios $\rho_{f,support}$ and $\rho_{f,span}$, equal to the linear elastic moment distribution. This results in a bending stiffness ratio $k_5 \approx m_{el}$ (see Table 2.6).

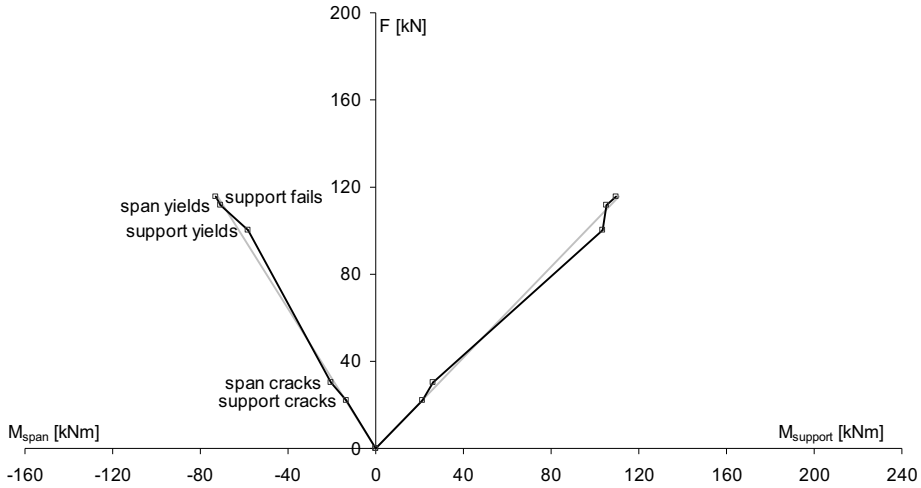

Fig. 2.16: Moment redistribution with $k_3 = m_{el}$ for case A

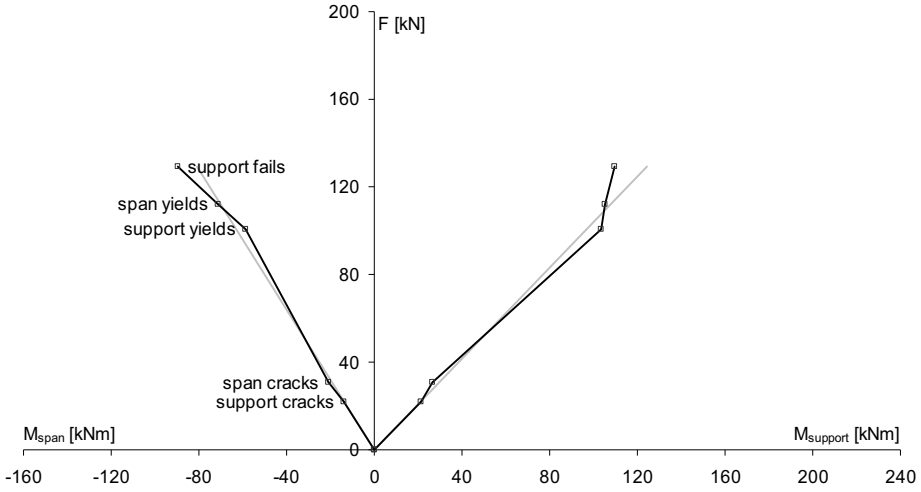

Fig. 2.17: Moment redistribution with $k_3 = m_{el}$ for case B

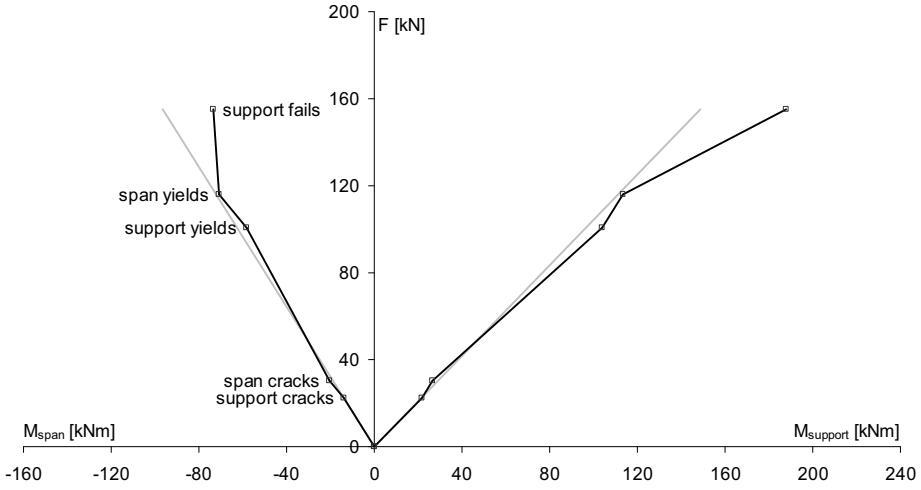

Fig. 2.18: Moment redistribution with $k_3 = m_{el}$ for case C

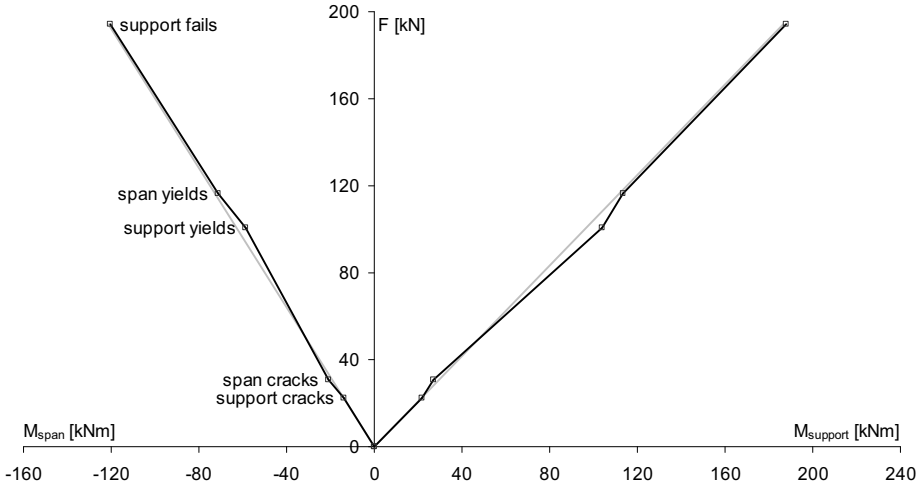

Fig. 2.19: Moment redistribution with $k_3 = m_{el}$ for case D

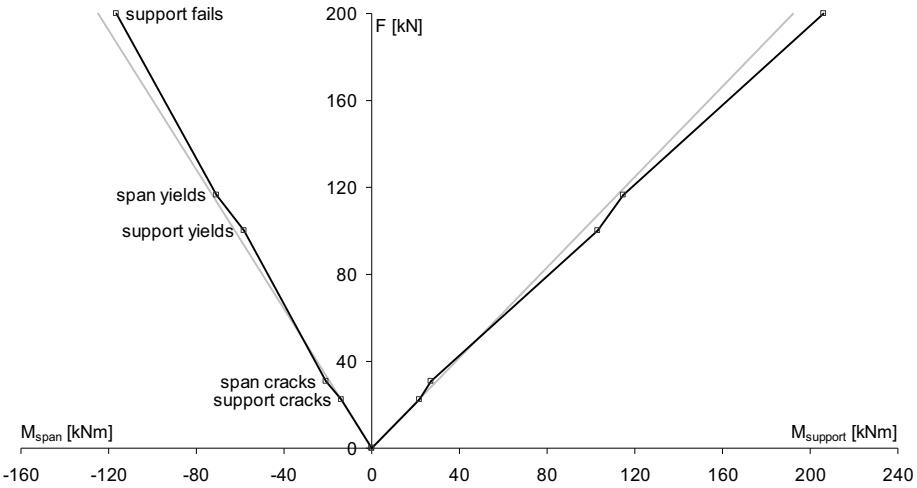

Fig. 2.20: Moment redistribution with $k_3 = m_{el}$ for case E

2.2.3.3 k = m

A last remarkable value in the k-m curve, is given by the intersection of the k-m curve with the 45°-line of k = m. The values k and m for this intersection are shown in both Table 2.7 and Fig. 2.21.

Table 2.7: Moment distribution ratios related to k = m

	bending stiffness ratio	moment distribution ratio
two-span beam (Fig. 2.1) with $\lambda = 2/3$	k = 0.9387	m = 0.9387
two-span beam (Fig. 2.1) with $\lambda = 3/2$	k = 4.1926	m = 4.1926
uniformly loaded infinitely long beam	k = 5.5616	m = 5.5616

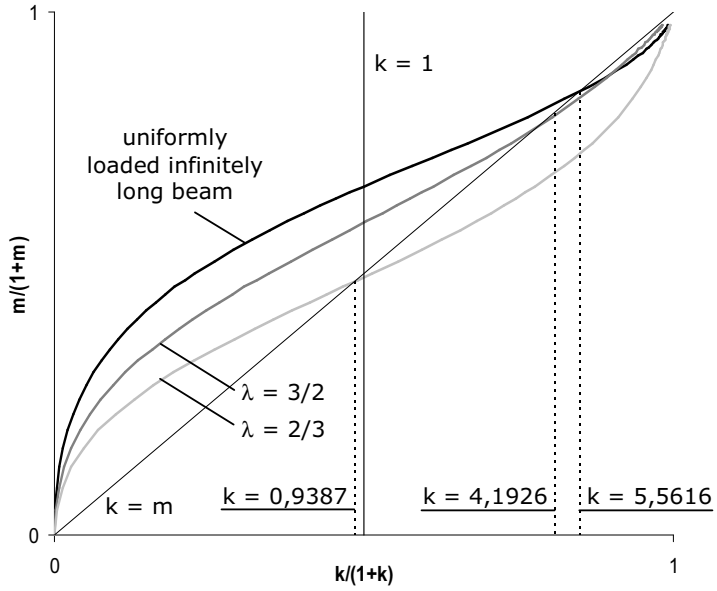

Fig. 2.21: Moment distribution ratios related to k = m

For the unstrengthened continuous beams in [12] it is demonstrated that the solution k = m (Eqs. 2.14, 2.15) gives a transition value (m_t). At this transition value, the location of the first yielding cross-section will change from the mid-support into the spans or vice versa. Or in other words, if $m_3 < m_t$, the mid-support yields first. On the contrary when $m_3 > m_t$, the span yields first. Hence by comparing m with m_t, the position of the first plastic hinge is known. By way of example for an unstrengthened two-span beam (length of one span equals 5 meter) with $\lambda = 2/3$, the mid-support will yield first as long as m_3 or $k_3 < 0.9387$ (see Fig. 2.21). On the contrary, if m_3 or $k_3 > 0.9387$, the critical cross-section in the span yields first and consequently, the first plastic hinges will be obtained in the spans.

In strengthened continuous beams, the above mentioned theory [12, 14] does not remain valid. The determination of the first yielding cross-section (intermediate support yields first or span yields first) in a strengthened continuous beam can be determined by the following approach. As mentioned in section 2.2.2, different stages can be distinguished in the moment redistribution curve. In Fig. 2.22, the increases of the moments at the mid-support and in the spans (based on a 2-span beam in Fig. 2.1) are given for the different stages up to yielding of both critical cross-sections.

To obtain the transition value m_t, it is assumed that both the mid-support and the spans are yielding at the same time. Hence, the fourth stage ($\min(F_{y,support};F_{y,span}) \leq F \leq \max(F_{y,support};F_{y,span})$) is negligible, or in other words: $\Delta M_{support,4} \approx 0$ and $\Delta M_{span,4} \approx 0$ (see Fig. 2.22). As a result $M_{y,support}$ and $M_{y,span}$ can be written as follows (see Fig. 2.22):

$$M_{y,support} = \Delta M_{support,3} + \Delta M_{support,2} + \Delta M_{support,1} \tag{2.35}$$

$$M_{y,span} = \Delta M_{span,3} + \Delta M_{span,2} + \Delta M_{span,1} \tag{2.36}$$

The transition value m_t, equals (taking into account Eqs. 2.28, 2.35 and 2.36):

$$\begin{aligned} m_t &= \frac{\Delta M_{support,3}}{\Delta M_{span,3}} \\ &= \frac{M_{y,support} - \Delta M_{support,2} - \Delta M_{support,1}}{M_{y,span} - \Delta M_{span,2} - \Delta M_{span,1}} \\ &\approx \frac{M_{y,support} - M_{cr}}{M_{y,span} - M_{cr}} \end{aligned} \tag{2.37}$$

Herewith, it is assumed approximately that the cracking moment at the intermediate support ($M_{cr,support}$) equals $\Delta M_{support,2} + \Delta M_{support,1}$ and the cracking moment in the span ($M_{cr,span}$) equals $\Delta M_{span,2} + \Delta M_{span,1}$. Both the cracking moment in the span and at the mid-support is taken equal (see Eq. 2.19).

Eq. 2.37 can be rewritten as:

$$m_t = \frac{\left(d - \frac{1}{3}x_{e,span}\right)A_{support,s}E_s + (h - \frac{1}{3}x_{e,span})A_{support,f}E_f\left(\frac{h - x_{e,support}}{d - x_{e,support}}\right) - \frac{M_{cr}}{\varepsilon_{sy}}}{\left(d - \frac{1}{3}x_{e,span}\right)A_{span,s}E_s + (h - \frac{1}{3}x_{e,span})A_{span,f}E_f\left(\frac{h - x_{e,span}}{d - x_{e,span}}\right) - \frac{M_{cr}}{\varepsilon_{sy}}} \quad (2.38)$$

with: d : the effective depth of the critical cross-section
h : the total depth of the critical cross-section
ε_{sy} : the yield strain of the internal steel reinforcement

and can be transformed into the following approximate equation:

$$m_t = \frac{d^2A_{support,s}E_s + h^2A_{support,f}E_f - M_{cr}d/\varepsilon_{sy}}{d^2A_{span,s}E_s + h^2A_{span,f}E_f - M_{cr}d/\varepsilon_{sy}} \quad (2.39)$$

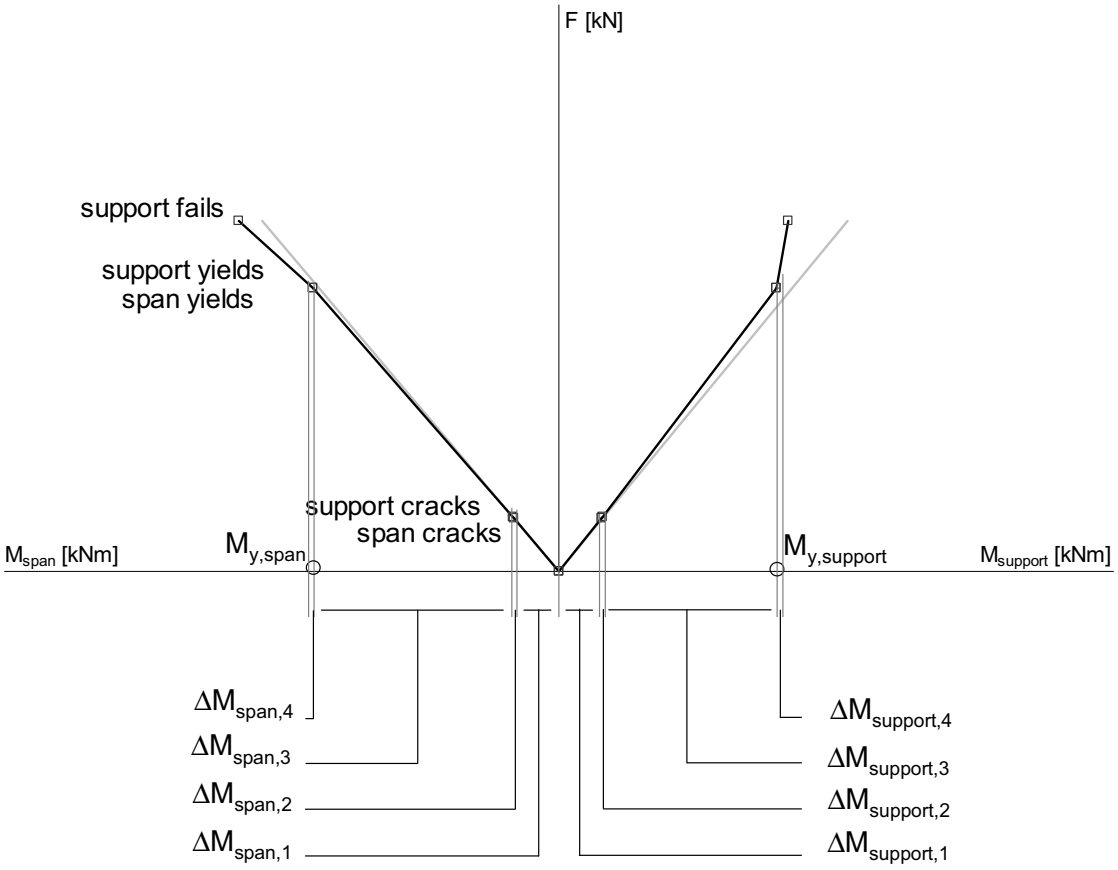

Fig. 2.22: Different subdivisions of the moment redistribution

Eq. 2.37 or 2.39 is derived easily from the moment redistribution graph, as presented in Fig. 2.22 and has to be interpreted as follows:

- If the moment distribution ratio in the fully cracked stage (m_3) is larger than the transition value (m_t) mentioned in Eq. 2.37 ($m_3 > m_t$), the critical cross-section at the mid-support yields first.
- If the moment distribution ratio in the fully cracked stage (m_3) is lower than the transition value (m_t) mentioned in Eq 2.37 ($m_3 < m_t$), the critical cross-section in the span yields first.

2.2.4 Simplifications

In applying the theoretical analysis as explained above, several simplifications have been introduced. Firstly, there is the assumption of three zones with each a constant bending stiffness over the length of these zones (see $K_{support}$ and K_{span} in Fig. 2.9). This bending stiffness is determined by the bending stiffness of the critical cross section in each particular zone (critical cross section = cross section where a maximum moment is noticed). In reality, no constant bending stiffness will be noticed. For example, after yielding of the critical cross section, each zone is characterized by yielding, cracked and uncracked sections. This results in reality, in a variable bending stiffness over the length of the sagging or hogging zone, which is not taken into account in the model presented above.

Secondly, in case of yielding of the internal reinforcement at the intermediate support, a rotation of the beam at this intermediate support will occur. Because these rotations are rather small, the influence of these rotations can be neglected, which is confirmed by means of calculations.

A third simplification is the used stress-strain model for concrete and steel reinforcement. As can be seen in Fig. 2.6 and Fig. 2.7, both materials are represented by a bilinear stress-strain curve.

Despite these simplifications which are introduced in the model, a good agreement is noticed between the analytical moment redistribution graphs and the experimental redistribution graphs (see further: section 3). Hence it is concluded that the assumed simplifications have a limited influence on the analytical moment redistribution graphs [15].

2.3 Theoretical approach for 2-span beams by the non-linear model

In this theoretical study, the non-linear theory, as explained in section 2.2 and in Appendix A, is applied to different 2-span beams in order to obtain the non-linear moment redistribution curves. In this study, the same concrete beam as treated in Fig. 2.1 is considered. The length of one span equals 5 meter and the parameter λ equals 2/3. The total depth of the beam equals 400 mm and the width 200 mm. The material characteristics are given in Table 2.2. In this theoretical study, for simplicity reasons the dead weight of the beam is not taken into account. In the analytical verification of the experimental tests mentioned further in section 3, the dead weight of the beam will be taken into account.

As can be seen in Table 2.8, three different reference beams are considered, each with a specific internal reinforcement ratio (ρ_s). The first configuration has the internal reinforcement as shown in Fig. 2.23 calculated according the linear elastic moment distribution (m_{el}). The second beam has a low internal

reinforcement ratio in the spans and a high concentration of reinforcement above the mid-support (Fig. 2.24). At last, a beam is considered with a high amount of internal reinforcement in the spans and a low reinforcement ratio at the mid-support (Fig. 2.25).

Table 2.8: Used steel reinforcement ratios in analytical study

Configuration	Mid-support ($\rho_{s,support}$)	Span ($\rho_{s,span}$)
1	0.78 %	0.78 %
2	1.43 %	0.53 %
3	0.31 %	0.95 %

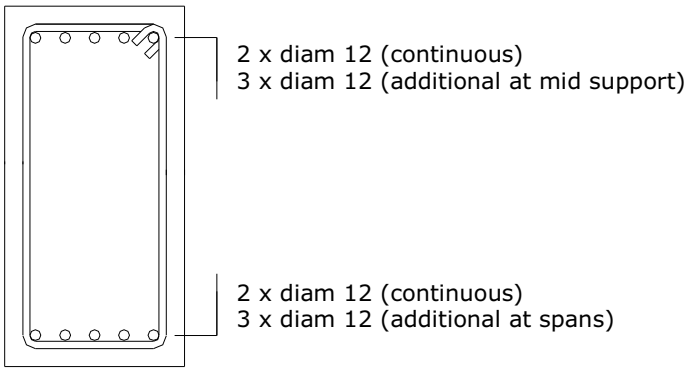

Fig. 2.23: Configuration 1 of internal steel reinforcement

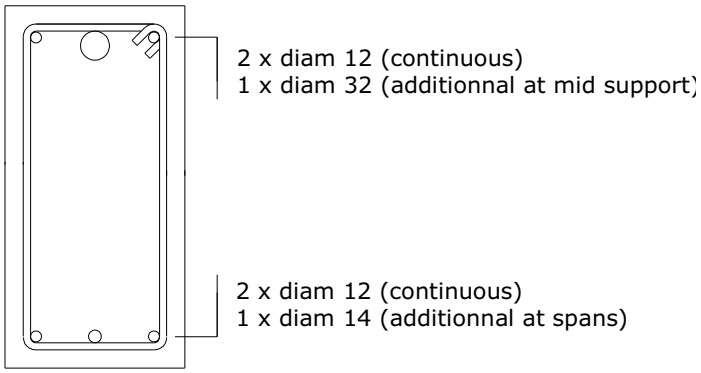

Fig. 2.24: Configuration 2 of internal steel reinforcement

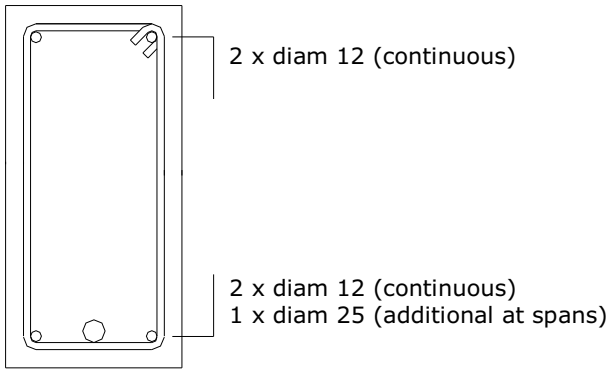

Fig. 2.25: Configuration 3 of internal steel reinforcement

As external reinforcement ratios (ρ_f), four different cases are investigated for each reference beam (Table 2.9): case A, the two-span beam without external reinforcement; case B, the beam with FRP EBR at top of the mid-support and at the soffit of the spans; case C, the beam with FRP EBR only in the spans and case D the beam with FRP EBR only at the top of the mid-support. The dimensions of the FRP laminates are: t_f = 1 mm and w_f = 100 mm. The length of the laminates at the soffit of the span is taken equal to 3750 mm, the length of the laminates at top of the mid-support is taken equal to 5000 mm (Fig. 2.26).

The lengths of the laminates are chosen in such a way they cross the point of contraflexure (location where the moment equals zero). As noted in Chapter 3, two out of the four debonding mechanisms can be avoided by enlarging the laminate beyond the point of contraflexure.

Table 2.9: Different used configurations of externally bonded FRP reinforcement (ρ_f)

Case	Mid-support ($\rho_{f,support}$)	Span ($\rho_{f,span}$)
A	-	-
B	0.13 %	0.13 %
C	-	0.13 %
D	0.13 %	-

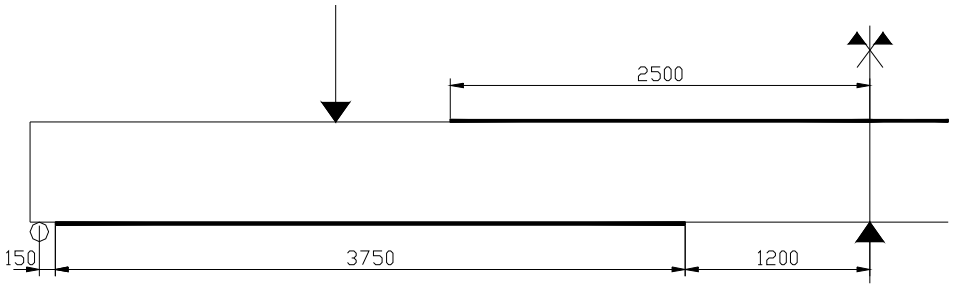

Fig. 2.26: Lengths of FRP-laminates used in analytical study

The results of the strengthening effect and the failure aspects are summarized in Table 2.10. Both the ultimate states, assuming full composite action (no bond loss) and assuming possible debonding mechanisms are considered in this table. In case failure is obtained by debonding of the laminate, the row in the table is

marked in grey. In this chapter no further elaboration of these debonding mechanisms is given. For this, reference is made to Chapter 3.

The moment redistribution of all different configurations is shown in Fig. 2.27 to Fig. 2.38. As explained in section 1.2, these graphs give the span moment M_{span} and the mid-support moment $M_{support}$ at the critical cross-sections (where the moment is maximum), as a function of the acting point load F. In each graph a linear curve and a non-linear curve is given which represents the moment distribution calculated by the classic theory and the non-linear theory respectively. In some graphs also a horizontal dashed line is observed. This line represents the ultimate load in case debonding failure is governing.

In the following sections, the different configurations for each case are explained.

Table 2.10: Results of analytical study

Configuration	Ult. load (excl. debond.) [kN]	Strength. ratio (excl. debond.)	Ult. load (incl. debond.) [kN]	Strength. ratio (incl. debond.)	Failure aspect
1 – A (ref.)	110.9	1.00	110.9	1.00	Concrete crushing
1 – B	223.8	2.02	156.8	1.41	Concrete rip-off
1 – C	165.7	1.49	143.2	1.29	Concrete rip-off
1 – D	142.2	1.28	142.2	1.28	Concrete Crushing
2 – A (ref.)	108.1	1.00	108.1	1.00	Concrete Crushing
2 – B	209.5	1.94	152.6	1.41	Crack bridging
2 – C	178.8	1.65	147.8	1.36	Concrete rip-off
2 – D	128.5	1.19	128.5	1.18	Concrete Crushing
3 – A (ref.)	106.9	1.00	106.9	1.00	Concrete Crushing
3 – B	220.3	2.06	143.8	1.34	Crack bridging
3 – C	141.0	1.32	112.3	1.05	Concrete rip-off
3 – D	148.3	1.39	130.4	1.22	Crack bridging

2.3.1 1st configuration: $\rho_{s,support}$ = 0.78 % and $\rho_{s,span}$ = 0.78 %

The calculated stiffness and moment redistribution ratios for all cases of the first configuration are given in Table 2.11. A bending stiffness ratio k_3 is obtained which is similar to the moment distribution ratio m_1 (= m_{el}). Hardly any moment redistribution is expected until the first critical cross-section starts to yield. This result is also noticed in Fig. 2.27 to Fig. 2.30, in which it can be observed that the moment redistribution curve follows quite well the linear elastic moment distribution.

In cases A and B (shown in Fig. 2.27 and Fig. 2.28 respectively) the entire moment distribution is quasi similar to the linear curve calculated by the elastic theory and no plastic hinges are observed. This observation is confirmed by Table 2.11 in which it is noticed that both bending stiffness ratios k_3 and k_5 are similar to m_1 (=m_{el}). Moreover, in the graphs of cases A and B it can be observed that span and mid-support start to yield at nearly the same moment. Nevertheless the span starts yielding first in both cases. By looking at Table 2.11, the same result is expected because the bending stiffness ratios m_3 of both cases are quasi

similar but smaller than the value noticed in the last column of Table 2.11 (values of m_t).

In case C, by using FRP EBR only in the spans, a plastic hinge is formed at the mid-support (vertical line in Fig. 2.29 after yielding of the internal reinforcement at the mid-support). By comparing the value of m_3 (= 0.867) and the value of m_t (= 0.818), found in Table 2.11, it is indeed expected that the mid-support starts yielding first. Although the spans start to yield shortly afterwards, almost all additional loads are taken by the spans, by means of the FRP. Furthermore in Table 2.11 for case C, a bending stiffness ratio k_5 can be noticed, which differs a lot from the linear elastic moment distribution value m_{el}. This observation results in the expectation of a considerable moment redistribution, once the critical cross-sections start yielding. This also is noticed in Fig. 2.29.

Case D (Fig. 2.30) is similar to case C, whereby the plastic hinge is formed in both spans and additional loads are taken by the strengthened mid-support. Also in this case, a considerable moment redistribution is observed after yielding of the critical cross-sections. This is related to the fact that k_5 differs a lot from m_1 (= m_{el}), as indicated in Table 2.11 for case D.

Table 2.11: Critical bending stiffness ratios k and moment distribution ratios m for configuration 1

	k_1	m_1 (=m_{el})	k_3	m_3	k_5	m_5	m_t Eq. 2.39
case A	1.000	0.972	1.000	0.972	1.000	0.972	1.000
case B	1.000	0.972	1.000	0.972	1.000	0.972	1.000
case C	0.961	0.951	0.812	0.867	0.030	0.155	0.818
case D	1.040	0.994	1.231	1.092	33.087	9.676	1.223

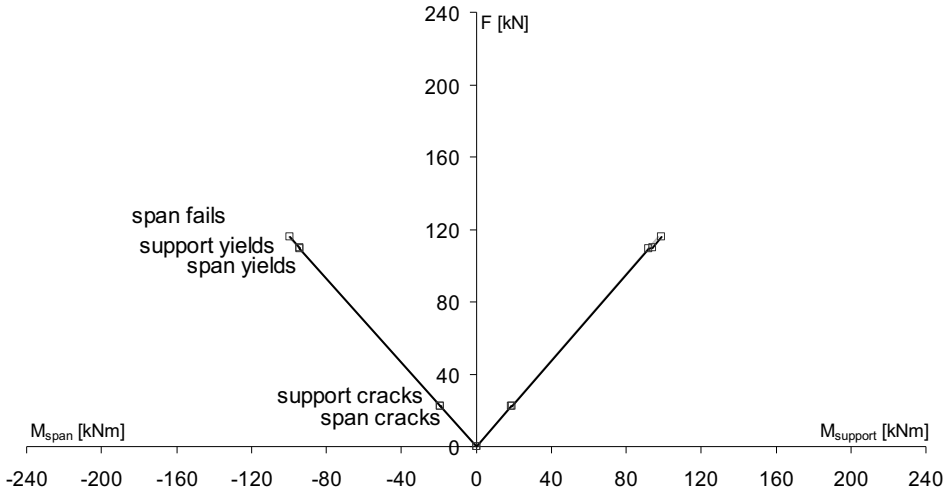

Fig. 2.27: Case A: moment redistribution without strengthening

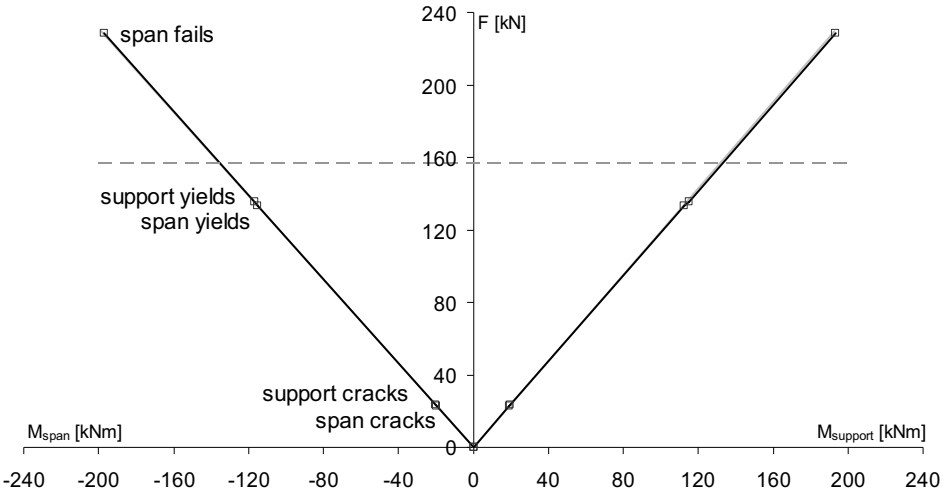

Fig. 2.28: Case B: moment redistribution with FRP EBR in the spans and the mid-support

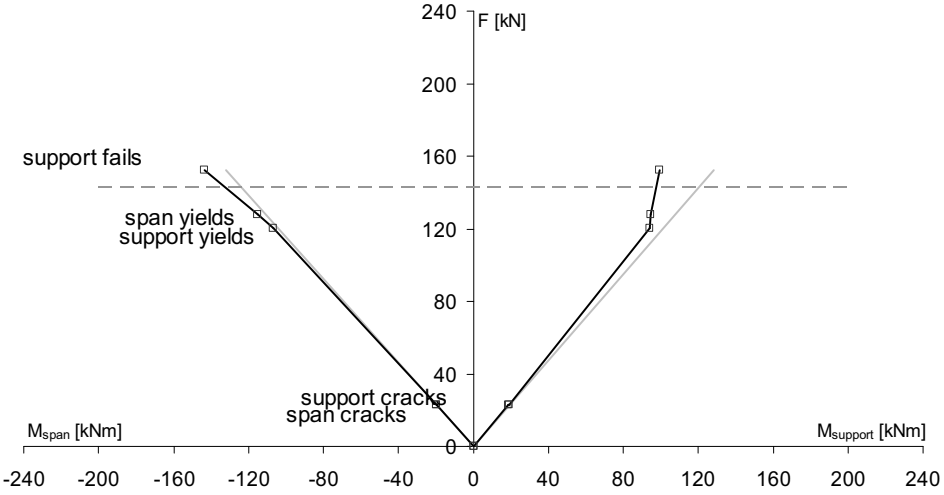

Fig. 2.29: Case C: moment redistribution with FRP EBR at the soffit of the spans

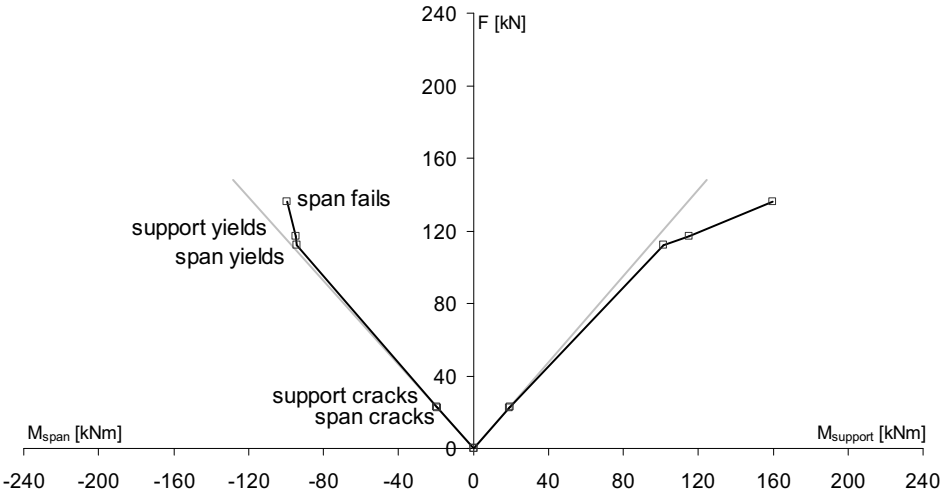

Fig. 2.30: Case D: moment redistribution with FRP EBR at top of the mid-support

2.3.2 2nd configuration: $\rho_{s,support}$ = 1.43 % and $\rho_{s,span}$ = 0.53 %

For the second configuration, the span yields first in all cases which is also indicated in Table 2.12: the values of m_3 are smaller than the values of m_t. This results in first yielding of the spans. Moreover in Table 2.12 also a considerable moment redistribution is expected for all cases. This results from the observed bending stiffness ratios k_3 and k_5, which differ a lot from the linear elastic moment distribution ratio m_{el} (= 0.972).

In the reference beam (case A, Fig. 2.31) the first plastic hinges occur in the spans from the moment the spans start to yield. All additional loads are taken up by the mid-support. By using FRP EBR at both locations (case B, Fig. 2.32), it is noticed that after yielding of both critical cross-sections the moment redistribution is parallel to the linear elastic moment distribution. This results also from factor k_5 (= 0.905) which is quite similar to m_{el} (= 0.972). In this case, additional load is taken by the FRP at both the spans and the mid-support.

In case C (strengthened in the spans, Fig. 2.33) it is observed that the first plastic hinge is formed at the mid-support instead of the spans, due to the strengthening of the latter. Although the strengthened spans still start to yield first, the FRP allows the spans to continue resisting the additional load. At increasing load, when the mid-support starts to yield, a plastic hinge is formed at this mid-support.

In case D (Fig. Fig. 2.34) the first plastic hinge formation is similar to case A but extends to a higher load level due to the additional moment redistribution at the strengthened mid-support zone. This strengthening technique (strengthening of the zone with high concentration of internal reinforcement) is not giving a significant strengthening ratio (see Table 2.10), as the first plastic hinge in the unstrengthened configuration is further exploited in the strengthened configuration.

Table 2.12: Critical bending stiffness ratios k and moment distribution ratios m for configuration 2

	k_1	m_1 (=m_{el})	k_3	m_3	k_5	m_5	m_t Eq. 2.39
case A	1.066	1.007	2.528	1.654	4.153	2.235	2.711
case B	1.063	1.006	2.021	1.450	0.905	0.920	2.285
case C	1.024	0.985	1.817	1.363	0.074	0.246	2.036
case D	1.107	1.029	2.812	1.762	50.653	13.747	3.042

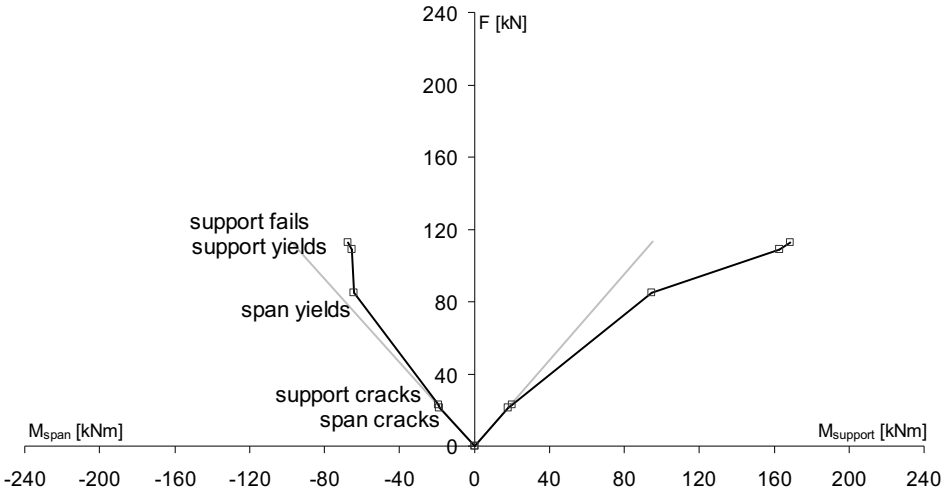

Fig. 2.31: Case A: moment redistribution without strengthening

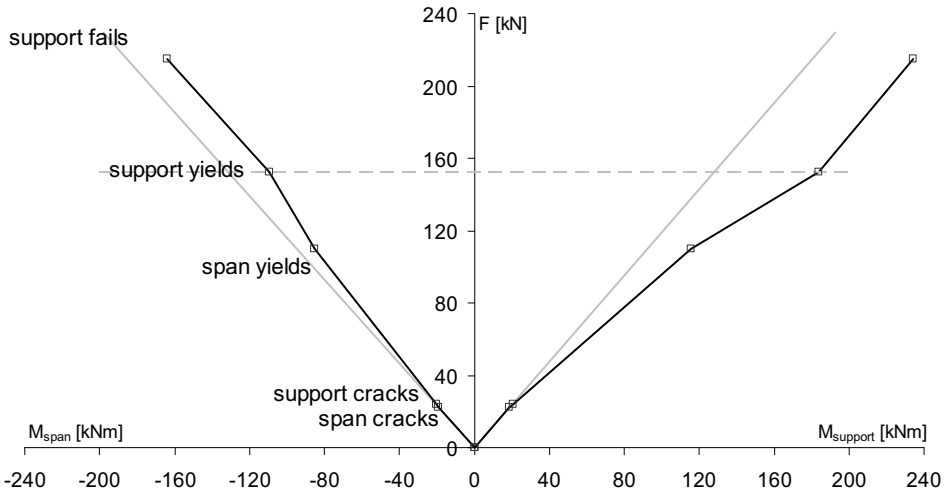

Fig. 2.32: Case B: moment redistribution with FRP EBR in the spans and the mid-support

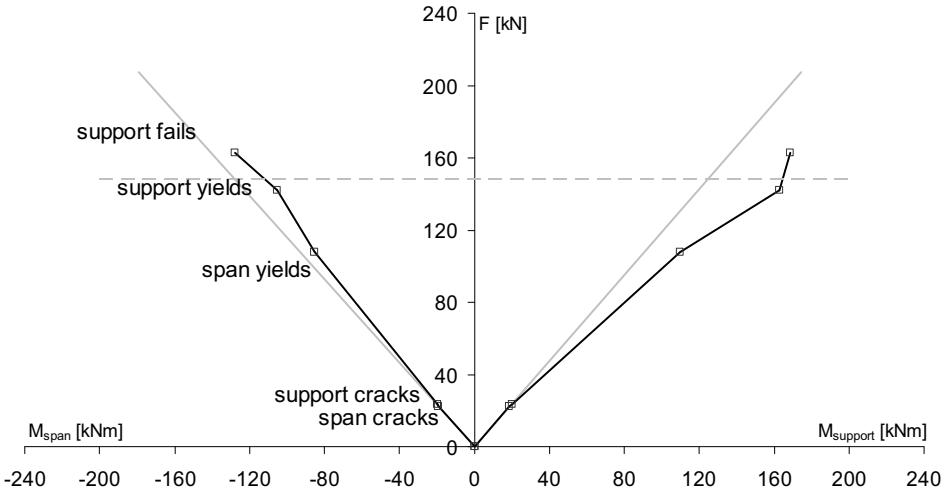

Fig. 2.33: Case C: moment redistribution with FRP EBR at the soffit of the spans

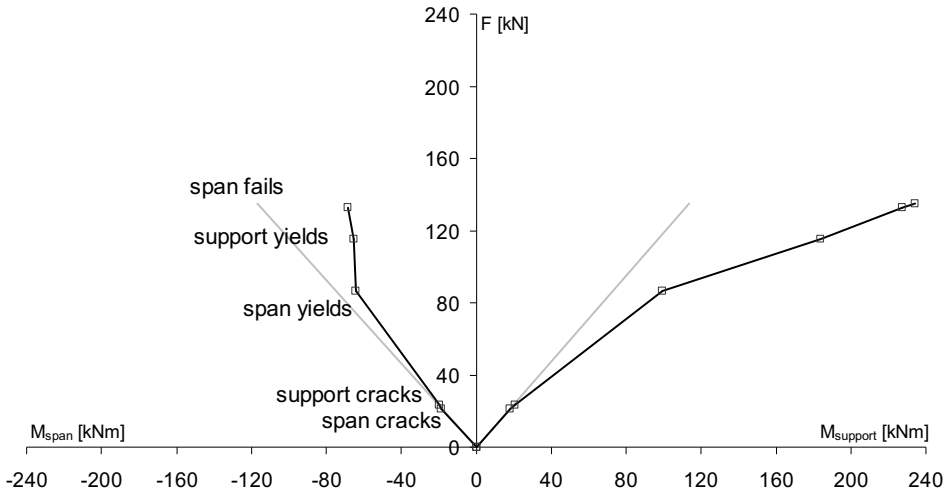

Fig. 2.34: Case D: moment redistribution with FRP EBR at top of the mid-support

2.3.3 3rd configuration: $\rho_{s,support}$ = 0.31 % and $\rho_{s,span}$ = 0.95 %

For this last configuration, the mid-support yields first in all cases which is also indicated in Table 2.13: the values of m_3 are larger than m_t. Moreover in Table 2.12 also a considerable moment redistribution is expected for all cases. This results from the observed bending stiffness ratios k_3 and k_5, which differ a lot from the linear elastic moment distribution ratio m_{el} (= 0.972).

The reference beam (case A, Fig. 2.35) is characterized by formation of a plastic hinge at the mid-support, from the moment the mid-support yields. Additional load is taken by the spans. By using FRP EBR at both locations (case B, Fig. 2.36) the same tendency is noticed as in the second configuration, namely after yielding of both critical cross-sections the moment redistribution is parallel to the linear elastic moment distribution. This is due to the fact that the factor k_5 (= 1.063) is quite similar to m_{el} (= 0.972) for case B. In this case, additional load is taken by the FRP at both the spans and mid-support.

In case C (strengthened in the spans, Fig. 2.37) the plastic hinge formation is similar to case A but extends to a higher load level due to the additional moment redistribution at the strengthened span zone. This strengthening technique (strengthening of the zone with high concentration of internal reinforcement) is not giving a significant strengthening ratio (see Table 2.10), as the first plastic hinge in the unstrengthened configuration is further exploited in the strengthened configuration.

In case D (Fig. 2.38) it is observed, similar to case C of the second configuration, that the plastic hinge has changed from location, due to strengthening of the mid-support. Although the strengthened mid-support still starts to yield first, the FRP allows the mid-support to continue resisting the additional load. At increasing load, when the spans start to yield, plastic hinges are formed in the spans.

Table 2.13: Critical bending stiffness ratios k and moment distribution ratios m for configuration 3

	k_1	m_1 ($=m_{el}$)	k_3	m_3	k_5	m_5	m_t Eq. 2.39
case A	0.944	0.942	0.260	0.471	0.294	0.502	0.329
case B	0.946	0.943	0.415	0.603	1.063	1.006	0.433
case C	0.908	0.922	0.220	0.431	0.012	0.097	0.278
case D	0.984	0.964	0.491	0.659	26.043	8.005	0.512

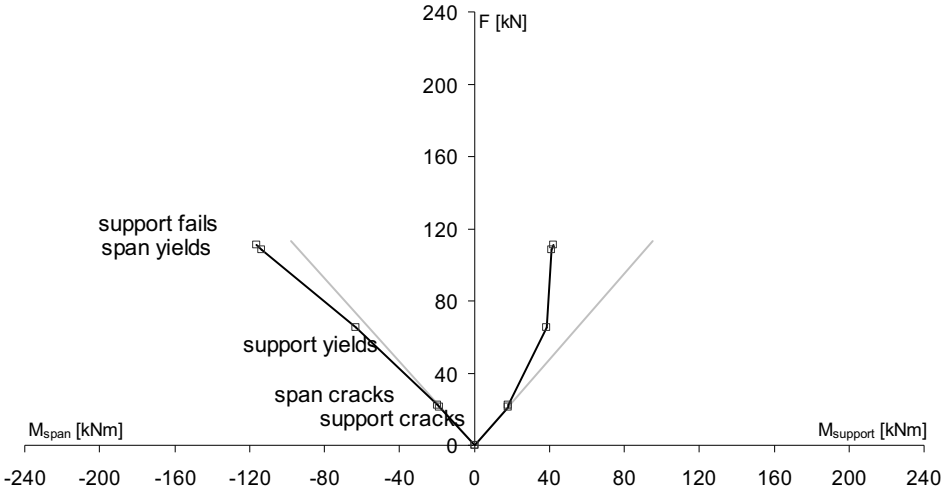

Fig. 2.35: Case A: moment redistribution without strengthening

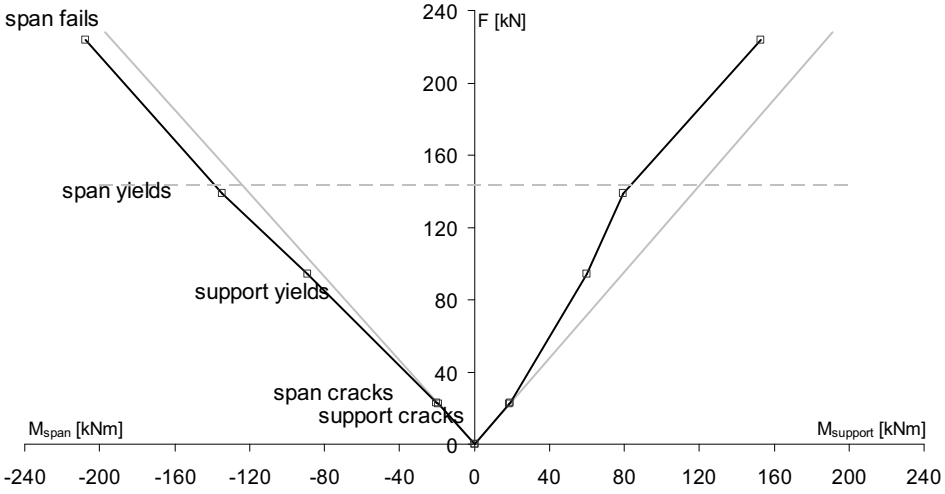

Fig. 2.36: Case B: moment redistribution with FRP EBR in the spans and the mid-support

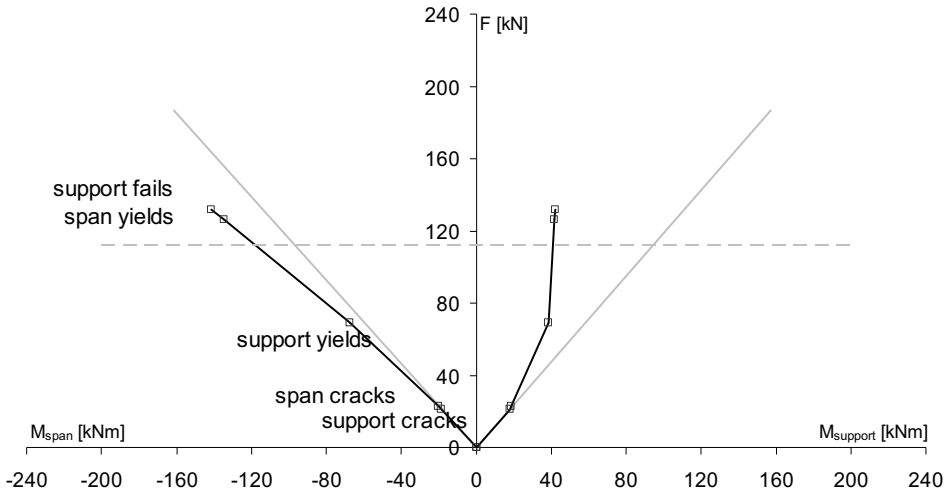

Fig. 2.37: Case C: moment redistribution with FRP EBR at the soffit of the spans

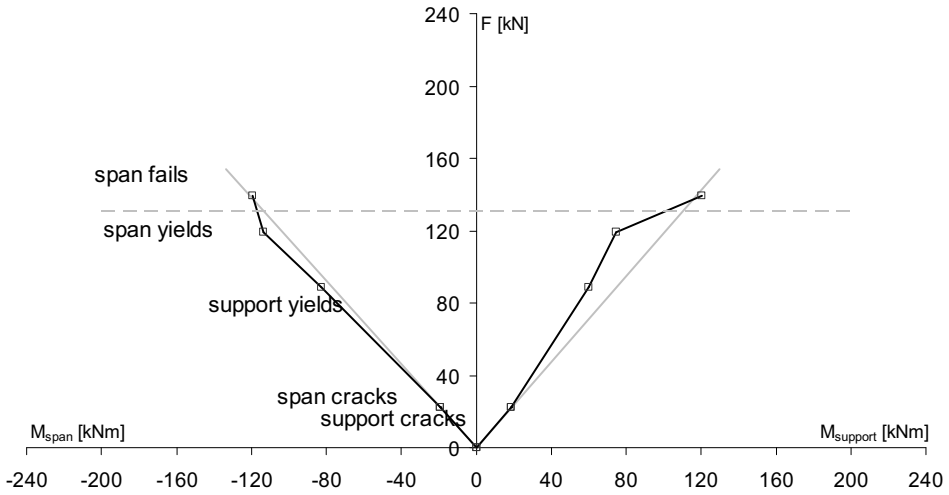

Fig. 2.38: Case D: moment redistribution with FRP EBR at top of the mid-support

3 Non-linear behaviour of strengthened continuous beam - Experimental analysis

3.1 Overview of test program

3.1.1 Test set-up

For the experimental study of the strengthened continuous beams, the used test configurations are based on a previous study concerning the non-linear behaviour of unstrengthened beams [12]. In this study eight different 2-span-beams were tested, each with a specific internal steel configuration. Despite of the different internal steel configurations, a similar failure load is obtained for all beams (see $F_{unstr,u}$ in Table 2.19). This relates to the internal steel configurations which were chosen in such a way that equation 2.40 (resulting from the plasticity theory, see Chapter 6) is giving equal results.

$$F_{u,plast} = M_{u,span}\frac{l}{ab} + M_{u,support}\frac{1}{b} \qquad (2.40)$$

In the experimental study, executed in the scope of this PhD, four 2-span-beams are tested. Both the dimensions and the internal reinforcement ratios in this experimental study are chosen equal to those used in the study [12, 14]. Given the results of these tests, no additional unstrengthened reference beams are included in this test program.

The total depth of the continuous concrete beams equals 400 mm and the width equals 200 mm (see Fig. 2.39). The continuous beams exist of two spans, each with a span length of 5 m. The beams are loaded with one point load in each span. The locations of the point loads are at a distance of 3 meter from the mid-support and 2 meter from the end supports. Hence, a equals 2 m, b equals 3 m and $\lambda = 2/3$ (referring to Eq. 2.10). Remark that this test set-up is equal to the beam configuration used in the theoretical approach (see section 2.3).

Concerning the reinforcement ratios reference is made to Fig. 2.39 and Table 2.14. As can be noticed in this table, four full-scale continuous beams are tested each with a different configuration of internal and external reinforcement. For the external reinforcement ratios, CFRP laminates with section 100 mm x 1.0 mm are applied in the zones with low internal reinforcement.

Beam CB1 is reinforced with a small amount of internal reinforcement in the spans and a large amount at the mid-support. To compensate the small amount in the spans, externally bonded reinforcement (EBR) is applied only in the spans. This configuration is equal to 'Configuration 2 - case C' in the theoretical approach.

A second beam is tested (CB2) with a large amount of internal reinforcement in the spans and a small amount at the mid-support (opposite to the first tested beam CB 1). As external reinforcement, EBR is only applied at the top of the beam above the mid-support (see Table 2.14). This configuration is equal to 'Configuration 3 - case D' in the theoretical approach.

The third beam (CB3) has internal reinforcement based on the linear elastic theory, which is similar to 'Configuration 1' of the theoretical approach. In this case almost the same amount of internal reinforcement is used in the spans and at the mid-support (as follows from the linear elastic theory). As external reinforcement, laminates are glued on top of the beam above the mid-support as well as at the soffit of the beam in the spans (see Table 2.14). This configuration is equal to 'Configuration 1 – case B' in the theoretical approach.

Finally a fourth beam is tested. Due to technical problems during testing of CB2, this specific configuration is repeated in a fourth tested beam (CB 4). Compared to the configuration of CB2, one change is made. The large amount of internal reinforcement in the spans is taken somewhat smaller, in order to obtain earlier yielding in the spans and, related to this, earlier yielding at the mid-support.

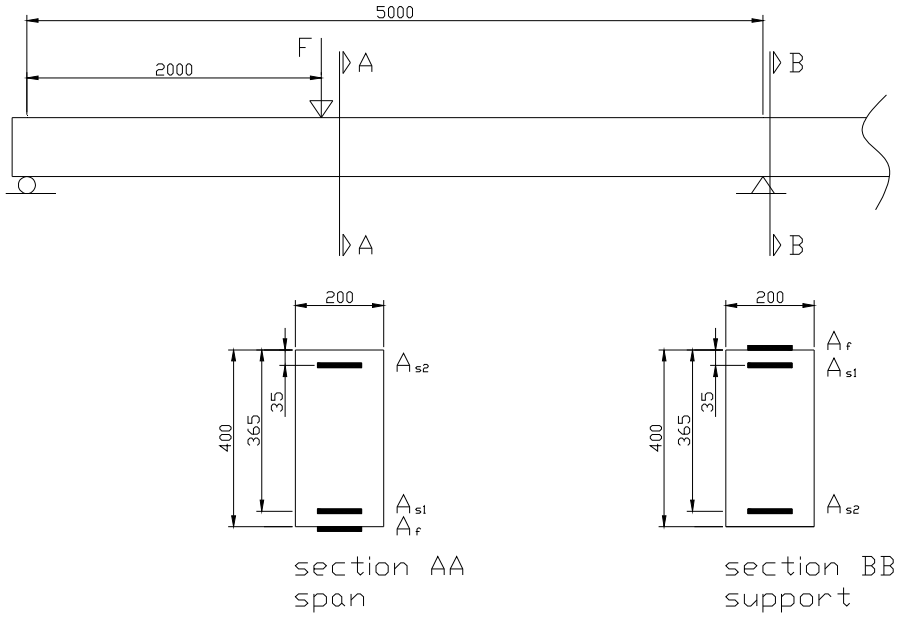

Fig. 2.39: Location of reinforcement sections over the length of the beam

Table 2.14: Reinforcement ratios used at mid-support and span

	Mid-support (related to section A_{s1} and A_f)			Span (related to section A_{s1} and A_f)		
	Steel reinf. ratio	FRP reinf. ratio	Eq. reinf. Ratio	Steel reinf. ratio	FRP reinf. ratio	Eq. reinf. Ratio
	$\rho_{s,support}$	$\rho_{f,support}$	$\rho_{eq,support}$	$\rho_{s,span}$	$\rho_{f,span}$	$\rho_{eq,span}$
CB 1	1.43 %	0.00 %	1.43 %	0.53 %	0.13 %	0.65 %
CB 2	0.31 %	0.13 %	0.43 %	0.99 %	0.00 %	0.99 %
CB 3	0.67 %	0.13 %	0.79 %	0.75 %	0.13 %	0.87 %
CB 4	0.31 %	0.13 %	0.43 %	0.75 %	0.00 %	0.75 %

The lengths of the laminates are chosen in such a way they cross the point of contraflexure (location where the moment equals zero) (see Fig. 2.26). As noted in Chapter 3, two out of the four debonding mechanisms can be avoided by extending the laminate beyond the point of contraflexure. In the spans, this results in a laminate in the spans with a length equal to 3750 mm, which is

applied as close as possible to the end-supports (to avoid anchorage failure near to the end supports). The laminate used on top of the mid-support has a length equal to 5000 mm and is applied centrically with respect to the mid-support.

3.1.2 Materials and specimen preparation

To avoid additional secondary moments in the continuous beams, introduced by non concordant supports, the beams are cast on the final supports. The tested beams are supported by one hinging support at the location of the mid-support and two roller supports (horizontally movable) at the location of the end-supports.

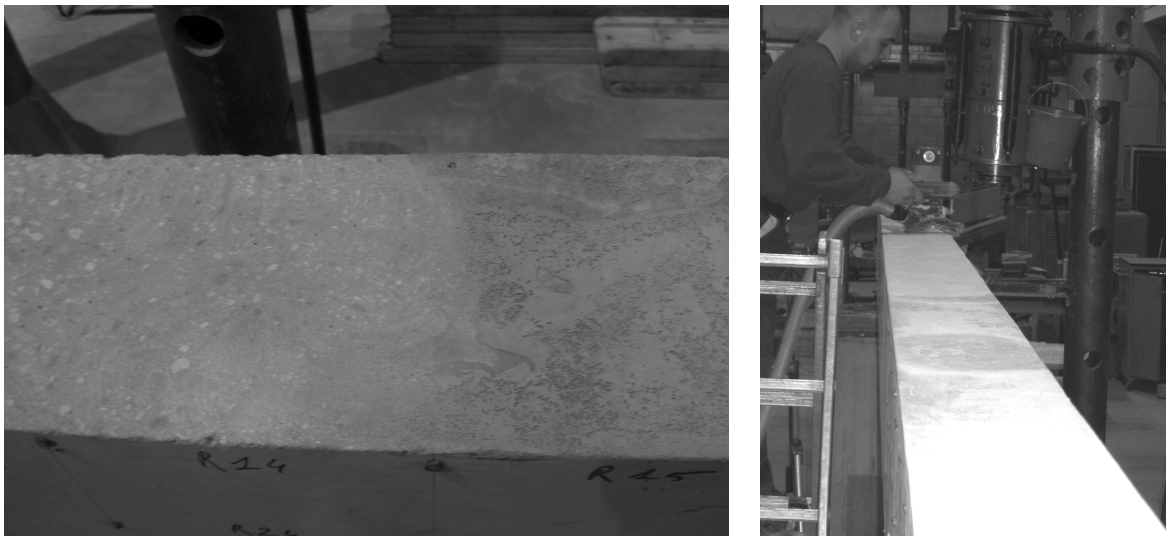

Fig. 2.40: Preparation of concrete surface before application of FRP-laminates

Fig. 2.41: Application of the FRP laminates

One day after casting, the side panels of the formwork are removed. Seven days after casting, the bottom panel of the formwork is removed and the beams

are submitted to their dead weight. Moreover, during these first seven days the concrete specimens are covered in a plastic foil, in order to avoid extensive drying.

At an age of 14 days, the FRP laminates are glued on top and/or soffit of the beams. First the concrete surface is roughened by means of a grinding disk (see Fig. 2.40). Further the laminates are covered with a two-component epoxy. To obtain a constant thickness of the epoxy layer, appropriate gluing equipment is used (see Fig. 2.41). Finally the laminates are pushed against the roughened concrete surface until the epoxy is squeezed out of the surface, in order to obtain a perfect contact between the concrete surface and the laminate.

The composition (per m³) of the concrete, used for all two-span beams is given in Table 2.15. Tested properties of the fresh concrete include slump, flow test and density (see Table 2.16). At an age of 28 days the properties of the hardened concrete are determined by means of standard tests [6, 16]. The mean compression strength $f_{c,cub}$ determined on cubes with side 150 mm, f_{cm} determined on cylinders (h = 300 mm and Ø = 150 mm) and the mean flexural tensile strength f_{ctf} determined on prisms (150 mm x 150 mm x 600 mm) are given in Table 2.17.

Table 2.15: Concrete mix of 1 m³

gravel	8/16	1120 kg
	2/8	190 kg
sand	0/5	655 kg
cement	CEM I 52,5 N	300 kg
water		165 l

Table 2.16: Properties of fresh concrete

	Slump [mm]	Flow test	Density [kg/m³]
CB1	50	1.68	2406
CB2	39	1.67	2388
CB3	31	1.45	2369
CB4*	-	-	-

* No test results are available

Table 2.17: Properties of hardened concrete

	$f_{c,cub}$ [N/mm²]	f_{cm} [N/mm²]	f_{ctf} [N/mm²]
CB1	54.7	48.9	3.22
CB2	53.7	44.4	2.74
CB3	51.9	47.1	2.59
CB4	45.6	42.1	2.45

3.1.3 Measurements

During the tests both manual and electronic measurements were performed as is indicated in Fig. 2.42. Electronic measurements are executed by a dedicated data acquisition system (type system 5000) at a sampling rate of 2-4 Hz during the loading stages.

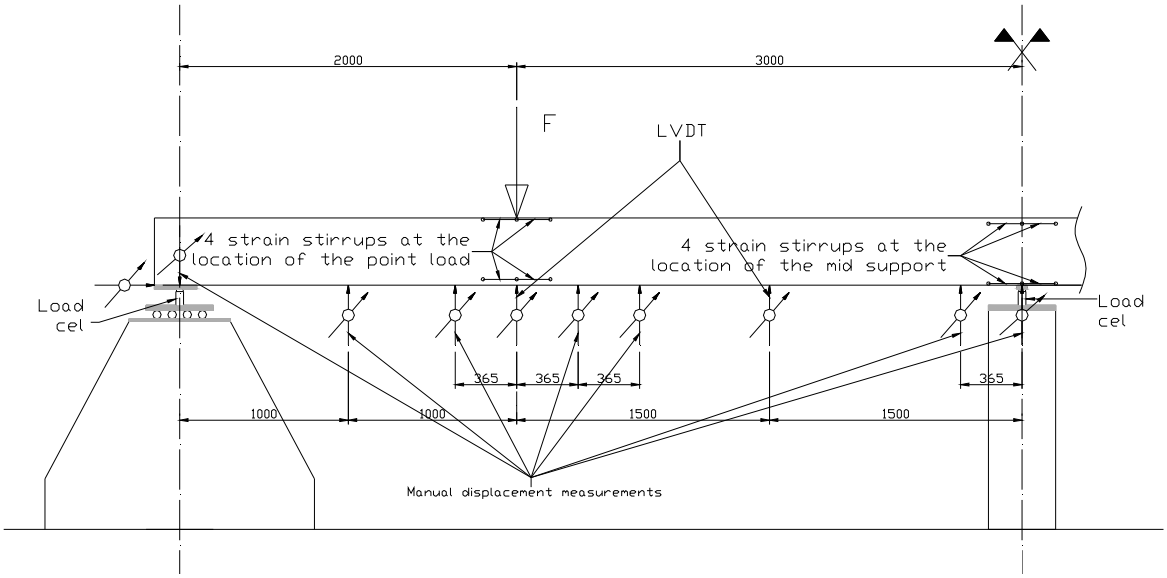

Fig. 2.42: Measurement equipment used during the experimental tests

Under each support two load cells are placed in order to obtain the reaction forces at the supports (see Fig. 2.43). The load cells at the location of the end-support have a capacity of 150 kN while the load cells at the location of the mid-support have a capacity of 300 kN. The applied load is recorded by means of a pressure transducer.

By means of the measured reactions, the applied load and the moment equilibrium (ME), the experimental moment distribution over the length of the beam can be evaluated.

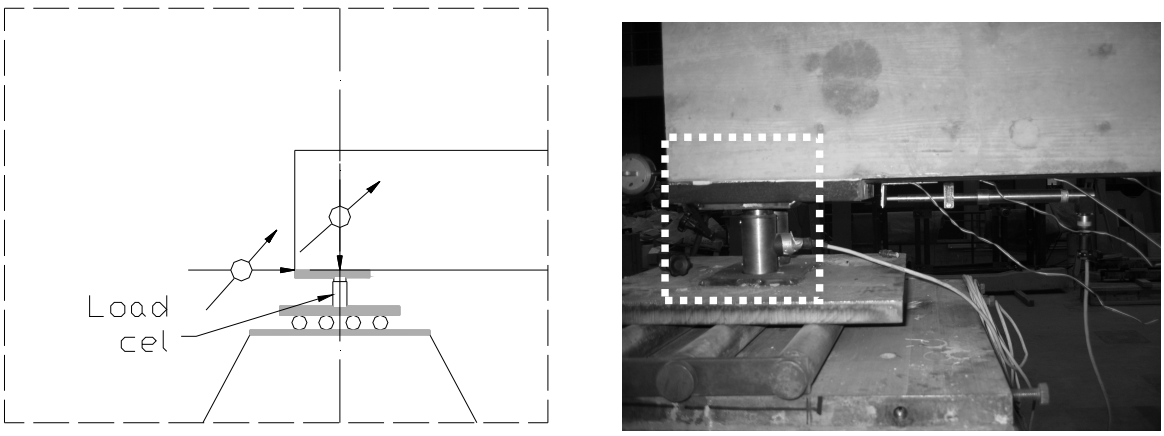

Fig. 2.43: Load cells at the location of a support: measurement of reaction force

The deflection of the beam is recorded electronically by means of LVDT's (Linear Variable Displacement Transducer) (see Fig. 2.44). In total four LVDT's are used: two per span, one at the location of the point load and one between the point load and the mid-support (Fig. 2.42). Furthermore, the displacement is also measured by means of manual displacement gauges at 19 locations.

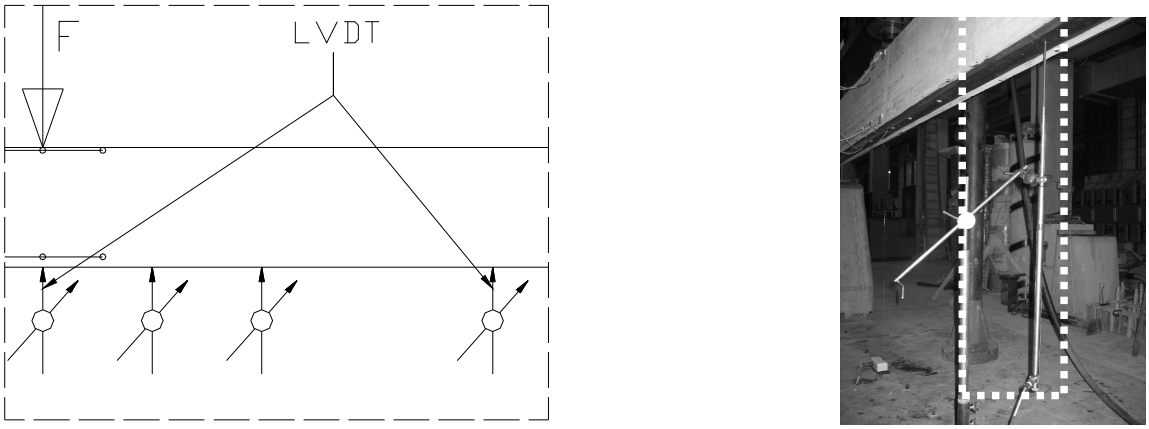

Fig. 2.44: LVDT (linear Variable Displacement Transducer): measurement of deflection

The strain in the critical cross-sections (at the point loads and at the mi-support) is measured electronically by means of strain stirrups. In each critical cross-section 4 strain stirrups are applied on one side of the beam. Two of them are measuring the strain of the concrete as close as possible to the level of the fibre with the maximum compressive strain. The other two strain stirrups are applied on a side face of the beam to record the concrete strain at the level of the internal steel reinforcement.

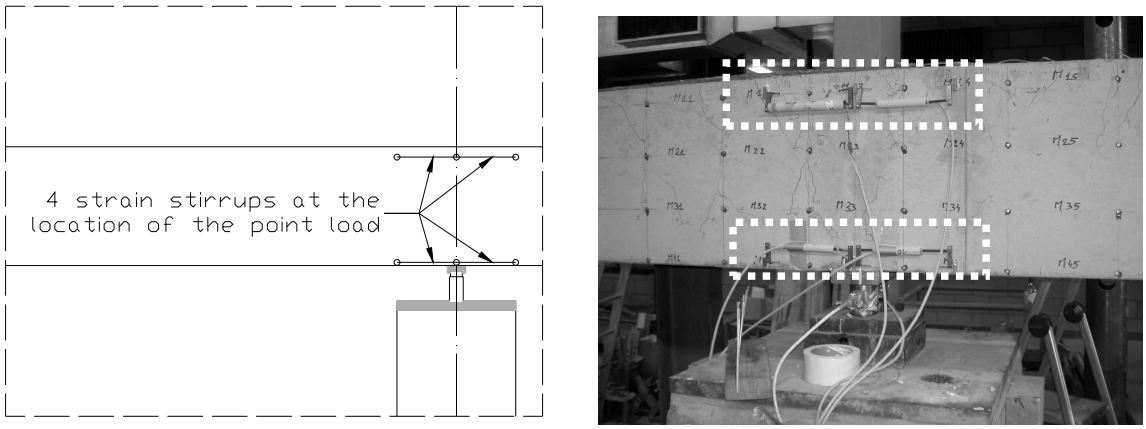

Fig. 2.45: Strain stirrups: measurement of strain

To measure the strain in the FRP laminates, strain gauges are glued on the laminates (see Fig. 2.46). Several strain gauges are used, to record strain distribution along the length of the laminate is obtained.

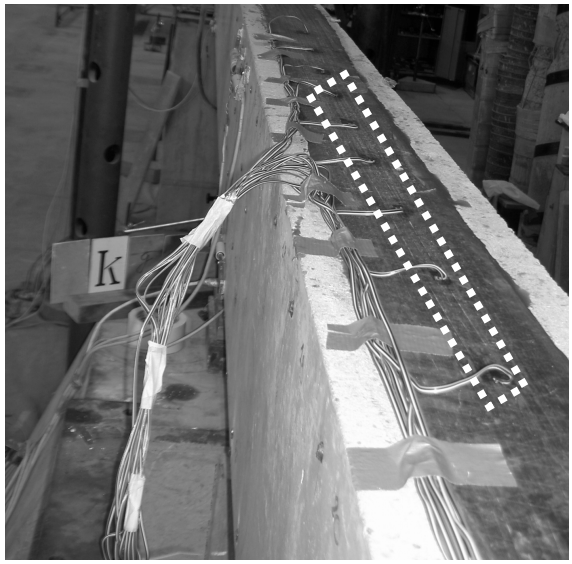

Fig. 2.46: Strain gauges glued on the FRP laminate

Finally, both the crack width and crack spacing are measured manually. The crack width is measured by means of a crack microscope with measuring scale 0.02 mm. The mean crack spacing is determined as the distance between the first and last crack in one zone divided by the number of cracks reduced with 1.

3.1.4 Loading scheme

At an age of 28 days, the static bending tests on the continuous beams are conducted by means of two hydraulic jacks, with a maximum capacity equal to 300 kN. At every step of 10 kN, the load is kept constant, in order to execute the manual measurements. At 80 % of the analytical obtained failure load, the beam is loaded continuously until failure.

3.2 Main test results

In this section the main experimental results are given. A more detailed discussion of the test results and analytical verification is given in section 3.3 (CB1), 3.4 (CB2), 3.5 (CB3) and 3.6 (CB4). Details on the analytical verification are given in Appendix A.

3.2.1 Moment distribution

The observed redistribution of each test beam is illustrated by means of two different graphs. Both type of graphs have been explained in detail in section 1.2. The first graph represents the span moment M_{span} and the mid-support moment $M_{support}$ at the critical sections (where the moment is maximum), in function of the acting point load F. For the tested beams, these graphs are shown in Fig. 2.50, Fig. 2.61, Fig. 2.72 and Fig. 2.83. In each graph four different curves concerning the moment distribution are given. First there is the linear curve which is the moment distribution calculated according to the elastic theory. Secondly, a non-

linear dashed curve is observed. This curve illustrates the non-linear moment distribution of the unstrengthened beam calculated according to the non-linear theory. In addition, there are two non-linear full-line curves, which represent the calculated and experimental non-linear moment distribution for the strengthened beam.

The second type of graph represents the moment redistribution factor δ for the mid-support (see Eq. 2.1) in function of the applied point load F. These graphs, are shown in Fig. 2.51, Fig. 2.62, Fig. 2.73 and Fig. 2.84. In each graph one linear curve (δ = 1) and two non-linear curves are observed. The linear curve represents the moment distribution factor calculated according to the linear elastic theory, for which δ = 1. The non-linear curves represent the calculated and experimental non-linear moment redistribution factor δ, in function of the applied point load F.

In Table 2.18 the maximum values of the redistribution factor δ_{max} are given for the four tested beams. Also the maximum moment redistribution is given.

Table 2.18: Maximum redistribution factors of tested beams (δ_{max})

	$\delta_{max,support}$	Max. redistribution
CB 1	1.32	31.5 %
CB 2	0.72	28.0 %
CB 3	0.87	12.7 %
CB 4	0.77	23.2 %

3.2.2 Ultimate loads

In Table 2.19, a comparison is made between the calculated ultimate loads of the unstrengthened test configuration ($F_{u,unstr}$) and the experimentally obtained failure loads ($F_{str,exp}$) of the strengthened beams. Besides the strengthening ratio is given. Remark that strengthened beams are characterized by debonding of the FRP laminate. This debonding is a specific phenomenon which is discussed further in Chapter 3.

Table 2.19: Overview of the ultimate and debonding loads of the continuous beams

	$F_{u,unstr}$ [kN]	$F_{str,exp}$ [kN]	Strengt. ratio
CB 1	124.3	152.8	1.24
CB 2	123.0	152.0	1.24
CB 3	118.7	170.5	1.44
CB 4	103.6	115.9	1.12

3.2.3 Strain at the critical cross-sections

In Table 2.20 the maximum concrete and FRP strains are given at the critical cross-sections under the left point load, at the mid-support and under the right point load. In this table absolute values of all strains are given. For the second beam no maximum values at the left point load were measured due to a problem with the data acquisition system.

From Table 2.20 it follows that for several cases the maximum strain in the FRP laminate is smaller than the maximum strain in the internal reinforcement. This phenomenon is noticeable in particular at the strengthened mid-supports, at which debonding of the laminates occurred.

Table 2.20: Overview of the maximum strains at the ultimate loads of the tested beams

		max. concrete strain	max. calculated strain at level of inter. reinf.	max. strain of external reinf.
CB1	Left point load	0.185 %	0.614 %	0.510 %
	Mid-support	0.122 %	0.442 %	-
	Right point load	0.151 %	0.501 %	0.563 %
CB2	Left point load	-	-	-
	Mid-support	0.108 %	0.669 %	0.458 %
	Right point load	0.150 %	0.351 %	-
CB3	Left point load	0.158 %	0.374 %	0.403 %
	Mid-support	0.117 %	0.665 %	0.406 %
	Right point load	0.178 %	0.496 %	0.437 %
CB4	Left point load	0.136 %	0.279 %	-
	Mid-support	0.076 %	0.534 %	0.418 %
	Right point load	0.126 %	0.272 %	-

3.2.4 Deflection

The maximum deflections can be found in Table 2.21. The entire curves of the deflection in function of the applied loads of CB1, CB2, CB3 and CB4 can be found in respectively Fig. 2.55, Fig. 2.66, Fig. 2.77 and Fig. 2.88. A comparison of these curves for CB1 till CB3 is given in Fig. 2.47.

Table 2.21: Measured maximum deflections at the position of the left and right point load

	Left point load [mm]	Right point load [mm]
CB1	20.4	24.9
CB2	16.1	13.1
CB3	19.2	17.9
CB4	23.4	22.0

In Fig. 2.47, for beams CB1, CB2 and CB3 it is noticed that the deflections follow a nearly similar curve. It can be concluded that a beam with low internal reinforcement ratio in a particular zone, which induces an early yielding of the steel reinforcement in this particular zone, does not result in excessively large deflections. This phenomenon is due to the higher stiffness of the other zones, which hinders the occurrence of large plastic deformations.

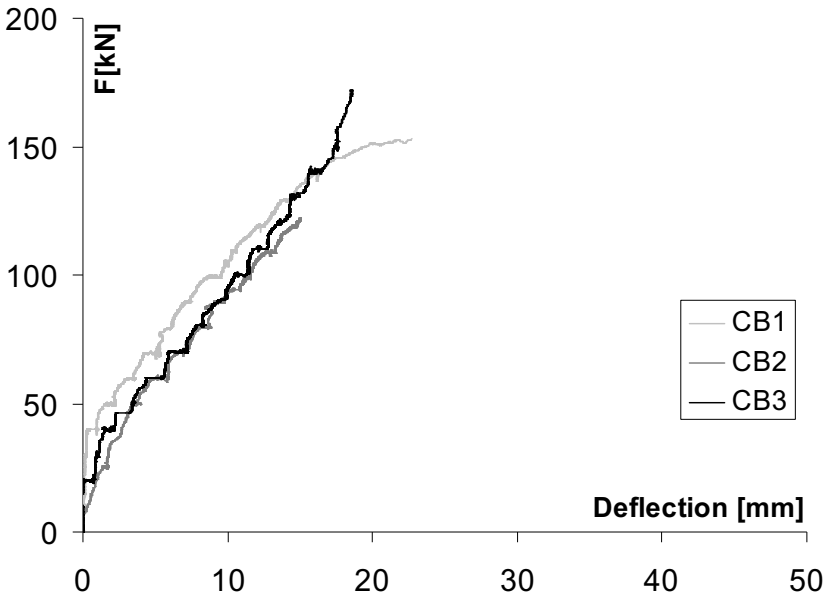

Fig. 2.47: Experimentally obtained deflections at the point loads of the two-span beams

3.2.5 Crack formation

In Table 2.22 and Table 2.23, an overview is given of the mean crack spacing and the mean crack width respectively at different zones of the tested beams at the last load step (= 80% of the calculated failure load). In this table, the shaded values are indicating the zones which are strengthened with FRP EBR.

Table 2.22: Overview of the mean crack spacings at different locations of the tested beams

	Left span zone [mm]	Mid-support [mm]	Right span zone [mm]
CB1	81.0	137.8	82.1
CB2	105.6	78.9	117.1
CB3	82.8	79.4	79.4
CB4	97.3	89.7	86.9

Table 2.23: Overview of the mean crack widths at different locations of the tested beams

	Left span zone [mm]	Mid-support [mm]	Right span zone [mm]
CB1	0.23	0.22	0.26
CB2	0.17	0.25	0.16
CB3	0.16	0.16	0.21
CB4	0.27	0.26	0.22

3.3 Continuous beam 1 (CB1)

3.3.1 Configuration

The first tested beam has internal reinforcement as shown in Fig. 2.48. The beam has low internal reinforcement ratio in the spans ($\rho_{s,span}$ = 0.53 %) and a high concentration of reinforcement above the mid-support ($\rho_{s,support}$ = 1.43 %). As external reinforcement, a CFRP laminate with a length of 3750 mm is applied in each span. The cross-section of the CFRP laminate equals 100 mm x 1.0 mm ($\rho_{f,span}$ = 0.13 %).

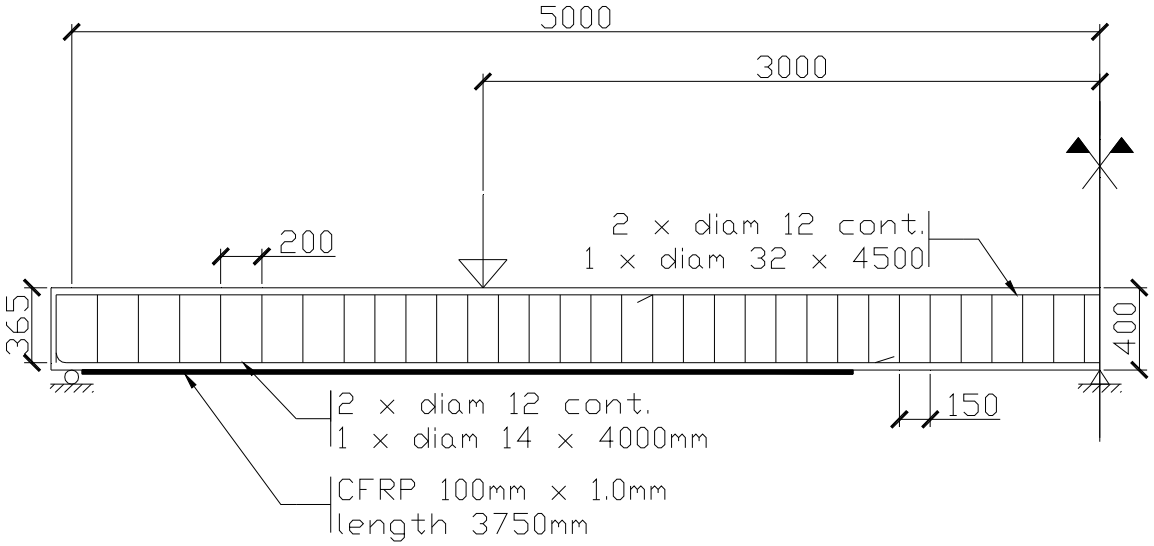

Fig. 2.48: Reinforcement configuration of CB1

The material properties are given in Table 2.24. These values result from standard tensile tests for the steel and FRP reinforcement [5, 7]. To determine the properties of the concrete, standard tests are conducted at the age of 28 days [6, 16].

Table 2.24: Material properties for CB1

	Concrete	CFRP	steel at span	steel at mid-supp.
Compres. strength (f_{cm})	46.0 N/mm²	-	-	-
Yield stress	-	-	601 N/mm²	474 N/mm²
Yield strain	-	-	0.28 %	0.23 %
Tensile stress	3.3 N/mm²*	2768 N/mm²	677 N/mm²	703 N/mm²
Failure strain	3.5 ‰ **	1.46 %	8.49 %	11.39 %
E-modulus	36 kN/mm²	190 kN/mm²	218 kN/mm²	210 kN/mm²

* Splitting test results and 3-point-bending tests results are converted to mean pure tensile strength according to EC2 [17]

** The failure strain of concrete is taken equal to 3.5 ‰, based on EC2 [17], as this value is not resulting from the standard tests

3.3.2 Moment-curvature diagram

In Fig. 2.49 the experimental and calculated moment-curvature diagrams for both the span and the mid-support sections of CB1 are given (based on Fig. 2.48 and Table 2.24). It can be noticed that the yielding moment in the span ($M_{y,span}$) is considerably lower than the yielding moment at the mid-support ($M_{y,support}$). The ultimate moments of the span ($M_{u,span}$) under the assumption of full composite action and the mid-support ($M_{u,support}$) are similar. In Table 2.25 the numerical values are given.

Table 2.25: Moment - curvature values of both the span and mid-support sections of CB1

	Span		Mid-support	
	moment [kNm]	curvature [10^{-6}.1/mm]	moment [kNm]	curvature [10^{-6}.1/mm]
cracking	22.7	0.55	23.9	0.57
yielding	98.3	9.90	172.8	10.45
ultimate	181.4	43.48	185.5	52.54

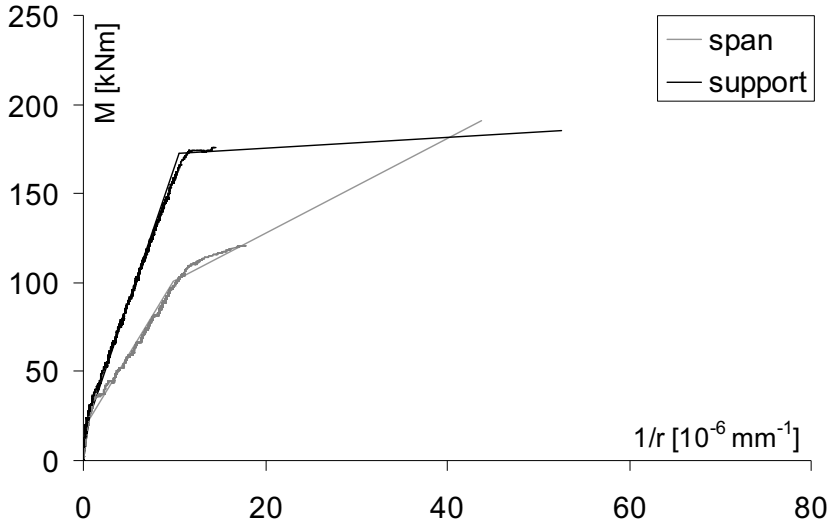

Fig. 2.49: Moment - curvature diagram of both the span and mid-support sections of CB1

3.3.3 Moment redistribution

In Table 2.26, the critical bending stiffness ratios and moment distribution ratios are given. As the moment ratio m_3 is smaller than m_t (Eq. 2.39), first yielding in the spans is expected.

Secondly, the bending stiffness ratio k_3 is considerable larger than the linear elastic moment distribution ratio (m_{el} = 0.972), which corresponds to the applied strengthening configuration different form the linear elastic configuration. By the use of this strengthening configuration, a redistribution of the moments characterized by a higher moment taken at the mid-support in comparison with the linear elastic theory is observed.

The bending stiffness ratio k_5 is considerably smaller than the linear elastic moment distribution ratio, which results in an additional moment redistribution starting from the yielding of both critical cross-sections. Now the redistribution is

characterized by a higher ΔM taken by the spans in comparison to the mid-supports, which is due to the used amount of FRP-EBR in the spans.

Table 2.26: Critical bending stiffness ratios k and moment distribution ratios m

k_1	m_1 ($=m_{el}$)	k_3	m_3	k_5	m_5	m_t
1.011	0.978	1.891	1.395	0.122	0.317	2.102

In Fig. 2.50, the experimental and analytical moment redistributions of CB1 are compared. For the unstrengthened beam, the formation of a plastic hinge can be noticed (vertical part of the dashed moment distribution curve). In case of the strengthened beam, although the strengthened spans still start to yield first (as mentioned above), the FRP allows the spans to continue resisting the additional load and a so-called restrained hinge is formed. At increasing load, when the mid-support starts to yield, a plastic hinge will be formed at the mid-support. Shortly after the plastic hinge formation, debonding of the laminates occurred at 153 kN. Clarification and prediction of this debonding load is given in Chapter 3. A good agreement is observed between the experimental curve and the calculated curve.

In Fig. 2.51 the moment redistribution factor δ is given in function of the applied load F. In this graph, during the first 20 kN of the loading scale, a big difference can be noticed between the theoretical and the experimental curve (up to 33 %). This problem is due to the relatively big difference between the analytical linear elastic moments and the experimental non-linear moments at the beginning of the loading test (see Eq. 2.1). In the upper part of the graph, a rather good agreement is noticed between the theoretical and experimental curve. Base on the experimental results a maximum redistribution factor of 1.32 is obtained, which means a maximum increase (at mid-support) of 31.5 %.

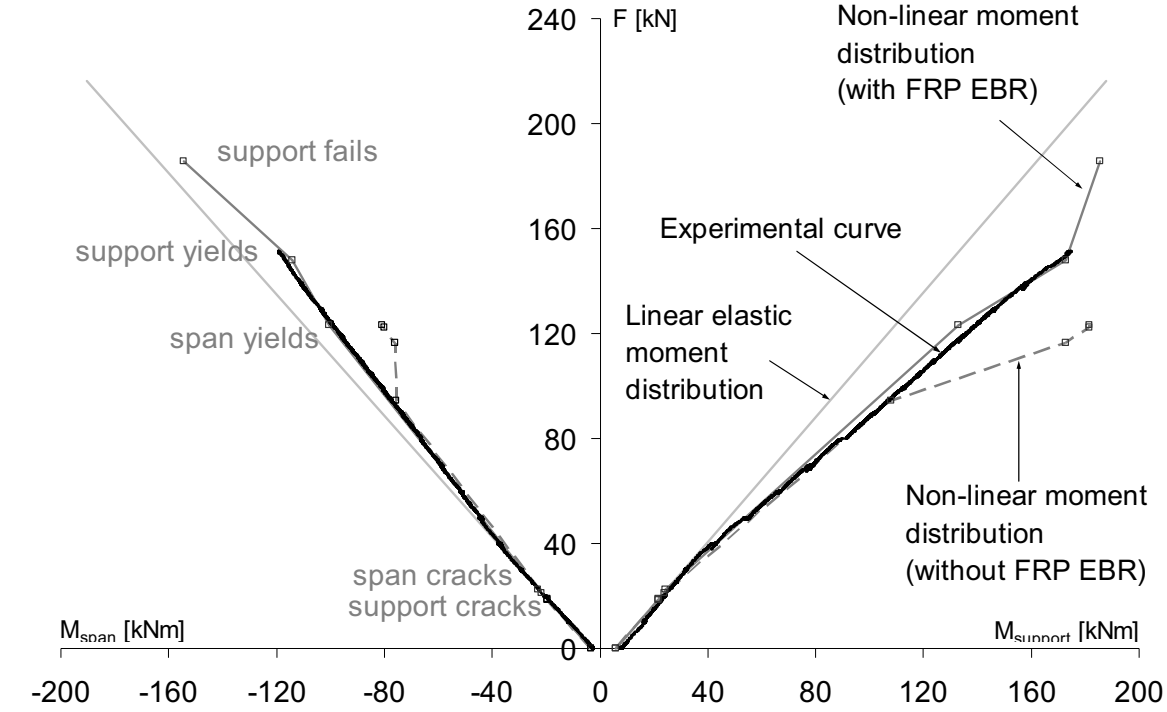

Fig. 2.50: Moment redistribution of CB1

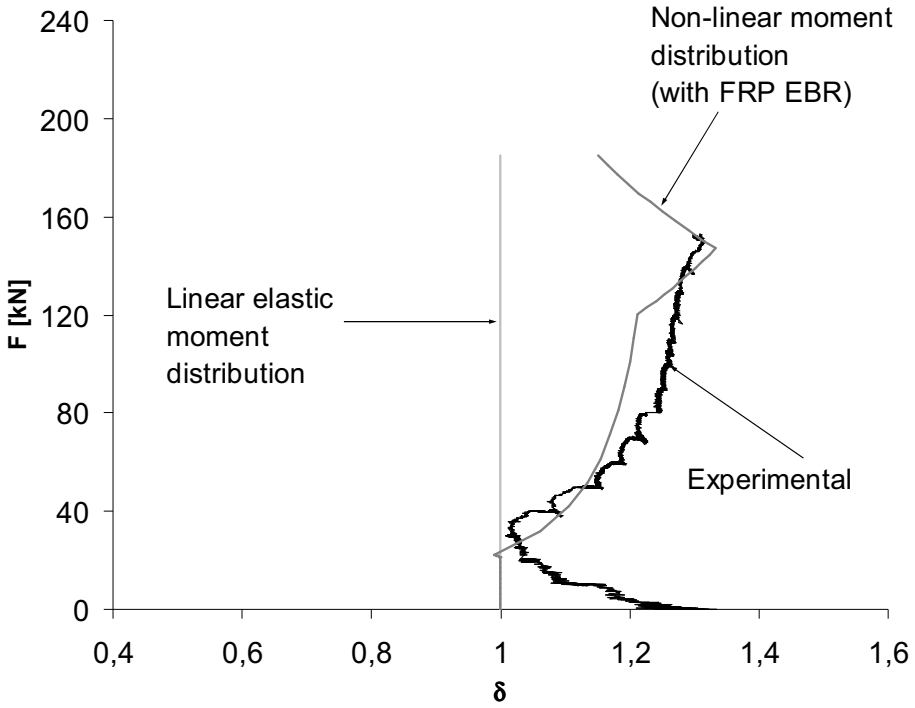

Fig. 2.51: Moment redistribution factor $\delta_{support}$ in function of the applied load F for CB1

3.3.4 Strain distribution at the critical cross-sections

In Fig. 2.52 to Fig. 2.54, the theoretical and experimental strain values at the critical cross-sections are given. The theoretical strain distribution shows a specific multi-linear shape in stead of the typical tri-linear shaped curves, due to the obtained moment redistribution in these continuous beams.

In Fig. 2.52 the strains at the critical cross-section at the left point load is shown. In Fig. 2.53 the strain at the mid-support is given and in Fig. 2.54 the strain distribution at the right point load is shown. In each graph the strain of the concrete in compression and of both the internal and external reinforcement is given (whereas for the internal reinforcement the concrete strain at the level of internal reinforcement has been measured).

In the graphs Fig. 2.52 to Fig. 2.54 all strains are presented by absolute values. A good to excellent agreement is noticed between the experimental values and the theoretically obtained values (multi-linear curve). Immediately after cracking of the critical cross-sections a difference is noticed between the experimental and analytical curves (see indication in Fig. 2.52). This is due to the tension stiffening effect, which is not taken into account in the analytical study. In Table 2.27, the maximum absolute values of the experimentally obtained strains are given.

Table 2.27: Absolute values of experimentally obtained maximum strains of CB1

	max. strain of concrete	max. strain of internal reinf.	max. strain of external reinf.
Left point load	0.185 %	0.614 %	0.510 %
Mid-support	0.122 %	0.442 %	-
Right point load	0.151 %	0.501 %	0.563 %

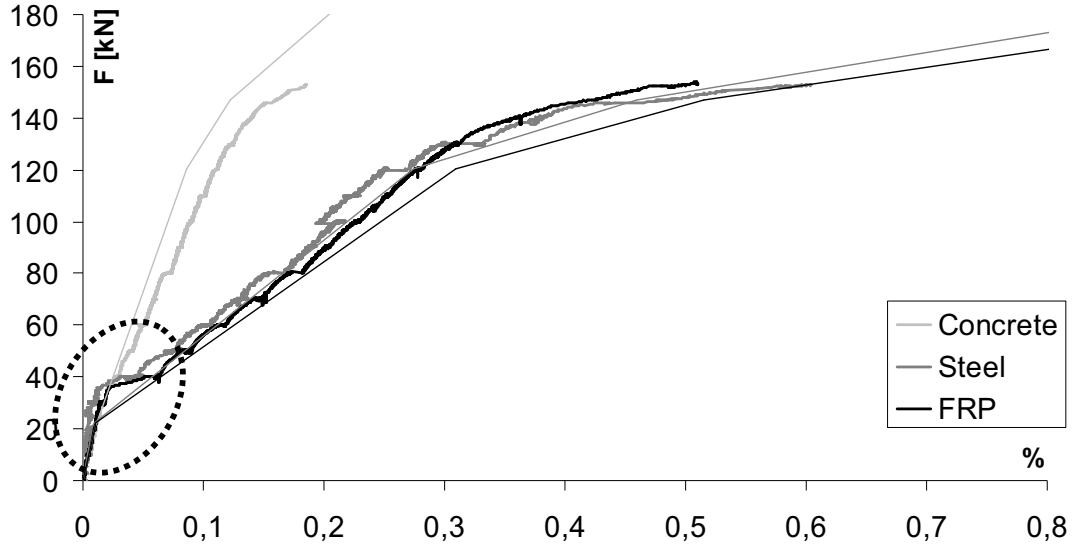

Fig. 2.52: Strain values at left point load.

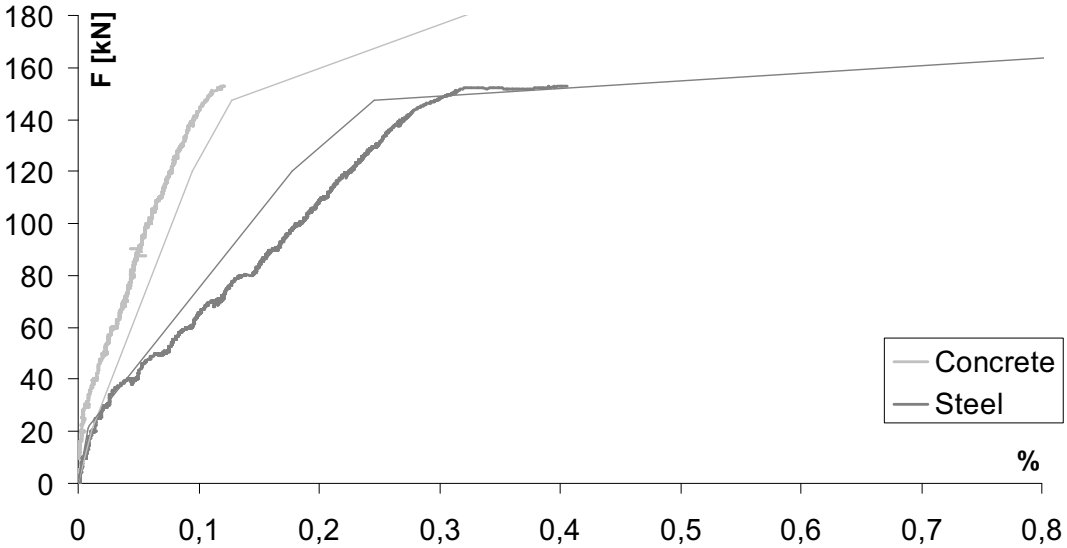

Fig. 2.53: Strain values at mid-support.

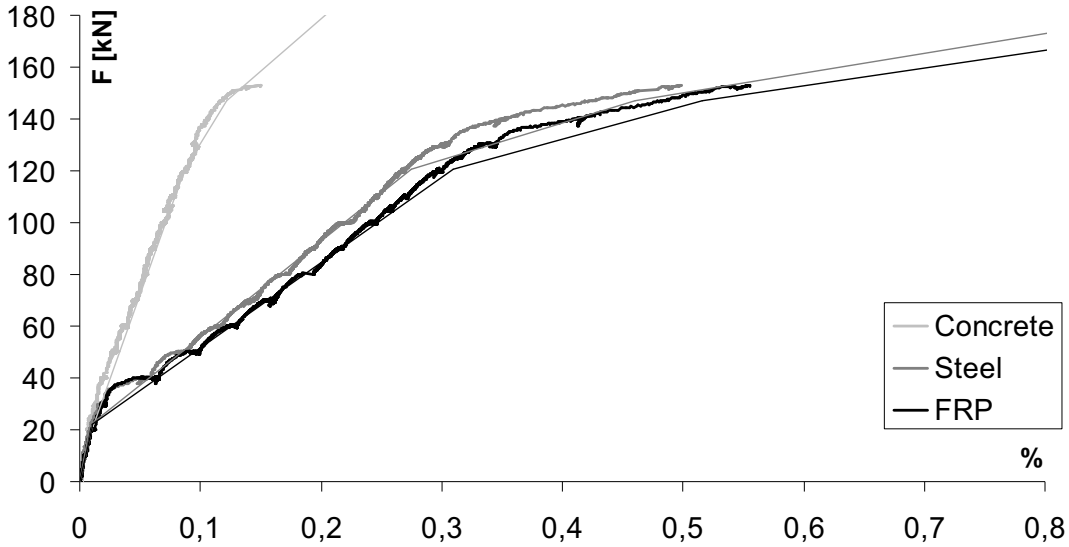

Fig. 2.54: Strain values at right point load.

3.3.5 Deflection

In Fig. 2.55 the deflection at the location of the point loads of CB1 is given in function of the applied load. In this figure also the analytically obtained deflection by numerical integration of curvatures along the beam length is shown. A reasonable agreement can be noticed between the analytical and experimental results.

Finally, in Fig. 2.55, also the measured deflection (see test results [12]) of the unstrengthened beam in function of the applied point load is given (dashed line). Comparing the unstrengthened situation with the curves of the strengthened continuous beam, a significant reduction of the ultimate deflection is observed, which is caused by the fact that the EBR is a linear elastic material which shows no plastic deformation.

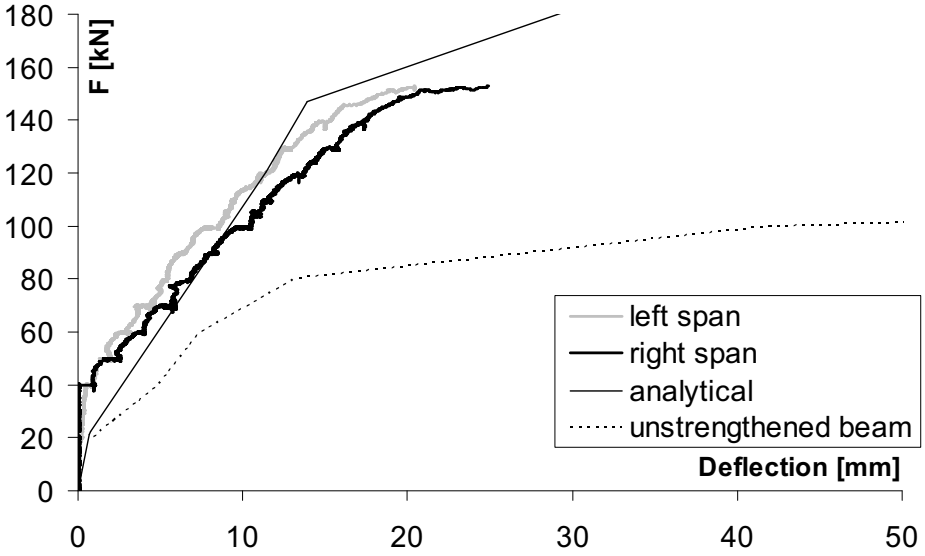

Fig. 2.55: Deflection of CB1 under the point loads

The deflection measured at the left span of the continuous beam CB1 (until F = 130 kN) is given in the left hand side of Fig. 2.56. In the right part of Fig. 2.56, the measured deflection of the unstrengthened continuous beam CB1 is given (until F = 100 kN). These latter experimental results are obtained from the earlier study about the non-linear behaviour of unstrengthened continuous beams [12].

As the deflections at the different measurement locations are connected by straight lines, the local rotation in the unstrengthened beam at the plastic hinge (under the point loads) is clearly visible. On the contrary, in the strengthened beam no local rotation neither at the point load, or at the mid-support, is visible. This also holds for the moment redistribution graph (Fig. 2.50), in which it can be observed that the formation of a plastic hinge will only be obtained at the mid-support after yielding of the latter ($F_{y,support}$ = 147 kN). Unfortunately this load is obtained after debonding of the externally bonded reinforcement.

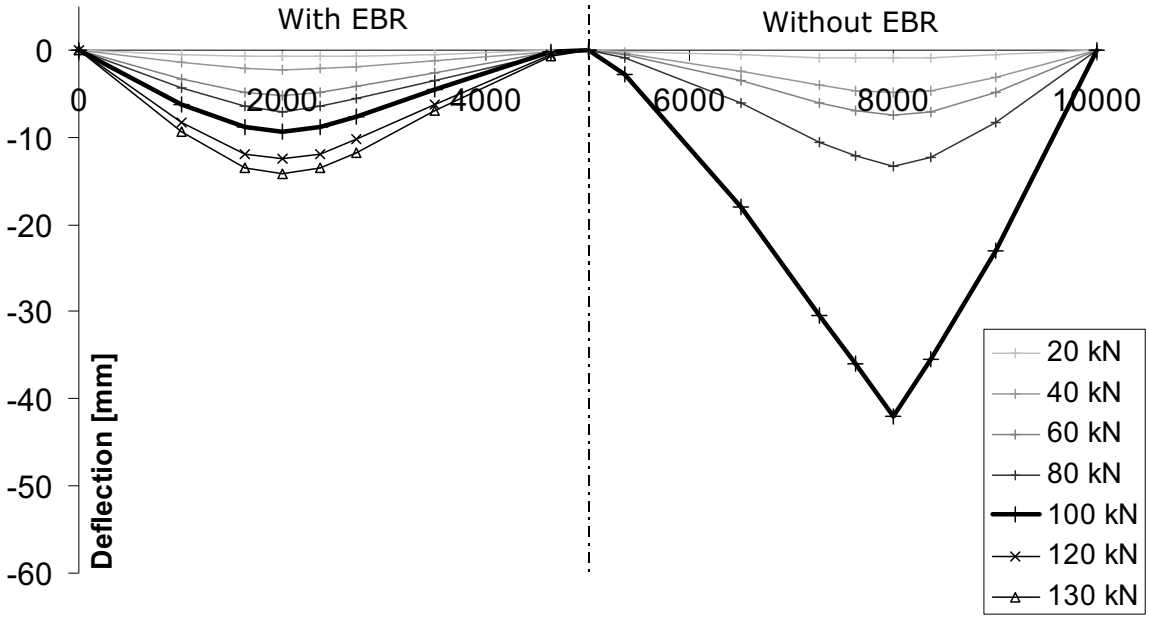

Fig. 2.56: Deflection of CB1 compared to the deflection of a similar beam without external strengthening for different load levels

3.3.6 Crack formation

In Fig. 2.57 the crack pattern of CB1 is given at three different load steps, namely F = 50 kN, F = 100 kN and the final load step at which the cracks are measured manually i.e. F = 130 kN. In the graphs a shorter crack spacing is observed for the zones with externally bonded reinforcement (span zones) in comparison with the zones without externally bonded reinforcement (mid-support zone). Nevertheless a smaller equivalent reinforcement ratio is used in the spans ($\rho_{eq,span}$ = 0.65 %) compared to the mid-support ($\rho_{eq,support}$ = 1.43 %). The mean crack spacing s_{rm}, at F = 130 kN, can also be found in Table 2.28. It follows that the mean crack spacing in the spans ($s_{rm,span}$) equals about 60% of the mean crack spacing at the mid-support ($s_{rm,support}$). The mean crack width is similar for

both the span zones and the mid-support zone. In Fig. 2.58 an analytical verification of the mean crack width is shown according to the fib Bulletin 14 [18] for the strengthened zones and according to EC2 [17] for the unstrengthened zones. Fairly accurate predictions are obtained.

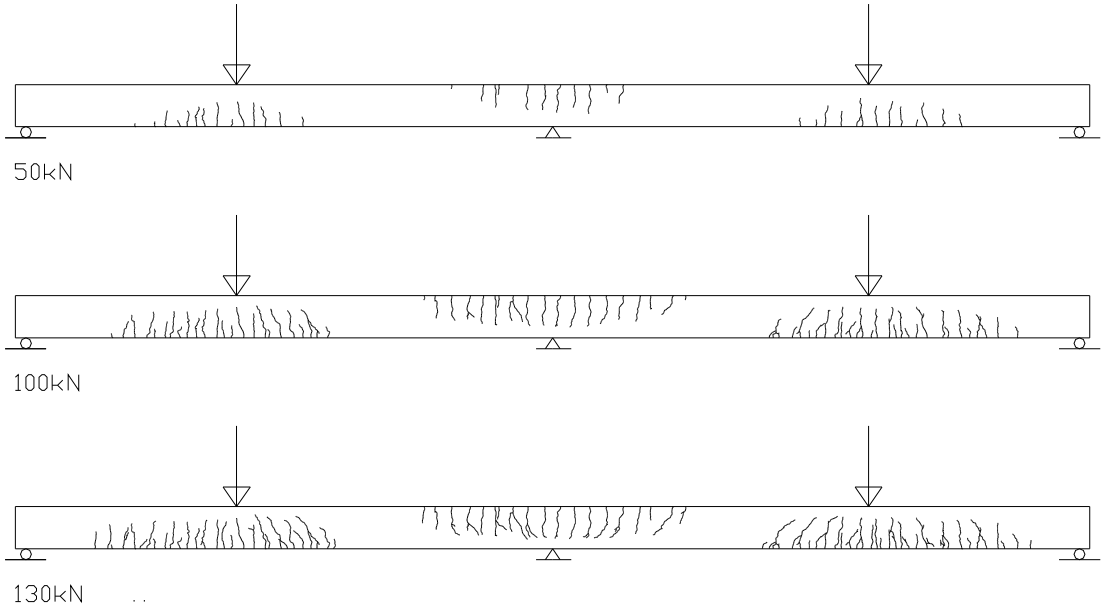

Fig. 2.57: Crack evolution of CB1.

Table 2.28: Mean crack spacing and mean crack width at F = 130 kN for CB1

	left span zone	mid-support zone	right span zone
Mean crack spacing [mm]	81.0	137.8	82.1
Mean crack width [mm]	0.23	0.22	0.26

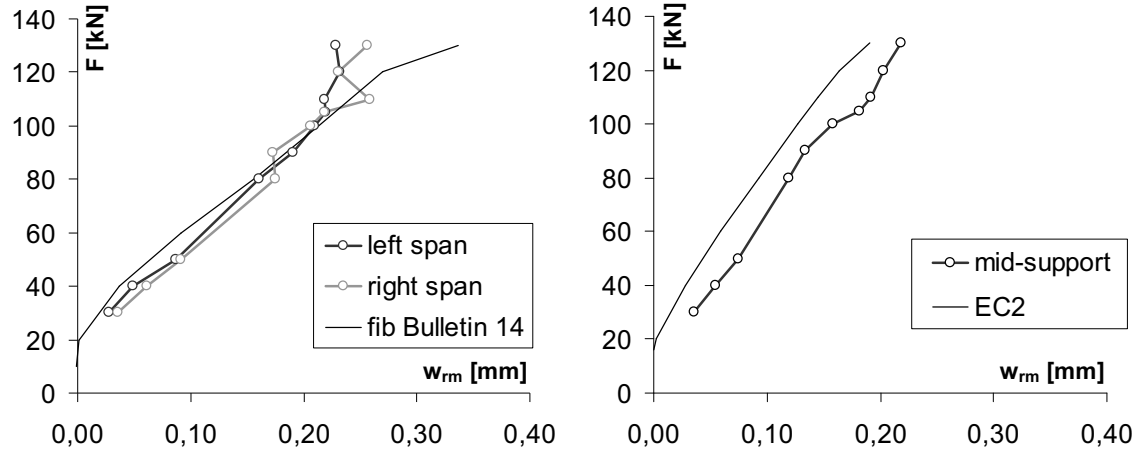

Fig. 2.58: Verification of the mean crack width of CB1

3.4 Continuous beam 2 (CB2)

3.4.1 Configuration

The second tested beam has internal reinforcement as shown in Fig. 2.59. The beam has a high internal reinforcement ratio in the spans ($\rho_{s,span}$ = 0.99 %) and a low concentration of reinforcement above the mid-support ($\rho_{s,support}$ = 0.31 %). As external reinforcement, one CFRP laminate with a length of 5000 mm is applied at the mid-support. The cross-section of the CFRP laminate equals 100 mm x 1.0 mm ($\rho_{f,support}$ = 0.13 %).

The material properties are given in Table 2.29. These values result from standard tensile and compression tests.

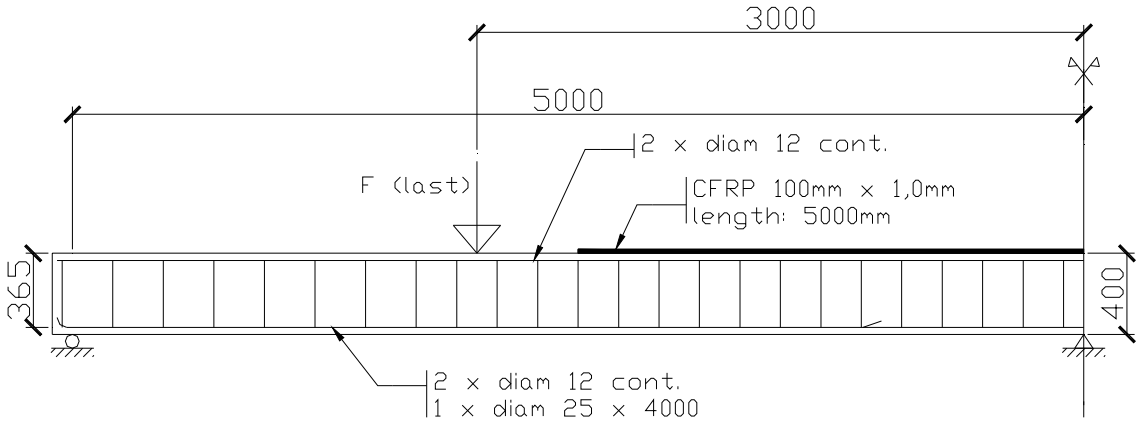

Fig. 2.59: Reinforcement configuration of CB2

Table 2.29: Properties of materials used for CB2

	Concrete	CFRP	steel at span	steel at mid-supp.
Compres. strength (f_{cm})	43.3 N/mm²	-	-	-
Yield stress	-	-	529 N/mm²	589 N/mm²
Yield strain	-	-	0.25 %	0.26 %
Tensile stress	3.2 N/mm²*	2768 N/mm²	628 N/mm²	674 N/mm²
Failure strain	3.5 ‰ **	1.46 %	10.59 %	9.62 %
E-modulus	36 kN/mm²	190 kN/mm²	213 kN/mm²	223 kN/mm²

* Splitting test results and 3-point-bending tests results are converted to mean pure tensile strength according to EC2 [17]

** The failure strain of concrete is taken equal to 3.5 ‰, based on EC2 [17], as this value is not resulting from the standard tests

3.4.2 Moment-curvature diagram

In Fig. 2.60 the moment-curvature diagrams of both the span and the mid-support sections of CB2 are given, calculated by using the data given in Fig. 2.59 and in Table 2.29 and compared to the experimental curves. It can be noticed that the yielding moment at the mid-support ($M_{y,support}$) is considerably lower than the yielding moment in the span ($M_{y,span}$). The ultimate moment of the span ($M_{u,span}$) is somewhat smaller than the ultimate moment at the mid-support

($M_{u,support}$) under the assumption of full composite action. In Table 2.30 the numerical values are given more into detail.

Table 2.30: Moment - curvature values of both the span and mid-support sections of CB2

	span		mid-support	
	moment [kNm]	curvature [10^{-6}.1/mm]	moment [kNm]	curvature [10^{-6}.1/mm]
cracking	22.0	0.54	21.3	0.53
yielding	123.4	9.73	66.3	9.09
ultimate	132.8	70.58	150.4	42.57

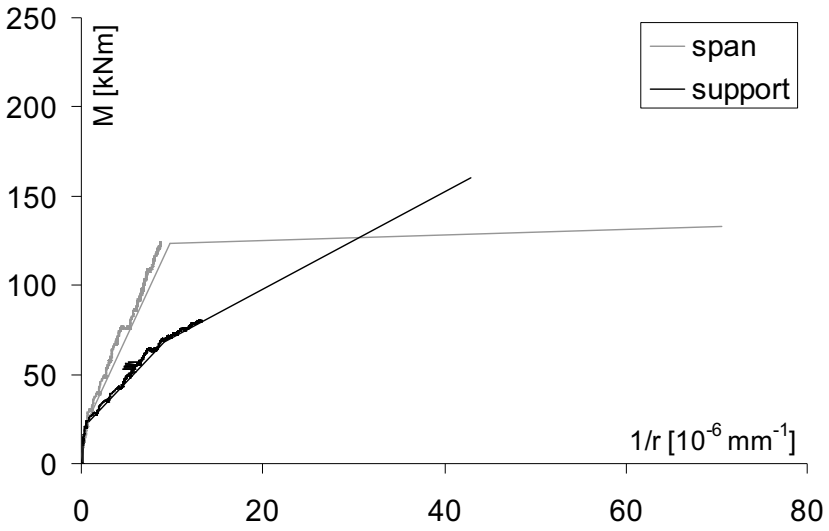

Fig. 2.60: Moment - curvature diagram of both the span and mid-support of CB2

3.4.3 Moment redistribution

In Table 2.31, the critical bending stiffness ratios and moment distribution ratios are given. As the moment distribution ratio m_3 is larger than m_t (Eq. 2.39), first yielding at the mid-support is expected.

Secondly, the bending stiffness ratio k_3 is considerable smaller than the linear elastic moment distribution ratio (m_{el} = 0.972), which corresponds to the applied strengthening configuration different form the linear elastic configuration. By the use of this strengthening configuration, a redistribution of the moments characterized by a higher moment taken in the spans in comparison with the linear elastic theory is observed.

Finally the bending stiffness ratio k_5 is considerable larger than the linear elastic moment distribution ratio, which results in an additional moment redistribution starting at the yielding of both critical cross-sections. Now the redistribution is characterized by a larger ΔM taken by the mid-support in comparison with the spans, which is due to the used amount of linear elastic FRP-EBR at the mid-support.

Table 2.31: Critical bending stiffness ratios k and moment distribution ratios m

k_1	m_1 (=m_{el})	k_3	m_3	k_5	m_5	m_t
0.999	0.972	0.476	0.649	16.253	5.604	0.479

In Fig. 2.61, the experimental and analytical moment redistribution of CB2 is compared. For the unstrengthened beam, the formation of a plastic hinge can be noticed at the mid-support (vertical part of the dashed moment distribution curve). In the case of the strengthened beam, although the strengthened mid-support section still starts to yield first (as mentioned above), the FRP allows the mid-support to continue resisting the additional load (restrained hinge formation). At increasing load, when the spans start to yield, a plastic hinge is formed in the spans. Somewhat later, the laminate debonded at 152 kN. Unfortunately no information about the moment redistribution for F > 122 kN is available, due to a technical problem by which the signals from the load cells were not recorded after 122 kN. Concerning the available experimental data, a good agreement is observed with the calculated curve.

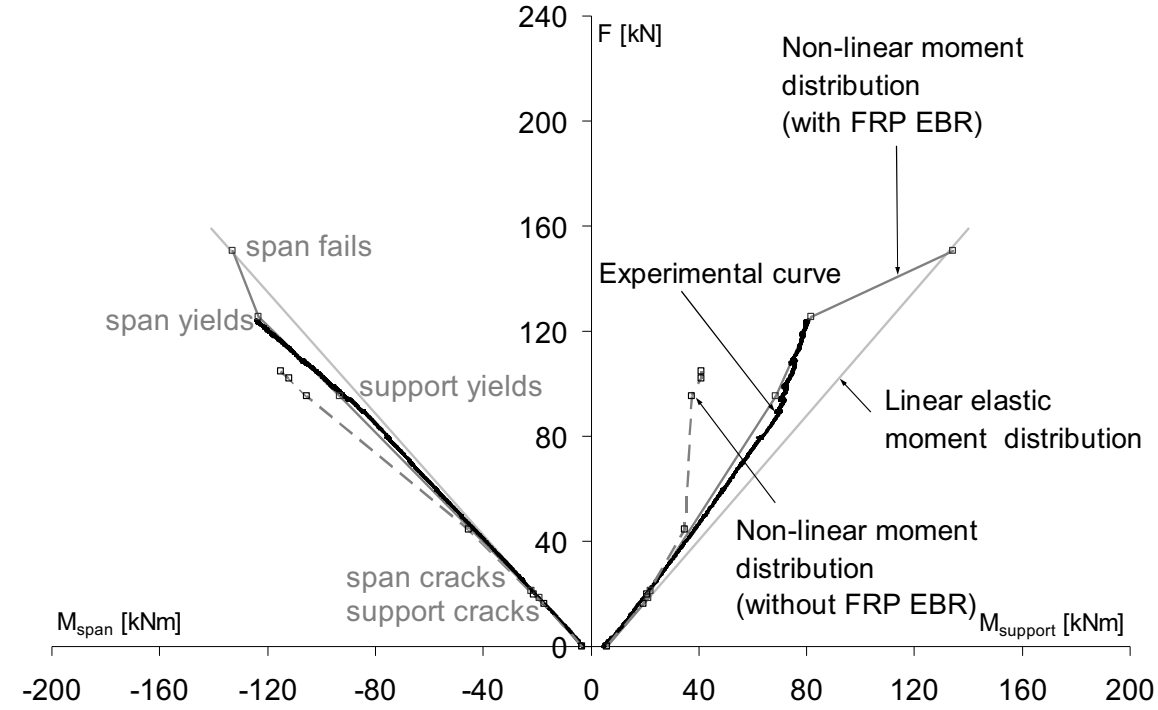

Fig. 2.61: Moment redistribution of CB2

In Fig. 2.62 the moment redistribution factor δ is given in function of the applied point load F. Similar to Fig. 2.51, a difference can be noticed between the theoretical and the experimental curve (up to 30 %) during the first 10 kN of the loading scale. In the upper part of the graph, a rather good agreement is noticed between the theoretical and experimental curve. Based on the experimental results a minimum redistribution factor of 0.72 is obtained, which corresponds to a maximum reduction (at mid-support) of 28.0 %.

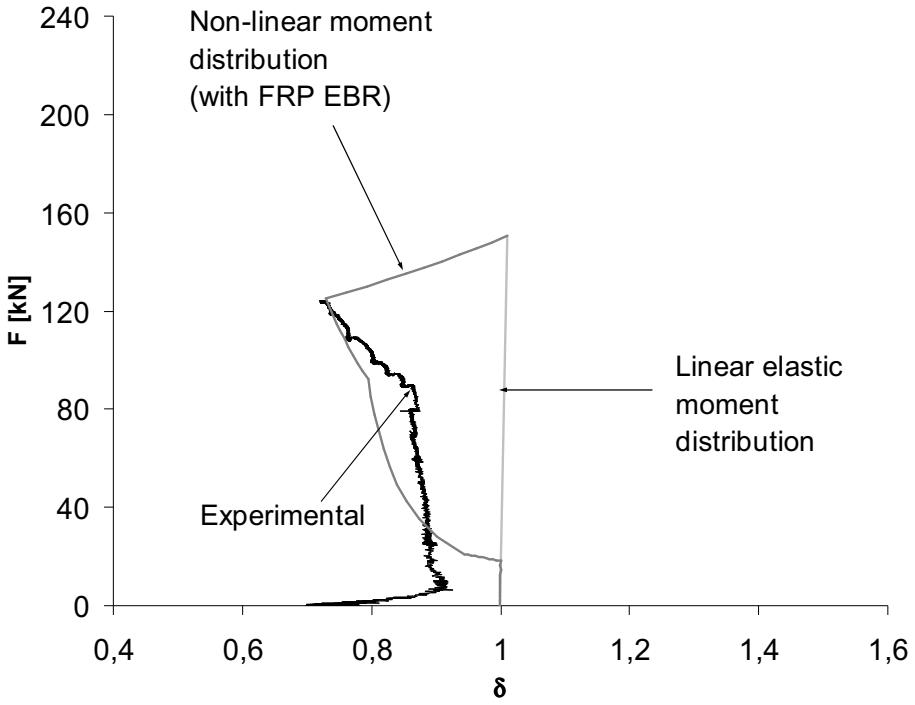

Fig. 2.62: Moment redistribution factor $\delta_{support}$ in function of the applied load F for CB2

3.4.4 Strain distribution at the critical cross-sections

In Fig. 2.63 to Fig. 2.65, the theoretical and experimental strain values at the critical cross-sections are given. In each graph the strain of the concrete and the internal and external reinforcement are given. The theoretical strain distribution is a multi-linear curve. Remark that in the graphs all strains are presented by their absolute values.

Comparing the electronic measurements with the analytically obtained multi linear curves, a good agreement is noticed. The experimentally obtained strain in the FRP is somewhat lower than expected. In Table 2.32, the maximum absolute values of these strains are given.

From Fig. 2.64 it can be noticed that the critical cross-section at the mid-support still is able to resist the additional load after yielding ($F_{y,support}$ = 92 kN), due to the use of FRP at the mid-support. At the load at which the spans start to yield, ($F_{y,span}$ = 125 kN), a change of stiffness in Fig. 2.64 is noticed.

Table 2.32: Absolute values of experimentally obtained maximum strains of CB2

	max. strain of concrete	max. strain of internal reinf.	max. strain of external reinf.
Left point load	0.119 %*	0.233 %*	-
Mid-support	0.108 %	0.669 %	0.458 %
Right point load	0.150 %	0.351 %	-

* these values are the maximum strains at 122 kN and not at failure load

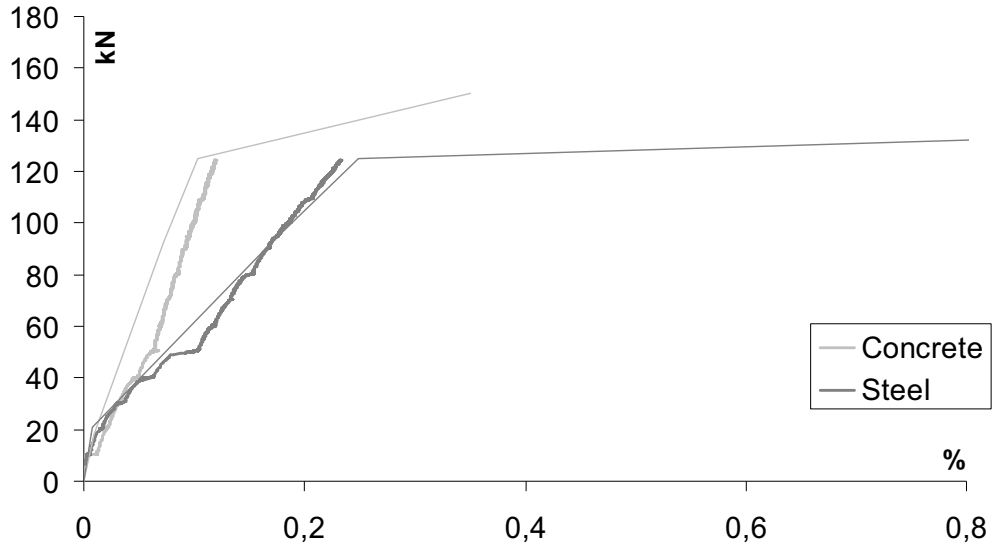

Fig. 2.63: Strain values at left point load.

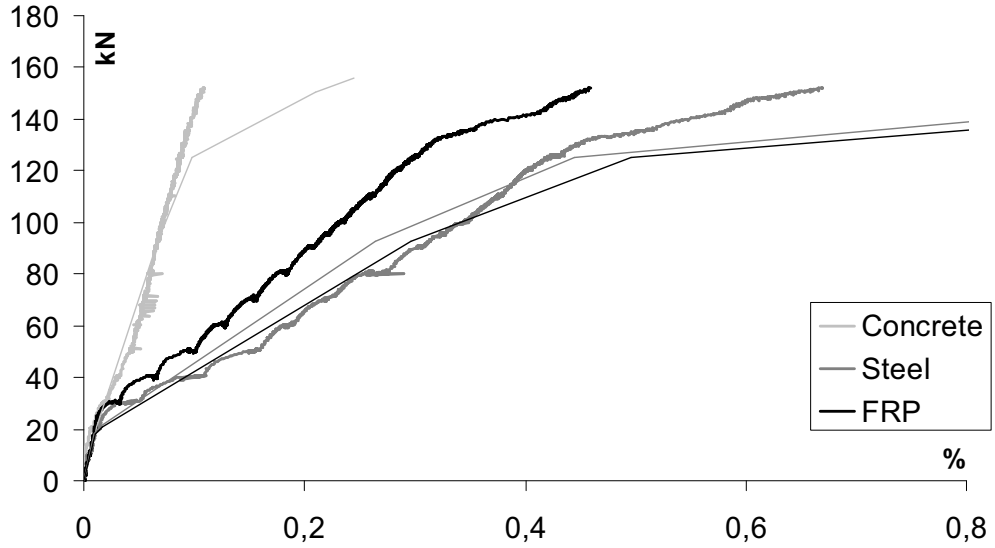

Fig. 2.64: Strain values at mid-support.

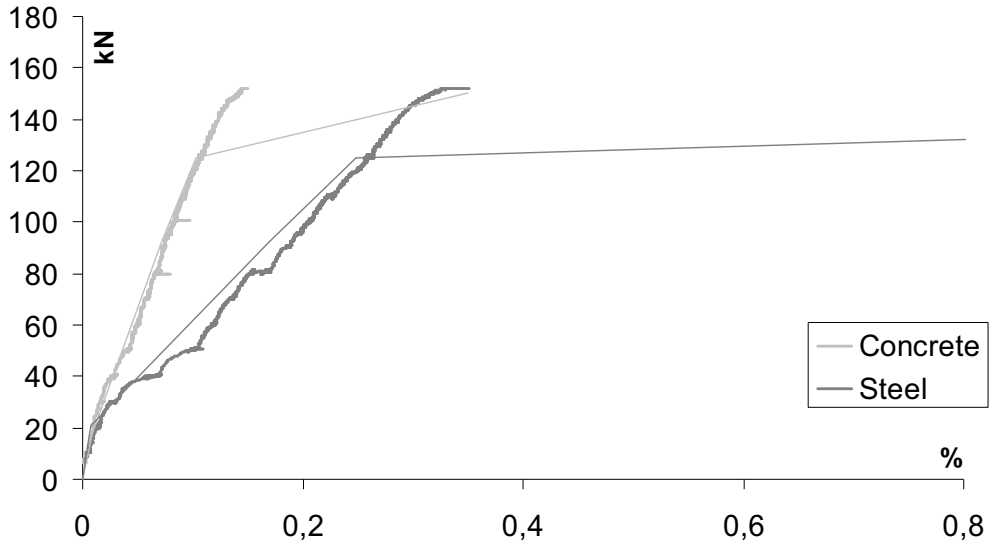

Fig. 2.65: Strain values at right point load.

3.4.5 Deflection

In Fig. 2.66 the deflection of the strengthened and unstrengthened (dashed line, data according to [12]) beam in function of the applied point load is given. Comparing these graphs, a significant reduction of the deflection is observed for the strengthened continuous beams, which is caused by the fact that the EBR is a linear elastic material which shows no plastic deformation. A good agreement is obtained between the analytical and experimental results.

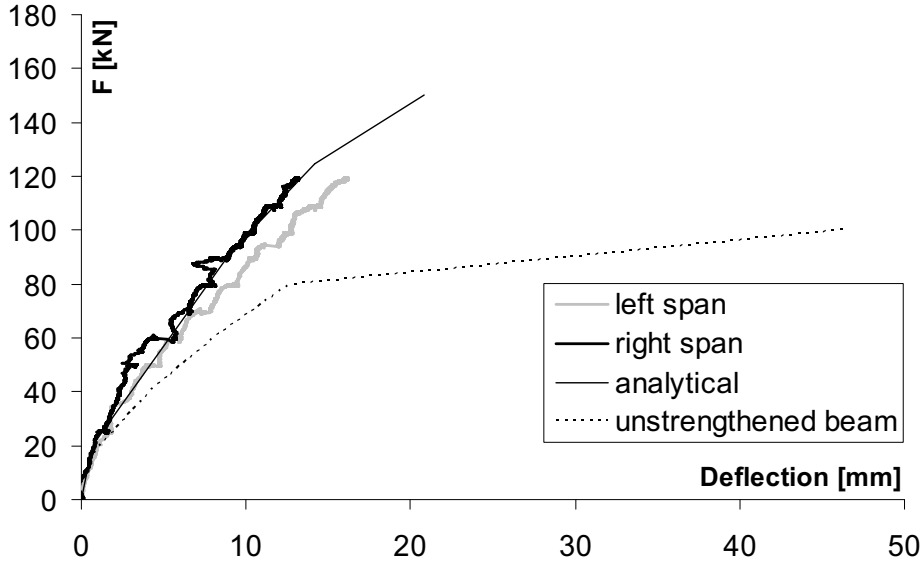

Fig. 2.66: Deflection of CB2 under the point loads

The deflection measured for the left span of the continuous beam CB2 (until F = 125 kN) is given in the left hand side of Fig. 2.67. In the right part the measured deflection of the unstrengthened continuous beam CB2 is given (until F = 100 kN) [12]. These latter experimental results are obtained from [12].

Similar to Fig. 2.56 the local rotation in the unstrengthened beam at the plastic hinges (under point loads) is visible. On the contrary, in the strengthened beam no local rotation neither at the point load, nor at the mid-support, is visible. This also holds for the moment redistribution graph (Fig. 2.61), in which nearly no formation of plastic hinges is observed.

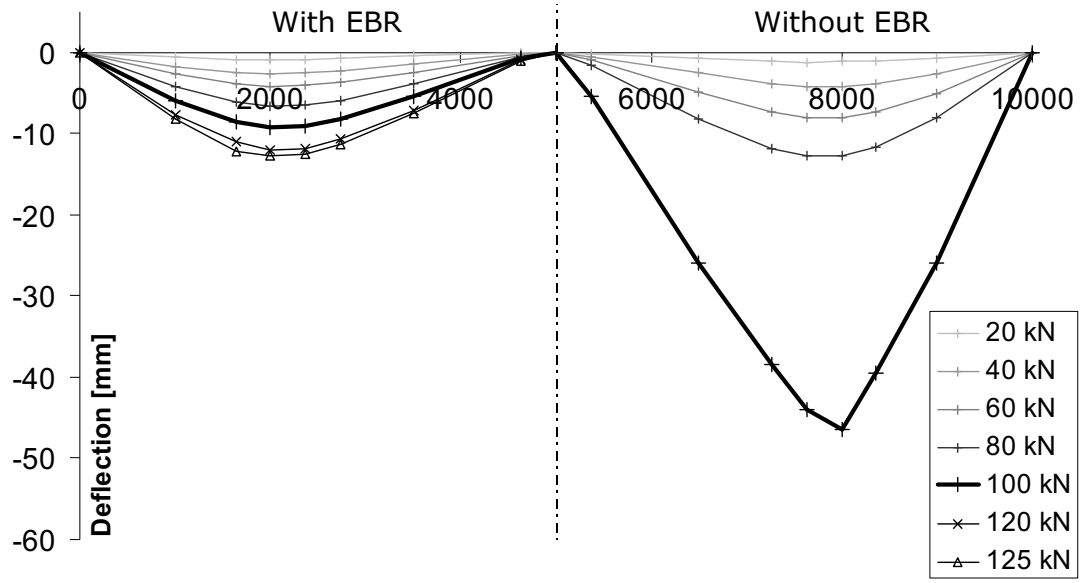

Fig. 2.67: Deflection of CB2 compared to the deflection of a similar beam without external strengthening for different load levels

3.4.6 Crack formation

In Fig. 2.68 the crack evolution of CB2 is given at three different load steps, namely F = 50 kN, F = 100 kN and the final load step at which the cracks are measured manually i.e. F = 110 kN. In the graphs and Table 2.33 a shorter crack spacing is observed for the zone with externally bonded reinforcement (mid-support zone) in comparison with the zones without externally bonded reinforcement (span zone). Nevertheless, a smaller equivalent reinforcement ratio is used at the mid-support ($\rho_{eq,support}$ = 0.43 %) compared to the spans ($\rho_{eq,span}$ = 0.99 %). It follows that the mean crack spacing at the mid-support ($s_{rm,support}$) equals about 70.9 % of the mean crack spacing in the spans ($s_{rm,span}$). The mean crack width, which is also shown in Fig. 2.69, is larger in the externally strengthened zone compared to the unstrengthened zone. Furthermore, as can be noticed in Fig. 2.69, a larger crack width at the mid-support is expected, according to fib Bulletin 14 [18]. For the unstrengthened zones (span zones), fairly accurate predictions are obtained.

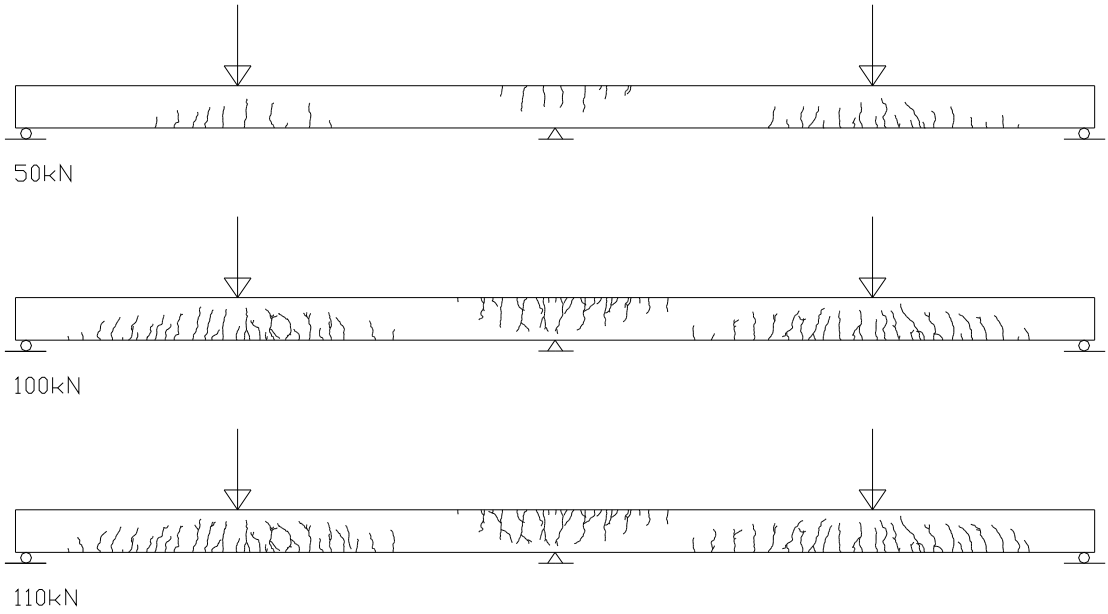

Fig. 2.68: Evolution of crack pattern of CB2

Table 2.33: Mean crack spacing and mean crack width at F = 110 kN for CB2

	left span zone	mid-support zone	right span zone
Mean crack spacing [mm]	105.6	78.9	117.1
Mean crack width [mm]	0.17	0.25	0.16

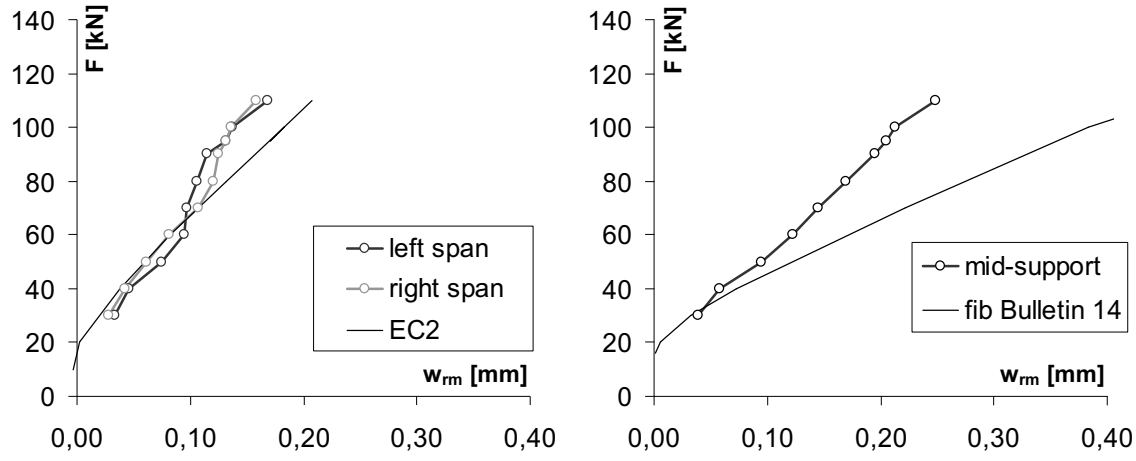

Fig. 2.69: Verification of the mean crack width of CB2

3.5 Continuous beam 3 (CB3)

3.5.1 Configuration

The third tested beam has internal reinforcement according to the linear elastic theory, as shown in Fig. 2.70. The internal reinforcement ratio in the spans ($\rho_{s,span}$ = 0.67 %) is slightly smaller than the reinforcement ratio at the mid-support ($\rho_{s,support}$ = 0.75 %). As external reinforcement, a CFRP laminate with a length of 3575 mm is applied in each span and one CFRP laminate with a length of 5000 mm is applied above the mid-support. The cross-section of all CFRP laminates equals 100 mm x 1.0 mm ($\rho_{f,span}$ = $\rho_{f,support}$ = 0.13 %), hence the total reinforcement ratios are still comparable with the ratios obtained from the linear elastic theory.

The material properties are given in Table 2.34. These values result from standard tensile and compression tests.

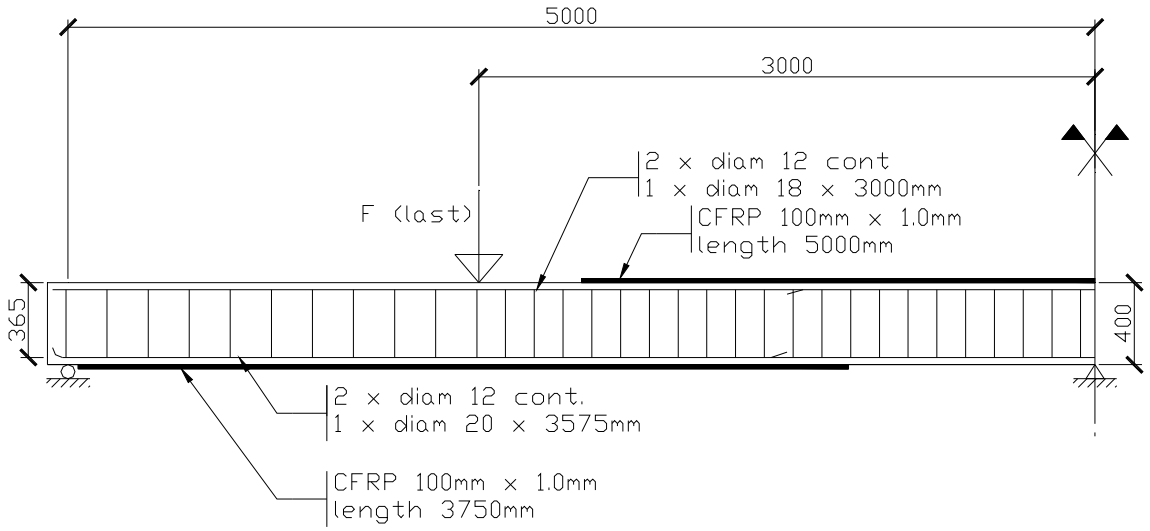

Fig. 2.70: Reinforcement configuration of CB3

Table 2.34: Properties of materials used for CB3

	Concrete	CFRP	steel at span	steel at mid-supp.
Compres. strength (f_{cm})	44.0 N/mm²	-	-	-
Yield stress	-	-	600 N/mm²	582 N/mm²
Yield strain	-	-	0.29 %	0.27 %
Tensile stress	2.8 N/mm²*	2768 N/mm²	695 N/mm²	665 N/mm²
Failure strain	3.5 ‰ **	1.46 %	8.78 %	9.56 %
E-modulus	36 kN/mm²	190 kN/mm²	210 kN/mm²	218 kN/mm²

* Splitting test results and 3-point-bending tests results are converted to mean pure tensile strength according to EC2 [17]

** The failure strain of concrete is taken equal to 3.5 ‰, based on EC2 [17], as this value is not resulting from the standard tests

3.5.2 Moment curvature diagram

In Fig. 2.71 the experimental and calculated moment-curvature diagrams for both the span and the mid-support sections of CB3 are given (based on Fig. 2.70 and Table 2.34). It can be noticed that the yielding moment at the mid-support ($M_{y,span}$) is higher than the yielding moment at the mid-support ($M_{y,support}$). The ultimate moment of the span ($M_{u,span}$) under the assumption of full composite action, also is higher than the ultimate moment at the mid-support ($M_{u,support}$) under the assumption of full composite action. In Table 2.35 the numerical values are given.

Table 2.35: Moment - curvature values of both the span and mid-support sections of CB2

	span		mid-support	
	moment [kNm]	curvature [10^{-6}.1/mm]	moment [kNm]	Curvature [10^{-6}.1/mm]
cracking	17.0	0.41	16.9	0.40
yielding	130.1	10.68	114.2	9.87
ultimate	212.1	44.84	197.8	44.26

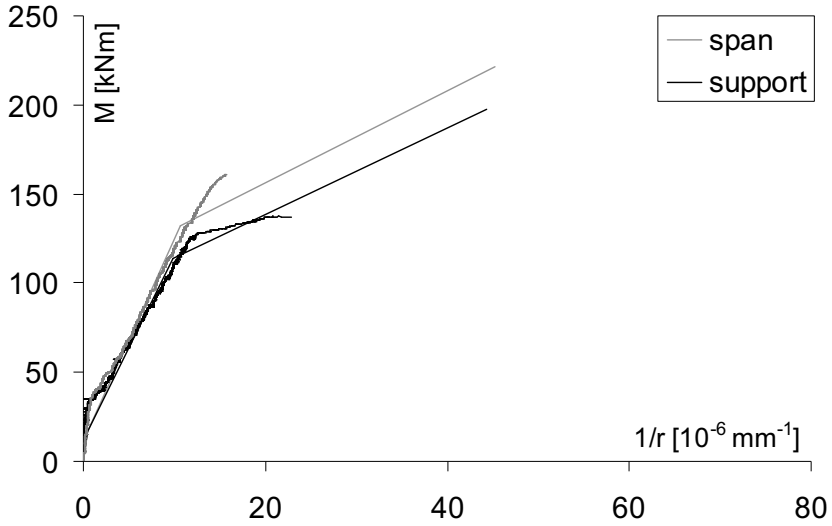

Fig. 2.71: Moment - curvature diagram of both the span and mid-support of CB3

3.5.3 Moment redistribution

In Table 2.36, the critical bending stiffness ratios and moment distribution ratios are found. As the moment distribution ratio m_3 is similar to m_t (Eq. 2.39), both the critical cross-section at the mid-support and in the span yield at nearly the same moment.

Secondly, the bending stiffness ratio k_3 is also similar to the linear elastic moment distribution ratio (m_{el} = 0.972), which corresponds to the applied strengthening configuration similar to the linear elastic configuration. Thus almost no redistribution of the moments is expected (see also Fig. 2.72).

Finally the bending stiffness ratio k_5 is also similar to the linear elastic moment distribution ratio (m_{el} = 0.972), which result in almost no moment redistribution after the yielding of both critical cross-sections.

Table 2.36: Critical bending stiffness ratios k and moment distribution ratios m for CB3

k_1	m_1 (=m_{el})	k_3	m_3	k_5	m_5	m_t
0.995	0.970	0.934	0.936	1.014	0.980	0.937

In Fig. 2.72, the experimental and analytical moment redistributions of CB3 are compared. Both for the unstrengthened and for the strengthened beam a moment distribution is observed similar to the distribution obtained from the linear elastic theory. At increasing load, when the spans and mid-support sections start to yield, the FRP allows both the spans and the mid-support to continue resisting the additional load (restrained hinge formation).

Concerning the available experimental data, a good agreement is observed with the calculated curve. Debonding of the laminate occurs at 170 kN, after both mid-support and spans already yield.

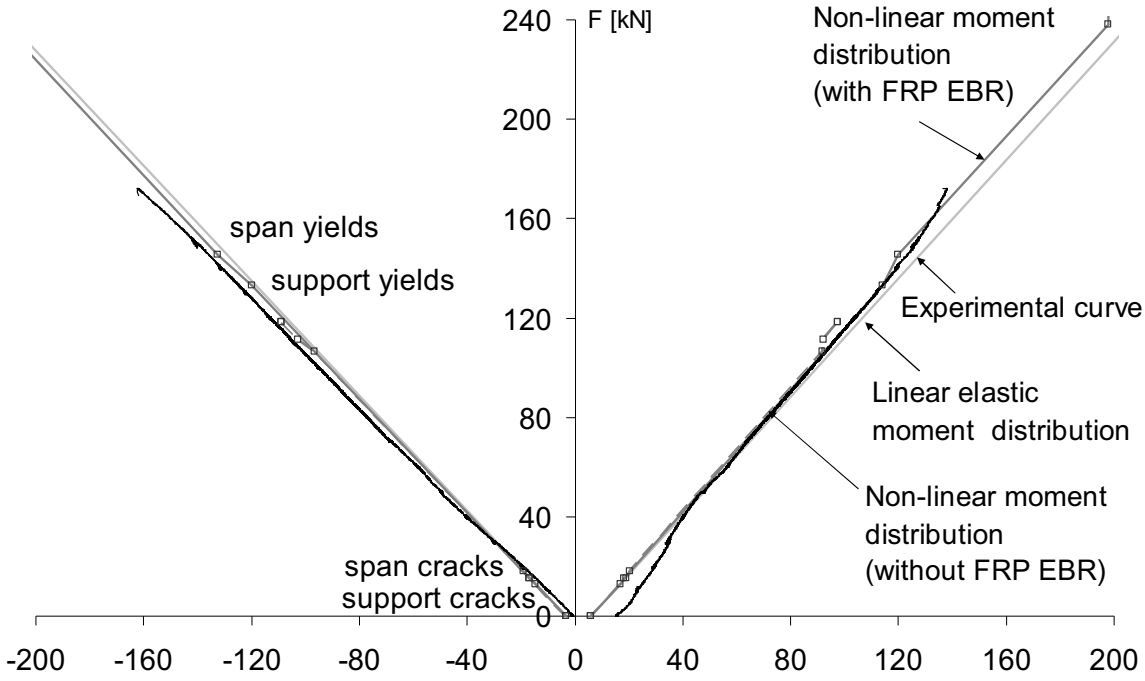

Fig. 2.72: Moment redistribution of CB3

In Fig. 2.73 the moment redistribution factor δ is given in function of the applied point load F. Similar to Fig. 2.51, a difference can be noticed between the theoretical and the experimental curve during the first 40 kN of the loading scale. In the upper part of the graph, a rather good agreement is noticed between the theoretical and experimental curve. Based on the experimental results a minimum redistribution factor of 0.87 is obtained, which corresponds to a maximum reduction (at the mid-support) of 12.7 %.

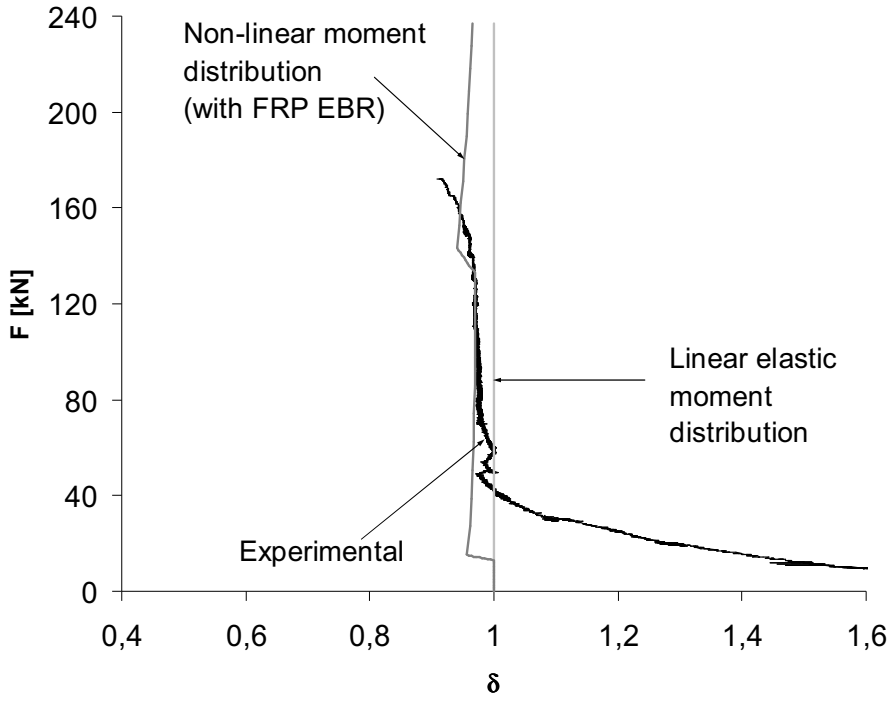

Fig. 2.73: Moment redistribution factor $\delta_{support}$ in function of the applied load F for CB3

3.5.4 Strain distribution at the critical cross-sections

In Fig. 2.74 to Fig. 2.76, the theoretical and experimental strain values of the critical cross-sections are given. In each graph the strain of the concrete and of both the internal and external reinforcement are given. The theoretical strain distribution is a multi-linear curve. Remark that the analytical multi-linear curves for this configuration are approximately tri-linear. This approximately tri-linear shape is caused by the fact that almost no redistribution is observed and hence both the span as the mid-support start to yield at nearly the same moment.

Remark that in the graphs all strains are presented by the absolute values. Comparing the electronic measurements with the analytically obtained multi linear curves, a good agreement is noticed.

Similar to Fig. 2.52, the experimentally obtained strain of the FRP laminate is smaller than the strain of the internal reinforcement, which is not expected. In Table 2.37, the maximum absolute values of these strains are given.

Table 2.37: Absolute experimental obtained values of maximum strains of CB3

	max. strain of concrete	max. strain of internal reinf.	max. strain of external reinf.
Left point load	0.158 %	0.374 %	0.403 %
Mid-support	0.117 %	0.665 %	0.497 %
Right point load	0.178 %	0.408 %	0.437 %

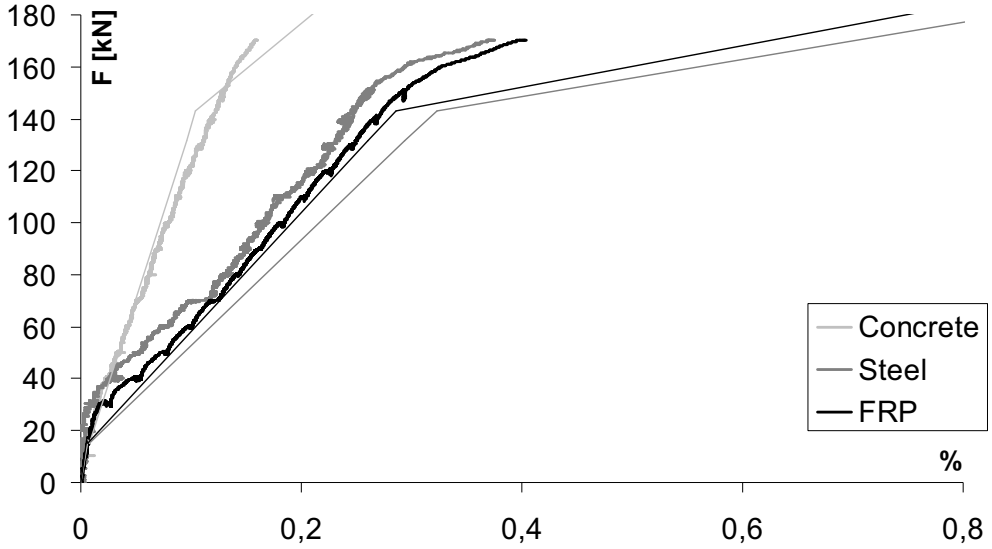

Fig. 2.74: Strain values at left point load.

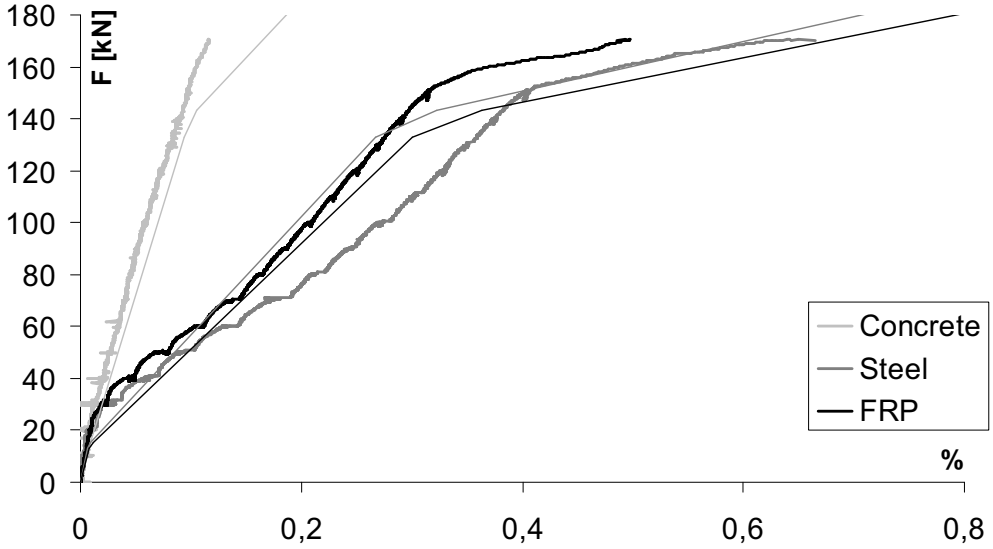

Fig. 2.75: Strain values at mid-support.

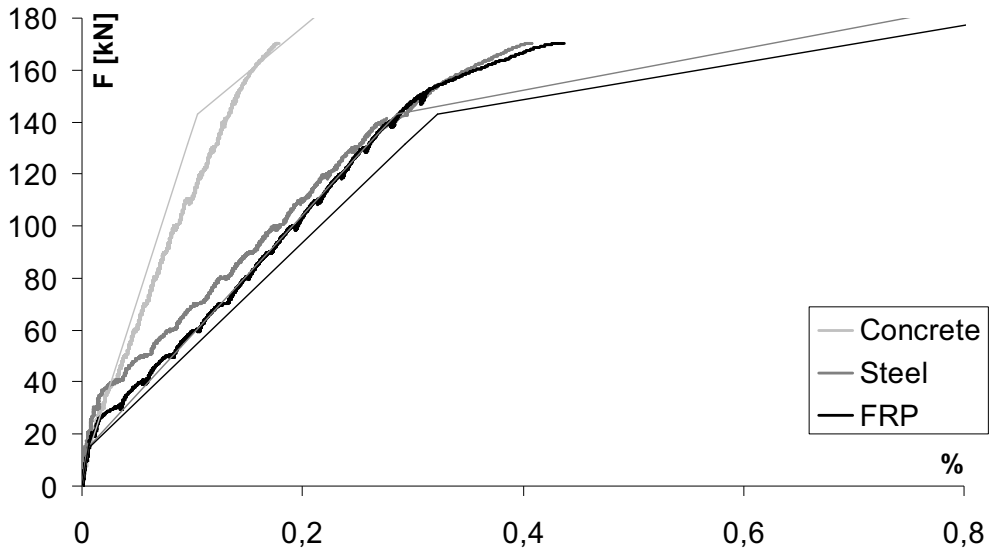

Fig. 2.76: Strain values at right point load.

3.5.5 Deflection

In Fig. 2.77, the deflection at the location of the point loads of CB3 is given in function of the applied load. In this figure also the analytically obtained deflection by numerical integration of curvatures along the beam length is shown. A reasonable agreement can be noticed between the analytical and experimental results.

Moreover, in Fig. 2.77, also the measured deflection (see test results [12]) of the unstrengthened beam in function of the applied point load is given (dashed line). Comparing the unstrengthened situation with the curves of the strengthened continuous beams, a significant reduction of the ultimate deflection is observed, which is caused by the fact that the EBR is a linear elastic material which shows no plastic deformation.

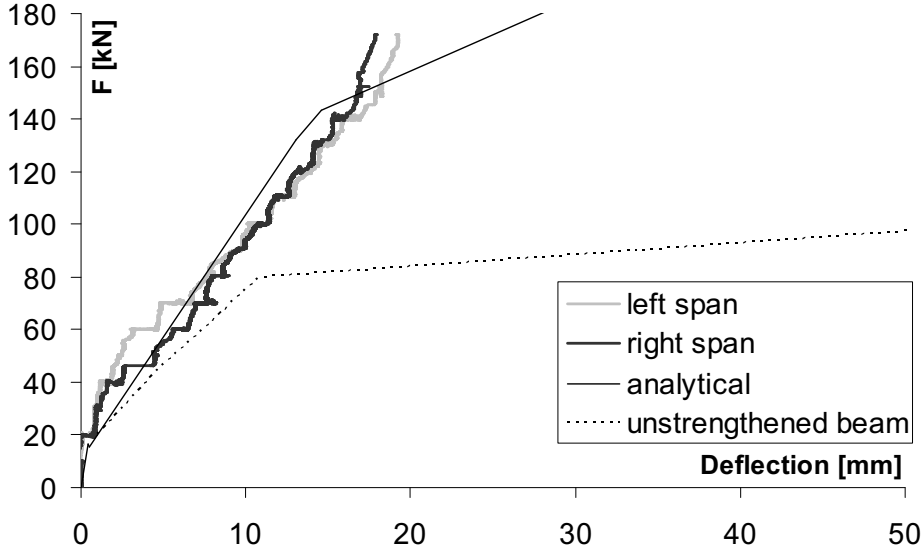

Fig. 2.77: Deflection of CB3 under the point loads

The deflection measured for the left span of the continuous beam CB3 (until F = 140 kN) is given in the left hand side of Fig. 2.78. In the right part the measured deflection of the unstrengthened continuous beam CB3 is given (until F = 100 kN) [12]. Similar to Fig. 2.56 the local rotation in the unstrengthened beam at the plastic hinges (under point loads) is visible. On the contrary, in the strengthened beam no local rotation neither at the point load, nor at the mid-support, is visible. This also holds for the moment redistribution graph (Fig. 2.72), in which nearly no formation of plastic hinges is observed.

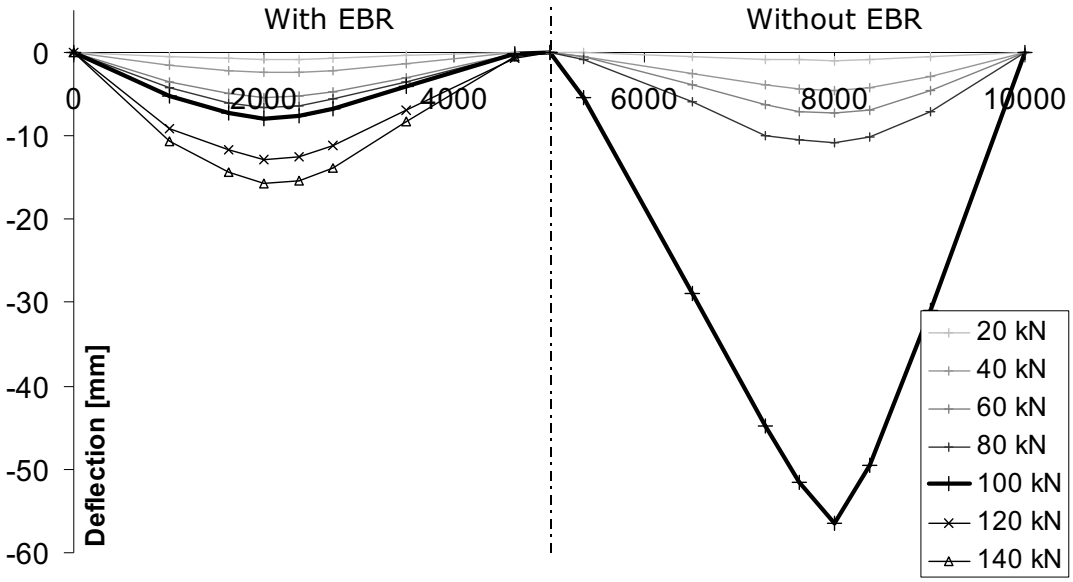

Fig. 2.78: Deflection of CB3 compared to the deflection of a similar beam without external strengthening for different load levels

3.5.6 Crack formation

In Fig. 2.79 the crack pattern of CB3 is given at three different load steps, namely F = 50 kN, F = 100 kN and the final load step at which the cracks are measured manually i.e. F = 140 kN. In the graphs and in Table 2.38 a similar crack spacing is observed for both the mid-support zone and the span zone. The mean crack width, shown in Fig. 2.80, is similar for both strengthened zones. Furthermore, as can be noticed in Fig. 2.80, a somewhat larger crack width at the support is expected, according to fib Bulletin 14 [18]. For the span zones a good agreement is noticed between the analytical and experimental graphs.

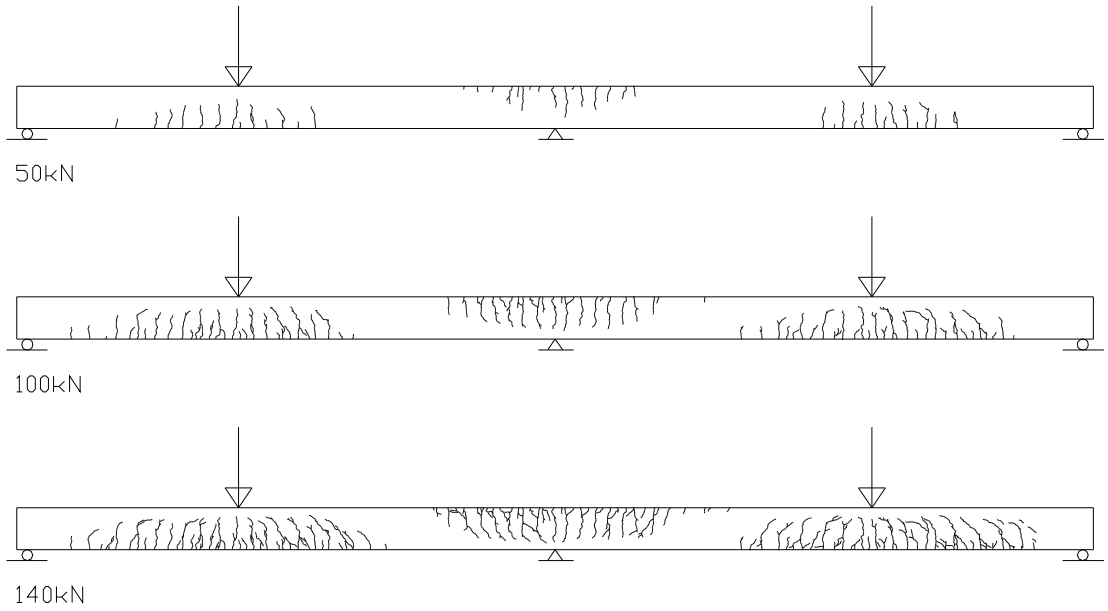

Fig. 2.79: Evolution of crack pattern of CB3

Table 2.38: Mean crack spacing and mean crack width at F = 140 kN for CB3

	left span zone	mid-support zone	right span zone
Mean crack spacing [mm]	82.8	79.4	79.4
Mean crack width [mm]	0.16	0.16	0.21

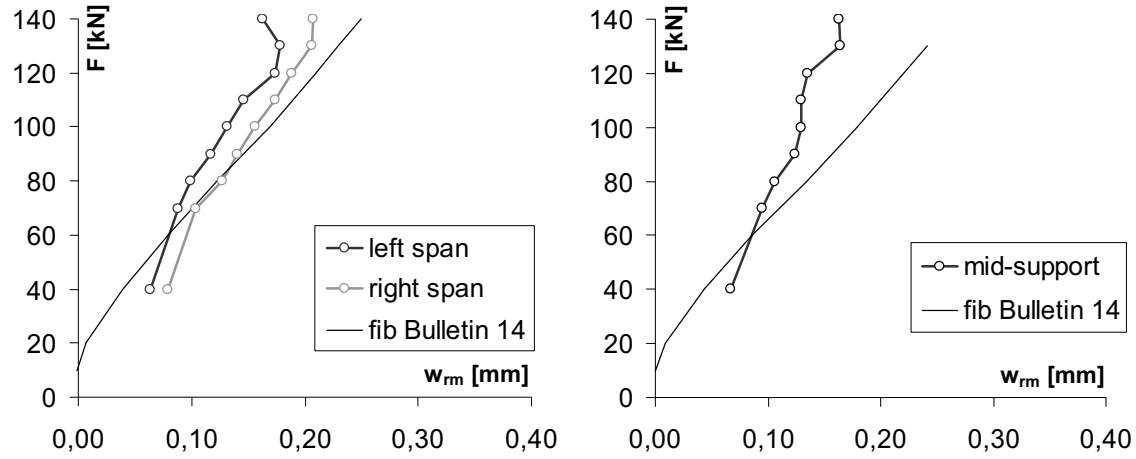

Fig. 2.80: Verification of the mean crack width of CB3

3.6 Continuous beam 4 (CB4)

3.6.1 Configuration

As mentioned in section 3.4, an electronical problem occurred with part of the recording of the measurements during the test on the second continuous beam (CB2). Due to this problem, it was decided to repeat the test of CB2, yet with a small modification of the internal reinforcement ratio. In the configuration of CB4, the internal reinforcement ratio in the spans is taken equal to 0.75 %. In the configuration of CB2 an internal steel reinforcement ratio equal to 0.99 % was used. By changing this internal steel reinforcement ratio, an earlier yielding of the spans and at the mid-support is obtained. In this way, the influence of yielding of the internal reinforcement on the FRP laminate can be investigated. The internal reinforcement ratio at the mid-support ($\rho_{s,support}$ = 0.31%) is taken equal to the internal reinforcement ratio of CB2. The entire internal reinforcement of CB4 is shown in Fig. 2.81. As external reinforcement, one CFRP laminate with a length of 5000 mm is applied at the mid-support. The cross-section of the CFRP laminate equals 100 mm x 1.0 mm ($\rho_{f,support}$ = 0.13 %).

The material properties are given in Table 2.39. These values result from standard tensile and compression tests.

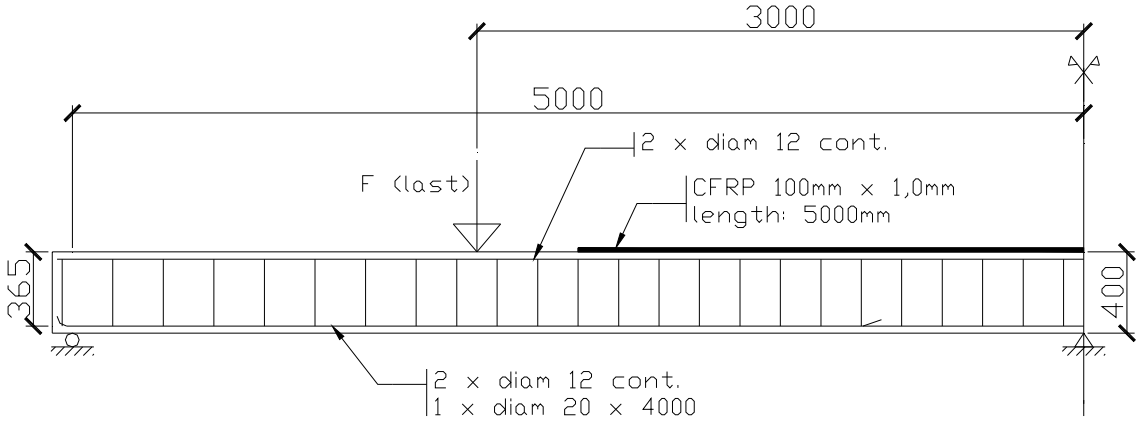

Fig. 2.81: Reinforcement configuration of CB4

Table 2.39: Properties of materials used for CB4

	Concrete	CFRP	steel at span	steel at mid-supp.
Compres. strength (f_{cm})	39.0 N/mm²	-	-	-
Yielding stress	-	-	600 N/mm²	589 N/mm²
Yield strain	-	-	0.29 %	0.26 %
Tensile stress	2.7 N/mm²*	2768 N/mm²	695 N/mm²	674 N/mm²
Failure strain	3.5 ‰ **	1.46 %	8.78 %	9.62 %
E-modulus	36 kN/mm²	190 kN/mm²	210 kN/mm²	223 kN/mm²

* Splitting test results and 3-point-bending tests results are converted to mean pure tensile strength according to EC2 [17]

** The failure strain of concrete is taken equal to 3.5 ‰, based on EC2 [17], as this value is not resulting from the standard tests

3.6.2 Moment curvature diagram

In Fig. 2.82 the moment-curvature diagrams of both the span and the mid-support sections of CB4 are given. Both experimental and calculated values are given (based on Fig. 2.82 and Table 2.40). Similar to the configuration of CB2, it can be noticed that the yielding moment at the mid-support ($M_{y,support}$) is considerably lower than the yielding moment in the span ($M_{y,span}$). The ultimate moment of the span ($M_{u,span}$) is smaller than the ultimate moment at the mid-support ($M_{u,support}$) under the assumption of full composite action.

Table 2.40: Moment - curvature values of both the span and mid-support sections of CB4

	span		mid-support	
	moment [kNm]	curvature [10^{-6}.1/mm]	moment [kNm]	curvature [10^{-6}.1/mm]
cracking	15.7	0.39	15.5	0.38
yielding	104.6	9.96	70.0	10.08
ultimate	111.7	77.18	150.9	43.01

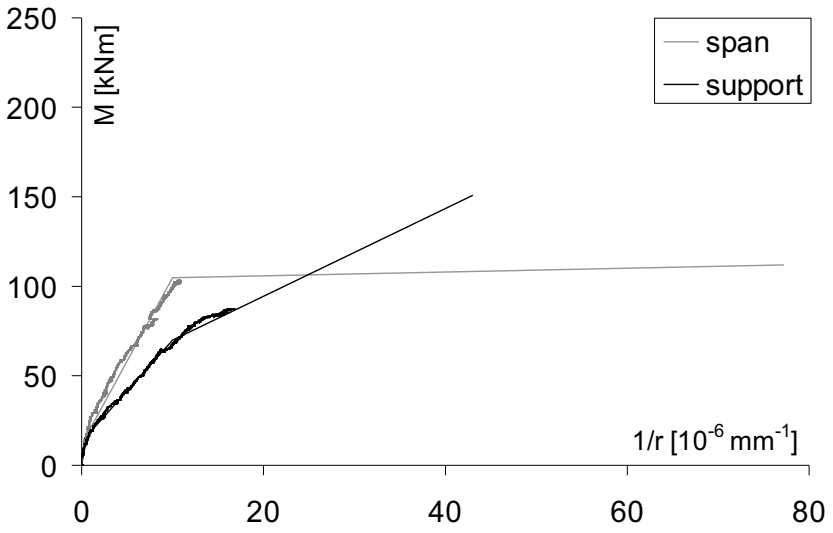

Fig. 2.82: Moment - curvature diagram of both the span and mid-support sections of CB4

3.6.3 Moment redistribution

In Table 2.41, the critical bending stiffness ratios and moment distribution ratios are given. As the moment distribution ratio m_3 is larger than m_t (Eq. 2.39), first yielding at the mid-support is expected.

Secondly, concerning the bending stiffness ratio k_3, a similar conclusion can be made compared to CB2. As the bending stiffness ratio k_3 is considerably smaller than the linear elastic moment distribution ratio (m_{el} = 0.972), a redistribution of the moments, characterized by a larger moment taken in the spans in comparison with the linear elastic theory is observed.

Finally the bending stiffness ratio k_5 is considerable larger than the linear elastic moment distribution ratio, which results in an additional moment redistribution starting at the yielding of both critical cross-sections. Now the redistribution is

characterized by a larger ΔM taken by the mid-support in comparison with the spans, which is due to the used amount of linear elastic FRP-EBR at the mid-support.

Table 2.41: Critical bending stiffness ratios k and moment distribution ratios m

k_1	m_1 ($=m_{el}$)	k_3	m_3	k_5	m_5	m_t
1.008	0.977	0.605	0.734	23.308	7.356	0.574

In Fig. 2.83, a similar moment redistribution for CB4 can be noticed as obtained for CB2. For the unstrengthened beam, the formation of a plastic hinge can be noticed at the mid-support (vertical part of the dashed moment distribution curve). In the case of the strengthened beam, although the strengthened mid-support section still starts to yield first (as mentioned above), the FRP allows the mid-support to continue resisting the additional load (restrained hinge). At increasing load, when the spans start to yield, a plastic hinge will be formed at the mid-support. Shortly afterwards, debonding of the laminate occurred at F = 115 kN. Concerning the experimental data, a good agreement is observed with the calculated curve.

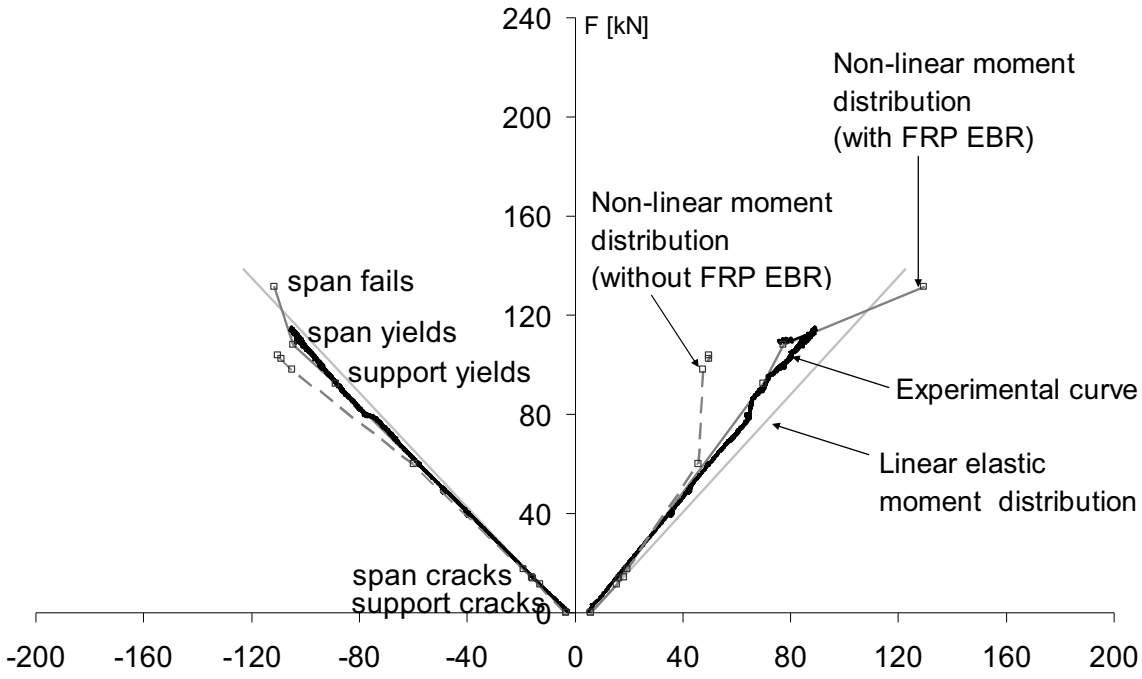

Fig. 2.83: Moment redistribution of CB4

In Fig. 2.84 the moment redistribution factor δ is given in function of the applied point load F. Similar to the previous graphs concerning the moment redistribution factor, a difference can be noticed between the theoretical and the experimental curve (up to 28 %) during the first 20 kN of the loading scale. In the upper part of the graph, a rather good agreement is noticed between the theoretical and experimental curves. Based on the experimental results a minimum redistribution

factor of 0.77 is obtained, which corresponds to a maximum reduction (at mid-support) of 23.2 %.

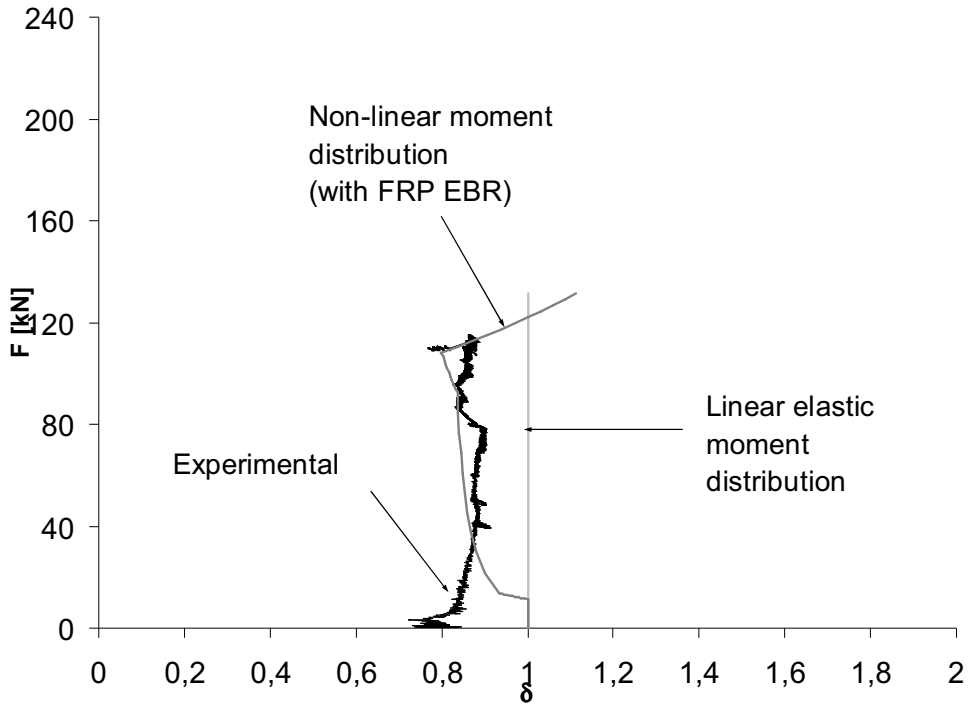

Fig. 2.84: Moment redistribution factor $\delta_{support}$ in function of the applied load F for CB4

3.6.4 Strain distribution at the critical cross-sections

In Fig. 2.85 to Fig. 2.87, the theoretical and experimental strain values at the critical cross-sections are given. In each graph the strain of the concrete and of both the internal and external reinforcement are given. The theoretical strain distribution is a multi-linear curve. Remark that in the graphs all strains are presented by the absolute values.

Comparing the electronical measurements with the analytically obtained multi-linear curves, a good agreement is noticed. In Table 2.42, the maximum absolute values of these strains are given.

From Fig. 2.86 it can be noticed that the critical cross-section at the mid-support still is able to resist the additional load after yielding ($F_{y,support}$ = 92 kN), due to the use of FRP at the mid-support. At the moment the spans start to yield, ($F_{y,span}$ = 108 kN), a change of stiffness in Fig. 2.86 is noticeable.

Table 2.42: Absolute experimental obtained values of maximum strains of CB4

	max. strain of concrete	max. strain of internal reinf.	max. strain of external reinf.
Left point load	0.136 %	0.279 %	-
Mid-support	0.076 %	0.534 %	0.418 %
Right point load	0.126 %	0.272 %	-

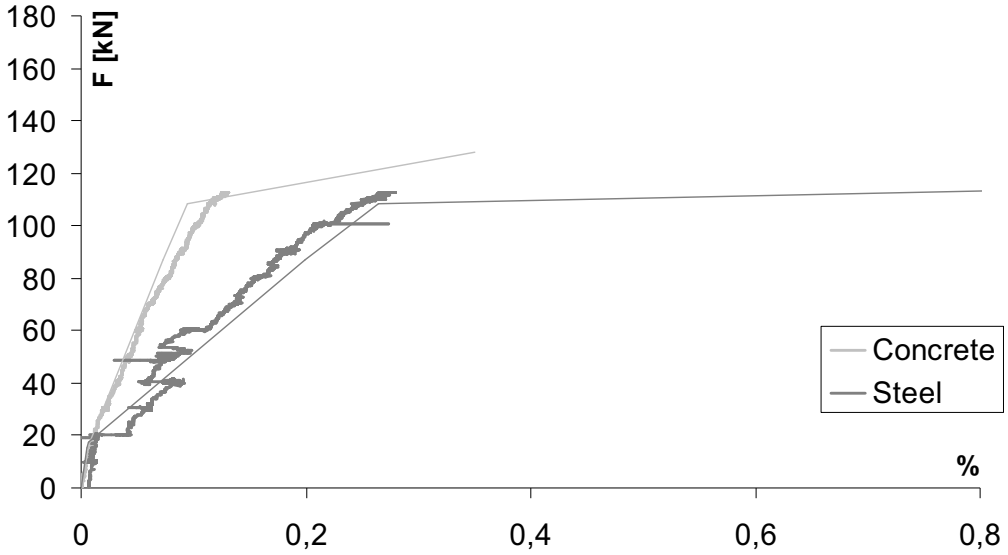

Fig. 2.85: Strain values at left point load.

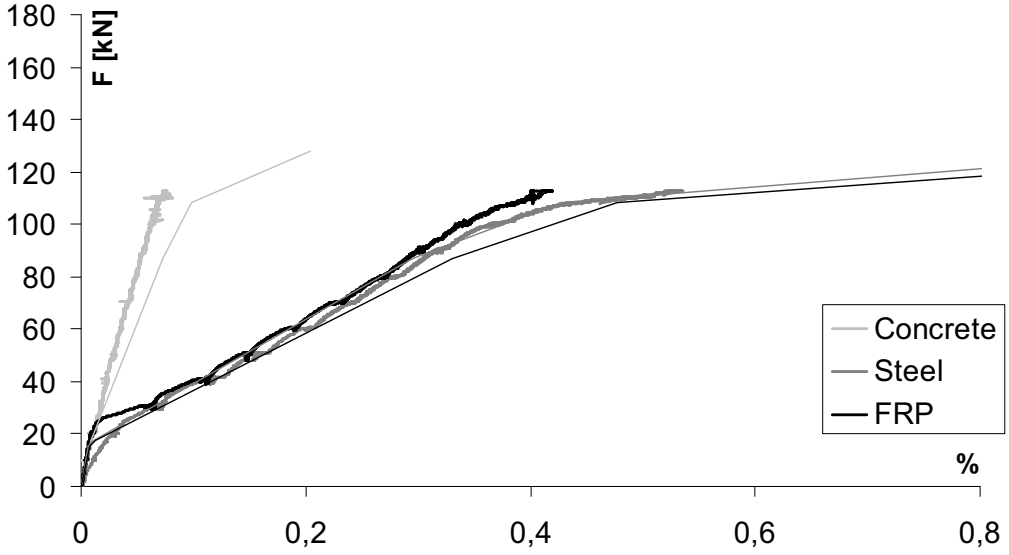

Fig. 2.86: Strain values at mid-support.

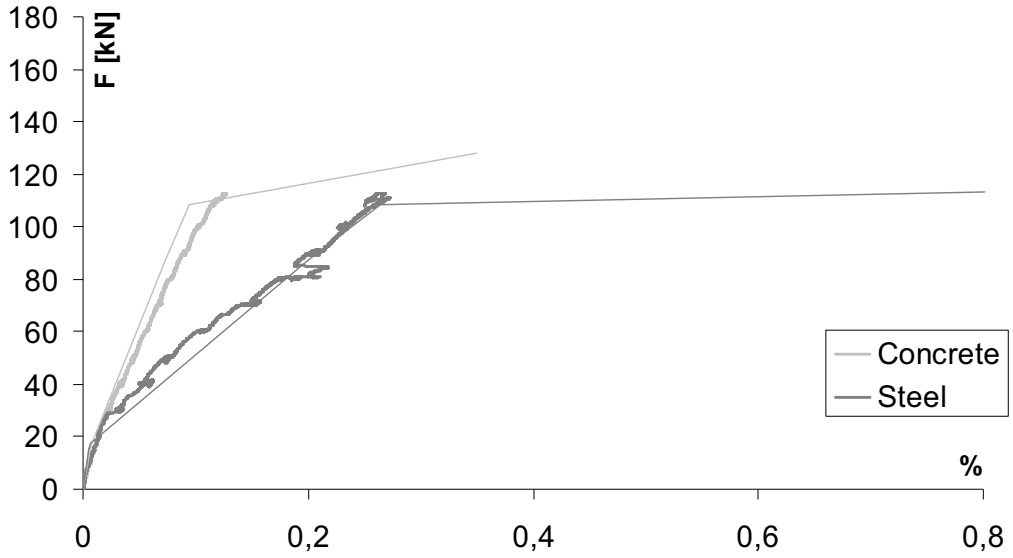

Fig. 2.87: Strain values at right point load.

3.6.5 Deflection

In Fig. 2.88 the measured deflection at the location of the point loads of CB4 is given in function of the applied load. Also the analytical deflection obtained by numerical integration is shown. A good agreement can be noticed between the analytical and experimental results.

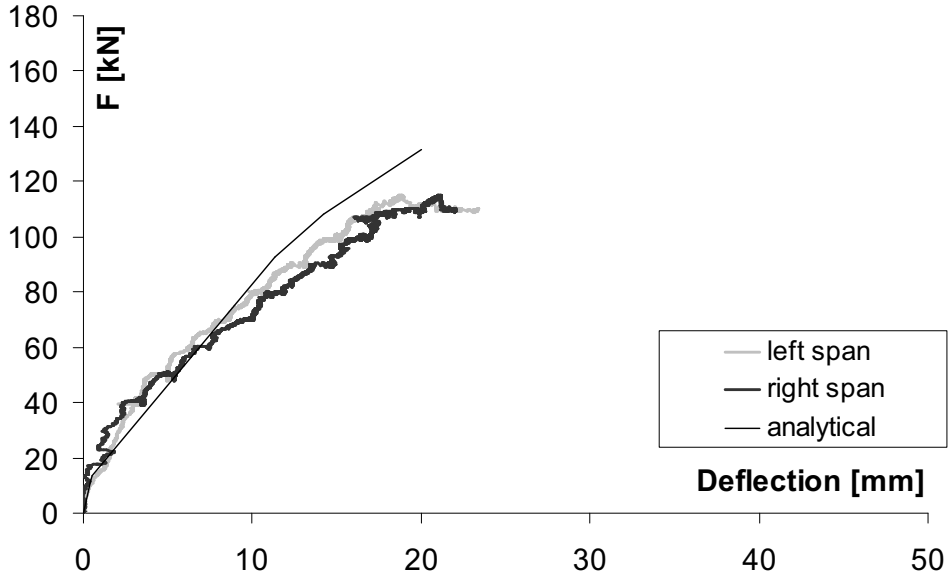

Fig. 2.88: Deflection of CB4 under the point loads

The deflection measured for the continuous beam CB4 (until F = 110 kN) is given in the left side of Fig. 2.89. No comparison is made with an unstrengthened

beam CB4 as this unstrengthened configuration has not been tested in [12]. In the strengthened beam no local rotation neither at the point load, nor at the mid-support, is visible. This also holds for the moment redistribution graph (Fig. 2.83), in which nearly no formation of plastic hinges is observed.

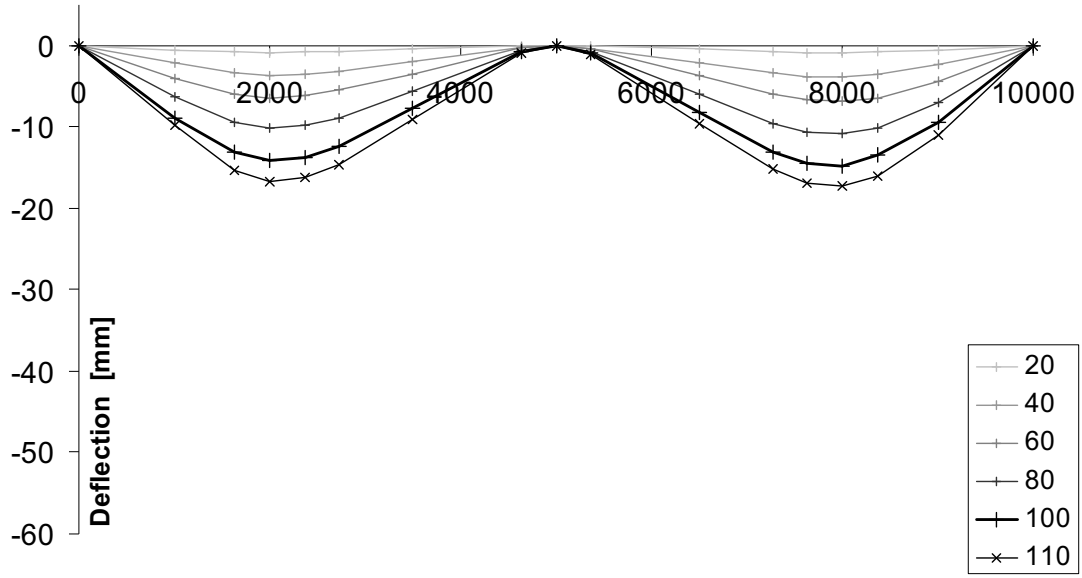

Fig. 2.89: Deflection of CB4 for different load levels

3.6.6 Crack formation

In Fig. 2.90 the crack evolution of CB4 is given at three different load steps, namely F = 50 kN, F = 100 kN and the final load step at which the cracks are measured manually i.e. F = 110 kN. In the graphs and in Table 2.43 a similar crack spacing is observed for the zone with externally bonded reinforcement (mid-support zone) in comparison with the zones without externally bonded reinforcement (span zone). Nevertheless a smaller equivalent reinforcement ratio is used at the mid-support ($\rho_{eq,support}$ = 0.43 %) compared to the spans ($\rho_{eq,span}$ = 0.75 %). It follows that the mean crack spacing at the mid-support ($s_{rm,support}$) equals about 94.0 % of the mean crack spacing in the spans ($s_{rm,span}$). The mean crack width, which is also shown in Fig. 2.91, is similar in the externally strengthened zone compared to the unstrengthened zone. Furthermore, as can be noticed in Fig. 2.91, a larger crack width at the mid-support is expected, according to fib Bulletin 14 [18]. For the unstrengthened zones (span zones), fairly accurate predictions are obtained.

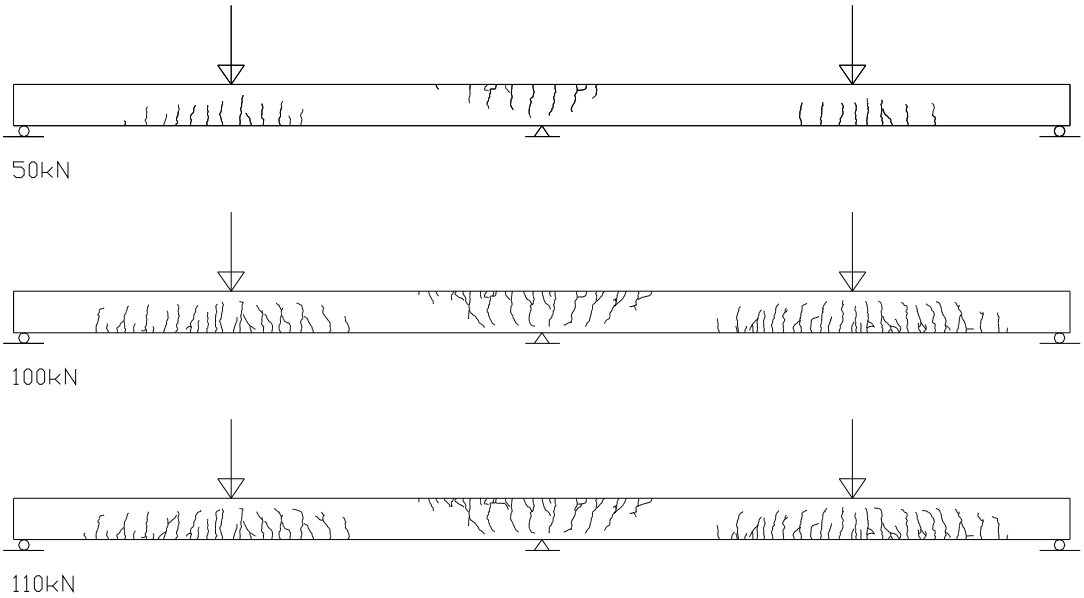

Fig. 2.90: Evolution of crack pattern of CB4

Table 2.43: Mean crack spacing and mean crack width at F = 110 kN for CB4

	left span zone	mid-support zone	right span zone
Mean crack spacing [mm]	97.3	86.7	86.9
Mean crack width [mm]	0.27	0.26	0.22

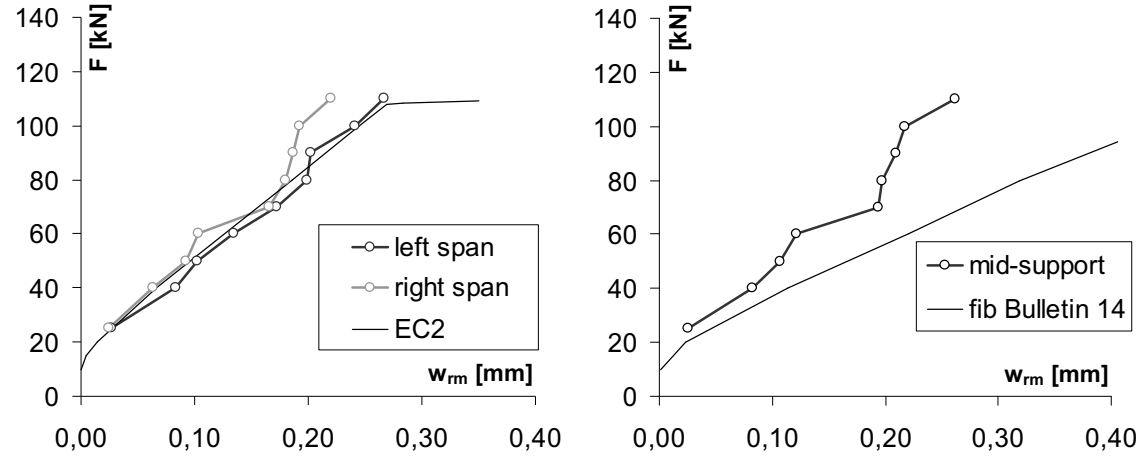

Fig. 2.91: Verification of the mean crack width of CB4

4 Conclusions

Analysing a continuous beam, four different types of analysis can be used (some of which are only valid for the ultimate state, see Chapter 6):

- linear elastic analysis
- linear elastic analysis with limited redistribution
- non-linear analysis
- plastic analysis

In this chapter the non-linear analysis of a two-span beam is presented. In this theory, in addition to the traditional equilibrium equations, a further equation is introduced to solve the statically indeterminate system by assuming no rotation of the beam at the mid-support. This additional equation is written in function of the bending stiffness ratio k (= $K_{support}/K_{span}$) and the moment distribution ratio m (=$M_{support}/M_{span}$) (see Eq. 2.10). To obtain the bending stiffness ratio k, the two-span beam is subdivided in three zones, each with a constant bending stiffness over the length of these zones (see $K_{support}$ and K_{span} in Fig. 2.9). To obtain the moment distribution ratio m the moments at the critical cross-sections of the spans and the mid-support are used (see $M_{support}$ and M_{span} in Fig. 2.9). Five different stages are assumed during the loading of the two-span beam (see also Appendix A) and from which the moment redistribution curve can be obtained:

- Stage k_1: $F \leq \min(F_{cr,span};F_{cr,support})$
- Stage k_2: $\min(F_{cr,span};F_{cr,support}) \leq F \leq \max(F_{cr,span};F_{cr,support})$
- Stage k_3: $\max(F_{cr,span};F_{cr,support}) \leq F \leq \min(F_{y,span};F_{y,support})$
- Stage k_4: $\min(F_{y,span};F_{y,support}) \leq F \leq \max(F_{y,span};F_{y,support})$
- Stage k_5: $\max(F_{y,span};F_{y,support}) \leq F \leq \min(F_{u,span};F_{u,support})$

Concerning this non-linear analysis and the experiments, the following conclusions can be made:

1/ The analytically obtained moment redistribution following from the non-linear analysis described in section 2, shows a good to excellent agreement with the experimentally obtained moment redistribution described in section 3.

2/ Also the analytically obtained strain distribution according the non-linear theory has a good to excellent agreement with the experimental obtained strain distribution described in section 3.

3/ In unstrengthened two-span beams, plastic hinges are expected in the zones with low internal reinforcement ratios (compared to the linear elastic reinforcement ratios). By strengthening only these zones with FRP EBR, the possibility exists to move the location of the plastic hinge to the zones with high internal reinforcement ratios (compared to the linear elastic reinforcement ratios).

4/ On the other hand, if it is opted to strengthen the zone with the high internal reinforcement ratio (compared to the linear elastic reinforcement ratios), the existing plastic hinge in the unstrengthened beam also acts as the plastic hinge in the strengthened beam. The plastic rotation of this plastic hinge is used to a further extent, in order to obtain a sufficient strengthening ratio. No high strengthening ratios can be achieved with this strengthening configuration.

5/ If both the internal and external reinforcement ratios of the two-span beam are calculated according to the linear elastic approach, a linear elastic moment distribution is obtained.

6/ Comparing the experimentally obtained deflection of a strengthened and unstrengthened beam, a significant reduction of the deflection is observed which is caused by the use of the linear elastic EBR and the early debonding of the EBR. Furthermore the local rotations at the plastic hinges in the unstrengthened beam are clearly visible, while in the strengthened beam no local rotations are visible, neither at the point loads nor at the mid-supports.

References

[1] A. Dall'Asta and A. Zona, *Comparison and validation of displacement and mixed elements for the non-linear analysis of continuous composite beams.* Computers & Structures. 2004. Vol. 82 (23-26): pp. 2117-2130.

[2] S. Coccia, U. Ianniruberto and Z. Rinaldi, *FRP Reinforcement at Sagging and Hogging Zones in Continuous Beams: Influence on Redistribution of Moment*. Proceedings of 2nd International fib Congress, Naples, Italy. 2006. Vol. 2: pp. 90-91

[3] L. Vasseur, S. Matthys and L. Taerwe, *Analytical study of a 2-span reinforced concrete beam strengthened with fibre reinforced polymer.* Proceedings of IABSE symposium: 'Responding to Tomorrow's Challanges in Structural Engineering', Budapest. 2006

[4] G. Macchi, *Elastic distribution of moments on continuous beams. Flexural mechanics of reinforced concrete*. Proceedings of International Symposium, Miami, Florida. 1964

[5] ISO-6892, *Metallic materials - Tensile testing at ambient temperature* 1998.

[6] NBN-B15-220, *Proeven op beton - Bepaling van de druksterkte*. 1990.

[7] NBN-EN-ISO-527, *Kunststoffen - Bepaling van de trekeigenschappen - Deel 1 : Algemene principes*. 1996.

[8] M.A. Aiello and L. Ombres, *Stiffness and Ductility of Continuous Reinforced Concrete Beams Strengthened with Externally Bonded FRP Sheets*. Proceedings of 2nd International fib Congress, Naples, Italy. 2006. Vol. 2: pp. 168-169

[9] W.M. Sebastian, *Optimisation of flexural stiffness profiles to compensate for reduced ductility in hyperstatic reinforced concrete structures.* Engineering Structures. 2006. Vol. 28 (6): pp. 893-902.

[10] L. Sowa, T. Wasniewski and M.E. Kaminska, *Flexural strengthening of RC continuous beams using CFRP laminates [Cement & Concrete Composites 26 (2004) 765-775].* Cement and Concrete Composites. 2005. Vol. 27 (9-10): pp. 958-961.

[11] D.J. Oehlers, et al., *Moment redistribution in continuous plated RC flexural members. Part 2: Flexural rigidity approach.* Engineering Structures. 2004. Vol. 26 (14): pp. 2209-2218.

[12] L. Taerwe and B. Espion, *Serviceability and the Nonlinear Design of Concrete Structures*. Proceedings of IABSE PERIODICA 2/1989. 1989: pp. 61-76

[13] CUR-rapport-83, *Doorgaande balken van gewapend beton*. Stichting voor onderzoek, voorschriften en kwaliteitseisen op het gebied van beton. 1980. pp. 124.

[14] L. Taerwe, *Doorlopende Liggers van gewapend beton.* Tijdschrift der openbare werken van België. 1981. Vol. 5: pp. 423-441.

[15] L. Vasseur, S. Matthys and L. Taerwe, *Load tests on 2-span reinforced concrete beams strengthened with fibre reinforced polymer*. Proceedings of ACIC 07: 'Advanced Composites in Construction Conference 2007', University of Bath, UK. 2007: pp. 422-429

[16] NBN-B15-214, *Proeven op beton - buigproef op betonprisma's*. 1990.

[17] CEN, *Eurocode 2: EN 1992-1-1: Design of concrete structures - Part 1-1: General rules and rules for buildings*. ed. CEN. 2004.

[18] fib, *fib bulletin 14, Externally bonded FRP reinforcement for RC structures*. International federation for structural concrete, Lausanne. 2001: pp. 138.

Chapter 3

BOND BEHAVIOUR OF EXTERNALLY BONDED FRP TO CONCRETE IN THE CASE OF CONTINUOUS BEAMS

1 Introduction

The use of EBR to strengthen reinforced concrete structures implies the possible occurrence of debonding of the laminates. In the design of a strengthened member, often full composite action is assumed to start with. In a second stage, different debonding mechanisms are considered or verified in the design. In this chapter, these different debonding mechanisms are checked in the case of continuous beams. As can be noticed in this chapter, some advantages are related to the use of FRP EBR in continuous beams. By anchoring the laminates into the compression zones, two of the four typical debonding mechanisms can be avoided.

On the other hand, special caution has to be taken during the verification of the debonding mechanisms. Due to the non-linear behaviour, several parameters influencing the debonding mechanisms are changing in a favourable or unfavourable way, depending on the degree of moment redistribution and the strengthening configuration. Indeed, the possibility exists that applying a larger section of FRP EBR in a tension zone of a continuous beam causes earlier debonding and related to this the bearing capacity of the beam may be lower than expected. This is contradictory to the axiom of Feinberg [1]: "*The bearing capacity of a structure can not be reduced if the yielding moment is increased in at least one section without reducing it in the other sections"*. However, the previous conclusion is not inconsistent with this axiom as the FRP laminates do not exhibit plastic behaviour. By applying a larger section of FRP laminates into a section, the yielding moment of this section will increase. Nevertheless, as mentioned above and discussed in section 4, the expected debonding load and related to this, the loading bearing capacity of the beam, can be underestimated if the non-linear behaviour is not properly considered in the design.

As a result, it is important to take into account the moment redistribution for the verification of the debonding mechanisms.

2 Loss of composite action

2.1 Overview of the different debonding mechanisms

For the design of an externally strengthened beam at the ultimate limit state (ULS), guidelines recommend a similar two stage analysis method [2-4]. First, the strengthened beam is being designed assuming a full composite action. Full composite action means that no debonding of the FRP EBR material from the concrete is taken into account. One of the following failure modes occurs:

- Steel yielding followed by concrete crushing
- Steel yielding followed by FRP fracture
- Concrete crushing without steel yielding (this failure mode is generally not allowed in design)

In the second design stage of an externally strengthened beam at the ultimate limit state (ULS), the loss of composite action has to be checked between the concrete and the FRP reinforcement. This type of failure is often very sudden and brittle. Bond failure can occur at different interfaces. A distinction can be made between:

- Debonding in the concrete, near to the surface
- Debonding in the concrete, along the embedded reinforcement
- Debonding in the adhesive
- Debonding in the FRP (interlaminate shear failure)
- Debonding at the interface between concrete and adhesive or adhesive and laminate

In practice, debonding in the adhesive or FRP is generally not noticed because the tensile and shear strength of the resin or adhesive is mostly higher than the tensile and shear strength of the concrete. The last type of debonding, debonding at one of the interfaces only occurs if one of the specific surfaces is insufficiently prepared. Hence, it can be concluded that debonding normally occurs in the concrete, near to the surface or along the embedded reinforcement. The exact location of debonding in the concrete cover is dependent on the type of debonding mechanism which is typical for a certain type of beam. According to fib Bulletin 14 [2] and Matthys [3] different bond failure aspects can be distinguished, among which:

- Debonding at flexural cracks (see section 2.1.1.1)
- Debonding at shear cracks (see section 2.1.1.2)
- Curtailment and anchorage length (see section 2.1.2)
- End shear failure (see section 2.1.3)

2.1.1 Crack bridging

Concerning the debonding phenomenon by crack bridging, often a distinction is made between the bridging of flexural cracks and the bridging of shear cracks by the FRP laminate. This is illustrated in Fig. 3.1.

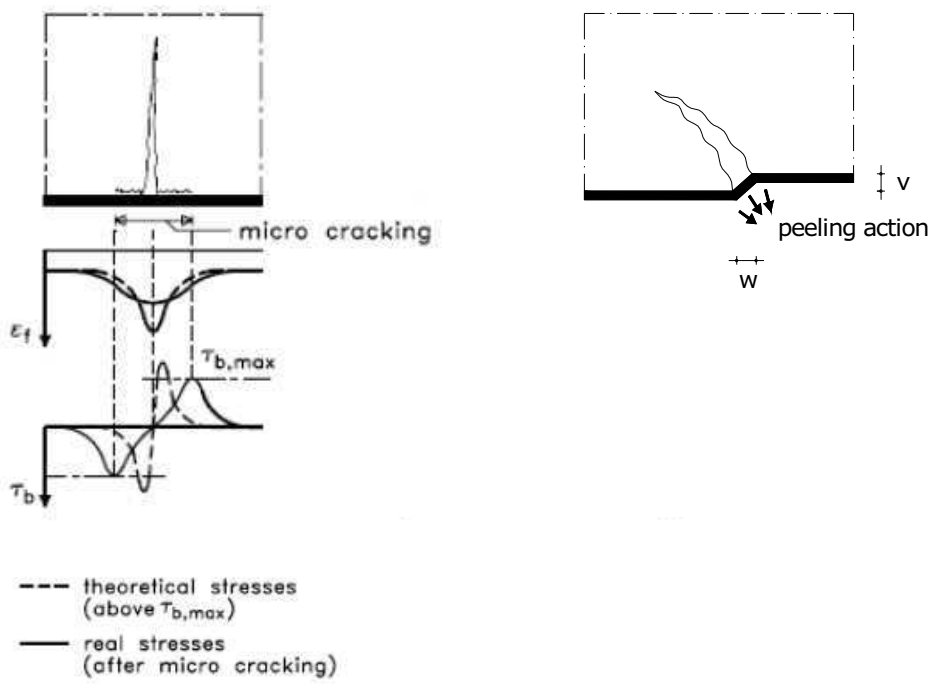

Fig. 3.1: A: Bridging a flexural crack [3] B: Bridging a shear cracks [2]

2.1.1.1 Debonding at flexural cracks

In a first approach attention is given to flexural cracks. These cracks are characterized by a horizontal crack opening (see Fig. 3.1.A). Near to this crack, at both sides of the opening, high peak shear stresses appear. When this peak shear stress exceeds the maximum shear stress ($\tau_{b,max}$), a gradual debonding is noticed, initiated by micro cracking and finally continuing in macro cracking.

When debonding is initiated, the shear stress redistributes and a smoothing effect occurs as illustrated in Fig. 3.1.A, for the ideal case of pure flexure. From this smoothing of the shear stresses, one could conclude that this debonding failure mode is less critical than crack bridging at flexural cracks in regions with also significant shear forces (and hence vertical crack displacement) [3]. As indicated by several authors [5-7], debonding at the location of a flexural crack can result in a complete debonding of the FRP laminate and has to be checked consequently. According to fib Bulletin 14 [2], the treatment of peeling off at flexural cracks can be done according to several approaches. A distinction is made between:

- Strain limitation in the FRP, assuming a nominal value of the strain limit. This is a simplified method, not recommended due to the lack of detailed information on proper values for a generic strain limit.
- Verification of the bond stresses due to force transfer at the FRP/concrete interface
- Verification according to the envelope line of the tensile stresses in the FRP. This detailed approach is the most complex to calculate of the three fib Bulletin approaches and is also independent on a proper prediction of the crack spacing.

Verification of the bond stresses due to force transfer

The variation of the tensile force in the FRP, due to the composite action between the FRP EBR and the concrete beam, initiates bond shear stresses τ_b at the interface. To avoid debonding of the laminate by this mechanism, the shear stress between the FRP and the concrete, resulting from the change of tensile forces along the length of the laminate, has to be limited. This shear stress is calculated as follows, based on the equilibrium of forces as can be seen in Fig. 3.2 and assuming constant bond stress.

$$\tau_b = \frac{\Delta N_{fd}}{b_f \Delta x} \tag{3.1}$$

This acting shear stress in the ULS has to be limited to the design bond shear strength (f_{cbd}), which is given by the following equation:

$$f_{cbd} = 1{,}8 \frac{f_{ctk}}{\gamma_c} \tag{3.2}$$

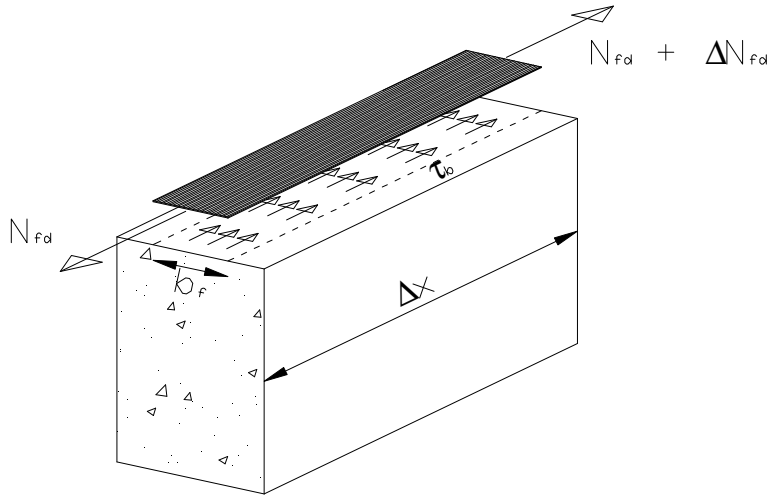

Fig. 3.2: Shear stresses along the FRP EBR laminate

Due to the considerable width of the bond interface, this limitation of the shear stress will not be critical in most cases. Except in case the internal steel reinforcement is yielding (resulting in high values of ΔN_{fd}), bond problems may occur.

Verification according to the envelope line of tensile stresses in the FRP

The model, proposed by Niedermeier [8], is based on the envelope line of tensile stresses in the FRP. More specifically this approach defines the maximum possible increase in tensile stress in the FRP laminate (max $\Delta\sigma_{fd}$), which can be transferred by the bond interface between two subsequent flexural cracks. In Fig.

3.3 max $\Delta\sigma_{fd}$ is given in function of the applied tensile stress in the externally bonded FRP laminate (σ_{fd}).

An analysis of the bond behaviour of the EBR based on a bilinear bond stress–slip relation (see Fig. 3.4) leads to equations which can be used to calculate the maximum increase in tensile stress max $\Delta\sigma_{fd}$ in an element between two cracks depending on the tensile stress σ_{fd}.

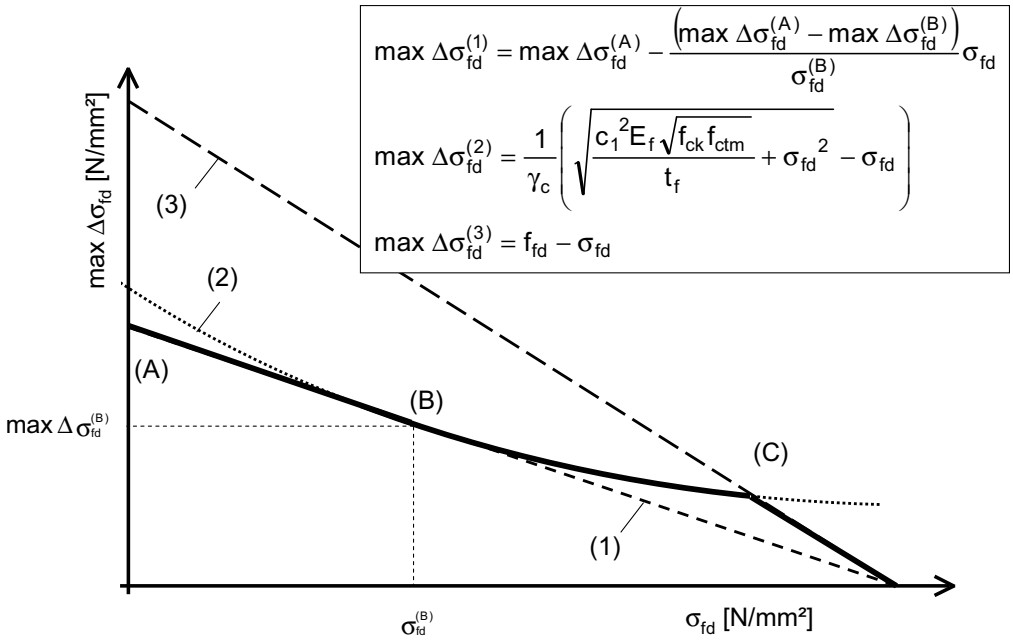

Fig. 3.3: Maximum possible increase in tensile stress between two subsequent cracks [2]

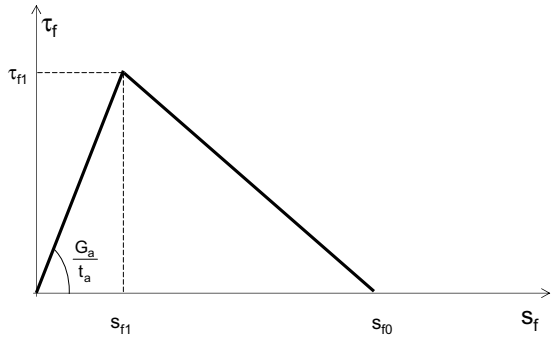

Fig. 3.4: Bilinear bond stress–slip relation

Point A (max $\Delta\sigma_{fd}^{(A)}$) in Fig. 3.3 is related to the debonding force, defined by a pure shear test with a bond length which equals the mean crack spacing. Hence point A can be seen and calculated as the debonding stress at the end anchorage. The coordinates of point B can be calculated with Eqs. 3.3 and 3.4.

$$\sigma_f^{(B)} = \frac{c_3 E_f}{s_{rm}} - c_4 \sqrt{f_{ck} f_{ctm}} \frac{s_{rm}}{4 t_f} \qquad (3.3)$$

$$\max \Delta\sigma_{fd}^{(B)} = \frac{1}{\gamma_c}\left[\sqrt{\frac{c_1{}^2 E_f \sqrt{f_{ck} f_{ctm}}}{t_f} + \left(\sigma_f^{(B)}\right)^2} - \sigma_f^{(B)}\right] \tag{3.4}$$

where c_1, c_3 and c_4 are constant values which equal 0.23; 0.185 and 0.285 respectively [2].

For high tensile stresses, the upper limit of the increase in stresses is determined by the tensile strength of the FRP (f_{fd}) as can be seen Eq. 3.5.

$$\max \Delta\sigma_{fd}^{(3)} = f_{fd} - \sigma_{fd} \tag{3.5}$$

For further information concerning this approach, reference is made to [2, 8]

In section 2.2 and section 4 of this chapter, debonding at flexural cracks is checked by means of the first model (Verification of the bond stresses due to force transfer). In section 5 of this chapter, an additional check of debonding at flexural cracks is executed, according to the last approach (verification according to the envelope line of tensile stresses in the FRP).

2.1.1.2 Debonding at shear cracks

Crack bridging models for shear cracks explicitly consider the combined effect of horizontal and vertical displacement.

In regions with significant shear forces, the shear cracks are inclined, and are associated with both horizontal (w) and vertical (v) crack displacements (see Fig. 3.1.B). Due to the horizontal crack displacement, peak shear stresses are induced. On the other hand, the vertical crack displacement results in an additional peeling-off effect of the laminate by inducing tensile stresses perpendicular to the FRP laminate.

To evaluate this latter debonding mechanism, several models can be found in literature [2, 3, 9]. fib Bulletin 14 proposes a model (Eurocode 2 approach), which may prevent peeling-off at shear cracks by limiting the acting shear force to the shear resistance V_{rd1} (see Eq. 3.6) of RC beams without shear reinforcement [9]. The following modifications to the characteristic shear strength of concrete τ_{Rk} and the equivalent longitudinal reinforcement ratio ρ_{eq} have to be made.

$$V_{Rd1} = \left[\tau_{Rd}\, k\, \left(1{,}2 + 40\rho_{eq}\right) + 0{,}15\sigma_{cp}\right] b_w d \tag{3.6}$$

$$\tau_{Rd} = \frac{\tau_{Rk}}{\gamma_c} = \frac{0{,}15 f_{ck}^{1/3}}{\gamma_c} \tag{3.7}$$

$$\rho_{eq} = \frac{A_s + A_f \dfrac{E_f}{E_s}}{b_w d} \tag{3.8}$$

with:
k : 1.6 – d ≥ 1 (d in [m])
b_w : minimum width within the effective height (d)
σ_{cp} : N_{Sd} / A_c
N_{Sd} : longitudinal force in the cross-section due to the loading configuration or prestressing
A : cross-sectional area of FRP reinforcement (index f) and longitudinal steel reinforcement (index s)
E : modulus of elasticity

In [3] another approach is applied, considering a crack appearing in between two successive stirrups, by which the following resisting shear force (V_{Rp}) is calculated:

$$V_{Rp} = \tau_{cza} b \left(x_e + (h - x_e)\left(1 - \frac{\varepsilon_0 + \varepsilon_f}{\varphi}\right)\right) + \chi_{da}\left(E_s A_s + E_l A_l\right) \qquad (3.9)$$

with:
τ_{cza} = the shear stress transferred in the compression zone and the shear crack (aggregate interlocking). From experimental results it follows that τ_{cza} = 0.71 N/mm²
$\varepsilon_0 + \varepsilon_f$ = strain at the extreme tension fibre
φ = w_{crit}/s_{rm} the ratio of the critical crack width at which no aggregate interlocking is noticed any more
χ_{da} = coefficient relating the dowel action to the axial stiffness of the reinforcement

As Eq. 3.9 results in a complex calculation of the resisting shear force, an alternative equation (see Eq. 3.10 and 3.11) is proposed in [3]. This equation is calibrated on experimental results obtained from 4-point bending tests for concrete strengths C25/30 and C30/37. Both CFRP prefab and wet lay-up types are considered.

$$V_{Rp} = \tau_{Rp} b d \qquad (3.10)$$

$$\tau_{Rp} = 0{,}38 + 151\rho_{eq} \qquad (3.11)$$

where $\rho_{eq}=\rho_s+\rho_f E_f/E_s$ the equivalent reinforcement ratio.

2.1.2 Curtailment and anchorage length

Theoretically the FRP reinforcement can be curtailed when the axial tensile force can be carried by the internal steel only. The remaining force in the FRP at this point needs to be anchored. Nevertheless, the FRP may need to be extended to zones corresponding to even lower FRP tensile stresses, as the anchorage capacity of the interface is limited (see Fig. 3.5).

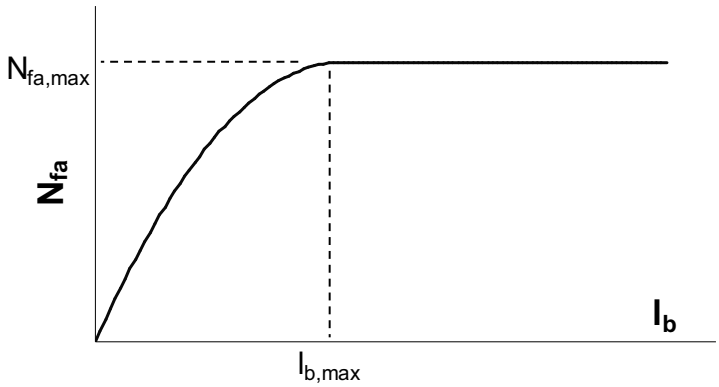

Fig. 3.5: Maximum FRP force which can be anchored in function of the bond length

The values of the maximum FRP force which can be anchored, $N_{fa,max}$, and the maximum anchorage length, $l_{b,max}$ (as can be noticed in Fig. 3.5) are equal to [2]:

$$N_{fa,max} = \alpha c_1 k_c k_b b_f \sqrt{E_f t_f f_{ctm}} \tag{3.12}$$

$$l_{b,max} = \sqrt{\frac{E_f t_f}{c_2 f_{ctm}}} \tag{3.13}$$

where α is a reduction factor, approximately equal to 0.9, to account for the influence of inclined cracks on the bond strength; k_c is a factor accounting for the state of compacting of concrete and k_b is a geometrical factor:

$$k_b = 1{,}06 \sqrt{\frac{2 - \frac{b_f}{b}}{1 + \frac{b_f}{400}}} \geq 1 \tag{3.14}$$

The anchorage length model given in Eqs. 3.12 and 3.13 is based on fracture mechanics considerations, e.g. [10]. Bond models assuming elastic behaviour (e.g. to verify debonding crack initiation) are also reported in literature, e.g. [11].

2.1.3 End shear failure (concrete rip-off)

By curtailing a laminate at a certain distance from a support, a shear crack can appear at the FRP-end. The propagation of this crack is hindered by the internal steel reinforcement (both the stirrups and the longitudinal reinforcement) and the aggregate interlocking. Although, due to the lack of internal steel stirrups between the internal steel reinforcement and the external FRP reinforcement (see Fig. 3.6), this shear crack may propagate as a debonding failure at the level of the internal steel reinforcement. In this case the laminate as well as a thick layer of concrete will rip off.

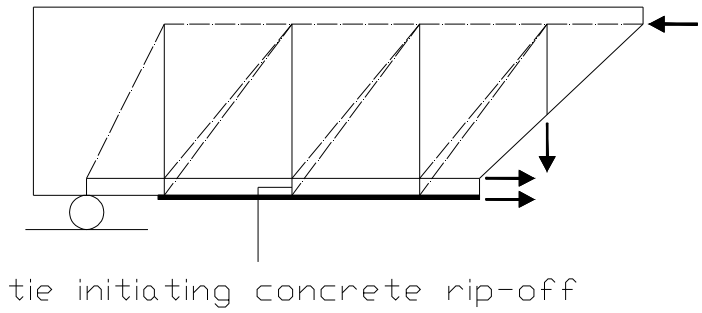

Fig. 3.6: Truss system in order to explain the tie initiating of concrete rip-off

An important parameter in the mechanism of concrete rip-off is the distance between the plate end and the support. Related to continuous beams, the latter has to be seen as the distance between the plate end and the point of contraflexure.

The modelling of concrete rip-off is based on the shear crack model. Herewith a comparison is made with a non-strengthened beam by which the shear crack appears at a distance a_c with respect to the distance a (see Fig. 3.7). Projecting this model on the strengthened configuration, the critical shear crack is observed at a distance L, to which a fictitious shear crack span a_L is corresponding. The magnitude of this fictitious shear crack span is obtained by the following equation:

$$a_L = \left(\frac{\left(1 - \sqrt{\rho_s}\right)^2}{\rho_s} L^3 d \right)^{1/4} \tag{3.15}$$

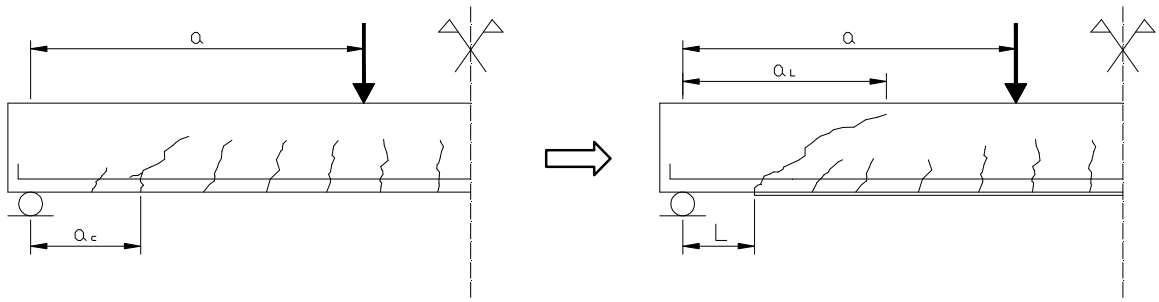

Fig. 3.7: Modelling of concrete rip-off

Based on the concept of the fictitious shear force zone a_L, it is possible to estimate the resisting shear force at the location of the plate end [2, 12]:

$$V_{Sd} \leq V_{Rd1} = \tau_{Rd1} b d \tag{3.16}$$

with: τ_{Rd1} equals the design value of the nominal maximum resisting shear stress

$$\tau_{Rd1} = 0{,}15\left(3\frac{d}{a_L}\right)^{1/3}\left(1+\sqrt{\frac{200}{d}}\right)(100\rho_s f_{ck})^{1/3} \quad (3.17)$$

In these equations only the internal reinforcement is taken into account. Moreover, it has to be mentioned that the model only is applicable if the following conditions are fulfilled:

$$a > L + d \text{ and } a_L < a \quad (3.18)$$

From experimental research it can be concluded that this model is an accurate lower bound limit for the prediction of concrete rip-off.

2.2 Control of debonding in case of a two span continuous beam

In Chapter 2, four different configurations of two span beams are described. By testing these different configurations an exact debonding load is obtained. In this section, an analytical study is conducted concerning the appearance of the debonding mechanisms in comparison to the test results given in Chapter 2, section 3. A shifted moment distribution over the distance z/2 is used. Herewith, z equals the lever arm of the critical cross-section.

The results of this study are shown in Fig. 3.9, Fig. 3.12, Fig. 3.15, Fig. 3.17 and Fig. 3.19. In these graphs the resisting bond strength is given as a function of the length of the FRP laminate. This is done for the different debonding mechanisms:

- Crack bridging at flexural cracks, calculated according to Eq. 3.1
- Crack bridging at shear cracks, calculated according to Eq. 3.11
- Curtailment and anchorage length, calculated according to Eq. 3.12
- End shear failure, calculated according to Eq. 3.16

The interpretation of the graphs is as follows. The length of the X-axis equals 5000 mm and corresponds to the left span of the two-span beam. The origin corresponds to the left support and the value 5000 corresponds to the mid-support. Along the Y-axis, the point load is given. The non-linear grey curve represents the position of the point of contraflexure, i.e. the location where the moment equals zero. As it is noticed from the graphs, the point of contraflexure is not fixed, but moves with increasing load. This phenomenon is caused by the non-linear moment redistribution. Different black curves can be noticed in the graphs. These curves represent the occurrence of the different debonding mechanisms calculated for the specific strengthening configuration, in function of the positions of the laminate ends over the length of the beam. The actual laminate ends as tested are indicated by vertical dashed lines. If the position of the laminate ends crosses one of the above mentioned black curves, debonding is expected. Or in other words, if one of the laminate ends is situated within the grey hatched zone at a certain load level (see Fig. 3.9 - Fig. 3.19), debonding will be expected, depending on the governing debonding mechanism, somewhere between the specific laminate end and the point load. For example, the

configuration of CB1 is given in Fig. 3.9, for which a 3750 mm long laminate is applied at the soffit of the spans. The distance between the laminate end and the centre of the outer support equals 150 mm. This results in the position of the laminate ends equalling 150 and 3900 (= 3750 + 150) on the X-axis (see vertical dashed lines in Fig. 3.9). By following these vertical dashed lines, in function of the applied load, it can be noticed that at the left side of the point load debonding is expected at 162 kN by concrete rip-off, while at the right side of the point load debonding is expected at 156 kN by crack bridging at shear cracks. From this analysis it can be concluded that the laminate will debond at an applied point load equal to 156 kN by crack bridging at shear cracks.

Finally a discontinuity in all graphs is noticed at the location of the point load at an X-value of 2000 mm. This discontinuity is caused by the investigation of the different debonding mechanisms in two different zones, i.e. the zone between the left laminate end and the point load and the zone between the point load and the right laminate end.

Regarding Fig. 3.12, Fig. 3.17 and Fig. 3.19, the different debonding mechanisms of the top laminate applied above the mid support are given, similar to the debonding mechanisms of the laminates applied at the soffit of the beam (see Fig. 3.9 and Fig. 3.15). Remark that only half of the top laminate is investigated, i.e. the zone between the left support and the mid-support. Due to the symmetry of the beam with respect to the mid-support, a similar graph is obtained for the right beam span.

Concerning the different debonding mechanisms it can be noticed that both debonding by crack bridging at shear cracks and debonding by crack bridging at flexural cracks are independent of the actual laminate length. This corresponds to horizontal lines, as can be seen from Fig. 3.9 to Fig. 3.19. Herewith, it can be concluded that these debonding mechanisms will occur at a certain load level (debonding load), independent of the used laminate length.

On the other hand, the debonding mechanisms related to anchorage length and end shear failure (concrete rip-off) are not characterized by a horizontal line. A non-linear curve is observed, as these debonding mechanisms depend indirectly on the FRP length (dependently on e.g. available anchorage capacity (section 2.1.2) or on the variable L (section 2.1.3).

In Fig. 3.9 to Fig. 3.19 also a horizontal dashed line is observed. This line represents the ultimate load of the unstrengthened configuration (indicated by $F_{u,unstr}$). As is noticed from the graphs, debonding of a short laminate can occur at a load level which is lower than the ultimate load of the unstrengthened beam. However, all beams with an early debonded laminate still are able to sustain additional loads until $F_{u,unstr}$.

A comparison between the experimental and analytical debonding loads and failure aspects is given in Table 3.1. A good agreement is noticed for CB1 and CB3. For CB2, later debonding is noticed in the test compared to the prediction (ΔF = 19.2 kN). For CB4 an earlier debonding is noticed compared to the analytical predictions (ΔF = 9.8 kN). More detailed information concerning these debonding phenomena is given in following sections.

Table 3.1: Calculated and experimental obtained debonding load

	$F_{deb,calc}$	Anal. obtained debonding mechanism	$F_{deb,exp}$	Exp. obtained debonding mechanism	F_{exp}/F_{calc}
CB1	156.1	crack bridging at shear cracks	152.8	crack bridging at flexural/shear cracks	0.98
CB2	132.8	crack bridging at shear cracks	152.0	crack bridging at flexural/shear cracks	1.14
CB3	162.3	concrete rip-off	170.5	crack bridging at flexural/shear cracks	1.05
CB4	125.7	crack bridging at shear cracks	115.9	crack bridging at flexural/shear cracks	0.92

2.2.1 Debonding mechanisms for beam configuration CB1

As can be noticed in Fig. 3.8, an FRP laminate of 3750 mm is applied at the soffit of both spans. These laminates are glued up to 150 mm from the centre line of the end supports. As a consequence, the other laminate end is situated at a distance equal to 3900 mm (see vertical dashed lines in Fig. 3.9). By following these vertical dashed lines starting from 0 kN, debonding is observed at the left laminate end at 162 kN and at the right laminate end at 156 kN. Hence, debonding is expected at 156 kN. This debonding is induced by crack bridging at shear cracks in the zone between the point loads and the mid-support.

During the test, debonding by crack bridging at shear cracks is noticed at 153 kN in the right span between the point load and the mid-support (see Fig. 3.10). This result is a good agreement between the analytical and experimental debonding loads.

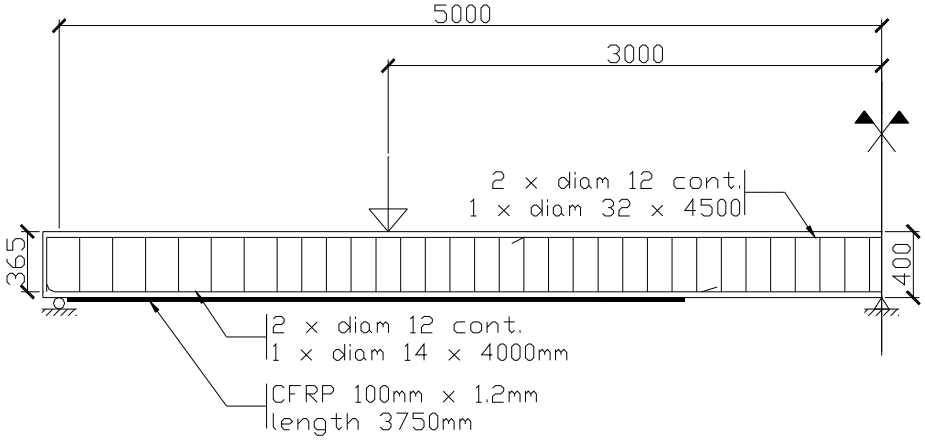

Fig. 3.8: Reinforcement configuration of CB1

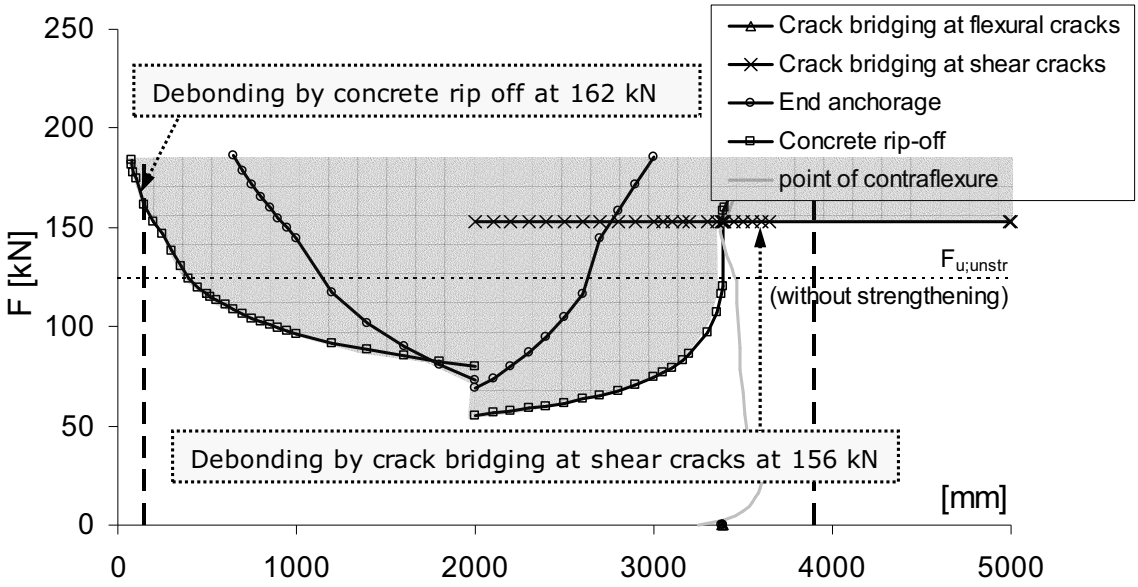

Fig. 3.9: Appearance of different debonding mechanisms in the span laminate (CB1)

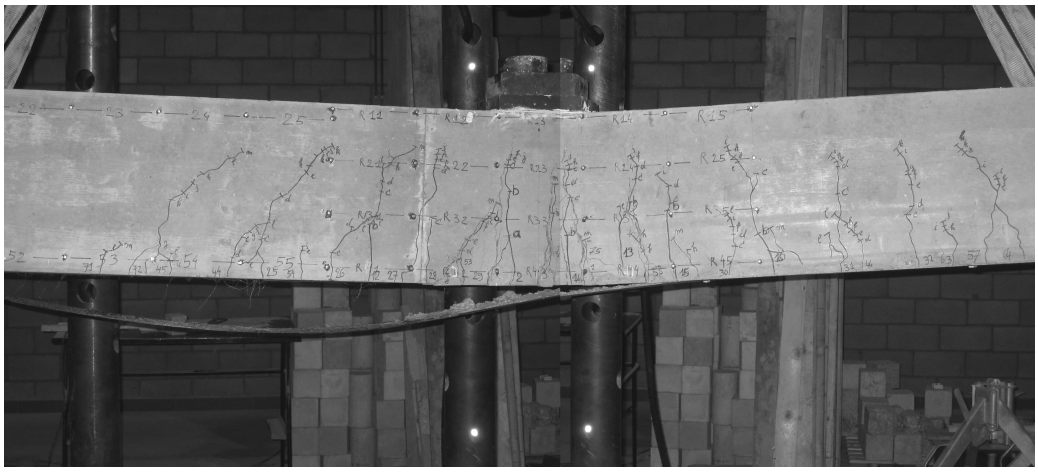

Fig. 3.10: Debonding of the laminate at the soffit of the right span by crack bridging.

2.2.2 Debonding mechanisms for beam configuration CB2

As can be noticed from Fig. 3.11 the FRP laminate is applied at the top of the beam above the mid-support. The length of the laminate is chosen equal to 5000 mm and the left laminate end corresponds to X = 2500 in Fig. 3.12 (see vertical dashed line). By following this dashed line, starting from 0 kN, an intersection is noticed with the curve representing debonding by crack bridging at shear cracks at 133 kN.

Concerning the test, debonding is noticed at 152 kN by crack bridging at flexural/shear cracks at the top laminate (see Fig. 3.13). This debonding load is considerably higher than the calculated debonding load.

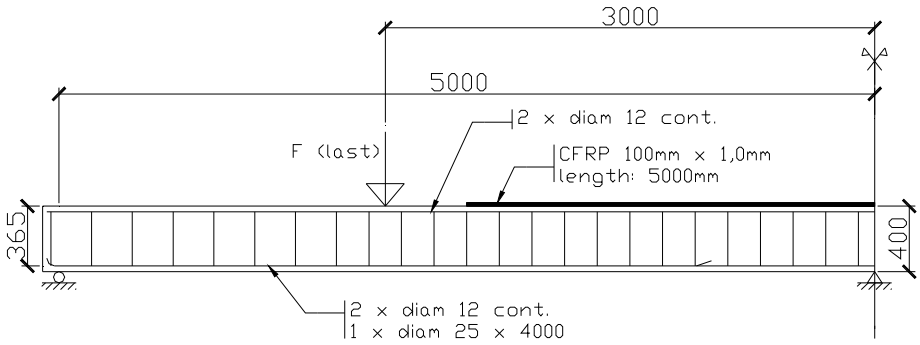

Fig. 3.11: Reinforcement configuration of CB2

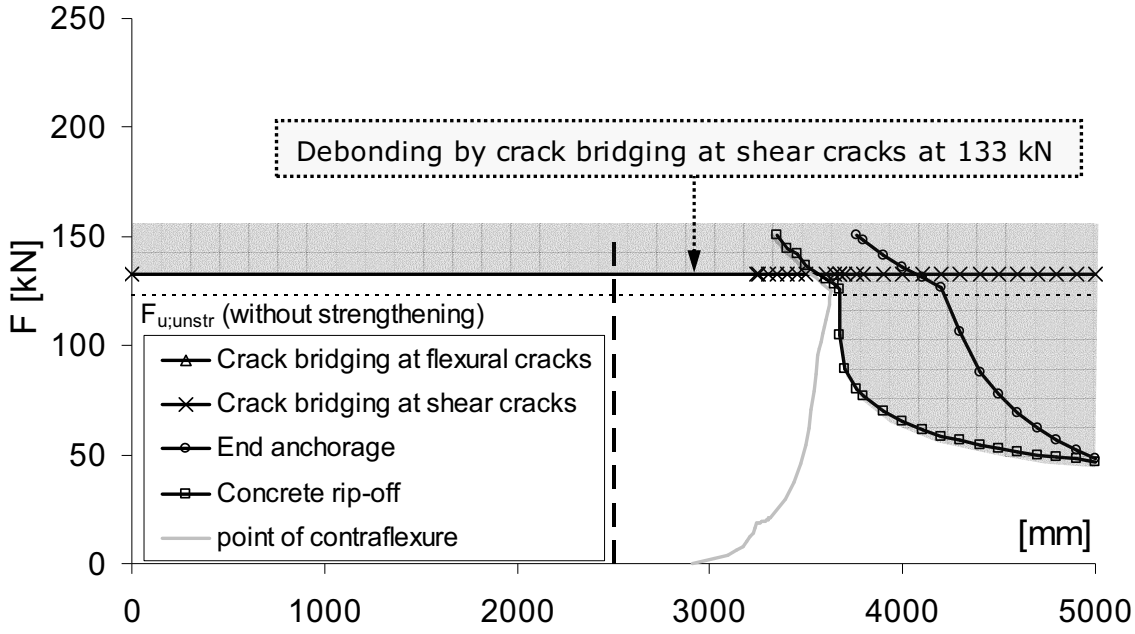

Fig. 3.12: Appearance of different debonding mechanisms at the top laminate (CB2)

Fig. 3.13: Debonding of the laminate at the top of the beam by crack bridging at flexural/shear cracks (CB2)

2.2.3 Debonding mechanisms for beam configuration CB3

As can be noticed from Fig. 3.14, three laminates are applied in this strengthening configuration. One laminate is applied at the top of the beam above the mid-support and two laminates are applied at the soffit of the beams, one in each span. Concerning the debonding mechanisms of the latter, reference is made to Fig. 3.15. As can be noticed in this figure, debonding by concrete rip – off is expected at 162 kN at the laminate end close to the outer supports, while debonding by crack bridging at shear cracks is expected at 212 kN at the other laminate ends. Concerning the debonding mechanisms of the top laminate, reference is made to Fig. 3.17. In this figure, debonding by crack bridging at shear cracks is predicted to occur at 196 kN.

In summary, debonding is first expected at 162 kN by concrete rip off at one of the laminates at the soffit of the beam in the region between the point load and the end support. Nevertheless during the test, debonding is noticed at 171 kN by crack bridging at a flexural/shear crack at the top laminate. Hence, it can be concluded that the prediction by the concrete rip off model is a conservative prediction [3].

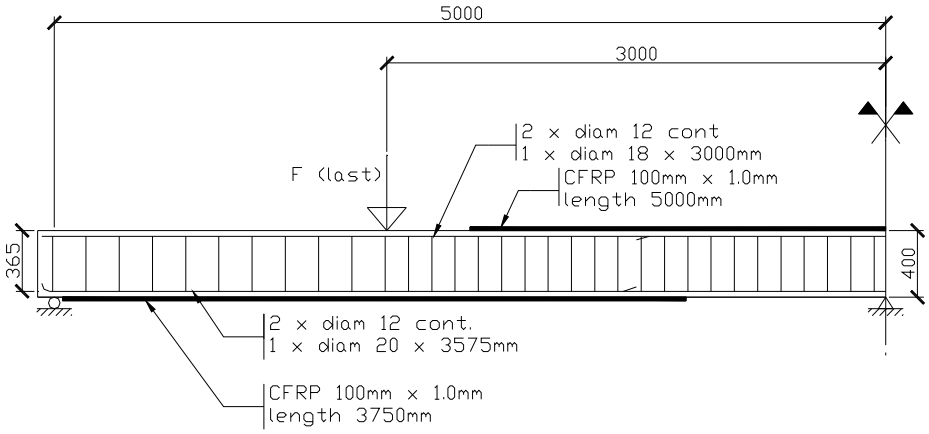

Fig. 3.14: Reinforcement configuration of CB3

Also the location of the point of contraflexure is shown in both Fig. 3.15 and Fig. 3.17. Although both point of contraflexure lines are related to the same moment distribution, a horizontal translation of the lines is noticed. The difference between these two graphs can be explained by the shifted moment distribution over the distance z/2, with z is the internal lever arm of the critical cross-section.

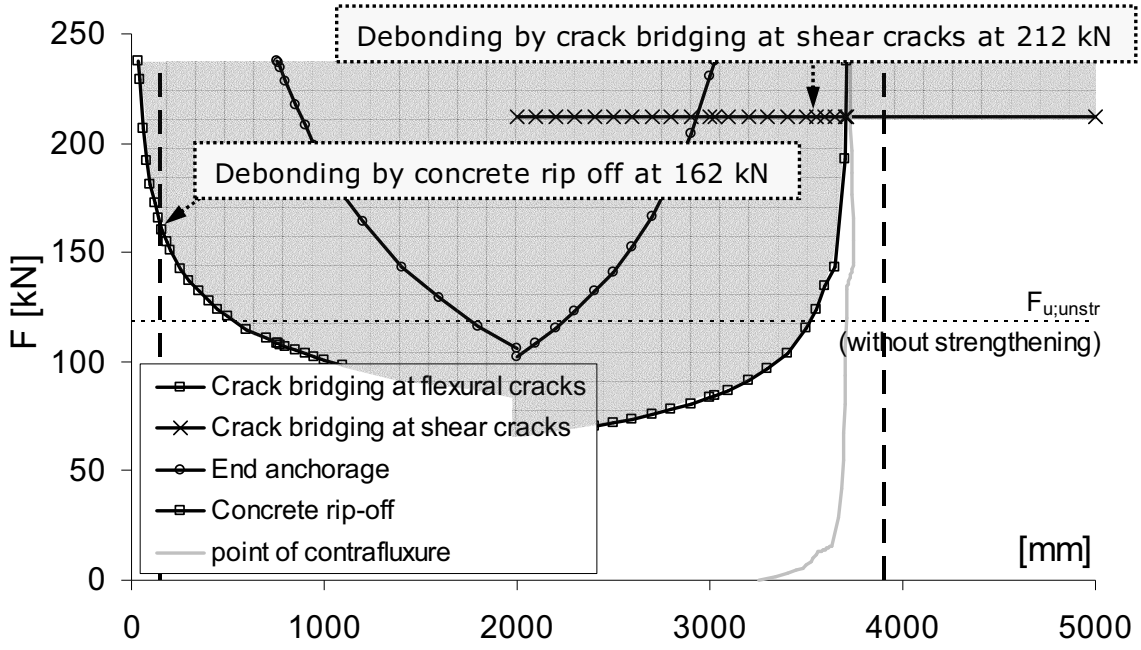

Fig. 3.15: Appearance of different debonding mechanisms in the span laminate (CB3)

Fig. 3.16: Debonding of the top laminate by crack bridging at a flexural/shear crack at 170.5 kN (CB3)

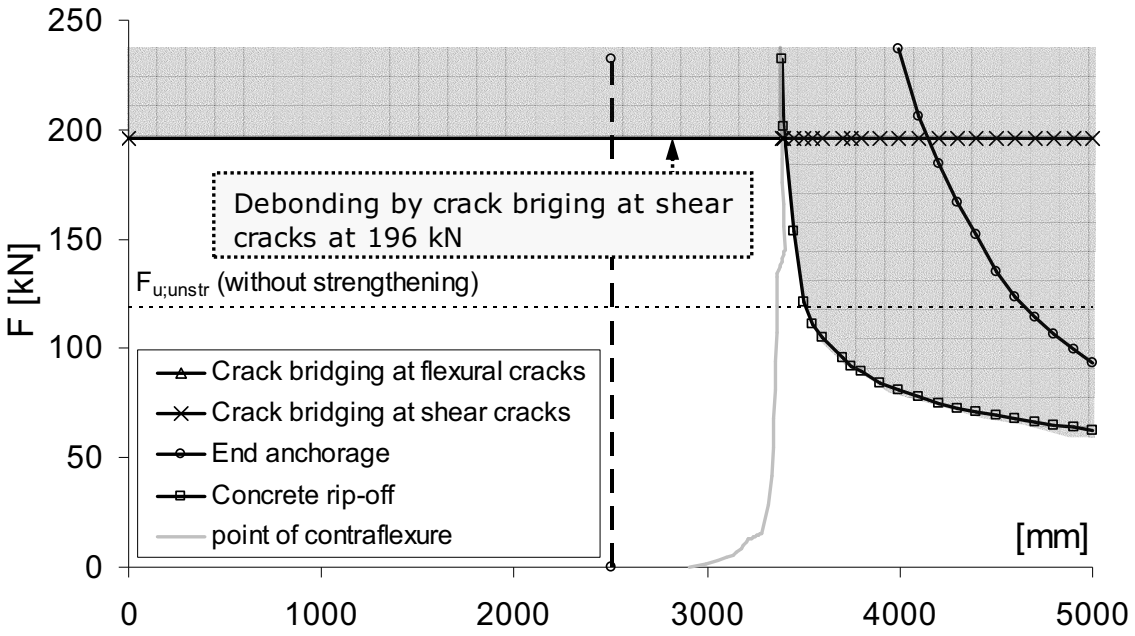

Fig. 3.17: Appearance of different debonding mechanisms at the top laminate (CB3)

2.2.4 Debonding mechanisms for beam configuration CB4

Finally the fourth tested beam is strengthened with one laminate at top of the beam, at the location of the mid-support (see Fig. 3.18). Debonding is expected at about 126 kN by crack bridging at shear cracks (see vertical dashed line in Fig. 3.19 at the value X = 2500 mm).

During the test, debonding of the top laminate is noticed at 116 kN, by the crack bridging at a flexural/shear crack mechanism. Debonding is noticed somewhat earlier in the tests, compared to the analytical prediction.

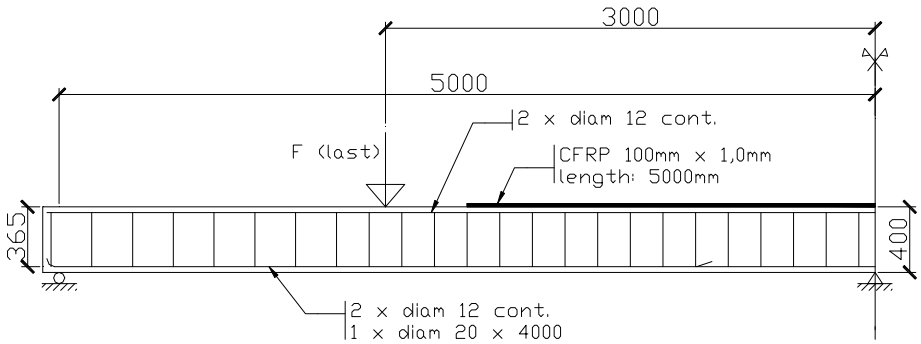

Fig. 3.18: Reinforcement configuration of CB4

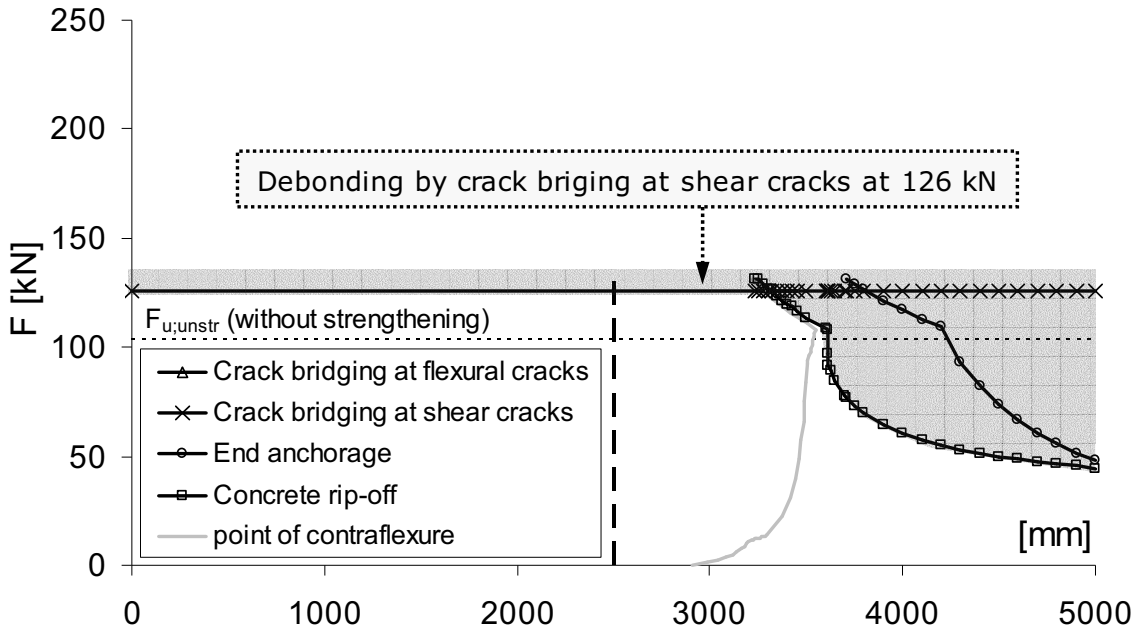

Fig. 3.19: Appearance of different debonding mechanisms at the top laminate (CB4)

Fig. 3.20: Debonding of the top laminate by crack bridging at a flexural/shear at 170.5 kN (CB4)

3 Avoiding some debonding mechanisms in continuous beams

3.1 Anchoring of the laminates into the compression zone

To predict the debonding load, the available calculation models [2] are based on formulas which basically relate to experiments on isostatic reinforced concrete beams and pure shear bond tests.

The difference between isostatic beams and continuous beams, which may influence the debonding mechanisms in continuous reinforced concrete beams, is the moment line with opposite signs. Whereas the moment in the span is negative, the moment at the mid-support is positive. As a result, the compression zones in the spans are situated at the top of the beam, while at the mid-support the compression zone is situated at the soffit of the beam (shaded zones in Fig. 3.21). In contrast to isostatic beams, this allows to anchor the FRP laminates in the compression zones (except for the outer supports). By extending a laminate into these compression zones, two out of the four different debonding mechanisms will be avoided: debonding by a limited anchorage length and debonding by end shear failure (concrete rip-off).

Debonding by limited anchorage length is prevented by extending the laminate into the compression zone because in this situation the tensile stress in the laminate is gradually reduced to zero, and anchored in a zone with small compressive stresses (no significant risk for buckling, see 3.2).

Debonding by end shear failure occurs when a shear crack appears at the end of the laminate. By extending the laminate into the compression zone, the plate-end reaches a zone where no shear cracks can start at the laminate end and neither concrete rip-off will appear.

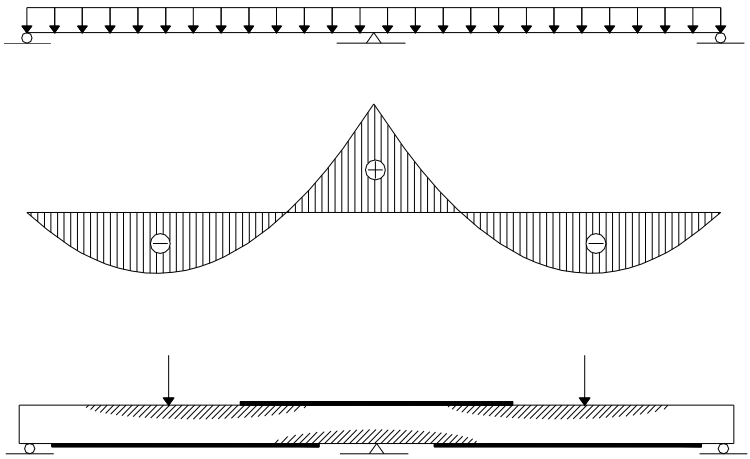

Fig. 3.21: Moments with opposite signs in continuous beams and anchoring laminates into compression zones

The above mentioned phenomena also can be deduced from Fig. 3.9, Fig. 3.12, Fig. 3.15, Fig. 3.17 and Fig. 3.19. In these figures it is remarkable that neither debonding by a too short anchorage length and debonding by concrete rip-off is

governing as long as the laminate end is situated beyond the point of contraflexure. On the other hand, the two other debonding mechanisms (debonding by crack bridging at shear cracks and debonding at flexural cracks) are independent of the location of the laminate end or with other words are independent of the length of the laminate. This is visualized by a horizontal line for these debonding mechanisms (see Fig. 3.12, Fig. 3.15, Fig. 3.17 and Fig. 3.19).

In literature [13] an analytical approach can be found, which calculates the adhesive shear stress and the interfacial transverse normal (peeling) stresses. In this approach it is concluded that bond failure initiation at the FRP laminate ends can be avoided by extending the laminates beyond the point of zero bending moment at any possible design load case; which is similar to the above obtained conclusion.

Remark that, the point of contraflexure, beyond which the laminates have to be anchored, is not a fixed position. This point moves in function of the increasing load, due to the non-linear moment redistribution (see the non-linear curve in Fig. 3.9, Fig. 3.12, Fig. 3.15, Fig. 3.17 and Fig. 3.19 which indicates the position of the point of contraflexure). In Table 3.2, the distance is given for each continuous beam, over which the point of contraflexure is moving.

Table 3.2: Interval over which point of contraflexure is moving

	Distance over which point of contraflexure is moving [mm]
CB 1	251
CB 2	378
CB 3	178
CB 4	335

3.2 Composites under compression

FRP EBR is normally applied to RC-structures in the tension zone of the member, to increase the cross-sectional area of the tension reinforcement of the RC members. In some applications it is possible that the FRP EBR is subjected to compression under specific variable load configurations (see Fig. 3.22). In continuous beams, the FRP EBR also can be subjected to compression as soon as the laminate is extended beyond the point of contraflexure (see Fig. 3.21). If the FRP laminate is subjected to compression, it has to be taken into account that due to the lower elastic modulus of FRP in compression and the low flexural rigidity of an EBR configuration, local buckling may occur at relatively low stresses [2].

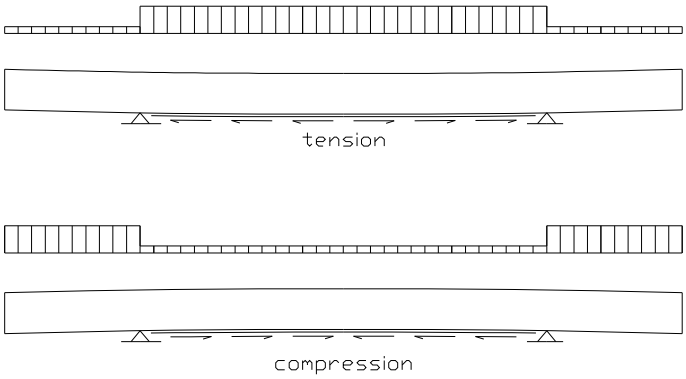

Fig. 3.22: FRP laminate in compression

In literature few information can be found concerning FRP in compression and related to this about buckling of FRP laminates. One experimental test with a FRP laminate glued in the compression zone of a RC beam is reported in [14]. In this test no buckling of the laminate was observed, until finally the concrete member failed by concrete crushing.

In [15] an analytical model can be found concerning the non-linear (buckling) effects in RC beams strengthened with composite materials subjected to compression. This model has shown analytically, in contrast with the above experimental result, that the buckling phenomenon can appear in FRP strengthened beams. Further, it is shown that the buckling effect is associated with considerable localized effects, especially in terms of stresses and deformations within the FRP laminate itself.

In none of the tests on the continuous beams (CB1 to CB4), buckling is noticed. The strain in the FRP laminate beyond the point of contraflexure was measured to check this buckling effect. The results of these strain distributions can be found in Fig. 3.23 until Fig. 3.27. In the graphs related to the laminates at the soffit of the span (Fig. 3.23 and Fig. 3.25), the origin of the X-axis refers to the laminate end in the compression zone. In the graphs related to the laminates above the mid-support (Fig. 3.24, Fig. 3.26 and Fig. 3.27), the origin of the X-axis refers to the centre of the top laminate, i.e. the mid-support. In Table 3.3 the maximum measured strains of the FRP laminates in the compression zones are given and also the stresses related to these maximum strains. As can be noticed in Table 3.3, the compression stresses in the laminates applied at the soffit of the spans are much lower than the stresses in the laminates applied above the mid-support. This difference is due to the length of the laminates: the top laminates are extended for about 1200 mm beyond the point of contraflexure while the laminates at the soffit of the span are only extended for about 500 mm beyond the point of contraflexure. Further in Table 3.3, a maximum compressive stress of 163 N/mm² is observed, which is a small stress level compared to the tensile stresses in the laminates. However, no buckling is noticed, because it is prevented by these low compression stresses.

The graphs of the strain distribution of the laminate in the compression zone are almost linear along the length of the laminate ends. By visual inspection of the laminates after the tests, no buckling of the laminate ends could be noticed (see Fig. 3.28).

Table 3.3: Maximum strain and stress in FRP laminates in compression

	$\varepsilon_{soffit,max}$ [%]	$\sigma_{soffit,max}$ [N/mm²]	$\varepsilon_{top,max}$ [%]	$\sigma_{top,max}$ [N/mm²]
CB1	0.018	34.0	-	-
CB2	-	-	0.066	126.2
CB3	0.011	20.5	0.086	162.6
CB4	-	-	0.055	104.7

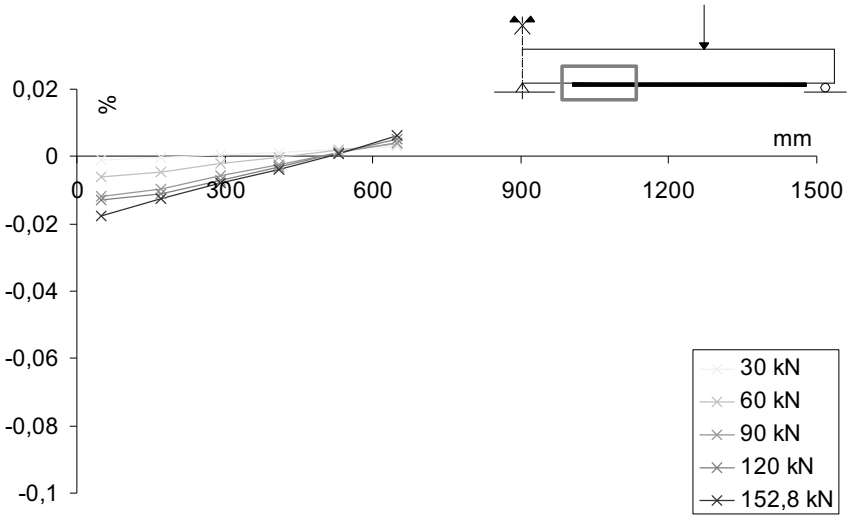

Fig. 3.23: Strain in FRP laminate at the soffit of the span beyond the point of contraflexure (CB1)

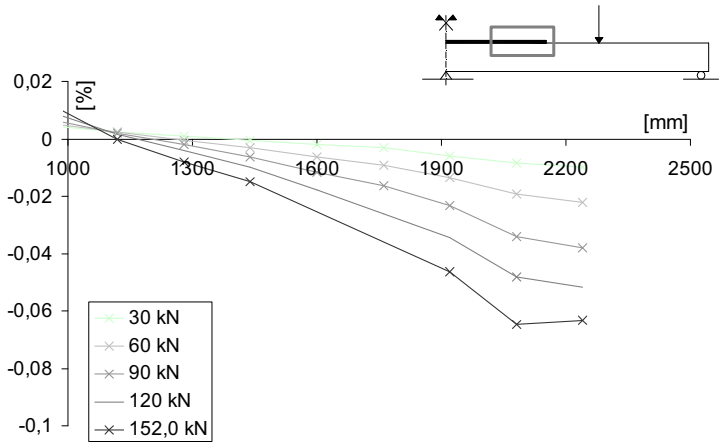

Fig. 3.24: Strain in FRP laminate at top of the mid-support beyond the point of contraflexure (CB2)

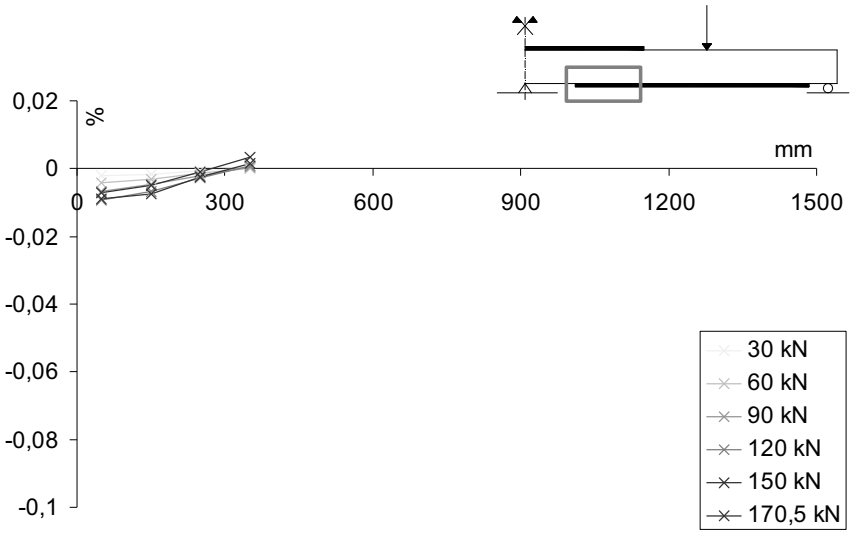

Fig. 3.25: Strain in FRP laminate at the soffit of the span beyond the point of contraflexure (CB3)

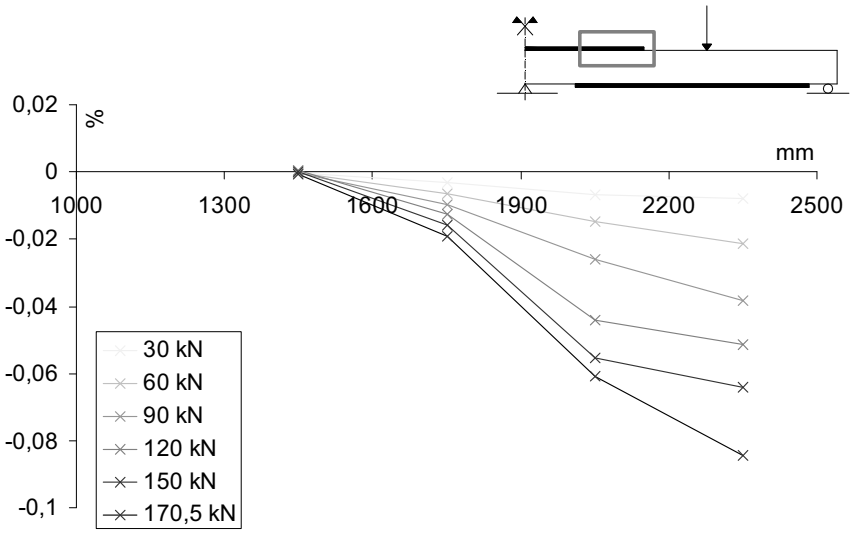

Fig. 3.26: Strain in FRP laminate at top of the mid-support beyond the point of contraflexure (CB3)

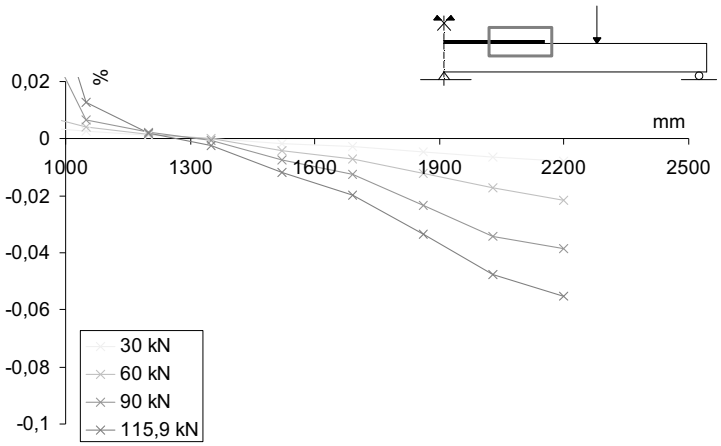

Fig. 3.27: Strain in FRP laminate at top of the mid-support beyond the point of contraflexure (CB4)

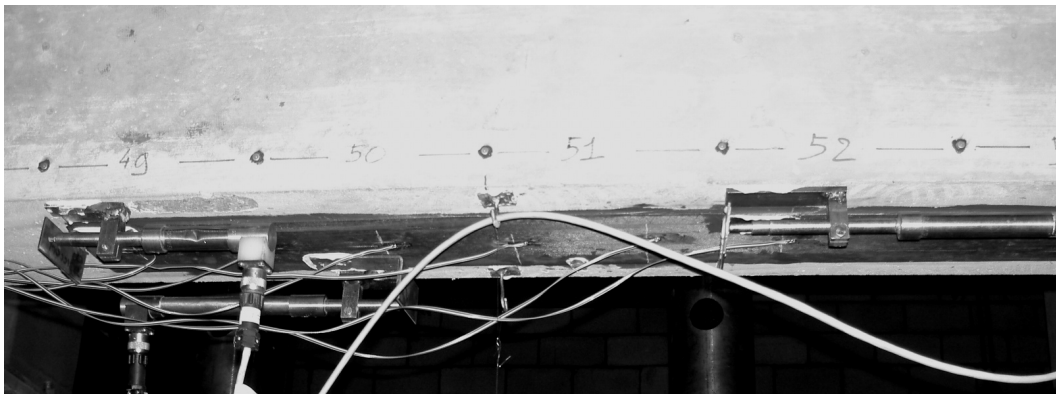

Fig. 3.28: No visual indication of buckling at the laminate end beyond the point of contraflexure is observed

4 Influence of non-linear behaviour on the different debonding mechanisms

In the case of strengthened continuous beams, some particular aspects can be noted, which may also influence the moment of debonding. This is illustrated in the following by means of an analytical study of a two span strengthened beam (see Fig. 3.29), where the length of one span equals 5 meter and a = 2 m and b = 3 m.

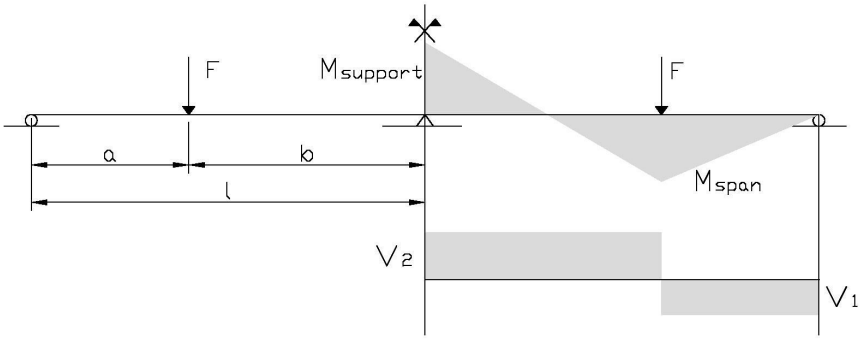

Fig. 3.29: Two span beam used in analytical study

The adopted internal and external reinforcement configuration is presented in Fig. 3.30. Herewith the applied internal reinforcement is kept constant during the analytical study and is based on the linear theory. In this case almost the same amount of internal reinforcement has to be used in the spans and at the mid-support (reinforcement ratios $\rho_{s,span}$ = 0.68 % and $\rho_{s,support}$ = 0.61 %). The properties assumed in the analysis are given in Table 3.4, whereas the amount of FRP strengthening in the spans and mid-support zone is varied (FRP widths of 60 mm, 100 mm, 150 mm and 200 mm are used in this study).

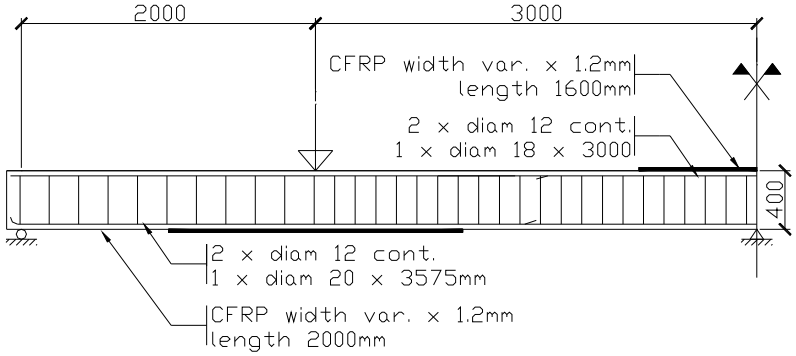

Fig. 3.30: Internal and external reinforcement configuration

Table 3.4: Properties of concrete and reinforcement materials

	Concrete	Steel	FRP
Compres. strength	36.0	-	-
Yield stress [N/mm²]	-	570	-
Yield strain [%]	-	0.28	-
Tensile strength [N/mm²]	3.3	670	2768
Failure strain [%]	0.35 *	12.40	1.46
E-modulus [N/mm²]	32000	210000	189900

* in compression

The length of the FRP is chosen in such a way that all four debonding mechanisms can occur. For this purpose, the laminates are not anchored into the compression zones as described in section 3.1. The length of the laminate at the soffit of the span equals 2000 mm and is applied in such a way that the centre of the laminate is just beneath the point load. The laminate at the top of the beam above the mid-support equals 1600 mm (see Fig. 3.30).

The influence of the amount of FRP strengthening on the acting shear forces is illustrated in Fig. 3.31, for a point load F of 100 kN. Herewith, V_1 (solid lines) is the shear force acting between the outer support and the point load. $V_2 = F - V_1$ (dashed lines) is the shear force acting between the point load and the mid-support (see Fig. 3.29). As can be noted, the value of V_1 (and hence V_2) is influenced by the FRP reinforcement ratios of both the span ($\rho_{f,span}$) and the mid-support ($\rho_{f,support}$). By increasing the width of the laminate above the mid-support (in-creasing $w_{f,support}$ or $\rho_{f,support}$), for $w_{f,span}$ = constant ($\rho_{f,span}$ = constant), V_1 decreases and V_2 increases. This is due to the moment redistribution which is dependent on both the external and internal reinforcement ratio used over the length of the beam. Hence, also the distribution of the reaction forces at the supports is dependent on the reinforcement ratios. As a result, that part of the applied load which is carried by the mid-support increases with an increasing amount of FRP at the mid-support. If $w_{f,span}$ (or $\rho_{f,span}$) is increased as well, the decrease of V_1 will be less pronounced and V_1 may even increase (compared to the unstrengthened beam).

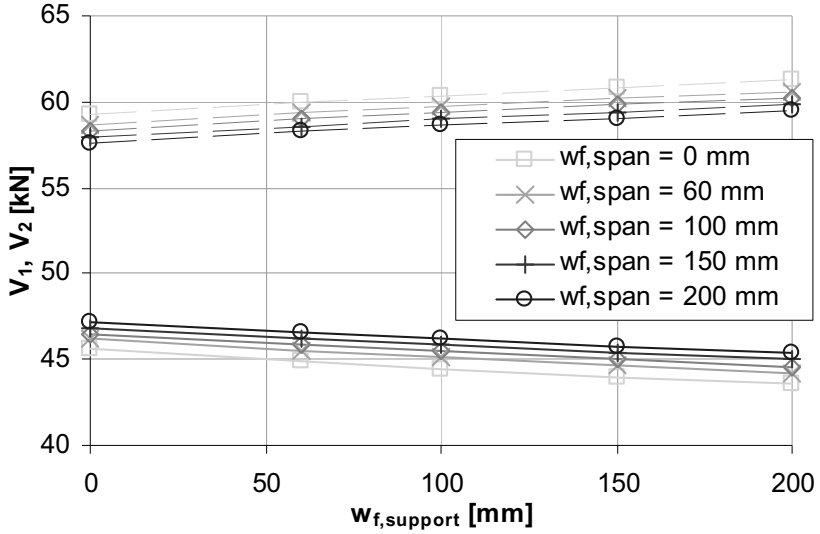

Fig. 3.31: Shear force V_1 and V_2 in function of width of laminates

As debonding phenomena often relate to the acting shear force, this means that possible debonding of a FRP laminate not only depends on the FRP configuration at that location, but also on the amount of FRP in the zone with opposite moment sign.

Another significant aspect with respect to the values of $\rho_{f,span}$ and $\rho_{f,support}$ relative to each other, is their influence on the point of contraflexure. Indeed, by increasing $\rho_{f,support}$ (increasing the width of the laminate above the mid-support), $M_{support}$ will increase and M_{span} will decrease and the point of contraflexure moves away from the mid-support. On the other hand, by increasing $\rho_{f,span}$ at the soffit of the span, $M_{support}$ will decrease and M_{span} will increase. As a result, the point of contraflexure moves towards the mid-support. Because of this, the distance between the laminate end and the point of contraflexure (L) changes. Indirectly, also the anchorage length (l_t) will change. This is a second reason why the debonding mechanisms 'anchorage failure' and 'concrete rip-off' depend on the amount of external reinforcement along the beam.

In the following sections, the load at which debonding occurs, for the different debonding mechanisms will be investigated in function of both $\rho_{f,span}$ and $\rho_{f,support}$. A distinction is made between debonding of the top laminate (case A), debonding of the laminate at the soffit of the span between the point load and the mid-support (case B) and debonding of the laminate at the soffit of the span between the point load and the outer support (case C) (Fig. 3.32).

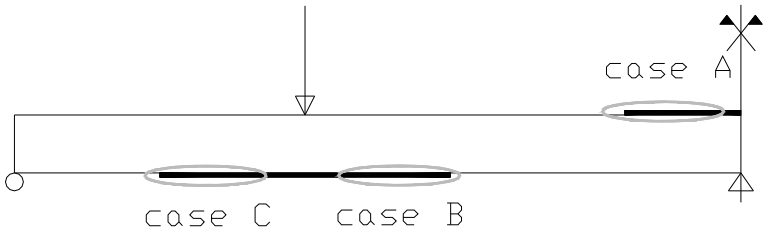

Fig. 3.32: Differentiation between places of debonding

The calculations are performed according to section 2.1 and fib-bulletin 14 [2]. The results obtained for the debonding load F_{deb} are given in Fig. 3.37 until Fig. 3.45. The results are represented by solid lines as far as they do not exceed the ultimate load of the strengthened beam assuming full composite action. If the calculated debonding load is higher than the ultimate load of the strengthened beam assuming full composite action, the results are represented by dashed lines. In the case of full composite action, it is assumed that debonding of the FRP does not occur, and that failure is characterized by concrete crushing or by exceeding the tensile strength of the FRP reinforcement.

In Table 3.5 a summary is given of the effect of the external reinforcement on the debonding load. In sections 4.1 till 4.4 a more detailed explanation is given about these findings. Also reference is made to [16-18].

Table 3.5: Effect of external reinforcement on debonding load

		Amount of top laminate above the mid-support ↗	Amount of laminate at the soffit of the span ↗
Crack bridging at flexural cracks	A	debonding load ↗	debonding load ↗
	B	debonding load ↙	debonding load ↗
	C	debonding load ↗	debonding load ↗
Crack bridging at shear cracks	A	debonding load ↗	debonding load ↗
	B	debonding load ↙	debonding load ↗
	C	debonding load ↗	debonding load ↗
Anchorage failure	A	debonding load ↙	debonding load ↗
	B	debonding load ↗	debonding load ↙
	C	debonding load ↗	debonding load ↙
Concrete rip-off	A	debonding load ↙	debonding load ↗
	B	debonding load ↗	debonding load ↙
	C	debonding load ↗	debonding load ↙

By means of the analytical study, it is demonstrated that the debonding load for continuous beams strengthened with FRP EBR is also governed by the shear force and moment redistribution (see sections 4.1 until 4.4). This redistribution occurs in statically indeterminate members and depends on the amounts of reinforcement (among which the externally bonded reinforcement) in the spans and at the mid-support, relative to each other. Depending on the situation (amount of FRP, type and location of the debonding phenomenon) both a higher or smaller value of the debonding load with respect to the values corresponding to the elastic moment distribution may be obtained.

In Fig. 3.33 the ratio is given of the debonding load considering the non-linear behaviour compared to the debonding load considering the linear elastic theory. For the configuration considered in this study, maximum differences are noticed up to 45.9 % higher (debonding by anchorage failure – case A) to 26.2 % lower (debonding by anchorage failure – case B) than the debonding load determined by neglecting the non-linear behaviour of continuous beams.

However, by extending the laminates into the compression zones, no debonding by anchorage failure and by end shear failure will occur in case A and case B. By eliminating these debonding mechanisms maximum differences are noticed up to 9.5 % higher (debonding by anchorage failure – case C) to 12.1 % lower (debonding by anchorage failure – case C) than the debonding load determined neglecting the non-linear behaviour of continuous beams.

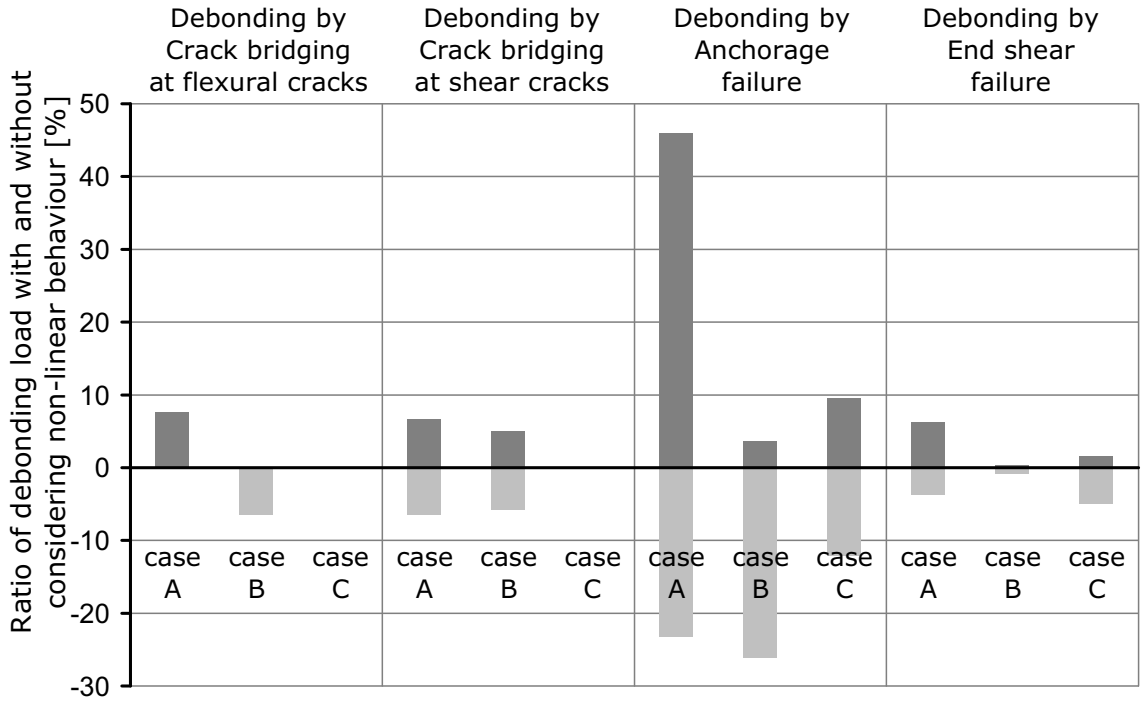

Fig. 3.33: Effect of non-linear behaviour on the debonding load

4.1 Debonding at flexural cracks

Firstly, there is the change of shear force ratio caused by the moment redistribution. By increasing the width of the top laminate above the mid-support, V_2 increases and V_1 decreases (Fig. 3.31). Hence a lower debonding load is expected in cases A and B and a higher debonding load is expected in case C. By increasing the width of the laminate at the soffit of the span, the opposite effect occurs.

Secondly, the width of the laminate (w_f) is also a basic factor in the calculation of the resisting shear force, V_{Rbd} [2]:

$$V_{Rbd} = f_{cbd}\, 0{,}95 d w_f \qquad (3.19)$$

with $f_{cbd} = 1.8 f_{ctk}/\gamma_c$, f_{ctk} the characteristic tensile strength of the concrete and γ_c the safety factor ($\gamma_c = 1.50$).

Increasing the width of the laminate has a positive influence on its debonding load. This effect is more pronounced than that of the acting shear force. The combined effect is illustrated in Fig. 3.34 until Fig. 3.36, for cases A, B and C respectively.

Increasing the width of the top laminate results in a large increase of the debonding load for case A (Fig. 3.34). Increasing the width of the laminate in the span also has a favourable influence, yet to a lesser extent.

In Fig. 3.35 the debonding load of case B is illustrated. In this graph only one curve ($w_{f,span}$ = 60 mm) is given. The curves ($w_{f,span}$ > 60 mm) are not shown, as these debonding loads are situated above 300 kN. There can be concluded that

the increase of the width of the laminate at the soffit of the span has an important favourable influence on the debonding load and will delay it, while the increase of the width of the top laminate has a negative influence and results in a lower debonding load.

In Fig. 3.36 the debonding load of case C is illustrated. Similar to case B only one curve ($w_{f,span}$ = 60 mm) is shown. As the other curves are situated above the 300 kN, it can be concluded that the increase of the width of both the laminates in the spans and at the mid-support increase the debonding load, whereas the laminate at the soffit has the most pronounced effect.

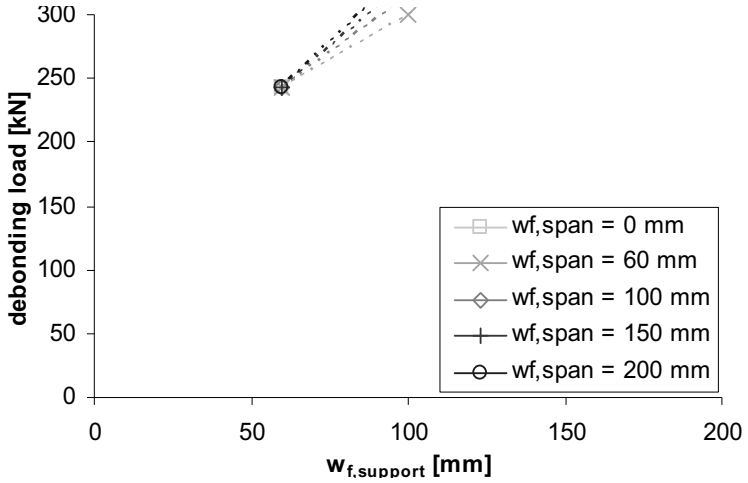

Fig. 3.34: Influence of external reinforcement on the debonding mechanism: debonding at flexural cracks (case A)

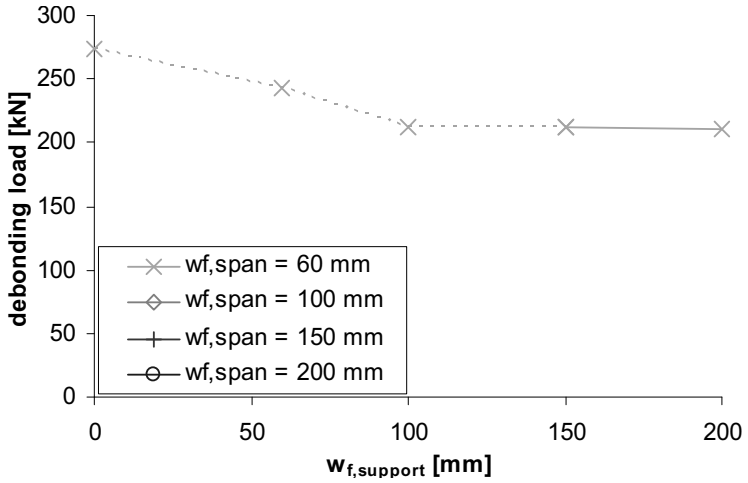

Fig. 3.35: Influence of external reinforcement on the debonding mechanism: debonding at flexural cracks (case B)

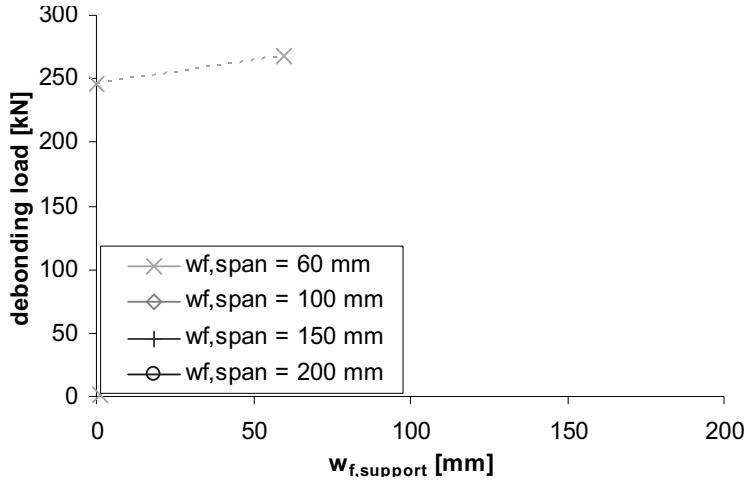

Fig. 3.36: Influence of external reinforcement on the debonding mechanism: debonding at flexural cracks (case C)

4.2 Debonding at shear cracks

Debonding by crack bridging at shear cracks in case of inclined shear cracks (vertical crack displacement) can be modelled according to [2], based on Eqs. 3.10 and 3.11 (see Eq. 3.20 and 3.21):

$$V_{Rpd} = \tau_{Rp} bd \tag{3.20}$$

$$\tau_{Rp} = 0{,}38 + 1{,}51\rho_{eq} \tag{3.21}$$

with $\rho_{eq} = (A_s + A_f E_f/E_s)/bd$ the equivalent reinforcement ratio and A and E the cross-section and modulus of elasticity of the reinforcement (s: steel and f: FRP).

This means that the debonding load will be dependent on both the acting shear force (influenced by both $\rho_{f,span}$ and $\rho_{f,support}$) and the resisting shear force (influenced by $\rho_{f,support}$ in case A and $\rho_{f,span}$ in cases B and C)

The debonding load of the top laminate (case A) is shown in Fig. 3.37. By increasing the width of the top laminate, the resistance V_{Rp} increases (increase of A_f in Eq. 3.21) and to a lesser extent the acting shear load V_2 also increases (Fig. 3.31). If at the same time the amount of FRP in the spans increases, this further enhances the debonding load due to a reduction of the acting shear force V_2.

The change in debonding load in case B is illustrated in Fig. 3.38. Increasing the widths of the laminate in the span (for $w_{f,support}$ = constant), increases the debonding resistance (increase of A_f) on the one hand and decreases the acting shear force (V_2) on the other hand. This results in a higher debonding load. Increasing also the width of the top laminate will result in a somewhat higher acting shear force V_2 (Fig. 3.31) and has a negative influence on the debonding load.

For the beam considered in this study (Fig. 3.30, Table 3.4), the debonding load calculated in case C appeared to be higher than the ultimate load of the strengthened beam assuming full composite action. However, similar to the above argumentation an increased debonding resistance can be expected for a

higher width of the laminate in the span. Increasing the amount of FRP at the mid-support, will further enhance the debonding load due to a reduction of the acting shear load V_1 (Fig. 3.31).

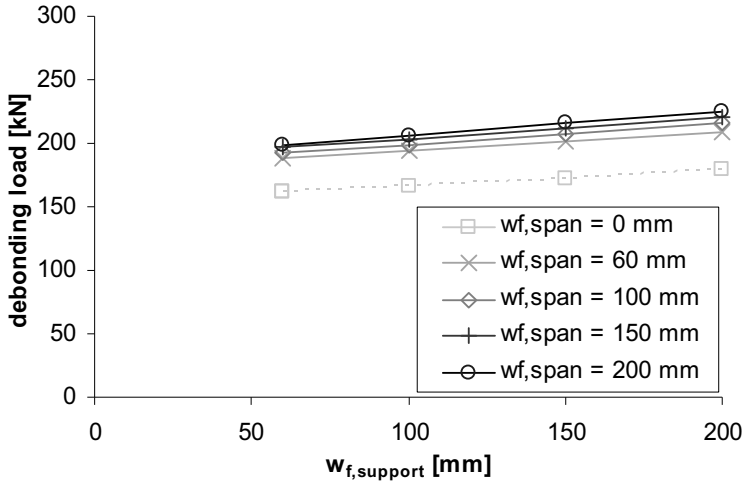

Fig. 3.37: Influence of external reinforcement on the debonding mechanism: debonding at shear cracks (case A)

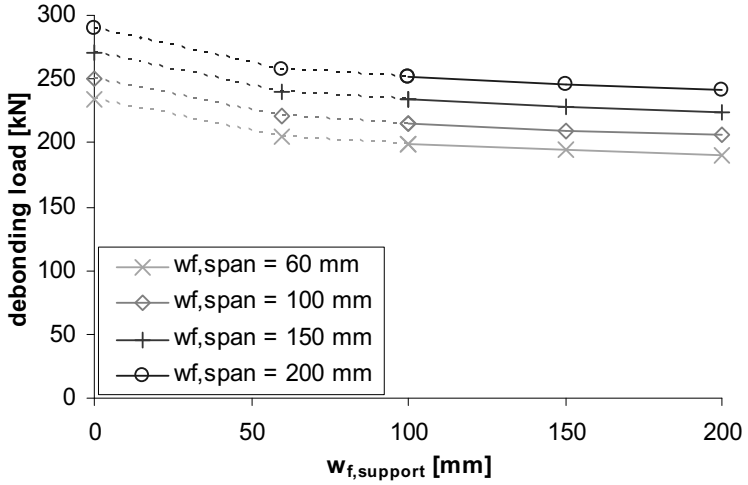

Fig. 3.38: Influence of external reinforcement on the debonding mechanism: debonding at shear cracks (case B)

4.3 Anchorage failure

Considering debonding by anchorage failure, the variability of the shear forces V_1 and V_2 according to the external reinforcement ratios is of no importance. However, the redistribution of the moments $M_{support}$ and M_{span} and its impact on the location of the section where the moment equals M_{curt} are important. Herewith, M_{curt} is the moment for which the axial tensile force can be carried by the internal steel only and consequently the external reinforcement theoretically can be curtailed. The section where M_{curt} is reached can also be seen as the

position along the length of the beam where the anchorage length l_t starts. Because of the change in position of M_{curt}, the available anchorage length is dependent on the moment redistribution and consequently on the reinforcement ratios along the continuous beam.

By increasing the amount of FRP reinforcement above the mid-support, $M_{support}$ increases and M_{span} decreases. This results in a shift of the position where the moment equals M_{curt}: (1) towards the laminate end (shorter anchorage length) for the laminate at the top of the beam (case A), and (2) away from the laminate end (larger anchorage length) for the laminates at the soffit of the beam (cases B and C).

By increasing the amount of FRP reinforcement at the soffit of the beam an opposite effect is obtained.

It can be concluded (keeping the total FRP length constant) that a reduced anchorage length is obtained in case A when the amount of FRP above the mid-support is increased and in cases B and C when the amount of FRP at the soffit of the span is increased. Due to this reduction of anchorage length, a lower debonding resistance may be obtained. This influence of the laminate widths (or ρ_f) on debonding at the anchorage zone is illustrated in Fig. 3.39 till Fig. 3.41 for the considered beam and strengthening configuration.

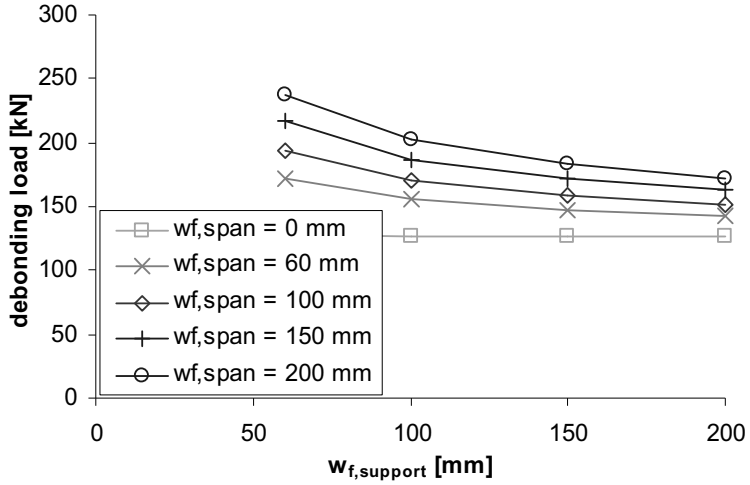

Fig. 3.39: Influence of external reinforcement on the debonding mechanism: 'anchorage failure' (case A)

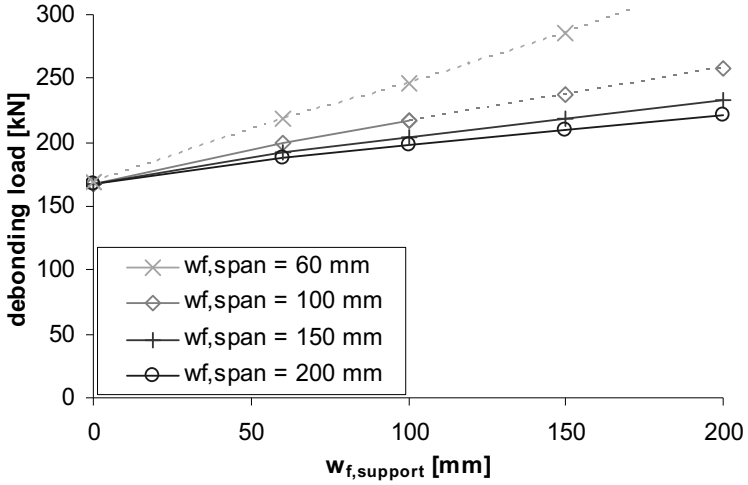

Fig. 3.40: Influence of external reinforcement on the debonding mechanism: 'anchorage failure' (case B)

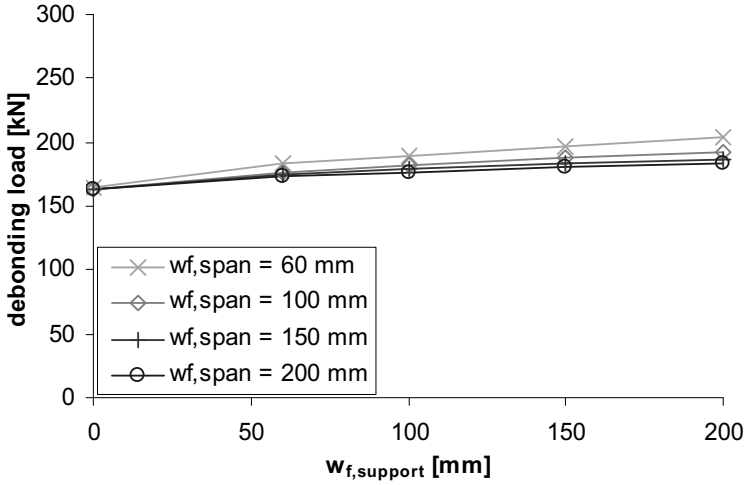

Fig. 3.41: Influence of external reinforcement on the debonding mechanism: 'anchorage failure' (case C)

4.4 Concrete rip-off

To check concrete rip-off, a resistant shear stress, τ_{Rd} (= V_{Rd}/bd), has to be calculated (see Eq. 3.22 and 3.23, [2]). In this case, the changes of the shear forces according to the reinforcement ratios play an important role. The influence will be similar as earlier discussed in sections 4.1 and 4.2.

$$\tau_{Rd} = 0{,}15 \sqrt[3]{3\frac{d}{a_L}\left(1+\sqrt{\frac{200}{d}}\right)} \sqrt[3]{100\rho_s f_{ck}} \qquad (3.22)$$

$$a_L = \sqrt[4]{\frac{\left(1-\sqrt{\rho_s}\right)^2}{\rho_s} dL^3} \qquad (3.23)$$

where $\rho_s = A_s/bd$, f_{ck} is the characteristic compressive strength of the concrete and L is the distance between the laminate end and the point where the moment equals zero (Fig. 3.42).

By increasing the amount of FRP above the mid-support, a larger part of the applied load is carried by the mid-support. As a result the internal shear force V_1 decreases and V_2 increases (Fig. 3.31). This decrease of V_1 has a beneficial influence on the debonding load for case C, while the increase of V_2 has a negative influence for cases A and B. By increasing the amount of FRP at the soffit of the beam, the opposite effect is obtained.

In addition to the redistribution of the acting shear force, the debonding load is also governed by the influence of L on the debonding resistance. In cases A and B this distance relates to the point of contraflexure (L_A and L_B). In case C, this distance relates to the outer support (L_C in Fig. 3.42). A higher debonding resistance is obtained for smaller values of L. As a result, debonding due to concrete rip-off will also depend on the moment redistribution.

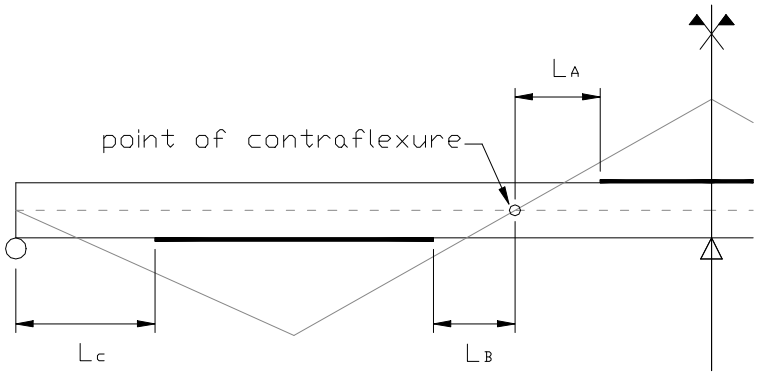

Fig. 3.42: The distance L between the laminate end and the point where the acting moment equals zero.

Consequently, increasing the amount of FRP above the mid-support moves the point of contraflexure to the left in Fig. 3.42. This causes an increase of L_A, and an equal decrease of L_B (for $L_A + L_B$ = constant). Hence, a decrease of the resisting debonding force of the FRP laminate at the top of the beam (case A) and an increased value of the debonding resistance of the FRP laminate at the soffit of the beam (case B) are obtained. An opposite effect is obtained when increasing the amount of FRP at the soffit of the beam.

The combined effect of shear and moment redistribution on the concrete rip-off debonding load is illustrated in Fig. 3.43 until Fig. 3.45. For the considered case, where the total length of the FRP is kept constant, the influence of the shear and moment redistribution appears less pronounced than for the other debonding mechanisms. Especially in case B (Fig. 3.44), for which the shear and moment redistribution effect counteract each other, the combined influence is insignificant.

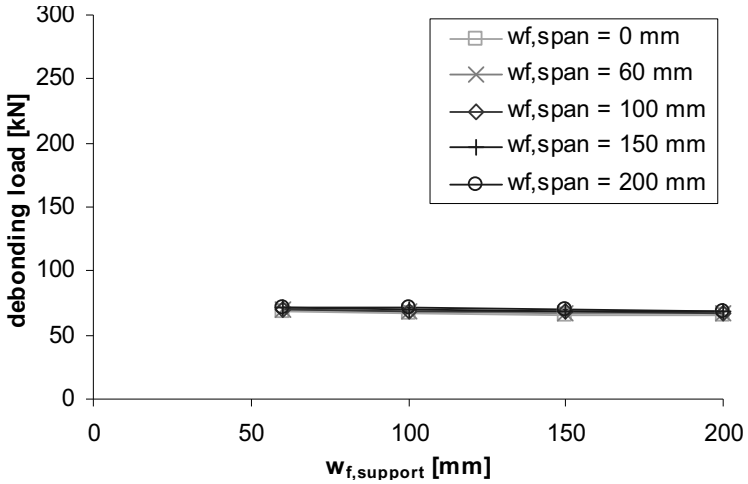

Fig. 3.43: Influence of external reinforcement on the debonding mechanism: 'concrete rip-off' (case A).

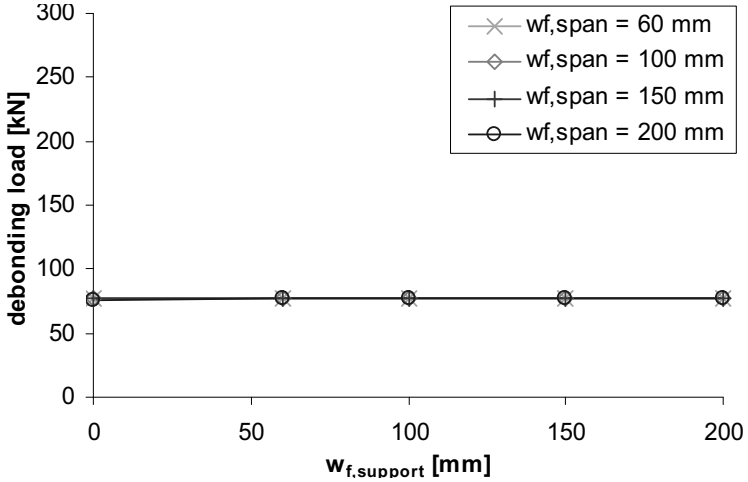

Fig. 3.44: Influence of external reinforcement on the debonding mechanism: 'concrete rip-off' (case B).

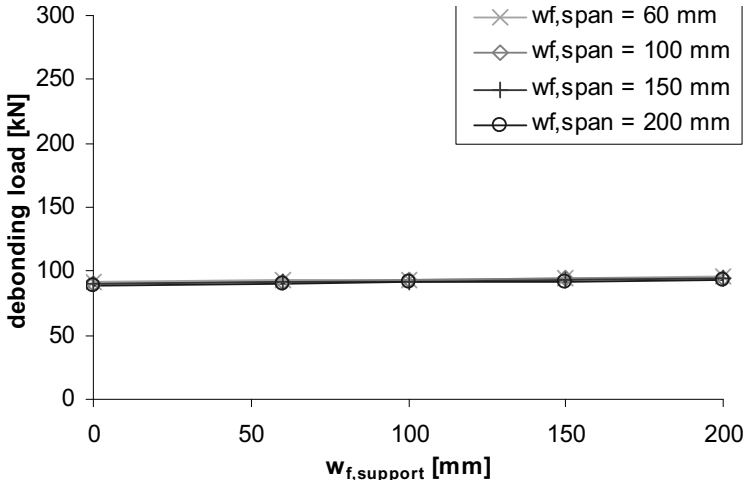

Fig. 3.45: Influence of external reinforcement on the debonding mechanism: 'concrete rip-off' (case C).

4.5 Shear force redistribution in infinitely long continuous beams

As can be noticed from the previous sections, the shear force (re)distribution can have a considerable influence on the expected debonding load. In the two-span beams a shear force redistribution occurs depending on the bending stiffnesses along the length of the beam (see Fig. 3.31).

For a multi-span beam (Fig. 3.46) the shear force redistribution will be less pronounced, depending on the distance from the outer support. In Fig. 3.46, two situations of a multi-span beam are given. The linear elastic shear force distribution is given in Fig. 3.46 by the grey coloured diagram. For the second situation a full rotation of the plastic hinges at the intermediate supports is assumed. The shear force redistribution of this configuration is given by the vertically hatched distribution. This shear force distribution is similar to the shear force distribution of separate isostatic beams situated next to each other.

Comparing the linear elastic shear force distribution with the non-linear shear force distribution, a noticeable difference can be seen in the first three spans. In the first span, the maximum difference is 21%, while in the second and third span the difference is reduced considerably to 6 % and 2 % respectively. From the fourth span on, no difference is noticed anymore.

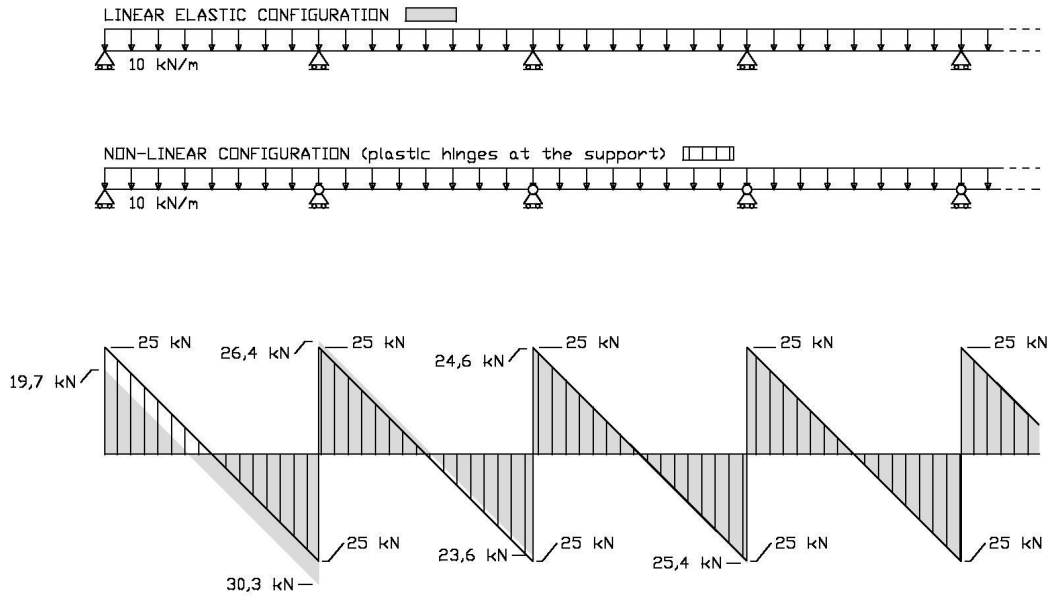

Fig. 3.46: Shear force distribution over the length of a continuous beam

Hence, the influence of the shear force redistribution on the expected debonding load will be noticed in the first span of a multi-span beam and to a lesser extent in the second and the third span. From the fourth span of a multi-span beam, no influence of the shear force redistribution will be noticed. Nevertheless, the moment redistribution still will be noticed in all spans of the multi-span beam. Related to this, both the location of M_{curt} (and so the anchorage length l_t) and the location of the point of contraflexure (and so the parameter L) will change. Moreover, also the resisting shear force at which debonding of a laminate is expected (V_{Rd}) is influenced in a positive way by an increasing section of the

particular laminate (see Eq. 3.20 until Eq. 3.19). The final effect of the strengthening ratios on the different debonding mechanisms at the different locations (case A and case B in Fig. 3.32) is given in Table 3.6. Remark that only case A and B are considered. Case C on the other hand is situated near to an end support and is not applicable here.

For the first two debonding mechanisms (debonding by crack bridging at shear cracks and at flexural cracks), it can be noticed that the expected debonding load is only influenced by the laminate at the location for which debonding is investigated. For the next two debonding mechanisms (debonding by limited anchorage length and debonding by concrete rip-off), it can be noticed that both reinforcement ratios along the length of the beam (hence both at intermediate supports and spans) influence the debonding load.

Table 3.6: Effect of external reinforcement on debonding load

		Amount of top laminate above the support ↗	Amount of laminate at the soffit of the span ↗
Crack bridging at flexural cracks	A	debonding load ↗	not applicable
	B	not applicable	debonding load ↗
	C	-	-
Crack bridging at shear cracks	A	debonding load ↗	not applicable
	B	not applicable	debonding load ↗
	C	-	-
Anchorage failure	A	debonding load ↙	debonding load ↗
	B	debonding load ↗	debonding load ↙
	C	-	-
Concrete rip-off	A	debonding load ↙	debonding load ↗
	B	debonding load ↗	debonding load ↙
	C	-	-

5 Debonding of the FRP EBR laminate at the location of a point load/mid-support

In the loading tests on the two-span beams mentioned in Chapter 2, debonding of the top laminate is often noticed. Peeling off of the laminate starts at a flexural–shear crack. This crack is located near the mid–support, as in this zone a combination of high shear forces and high moments can be found. The high shear forces are mainly responsible for vertical crack displacement, which induces direct tension in the concrete layer between the FRP and the concrete. On the other hand, both the high moments and shear forces are responsible for shear stress peaks in the bond interface between the FRP and the concrete. Previous research [19] has shown that the interfacial shear stresses in a FRP-strengthened RC beam can be divided into two types (see Fig. 3.47):

- Shear stresses related to force transfer, which is proportional to the shear force in the beam. In a pure bending zone these shear stresses are zero.
- Shear stresses related to the opening of cracks (crack bridging).

As the calculated debonding loads of the laminates above the mid-support differed significantly from the experimental debonding loads, additional 3-point-bending tests have been conducted [20] to obtain additional information. As can be noticed in Fig. 3.48, a good correspondence is noticed between the combination of moments and shear forces at the location of the mid-support in the two-span beam and the corresponding values in the 3-point-bending test. The results of these tests are given in the following sections.

In the first section (section 5.1) an overview is given of the different models found in literature, which can be applied to calculate debonding at a flexural/shear crack, also known as intermediate crack debonding (IC-debonding).

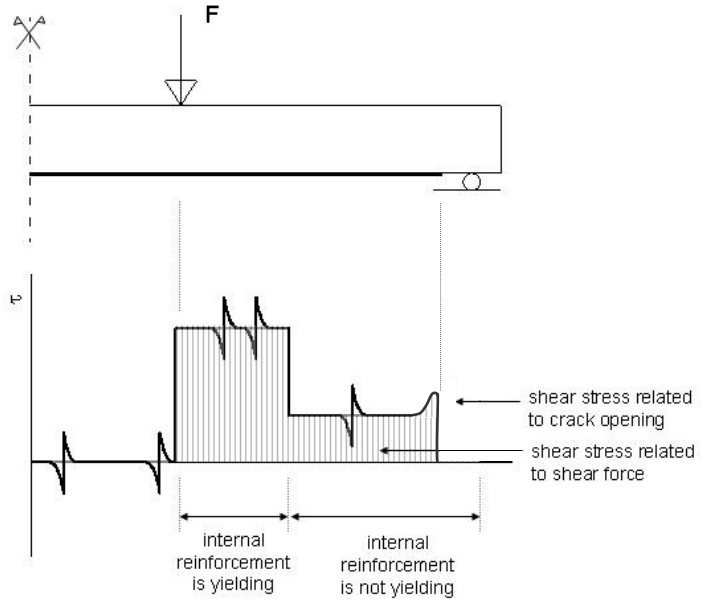

Fig. 3.47: Interfacial shear stresses in a FRP-strengthened RC beam

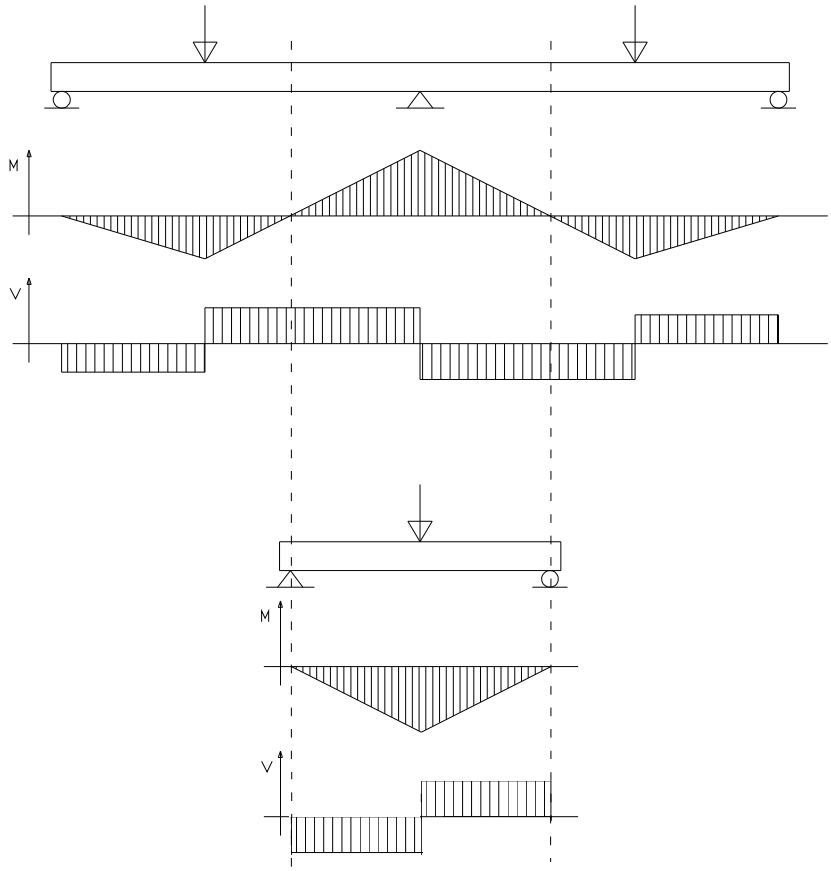

Fig. 3.48: Similarity 3-point-bending test and the central support of a two-span beam

5.1 Models for IC-debonding

A first approach is based on the method given in fib Bulletin 14 [2]. In this approach the IC-debonding is split up in two parts: peeling-off at flexural cracks and peeling-off at shear cracks. A second approach, developed by E. Oller [21], is based on a maximum shear force - bending moment relationship associated to the theoretical maximum transferable force between cracks [21]. Finally, the third approach is the one developed by Teng et al. [5].

5.1.1 Intermediate crack debonding according to fib Bulletin 14

By calculating the intermediate crack debonding load according to fib Bulletin 14, two models have to be considered, among which debonding at flexural cracks and debonding at shear cracks.

For the first model, debonding at flexural cracks, three approaches can be applied (see section 2.1.1.1):

1. By strain limitation in the FRP.
2. By verifying the bond stresses due to force transfer at the FRP/concrete interface
3. Verification according to the envelope line of tensile stresses in the FRP.

Approach (1) is not considered further in this section, as it oversimplifies the physical behaviour. Approach (2) has been discussed in sections 2.1.1.1 and 4.1. Approach (3), proposed by Niedermeier, has been also discussed in section 2.1.1.1. In this approach the gradient of the tensile force in the laminate between two successive cracks is of importance. Herewith, a maximum gradient of the tensile stress (max $\Delta\sigma_{fd}$) is given in function of the applied tensile stress (σ_{fd}) in the externally bonded FRP laminate (see Fig. 3.3).

The second model, debonding at shear cracks, has been discussed in sections 2.1.1.2 and 4.2. This model calculates debonding at inclined shear cracks, at which mainly the vertical crack displacement is of importance. There can be noticed that this is a simplified model calibrated on 4-point-bending test results, while in this section 3-point bending is considered.

5.1.2 Intermediate crack debonding according to Oller et al.

To verify peeling-off failure of a FRP laminate from a concrete member, a simplified model based on a maximum shear force versus the moment was developed by Oller et al. In the following, a short introduction is given to this model. For further details and equations, reference is made to [6, 21, 22].

To use this model, an assumption about the crack spacing s_{rm} has to be made by using for example the model provided in [2]. A reinforced element is considered with a length equal to s_{rm} and bounded by cracks I and J (Fig. 3.49). Also a moment-curvature analysis should be available for the strengthened section, in order to obtain the internal yielding moment M_y and the internal ultimate moment assuming full composite action.

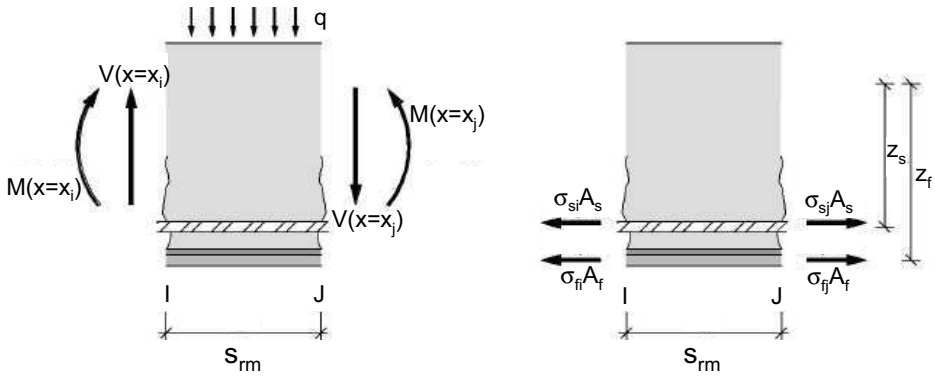

Fig. 3.49: Element between cracks I and J [21]

To calculate the curve giving the maximum shear force in relation to the moment, three different cases are distinguished, depending on the stiffness of both sections I and J:

Case 1: $M_J < M_y$ $M_I < M_y$
No yielding of internal steel reinforcement in both crack I and crack J.
Case 2: $M_J \geq M_y$ $M_I < M_y$
Internal steel reinforcement yields in crack J but not in crack I.
Case 3: $M_J \geq M_y$ $M_I \geq M_y$
Internal steel reinforcement yields in both crack J and crack I.

In Fig. 3.50 these three cases can be distinguished:

- Case 1 can be found between the points (*) and (3).
- Case 2 can be found between the points (3) and (2).
- Case 3 can be found between the points (2) and (**).

For each case, a relation between the maximum allowable shear force in function of the moment at crack J can be obtained. In the simplified model, these relations are assumed to be linear. Hence, the entire model is represented by linear segments connecting the successive points (**), (2), (3) and (*).

In Fig. 3.50 two additional lines are drawn: one between the points (0) and (1) and one between point (4) and the origin of the coordinate system. The first additional line is a horizontal line between (0) and (1) which represents the minimum of the following two moments.

- The ultimate moment assuming full composite action, associated to a classical failure mode (concrete crushing or FRP rupture).
- The moment in the pure flexural case (V = 0) which causes peeling failure when the slip is maximal (s_{f0}, ultimate slip in the shear stress-slip relationship) at both crack I and crack J.

The second additional line, which connects point (4) and the origin of the coordinate system, is called the upper limit. This curve is found by applying the force and moment equilibrium of the element in Fig. 3.49 and requiring that the moment in crack I (M_I), is not allowed to become negative.

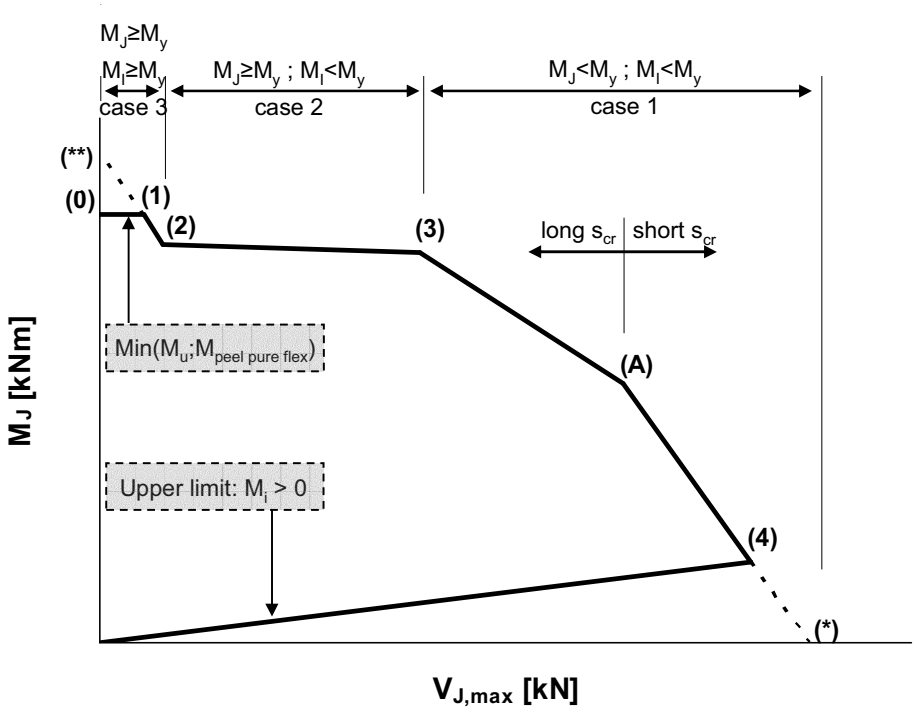

Fig. 3.50: Simplified model for the maximum shear force versus the moment

Finally in Fig. 3.50 an additional point (A) can be noticed, which corresponds to the transition between so-called short and long crack spacing. For short crack spacing bond transfer is characterized by shear stresses along the entire crack spacing, if the maximum transferable force is reached. While for long crack

spacing, the maximum transferable force is reached after a debonding crack between the laminate and the concrete already has appeared by exceeding the ultimate slip (s_{f0}) in the shear stress-slip relationship. The limit between short and long crack spacing equals $s_{rm,lim}$. Herewith, for short crack spacing ($s_{rm} < s_{rm,lim}$), the bond length (L_b) equals the crack spacing s_{rm}. While for long crack spacing ($s_{rm} \geq s_{rm,lim}$), the bonded length (L_b) equals the limited crack spacing ($s_{rm,lim}$)

To define the maximum shear force envelope line, all successive key points (0.1.2.3.4 and A) have to be calculated (see [21]).

5.1.3 Intermediate crack debonding according to Teng et al.

According to Teng et al. [5, 23, 24] it is assumed that debonding is not induced by a major flexural crack but by a flexural-shear crack. These flexural-shear cracks are characterized by a relative vertical displacement between the two faces of the crack, which causes transverse tensile stresses on the FRP plate-to-concrete interface (similar to the assumption in the fib Bulletin [2]). Nevertheless, Teng et al. assume that the widening of the crack is the main factor for intermediate crack debonding, with the vertical displacement of the crack faces being secondary. This, because even if significant transverse tensile stresses exist at the initiation of debonding, these stresses are expected to reduce rapidly as debonding propagates. The resulting peak stress in the FRP laminate in a beam with debonding induced by a flexural-shear crack is expected to be not too different from that corresponding to debonding induced by a flexural crack.

In Fig. 3.51 the simplified model according to [24] is given, on which an analytical solution for the prediction of the intermediate crack debonding load is based. In this model, the behaviour of the FRP-concrete interface between two successive cracks is considered. The model is similar to a pure shear model, but with the difference that in this model both ends of the FRP laminate are subjected to a tensile force. The forces F_2, F_3 and F_4 indicated in Fig. 3.51 can be expressed as fractions of F_1 (see Eq. 3.24 to 3.26).

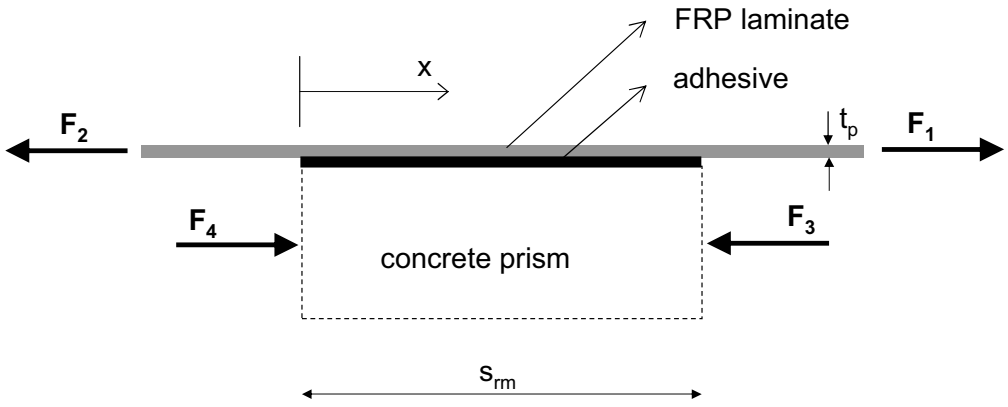

Fig. 3.51: Idealized model of FRP-to-concrete bonded joint between two adjacent cracks [24]

$$F_2 = \beta F_1 \tag{3.24}$$

$$F_3 = \eta F_1 \tag{3.25}$$

$$F_4 = (\beta + \eta - 1) F_1 \tag{3.26}$$

Resulting from an analytical study [24] based on a differential equation determined from the above mentioned model, the debonding load $F_{1,u}$ is given in function of the parameter s_{rm}/a_u (see Fig. 3.52), with s_{rm} equalling the crack spacing, $F_{1,u}$ equal to the force F_1 (see Fig. 3.51) at ultimate and a_u equalling the length of the bond interface at ultimate taken by second decreasing branch of the bilinear τ-s model (see Fig. 3.4) over the length of the crack spacing (length of softening interface [24]).

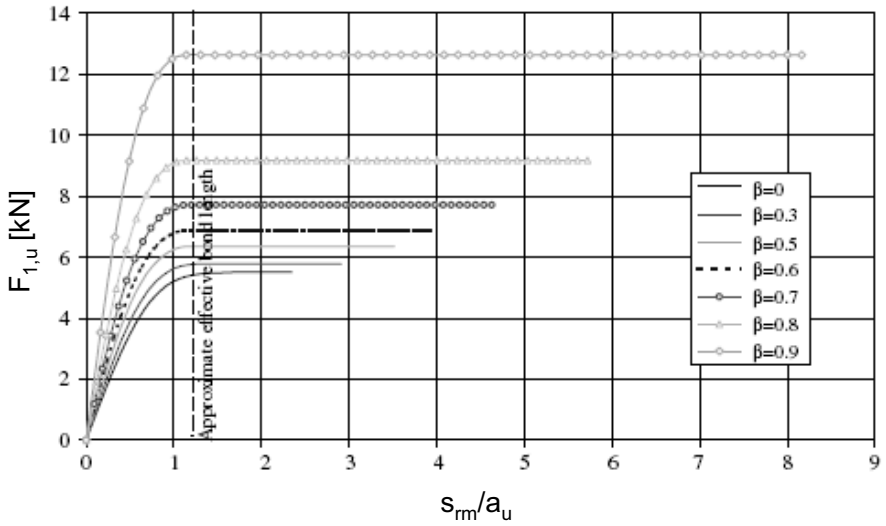

Fig. 3.52: Ultimate load versus normalized bond length for different β values [24]

From Fig. 3.52 the following can be derived: for a given β value, $F_{1,u}$ increases with the crack spacing s_{rm} but remains constant after s_{rm} reaches a certain value. Moreover, the debonding load $F_{1,u}$ also increases with increasing values of β. As β is a function of F_1 and F_2 (see Eq. 3.24), it can be concluded that β is related to the stress gradient in the FRP laminate ($\Delta\sigma_f$) and related to this to the acting shear force. Herewith a similarity is found between the model proposed by Teng et al. and the models proposed by respectively fib Bulletin 14 [2] and by Oller et al. [21].

Finally from Fig. 3.52, it can be noticed that the curve for β = 0, represents the maximum anchoring FRP force in function of the bond length for a pure shear test. Herewith it can be noticed that the curve for β = 0 in Fig. 3.52 is identical to the maximum FRP force which can be anchored in function of the bond length as illustrated in Fig. 3.5.

5.2 M – V diagrams

As all three models presented in previous sections are related to both the stress gradient in the FRP laminate ($\Delta\sigma_f$) and to the real acting stress in the FRP laminate (σ_f), or in other words are related to respectively the shear force (V) and to the moment (M), it is useful to draw the real acting shear force in function of the moment for different load configurations. With these graphs the effect of the load configuration on the debonding load can be investigated. As an example, the relation between shear force and moment is investigated for a 3-point-bending test, for a 4-point bending test and for a uniformly loaded isostatic beam (Fig. 3.53). The length of each beam is taken equal to 3.6 meter, which equals the length of the tested beams discussed in the following section (section 5.3).

The total applied load on each beam is assumed to be equal for all test set-ups. In this investigation, the total load is taken equal to 115 kN. With this assumption one point load of 115 kN is considered in the 3-point-bending configuration, two point loads of 57.5 kN are considered in the 4-point-bending configuration and a uniform load of 32.0 kN/m is considered in the uniformly loaded beam (see Fig. 3.53). The choice of the total load equal to 115 kN, is explained further in this section.

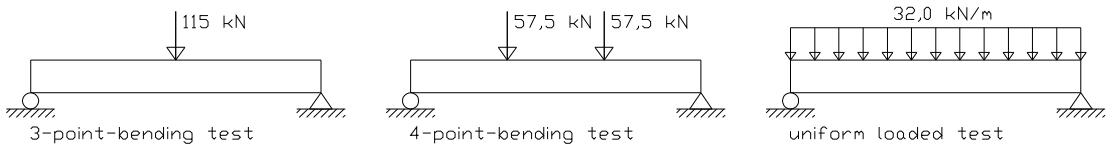

Fig. 3.53: Different loading configurations

In Fig. 3.54, the relation of the shear force versus the moment is shown for the three different load configurations. Notice that only half of the total graph is shown, i.e. the part corresponding to the zone between the left support and the centre of the beam.

Further investigation of Fig. 3.54 reveals that the shear force-moment relation for a 3-point-bending configuration is a vertical line at V = 57.5 kN, with a maximum moment which equals 103.5 kNm (see point A). The relation for a 4-point-bending configuration also partly exists of the vertical line at V = 57.5 kN, but with a lower maximum moment (69 kNm) (see line BC). The second part of this relation is a horizontal line at M = 69 kN (see line BD). In fact this horizontal line is a connection between the M-V combination under the point load (M = 69 kNm and V = 57.5 kN) and the M-V combination at the pure bending zone between the point loads. In this zone, the moment is constant (M = 69 kNm) and the shear force equals zero. Finally the relation of the uniformly loaded beam is a non-linear relation, with a maximum moment of 51.75 kNm at a shear force equal to 0 kN (see point E) and the other extreme at V = 57.5 kN for M = 0 kNm (see point C).

From Fig. 3.54, it can be noticed that the maximum shear force for all three different load configurations equals the same maximum value (57.5 kN). The value of the maximum moment on the other hand differs between 103.5 kNm (point A for 3-point-bending configuration) and 51.75 kNm (point E for uniformly loaded configuration). Given that the shear resistance is limited for debonding

reasons in function of the real acting moment (see e.g. the model proposed by Oller in Fig. 3.50), it is obvious that IC-debonding is expected earlier in a 3-point-bending situation compared to the uniformly loaded test. Referring to the model proposed in fib Bulletin 14 [2], by which IC-debonding at inclined shear cracks is evaluated by a simplified model calibrated on 4-point-bending test results (see section 2.1.1.2), it can be expected that the predictions of debonding loads will be at the safe side for uniformly loaded beams and for 4-point-bending situations but will be at the unsafe side for 3-point-bending situations.

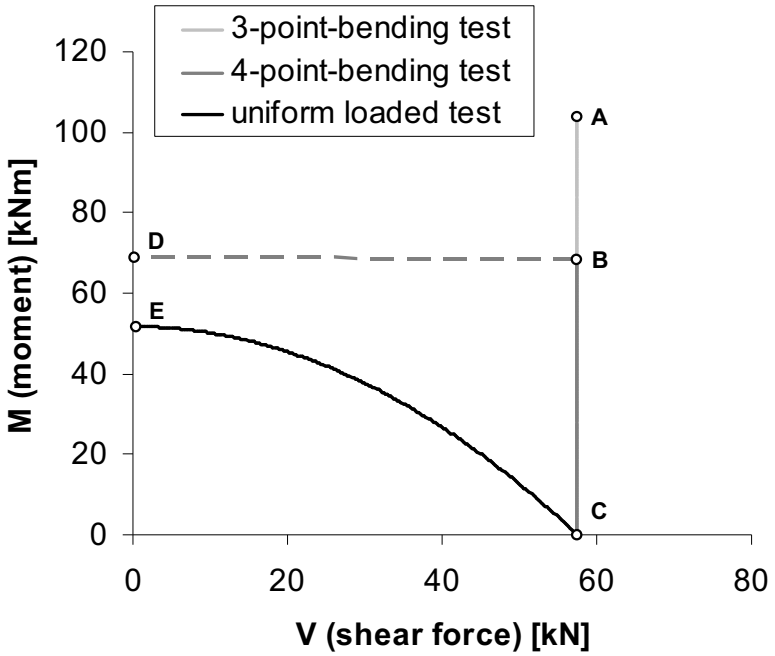

Fig. 3.54: Shear force versus moment for different load configurations

Next, the relationship between the shear forces and the linear elastic moment distribution is also elaborated for three different two-span beams configurations. The first investigated configuration (case 1 in Fig. 3.55) is the configuration used in the experimental and analytical studies of Chapter 2. One point load is applied in each span at a distance of 2 meters from the outer support and 3 meters from the mid-support. The point load in this configuration is taken equal to 100 kN, which results in a reaction at the mid-support of 113.6 kN. This reaction force roughly equals the load of 115 kN applied in the 3-point-bending configuration mentioned above (see Fig. 3.53).

In a second configuration (case 2) two point loads are applied in each span. The distance between each support and the nearest point load is taken equal to 1.66 m, which equals 1/3 of the span length. In the last configuration (case 3), a uniformly loaded configuration is supposed. For all cases, the applied total load equals 100 kN for each span.

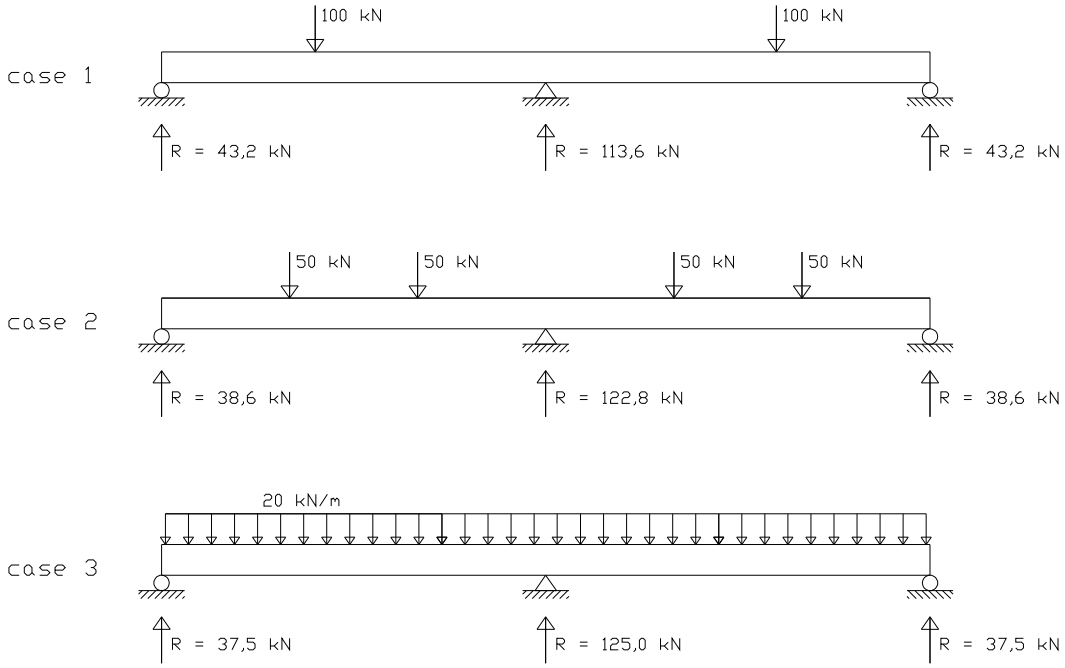

Fig. 3.55: Different load configurations for two-span beams

In Fig. 3.56, the relation between the shear forces and the linear elastic moment distribution are given for the three different test configurations shown in Fig. 3.55. Again, only half of the total graph is shown, i.e. the part corresponding to the zone between the left support and the mid support (left span in Fig. 3.55).

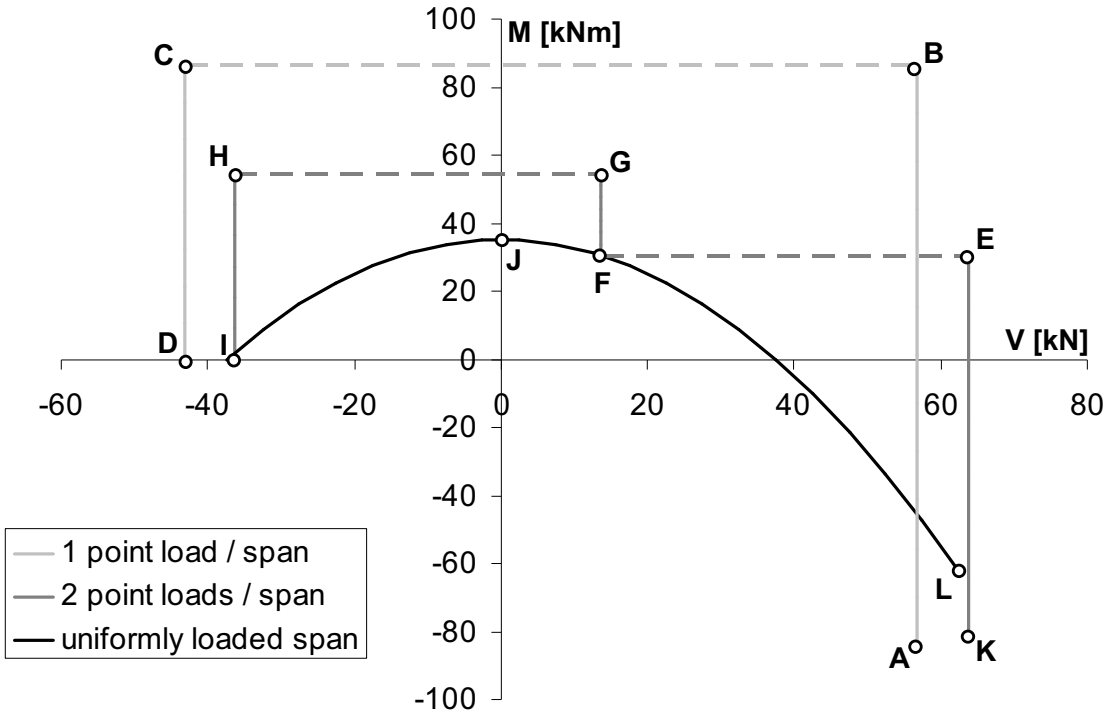

Fig. 3.56: Shear force versus moment for different load configurations

Table 3.7: M – V coordinates of specific locations at the M – V curves

Test configuration	Location in Fig. 3.56	M [kNm]	V [kN]	Location at beam
Case 1:	A	-84.0	56.8	Mid-support
1 – point load / span	B	86.4	56.8	Point load (right side)
	C	86.4	-43.2	Point load (left side)
	D	0.0	-43.2	Outer support
Case 2:	K	-81.0	63.7	Mid-support
2 – point loads / span	E	30.4	63.7	Point load 1 (right side)
	F	30.4	13.7	Point load 1 (left side)
	G	54.4	13.7	Point load 2 (right side)
	H	54.4	-36.3	Point load 2 (left side)
	I	0.0	-36.3	Outer support
Case 3:	L	-62.5	62.5	Mid-support
Uniformly loaded span	J	35.0	0.0	Location of M_{max}
	I	0.0	-37.5	Outer support

The M - V relation for case 1, exists of two vertical parts and one horizontal part (curve characterized by the points A – B – C – D in Fig. 3.56). The M – V coordinates and the related position in the continuous beam of each point in Fig. 3.56 are given in Table 3.7. The horizontal segment is given as a dashed line, because it is the connection in the M – V curve between the right hand side of the point load (point B) and the left hand side of the point load (point C). By adding the model of Oller (section 5.1.2) in this graph, it becomes obvious that the extremities (e.g. point A, B and C) of this graph become potential locations where IC-debonding of the FRP laminate is expected. In the left span of the 2-span beam, these extremities are respectively found at the location of the mid-support, the right hand side of the point load and the left hand side of the point load. As point B is located further from the origin (coordinates (0;0)) compared to point C, point B will be more critical than point C. Hence IC-debonding of the soffit laminate applied beneath the point load, will be initiated at the right hand side of the point load and will continue in the direction of the mid-support. This outcome for two-span beams with one point load in each span is in agreement with the experimental observation for beam CB1, for which IC-debonding of the bottom laminate is observed starting from the point load and moving to the mid-support (see Fig. 3.57).

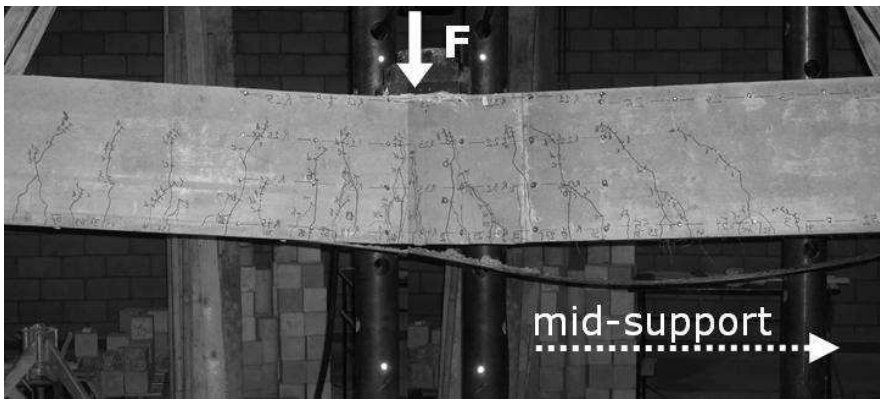

Fig. 3.57: Debonding of the soffit laminate at a flexural/shear crack.

The M – V relation of case 2 exists of 3 vertical parts and two horizontal parts. Again, each horizontal line is a connection between the left and right hand side of one point load. On the other hand the vertical lines are the real acting M – V relations. In the graph four critical points are observed at which IC-debonding can be expected: i.e. points K, E, G and H. From Fig. 3.56 it can be noticed that points E and G are less critical, while point K is more critical.

In the M – V relation of case 3, point L is the most critical point. IC-debonding of the laminate in a uniformly loaded continuous beam is expected at the top laminate.

Summarizing the three different loading configurations, it is noticed that the mid-support (points A, K and L) is critical in all loading configurations. Hence, special attention is needed for the verification of debonding at the location of the top laminates for all types of loading configuration.

Finally also the M – V relation is given for the loading configuration where only one span is loaded (see Fig. 3.58). In Fig. 3.59 both the M – V relations are given for the beam uniformly loaded over its full length (case 3) and the two-span beam uniformly loaded in only one span. Comparing these two relations with each other, an upward translation of the curve is noticed. This results in both a reduction of the shear force and a considerable reduction of the moment (about 50%) at the mid-support (mid-support corresponds to the above mentioned critical point L). In this case the debonding of the top laminate by IC debonding becomes less critical. On the other hand, extra attention is needed, for the soffit laminates, as the moment is increasing at that location. Nevertheless in design stadium all possible loading configurations need to be taken into account, or in other words design of a structural element is based on the envelope line of both internal moments and shear forces.

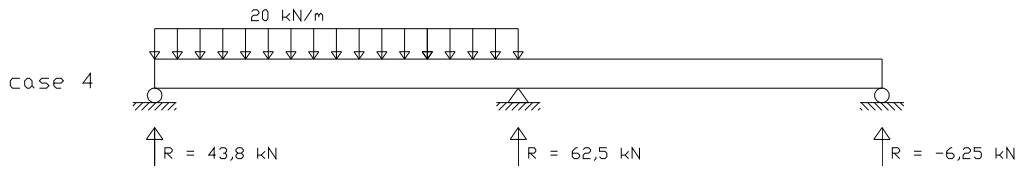

Fig. 3.58: Load configuration of two-span beam

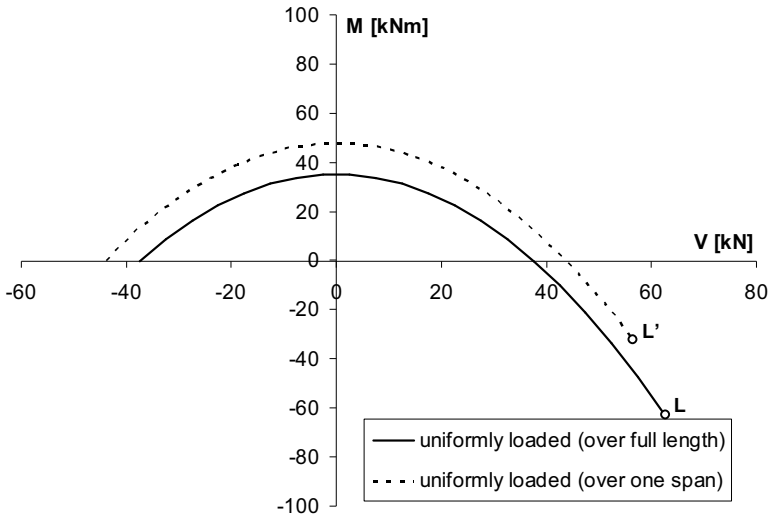

Fig. 3.59: Shear force versus moment for one span uniformly loaded

5.3 Debonding of the FRP EBR laminate in 3-point-bending tests

The analytical approach of IC-debonding has been experimentally verified for the specific case of 3-point-bending. A 3-point-bending configuration is chosen because of the similarity with both the moment and shear force distribution at the mid-support of a two-span beam (see Fig. 3.48). Four tests have been conducted on flexural strengthened beams with a span length of 3.6 m. The test set-up is shown in Fig. 3.60. As can be seen in Table 3.8 the main test parameters are the internal steel reinforcement ratio and the stirrup spacing.

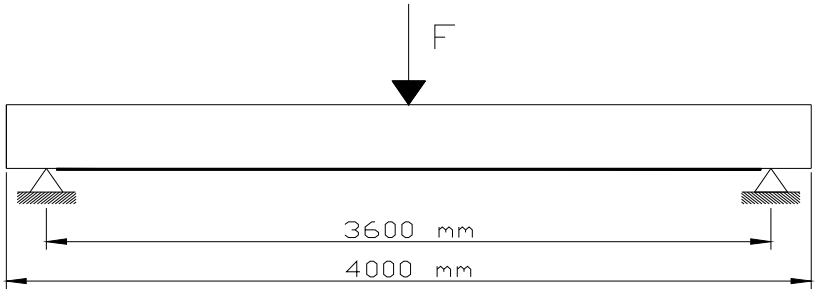

Fig. 3.60: Test set-up for 3-point-bending test

Table 3.8: Test parameters

	Internal reinforcement ratio (ρ_s)	External reinforcement ratio (ρ_f)	Stirrup spacing
IB1	0.31 %	0.13 %	150 mm
IB2	0.64 %	0.13 %	150 mm
IB3	1.43 %	0.13 %	150 mm
IB4	0.64 %	0.13 %	75 mm

The width of the cross-section (b) equals 198 mm and the height equals 400 mm (h). The cross-section of the FRP laminate equals 100 mm (w_f) x 1.0 mm (t_f). The external reinforcement ratio (ρ_f) equals 0.13 % for all strengthened beams (Table 3.8). The laminates are applied over the entire free distance between the supports (length of laminate = 3500 mm), to avoid both debonding by a too short anchorage length or debonding by concrete rip-off (see section 3 and [16]).

The properties of the materials are given in Table 3.9 and Table 3.10.

Table 3.9: Properties of concrete

		IB1	IB2	IB3	IB4
modulus of elasticity (E_c)	[N/mm²]	33900	35500	35600	33900
compressive strength (f_c)	[N/mm²]	39.0	40.5	38.7	39.0
tensile strength (f_{ct})	[N/mm²]	2.8	2.7	3.0	2.6
ultimate strain (ε_u)	[%]	0.35	0.35	0.35	0.35

f_c, cylindrical compressive strength (diam: 150 mm x height: 300 mm)
f_{ct}, pure tensile strength, obtained by converting the experimentally obtained flexural tensile strength and the splitting tensile strength, according to Eurocode 2.

Table 3.10: Properties of the reinforcement

		FRP	Steel reinforcement			
			IB1	IB2	IB3	IB4
modulus of elasticity (E_s or E_f)	[kN/mm²]	180.0	223	212	212	212
yield stress (f_y)	[N/mm²]	-	589	618	495	618
tensile strength (f_s or f_f)	[N/mm²]	2981	674	682	698	682
ultimate strain (ε_u)	[%]	1.65	9.62	6.82	11.1	6.82

In Table 3.11 an overview is given of both the experimental and analytical debonding loads. For the analytical debonding loads, both models of fib Bulletin 14 are considered, i.e.:

- debonding at flexural cracks represented by the model according to the envelope line of tensile stresses in the FRP (according to Fig. 3.3).
- debonding at shear cracks (according to Eqs. 3.10 and 3.11)

Further, also the model proposed by Oller is considered. In addition, the ratio is given for all analytically obtained debonding loads in comparison with the experimental one's. The analytical values are obtained by using the material properties mentioned in Table 3.9 and Table 3.10 and by taking all safety factors equal to 1 in the design models. The crack spacing (s_{rm}) is taken equal to the experimentally obtained crack spacing, and the bilinear bond slip relation is taken as defined in [2]. Values of s_{rm} are reported in Table 3.11.

Remark that the model proposed by Teng (see section 5.1.3) is not further considered in the analytical verification.

Table 3.11: Overview of experimental and analytical results

	$F_{deb,exp}$	s_{rm}	$F_{deb,Bull14}$ at flexural cracks		$F_{deb,Bull14}$ at shear cracks		$F_{deb,Oller}$	
	[kN]	[mm]	[kN]	[%]	[kN]	[%]	[kN]	[%]
IB1	100.3	87.4	81.5	81	150.1	150	81.3	81
IB2	153.0	76.8	139.1	91	222.6	146	138.8	91
IB3	218.8	84.7	211.5	97	394.3	180	209.9	96
IB4	147.6	80.3	139.0	94	222.6	151	138.7	94

Table 3.11 shows that the model of fib Bulletin 14 (peeling-off caused at flexural cracks) and the model of Oller et al. [21] give fairly good predictions for the intermediate crack debonding load in these tests although they appear to be slightly conservative. In addition it seems that the other model of the fib Bulletin 14 (peeling-off caused at shear cracks) gives unrealistic predictions for the three-point-bending tests. A possible reason for this can be that the experimental calibration of the formula was based on four-point-bending tests.

5.3.1 Debonding at flexural cracks according to fib Bulletin 14

In Fig. 3.61 to Fig. 3.64, the maximum allowable increase of the stress in the FRP laminate (max $\Delta\sigma_f$) is given versus the related tensile stress in the FRP laminate for all tested beams. The acting $\Delta\sigma_f$ - σ_f relation at the location of the point load in the centre of this beam is given by the grey line.

The debonding characteristics obtained from this model, correspond to the intersection of the two curves, and are given in Table 3.12: the maximum

possible increase in tensile stress between two adjacent cracks (max $\Delta\sigma_f$) at debonding load and the tensile stress in the laminate (σ_f) at debonding load. The corresponding calculated debonding load F_{deb} is given in Table 3.12, as well as in Fig. 3.61 to Fig. 3.64.

Table 3.12: max $\Delta\sigma_f$ at debonding load and σ_f at debonding load of all tested beams

		IB1	IB2	IB3	IB4
max $\Delta\sigma_f$	[N/mm²]	69.8	67.3	80.0	67.6
σ_f	[N/mm²]	589.6	640.0	542.2	638.6
F_{deb}	[kN]	81.5	139.1	211.5	139.0

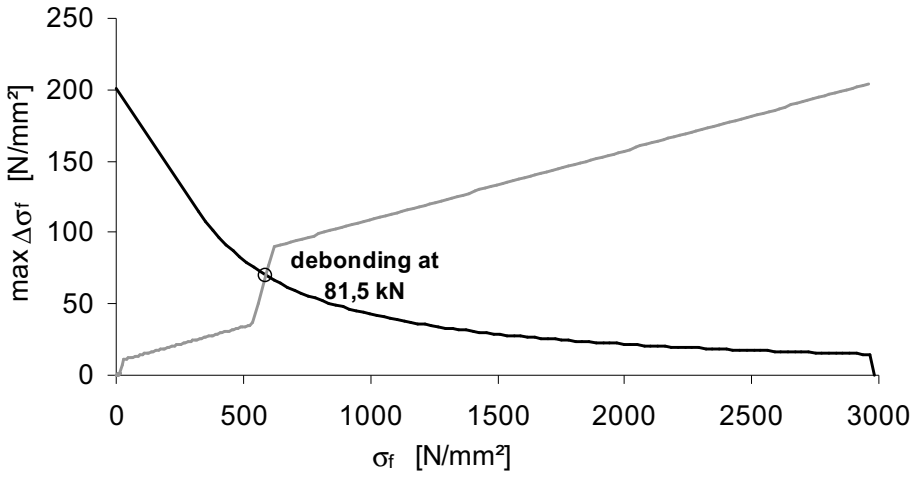

Fig. 3.61: Maximum $\Delta\sigma_f$ versus the applied tensile stress in the laminate (σ_f) for IB1

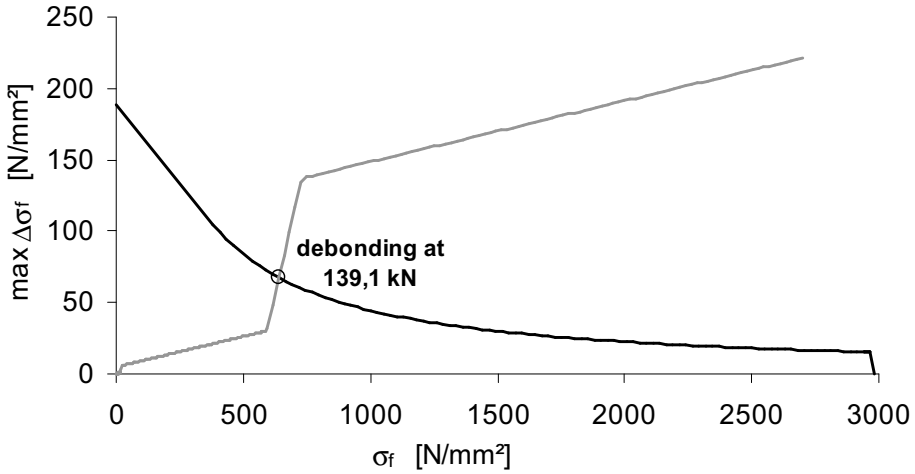

Fig. 3.62: Maximum $\Delta\sigma_f$ versus the applied tensile stress in the laminate (σ_f) for IB2

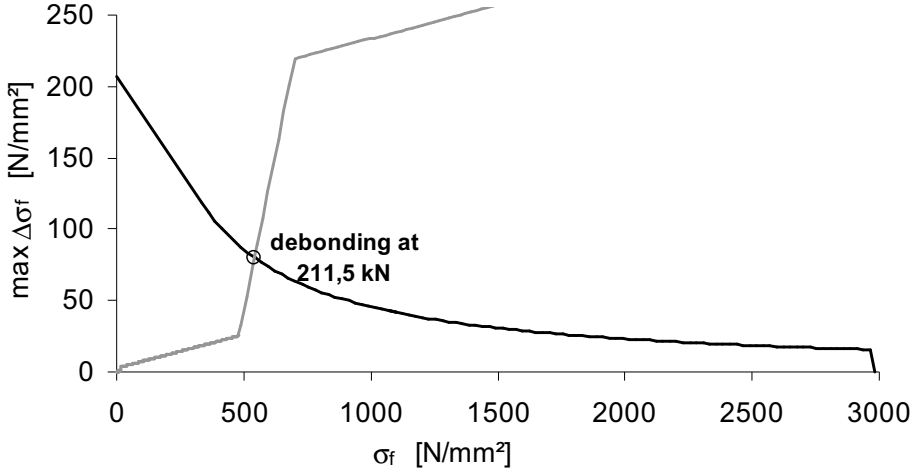

Fig. 3.63: Maximum $\Delta\sigma_f$ versus the applied tensile stress in the laminate (σ_f) for IB3

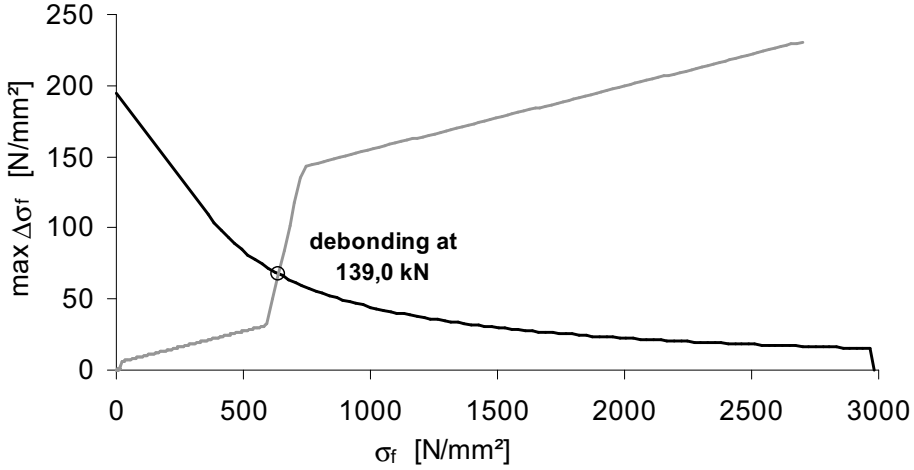

Fig. 3.64: Maximum $\Delta\sigma_f$ versus the applied tensile stress in the laminate (σ_f) for IB4

5.3.2 Debonding according to Oller et al.

In Fig. 3.65 to Fig. 3.68, the relation of the maximum shear force versus the moment at the location of the point load of all tested beams is shown. The acting V – M relation at the location of the point load in the centre of the beam is given by the grey line. The intersection of the two curves represents the shear force and the moment at debonding. These values are given in Table 3.13. The corresponding calculated debonding load F_{deb} is given in Table 3.13, as well as in Fig. 3.65 to Fig. 3.68.

Table 3.13: Shear force and moment related to the debonding load of all tested beams

		IB1	IB2	IB3	IB4
V_{max}	[kN]	40.6	69.4	104.9	69.4
M	[kNm]	69.2	120.9	184.9	120.9
F_{deb}	[kN]	81.3	138.8	209.9	138.7

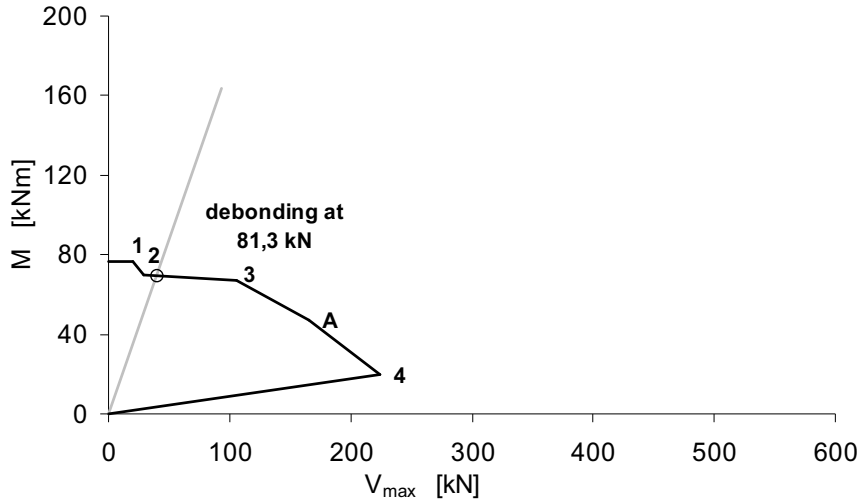

Fig. 3.65: Maximum shear force versus the moment for IB1

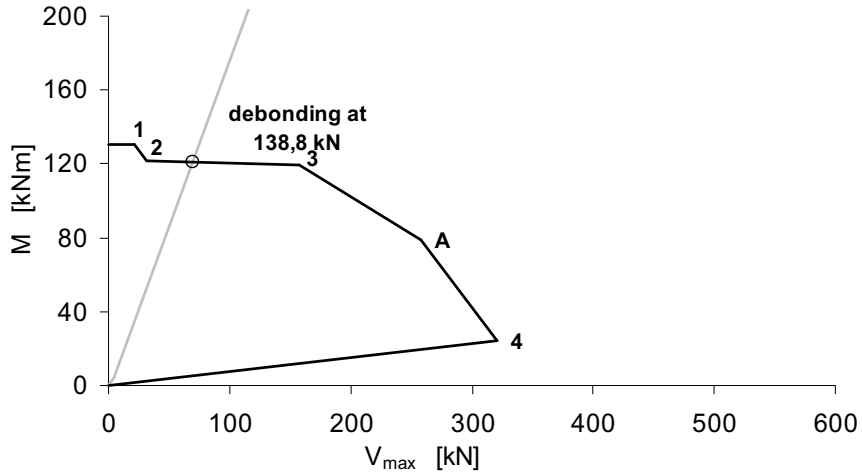

Fig. 3.66: Maximum shear force versus the moment for IB2

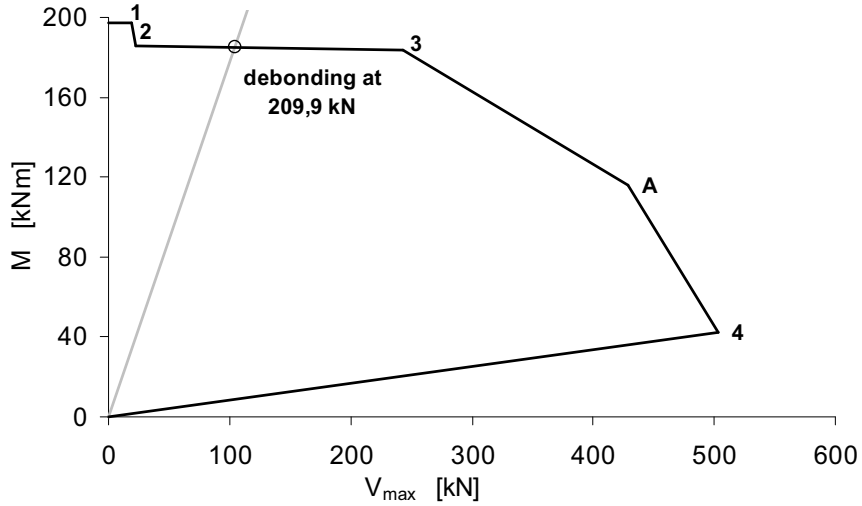

Fig. 3.67: Maximum shear force versus the moment for IB3

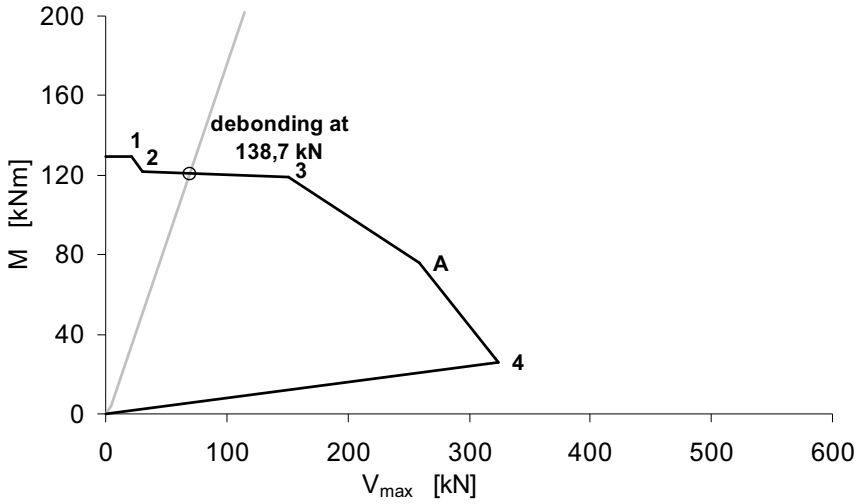

Fig. 3.68: Maximum shear force versus the moment for IB4

5.4 Debonding of laminate at the mid-support of two-span beams

The analytical approach for IC-debonding has also been verified given the experimental results on two-span beams, for which debonding of the laminate occurred above the mid-support. For this, the continuous beams CB2, CB3 and CB4, discussed in section 2.2 and in Chapter 2, are considered.

In Table 3.14, both the experimental IC-debonding loads and the analytical debonding loads are given. The analytical debonding loads were calculated according to:

- fib Bulletin 14 model: debonding at flexural cracks (see section 2.1.1.1), represented by the model according to the envelope line of tensile stresses in the FRP (according to Fig. 3.3).
- fib Bulletin 14 model: debonding at shear cracks (see section 2.1.1.2), according to Eqs. 3.10 and 3.11.
- Model proposed by Oller et al. (see section 5.1.2).

Remark that the model proposed by Teng (see section 5.1.3) is not further considered in the analytical verification.

Table 3.14: Overview of experimental and analytical results

	$F_{deb,exp}$	s_r	$F_{deb,Bull14}$ at flexural cracks		$F_{deb,Bull14}$ at shear cracks		$F_{deb,Oller}$	
	[kN]	[mm]	[kN]	[%]	[kN]	[%]	[kN]	[%]
CB2	152.0	44.6	121.2	80	132.8	87	115.7	76
CB3	170.5	66.8	138.7	81	196.6	115	140.3	82
CB4	115.9	64.7	96.8	84	125.7	108	96.8	84

The crack spacing introduced in the three models, is taken equal to the experimental crack spacing at the location where IC-debonding was observed.

From Table 3.14, it can be observed that the predictions by the fib Bulletin 14 model at flexural cracks (model according to the envelope line of tensile stresses in the FRP) and by the model of Oller are very similar to each other, but are quite

conservative. These models result in an average of respectively 81.5 % and 80.6 % of the experimental debonding loads. Finally, the fib Bulletin 14 model at shear cracks is giving the best predictions, with an average of 103.7 % of the experimental debonding load. However, the fib Bulletin 14 model at shear cracks is giving an unsafe prediction for CB3 (up to 15 %) and for CB4 (up to 8 %).

5.4.1 Debonding at flexural cracks according to fib Bulletin 14

In Fig. 3.69 to Fig. 3.71, the maximum allowable increase of the stress in the FRP laminate (max $\Delta\sigma_f$) is given versus the related tensile stress in the FRP laminate for all tested beams. The acting $\Delta\sigma_f$ - σ_f relation at the location of the point load in the centre of this beam is given by the grey line. The values of $\Delta\sigma_f$ and σ_f at the calculated moment of debonding are given in Table 3.15.

Table 3.15: Max $\Delta\sigma_f$ at debonding load and σ_f at debonding load of all tested beams

		CB2	CB3	CB4
max $\Delta\sigma_f$	[N/mm²]	71.0	82.2	71.7
σ_f	[N/mm²]	839.9	637.3	682.1
F_{deb}	[kN]	121.2	138.7	96.8

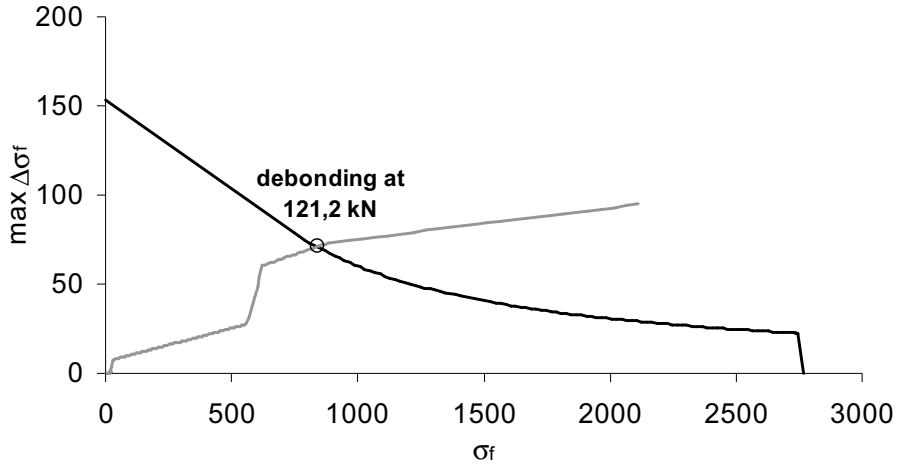

Fig. 3.69: Maximum $\Delta\sigma_f$ versus the applied tensile stress in the laminate (σ_f) for CB2

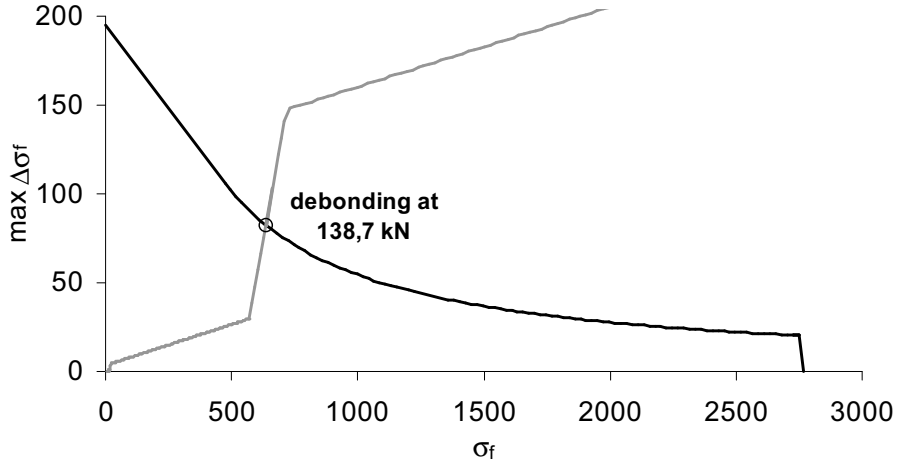

Fig. 3.70: Maximum $\Delta\sigma_f$ versus the applied tensile stress in the laminate (σ_f) for CB3

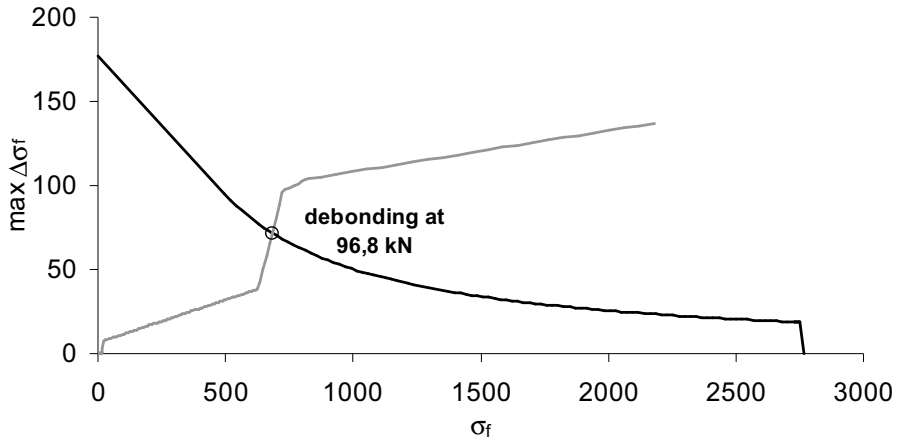

Fig. 3.71: Maximum $\Delta\sigma_f$ versus the applied tensile stress in the laminate (σ_f) for CB4

5.4.2 Debonding according to Oller et al.

In Fig. 3.72 till Fig. 3.74 both the maximum transferable shear force in function of the moment and the acting shear force in function of the moment at the location of the mid-support are given. It is observed that the acting shear force – moment relation is a non-linear curve, which is caused by the non-linear behaviour (moment redistribution) at the two-span beams. As mentioned in Chapter 2 and looking to Fig. 3.73, hardly any non-linear behaviour (moment redistribution) is observed in CB3 as the internal and external reinforcement ratios are chosen according to the linear elastic theory.

The shear force and moment at debonding are given in Table 3.16, as well as the corresponding debonding load.

Table 3.16: Shear force and moment related to the debonding load of all tested beams

		CB2	CB3	CB4
V_{max}	[kN]	63.7	81.5	55.1
M	[kNm]	77.4	117.4	72.0
F_{deb}	[kN]	115.7	140.3	96.8

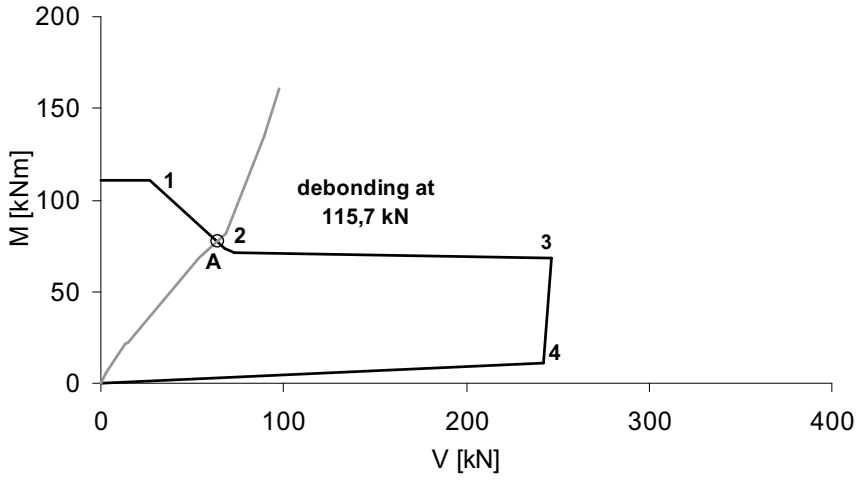

Fig. 3.72: Maximum shear force versus the moment for CB2

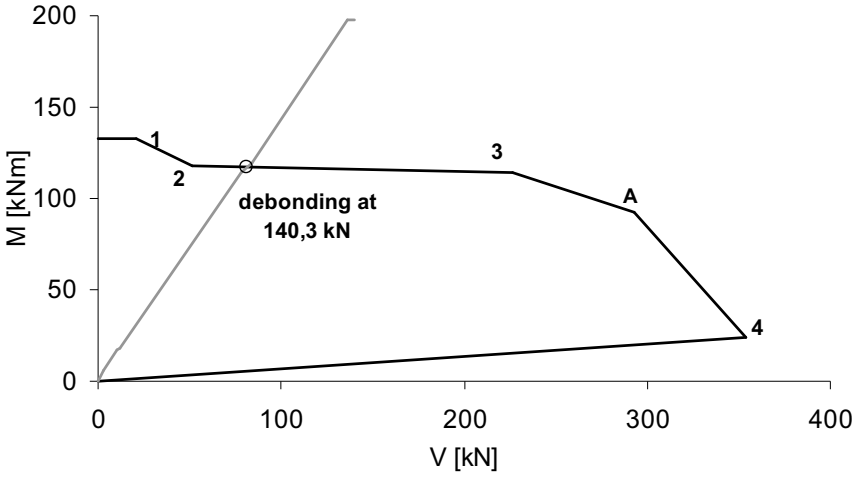

Fig. 3.73: Maximum shear force versus the moment for CB3

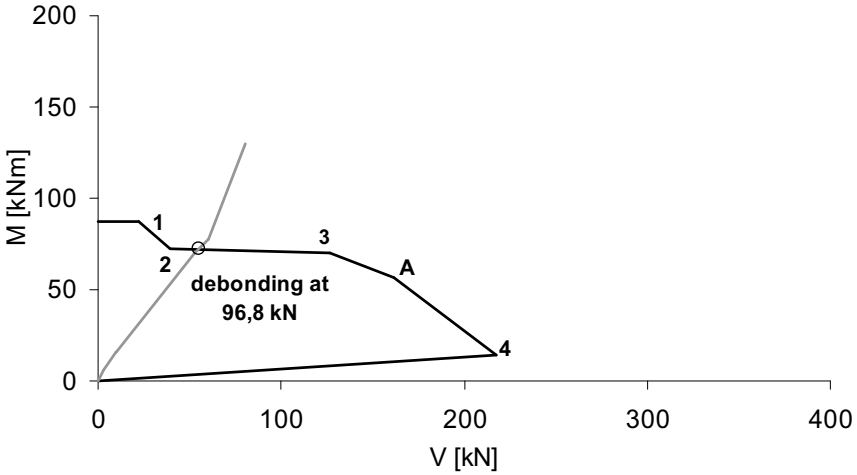

Fig. 3.74: Maximum shear force versus the moment for CB4

6 Conclusions

The use of EBR to strengthen reinforced concrete structures implies the possible occurrence of debonding of the laminates. In the design of a strengthened member, often full composite action is assumed to start with. In a second stage, different debonding mechanisms are considered or verified in the design. The different debonding mechanisms which can appear in the strengthened regions of a continuous beam are similar to the mechanisms which appear in isostatic beams. These mechanisms have been investigated by various researchers. A distinction is made between the following mechanisms [2, 3]:

- Debonding at flexural cracks
- Debonding at shear cracks
- Debonding by a limited anchorage length
- Debonding by end shear failure

By investigating these mechanisms in continuous beams, certain differences between continuous beams and isostatic beams have to be mentioned. A first difference which may influence the debonding mechanisms in continuous reinforced concrete beams is the moment line with opposite signs. Whereas the moment in the span is positive, the moment at the mid-support is negative. In contrast to reinforced isostatic beams, this allows to anchor the FRP laminates in compression zones. By extending a laminate into these compression zones, two out of the four different debonding mechanisms will be avoided: debonding by a limited anchorage length and debonding by end shear failure (concrete rip-off). By executing strain measurements in the compression zone of the laminates no indication of local buckling has been noticed. Due to the limited length of which the laminate is extended in the compression zone, the compressive stress in the laminate is restricted and the probability of buckling is negligible.

A second difference between continuous and isostatic beams is the non-linear behaviour. By using reinforcement ratios different from those corresponding to the linear elastic theory, both a moment and shear force redistribution is observed. These redistributions on their turn do influence both the real acting shear force as well as some parameters which are necessary to calculate the debonding load (the anchorage length l_t and the distance between laminate end and point of contraflexure L). As the non-linear behaviour is dependent on the stiffness distribution along the length of the beam or, in other words on the reinforcement/strengthening ratios, also the debonding load will be dependent on the different reinforcement/strengthening ratios along the length of the beam. This dependency can result in earlier or later debonding of the laminates compared to the linear elastic theory. As a result, it is of importance to check all different debonding mechanisms by taken into account the real acting moment redistribution.

Finally, IC-debonding has been observed at the location of the mid-support of two span-beams. The location of the mid-support acts as a concentrated point-load, for which a combination of high shear forces and high moments can be found. As a result, this configuration is comparable with a 3-point-bending test (see Fig. 3.54 and Fig. 3.56). As most of the experimentally calibrated debonding models are based on 4-point-bending tests, it is interesting to investigate IC-

debonding for 3-point bending configurations and related to this the IC-debonding at the location of the mid-support.

For the 3-point-bending test program, it has been observed that fib Bulletin 14 gives good predictions of the intermediate crack debonding load in 3-point-bending tests, on average 9.2 % lower compared to the real debonding load. For all beams these predictions correspond to the 'debonding at flexural cracks' model (represented by the envelope line of tensile stresses in the FRP) while the 'debonding at shear cracks' model appeared not to be representative.

An alternative model to evaluate intermediate crack debonding is proposed by Oller et al. [21]. This model gives the impression to combine both debonding at shear cracks and at flexural cracks, as it combines a maximum shear force and the moment. However, vertical crack displacement is not explicitly considered in the model. An experimental verification by means of the conducted 3-point-bending-tests, shows that this model is as conservative as the fib Bulletin 14 model (on average 9.6 % lower compared to the real debonding load). It can be concluded that both the 'debonding at flexural cracks' model of fib Bulletin 14 (represented by the envelope line of tensile stresses in the FRP) and the model by Oller give accurate predictions of the debonding load in the case of 3-point-bending tests. Compared to the fib Bulletin 14 model, the model by Oller is less complex to calculate.

Considering IC-debonding at the location of the mid-support of the two span beams, again both predictions by fib Bulletin 14 and by Oller are verified. As is noticed in the 3-point-bending configurations, the model at flexural cracks proposed by fib Bulletin 14 and the model proposed by Oller et al. give similar and accurate predictions. However, too conservative results are obtained for the top laminate in the case of two span beams. The other model proposed by fib Bulletin 14 (debonding at shear cracks), gives better predictions, but at the unsafe side for both CB3 and CB4.

Due to the better predictions of the latter model, it seems that IC-debonding of the laminate above the mid-support in a two-span beam is induced by the vertical crack displacement at a flexural-shear crack. This vertical crack displacement can be observed in both Fig. 3.75 and Fig. 3.77 as well as in the vertical displacement schemes resulting from DICT (Digital Image correlation Technique) measurements (Fig. 3.76 and Fig. 3.78). The latter figures display, by means of a colour range, the vertical displacement of the top face of the beam. The vertical displacement, with respect to the loaded configuration, is given for both the top laminate and the two zones of concrete just next to it. In these figures it is remarkable that just before debonding of the laminate, already a peeling off of the laminate is observed at the location where debonding will occur. This peeling-effect (vertical crack displacement (v)) amounts to only several tenths of a millimetre ($v \approx 0.6$ mm) and is hardly observable during testing by the naked eye.

Fig. 3.75: IC-debonding of the laminate applied at top of the mid-support (CB3)

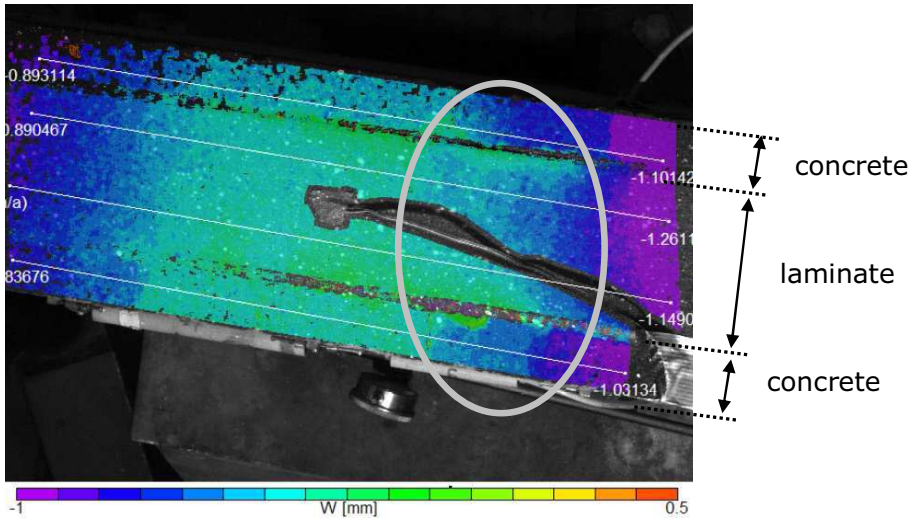

Fig. 3.76: Vertical crack displacement between laminate and concrete just before debonding (CB3)

Fig. 3.77: IC-debonding of the laminate applied at top of the mid-support (CB4)

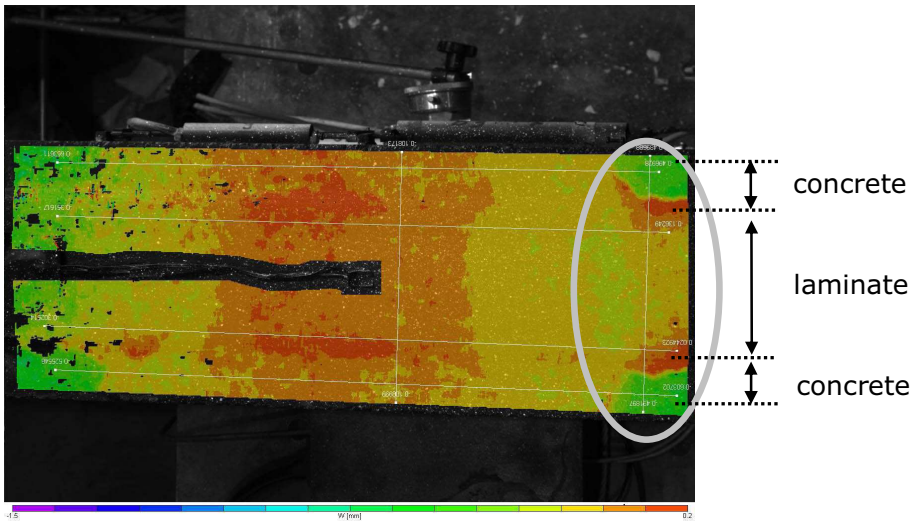

Fig. 3.78: Vertical crack displacement between laminate and concrete just before debonding (CB4)

References

[1] D. Vandepitte, *Berekening van constructies*. E. Story-Scientia. Ghent. 1979. Vol. 3: pp. 721.

[2] fib, *fib bulletin 14, Externally bonded FRP reinforcement for RC structures*. International federation for structural concrete, Lausanne. 2001: pp. 138.

[3] S. Matthys, *Structural behaviour and design of concrete members strengthened with externally bonded FRP reinforcement*. PhD thesis. Department of Structural Engineering, Ghent University. Ghent, Belgium. 2000. pp. 345.

[4] A.C. 440, *ACI 440.2R-02, Guide for the Design and Construction of externally Bonded FRP Systems for strengthening Concrete Structures*. 2002.

[5] J.G. Teng, et al., *Intermediate crack-induced debonding in RC beams and slabs.* Construction and Building Materials. 2003. Vol. 17 (6-7): pp. 447-462.

[6] E. Oller, D. Cobo and A.R. Mari, *A new design proposal to prevent failure in beams strengthened by plate debonding*. Proceedings of FRPRCS-8, Patras, Greece. Thanasis C. Triantafillou. 2007

[7] J.F. Chen, H. Yuan and J.G. Teng, *Debonding failure along a softening FRP-to-concrete interface between two adjacent cracks in concrete members.* Engineering Structures. 2007. Vol. 29 (2): pp. 259-270.

[8] R. Niedermeier, *Envelope line of tensile forces while using externally bonded reinforcement*. PhD thesis, TU Münich. Munchen. 2000.

[9] M. Blaschko, *Strengthening with CFRP*. Proceedings of Münchner Massivbau Seminar, Münich. 1997

[10] P. Holzenkämpfer, *Ingenieurmodelle des Verbunds geklebter Bewehrung für Betonbauteile*. Berlin. 1997. Vol. DAS - Heft 473.

[11] B. Täljsten, *Plate Bonding - Strengthening of Existing Concrete Structures with Epoxy Bonded Plates of Steel or Fibre Reinforced Plastics*. PhD thesis. Division of structural engineering, University of Technology. Lulea. 1994. pp. 281.

[12] W. Jansze, *Strengthening of reinforced concrete members in bending by externally bonded steel plates*. PhD thesis, TU Delft. Delft, The Netherlands. 1997.

[13] O. Rabinovitch and Y. Frostig, *Edge effects in retrofitting of concrete beams using fibre reinforced polymer stripes*. Proceedings of FRPRCS-4, Baltimore. ACI. 1999: pp. 179-191

[14] M. Deuring, *Verstärken von Stahlbeton mit gespannten Faserverbundwerkstoffen*. EMPA, Dübendorf, Switzerland. 1993. Vol. 224: pp. 279.

[15] O. Rabinovitch, *Nonlinear (buckling) effects in RC beams strengthened with composite materials subjected to compression.* International Journal of Solids and Structures. 2004. Vol. 41 (20): pp. 5677-5695.

[16] L. Vasseur, S. Matthys and L. Taerwe, *Debonding mechanisms in continuous RC beams externally strengthened with FRP.* Proceedings of FraMCoS, Catania, Italy. A. Carpinteri, et al.: Taylor & Francis/Balkema. 2007. Vol. 2 ('Design, Assessment and retrofitting of RC Structures'): pp. 1101-1110

[17] L. Vasseur, S. Matthys and L. Taerwe, *Debonding mechanisms and moment redistribution of 2 span RC beams*. Proceedings of FRPRCS 8, Patras, Greece. Thanasis C. Triantafillou. 2007

[18] L. Vasseur, S. Matthys and L. Taerwe, *An analytical study on the bond behaviour between an externally bonded FRP and concrete in the case of continuous beams.* Mechanics of Composite Materials. 2008. Vol. 44 (3 / May, 2008): pp. 269-278.

[19] L. Vasseur, S. Matthys and L. Taerwe, *Analytical study of a 2-span reinforced concrete beam strengthened with fibre reinforced polymer*. Proceedings of IABSE symposium: 'Responding to tomorrow's challenges in structural engineering', Budapest. IABSE Hungarian Group 2006

[20] L. Vasseur, S. Matthys and L. Taerwe, *Bond behaviour of externally bonded FRP to concrete in the case of 3-point-bending tests*. Proceedings of CCC2008: 'Challanges for Civil Construction', Porto. A.Marques. 2008. Vol. 1: pp. 164 - 165

[21] E. Oller, *Peeling failure in beams strengthened by plate bonding. A design proposal*. PhD thesis. Departament d'Enginyeria de la construcció, Universitat Politècnica de Catalunya. Barcelona. 2005. pp. 334.

[22] E. Oller, D. Cobo and A.R. Mari, *Maximum transferred Force along the interface in an FRP - strengthened beam subjected to transverse loads*. Proceedings of FRPRCS-8, Patras, Greece. Thanasis C. Triantafillou. 2007

[23] J.G. Teng, S.Y. Cao and L. Lam, *Behaviour of GFRP-strengthened RC cantilever slabs.* Construction and Building Materials. 2001. Vol. 15 (7): pp. 339-349.

[24] J.G. Teng, H. Yuan and J.F. Chen, *FRP-to-concrete interfaces between two adjacent cracks: Theoretical model for debonding failure.* International Journal of Solids and Structures. 2006. Vol. 43 (18-19): pp. 5750-5778.

Chapter 4

PLASTIC HINGES AND ROTATION CAPACITY OF EXTERNALLY STRENGTHENED SECTIONS

1 Plastic hinges: Introduction

Considering the non-linear behaviour of statically indeterminate structures and continuous beams in particular, it is necessary to have a good insight in the deformation capacity of the concrete members. For beams, the formation of plastic hinges allows the member to fail gradually, absorb dynamic loads and redistribute moments for unexpected loading scenarios. To illustrate the failing mechanism of a two-sided clamped beam, uniformly loaded and characterized by a similar reinforcement ratio in both the supports and in the span, reference is made to Fig. 4.1. By increasing the uniform load, first two plastic hinges are formed at the clamped supports. By increasing the uniform load, a third plastic hinge occurs at the centre of the span and the two-side clamped beam fails as n+1 plastic hinges are needed to transform an n-times statically indeterminate structure into a mechanism.

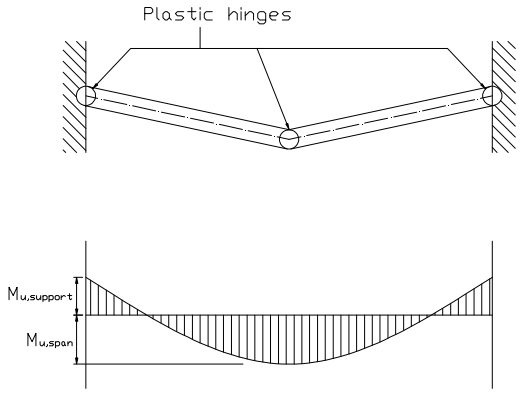

Fig. 4.1: Non-linear behaviour of a statically indeterminate structure

The advantage of the formation of plastic hinges in a statically indeterminate structure is in obtaining a favourable moment redistribution by which an increase of the final load bearing capacity is obtained. A theoretical and experimental investigation on this moment redistribution is given in Chapter 2. However, by assuming a certain moment redistribution in design, a certain rotation capacity at the plastic hinges is required. This design requirement has to be fulfilled in order to obtain a full moment redistribution:

$$\theta_d \leq \theta_{pl} \qquad (4.1)$$

In this equation θ_d equals the acting plastic rotation in the first plastic hinges up to appearance of the last plastic hinge. This rotation can be calculated from the deformation of the adjacent spans. This is illustrated for a two-span beam with a plastic hinge at the mid-support in Fig. 4.2.

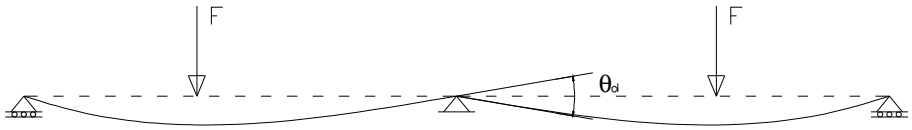

Fig. 4.2: Needed plastic rotation in order to obtain the intended moment redistribution

On the other hand, the rotation capacity θ_{pl} equals the maximum plastic rotation, a plastic hinge can supply. This maximum rotation depends on the geometry and material properties at the location of the hinge. To quantify the plastic rotation capacity θ_{pl}, reference is made to the moment-curvature diagram (see Fig. 4.3). In this figure both a diagram is given of an externally strengthened and an unstrengthened cross-section. The curvatures at yielding for both configurations are quite similar. The ultimate curvatures on the other hand are differing largely, depending if FRP strengthening is applied or not. Herewith, a rather high value of χ_u is observed for the unstrengthened configuration while a rather small value of χ_u is observed for the strengthened configuration, as the ultimate curvature is amongst other aspects related to the moment of debonding of the FRP laminate.

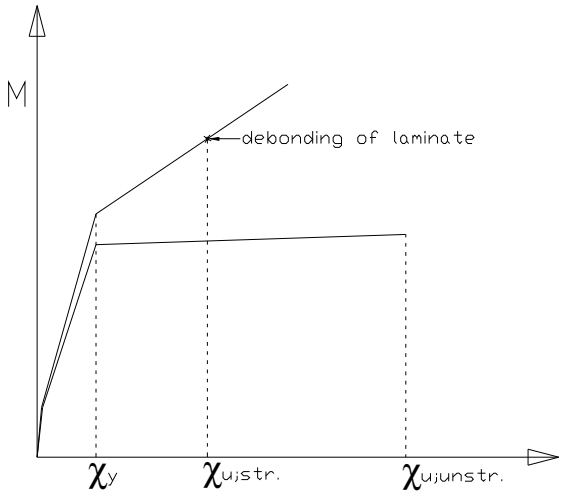

Fig. 4.3: Moment-curvature diagram (M-χ diagram)

Due to the limitation of the ultimate curvature of the strengthened cross-section, also the plastic rotation capacity will be limited. The rotation capacity of a critical cross-section, can be calculated as [1, 2]:

$$\theta_{pl} = \int_{l_{pl}} \left(\chi(x) - \chi_y\right) dx \qquad (4.2)$$

where l_{pl} equals the length of the plastic hinge. This length is the zone where $M_y \leq M \leq M_u$ (see Fig. 4.4). Eq. 4.2 can be rewritten, by introducing the conventional plastic length l_{pl}* shown in Fig. 4.4.

$$\theta_{pl} = \left(\chi_u - \chi_y\right) l_{pl}^* \tag{4.3}$$

By approximation [3], one could conclude that l_{pl}* = 2d, so that:

$$\theta_{pl} = \left(\chi_u - \chi_y\right) 2d \tag{4.4}$$

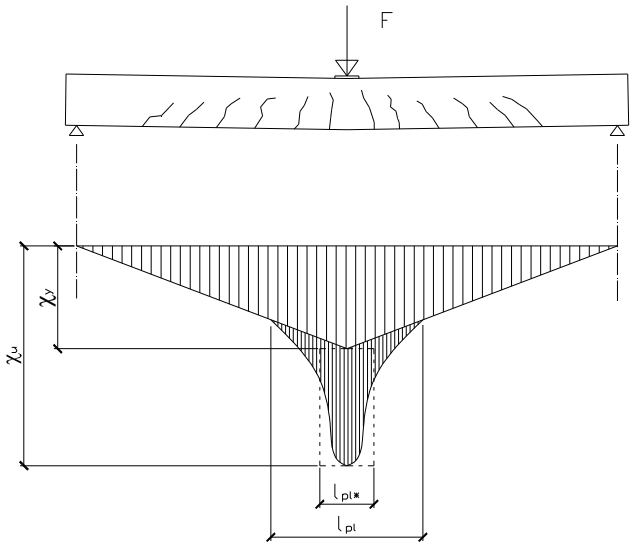

Fig. 4.4: Curvature over the length of the beam

Another noticeable difference between the strengthened and unstrengthened cross-section is the difference between the internal moment at yielding and the ultimate internal moment. The difference between the two internal moments is negligible in the unstrengthened configuration ($M_y \cong M_u$). This is not longer the case for the strengthened configuration ($M_y < M_u$). This relates to the remaining stiffness of the strengthened cross-section after yielding of the internal steel reinforcement (see Fig. 4.3). Or in other words, a small increase of the internal moment does not result in a big increase of the curvature, as can be noticed in the moment-curvature relation after yielding in the unstrengthened configuration. Hence, increase of the post-yield curvature of a strengthened cross-section can only occur in relation to significant increase of the internal moment at that location. The formation of large plastic rotation is restrained. To express this different behaviour, in this work, the term 'plastic hinge' is replaced by 'restrained hinge' in the case of a FRP strengthened post-yielding cross-section.

2 Rotation capacity

2.1 Rotation capacity related to flexure

To start, the rotation capacity is considered in a pure flexural zone, with the absence of both shear and normal forces, for example in the central zone of a four-point-bending test [4]. The maximum obtained rotation capacity in this configuration equals [1, 2]:

$$\theta_{pl} = \int_{l_{pl}} (\chi_u - \chi_y) dx \tag{4.5}$$

where, l_{pl} equals the length of the plastic hinge. For further discussion about this equation, reference is made to section 1.

Referring to a strengthened cross-section with FRP EBR, a restricted rotation capacity is obtained. This restricted rotation capacity is caused by:

- First, the linear elastic behaviour of the used FRP laminates and the limited ultimate strain.
- Secondly, the early debonding phenomena (see Fig. 4.3), by which no full composite action can be taken into account.

2.1.1 Rotation capacity of an unstrengthened cross-section

In the following, an overview is given of the parameters which have an influence on the rotation capacity of an unstrengthened cross-section. As can be noticed in Eq. 4.5, one of the crucial parameters in the plastic rotation capacity is the ultimate curvature χ_u (see Eq. 4.6 and Fig. 4.5). In literature [2-4] this ultimate curvature χ_u often is related to ξ_u ($=x_u/d$) by means of Eq. 4.7.

$$\chi_u = \frac{\varepsilon_{cu} + \varepsilon_{su}}{d} = tg(\beta) = \frac{\varepsilon_{cu}}{x_u} \tag{4.6}$$

$$\chi_u d = \frac{\varepsilon_{cu}}{\xi_u} \tag{4.7}$$

$$\text{with} \quad \xi_u \sim \omega = \rho \frac{f_{yd}}{f_{cd}} \tag{4.8}$$

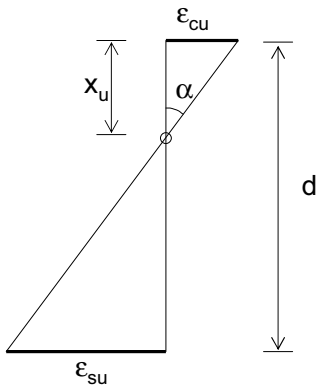

Fig. 4.5: Strain distribution at ultimate

As ξ_u is proportional to the mechanical reinforcement ratio ω (see Eq. 4.8), the following conclusions can be made concerning the different parameters influencing the plastic rotation capacity (see also Table 4.1):

- An increasing geometric reinforcement ratio ρ results in a decreasing rotation capacity.
- Increasing the yielding strength of the internal steel reinforcement also results in a decrease of the rotation capacity (see Eq. 4.5 - 4.8).
- Increasing the compressive strength of the concrete results in a positive influence on the rotation capacity. This influence is only limited, as the ultimate strain ε_{cu} tends to decrease with an increasing compressive strength f_c.
- A next possibility to increase the plastic rotation capacity is increasing the amount of compressive reinforcement A_{s2}, as can be noticed from Eq. 4.9. Notice that only a limited effect is obtained.

$$\xi_u \sim \Delta\omega = \frac{(A_{s1} - A_{s2})}{bd}\frac{f_{yd}}{f_{cd}} \tag{4.9}$$

- Increasing the effective depth d of the concrete member results in a slight increase of the plastic rotation capacity.

Table 4.1: Influence of different parameters on the rotation capacity of an unstrengthened cross-section

Increasing of:			Influence on θ_{pl}
A_{s1}	↗	(tensile reinforcement)	↙
f_y	↗		↙
f_c	↗		↗ (limited)
A_{s2}	↗	(compression reinforcement)	↗ (limited)
d	↗		↗ (limited)

2.1.2 Rotation capacity of a strengthened cross-section

Referring to strengthened concrete beams, some of the previous derivations have to be revised. Due to the typical failure aspect of a strengthened concrete structure, characterized by the debonding of the externally bonded laminates, the

ultimate strain in the concrete ε_{cu} may not be reached. Hence, it is incorrect to relate the ultimate curvature χ_u to the ultimate strain ε_{cu} as given in Eq. 4.6.

In order to verify the influence of the different parameters on the rotation capacity θ_{pl}, a parametric study is executed. The results in terms of M-χ diagrams are shown in Fig. 4.6 till Fig. 4.11. Each figure shows the influence of a parameter, whereas the cross-section of beam IB2 in Chapter 3 (section 5.3) is taken as a basis and each time one parameter is altered. The basic characteristics of the IB2 cross-section are as follows. The width (b) equals 198 mm and the height equals 400 mm (h), the cross-section of the FRP laminate equals 100 mm (w_f) x 1.0 mm (t_f), corresponding to a strengthening ratio (ρ_f) of 0.13 % and the reinforcement ratio (ρ_s) equals 0.64 %. The material properties can be found in Table 4.2.

Table 4.2: Material properties in parametric study

		Concrete	Steel	FRP
modulus of elasticity	[N/mm²]	32000	210000	180000
compression strength	[N/mm²]	35		-
yielding stress	[N/mm²]	-	500	-
tensile strength	[N/mm²]	3.2	550	2981
failure strain	[%]	0.35	10.00	1.65

Concerning the M-χ diagrams of the strengthened cross-sections (found in Fig. 4.7 - Fig. 4.11), initially a full-composite-action is assumed. The end of this assumed full-composite-action M-χ diagram is characterized by a symbol (small cross).

In addition, a white dot is found on every curve, which represents a strain in the FRP equal to 0.40 %. For simplicity, it is assumed that debonding occurs at 0.40 %, which is verified on two span strengthened beams (see Table 2.20 in Chapter 2) and can be compared with other experimentally obtained or recommended strains at debonding (see Table 4.3). The curvature related to this situation (ε_f = 0.40 %) is assumed as the ultimate curvature χ_u, at which the plastic rotation capacity is determined (see Eq. 4.5).

Table 4.3: FRP debonding resistances

Source	$\varepsilon_{debonding}$
Chen and Teng	0.53 %
Neubauer and Rostasy	0.26 % *
Concrete Society	0.60 – 0.80 %
German Inst. Of structure	0.65 – 0.85 %
Oehlers and Seracino	0.25 – 0.52 %

* This value represents the 0.95 % characteristic value of $\varepsilon_{debonding}$

In every graph, two curves are noticed. One curve is representing the original cross-section, the other curve is representing a similar cross-section with the investigated parameter having been increased by 25 % compared to the original value. Resulting from the parametric study the following conclusions can be drawn (see also Table 4.4):

- An increase of the reinforcement section, considering an increase of A_{s1} and/or A_f, results in a slight increase of the plastic rotation capacity θ_{pl} (see Fig. 4.6 and Fig. 4.7).

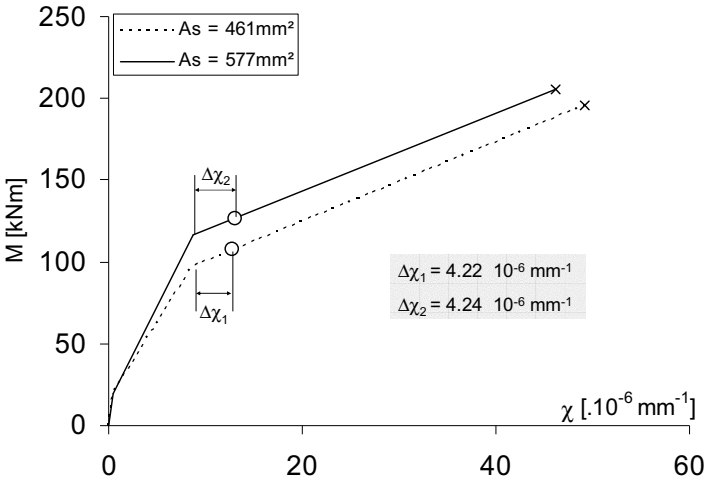

Fig. 4.6: Influence of the internal reinforcement section A_s (increase of 25 %) on the curvature

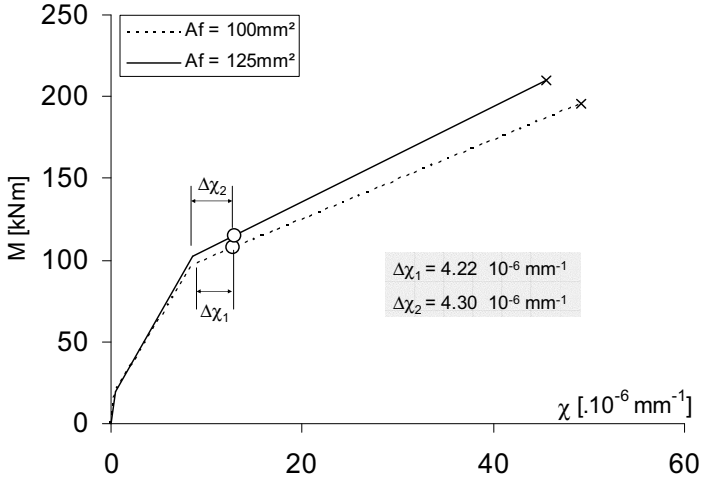

Fig. 4.7: Influence of the external reinforcement section A_f (increase of 25 %) on the curvature

- Secondly an increase of the yield stress f_y of the internal reinforcement, results in a considerable decrease of the rotation capacity θ_{pl} (see Fig. 4.8). The decrease of the plastic rotation capacity is caused, for the greatest part by the increase of the curvature at yielding χ_y corresponding to the increased yield stress f_y.

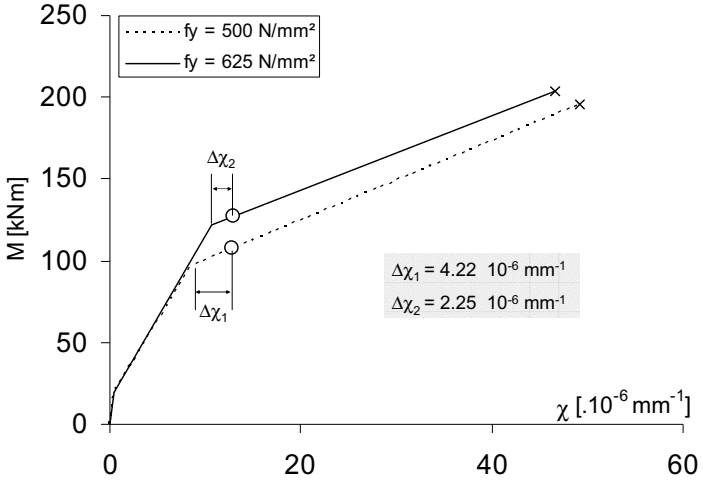

Fig. 4.8: Influence of the steel yield stress f_y (increase of 25 %) on the curvature

- Thirdly the influence of the compressive strength of the concrete is investigated. An increase of this compressive strength results in a very slight decrease of the rotation capacity θ_{pl} (see Fig. 4.9).

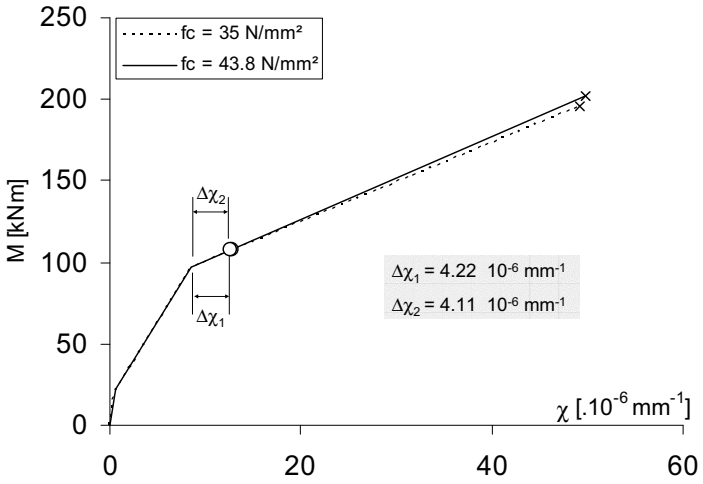

Fig. 4.9: Influence of the concrete compressive strength f_c (increase of 25 %) on the curvature

- Increasing the amount of compression steel reinforcement results in only a small decrease of the plastic rotation capacity θ_{pl} (see Fig. 4.10).

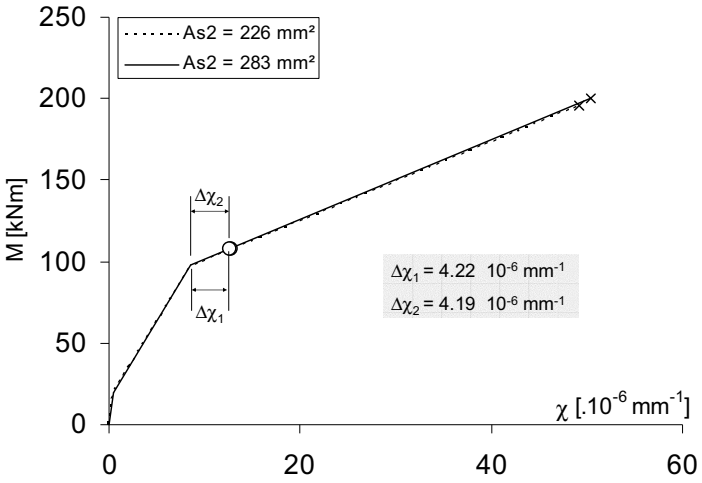

Fig. 4.10: Influence of the internal reinforcement section A_{s2} (increase of 25 %) on the curvature

- Finally, by increasing the effective depth d, a negative influence on the plastic rotation capacity θ_{pl} is obtained (see Fig. 4.11).

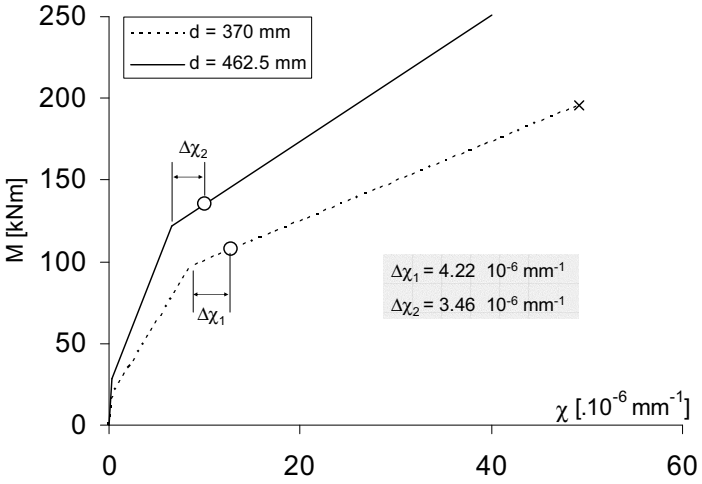

Fig. 4.11: Influence of the effective depth d (increase of 25 %) on the curvature

In Table 4.4, an overview is given concerning each parameter separately.

Table 4.4: Influence of different parameters on the rotation capacity of a strengthened cross-section

Increasing of:		Influence on θ_{pl}
A_{s1} ↗	(tensile reinforcement - steel)	↗ (limited)
A_f ↗	(tensile reinforcement - FRP)	↗ (limited)
f_y ↗		↙
f_c ↗		↙ (limited)
A_{s2} ↗	(compression reinforcement)	↙ (limited)
d ↗		↙

2.2 Rotation capacity related to flexure and shear

The influence of inclined cracks on the forces in the tensile reinforcement can be modelled by a horizontal translation of the bending moment line away from the plastic hinge. Hence, a positive influence on the plastic rotation capacity is obtained, as the plastic hinge is appearing over a longer distance. This is illustrated schematically in Fig. 4.12 for a mid-support of a continuous beam. A distinction is made between the internal moment contribution and the shear force contribution to the rotation capacity.

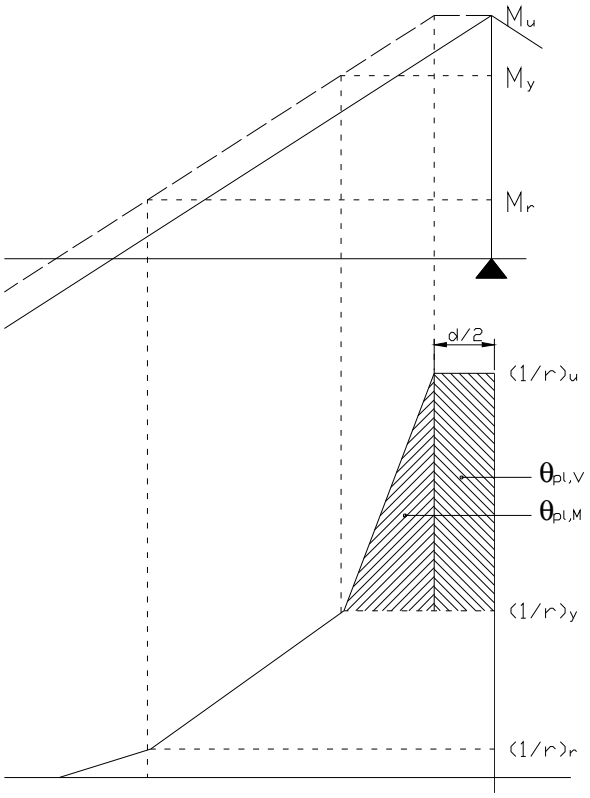

Fig. 4.12: Influence of shear forces on θ_{pl}

Nevertheless a considerable decrease of the rotation capacity may be obtained, as the concrete needs also to contribute in taking up shear forces [2, 5]. In [2], an empirical expression is obtained for the rotation capacity related to flexure and shear in function of the parameter r (see Eq. 4.10). For an increasing value of r an increasing part of the shear force is taken by the concrete.

$$r = \frac{V_d - V_{wd}}{V_c} \qquad (4.10)$$

herewith: V_d = design value of the real acting shear force at the plastic hinge
V_{wd} = shear force taken by the stirrups
V_c = 0.5 f_{ct} b d

Based on an empirical study [2], the rotation capacity is expressed as a function of the rotation capacity calculated in a pure flexural zone (Eq. 4.5) and of the introduced parameter r (Eq. 4.10). A distinction is made between three different zones, i.e. $r < 0$; $0 \le r < 0{,}5$ and $0{,}5 \le r$. In Fig. 4.13 a schematic overview is given of the finally obtained rotation capacity in function of the parameter r.

$$\theta_{pl} = \theta_{pl;max} \qquad \text{with } r < 0 \tag{4.11}$$

$$\theta_{pl} = (1 - 2r)\ \theta_{pl;max} \qquad \text{with } 0 \le r < 0.5 \tag{4.12}$$

$$\theta_{pl} = 0 \qquad \text{with } 0.5 \le r \tag{4.13}$$

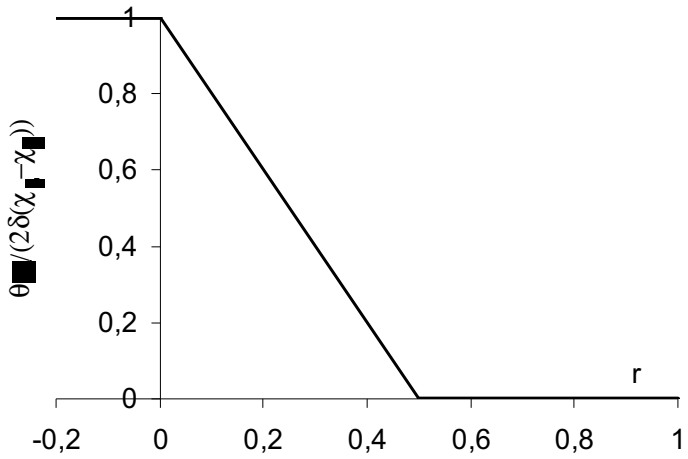

Fig. 4.13: (Relative) rotation capacity as function of the parameter r

As can be deduced from Fig. 4.13, the maximum rotation capacity ($\theta_{pl,max}$) is found if r is negative. Theoretically, this situation is found if the acting shear force V_d is taken completely by the stirrups ($V_d = V_{wd}$). The influence of the shear force on the rotation capacity is given by means of a linear relation (Eq. 4.12). However, once the parameter r is larger than 0.5, no plastic rotation capacity is left.

2.3 Experimentally obtained rotation capacity

In Fig. 4.14, Fig. 4.16, Fig. 4.18 and Fig. 4.20, both the experimental and analytically obtained curvatures are given of the tested isostatic beams and of the mid-supports of the tested 2-span beams. The material properties and the 3-point-bending test set-up for the isostatic beams are given in section 5.3 of Chapter 3, the material properties and the 2-span test set-up of the continuous beams are given in section 3 of Chapter 2. In Table 4.5, an overview is given of the strengthening and internal reinforcement ratios used in these critical cross-sections.

For the isostatic beams, two specific reinforcement configurations are used, considered in addition to IB1 till IB3:

- In IB4, a stirrup spacing of 75 mm instead of 150 mm is used.
- In IB5, the central zone of the beam, inclusive the externally bonded laminate, is wrapped by means of an externally applied carbon textile (see Fig. 4.19).

Both these configurations are tested to investigate their influence on the plastic rotation capacity.

In Table 4.5, the experimentally obtained plastic rotation capacities ($\theta_{pl,exp}$) of both the continuous beams (see Chapter 2) and the isostatic beams (see Chapter 3) are given. $\theta_{pl,exp}$ is derived as follows. The strains in the critical cross-section are measured by means of 4 strain stirrups (each with measurement base = 200 mm). Two of them are measuring the strain of the concrete and are placed as close as possible to the fibre with the maximum compressive strain. The other two strain stirrups are applied on the side of the beam at the height of the internal steel reinforcement. The latter register the concrete strain at the level of the internal steel reinforcement. The mean values of the measured strains are applied to calculate the curvature at yielding and at failure. By introducing the latter two into Eq. 4.4, the values of Table 4.5 are obtained.

It is noticed that the plastic rotation capacity of the unstrengthened beam (IB ref.) is much higher than the ones of the strengthened beams. Hereby, the plastic rotation capacity of the wrapped strengthened beam (IB5) is considerably higher compared to the other strengthened beams. A more detailed analysis of the results is given further, based on the moment-curvature graphs given in Fig. 4.14, Fig. 4.16, Fig. 4.18 and Fig. 4.20.

Table 4.5: Experimentally obtained plastic rotation capacity of isostatic and continuous beams

		ρ_s [%]	ρ_f [%]	$\theta_{pl,exp}$ [rad]	$\theta_{pl,exp}$ [°]
Fig. 4.14	IB ref.	0.64	0.00	0.0425	2.44
Fig. 4.16	IB1	0.31	0.13	0.0075	0.43
	CB2	0.31	0.13	0.0091	0.52
	CB4	0.31	0.13	0.0033	0.19
Fig. 4.18	IB2	0.64	0.13	0.0057	0.33
	IB4 *	0.64	0.13	0.0115	0.66
	IB5 **	0.64	0.13	0.0288	1.65
	CB3	0.67	0.13	0.0053	0.30
Fig. 4.20	IB3	1.43	0.13	0.0112	0.64

* the spacing of the stirrups in IB4 is half of the spacing applied in the other isostatic beams

** the central zone of IB5 is completely wrapped with one layer of carbon textile

In Fig. 4.14 both the experimental and analytical curvatures are given of an unstrengthened isostatic beam with reinforcement ratio (ρ_s) equal to 0.64 %. Analysing both curves, generally a good agreement is noticed between the experimental and analytical data. Nevertheless, a difference is noticed between the ultimate curvatures $\chi_{u,exp.}$ (= 6.92 10^{-5} 1/mm) and $\chi_{u,anal.}$ (= 8.51 10^{-5} 1/mm). This difference may be explained by a measurement problem. Due to the large deformations of the plastic hinge, the measurement equipment was not able any more to register the deformations. Nevertheless, by linear extrapolation of the measured curvatures, it can be concluded that the experimentally obtained ultimate curvature is similar to the analytically obtained ultimate curvature.

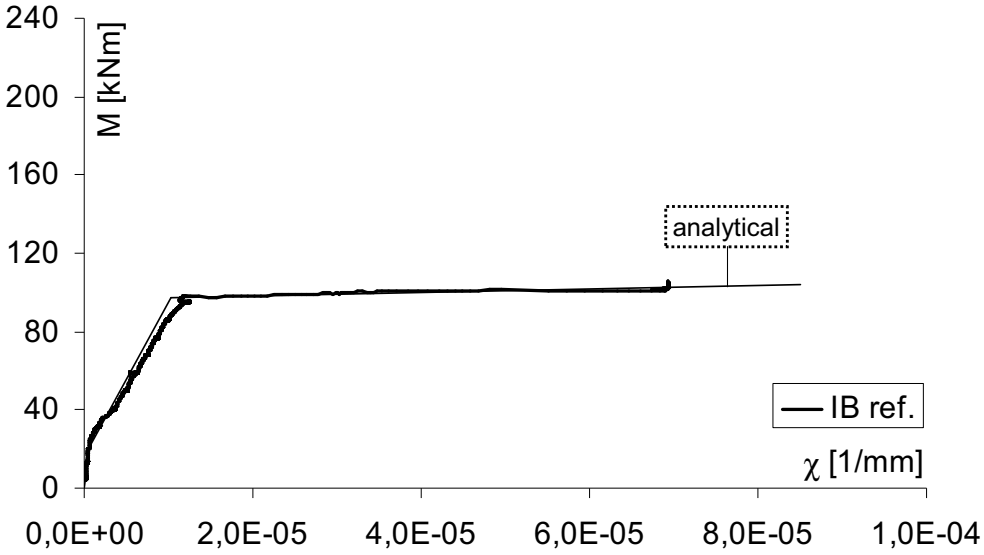

Fig. 4.14: Curvature of unstrengthened isostatic beam (ρ_s = 0.64 %)

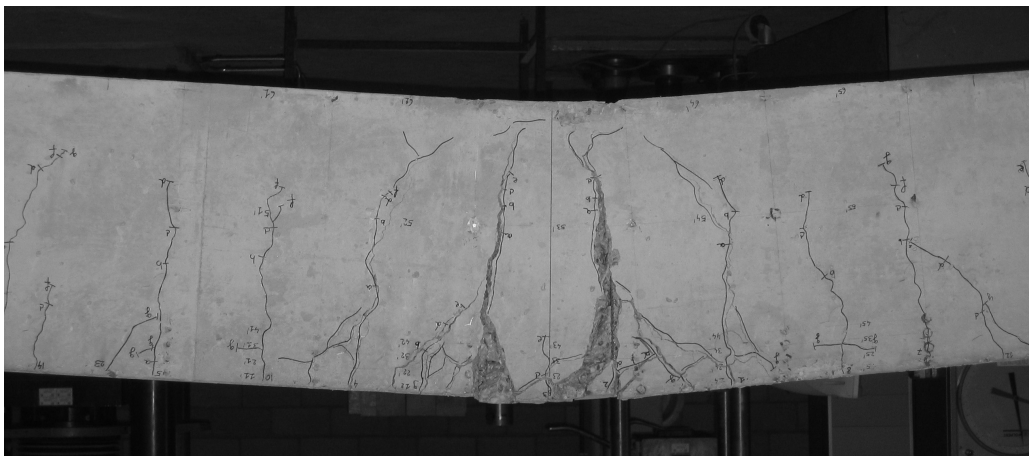

Fig. 4.15: Plastic hinge zone after failure (IB ref.)

In Fig. 4.16, both the analytical and experimental curvatures are shown for different cross-sections with an internal reinforcement ratio (ρ_s) equal to 0.31 % and an external strengthening ratio (ρ_f) equal to 0.13 %. Again a good agreement is noticed between the analytical and experimental data until debonding of the laminate. Nevertheless, the obtained ultimate curvature is considerably lower than the analytically derived ultimate curvature (assuming full composite action), which is due to debonding of the FRP laminate. Compared to the reference beam IB ref. a rotation capacity is obtained which is about 20% of the rotation capacity of the unstrengthened beam.

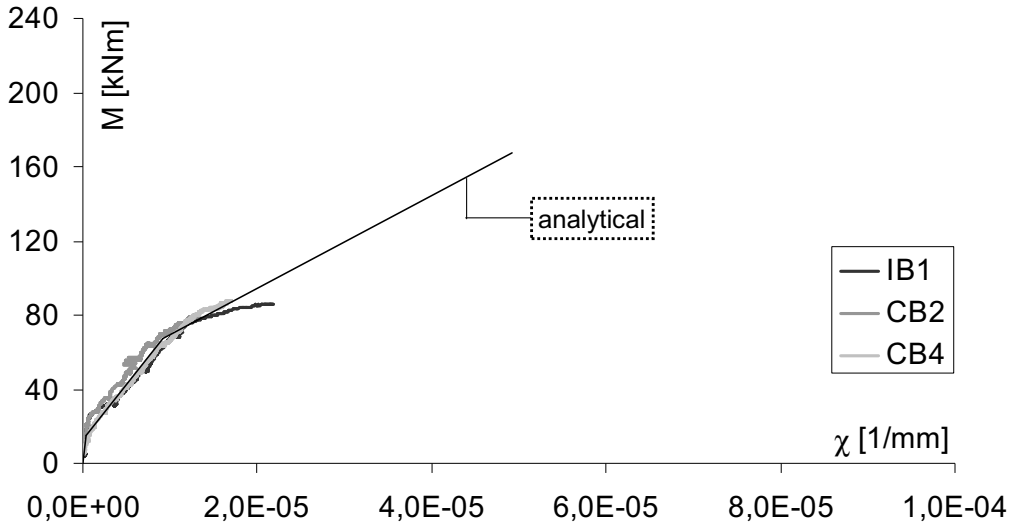

Fig. 4.16: Curvature of strengthened isostatic beam (ρ_s = 0.31 %) and the mid-support of two continuous beams (ρ_s = 0.31 %)

Fig. 4.17: Debonding of the top laminate at the mid-support of CB4 which induces a limited rotation capacity

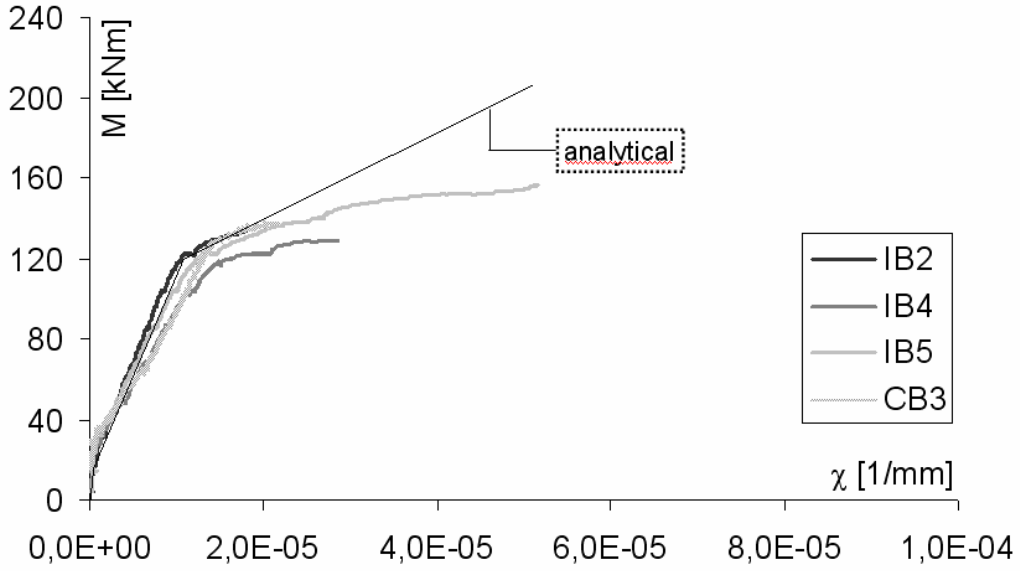

Fig. 4.18: Curvature of strengthened isostatic beams (ρ_s = 0.64 %) and the mid-support of the continuous beam CB2 (ρ_s = 0.66 %)

In Fig. 4.18, both the analytical and experimental rotation capacity is given of different cross-sections with an internal reinforcement ratio (ρ_s) equal to 0.64 % for the isostatic beams (IB2, IB4 and IB5) and ρ_s equal to 0.67 % for the continuous beam (CB3). The external strengthening ratio (ρ_f) is equal to 0.13 % in all cases. Further, as mentioned above, additional stirrups are placed in IB4 and a wrapping with carbon textile is applied to IB5 (see Fig. 4.19).

Focussing on IB4 (see Table 4.5 and Fig. 4.18) an increase of the rotation capacity is observed compared to IB2 and CB3. Indeed $\theta_{pl,IB4}$ equals 0.66° while $\theta_{pl,IB2}$ equals 0.33° and $\theta_{pl,CB3}$ equals 0.30°, which is about a doubling of the capacity. Due to the additional stirrups, it is possible that a larger amount of the shear force is taken by the stirrups which results in a smaller value of the r-factor and consequently in a larger rotation capacity. However, looking to Table 4.6, the r-factors of IB2, IB4 and CB3 all are negative, which means, referring to Fig. 4.13, that there is no influence on the expected plastic rotation capacity. Neither a higher ultimate moment nor later debonding of the laminate is observed (see Table 4.6) which may have a beneficial effect on the rotation capacity. Hence, it may be concluded that the higher number of stirrups has a positive effect on the plastic rotation capacity, due to the confining effect of the additional stirrups.

For IB5, an even higher increase of the rotation capacity is observed. Due to the wrapping of the cross-section with carbon textile (see Fig. 4.19), again an increasing shear force may be taken by the (internal and external) stirrups, and as a consequence the r-factor is decreasing (see Table 4.6). As the r-factor of the unwrapped cross-section is already negative, the additional effect of the carbon textile on the shear resistance would not be beneficial for the rotation capacity. Nevertheless, similar to IB4 a positive effect can be expected due to the confining action on the concrete. Besides, due to the wrapping of the beam, also the externally bonded FRP laminate is wrapped, which delays the debonding of the laminate to a considerable extent. Hence a higher ultimate moment is obtained (see Table 4.6) and moreover the third branch of the experimental moment-

curvature graph is continued, which is of importance for the rotation capacity. As can be noticed from Fig. 4.18, the experimental ultimate curvature $\chi_{u,exp.}$ (= 5.16 10^{-5} 1/mm) is similar to the analytical ultimate curvature $\chi_{u,anal.}$ (= 5.09 10^{-5} 1/mm). This positive effect of wrapping is also discussed in the literature [6].

On the other hand it has to be noticed that the ultimate moment, assuming full composite action, is not reached. It appears that the cross-section loses a certain degree of stiffness after yielding of the internal reinforcement. This raises the idea that the laminate shows a certain degree of local debonding under the carbon textile.

Table 4.6: Parameter r of considered beams

	M_u [kNm]	V_d [kN]	V_{wd} [kN]	V_c [kN]	$r = (V_d-V_{wd})/V_c$ [-]
IB2	135.3	75.2	110.1	98.3	-0.355
IB4	132.8	73.8	220.2	102.6	-1.427
IB5	160.6	89.2	186.0	108.4	-0.893
CB3	137.9	105.6	110.1	101.5	-0.045

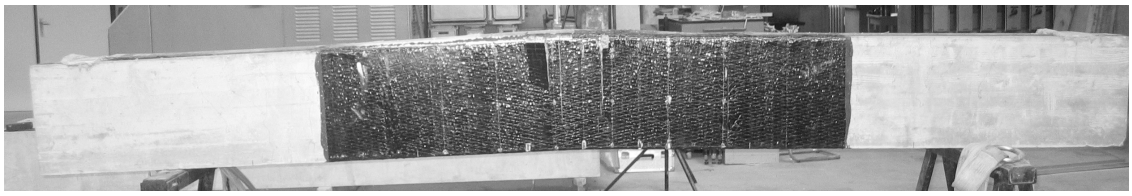

Fig. 4.19: Wrapping of IB5 by carbon textile

Finally the curvature of IB3, isostatic beam with a high internal reinforcement ratio (ρ_s = 1.43) is investigated in Fig. 4.20. A fairly good agreement is noticed between the analytical and experimental curvatures. Similar to the other tested strengthened beams, a low plastic rotation capacity is obtained compared to the unstrengthened beam (IB ref.). Again, the early debonding of the laminate is the main reason of the restriction of the rotation capacity

By these tests, the conclusion mentioned in section 2.1 for externally strengthened beams, of an increasing rotation capacity resulting from an increasing internal reinforcement section is confirmed (see Table 4.7). In this table, the beams IB4 and IB5 are not taken into account, due to the deviating stirrup section. Remark that for the internal reinforcement ratio of 0.31 % a rather high rotation capacity is obtained which is due to the later experimental debonding load of the laminate.

Table 4.7: Mean plastic rotation capacity from tests

ρ_s [%]	ρ_f [%]	$\theta_{pl,mean}$ [°]
0.31	0.13	0.38
0.64	0.13	0.32
1.43	0.13	0.64

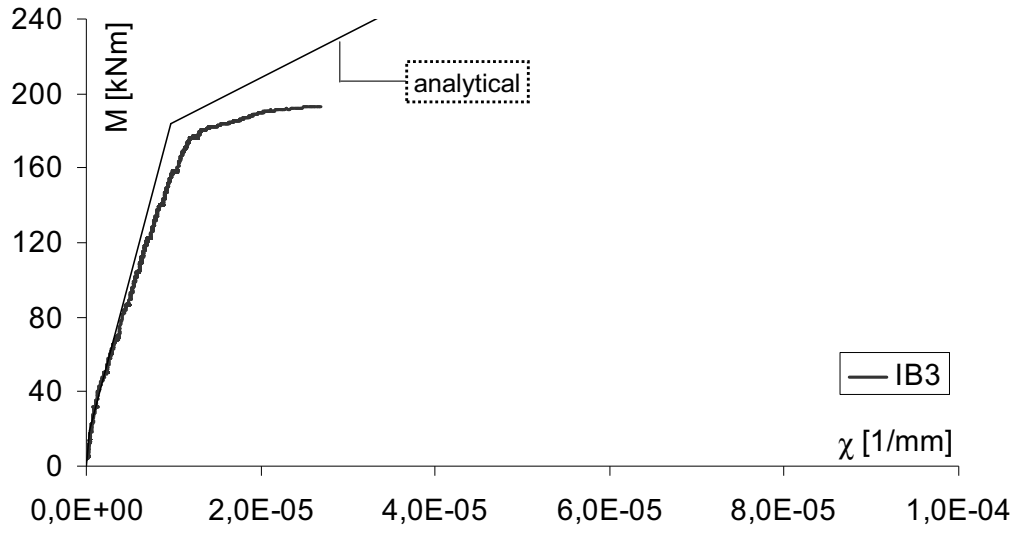

Fig. 4.20: Curvature of strengthened isostatic beam (ρ_s = 1.43 %)

3 Control of plastic rotation

3.1 Control of plastic rotation in unstrengthened hinges

In an unstrengthened concrete member, for which a certain degree of moment redistribution is introduced, a check of the plastic rotation capacity has to be fulfilled based on the following equation:

$$\theta_d \leq \theta_{pl} \tag{4.14}$$

Depending on the used analysis method, one of the following design procedures can be used.

3.1.1 Linear elastic methods of structural analysis with limited redistribution

By using the linear elastic methods of structural analysis with limited redistribution, explicit control of the plastic rotation according to Eq. 4.14 is not needed if the following ductility conditions are fulfilled [7]:

a) based on concrete strength:

$$\delta \geq k_1 + k_2 \xi_u \qquad \text{for } f_{ck} \leq 50 \text{ MPa} \tag{4.15}$$

$$\delta \geq k_3 + k_4 \xi_u \qquad \text{for } f_{ck} > 50 \text{ MPa} \tag{4.16}$$

with $\xi_u = x_u/d$: the neutral axis depth in ULS over the effective depth of the beam. The recommended value for k_1 is 0.44, for k_2 is $1.25(0.6+0.0014/\varepsilon_{cu2})$, for k_3 is 0.54 and for k_4 is $1.25(0.6+0.0014/\varepsilon_{cu2})$ [7].

b) based on ductility of steel:

$$\delta \geq 0.7 \qquad \text{where Class B and Class C reinforcement is used} \tag{4.17}$$

$$\delta \geq 0.8 \qquad \text{where Class A reinforcement is used} \tag{4.18}$$

The ductility of the different classes of steel reinforcement are characterized by the factors ε_{uk} and $(f_u/f_y)_k$ (see Table 4.8) [7], based on characteristic values (subscript k).

Table 4.8: Classification of different steel classes

Class	A	B	C
Minimum value of $k = (f_u/f_y)_k$	≥1.05	≥1.08	≥1.15 <1.35
Characteristic strain at maximum force, ε_{uk} (%)	≥2.5	≥5.0	≥7.5

These ductility conditions are shown in Fig. 4.21 and are fulfilled for the grey area. As can be noted in this figure and from Eq. 4.15 - 4.16 the control of the rotation capacity is related to a limitation of the ξ_u value, which is the ratio of the neutral axis depth to the effective depth of the beam ($\xi_u = x_u/d$). It is related to the ultimate curvature by means of Eq. 4.19.

$$\chi_u d = \frac{\varepsilon_{cu}}{\xi_u} \tag{4.19}$$

In this equation it is assumed that concrete crushing (ε_{cu}) occurs at failure.

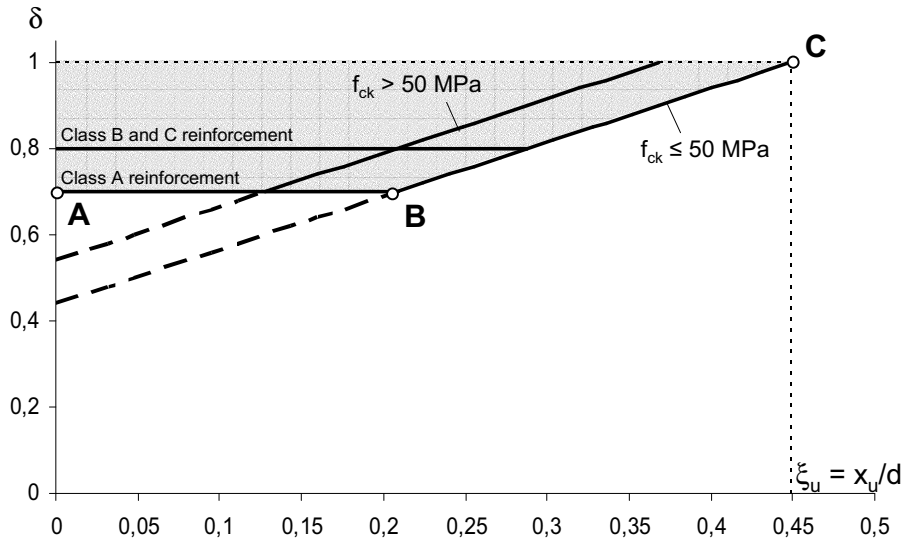

Fig. 4.21: Limitation of ξ_u factor in order to obtain a sufficient rotation capacity

In Fig. 4.21, the restriction of the ξ_u-value is given by different linear relations, as for example the relation A-B and the relation B-C for Class A steel reinforcement and a concrete class with $f_{ck} \leq 50$ MPa. Herewith point C represents the classical 'balanced strain condition' where concrete crushes at the same time as the internal steel reinforcement yields. In reality this 'balanced strain condition' is found at $\xi_u \approx 0.6$ [3, 8], but due to safety considerations a shift is introduced in this European approach. Further the horizontal plateau A-B is a limit that is governed by the steel quality.

3.1.2 Non-linear methods of structural analysis

In case the non-linear analysis approach is used as presented in Chapter 2, (taking into account both the bending stiffnesses K_0, K_1 and K_2 and the critical internal moments M_{cr}, M_y and M_u of all critical cross-sections), no explicit check of the rotation capacity at he plastic hinges is needed. Because the entire moment-curvature diagram of all critical cross-sections is taken into account in order to obtain the moment redistribution, the exact ultimate load is obtained when the structure fails by concrete crushing or steel rupture at one of the plastic hinges.

In other cases the non-linear approach is used, just by taking into account the bending stiffnesses K_0 and K_1 and the critical internal moments M_{cr} and M_y (under the assumption that $K_2 = 0$ and $M_y = M_u$). By this assumption, a constant internal moment is applicable for the plastic hinges. This means that sufficient plastic rotation capacity of the plastic hinges needs to be available, by which the condition given by Eq. 4.14 has to be checked explicitly for all critical cross-sections where a plastic rotation is expected.

In this case, the value of θ_d needs to be determined on the basis of the design values for actions and materials. For this, the model in order to calculate the discontinuity of rotations given in [9] can be applied. The value of θ_{pl} is derived from Fig. 4.22 [7]. The increasing branch of these curves corresponds to failure of the internal reinforcement. Similar to the 'balanced strain condition' limitation mentioned in section 3.1.1, ξ_u shall not exceed the value 0.45. In the graph, a distinction is made between two different types of steel reinforcement, classes B and C, based on the ductility (see Table 4.8). The use of Class A steel is not recommended for plastic analysis.

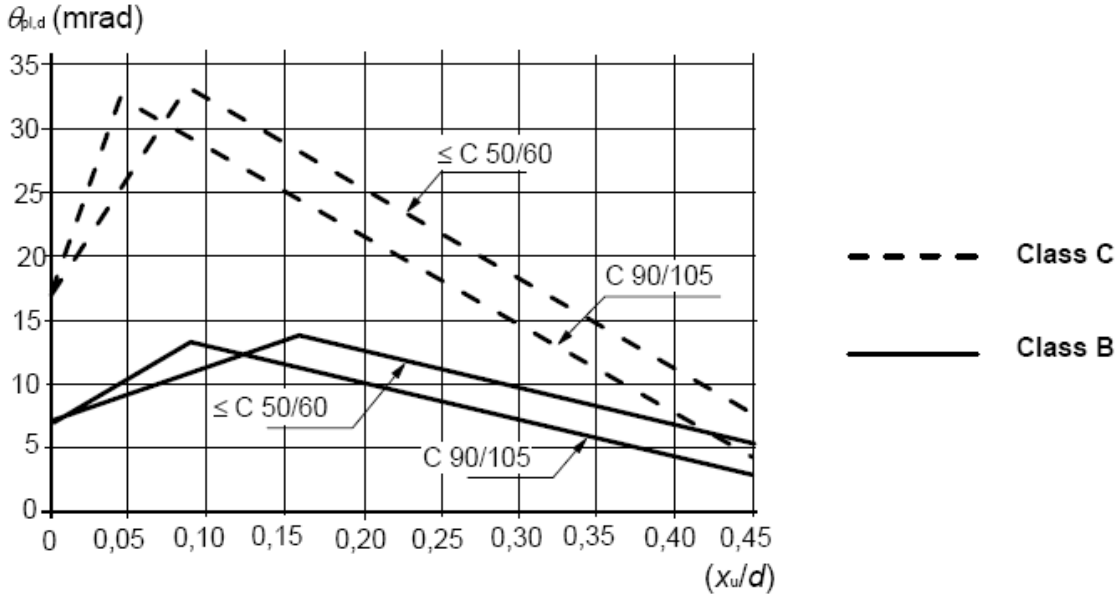

Fig. 4.22: Basic value of allowable rotation, $\theta_{pl,d}$ of reinforced concrete sections for Class B and C reinforcement [7]

3.1.3 Plastic methods of structural analysis

By using the plastic method of structural analysis, a sufficient rotation capacity in the plastic hinges is required. The required ductility is deemed to be satisfied without explicit verification if all the following are fulfilled [7]:

- the area of tensile reinforcement is limited such that, at any section
  $\xi_u = x_u/d \leq 0.25$ for concrete strength classes ≤ C50/60
  $\xi_u = x_u/d \leq 0.15$ for concrete strength classes ≥ C55/67
- reinforcing steel is either Class B or C
- the ratio of the moments at intermediate supports to the moments in the span should be between 0.5 and 2.

3.2 Control of plastic rotation in unstrengthened hinges in a FRP strengthened structure

In strengthened statically indeterminate structures, moment redistribution basically relates to plastic hinge formation in unstrengthened cross-sections (see also Chapter 6). As the plastic hinges in this case are not strengthened with FRP EBR, the needed plastic rotation can be checked by means of the approaches mentioned in section 3.1.

Besides it is noticed that in a FRP EBR strengthened structure a lower plastic rotation is needed compared to a steel EBR strengthened configuration. To explain this into detail, two different cases are considered resulting from the study in Chapter 6:

- case A: a two-span beam with internal reinforcement ratios following the linear elastic theory. In order to increase the load bearing capacity, the spans are strengthened with FRP EBR. The mid-support on the other hand is not needed to be strengthened as a moment reduction of 30 % at the mid-support is introduced (Fig. 4.23 and Fig. 4.26 left side)
- case B: a two-span beam with equal internal reinforcement ratios as in case A. In order to increase the load bearing capacity, the spans are strengthened with steel EBR. The mid-support on the other hand is not needed to be strengthened as a moment reduction of 30 % at the mid-support is introduced (Fig. 4.24 and Fig. 4.26 right side).

After yielding of both the spans and the mid-support in case A, the span zone retains a considerably higher stiffness compared to the mid-support. As a result the internal moments in the spans are increasing strongly and the internal moment at the mid-support is increasing slowly (see Fig. 4.23 and Fig. 4.25).

In case B, on the other hand, after yielding of both the spans and the mid-support, both these zones show a similar stiffness. As a result, both the internal moments at the mid-support and the spans are increasing in an equal way (see Fig. 4.24 and Fig. 4.25).

In Fig. 4.25, a detail is given of the difference of the increasing internal moments at the mid-support. Due to the slower increase of the internal moment at the mid-support in case A, a considerably smaller curvature is needed in order to obtain a similar moment redistribution (see Table 4.9 and Fig. 4.26). On the other hand, a similar plastic rotation capacity at the mid-support is available. This results in a more favourable situation for the FRP EBR configuration compared to the steel EBR configuration.

Table 4.9: Needed curvature according Fig. 4.26 related to a redistribution of 30 % in case A and case B

	Redistribution	Curvature	ratio
Case A – FRP EBR	30 %	$69.6 \cdot 10^{-6}$ 1/mm	64 %
Case B – Steel EBR	30 %	$108.6 \cdot 10^{-6}$ 1/mm	100 %

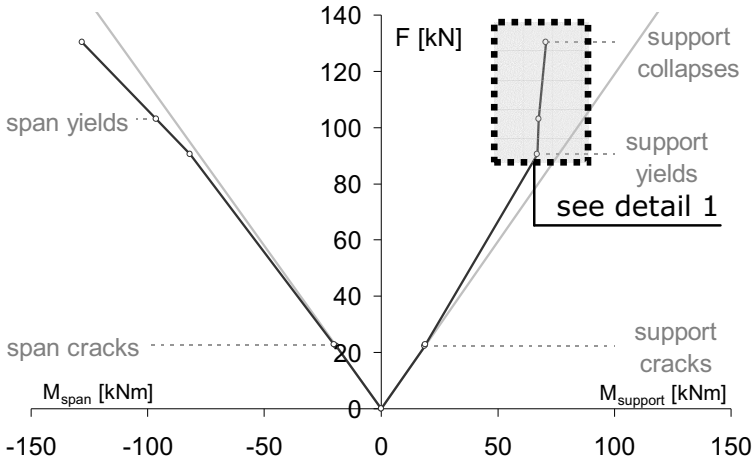

Fig. 4.23: case A – moment redistribution of 30 % at the mid-support and strengthening of the spans with FRP EBR

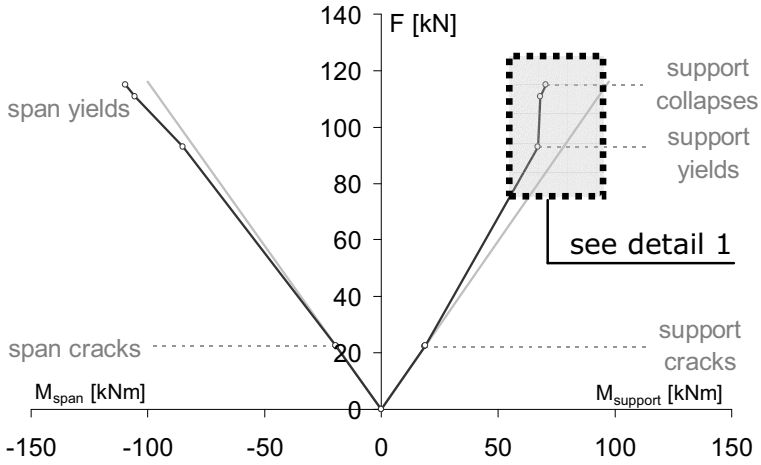

Fig. 4.24: case B – moment redistribution of 30 % at the mid-support and strengthening of the spans with steel EBR

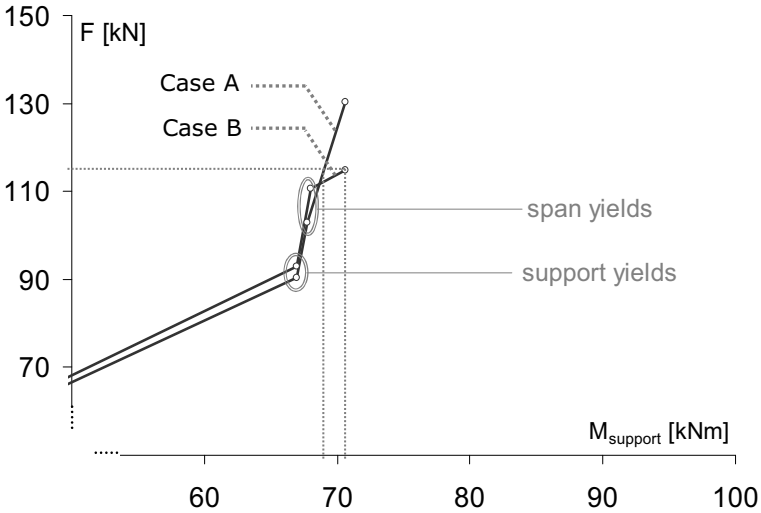

Fig. 4.25: Detail 1 of Fig. 4.23 and Fig. 4.24

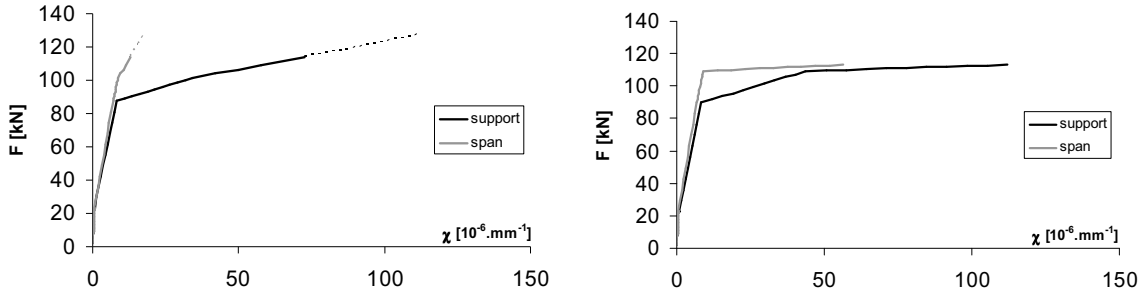

Fig. 4.26: Curvature at 30 % of redistribution (left fig. – FRP – case A; right fig. – steel reinf. – case B)

3.3 Control of plastic rotation in strengthened hinges in a FRP strengthened structure

Current design rules give ductility conditions (e.g. the neutral axis depth approach) to implicitly verify $\theta_d \leq \theta_{pl}$. These are based on the assumption that failure always occurs by concrete crushing, which is often not the case in externally strengthened concrete members. Hence these approaches should not be used for members where concrete crushing does not occur. This results in the explicit need to check the plastic rotation of all critical strengthened cross-sections by means of Eq. 4.14. In order to apply Eq. 4.14, an estimation of the plastic rotation capacity has to be made. In literature two analytical models about the rotation capacity of externally strengthened cross-sections have been found [8, 10].

Nevertheless, by referring to Chapter 6, it is demonstrated that strengthening the first plastic hinges assumed in design, a linear elastic FRP-material is not advisable. In the latter case (see also case 3 in section 3.2.5 of Chapter 6) the plastic rotation capacity is insufficient to achieve the required moment redistribution. Based on these conclusions, it is proposed to perform a non-linear analysis in order to obtain a realistic analysis of these structures. As demonstrated in Chapter 6, different strengthening strategies are applicable. In most cases, no moment redistribution is related to the FRP strengthened section, in which case no control of plastic rotation in strengthened sections is needed.

4 Conclusions

The plastic rotation capacity is dependent on several parameters, among which the reinforcement ratio, the tensile strength of the internal steel reinforcement, the compressive strength of the concrete and the effective depth. Depending on the considered configuration, the parameters are resulting in a higher or lower rotation capacity.

Regarding to an unstrengthened cross-section, a large plastic rotation capacity is obtained due to the yielding capacity of the internal steel reinforcement. This rotation capacity results from the large horizontal third branch in the M-χ diagram. Regarding to a FRP-strengthened cross-section, the rotation capacity of the cross-section is considerably decreased due to the use of the linear elastic FRP-material. Besides, failure of a FRP-strengthened cross-section is characterized by debonding of the externally bonded laminates, which reduces also the plastic rotation capacity to an important degree. As evidence by the experimental results, this early debonding of the FRP laminate can be delayed by wrapping the cross-section with carbon textile. Herewith a higher ultimate moment is obtained and the third branch of the experimental moment-curvature graph is continued, which is of importance for the rotation capacity.

Given the restrained rotation at post-yielding FRP-strengthened cross-section and the related impact on the moment redistribution as explained in Chapter 2 and 6, FRP strengthening is not advisable in cross-sections where plastic rotations are required to invoke the required moment redistribution.

References

[1] CUR-rapport-83, *Doorgaande balken van gewapend beton*. Stichting voor onderzoek, voorschriften en kwaliteitseisen op het gebied van beton. 1980. pp. 124.

[2] CUR-rapport-108, *Plastische scharnieren*. Stichting voor onderzoek, voorschriften en kwaliteitseisen op het gebied van beton. 1982. pp. 80.

[3] L. Taerwe, *Niet-lineaire analyse van betonconstructies*. Department of structural Engineering, Ghent University. 2000. pp. 61.

[4] F.B. Gijsbers, *Onderzoek naar de rotatiecapaciteit van op buiging belaste liggers met een rechthoekige doorsnede van met FeB 400 HK gewapend beton.*, in *nr. BI-74-6*. 1974.

[5] W.B. Cranston and G.C. Reynolds, *Influence of shear on rotation capacity of reinforced concrete beams*, in *Technical Report nr; 42.439*. 1970.

[6] U. Husemann and H. Budelmann, *Influence of the external enclousure of RC beams strengthened with CFRP plates*. Proceedings of CICE2008, Zurich, Switzerland. 2008

[7] CEN, *Eurocode 2: EN 1992-1-1: Design of concrete structures - Part 1-1: General rules and rules for buildings*. ed. CEN. 2004.

[8] J.E. Daniell, et al., *The softening rotation of reinforced concrete members.* Engineering Structures. 2008. Vol. In Press, Corrected Proof.

[9] D. Vandepitte, *Berekening van constructies*. E. Story-Scientia. Ghent. 1979. Vol. 3: pp. 721.

[10] I. Liu, et al., *Moment redistribution parametric study of CFRP, GFRP and steel surface plated RC beams and slabs.* Construction and Building Materials. 2006. Vol. 20 (1-2): pp. 59-70.

Chapter 5

INFLUENCE OF EXTERNALLY BONDED REINFORCEMENT ON THE CRACK SPACING

1 Introduction

In case of EBR strengthened beams, the external reinforcement bridges cracks and as a consequence influences the crack pattern. Especially in relation to the prediction of debonding due to crack bridging, also called intermediate crack debonding, the crack spacing s_{rm} is one of the main influencing parameters [1-3]. Hence, it is important to estimate the crack spacing as accurately as possible. In this chapter, different approaches are evaluated and compared to experimental observations.

2 Theoretical evolution of crack spacing

2.1 Crack spacing and transfer length

Generally the maximum crack spacing is equal to the length over which slip between the reinforcement and the concrete occurs, or the length which contributes to the crack width. This length equals two times the transfer length l_t. According to MC 90 [4] , the mean crack spacing at stabilized cracking s_{rm} for steel reinforced structures can be assumed 2/3 s_{rmax}.

$$s_{rm} = \frac{2}{3} s_{r\,max} = \frac{4}{3} l_t \qquad (5.1)$$

The transfer length l_t is the length over which the force in the reinforcement is transmitted to the concrete through bond interaction. This is related to the shear stress (τ) – slip (s) relation at the bond interface. For the τ-s relationship, different models are proposed, among which a linear elastic relation (see Fig. 5.1) [5], a non-linear relation [6] and a bilinear relation (see Fig. 5.1) [7]. In the following a linear τ-s relation is considered, as often assumed for serviceability limit state conditions. Given or assuming the τ-s relationship, different approaches for the modelling of the transfer length are possible, as discussed hereafter.

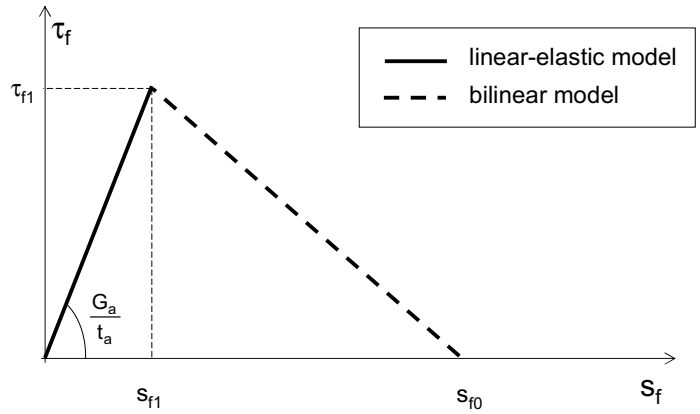

Fig. 5.1: Linear elastic and bilinear τ-s model

2.2 1st approach based on pure shear model

The first model used in this chapter to estimate the transfer length is based on the simple pull test of FRP-to-concrete bonded joints (Fig. 5.2- a). Note that this model only focuses on the behaviour between the externally applied FRP reinforcement and the concrete, without any interaction with internal steel reinforcement.

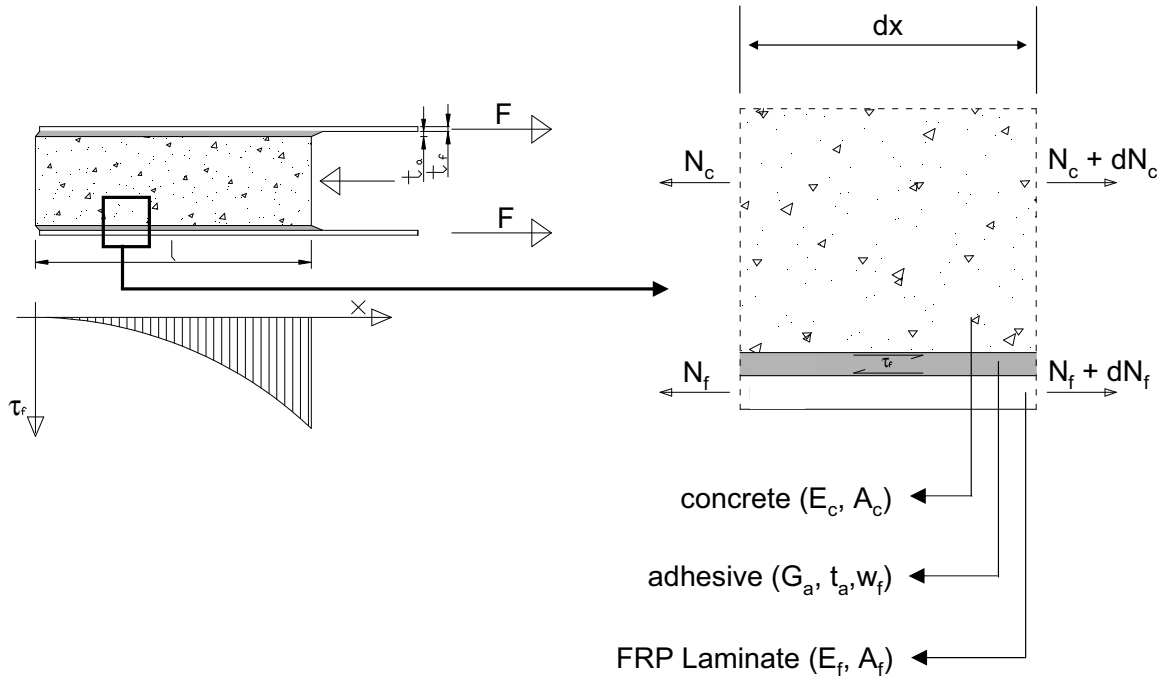

Fig. 5.2: a) Pure shear model; b) Differential element

By analyzing a differential element taken from this model (Fig. 5.2 - b), the following differential equation can be derived (e.g. [8]):

$$s_f'' - \frac{(1+\alpha_f\rho_f)}{E_f t_f} f(s_f) = 0 \tag{5.2}$$

$$\text{with} \quad s_f'' = \frac{d^2 s_f}{dx^2} \tag{5.3}$$

with $\tau_f = f(s_f)$ and s_f equals the slip between the FRP and the concrete. To solve Eq. 5.2, boundary conditions with respect to the normal force in the concrete N_c and the FRP N_f (Eq. 5.4) have to be considered, which results in expression 5.5 for τ_f. This relationship has been derived by several authors [9-11].

$$\begin{aligned} &BC1: N_c(x=0) = 0; \quad N_f(x=0) = 0; \\ &BC2: N_c(x=l) = -F; \quad N_f(x=l) = F; \end{aligned} \tag{5.4}$$

$$\tau_f(x) = \frac{F\,\omega\cosh(\omega x)}{b_f \sinh(\omega l)} \tag{5.5}$$

$$\text{where} \quad \omega^2 = \frac{G_a(1+\alpha_f\rho_f)}{t_a E_f t_f} \tag{5.6}$$

with G_a the shear modulus of the adhesive, t_a the thickness of the adhesive, t_f the thickness and w_f the width of the FRP laminate (see Fig. 5.2). Further $\alpha_f = E_f/E_c$ and $\rho_f = A_f/A_c$.

To derive the transfer length l_t, Eq. 5.5 has to be solved for x = 0 ($\tau_f(0) = 0$), which is theoretically obtained for $l_t = \infty$. For practical calculations $\tau_f(0) = 2\zeta_f$ with $\sinh(\omega l) \approx e^{\omega l}/2$ ($\omega l > 0$) and $F_{max} = (\tau_{f,max}\, w_f)/\varphi$ [10, 12]:

$$l_t \approx \frac{1}{\omega} \ln\left(\frac{\omega F_{max}}{\zeta_f w_f}\right) = \frac{1}{\omega} \ln\left(\frac{\tau_{f,max}}{\zeta_f}\right) \tag{5.7}$$

where a boundary condition $\zeta_f = 0.0002$ N/mm² is proposed.

2.3 2nd approach based on a tensile member

The second approach to evaluate the transfer length is based on the model illustrated in Fig. 5.3. In this case interaction between FRP and concrete is assumed over the entire length of a tensile member which creates the possibility of multiple crack formation. This causes multiple peak stress zones in the laminate, and high shear stresses in the bond interface at both sides of every crack (see Fig. 5.3).

By evaluating this model a similar differential element as in Fig. 5.2-b is obtained, from which the same differential equation (5.2) can be derived. Nevertheless other boundary conditions apply in this model (Eq. 5.8), which results in a specific solution for $s_f(x)$ according to Holzenkämpfer [8] (Eq. 5.9).

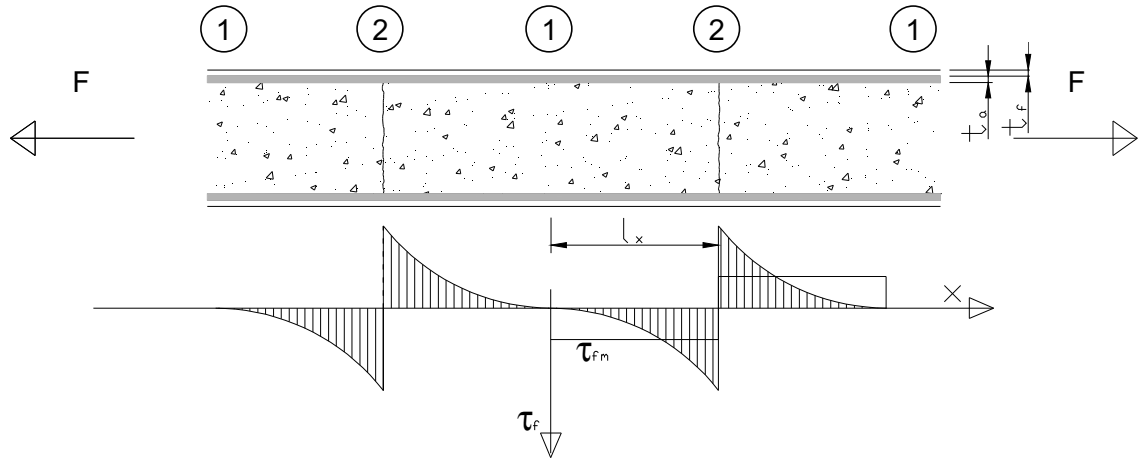

Fig. 5.3: Model based on crack formation in a tensile member

$$BC1: \tau_f(x=0)=0 \qquad BC2: s_f(x=l_x)=s_{f0} \tag{5.8}$$

$$s_f(x)=s_{f0}\frac{\sinh(\omega x)}{\sinh(\omega l_x)} \tag{5.9}$$

where s_{f0} equals the slip when debonding initiation between the laminate and the concrete is observed, determined by the bilinear τ-s model (see Fig. 5.1).

Based on the horizontal equilibrium of a differential element, Holzenkämpfer [8] defined the transfer length l_t according to Eq. 5.10. Herewith a simplification is introduced by assuming a constant shear stress τ_{fm} over the transfer length (see Fig. 5.3).

$$l_t=\Delta\sigma_f.\frac{t_f}{\tau_{fm}} \tag{5.10}$$

with τ_{fm} = $1.25f_{ct}$ [8]
$\Delta\sigma_f$ = σ_{f2} - σ_{f1}
σ_{f2} : tension in FRP laminate at the location of a crack (see Fig. 5.3)
σ_{f1} : tension in FRP laminate at the location of full composite bond (see Fig. 5.3)

2.4 3rd approach based on a mixed reinforced tensile member

The third approach to evaluate the transfer length is based on the model presented in Fig. 5.4 [4, 12]. The different bond behaviour of both reinforcement types is taken into account.

By analyzing a differential element from this model, two coupled differential equations can be derived:

$$s_f'' - \frac{(1+\alpha_f\rho_f)}{E_f t_f} f(s_f) - \frac{4\alpha_s\rho_s}{E_s d_s} f(s_s) = 0 \qquad (5.11)$$

$$s_s'' - \frac{(1+\alpha_s\rho_s)}{E_s d_s} f(s_s) - \frac{4\alpha_f\rho_f}{E_f t_f} f(s_f) = 0 \qquad (5.12)$$

with $\alpha_f = E_f/E_c$, $\alpha_s = E_s/E_c$, $\rho_f = A_f/A_c$, $\rho_s = A_s/A_c$, $\tau_f = f(s_f)$, $\tau_s = f(s_s)$ and s equals the slip between the reinforcement and the concrete (subscript f: FRP and s: steel).

To evaluate the transfer length, two different stages are considered. The first stage corresponds to a single crack (Fig. 5.4-a) where different transfer lengths l_s and l_f are obtained for the steel rebars and the FRP respectively:

$$l_s = \frac{\sigma_s A_s}{\tau_{sm} u_s} \qquad \text{with } \tau_{sm} = 1.80\, f_{ct} \text{ [4]} \qquad (5.13)$$

$$l_f = \frac{\sigma_f A_f}{\tau_{fm} u_f} \qquad \text{with } \tau_{fm} = 1.25\, f_{ct} \text{ [8]} \qquad (5.14)$$

with u_s and u_f the bond perimeter of the reinforcement ($u_s=\pi d_s$ (with d_s, the diameter of the steel bar) and u_f = b (width of laminate)). Remark the similarity between l_f in Eq. 5.14 and l_t in Eq. 5.10.

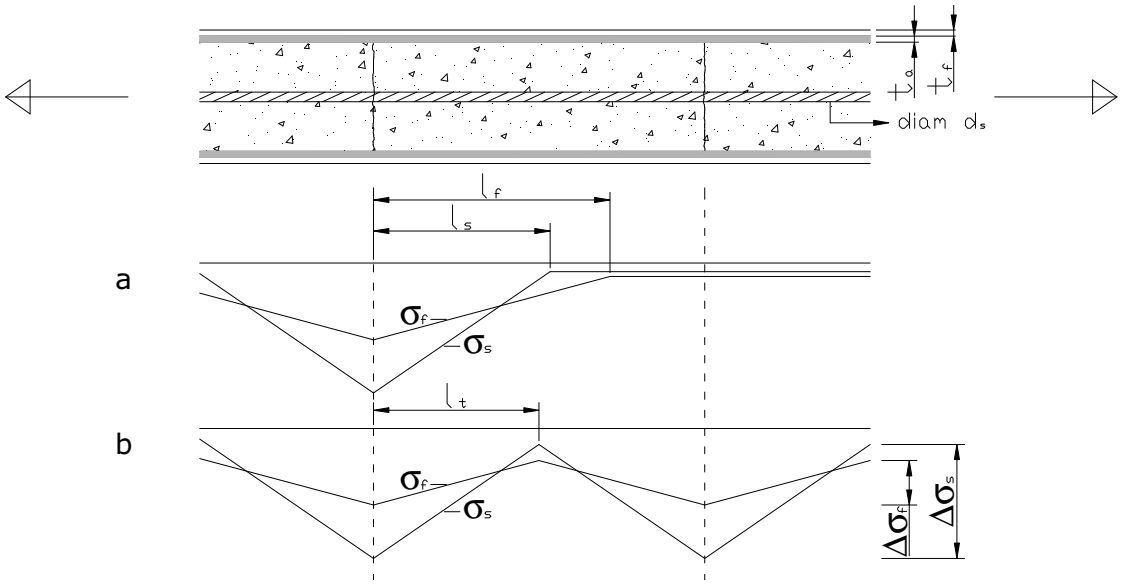

Fig. 5.4: Model based on the crack formation in a mixed reinforced tensile member

For the single crack stage, a remark can be made concerning the different transfer lengths. Assuming an equal force in the steel and the FRP reinforcement ($N_s = N_f$), results in the following equality:

$$\sigma_s A_s = \sigma_f A_f \qquad (5.15)$$

Herewith, the ratio of the two transfer lengths will only be dependent on the ratio of the bond perimeter multiplied by the factor 1.80 or 1.25, for steel and FRP reinforcement respectively.

In Fig. 5.5 the factors $1/(1.25u_s)$ and $1/(1.80u_f)$ are plotted in function of the reinforcement area (A_s or A_f). For the transfer length of the steel reinforcement, three different curves are plotted: 1, 2 or 3 steel rebars, with the same diameter.

From the figure it is clear that for a similar reinforcement section, the transfer length of the steel reinforcement, existing of bars embedded in concrete, will be considerably longer than the transfer length of the FRP reinforcement. E.g., for a reinforcement area of 150 mm² the transfer length of the FRP is 2.4 times smaller than for the single steel bar reinforcement, 1.7 times smaller than for 2 steel rebars and 1.4 times smaller than for 3 steel rebars.

It can be concluded that the transfer length for FRP tends to be smaller than the transfer length for steel rebars. This would logically result in smaller crack spacing in the neighbourhood of the FRP laminate than in the neighbourhood of the internal steel reinforcement. Indeed in the experimental study mentioned in section 3, a smaller crack spacing is observed under the laminate, by which these findings are confirmed.

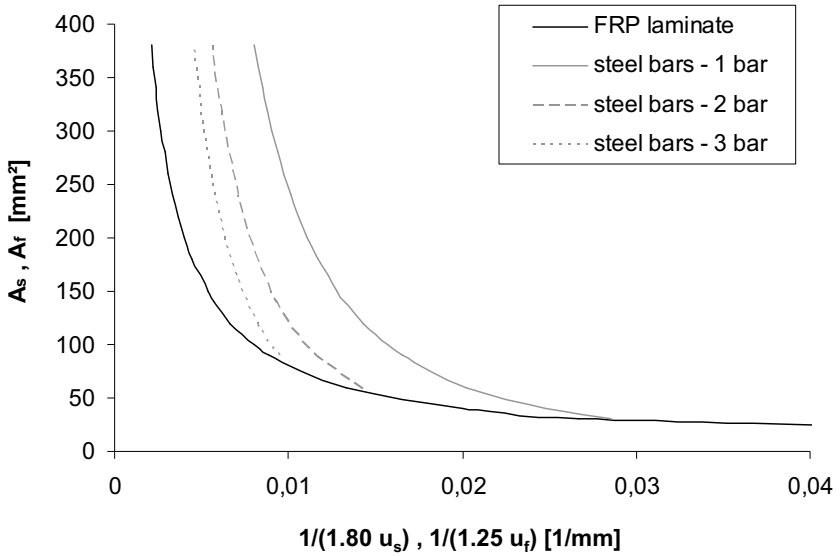

Fig. 5.5: Factors to calculate transfer lengths (l_s and l_f) in function of applied reinforcement section

At higher loads (second stage - Fig. 5.4-b) a stabilized crack pattern occurs (see Fig. 5.4-b), which results in an identical transfer length $l_{cr,n}$ for steel and FRP (Eq. 5.16). The following expression for the transfer length is presented by several authors [12-14].

$$l_{cr,n} = \frac{N_{cr}}{\tau_{sm} u_s} \frac{E_s A_s}{E_s A_s + \xi_b E_f A_f} = \frac{N_{cr}}{\tau_{fm} u_f} \frac{\xi_b E_f A_f}{E_s A_s + \xi_b E_f A_f} \quad \text{with } \xi_b = \frac{\tau_{fm} E_s A_s u_f}{\tau_{sm} E_f A_f u_s} \tag{5.16}$$

3 Experimental evolution of the crack width and crack spacing

3.1 Macro cracks of tested 2-span beams

In the following, verification of the analytical and experimental results regarding the crack pattern is performed at the load level:

$$N_{cr,m} \approx \frac{N_{cr,n} + N_y}{2} \tag{5.17}$$

where $N_{cr,n}$ is the load at which the concrete element is in the stabilized cracking phase and N_y is the load at which the internal reinforcement is yielding. As the experimental crack spacing is measured every 10 kN, the load level $N_{cr,m}$ is rounded to the nearest 10 kN value. In Table 5.1, both the rounded value of $N_{cr,m}$ and the mean value of the experimental crack spacing is given. The crack spacing is only given for locations where both internal steel reinforcement and external bonded reinforcement is provided. In Table 5.1, the calculated crack spacings according to Eq.5.7, Eq.5.10 and Eq.5.16 are given, as well as the ratio of the calculated crack spacing to the measured crack spacing.

Table 5.1: Experimental and analytical macro crack spacing of two-span beams

	Experimental		Analytical*					
	$N_{cr,m}$	$s_{rm,exp}$	M1 (Eq.5.7)		M2 (Eq.5.10)		M3 (Eq.5.16)	
	[kN]	[mm]	[mm]	ratio	[mm]	ratio	[mm]	ratio
CB 1 (bottom)	80	96	177	1.84	47	0.49	101	1.05
CB 2 (top)	60	87	177	2.04	70	0.81	110	1.26
CB 3 (top)	80	88	179	2.04	35	0.40	90	1.03
CB 3 (bottom)	80	102	179	1.75	33	0.32	85	0.83
CB 4 (top)	60	110	177	1.60	60	0.55	116	1.06
Mean ratio				1.85		0.51		1.04

* For Model 1 and Model 2 s_{rm} equals 4/3 l_t (see Eq. 5.1), for Model 3 s_{rm} equals 2 $l_{cr,n}$

As can be noticed from Table 5.1, the third approach, based on the crack formation in a mixed reinforced tensile member (section 2.4 - Eq.5.16), is giving the best prediction of the crack spacing. The first and second approach yield respectively a too large and a too small prediction of the crack spacing.

Finally, the recorded crack patterns of the tested continuous beams are shown in Fig. 5.6. Also the position of the externally bonded reinforcement is indicated. The smaller crack spacing of the strengthened regions compared to the unstrengthened regions can clearly be noticed.

Further information concerning the crack pattern and crack width of the continuous beams is found in section 3 of Chapter 2.

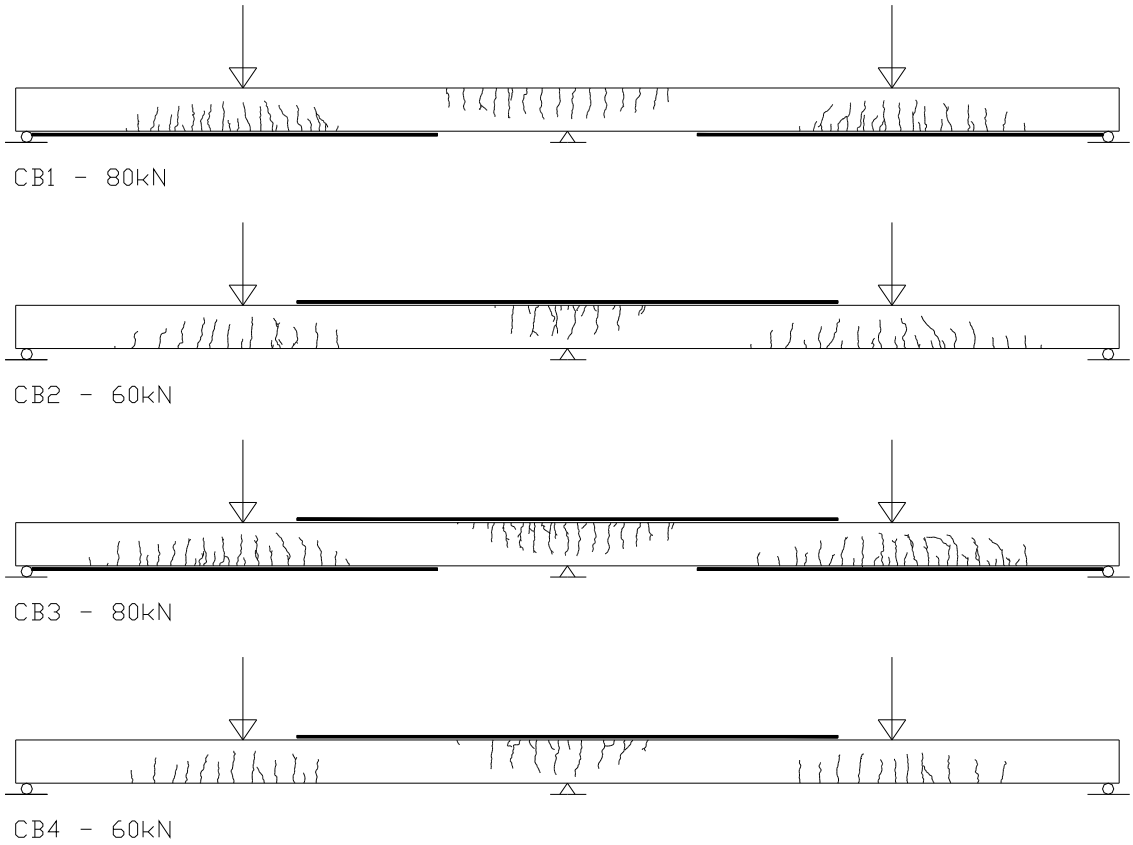

Fig. 5.6: Crack pattern of two-span beams at $N_{cr,m}$

3.2 Micro cracks of tested 2-span beams

More detailed microscopic investigations on crack spacing have been conducted on the two-span continuous beams [15]. Concrete cores have been drilled from the fourth beam (CB4) after testing. Three cores of 100 mm in diameter have been drilled at the top of the beam at the mid-support zone (Fig. 5.7). The first core was drilled at a location where the FRP laminate has debonded from the concrete top layer. Core 2 and 3 were drilled in a zone where no debonding was noticed. The cores are drilled through the FRP laminate as well as through the upper horizontal part of the closed steel stirrups, until a depth of about 170 mm into the concrete. The location of the cores is chosen in order to cover each time a major crack, visible at the outside of the tested beam, and to investigate the crack pattern near the FRP laminate.

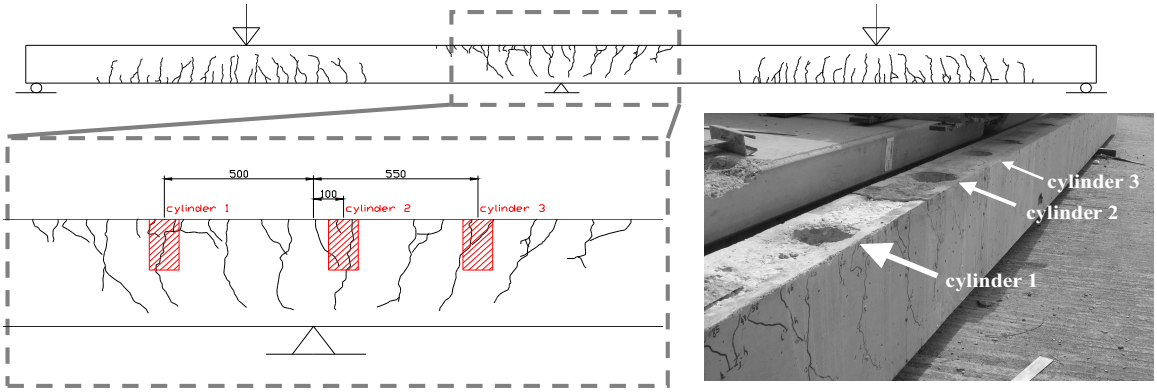

Fig. 5.7: Drawing and photograph of location of drilled cores at the mid-support.

After drilling, the cores are sawn in two halves, according to the longitudinal axis of the beam. The cross-section of one halve is polished and finally a microscopic investigation on the polished surfaces is executed. A graphical representation of all cracks visible in the cross-section of the cores is made (Fig. 5.8). Notice that the FRP laminate is missing at the top of the first core (Fig. 5.8), as it was drilled in the debonded zone.

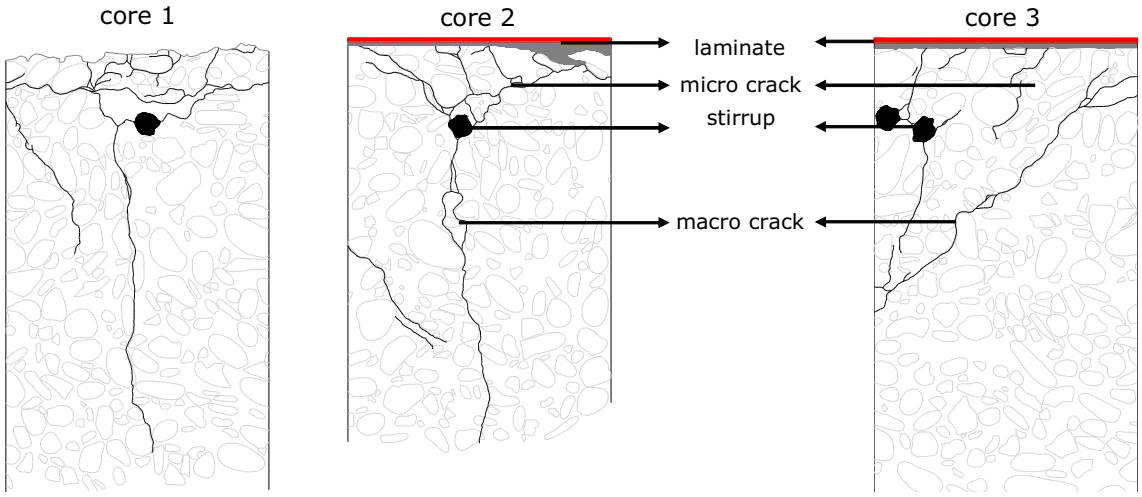

Fig. 5.8: Visualization of cracks in the cross sections of the cores

Cracks, which are visible at the side faces of the beam (Fig. 5.7), are also visible in the cross-section of the cores (Fig. 5.8). However, in the top layer of the concrete, between the FRP laminate and the internal reinforcement, additional cracks are observed. Observations by means of the microscopic study show that these additional cracks are smaller compared to the macro cracks (see Table 5.2). Whereas the mean crack width of the macro cracks after failure equals 0.97 mm (mean value of all macro cracks in the mid-support zone of the continuous beam), the mean crack width of the micro cracks measures 0.16 mm (mean value of micro cracks found in cross sectional areas of the cores). This results in a ratio of about 0.16.

A comparison of the macro crack spacing (mean value of spacing between all major cracks at the mid-support zone) and the micro crack spacing (mean value of spacing between micro cracks found in cross sectional areas of the cores) is

given in Table 5.3. The smaller crack spacing in the concrete layer nearby the FRP bond interface can be noticed (more, yet smaller cracks). The ratio between macro and micro crack spacing equals 0.23.

Table 5.2: Crack widths of macro and micro cracks

	Cyl. 1	Cyl. 2	Cyl. 3	mean
Mean crack width of micro cracks [mm]	0.24	0.17	0.13	0.16
Crack width of macro crack [mm]	0.95	1.75	1.15	0.97
Ratio	0.25	0.10	0.11	0.16

Table 5.3: Crack spacing of macro and micro cracks

	Crack spacing after N_u
crack spacing micro cracks	20 mm
crack spacing macro cracks	87 mm

As reported in many research projects (e.g. [12]), the (macro) crack spacing of beams strengthened for flexure is smaller compared to unstrengthened reference members. In this study it is demonstrated, that additional crack formation occurs in the concrete cover nearby the laminate, resulting in even smaller crack spacing at the location of the FRP laminate. This phenomenon is also confirmed by the analytical study summarized in Fig. 5.5, whereby the transfer length for FRP laminates tends to be smaller than the transfer length for steel rebars.

3.3 Macro cracks of tested isostatic beams

Similar to section 3.1, the analytically obtained crack spacing of the three-point-bending test configuration is compared to the measured crack pattern at the load level $N_{cr,m}$. As can be noticed from Table 5.4, again the best predictions for the crack spacing are given by the third model.

Finally the recorded crack patterns of the tested isostatic beams are shown in Fig. 5.9. In this figure also the position of the externally bonded reinforcement is indicated. For further information concerning the recorded crack patterns of these beams and the measured crack widths, reference is made to Appendix B.

Table 5.4: Experimental and analytical macro crack spacing of one-span beams

	Experimental		Analytical*					
	$N_{cr,m}$	$s_{rm,exp}$	M1 (Eq.5.7)		M2 (Eq.5.10)		M3 (Eq.5.16)	
	[kN]	[mm]	[mm]	ratio	[mm]	ratio	[mm]	ratio
IB 1	50	128	177	1.38	54	0.42	133	1.04
IB 2	80	118	177	1.51	35	0.30	93	0.79
IB 3	120	130	177	1.36	20	0.15	67	0.51
IB 4	80	101	177	1.76	35	0.34	92	0.91
Mean ratio				1.50		0.30		0.81

* For Model 1 and Model 2 s_{rm} equals 4/3 l_t (see Eq. 5.1), for Model 3 s_{rm} equals 2 $l_{cr,n}$

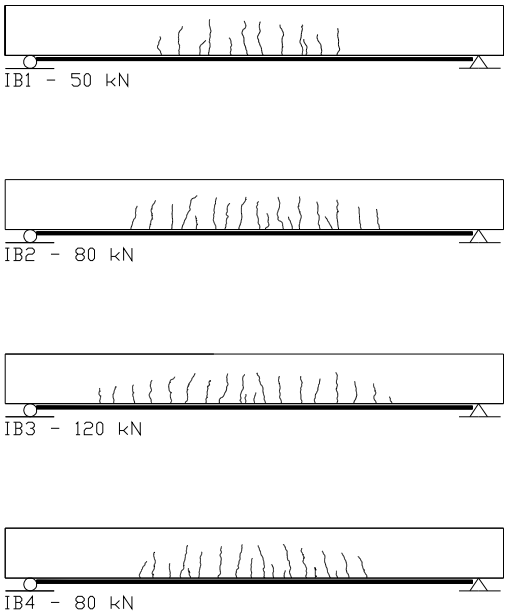

Fig. 5.9: Crack pattern of isostatic beams

3.4 Micro cracks of tested isostatic beams

During some of the tests, a Digital Image Correlation Technique (DICT) was used to record both the displacements and strains of the laminate and the adjacent concrete zones. The measurements were performed by a team of the Department of Materials and Structures of the Free University Brussels (Prof. D. Van Hemelrijck).

A measurement area of ~ 120 mm x 120 mm[1] was used which resulted in a sufficiently small optical gauge length and in a detailed recorded strain distribution. In Fig. 5.10 a picture is given of the strain distribution 10 kN before debonding of the laminate. A clear distinction can be seen between the macro cracks, appearing in the concrete zone and the micro cracks appearing underneath the laminate. Additionally in Fig. 5.11 the detailed strain distribution is given of section A (concrete zone) and section B (border of laminate and concrete zone) indicated in Fig. 5.10. Again, a good distinction is obtained between the macro and micro crack formation of the strengthened beam. Finally, the crack spacing derived from Fig. 5.11 is summarized in Table 5.5. A similar ratio between the macro crack spacing and the micro crack spacing is obtained as for the two-span beam (see Table 5.3).

[1] A similar measurement was first applied on the tested continuous beam. No useful information concerning the peak stresses at crack bridging was obtained, because the measuring area (~ 500 mm x 200 mm) was too large. This large area results in a too large optical gauge length which is used to handle the data. Herewith, the expected peak stresses are smoothed and as a consequence not visible in the strain graphs.

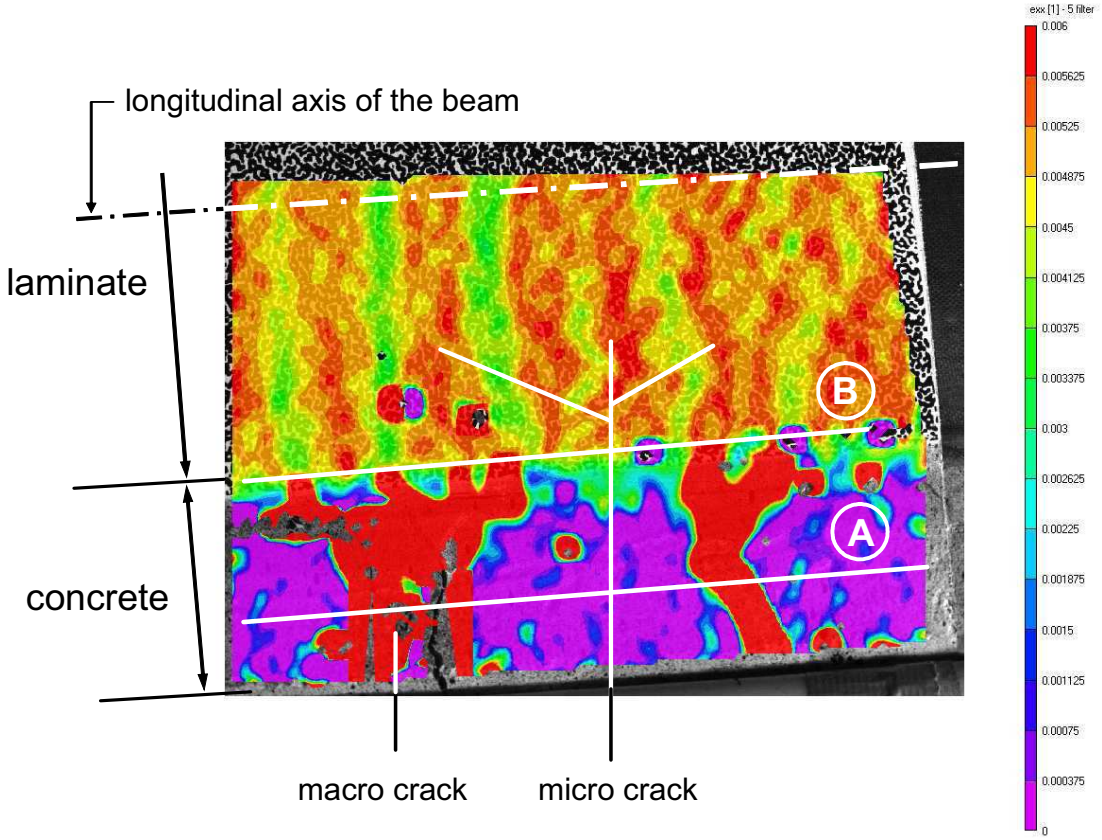

Fig. 5.10: Recorded strain concrete and FRP under point load of IB6 (range 0.0 % - 0.6 %)

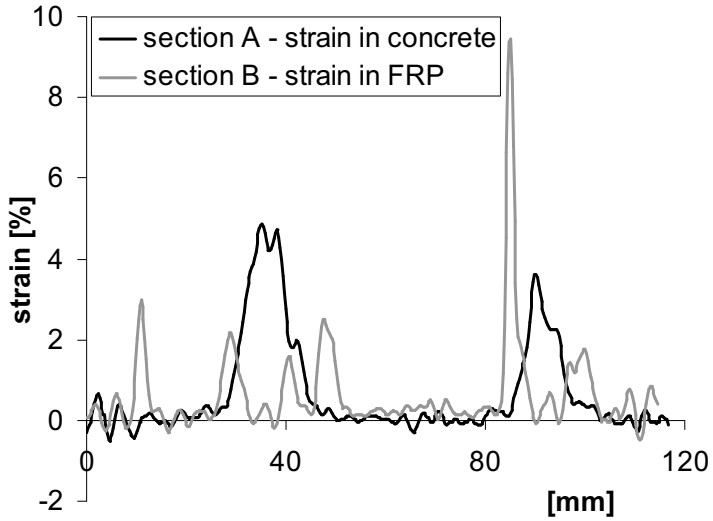

Fig. 5.11: Strain distribution in section A (Concrete) and in section B (FRP laminate) of IB6

Table 5.5: Crack spacing of macro and micro cracks

	Crack spacing 10 kN before debonding	
crack spacing micro cracks	18 mm	32 %
crack spacing macro cracks	55 mm	100 %

4 CONCLUSIONS

Analytical models to predict crack spacing have been compared. The best prediction of the crack spacing of a strengthened reinforced concrete beam is obtained by the model based on the crack formation in a mixed reinforced tensile member.

According to a microscopic investigation of the crack pattern underneath the FRP laminate of a continuous beam and a DICT-monitoring of an isostatic beam, it has been observed that macro cracks visible at the side-faces of the beam split up into multiple micro cracks under the laminate. This phenomenon is also confirmed by the analytical study which compares the transfer length in the neighbourhood of embedded steel rebars and the transfer length in the neighbourhood of an FRP laminate. Both from the experimental and analytical investigation, a smaller crack spacing is observed under the laminate compared to the crack spacing around the steel rebars.

For the considered beams the crack spacing of these micro cracks appeared to be equal to 27.5 % of the macro crack spacing on the mean (respectively 23 % for the continuous beam and 32 % for the isostatic beam). The depth over which the micro cracks expands, roughly corresponds to the concrete layer between the FRP laminate and the internal steel reinforcement.

From this study it appears that strengthened flexural members have not the same crack pattern underneath the FRP compared to the overall crack pattern of the beam, opposite to what is generally assumed in design models for externally bonded reinforcement. Taking into account the local crack pattern underneath the FRP, may allow more refined modelling of FRP debonding in the future.

References

[1] E. Oller, *Peeling failure in beams strengthened by plate bonding. A design proposal*. PhD thesis. Departament d'Enginyeria de la construcció, Universitat Politècnica de Catalunya. Barcelona. 2005. pp. 334.

[2] J.G. Teng, et al., *Intermediate crack-induced debonding in RC beams and slabs.* Construction and Building Materials. 2003. Vol. 17 (6-7): pp. 447-462.

[3] fib, *fib bulletin 14, Externally bonded FRP reinforcement for RC structures*. International federation for structural concrete, Lausanne. 2001: pp. 138.

[4] CEB, *CEB-FIP Model Code 1990, Design Code*. ed. Comité Euro-International du Béton. Thomas Telford. Lausanne, Switzerland. 1993: pp. 437.

[5] J. Bresson, *Nouvelles recherches at applications concernant l'utilisation des collages dans les structures. Béton plaqué.* Annales de l'ITBTP. 1971. Vol. 278: pp. 22-25.

[6] M. Wicke and D. Pichler, *Geklebte Bewehrung - Endverankerung mit und ohne Anpressdruck - Bemessungskonzept.* HILTI-Konzern-Forschung. 1991.

[7] E.-H. Ranisch, *Zur Tragfähigkeit von Verklebungen zwisschen Baustahl und beton - Geklebte Bewehrung.* TU Braunschweig. 1982. Vol. 54.

[8] P. Holzenkämpfer, *Ingenieurmodelle des Verbunds geklebter Bewehrung für Betonbauteile*. Berlin. 1997. Vol. DAS - Heft 473.

[9] H. Kaiser, *Bewehren von Stahlbeton mit kohlenstoffaserverstärkten Epoxidharzen*. PhD thesis, Technical University of Zurich. Switzerland. 1989. pp. 240.

[10] M. Deuring, *Verstärken von Stahlbeton mit gespannten Faserverbundwerkstoffen*. EMPA, Dübendorf, Switzerland. 1993. Vol. 224: pp. 279.

[11] B. Täljsten, *Plate Bonding - Strengthening of Existing Concrete Structures with Epoxy Bonded Plates of Steel or Fibre Reinforced Plastics*. PhD thesis. Division of structural engineering, University of Technology. Lulea. 1994. pp. 281.

[12] S. Matthys, *Structural behaviour and design of concrete members strengthened with externally bonded FRP reinforcement*. Department of Structural Engineering, Ghent University. Ghent. 2000. pp. 345.

[13] F. Ceroni and M. Pecce, *Cracking behaviour of RC beams externally strengthened with emerging materials.* Construction and Building Materials. 2007. Vol. 21 (4): pp. 736-745.

[14] F.S. Rostásy, P. Holzenkämpfer and C. Hankers, *Geklebte Bewehrung für die Verstärkung von Betonbauteilen.* Betonkalender 1996. 1996. Vol. II: pp. 547-576.

[15] L. Vasseur, S. Matthys and L. Taerwe, *Influence of externally bonded reinforcement on the crack spacing*. Proceedings of CICE2008: 'FRP Composites in Civil Engineering', Zurich. Masoud Motavalli. 2008. Vol. 1: pp. 116

Chapter 6
DESIGN RECOMMENDATIONS

1 Introduction

While in previous chapters the study was mainly focussed on beams, the design recommendations given in this chapter can also be extended to slabs.

If the linear elastic theory is applied for the design of continuous beams and slabs strengthened in flexure, a certain section of external reinforcement has to be applied both in the spans and at the intermediate supports. This strengthening configuration is often difficult to apply in practice due to the existence of:

- a finishing layer at top of the beam/slab
- a finishing layer at the soffit of the beam/slab
- a wall on top of the intermediate supports
- technical installations at the soffit of the beam/slab
- ...

Hence, in many practical cases only one location can be strengthened: either the soffit of the spans, or the top of the intermediate supports. Due to this selective strengthening of the beam, a certain redistribution of the moments will occur. By means of the moment redistribution, it is possible to keep the moment at a critical cross section constant, which can result in the following two strengthening configurations:

- Firstly the bending moment at the intermediate support is kept constant and FRP EBR is applied at the soffit of the span. In this case a first plastic hinge is expected to occur at the support.
- Secondly the maximum resisting moment in the spans is kept constant, whereas FRP EBR is applied at top of the supports. In this case a plastic hinge is expected to occur in the spans.

Analysing a continuous beam or slab, four different theories can be used [1]. Some of the design models are based on the linear elastic theory, while others are based on the non-linear theory. In the following sections the four different theories will be shortly introduced, among which:

- the linear elastic theory (see section 2)
- the linear elastic theory with limited redistribution (see section 3)
- the non-linear theory (see section 4)
- the plasticity theory (see section 5)

In each of these theories it should be verified, implicitly or explicitly, that the rotation occurring in the plastic hinges is smaller than the rotation capacity of the critical sections under consideration (see equation 6.1)

$$\theta_d \leq \theta_{pl} \tag{6.1}$$

with θ_d = the occurring plastic rotation (needed for the required moment redistribution) between the onset of the plastic hinge at the critical section considered and the occurrence of the failure mechanism
θ_{pl} = the plastic rotation capacity

Often in basic design, the design procedure directly addresses the flexural strength and indirectly addresses the rotation capacity (flexural ductility). This rotation capacity can be guaranteed in the linear elastic theory with limited redistribution by limiting the neutral axis depth. Given the sometimes brittle failure mechanisms, such as the debonding mechanisms which are typical for structures strengthened with externally bonded reinforcement, this approach is not sufficient any more. Herewith other approaches such as for example the non-linear theory need to be applied.

2 Linear elastic theory

2.1 Unstrengthened continuous beams

If the linear elastic theory is applied, reinforcement ratios according to this linear elastic theory are used. As a result, no redistribution of the theoretical moments is obtained. As the practical reinforcement ratios differ slightly from the theoretical reinforcement ratios, only a limited moment redistribution is expected.

Because no or only a limited moment redistribution is expected in a linear elastic reinforced concrete beam, a basically linear relation between the moment and externally applied load is obtained. The linear elasticity model can be used for both serviceability limit state (SLS) and ultimate limit state (ULS).

2.2 Strengthened continuous beams

For the design of a strengthened continuous beam according to the linear elastic theory, reference is made to section 2.2.3.2 of Chapter 2. From the study in Chapter 2 it appears that no, or only a limited, moment redistribution is obtained in the case of a continuous beam with internal steel reinforcement ratios calculated according to the linear elastic theory and with additional externally bonded reinforcement ratios also designed according to the linear elastic theory. In this case it is allowed to apply the linear elastic theory. Again, the linear elasticity model can be used for both serviceability state and ultimate state.

In case the internal reinforcement ratios or the external reinforcement ratios are differing from the linear elastic moment distribution a considerable moment redistribution can be obtained and as a consequence, the linear elastic theory should not be applied.

3 Linear elastic theory with limited redistribution

3.1 Theoretical approach

3.1.1 Unstrengthened continuous beams

The moment distribution obtained from the linear elastic theory, can be partly redistributed [1]. This redistribution can be applied under the condition that the static equilibrium conditions are still satisfied for the new bending moment diagram.

The redistribution is obtained by reducing the bending moment at critical sections according to the linear elastic theory with a factor δ (see equation 6.2 and Fig. 6.1).

$$\delta = \frac{M_{red}}{M_{el}} \tag{6.2}$$

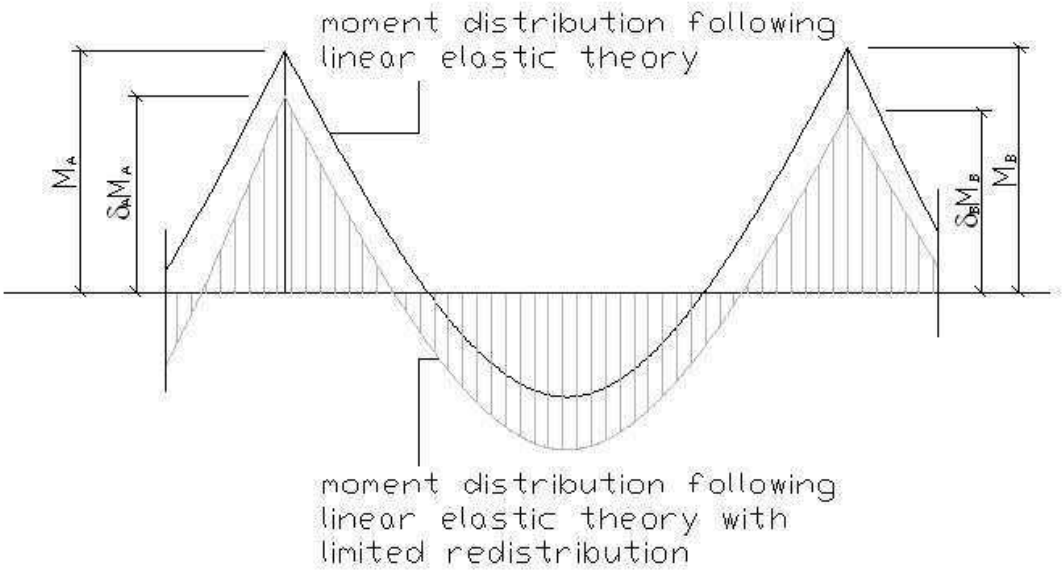

Fig. 6.1: Moment distribution according to linear elastic theory and according to linear elastic theory with limited redistribution

In beams or slabs which are predominantly subjected to flexure and where the ratio of the lengths of adjacent spans is smaller than 2, sufficient rotation capacity is available to allow a limited moment redistribution [1]. Nevertheless the following ductility conditions (in function of the applied redistribution δ, see Eq. 6.3 and 6.4) and limitations of δ (see Eq. 6.5 and 6.6) at the location of the plastic hinges have to be fulfilled:

a) based on concrete strength:

$$\delta \geq k_1 + k_2 \xi_u \qquad \text{for } f_{ck} \leq 50 \text{ MPa} \qquad (6.3)$$

$$\delta \geq k_3 + k_4 \xi_u \qquad \text{for } f_{ck} > 50 \text{ MPa} \qquad (6.4)$$

with $\xi_u = x_u/d$: the ratio of the neutral axis depth in the ULS to the effective depth of the beam.

The recommended value for k_1 is 0.44, for k_2 is $1.25(0.6+0.0014/\varepsilon_{cu2})$, for k_3 is 0.54 and for k_4 is $1.25(0.6+0.0014/\varepsilon_{cu2})$, with ε_{cu2} is ultimate strain of the parabola-rectangle diagram for concrete under compression [1].

b) based on ductility of steel:

$$\delta \geq 0.7 \qquad \text{where Class B and Class C reinforcement is used} \qquad (6.5)$$

$$\delta \geq 0.8 \qquad \text{where Class A reinforcement is used} \qquad (6.6)$$

The ductility of the different classes of steel reinforcement are characterized by the factors ε_{uk} and $(f_u/f_y)_k$ (see Table 4.8 in Chapter 4)

The allowable limited redistribution, corresponding to these conditions is given in Fig. 6.2 by the shaded area.

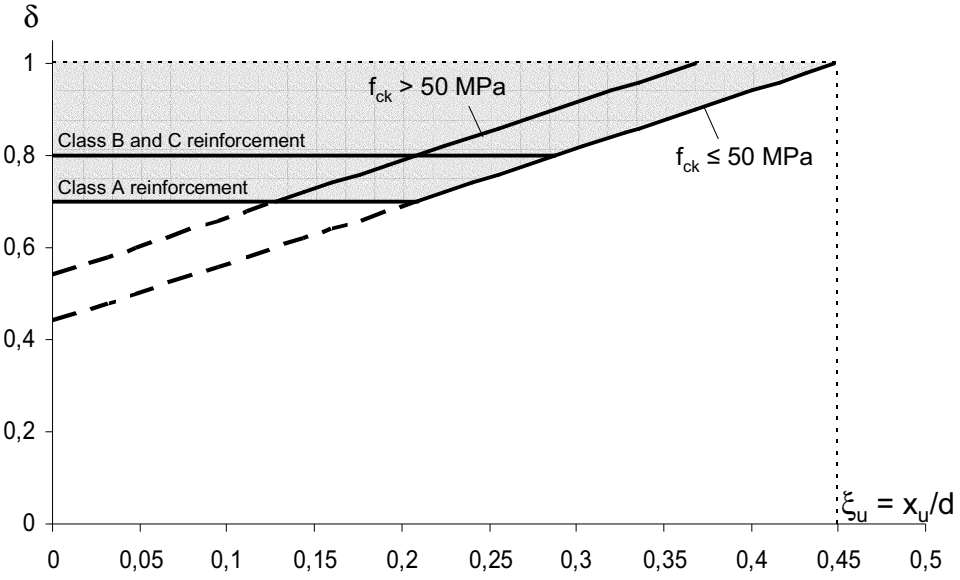

Fig. 6.2: Moment redistribution coefficient δ in function of ξ_u

Due to the restrictions of ξ_u, this approach is also known as the 'neutral axis depth approach' [2, 3]. In this approach, it is assumed that the concrete in the compression zone crushes at failure (ultimate strain ε_c equal to 0.0035).

3.1.2 Strengthened continuous beams

For a strengthened continuous beam a redistribution of moments can be introduced under the condition that the static equilibrium conditions are satisfied. The redistribution is obtained by reducing the bending moment at critical sections obtained from the linear elastic theory with a factor δ (see Eq. 6.2 and Fig. 6.1).

As EC2 [1] requires a maximum ξ_u-factor equal to 0.2 for a moment redistribution of 30%, a minimum FRP strain of 0.0140 is required (see Fig. 6.3). Looking to the obtained strain in the FRP laminates of the tested strengthened beams (see Table 2.20 in Chapter 2), an average strain is obtained equal to 0.0042, while the maximum experimental strain equals 0.0056.

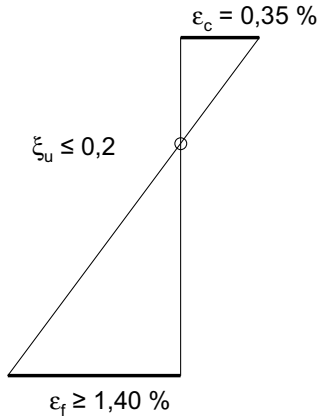

Fig. 6.3: Strain distribution for a moment redistribution equal to 30% according to EC2 [1].

In fact the assumption of concrete crushing at failure can be questioned for FRP strengthened critical sections. Because the failure of a strengthened cross-section is often characterized by a debonding mechanism, the ultimate strain obtained at the compression face is smaller than the above mentioned 0.0035. This requires a smaller tension face strain to achieve the required ξ_u-factor, given in Fig. 6.2. Hence, it is suggested that the ξ_u-factor should not be used to control the moment redistribution for strengthened structures, where concrete crushing does not control the failure [4].

On the other hand, at strengthened critical sections, it is interesting to check the curvature which is related to the predicted ξ_u-factors (under the assumption that ε_c = 0.0035). In order to obtain a limitation of the curvature, independent of the effective depth, the product χd is considered. From Eq. 6.7, it follows that χd is obtained by dividing the strain at the compression face (ε_c) by the ξ_u-factor.

$$\chi = \frac{\varepsilon_c}{x_u} = \frac{\varepsilon_c}{\xi_u d} \tag{6.7}$$

$$\chi d = \frac{\varepsilon_c}{\xi_u} \tag{6.8}$$

The obtained limitation of the χd-factor, related to the limitation of the ξ_u-factor and ε_c = 0.0035, is given in Fig. 6.4. Herewith the shaded area of Fig. 6.2 corresponds to the shaded area in Fig. 6.4.

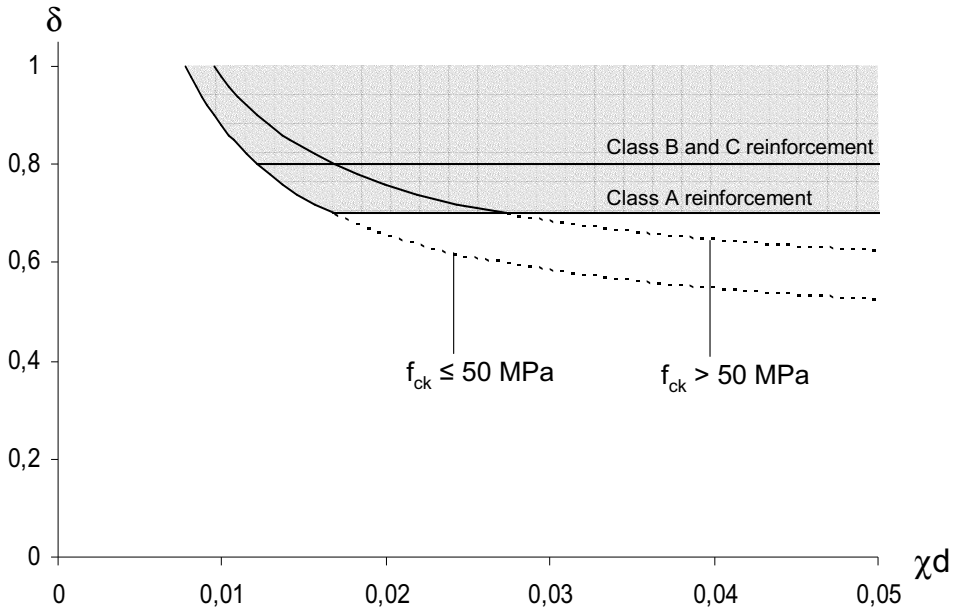

Fig. 6.4: Moment redistribution coefficient δ in function of χ.d

Indeed, both the curvature and the ξ_u-factor control the rotation of a plastic hinge θ_{hinge} (see equation 4.4 and 4.7 in Chapter 4) if it is assumed that $L_{hinge} \approx$ 2d (= twice the effective depth). [4].

3.2 Verification of linear elastic theory with limited redistribution by means of examples

In this section the linear elastic theory with limited redistribution applied on a two span beam (see Fig. 6.5) is discussed. The results of the linear elastic theory with limited redistribution are verified by comparing them with a more detailed non-linear analysis. This investigation will be conducted by means of three cases:

- Case 1 strengthening configuration for which externally bonded reinforcement is used in the spans (section 3.2.2).
- Case 2 strengthening configuration for which externally bonded reinforcement is used at the mid-support (section 3.2.3).
- Case 3 strengthening configuration for which externally bonded reinforcement is used both in the spans and at the mid-support (section 3.2.5).

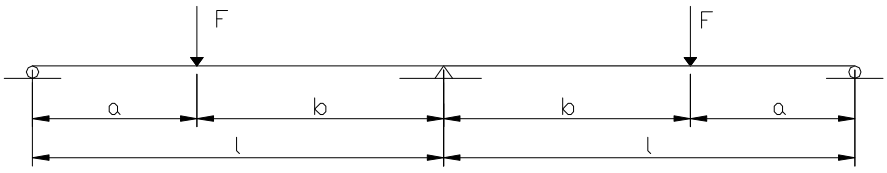

Fig. 6.5: Continuous beam with two spans

For the verification of the moment redistribution according to the non-linear theory, the following material properties are used:

Table 6.1: Material properties

	C35/45		S500		CFRP	
Compressive strength	35	N/mm²				
Yielding strength			500	N/mm²		
Tensile strength	3.5	N/mm²	550	N/mm²	2850	N/mm²
Failure strain	0.35	%	12.40	%	1.81	%
E-modulus	32000	N/mm²	200000	N/mm²	175000	N/mm²

These values are the same as the material properties used in the theoretical study of Chapter 2. Further, for the calculations no material safety factors are taken into account.

In addition to the strengthening by means of FRP EBR, also strengthening by means of externally bonded steel plates (Steel EBR – S500) is considered. For the calculation of FRP EBR, it is assumed that debonding of the FRP laminates occurs at a strain of 0.40 % (see section 2.1.2 in Chapter 4). For the calculation of Steel EBR it is assumed that debonding is prevented and hence that failure corresponds to concrete crushing.

For all beams, the internal reinforcement configuration is assumed to be calculated according to the linear elastic theory. This reinforcement configuration is used, as it is the configuration which is found in the majority of practical cases. For a discussion of the linear elastic theory with limited redistribution applied to two-span beams with a non-elastic reinforcement distribution, reference is made to Chapter 2 and Appendix C.

3.2.1 Unstrengthened beam

As can be seen in Fig. 6.5 a two span beam is considered, which is loaded with one point load in every span. This configuration is identical to the test set-up mentioned in Chapter 2 and Chapter 3. It is assumed that the reference unstrengthened two span beam is able to sustain a loading configuration consisting of two point loads of 80 kN. The linear elastic moment distribution is shown in Fig. 6.6. The reference beam is reinforced according to this linear elastic moment distribution. As the absolute values of the critical cross-sections are quite similar, an identical reinforcement section is taken both in the spans and at the mid-support, equal to 393mm², which is only a theoretical value.

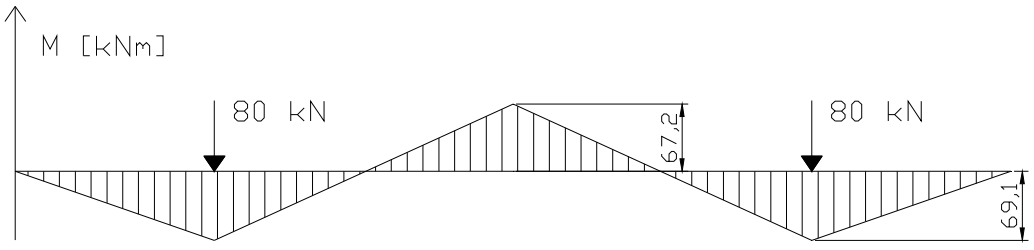

Fig. 6.6: Linear elastic moment redistribution of unstrengthened the two span reference beam

By applying this reinforcement configuration, almost no moment redistribution is observed (see Fig. 6.7 and Fig. 6.8). In Fig. 6.7 the bending moment at the mid-support and in the spans, calculated according to the non-linear theory, are shown in function of the applied point load F. In Fig. 6.8, the redistribution factor δ of the mid-support (see Eq. 6.9) is also shown in function of the applied load F.

$$\delta_{support} = \frac{M_{red,support}}{M_{el,support}} \tag{6.9}$$

Because the reinforcement configuration corresponds to the linear elastic theory, almost no redistribution is noticed. The beam will fail at an ultimate point load of 82.3 kN, which is the failure load resulting from a non-linear analysis. Notice that this failure load agrees well with the failure load obtained from the linear elastic theory (= 80 kN (see Fig. 6.6)). A maximum moment redistribution of 2.0 % is obtained, for which 0.4 % is caused by elastic redistribution and 1.6 % is caused by plastic redistribution.

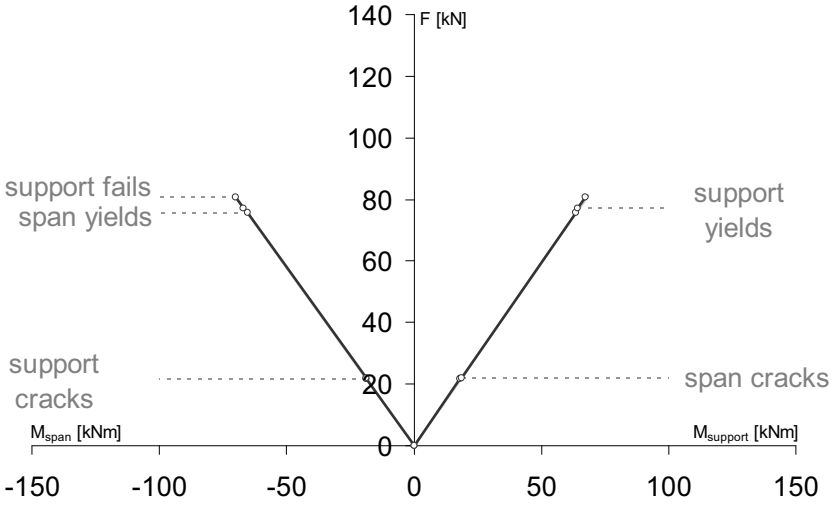

Fig. 6.7: Moment distribution of unstrengthened reference beam

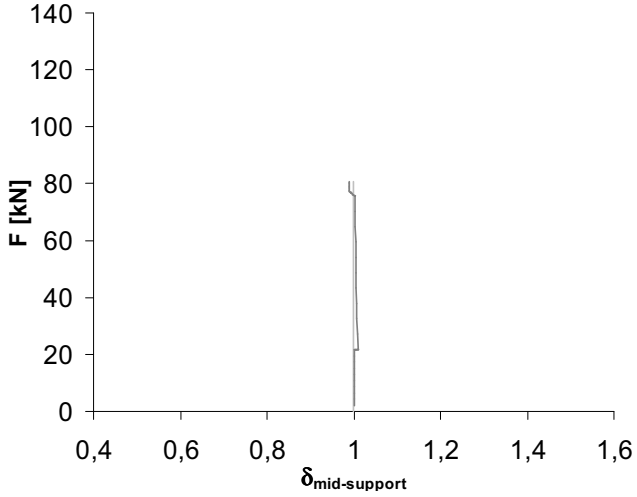

Fig. 6.8: Redistribution factor of unstrengthened reference beam

3.2.2 Strengthened beam – case 1

3.2.2.1 Strengthening with limited redistribution

In practical applications it can happen that no possibility exists to strengthen a continuous beam at the intermediate supports. In such a situation, a moment redistribution has to be introduced in order to keep the moment at the intermediate support constant and to increase the applied load until the required ultimate load. By keeping the moment at the intermediate support constant, no strengthening is needed at the intermediate support but a plastic hinge is expected to be formed.

In the following, three different cases of moment redistribution at the support (10 %, 20 % and 30 %) will be discussed. In Table 6.2 and Fig. 6.9 both the moment distribution according to the linear elastic theory (grey lines in Fig. 6.9) and the moment redistribution according to the linear elastic theory with limited redistribution (black curve in Fig. 6.9) are given. The bending moment at the mid-support of all redistributed configurations is equal to the bending moment of the unstrengthened reference beam. As mentioned above, no strengthening is applied at the mid-supports, while in the spans, strengthening is required to resist the higher moments, for which FRP EBR is used.

Further in Table 6.2, the strengthening ratio is noticed and the ratios of the moments according to the linear elastic theory with limited redistribution compared to the moments according to the linear elastic theory at the critical cross-sections are given. Concerning the latter ratio, reference is made to Eq. 6.10.

$$ratio_{mom.} = \frac{M_{LE-LR}}{M_{el}} \tag{6.10}$$

with M_{LE-LR} = the bending moment following the linear elastic theory with limited redistribution

M_{el} = the bending moment following the linear elastic theory

Table 6.2: Ultimate loads and moment redistribution according to the linear elastic theory with limited redistribution for configurations with strengthening in the spans

Redistr.	F_u [kN]	strength. ratio [%]	Span		Mid-support	
			M_{LE-LR} [kNm]	$ratio_{mom.}$ [%]	**M_{LE-LR} [kNm]**	$ratio_{mom.}$ [%]
0 %	80.0	1.00	**69.1**	1.00	**67.2**	1.00
10 %	88.9	1.11	**79.9**	1.04	**67.2**	0.90
20 %	100.0	1.25	**93.3**	1.08	**67.2**	0.80
30 %	114.3	1.43	**110.6**	1.12	**67.2**	0.70

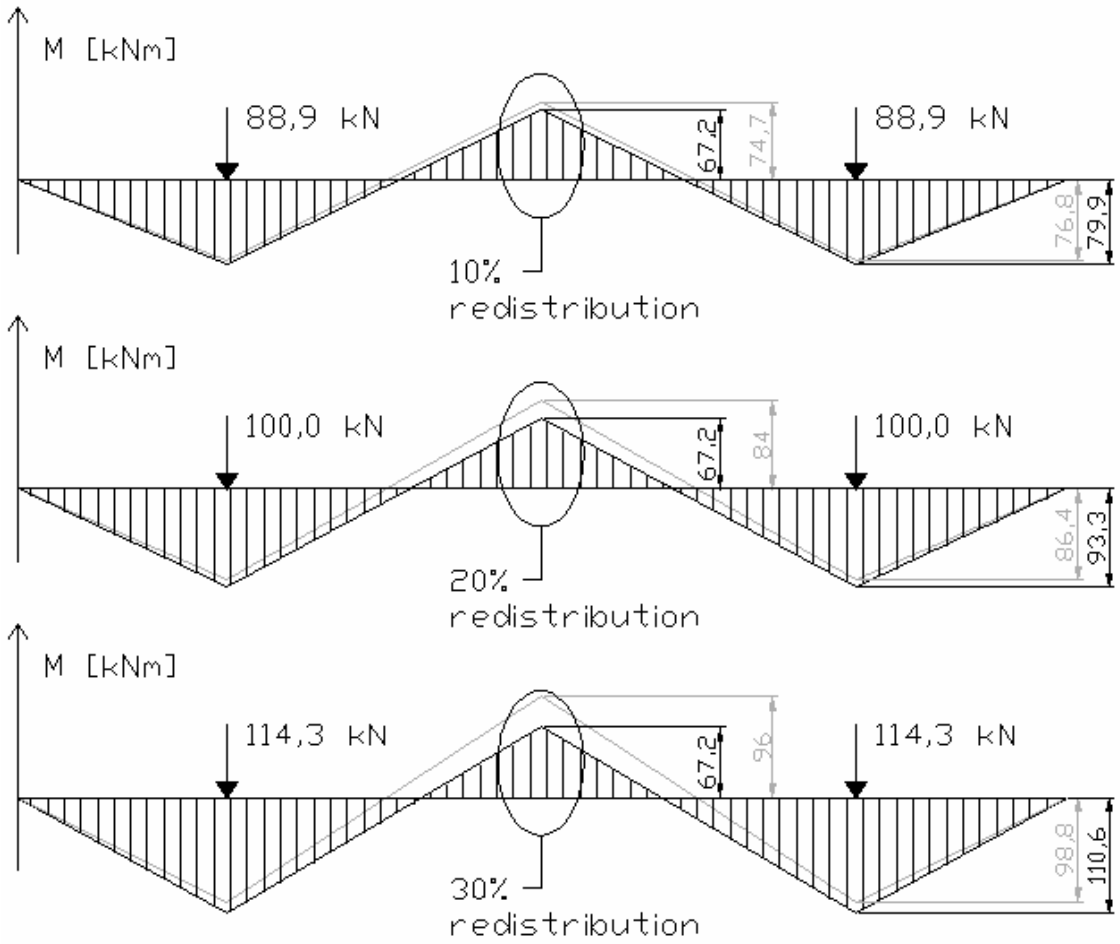

Fig. 6.9: Moment redistributions (10%, 20% and 30%) at ultimate of configurations with strengthening in the spans

In Table 6.3, the sections of the FRP which are needed to resist the increased span moments are given based on Fig. 6.9. Moreover, also the yielding moment of the span ($M_{y,span}$) and the ultimate moment at which a strain of 0.4 % in the laminates is obtained ($M_{u,0.4\%,span}$) are given.

Table 6.3: Strengthening configuration of the different redistribution cases

Redistr	FRP EBR			Steel EBR		
	$\rho_{f,span}$ [%]	$M_{y,span}$ [kNm]	$M_{u,0.4\%,span}$ [kNm]	$\rho_{s,add,span}$ [%]	$M_{y,span}$ [kNm]	$M_{u,span}$ [kNm]
10 %	0.05	75.3	79.9	0.07	75.9	79.9
20 %	0.11	84.2	93.3	0.18	88.6	93.3
30 %	0.18	95.7	110.6	0.32	105.2	110.6

The obtained results based on the linear elastic analysis with limited redistribution are verified in the next section (section 3.2.2.2). A verification of the ductility conditions of these strengthened beams is given in section 3.2.2.3.

3.2.2.2 Verification by means of non-linear theory

In Fig. 6.10 to Fig. 6.21, several graphs concerning both the FRP EBR strengthened configuration (left side of figure) and the Steel EBR strengthened configuration (right side of figure) are shown. For every configuration, two different moment redistribution graphs are given. First, in Fig. 6.10, Fig. 6.14 and Fig. 6.18, the critical moment at both the mid-support and the span are given in function of the applied point load. Secondly, in Fig. 6.11, Fig. 6.15 and Fig. 6.19, the redistribution factor at the mid-support is given in function of the applied point load. Finally both the ξ_u-factor (Fig. 6.12, Fig. 6.16 and Fig. 6.20) and the curvature (Fig. 6.13, Fig. 6.17 and Fig. 6.21) of the different critical sections are given. Most graphs for the FRP strengthened configuration exist out of two lines:

- full line: which corresponds to $\varepsilon_f \leq 0.40$ %
- dashed line: which corresponds to $\varepsilon_f > 0.40$ %

In the graphs of the neutral axis depth and the curvature, a vertical dashed line is noticed. These lines represent respectively the limitation of the neutral axis depth according to [1] (see Fig. 6.2) and the limitation of the curvature (see Fig. 6.4). In Table 6.4, the exact values of these limitations are given. Notice that limitation of the neutral axis depth is represented by a maximum value while the limitation of the curvature is represented by a minimum value. This minimum value of the curvature is obtained by applying Eq. 6.7 (with the effective depth, d = 370 mm).

Table 6.4: Limit values of neutral axe depth and curvature

	ξ_{max} [-]	χ_{min} [10^{-6} mm^{-1}]
0 %	0.448	21.1
10 %	0.368	25.7
20 %	0.288	32.9
30 %	0.208	45.5

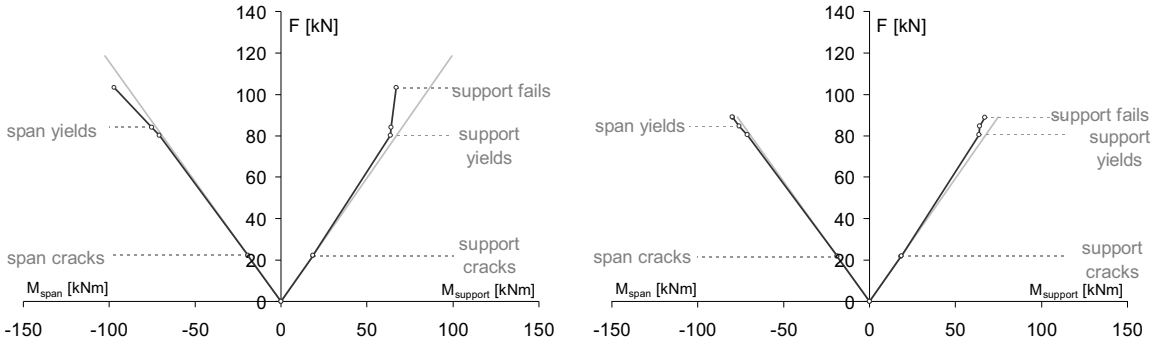

Fig. 6.10: 10% redistribution by applying FRP EBR in the spans (left figure) and by applying Steel EBR in the spans (right figure)

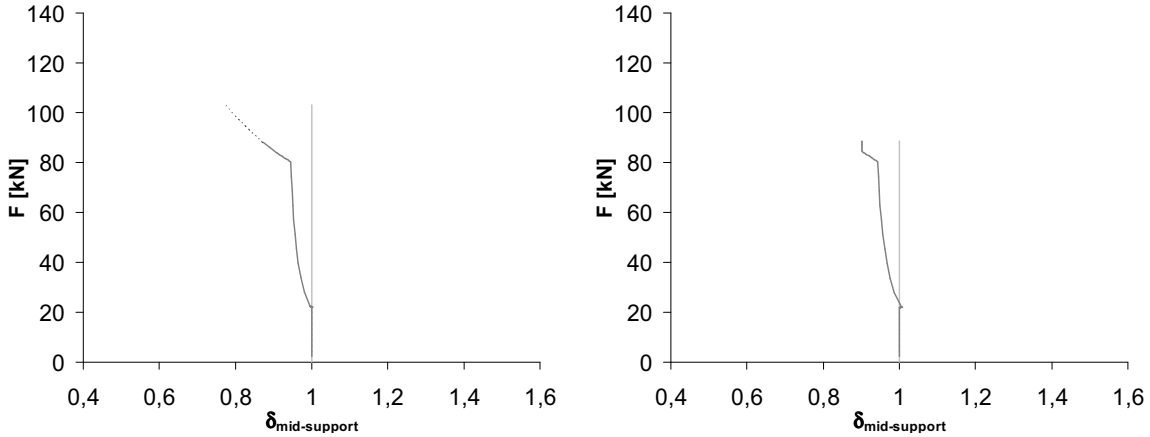

Fig. 6.11: Redistribution factor δ for 10 % redistribution (left – FRP EBR; right – Steel EBR)

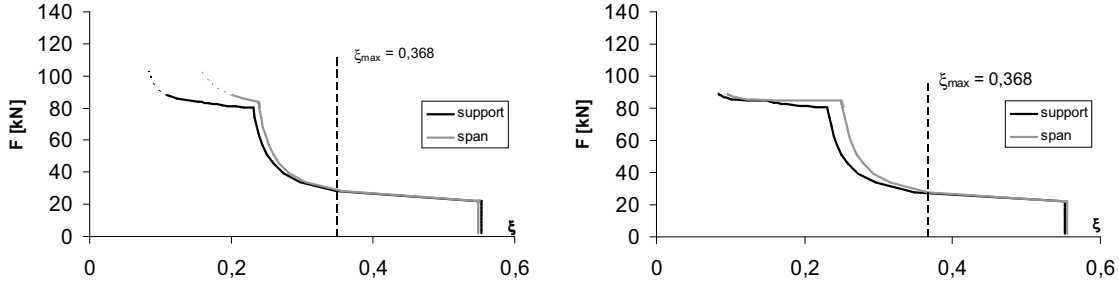

Fig. 6.12: ξ-factor for 10 % redistribution (left – FRP EBR; right – Steel EBR)

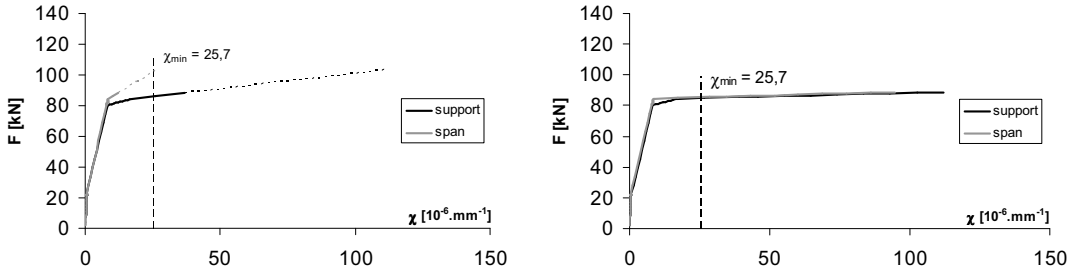

Fig. 6.13:Curvature for 10 % redistribution (left – FRP EBR; right – Steel EBR)

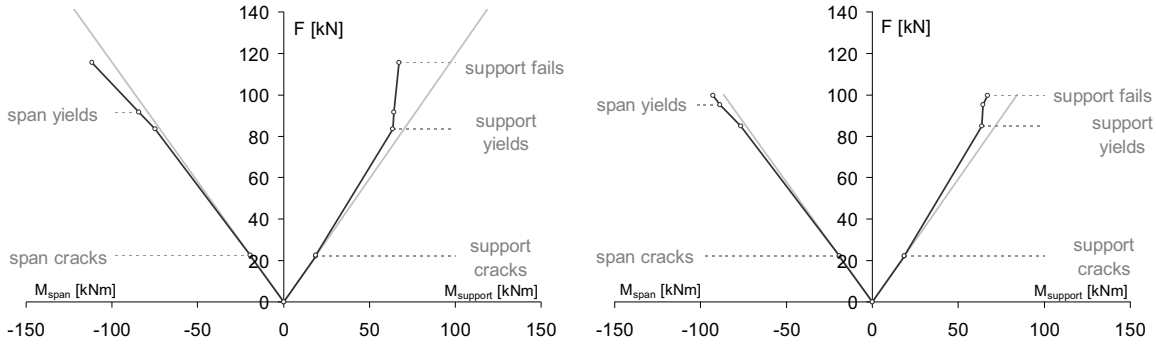

Fig. 6.14: 20% redistribution by applying FRP EBR in the spans (left figure) and by applying Steel EBR in the spans (right figure)

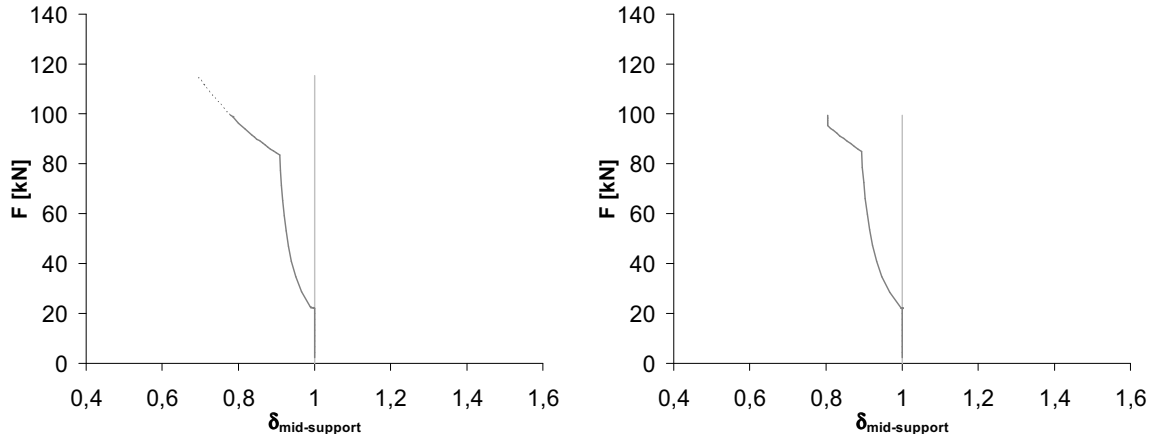

Fig. 6.15: Redistribution factor δ for 20 % redistribution (left – FRP EBR; right – Steel EBR)

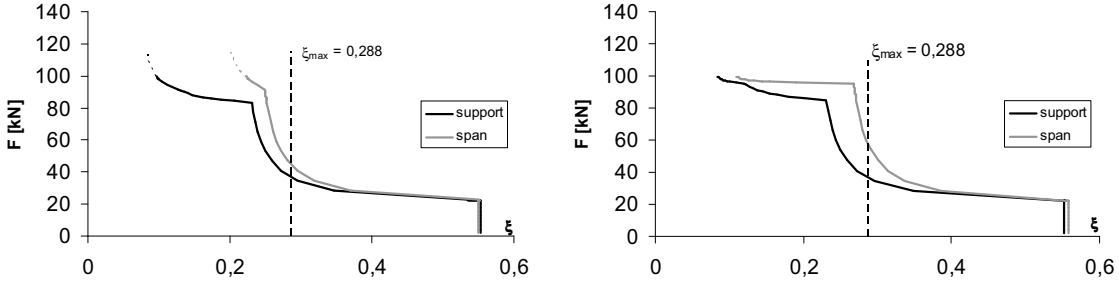

Fig. 6.16: ξ-factor for 20 % redistribution (left – FRP EBR; right – Steel EBR)

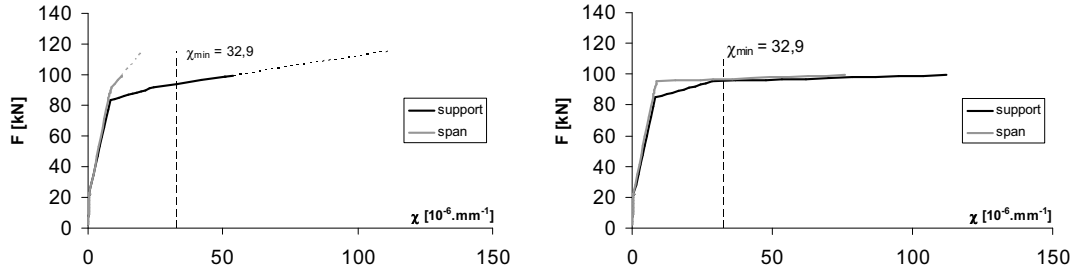

Fig. 6.17: Curvature for 20 % redistribution (left – FRP EBR; right – Steel EBR)

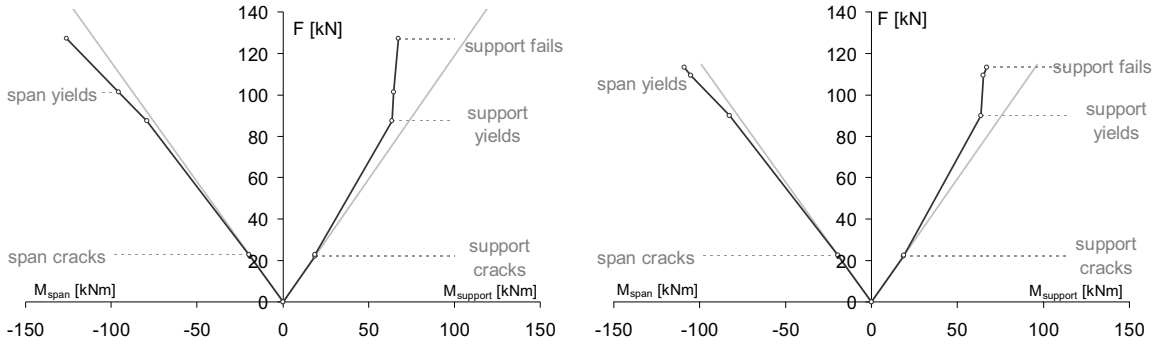

Fig. 6.18: 30% redistribution by applying FRP EBR in the spans (left figure) and by applying Steel EBR in the spans (right figure)

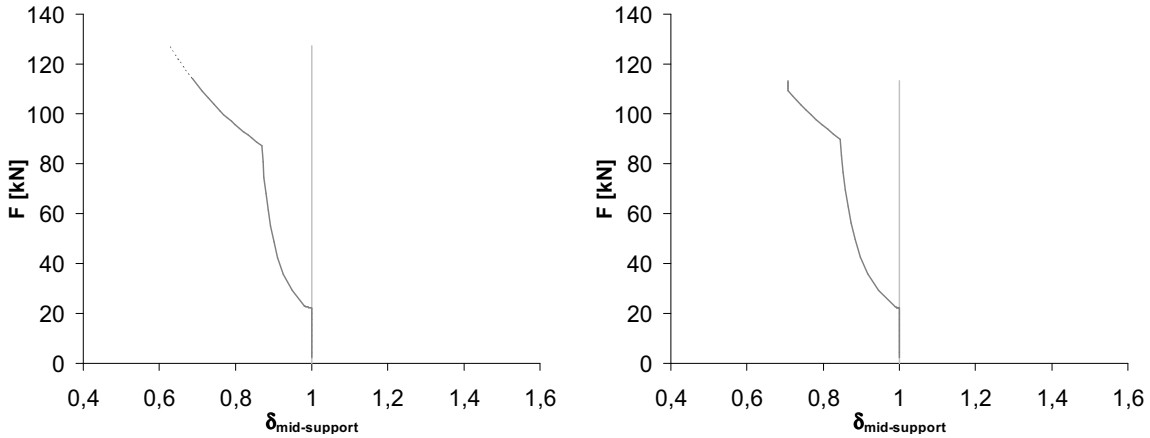

Fig. 6.19: Redistribution factor δ for 30 % redistribution (left – FRP EBR; right – Steel EBR)

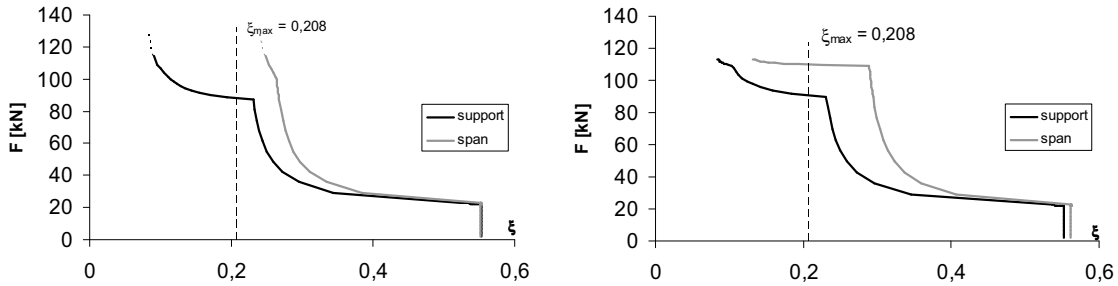

Fig. 6.20: ξ-factor for 30 % redistribution (left – FRP EBR; right – Steel EBR)

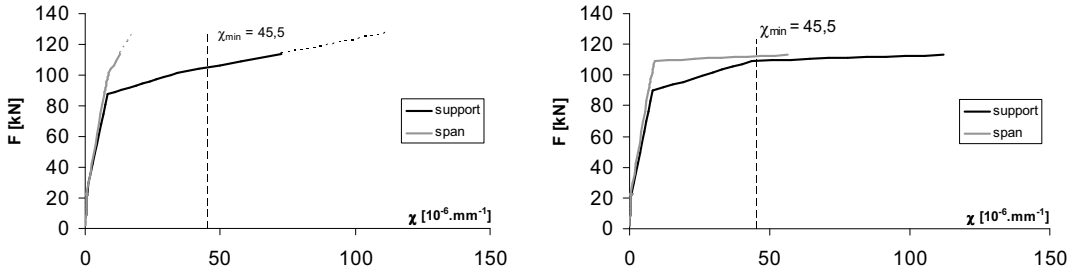

Fig. 6.21: Curvature for 30 % redistribution (left – FRP EBR; right – Steel EBR)

By analysing the moment redistribution graphs, it can be noticed that the redistribution of the FRP EBR and Steel EBR configurations are quite similar. In Table 6.5 the ultimate load according the linear elastic theory with limited redistribution and the ultimate load obtained from the non-linear theory are given. A good correspondence between these two ultimate loads is obtained. Regarding the FRP EBR configuration, it has to be noticed that these ultimate loads represent the values for which a strain of 0.40 % in the external FRP reinforcement is obtained, as mentioned above. Regarding the Steel EBR configuration, failure is obtained by concrete crushing of the first plastic hinge.

Furthermore the yielding loads of the different critical cross-sections (at the span and at the mid-support) are given in Table 6.5.

- Focussing on the yielding loads of the spans, the critical cross-sections of the FRP EBR configuration yield a little earlier compared to the Steel EBR configuration. This can also be noticed in Fig. 6.22.
- Focussing on the yielding loads of the mid-support, it is noticed that the critical cross-sections yield at almost the same load for both the FRP EBR and Steel EBR configuration.

Table 6.5: Ultimate and yielding loads for different strengthening configurations

Linear el. theory with limited red.	Non-linear theory						
		FRP EBR			Steel EBR		
	F_u [kN]	$F_{u,0.4\%}$ [kN]	$F_{y,span}$ [kN]	$F_{y,support}$ [kN]	F_u [kN]	$F_{y,span}$ [kN]	$F_{y,support}$ [kN]
0 %	80.0	80.8	77.2	75.6	80.8	77.2	75.6
10 %	88.9	88.1	84.0	80.3	88.8	84.6	80.4
20 %	100.0	99.5	91.5	83.5	99.5	95.3	84.9
30 %	114.3	114.1	101.3	87.3	113.2	109.3	89.9

The occurring amount of moment redistribution calculated according the non-linear theory is given in Table 6.6. A distinction is made between the total, the elastic and the plastic redistribution (see Fig 2.3 in Chapter 2).

- Concerning the total redistribution: similar values are obtained for both strengthening configurations. Moreover a good agreement is noticed between the required moment redistribution according the linear elastic theory with limited redistribution and the obtained moment redistribution (verified according to the non-linear theory)
- Concerning the elastic redistribution: a smaller elastic redistribution is noticed in the FRP EBR configuration compared to the Steel EBR configuration. This is due to the somewhat lower stiffness until yielding at the critical cross-section in the spans in the FRP EBR compared to the Steel EBR configuration (see Fig. 6.22).
- Concerning the plastic redistribution: a higher plastic redistribution is noticed in the FRP EBR configuration compared to the Steel EBR configuration. This is due to the remaining high stiffness after yielding at the critical cross section in the spans in the FRP EBR compared to the Steel EBR configuration (see Fig. 6.22). In the FRP EBR configuration, a continuously increasing value of redistribution is noticed after yielding of both critical cross-sections (see Fig. 6.11, Fig. 6.15 and Fig. 6.19). In the Steel EBR configuration on the other hand, a constant value of

redistribution (vertical line) is noticed (see Fig. 6.11, Fig. 6.15 and Fig. 6.19). This phenomenon is caused by a similar stiffness of all critical cross-sections after yielding in the Steel EBR configuration.

Table 6.6: Elastic, plastic and total redistribution for different strengthening configurations

Linear el. theory with limited red.	Non-linear theory					
	FRP EBR			Steel EBR		
	tot. red. [%]	el. red. [%]	pl. red. [%]	tot. red. [%]	el. red. [%]	pl. red. [%]
0 %	1.0	0.3	1.0	1.0	0.3	1.0
10 %	12.7	5.5	7.1	9.9	5.7	4.2
20 %	22.0	9.2	12.8	19.6	10.7	8.9
30 %	31.3	13.1	18.1	29.3	15.7	13.7

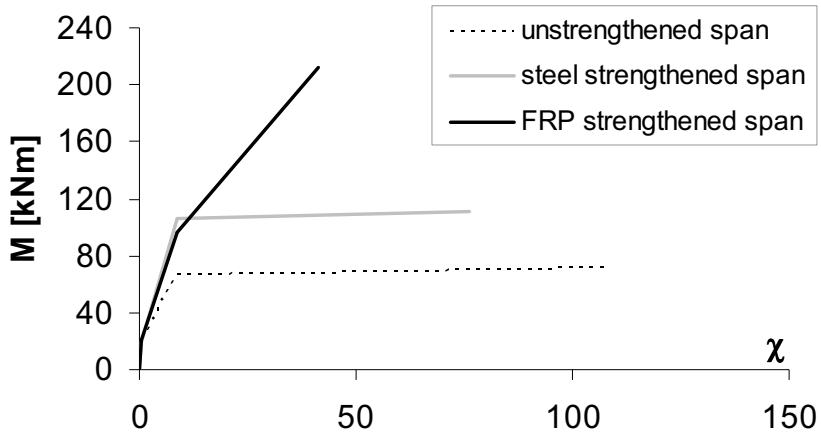

Fig. 6.22: Moment curvature of unstrengthened and strengthened critical cross-section at the span

3.2.2.3 Comparison between neutral axis depth (related to ξ_u-factor) and curvature (χ)

To check the plastic rotation capacity when applying the linear elastic theory with limited redistribution, the ultimate neutral axis depth (represented by the ξ_u-factor) of the first plastic hinge needs to be checked (see limitations in Table 6.4). The first plastic hinge in the strengthened configurations is obtained at the unstrengthened mid-support. The minimum ξ-factor at ultimate at this mid-support equals 0.084 (see Table 6.7) and fulfils consequently the limitations of the neutral axis depth (see Table 6.4). As a result, a sufficient plastic rotation capacity can be assumed.

As verification, the needed curvature (and related to this the needed rotation capacity) of the first plastic hinge is also determined according the non-linear theory (see Table 6.7). From this table it is noticed that the needed curvature in the first plastic hinge (mid-support) is smaller or equal to the maximum obtained curvature at the mid-support ($\chi_{u,support}$ = 112.0 10^{-6} mm^{-1}). In Fig. 6.13, Fig. 6.17 and Fig. 6.21 a similar result is obtained as the needed curvatures (at the end of the full lines) are smaller or equal than the maximum possible curvatures (end of dashed lines).

Table 6.7: Minimum neutral axis depth and maximum curvature at failure according to the non-linear theory

	Non-linear theory							
	FRP EBR				Steel EBR			
	$\xi_{u,span}$ [-]	$\chi_{u,span}$ [10^{-6} mm^{-1}]	$\xi_{u,support}$ [-]	$\chi_{u,support}$ [10^{-6} mm^{-1}]	$\xi_{u,span}$ [-]	$\chi_{u,span}$ [10^{-6} mm^{-1}]	$\xi_{u,support}$ [-]	$\chi_{u,support}$ [10^{-6} mm^{-1}]
0 %	0.087	108.6	0.084	112.0	0.087	108.6	0.084	112.0
10 %	0.201	12.3	0.109	36.8	0.096	94.8	0.084	112.0
20 %	0.223	12.6	0.097	53.7	0.110	76.1	0.084	112.0
30 %	0.248	13.0	0.091	72.5	0.131	56.5	0.084	112.0

Finally a considerable reduction of the needed curvature in the FRP EBR configuration compared to the Steel EBR configuration is observed (see Table 6.7). Nevertheless a similar moment redistribution is obtained.

3.2.2.4 Conclusions

The following conclusions concerning moment redistribution can be made for a two span beam strengthened with FRP in the spans:

- The required moment redistribution in the ultimate state according to the linear elastic theory with limited redistribution, corresponds very well with the obtained moment redistribution (verified according to the non-linear theory).
- The moment redistribution in the ultimate state exists out of an elastic redistribution (~ 40 %) and a plastic redistribution (~ 60 %).
- The plastic hinge in this configuration is expected at the unstrengthened mid-support. According to the limitations of the linear elastic theory with limited redistribution (Table 6.4), a sufficient plastic rotation capacity is available. This is also verified according the non-linear theory.
- A considerable reduction of the needed curvature in the FRP EBR configuration compared to the Steel EBR configuration is observed

3.2.3 Strengthened beam – case 2

3.2.3.1 Configuration based on strengthening with limited redistribution

Similar to the restrictions for strengthening the mid-supports in practical applications (see section 3.2.2), it also can happen that strengthening of the spans is not possible in practical applications. This is e.g. the case if a finishing layer, which is not allowed to be removed, is applied at the soffit of the beam or if only a too restricted working space is available due to technical installations at the soffit of the beam. In these situations, a redistribution of moments has to be introduced in order to keep the moment at the spans constant and to increase the applied load until the required ultimate load. By keeping the moment at the spans constant, no strengthening is needed at the spans but plastic hinges are expected to be formed at the critical cross-section in the spans (under the point loads).

A redistribution of the moments at the span of 10%, 20% and 30% will be discussed. In Table 6.8 the increased moments (after redistribution) are given which the mid-supports have to resist. In Fig. 6.23 both the moment distribution according to the linear elastic theory (grey lines) and the moment redistribution according to the linear elastic theory with limited redistribution (black curves) are given. It can be noticed that the bending moment in the spans of all redistributed configurations is similar to the bending moment of the unstrengthened reference beam.

Table 6.8: Ultimate loads and moment redistribution according to the linear elastic theory with limited redistribution for configurations with strengthening in the spans

Redistr.	F_u [kN]	strength. ratio [%]	Span M_{LE-LR} [kNm]	Span ratio$_{mom.}$ [%]	Mid-support M_{LE-LR} [kNm]	Mid-support ratio$_{mom.}$ [%]
0 %	80.0	1.00	**69.1**	1.00	**67.2**	1.00
10 %	88.9	1.11	**69.1**	0.90	**93.9**	1.26
20 %	100.0	1.25	**69.1**	0.80	**127.2**	1.51
30 %	114.3	1.43	**69.1**	0.70	**170.0**	1.77

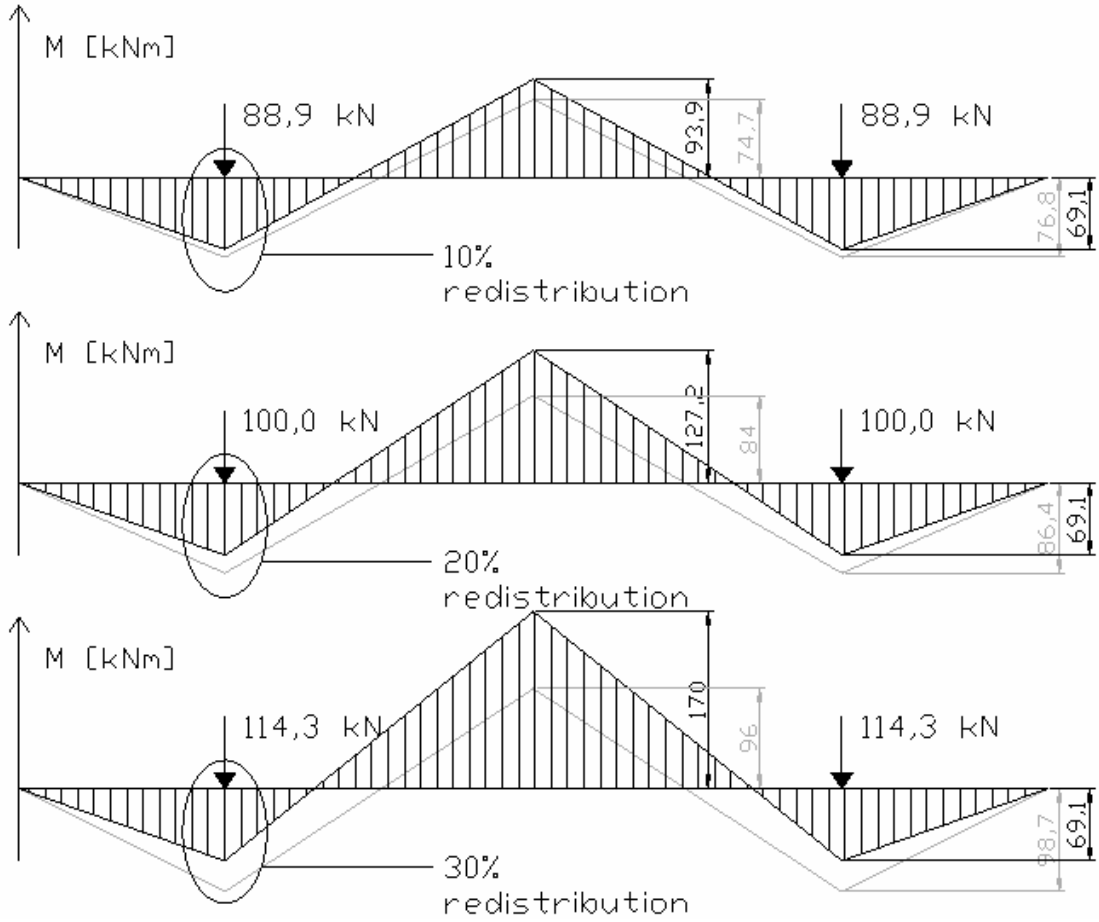

Fig. 6.23: Moment redistributions (10%, 20% and 30%) at ultimate state of configurations with strengthening at the mid-supports

Further in Table 6.8, the strengthening ratio is noticed and the ratios of the moments according to the linear elastic theory with limited redistribution compared to the moments according to the linear elastic theory at the critical cross-sections ($ratio_{mom}$) are given. Concerning the latter ratio, reference is made to Eq. 6.10.

In Table 6.9 the sections of the FRP which are needed to resist the increased moments at the supports can be noticed (according to Fig. 6.23). Also the yielding moment at the support ($M_{y,support}$) and the ultimate moment at which a strain of 0.4 % in the laminates is obtained ($M_{u,0.4\%,support}$) are given.

Further in Table 6.9 also strengthening by means of externally bonded steel plates (Steel EBR) is mentioned.

Table 6.9: Strengthening configuration of the different redistribution cases

Redistr	FRP EBR			Steel EBR		
	$\rho_{f,support}$ [%]	$M_{y,support}$ [kNm]	$M_{u,0.4\%,support}$ [kNm]	$\rho_{s,add,support}$ [%]	$M_{y,support}$ [kNm]	$M_{u,support}$ [kNm]
10 %	0.11	84.5	93.9	0.21	89.2	93.9
20 %	0.26	107.0	127.3	0.48	121.2	127.2
30 %	0.44	136.2	170.0	0.84	162.5	170.0

The obtained results based on the linear elastic analysis with limited redistribution are verified in the next section (section 3.2.3.2). A verification of the ductility conditions of these strengthened beams is given in section 3.2.3.3.

3.2.3.2 Verification by means of non-linear theory

In Fig. 6.24 to Fig. 6.35, the graphs for the different moment redistribution ratios are given. In these graphs, the moment redistribution, the redistribution factor, the neutral axis depth of the critical cross-sections and the curvature of the critical cross-sections are given in function of the applied point load. The graphs at the left concern the FRP EBR configuration, while the graphs at the right concern the Steel EBR configuration. Remark that some graphs exist out of two lines:

- full line: represents the parameter evolution for $\varepsilon_f \leq 0.40$ %
- dashed line: represents the parameter evolution for $\varepsilon_f > 0.40$ %

In the graphs of the neutral axis depth and the curvature, a vertical dashed line is noticed. These lines represent respectively the limitation of the neutral axis depth according to [1] (see Fig. 6.2) and the limitation of the curvature (see Fig. 6.4). In Table 6.4, the exact values of these limitations are given.

Regarding to the ultimate loads given in Table 6.10 according the non-linear theory, similar values are obtained for all strengthening configurations. Moreover, these values agree very well with the required ultimate loads according to the linear elastic theory with limited redistribution.

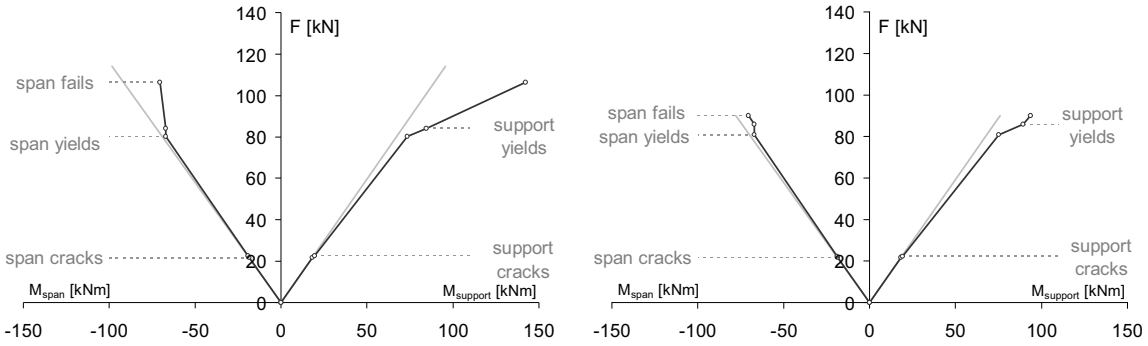

Fig. 6.24: 10% redistribution by applying FRP EBR at the mid-support (left figure) and by applying Steel EBR at the mid-support (right figure)

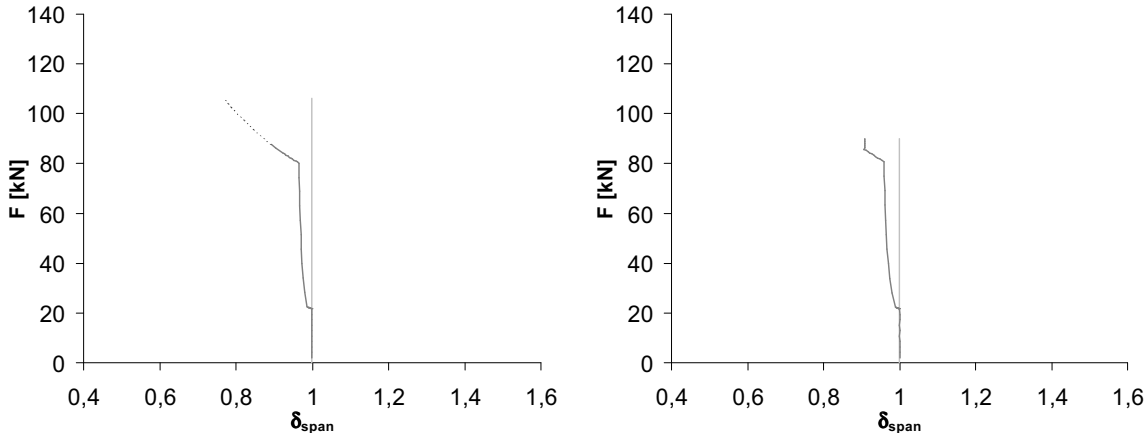

Fig. 6.25: Redistribution factor δ for 10 % redistribution (left – FRP EBR; right – Steel EBR)

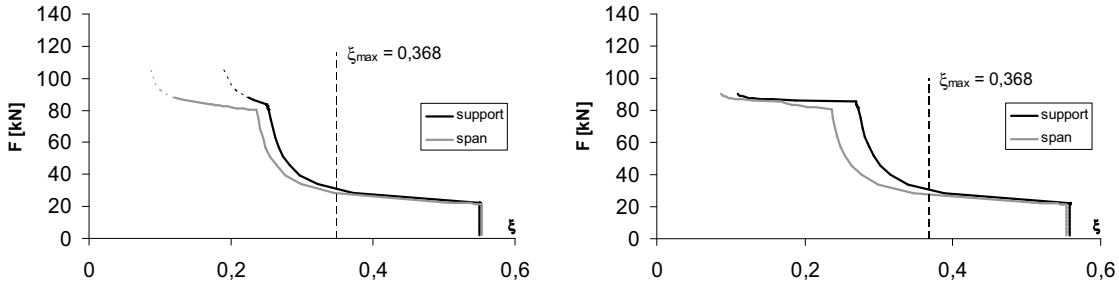

Fig. 6.26: ξ-factor for 10 % redistribution (left – FRP EBR; right – Steel EBR)

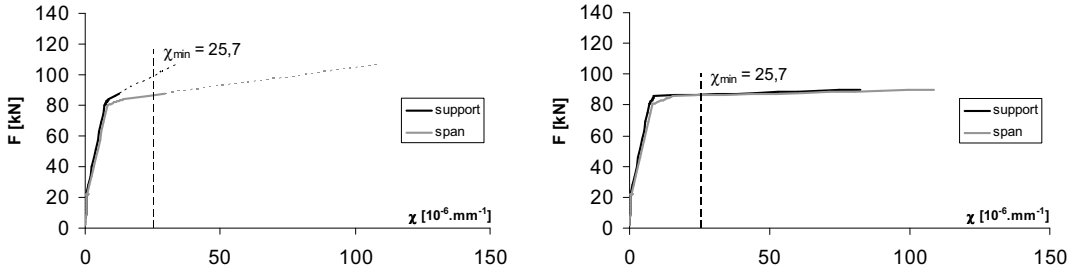

Fig. 6.27:Curvature for 10 % redistribution (left – FRP EBR; right – Steel EBR)

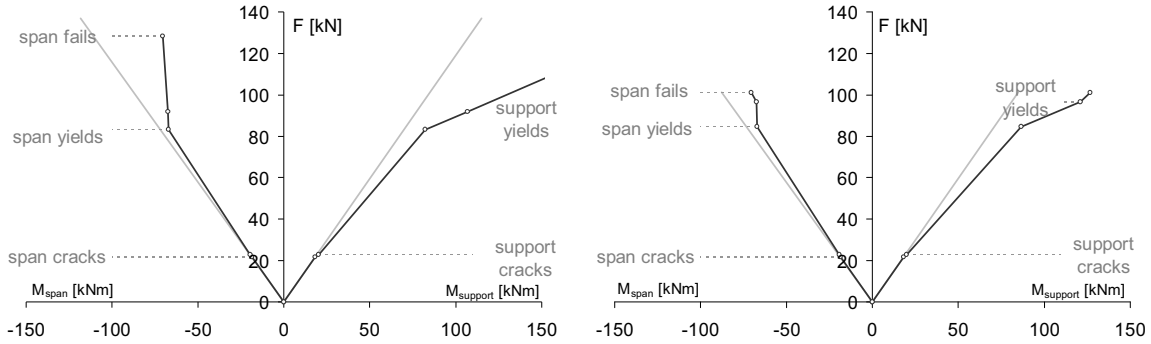

Fig. 6.28: 20% redistribution by applying FRP EBR at the mid-support (left figure) and by applying Steel EBR at the mid-support (right figure)

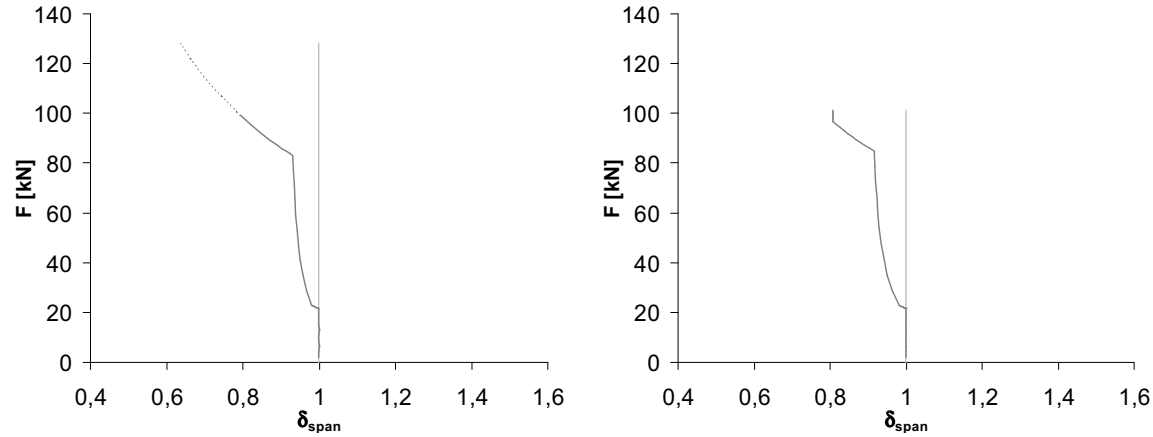

Fig. 6.29: Redistribution factor δ for 20 % redistribution (left – FRP EBR; right – Steel EBR)

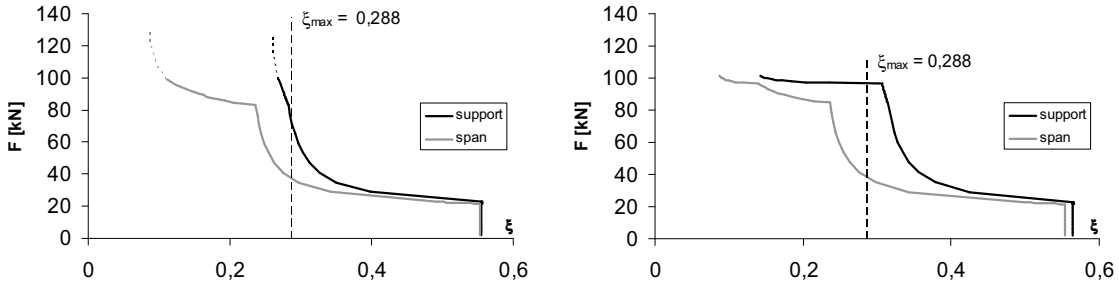

Fig. 6.30: ξ-factor for 20 % redistribution (left – FRP EBR; right – Steel EBR)

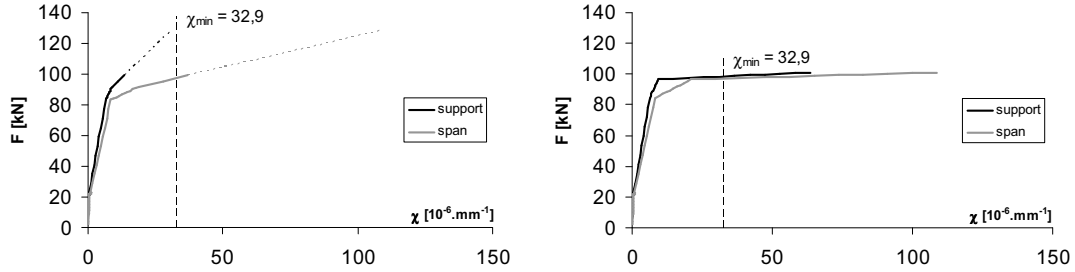

Fig. 6.31: Curvature for 20 % redistribution (left – FRP EBR; right – Steel EBR)

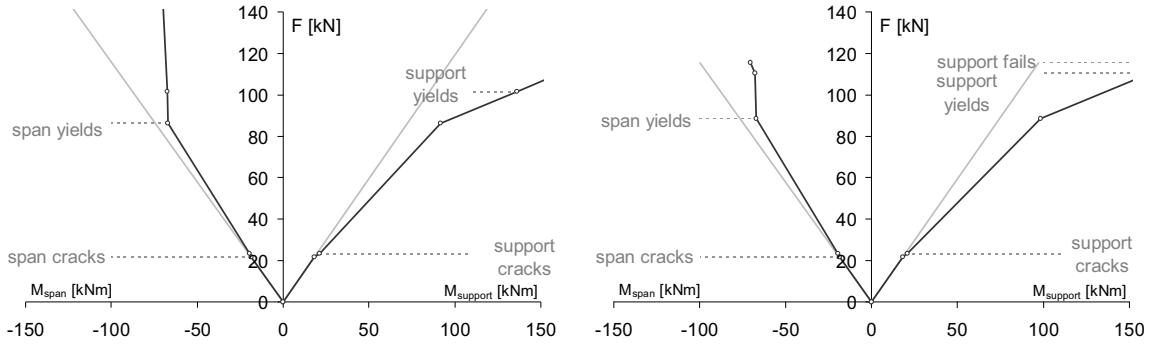

Fig. 6.32: 30% redistribution by applying FRP EBR at the mid-support (left figure) and by applying Steel EBR at the mid-support (right figure)

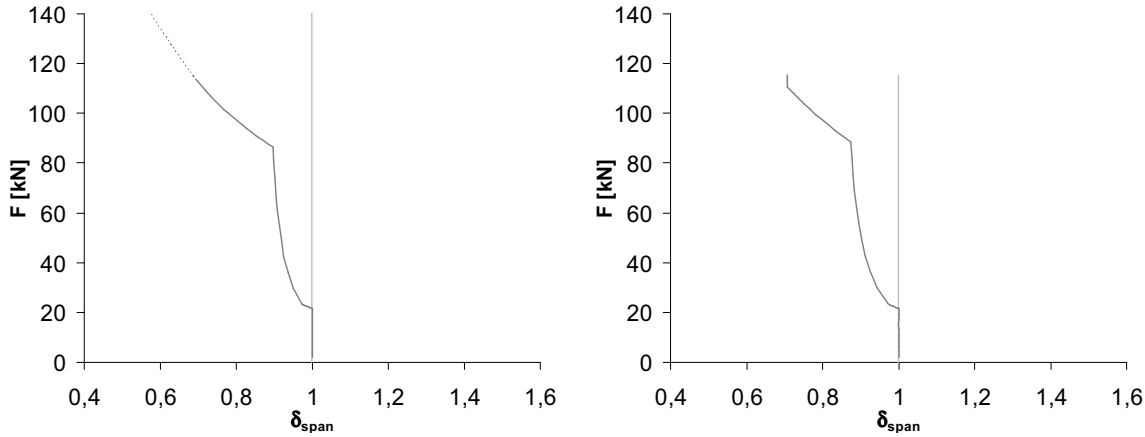

Fig. 6.33: Redistribution factor δ for 30 % redistribution (left – FRP EBR; right – Steel EBR)

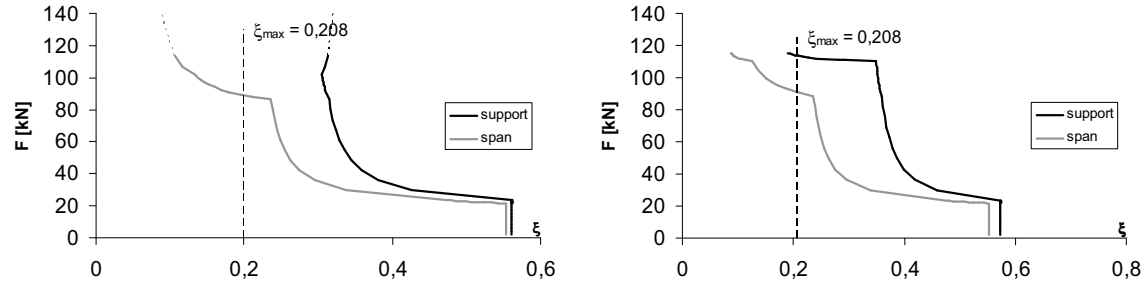

Fig. 6.34: ξ-factor for 30 % redistribution (left – FRP EBR; right – Steel EBR)

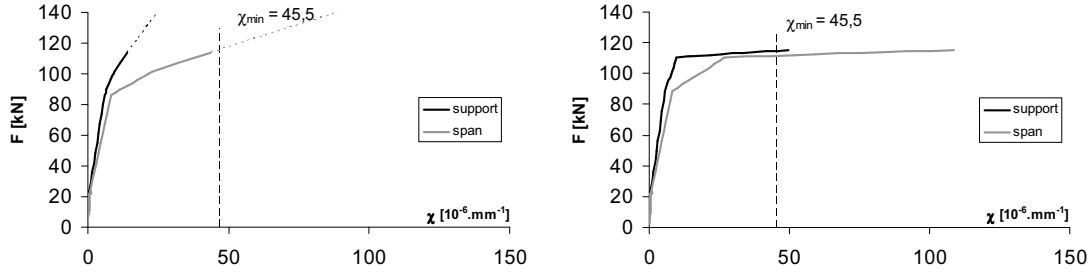

Fig. 6.35: Curvature for 30 % redistribution (left – FRP EBR; right – Steel EBR)

Furthermore in Table 6.10, the yielding loads of the different critical cross-sections (at the span and at the mid-support) are given.

- Focussing on the yielding loads of the mid-support, the critical cross-section of the FRP EBR configuration yields a little earlier compared to the Steel EBR configuration. This is confirmed by Fig. 6.36, in which it is noticed that the critical cross-section of the FRP strengthened mid-support yields earlier compared to the steel strengthened mid-support.
- Focussing on the yielding loads of the spans, it is noticed that the critical cross-sections yield at almost the same load for both the FRP EBR and Steel EBR configuration.

Table 6.10: Ultimate and yielding loads of different strengthening configurations

Linear el. theory with limited red.	Non-linear theory						
		FRP EBR			Steel EBR		
	$F_{u,required}$ [kN]	$F_{u,0.4\%}$ [kN]	$F_{y,span}$ [kN]	$F_{y,support}$ [kN]	F_u [kN]	$F_{y,span}$ [kN]	$F_{y,support}$ [kN]
0 %	80.0	80.8	77.2	75.6	80.8	77.2	75.6
10 %	88.9	87.7	80.3	84.1	90.0	80.8	85.7
20 %	100.0	99.1	83.1	91.7	101.1	84.6	96.6
30 %	114.3	113.5	86.4	101.6	115.4	88.6	110.5

In Table 6.11, the total, the elastic and the plastic amount of redistribution at the spans is given.

- Concerning the total redistribution: similar values are obtained for both strengthening configurations. Moreover a good agreement is noticed between the required moment redistribution according the linear elastic theory with limited redistribution and the obtained moment redistribution (verified according to the non-linear theory)
- Concerning the elastic redistribution: a smaller elastic redistribution is noticed in the FRP EBR configuration compared to the Steel EBR configuration. This is due to the somewhat lower stiffness until yielding at the critical cross-section in the mid-support in the FRP EBR compared to the Steel EBR configuration (see Fig. 6.36). Further it is remarkable that only $1/3^{rd}$ of the redistribution at the spans in the FRP EBR configuration is obtained in the elastic stage.
- Concerning the plastic redistribution: a higher plastic redistribution is noticed in the FRP EBR configuration compared to the Steel EBR configuration. This is due to the remaining high stiffness after yielding at the critical cross section in the mid-support in the FRP EBR configuration compared to the Steel EBR configuration (see Fig. 6.36). In the FRP EBR configuration, a continuously increasing value of redistribution is noticed after yielding of both critical cross-sections. In the Steel EBR configuration on the other hand, a constant value of redistribution (vertical line) is noticed (see Fig. 6.25, Fig. 6.29 and Fig. 6.33). This phenomenon is caused by a similar stiffness of all critical cross-sections after yielding in the Steel EBR configuration.

Table 6.11: Elastic, plastic and total redistribution of different strengthening configurations

Linear el. theory with limited red.	Non-linear theory					
	FRP EBR			Steel EBR		
	tot. red. [%]	el. red. [%]	pl. red. [%]	tot. red. [%]	el. red. [%]	pl. red. [%]
0 %	1.0	0.3	1.0	1.0	0.3	1.0
10 %	10.7	3.5	7.2	9.2	4.2	5.1
20 %	20.6	6.8	13.8	19.2	8.5	10.7
30 %	30.4	10.3	20.1	29.3	12.6	16.7

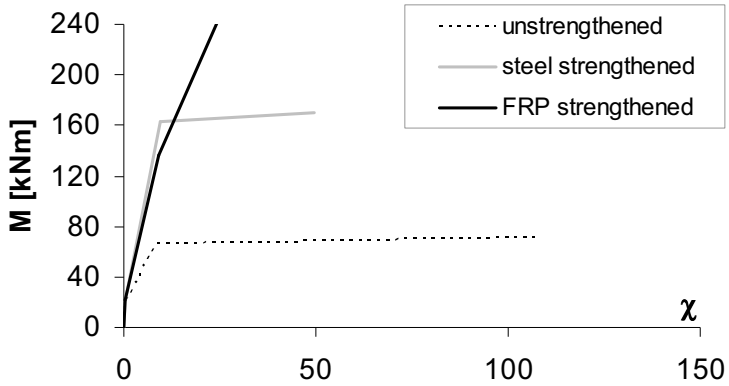

Fig. 6.36: Moment curvature of unstrengthened and strengthened critical cross-section at the mid-support

3.2.3.3 Comparison between neutral axis depth (related to ξ-factor) and curvature (χ)

To check the plastic rotation capacity when applying the linear elastic theory with limited redistribution, the ultimate neutral axis depth (represented by the ξ_u-factor) of the first plastic hinge needs to be checked (see limitations in Table 6.4). The first plastic hinge in the strengthening configurations is obtained in the unstrengthened spans. The minimum ξ-factor at these spans equals 0.087 (see Table 6.12) and fulfils consequently the limitations of the neutral axis depth (see Table 6.4). As a result a sufficient plastic rotation capacity can be assumed.

As verification, the needed curvature (and related to this the needed rotation capacity) of the first plastic hinge is determined according the non-linear theory (see Table 6.12). From this table it is noticed that the needed curvature in the first plastic hinges (spans) are smaller or equal to the maximum possible curvature at the spans ($\chi_{u,span}$ = 108.6 10^{-6} mm^{-1}). In Fig. 6.27, Fig. 6.31 and Fig. 6.35 a similar result is obtained, as the needed curvatures (at the end of the full lines) are smaller or equal than the maximum possible curvatures (end of dashed lines).

Table 6.12: Minimum neutral axis depth and maximum curvature at failure according to the non-linear theory

	Non-linear theory							
	FRP EBR				Steel EBR			
	ξ_{span} [-]	χ_{span} [10^{-6} mm^{-1}]	$\xi_{support}$ [-]	$\chi_{support}$ [10^{-6} mm^{-1}]	ξ_{span} [-]	χ_{span} [10^{-6} mm^{-1}]	$\xi_{support}$ [-]	$\chi_{support}$ [10^{-6} mm^{-1}]
0 %	0.087	108.6	0.084	112.0	0.087	108.6	0.084	112.0
10 %	0.121	29.6	0.224	12.6	0.087	108.6	0.109	82.4
20 %	0.112	36.8	0.268	13.3	0.087	108.6	0.142	63.7
30 %	0.106	43.6	0.314	14.1	0.087	108.6	0.190	49.7

3.2.3.4 Conclusions

The following conclusions concerning moment redistribution can be made for two span beams strengthened with FRP at the mid-support:

- The required moment redistribution in the ultimate state according to the linear elastic theory with limited redistribution corresponds very well with the obtained moment redistribution (verified according the non-linear theory).
- The moment redistribution in ultimate state exists out of an elastic redistribution (~ 33 %) and a plastic redistribution (~ 66 %).
- The plastic hinges in this configuration are expected at the unstrengthened spans. According to the limitations of the linear elastic theory with limited redistribution (Table 6.4), a sufficient plastic rotation capacity is available. This is also verified according the non-linear theory.
- A considerable reduction of the needed curvature in the FRP EBR configuration compared to the Steel EBR configuration is observed, especially for the low redistribution ratios (10 % and 20 %).

3.2.4 Comparison between case 1 and case 2

In Table 6.13, the ultimate moments at the mid-support and in the spans are given. Remark that for a given redistribution ratio, independent of case 1 and case 2, an equal ultimate load according to 'the linear elastic theory with limited redistribution' is obtained.

Table 6.13: Ratio of ultimate moments of strengthened beam to ultimate moments of unstrengthened beam in case 1 and case 2

		case 1				case 2			
Red. [%]	F_u [kN]	$M_{u,sprt}$ [kNm]	ratio [%]	$M_{u,span}$ [kNm]	ratio [%]	$M_{u,sprt}$ [kNm]	ratio [%]	$M_{u,span}$ [kNm]	ratio [%]
0	80	67.2	1.00	69.1	1.00	67.2	1.00	69.1	1.00
10	89.9	67.2	1.00	79.9	1.16	93.9	1.40	69.1	1.00
20	100.0	67.2	1.00	93.3	1.35	127.2	1.89	69.1	1.00
30	114.3	67.2	1.00	110.6	1.60	170.0	2.53	69.1	1.00

By comparing case 1 and case 2, applied on a two-span beam, it has to be taken into account that in case 1 two span zones need to be strengthened while

in case 2 only the mid-support zone needs to strengthened. The amount (cross-section) of needed reinforcement (both FRP EBR and Steel EBR) to obtain the intended strengthening ratio is given in Table 6.14. Fig. 6.37 is giving a visualisation of the amounts. The first strengthening configuration (case 1 – EBR in the spans and $M_{support}$ remains constant) is more economical compared to the second strengthening configuration (case 2 - EBR at the mid-support and M_{span} remains constant).

Table 6.14: Total amount (cross-section) of additional reinforcement needed to obtain the intended strengthening ratio

		case 1		case 2	
Red. [%]	F_u [kN]	FRP EBR [mm²]	Steel EBR [mm²]	FRP EBR [mm²]	Steel EBR [mm²]
0	80	0	0	0	0
10	89.9	42 (2 x 21)	55 (2 x 27)	89	137
20	100.0	87 (2 x 43)	133 (2 x 66)	204	337
30	114.3	146 (2 x 73)	237 (2 x 118)	355	603

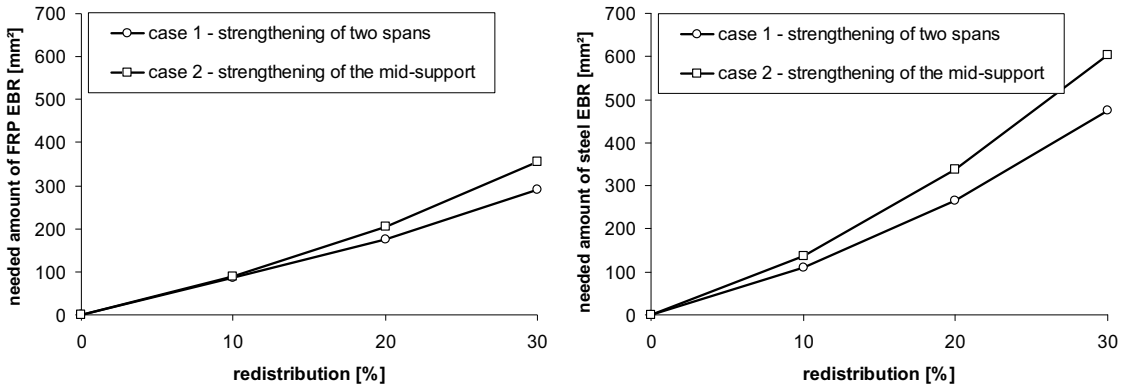

Fig. 6.37: Total amount of additional reinforcement needed to obtain the intended strengthening ratio

Further from Fig. 6.37, it can be concluded that a considerably smaller amount of reinforcement is needed in the FRP-EBR configuration compared to the Steel-EBR configuration. This despite the fact that the example considers FRP debonding at 0.40 % versus no premature debonding for steel EBR.

The above mentioned values are only valid for the two span beam given in Fig. 6.5 (λ = 2/3). Similar results can be obtained for two-span beams with other λ-values.

For infinitely beams with uniformly distributed loading an opposite conclusion is obtained. In Table 6.15 the ultimate moments of the spans and the intermediate supports are given for an infinitely long beam with span lengths equal to 4 meter. From Table 6.15 it can be noticed that the needed strengthening of the span zones in case 1 is twice the value needed for strengthening of the support zones in case 2. With this in mind, contrary to the two-span beams, it seems that for an infinitely long continuous beam the strengthening configuration of case 2 is more economical compared to the strengthening configuration of case 1.

Table 6.15: Ratio of ultimate moments in strengthened beam to ultimate moments in unstrengthened beam for case 1 and case 2

		case 1				case 2			
Red. [%]	p_u [kN/m]	$M_{u,sprt}$ [kNm]	ratio [%]	$M_{u,span}$ [kNm]	ratio [%]	$M_{u,sprt}$ [kNm]	ratio [%]	$M_{u,span}$ [kNm]	ratio [%]
0	20.0	26.7	1.00	13.3	1.00	26.7	1.00	13.3	1.00
10	22.2	26.7	1.00	17.8	1.33	31.1	1.17	13.3	1.00
20	25.0	26.7	1.00	23.3	1.75	36.7	1.38	13.3	1.00
30	28.6	26.7	1.00	30.5	2.29	43.8	1.64	13.3	1.00

3.2.5 Strengthened beam – case 3

3.2.5.1 Configuration based on strengthening with limited redistribution

Also in case 3, the linear elastic internal steel configuration is adopted for the unstrengthened reference beam (see section 3.2.1). This time, the bearing capacity of this reference beam is increased by using FRP EBR in both the spans and at the mid-support. In the strengthened configuration a failure load equal to 114.3 kN is required, similar to the 30 % redistribution configurations of case 1 and case 2 (see sections 3.2.2 and 3.2.3 respectively). This failure load corresponds to the linear elastic moment distribution shown in Fig. 6.38. Instead of applying a redistribution of 30 %, this time a redistribution of only 20 % and 10 % is introduced. The difference of the moment redistribution ratios used in this section compared to the redistribution ratio of 30 % used in case 1 and case 2, is taken by FRP EBR at the critical sections. Hence, not one zone but both the mid-support and the span zones need to be strengthened. As the FRP EBR is a fully linear elastic material, the plastic rotation capacity at the hinges is restrained (see Chapter 4). Therefore in this section, the term 'plastic hinge' is replaced by 'restrained hinge'.

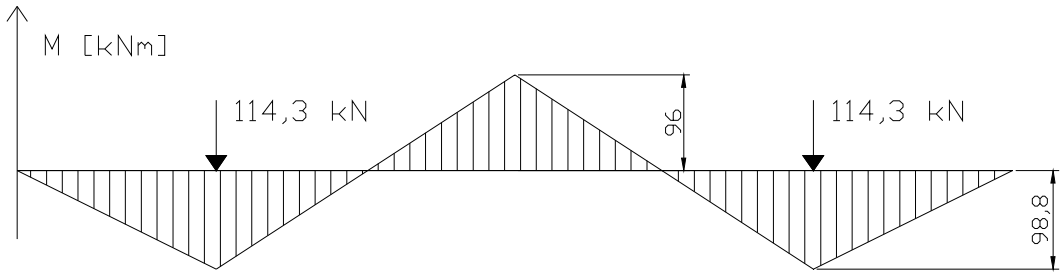

Fig. 6.38: Linear elastic moment distribution as starting point for case 3

Remark that the above mentioned moment redistribution can be introduced at the mid-support (case 3.A – first restrained hinge at the mid-support) or at the spans (case 3.B – first restrained hinges at the spans). Following distinction is made:

- case 3.A: Redistribution of the mid-support moments, by which a restrained hinge is expected at this mid-support (see Fig. 6.39)
  - case 3.A–30%: Redistribution of 30 % of the mid-support moment: there is no need for strengthening of the mid-support (see the 30 % redistribution configuration in case 1)
  - case 3.A–20%: Redistribution of 20 % of the mid-support moment: this results in a needed strengthening of the mid-support.
  - case 3.A–10%: Redistribution of 10 % of the mid-support moment: this results in a needed strengthening of the mid-support.
- case 3.B: Redistribution of the span moments, by which restrained hinges are expected in these spans (see Fig. 6.40)
  - case 3.B–30%: Redistribution of 30 % of the span moments: there is no need for strengthening of the spans (see the 30 % redistribution configuration in case 2; section 3.2.3)
  - case 3.B–20%: Redistribution of 20 % of the span moments: this results in a needed strengthening of the spans
  - case 3.B–10%: redistribution of 10 % of the span moments. this results in a needed strengthening of the spans

In Table 6.16, Fig. 6.39 and Fig. 6.40 both the moment distribution according to the linear elastic theory (grey curve in Fig. 6.39 and Fig. 6.40) and the moment redistribution according to the linear elastic theory with limited redistribution (black curve in Fig. 6.39 and Fig. 6.40) are noticed.

Table 6.16: Ultimate loads and moment redistribution according to the linear elastic theory with limited redistribution for configurations with strengthening in both the spans and the support

case	Redistr.	F_u [kN]	strength. ratio [%]	Span $\mathbf{M_{LE\text{-}LR}}$ **[kNm]**	Span $ratio_{mom.}$ [%]	Mid-support $\mathbf{M_{LE\text{-}LR}}$ **[kNm]**	Mid-support $ratio_{mom.}$ [%]
	0 %	80.0	1.00	**69.1**	1.00	**67.2**	1.00
3.A–30%	30 %	114.3	1.43	**110.3**	1.12	**67.2**	0.70
3.A-20%	20 %	114.3	1.43	**106.5**	1.08	**76.8**	0.80
3.A-10%	10 %	114.3	1.43	**102.6**	1.04	**86.4**	0.90
3.B–30%	30 %	114.3	1.43	**69.1**	0.70	**170.1**	1.77
3.B-20%	20 %	114.3	1.43	**79.0**	0.80	**145.4**	1.51
3.B-10%	10 %	114.3	1.43	**88.9**	0.90	**120.7**	1.26

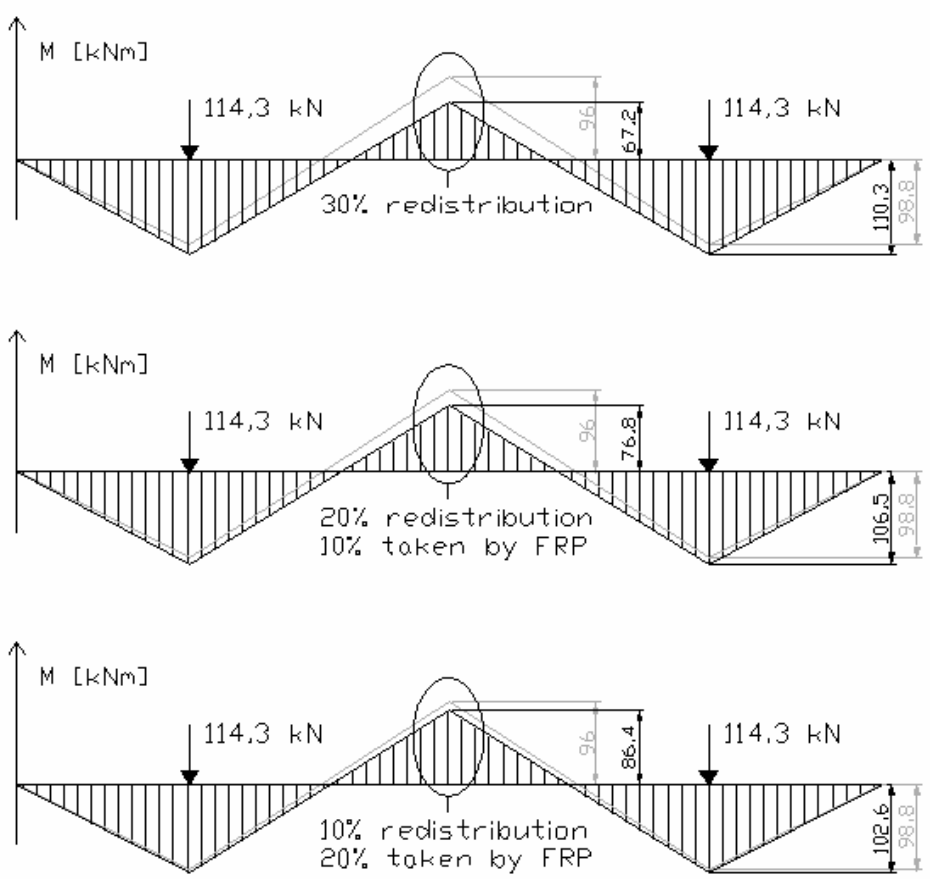

Fig. 6.39: Moment redistributions of case 3.A-30%, case 3.A-20% and case 3.A-10%

The material properties used in this analytical study again are equal to the properties used in previous sections (see Table 6.1). In Table 6.17, both the internal and external reinforcement ratios of all different cases considered above are given.

Table 6.17: Reinforcement ratios for the different cases considered

	case	$\rho_{f,span}$ [%]	$\rho_{s,span}$ [%]	$\rho_{f,support}$ [%]	$\rho_{s,support}$ [%]
see section 3.2.2	3.A–30%	0.18	0.53	0.00	0.50
	3.A-20%	0.17	0.53	0.05	0.50
	3.A-10%	0.15	0.53	0.09	0.50
see section 3.2.3	3.B–30%	0.00	0.53	0.44	0.50
	3.B-20%	0.05	0.53	0.35	0.50
	3.B-10%	0.09	0.53	0.24	0.50

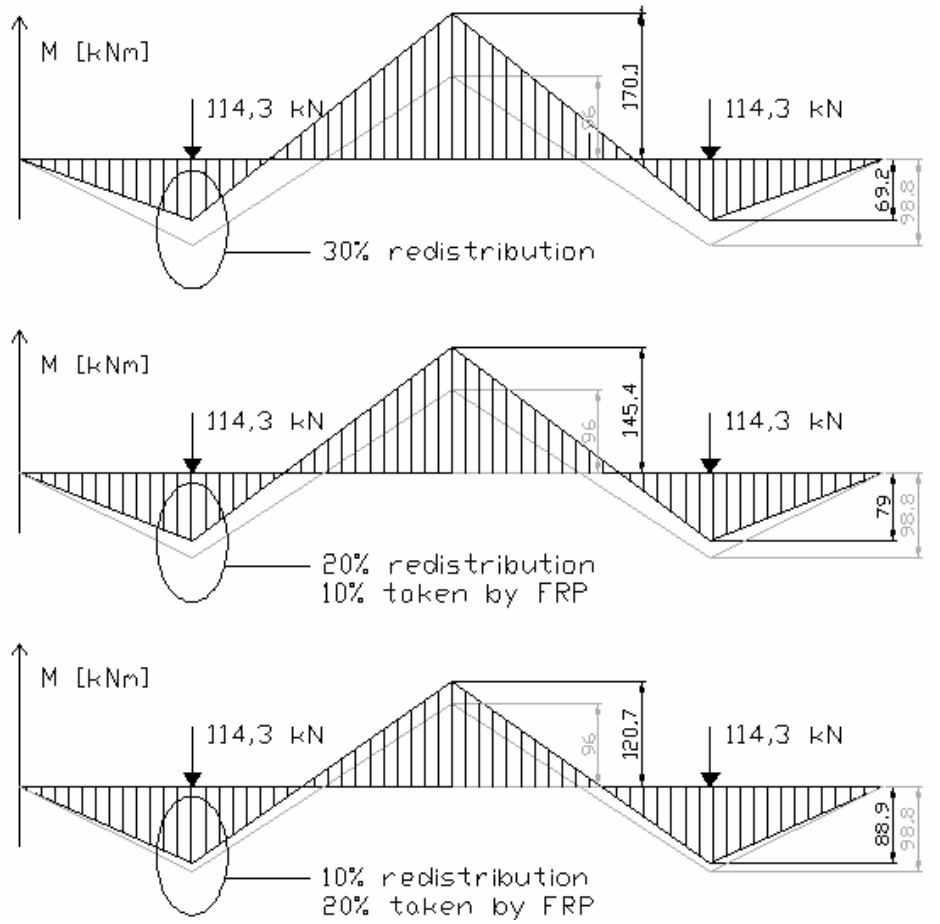

Fig. 6.40: Moment redistributions of case 3.B-30%, case 3.B-20% and case 3.B-10%

The obtained results based on the linear elastic analysis with limited redistribution are verified in the next section (section 3.2.5.2). A verification of the ductility conditions of these strengthened beams is given in section 3.2.5.3.

3.2.5.2 Verification by means of non-linear theory

In Fig. 6.41 to Fig. 6.48, the graphs for the different redistribution ratios are given. The graphs at the left hand side concern the strengthening configurations with redistribution of the mid-support moment (case 3.A). The graphs at the right hand side concern the strengthening configurations with redistribution of the span moments (case 3.B). For case 3.A-30% and case 3.B-30% no results are given as reference is made to sections 3.2.2 and 3.2.3 respectively.

In Table 6.18, the ultimate loads according to the linear elastic theory with limited redistribution and the obtained ultimate loads according to the non-linear theory are given. For simplicity, it is assumed again that debonding occurs at a FRP strain of 0.40 %.

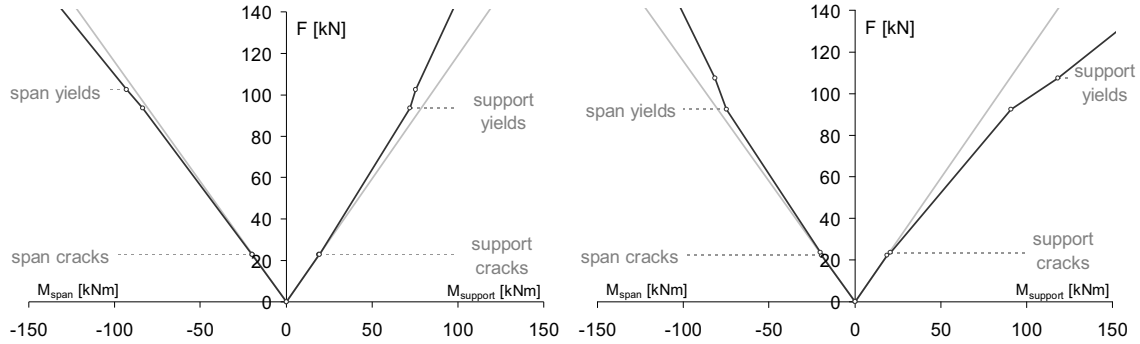

Fig. 6.41: 20% redistribution by applying FRP EBR in both the spans and the mid-support (left - case 3.A-20%; right - case 3.B-20%)

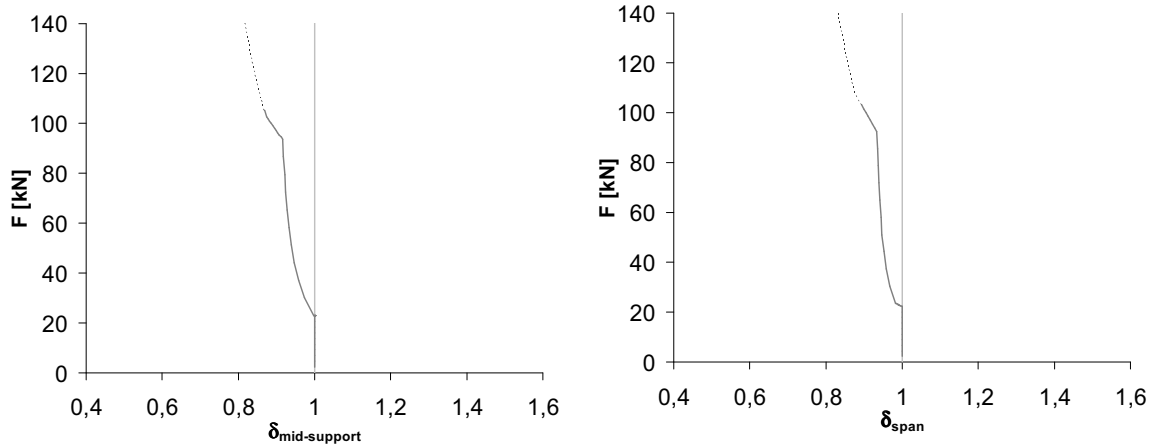

Fig. 6.42: Redistribution factor δ for 20 % redistribution (left - case 3.A-20%; right - case 3.B-20%)

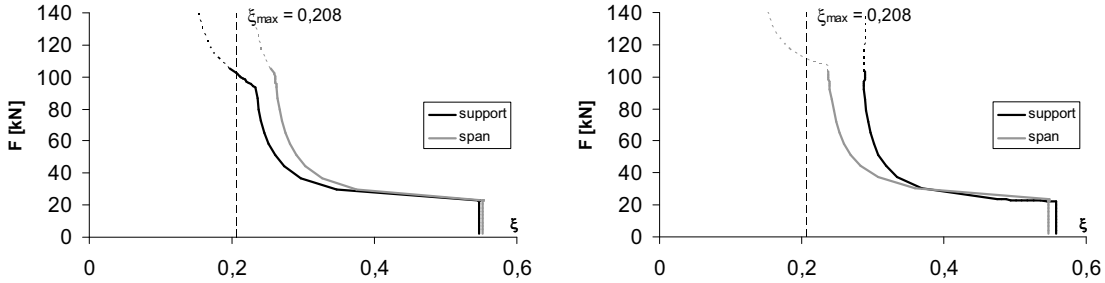

Fig. 6.43: ξ-factor for 20 % redistribution (left - case 3.A-20%; right - case 3.B-20%)

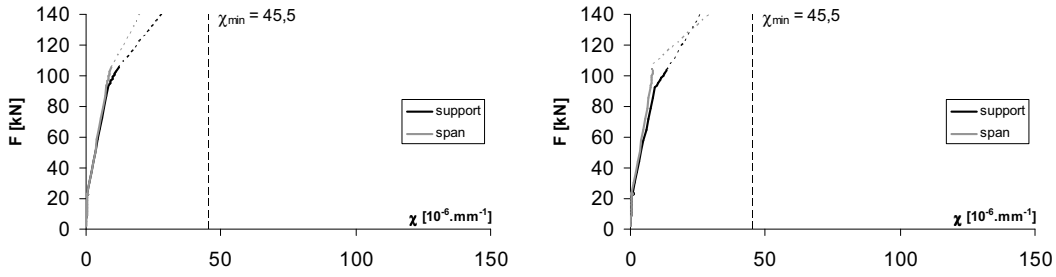

Fig. 6.44: Curvature for 20 % redistribution (left - case 3.A-20%; right - case 3.B-20%)

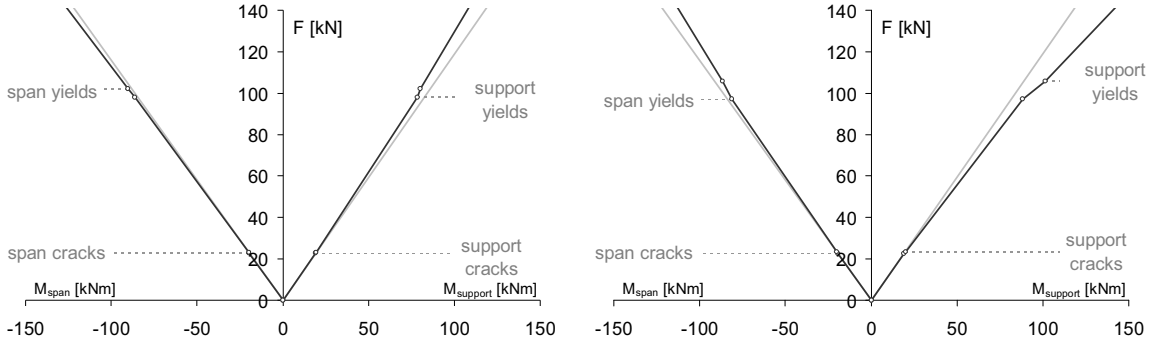

Fig. 6.45: 10% redistribution by applying FRP EBR in both the spans and the mid-support (left - case 3.A-10%; right - case 3.B-10%)

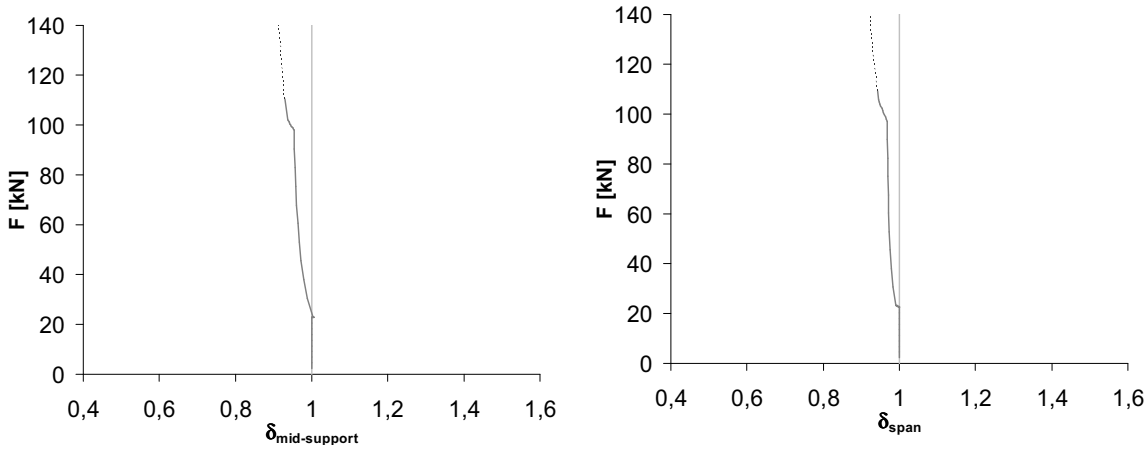

Fig. 6.46: Redistribution factor δ for 10 % redistribution (left - case 3.A-10%; right - case 3.B-10%)

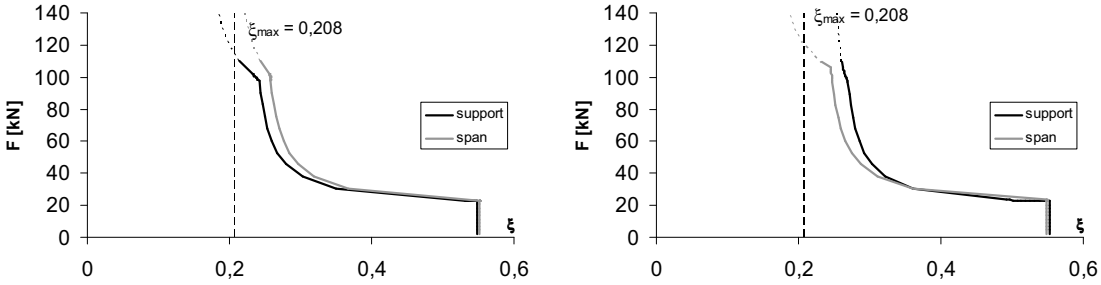

Fig. 6.47: ξ-factor for 10 % redistribution (left - case 3.A-10%; right - case 3.B-10%)

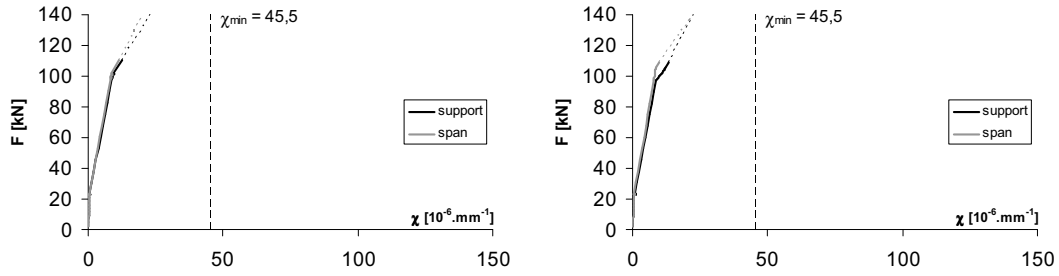

Fig. 6.48: Curvature for 10 % redistribution (left - case 3.A-10%; right - case 3.B-10%)

From Table 6.18 it can be noticed that, as soon as a moment redistribution is introduced by which a plastic hinge needs to be strengthened with FRP and hence becomes a restrained hinge, the required ultimate load according following the linear elastic theory with limited redistribution, is not achieved any more (see case 3.A – 20%, case 3.A – 10 %, case 3.B – 20% and case 3.B – 10 %). In Fig. 6.49 and Fig. 6.50, a comparison of the moment redistribution for case 3.A and case 3.B is given. Due to the strengthening with FRP, the moment redistribution is forced to follow more close the linear elastic distribution. As a result, a limited plastic redistribution is obtained in the restrained hinges (no vertical branch in the moment redistribution graphs) and related to this, the ultimate moment at the restrained hinges is achieved at a lower (ultimate) load.

The restrained plastic redistribution, can also be noticed in Fig. 6.51 and Table 6.19. In these graphs, it is remarkable that only two cases obtain a redistribution ratio (according to the non-linear theory) equal to the required redistribution ratio (according to the lin. el. theory with lim. red.). These two cases are indicated in Fig. 6.51 and can be described as follows:

- The first cases are case 3.A – 30% and case 3.B – 30%. As indicated in sections 3.2.2 and 3.2.3 no plastic hinges need to be strengthened with FRP EBR.
- The second case equals the strengthening configuration in which no redistribution is required (origin of the graph - coordinates (0;0) in Fig. 6.51). This is the case when both internal and external reinforcement are based on the linear elastic theory (see section 2.2).

Al other configurations in Fig. 6.51 do not reach the redistribution ratio assumed according to the linear elastic theory with limited redistribution. Remarkable is that the lack of redistribution is attributed to the plastic redistribution, which decreases considerable by using FRP EBR (restrained hinges).

In the last column of Table 6.18, the location where debonding is expected, is given. As soon as a FRP strengthening is used at a restrained hinge, debonding is expected at these restrained hinges. For case 3.A the restrained hinge is obtained in the mid-support and, for case 3.B the restrained hinge is obtained at the spans.

Table 6.18: Ultimate and yielding loads for different strengthening configurations

Linear el. theory with limited red.			Non-linear theory			
	case	$F_{u,required}$ [kN]	$F_{u,0,4\ \%}$ [kN]	$F_{y,span}$ [kN]	$F_{y,support}$ [kN]	'Debonding' expected at
see section 3.2.2	3.A–30%	114.3	114.1	101.3	87.3	span
	3.A-20%	114.3	105.3	102.6	93.6	mid-support
	3.A-10%	114.3	110.5	102.0	97.9	mid-support
see section 3.2.3	3.B–30%	114.3	113.5	86.4	101.6	mid-support
	3.B-20%	114.3	103.1	92.5	107.3	span
	3.B-10%	114.3	109.2	97.1	105.8	span

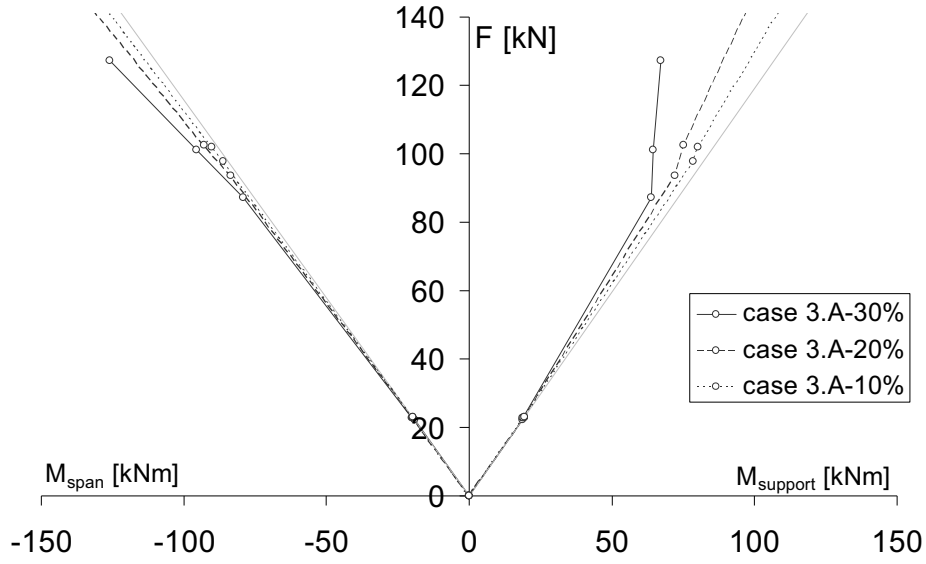

Fig. 6.49: Moment redistribution graphs for case 3.A

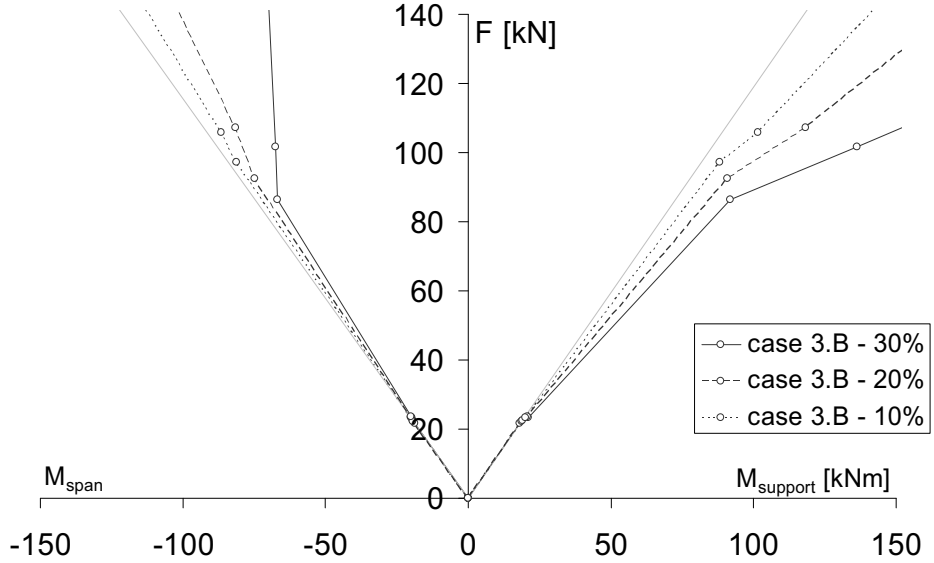

Fig. 6.50: Moment redistribution graphs for case 3.B

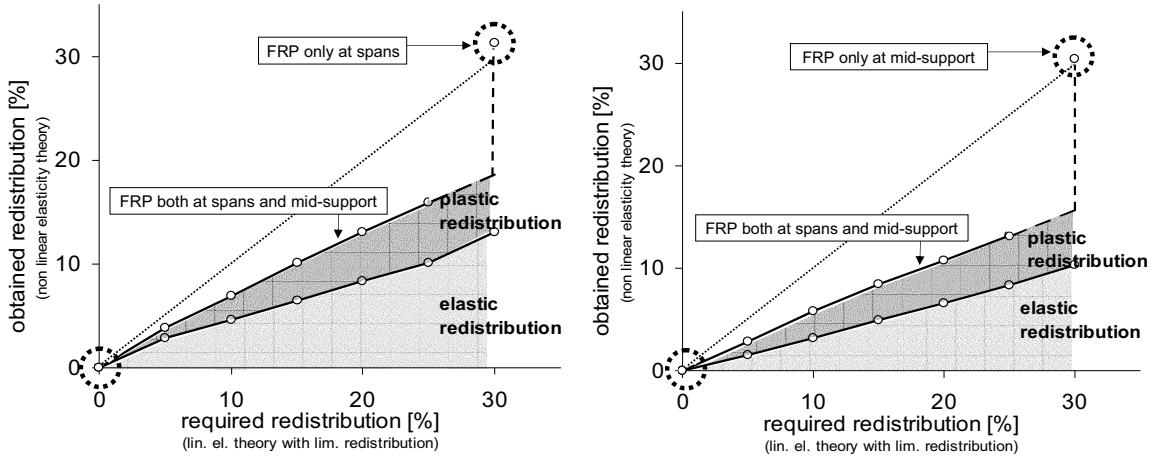

Fig. 6.51: Total, elastic and plastic redistribution for case 3.A (left fig.) and case 3.B (right fig.).

Table 6.19: Elastic, plastic and total redistribution for different cases considered

Linear el. theory with limited red.		Non-linear theory					
		case 3.A			case 3.B		
		tot. red. [%]	el. red. [%]	pl. red. [%]	tot. red. [%]	el. red. [%]	pl. red. [%]
case 3-30%	30 %	31.3	13.1	18.1	30.4	10.3	20.1
case 3-20%	20 %	13.1	8.3	4.8	10.7	6.6	4.1
case 3-10%	10 %	6.9	4.6	2.3	5.8	3.2	2.6

3.2.5.3 Comparison between neutral axis depth (related to ξ_u-factor) and curvature (χ)

In Fig. 6.43 and Fig. 6.47, the neutral axis depth is given in function of the applied load. In Fig. 6.44 and Fig. 6.48 the curvature is given in function of the applied load. In Table 6.20 the ξ_u-factor and curvature of the critical cross-sections at failure are given

To check the plastic rotation capacity in the linear elastic theory with limited redistribution, the neutral axis depth at failure of the first restrained hinge needs to be checked (see limitations in Table 6.4). However, as the restrained hinges are strengthened with FRP, debonding of the laminate will appear earlier than concrete crushing. Hence no check of the ξ_u-factor can be conducted.

On the other hand, it is possible to check the maximum curvature of the expected restrained hinges. In Table 6.20 a large reduction of the curvature at the restrained hinges is noticed. Moreover, once a hinge is strengthened with FRP (restrained hinge in case 3 – 20 % and case 3 - 10 %), the curvature will not exceed the minimum curvature values given in Table 6.4.

Table 6.20: Minimum neutral axis depth and maximum curvature at failure according to the non-linear theory

	Non-linear theory							
	case 3.A				case 3.B			
	ξ_{span} [-]	χ_{span} [10^{-6} mm^{-1}]	$\xi_{support}$ [-]	$\chi_{support}$ [10^{-6} mm^{-1}]	ξ_{span} [-]	χ_{span} [10^{-6} mm^{-1}]	$\xi_{support}$ [-]	$\chi_{support}$ [10^{-6} mm^{-1}]
case 3-30 %	0.248	13.0	0.091	72.5	0.106	43.6	0.314	14.1
case 3-20 %	0.255	9.5	0.198	12.2	0.238	8.2	0.289	13.4
case 3-10 %	0.243	11.3	0.213	12.5	0.232	9.9	0.261	13.4

3.2.5.4 Conclusions

The following conclusions concerning moment redistribution can be made for a two span beam strengthened with FRP EBR in both the spans and the mid-support.

- By using FRP EBR at a hinge (= restrained hinge), the moment redistribution is forced to approach the linear elastic moment distribution. As a result, the moment redistribution is lower than the one assumed by the linear elastic theory with limited redistribution and hence the ultimate moment at the restrained hinges is achieved at a lower (ultimate) load.
- The linear elastic theory with limited redistribution is not a valid design method in case FRP EBR is applied to both the spans and the mid-support.
- The required moment redistribution at the ultimate state according to the linear elastic theory with limited redistribution only corresponds with the obtained moment redistribution (verified according to the non-linear theory) if a plastic hinge can appear in the statically indeterminate structure.
- If a restrained hinge is introduced in a statically indeterminate structure, a considerable reduction of the plastic redistribution is obtained.
- The minimum curvature values given in Table 6.4 are not exceeded at the restrained hinges.

4 Non-linear theory

4.1 Theoretical approach

4.1.1 Unstrengthened continuous beams

The non-linear theory will be applied in case a moment reduction of more than 30 %, compared to the linear elastic moment distribution, is desired or in the case a reliable calculation of crack widths and deflections is needed [5-8].

As mentioned in [2, 9] this non-linear theory is known as the flexural rigidity approach. This designation results from the different flexural stiffnesses which are used over the length of the beam to calculate the evolution of the redistribution of the statically indeterminate structure (see Fig. 6.52). In most cases two different types of zones with a constant stiffness are used. These two zones are the hogging and the sagging zone. The hogging zone is seen as the zone at a mid-support, where positive moments are found. The sagging zone is seen as the zone in the spans, where negative moments are found (see Fig. 6.52).

A non-linear relation between the internal force and the curvature is taken into account. Herewith different bending stiffnesses (see K_0, K_1 and K_2 in Fig. 1.6 in Chapter 1), which are mainly dependent on the used reinforcement ratios, are applied in this theory. As this approach is taking the three different bending stiffnesses into account, a complete moment redistribution in function of the applied load is obtained. Herewith, the non-linear elasticity approach can be applied for both the SLS and the ULS.

In case of applied reinforcement ratios, which are comparable to the ratios obtained from the linear elastic theory, a minimum moment redistribution will occur. By applying reinforcement ratios, different from those obtained by linear elastic calculations, a considerable moment redistribution will appear.

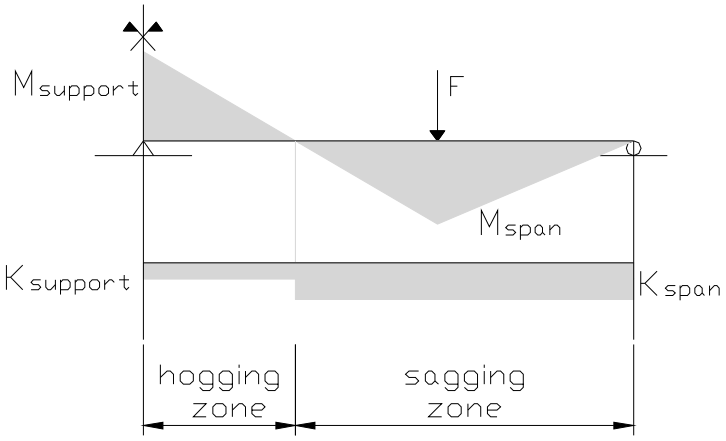

Fig. 6.52: Hogging and sagging zone in non-linear theory

Because the applied reinforcement ratios have to be known to apply the non-linear elasticity calculation, this model can be seen as a verification calculation.

For applying this approach, an elementary beam stiffness computer program is ideal for the analysis. To simplify the calculations, different approaches have been developed to calculate simple beams by hand. Early examples are the design method of BAKER [10] and the method of the enforced rotations by MACCHI [11, 12]. Moreover, also closed form solutions for simple load configurations can be found in literature [6, 9, 13, 14]. For the theoretical approach of a two span beam with one point load in each span, reference is made to Chapter 2.

As an example the m-k relationship of an infinitely long continuous beam is given (see Fig. 6.53).

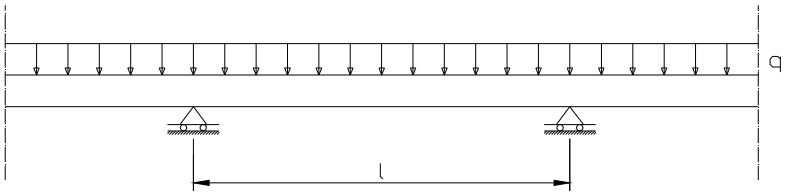

Fig. 6.53: Infinitely long continuous beam

Introducing the variable k equal to the bending stiffness ratio ($k = K_{support}/K_{span}$) and the variable m equal to the moment ratio ($m = M_{support}/M_{span}$) and assuming that the angular rotation of the beam at an intermediate support equals zero, equation 6.11 is obtained [13]. In Fig. 6.54 the non-linear relation between the bending stiffness ratio k and the moment ratio m is given. It can be noticed that for k = 1 (linear elastic distribution), m equals 2.

$$(m-2)\sqrt{1+m} = 2(k-1) \qquad (6.11)$$

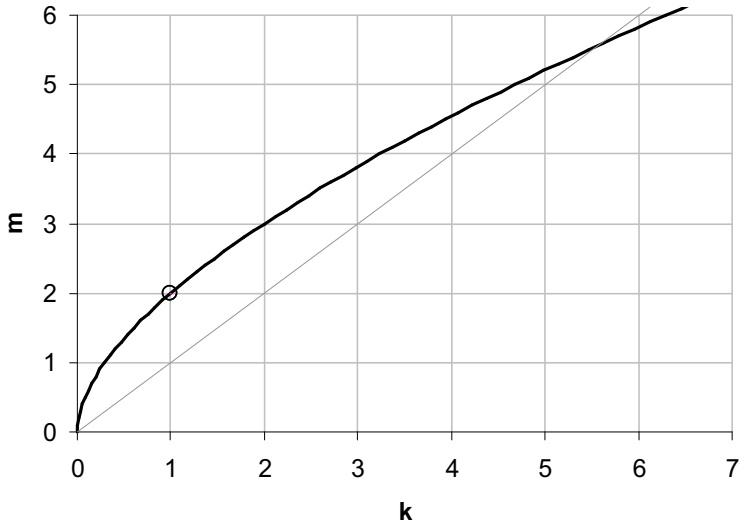

Fig. 6.54: Non-linear relation between k and m for an infinitely long continuous beam

4.1.2 Strengthened continuous beams

In case a moment redistribution of more than 30 % is needed, a detailed analysis of the non-linear behaviour is wanted or in case redistribution via restrained hinges is assumed in the design, the non-linear theory needs to be applied.

To apply the non-linear theory to a strengthened continuous beam, the same procedure is followed as for the unstrengthened continuous beams. Different flexural stiffnesses over the length of the beam are used to calculate the evolution of the redistribution. Herewith different bending stiffnesses (see K'_0, K'_1 and K'_2 in Fig. 1.6 in Chapter 1), which are mainly dependent on the used internal and external reinforcement ratios are introduced in this theory. The applied internal and external reinforcement ratios have to be known to use the non-linear elasticity.

For further information concerning the non-linear theory of (un)strengthened continuous girders, reference is made to Chapter 2.

4.2 Verification of the non-linear theory

The verification of the non-linear theory for strengthened beams has been executed, by means of experimental tests, for which reference is made to Chapter 2. In this chapter, four different two-span beams are tested (see Fig. 6.5). Concerning the internal reinforcement ratios used in the tests, two cases are considered:

- An internal reinforcement configuration calculated according to the linear elastic theory
- An internal reinforcement configuration different from the linear elastic theory

A good to excellent agreement is noticed between the theoretical and experimental results for both configurations. It can be concluded that the non-linear theory, as explained in Chapter 2, is a reliable verification method. On the other hand, more calculations are needed when applying this method.

5 Plasticity theory

5.1 Theoretical approach

5.1.1 Unstrengthened continuous beams

A last method to analyse a statically indeterminate structure is the plasticity method of structural analysis. As mentioned in [2] the plasticity theory is also known as the plastic hinge approach. This theory is related to the failure stage at which only the equilibrium conditions have to be fulfilled. Hence, the plasticity approach can only be applied for the ULS.

According to the plasticity theory, a continuous beam is transformed into a mechanism. The beam is subdivided into different rigid parts, connected to each other by plastic hinges. As a first example, the failure mechanism of a span of an infinitely long continuous beam loaded with a uniform load p is shown in Fig. 6.55.

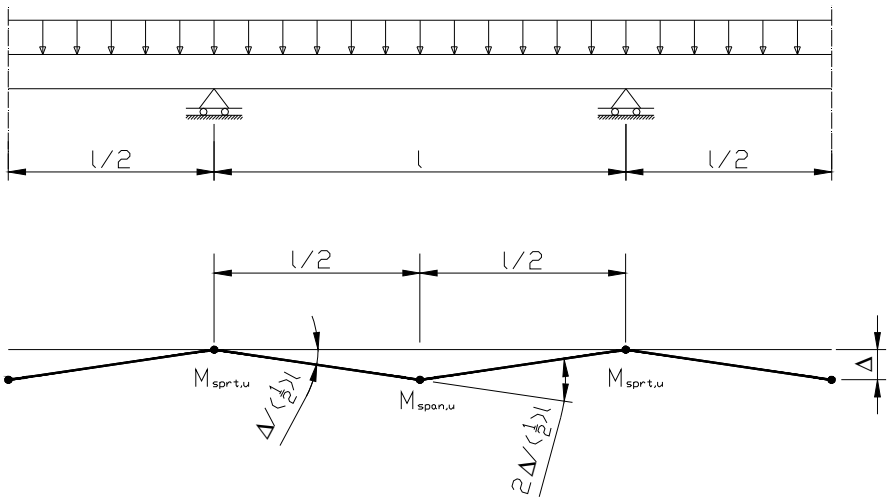

Fig. 6.55: Failure mechanism of a continuous beam according to the plasticity theory

Once the failure mechanism is known, the failure load can be calculated by applying the principle of virtual work. Based on this, an expression between the ultimate load and the ultimate moments at plastic hinges is obtained (see Eq. 6.14). If the ultimate moments of the different critical cross-sections are known (this is the case for a control calculation), the failure load can be obtained. If, on the other hand, the failure load is known (this is the case for design calculations), the required ultimate moments can be calculated. From these ultimate moments, the reinforcement ratios of the critical cross-sections can be defined.

It is important to consider to the correct failure mechanism, which is the mechanism with the most unfavourable position of the plastic hinges, hence, corresponding to the lowest failure load.

Considering the failure mechanism of Fig. 6.55 and the equilibrium of internal and external work, the ultimate load can be found as:

External work $$W_e = 2\left(\frac{1}{2}p_u l\right)\left(\frac{1}{2}\Delta\right) \tag{6.12}$$

Internal work $$\begin{aligned} W_i &= 2M_{u,support}\frac{\Delta}{(1/2)l} + M_{u,span}\frac{2\Delta}{(1/2)l} \\ &= 4\left(M_{u,support} + M_{u,span}\right)\frac{\Delta}{l} \end{aligned} \tag{6.13}$$

$$W_e = W_i \quad \Rightarrow \quad p_{u,plast} = \frac{8\left(M_{u,support} + M_{u,span}\right)}{l^2} \tag{6.14}$$

with: $M_{u,span}$ = ultimate moment of the span
$M_{u,support}$ = ultimate moment of the mid-support

As second example a two-span beam is considered loaded with two point loads (see Fig. 6.5). The ultimate load according to the plasticity approach of these two-span beams again is obtained by equalling the internal and external work:

External work $$W_e = 2F(a\theta) \tag{6.15}$$

Internal work $$W_i = 2M_{u,span}\theta_{u,span} + 2M_{u,support}\theta_{u,support} \tag{6.16}$$

$$W_i = 2M_{u,span}\left(\frac{l}{b}\theta\right) + 2M_{u,support}\left(\frac{a}{b}\theta\right) \tag{6.17}$$

$$W_e = W_i \quad \Rightarrow \quad F_{u,plast} = M_{u,span}\frac{l}{ab} + M_{u,support}\frac{1}{b} \tag{6.18}$$

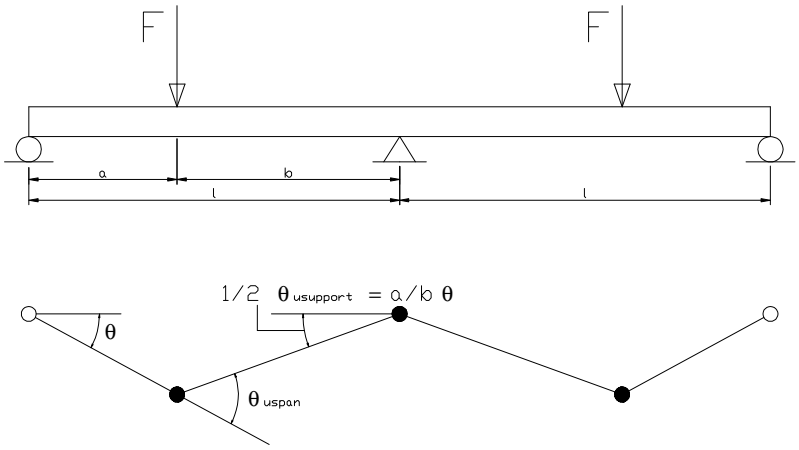

Fig. 6.56: Failure mechanism of a two span beam according to the plasticity theory

The ultimate moments of the critical cross-sections ($M_{u,support}$ and $M_{u,span}$ in Eq. 6.14) in unstrengthened reinforced concrete beams are dependent on the used internal steel reinforcement. It is possible to vary the different steel reinforcement ratios within a certain extent, without changing the failure load, on the condition that the right part of Eq. 6.14 keeps a constant value. As a consequence, related to the failure load, it is not necessary to retain the classic moment distribution according to the linear elastic theory, but it is possible to use an alternative moment distribution. The freedom of varying reinforcement ratios is restricted by the criteria of rotation capacity or by a limitation of deflection and crack formation in service state.

In the ultimate state, a sufficient rotation capacity in the plastic hinges is required. The required ductility is deemed to be satisfied without explicit verification if all the following conditions are fulfilled:

- the area of tensile reinforcement is limited such that, at any section
  $\xi_u = x_u/d \leq 0.25$ for concrete strength classes ≤ C50/60
  $\xi_u = x_u/d \leq 0.15$ for concrete strength classes ≥ C55/67
- reinforcing steel is either Class B or C
- the ratio of the moments at intermediate supports to the moments in the span should be between 0.5 and 2.

5.1.2 Strengthened continuous beams

In a strengthened continuous beam the same theory as mentioned above can be applied in order to obtain the ultimate load capacity of the beam. Again the beam is subdivided in different rigid parts, connected to each other by plastic hinges. However, it has to be taken into account that the deformation of these hinges is restricted if they are strengthened with FRP EBR (= restrained hinges).

The validity of the plasticity theory is discussed in the following sections. Similar as for the case of linear elastic theory with limited redistribution, it is demonstrated that the plastic theory can only be used in those cases where the first plastic hinges are related to unstrengthened critical cross-sections.

5.2 Verification of plasticity theory

As verification for the strengthened beams, the plasticity theory is applied for all cases mentioned in section 3.2 (Verification of linear elastic theory with limited redistribution by means of examples) on the basis of Eq. 6.18.

In Table 6.21, the ultimate moments according to EC2 [1] for unstrengthened critical cross-sections or according to fib Bulletin 14 [15] for strengthened critical cross-sections are given. For simplicity, it is assumed that debonding occurs at a FRP strain of 0.40 %. For the calculation of these ultimate loads, mechanical properties are used as presented in Table 6.1.

Also the ultimate load calculated according to the plasticity theory (see $F_{u,plast.}$ in Eq. 6.18) and the ultimate load calculated according to the non-linear theory ($F_{u,non-lin.}$ obtained in sections 3.2.2, 3.2.3 and 3.2.5) are given in Table 6.21. These two ultimate loads are compared for different strengthening configurations. The same strengthening configurations are investigated as used in the non-linear elasticity approach, among which:

- Strengthening of the spans by means of FRP EBR, by keeping the moment at the mid-support constant (see Fig. 6.9 in case 1 (section 3.2.2))
- Strengthening of the spans by means of additional steel reinforcement, by keeping the moment at the mid-support constant (see Fig. 6.9 in case 1 (section 3.2.2))
- Strengthening of the mid-support by means of FRP EBR, by keeping the moment at the span constant (see Fig. 6.23 in case 2 (section 3.2.3))
- Strengthening of the mid-support by means of additional steel reinforcement, by keeping the moment at the span constant (see Fig. 6.23 in case 2 (section 3.2.3))
- Strengthening of both the spans and the mid-support by means of FRP EBR, by introducing a partial redistribution at the location of the mid-support (see Fig. 6.39 in case 3.A (section 3.2.5)) or by introducing a partial redistribution at the location of the spans (see Fig. 6.40 in case 3.B (section 3.2.5)).

Table 6.21: Ultimate moments and ultimate loads of different strengthening configurations

		Red. [%]	$M_{u,span}$ [kNm]	$M_{u,support}$ [kNm]	$F_{u,plast.}$ [kN]	$F_{u,non-lin.}$ [kN]	[%]
Strength. of span (by FRP)	case 1	10	79.9	67.2	89.0	88.1	99
	case 1	20	93.3	67.2	100.2	99.5	99
	case 1	30	110.6	67.2	114.6	114.1	100
Strength. of span (by steel)	case 1	10	79.9	67.2	89.0	88.8	100
	case 1	20	93.3	67.2	100.2	99.5	99
	case 1	30	110.6	67.2	114.6	113.2	99
Strength. of support (by FRP)	case 2	10	70.6	93.9	90.1	87.7	97
	case 2	20	70.6	127.3	101.3	99.1	98
	case 2	30	70.6	169.9	115.5	113.5	98
Strength. of support (by steel)	case 2	10	70.6	93.9	90.1	90.0	100
	case 2	20	70.6	127.2	101.2	101.1	100
	case 2	30	70.6	170.0	115.5	115.4	100
Strength. of span and support (by FRP)	case 3.A-20	20*	106.5	76.9	114.4	105.3	92
	case 3.A-10	10*	102.6	86.4	114.3	110.5	96
	case 3.B-20	20**	79.0	145.4	114.3	103.1	90
	case 3.B-10	10**	88.9	120.7	114.3	109.2	95

* partial redistribution at the mid-support
** partial redistribution at the spans

Looking to Table 6.21, a good to excellent agreement is noticed between the ultimate loads calculated according to the non-linear theory and the ultimate loads according to the plasticity theory. Except for the last strengthening configuration, for which strengthening of both the spans and the mid-support by means of FRP EBR is considered. In this configuration an ultimate load according

to the plasticity theory is obtained which is considerably higher compared to the ultimate load calculated according to the non-linear theory.

Concerning the plasticity theory, it can be concluded that good to excellent predictions of the failure load are obtained on the condition that no FRP strengthening is applied at the first plastic hinges. This recommendation is logical, as the plasticity approach is based on a failure mechanism caused by the full development of first plastic hinges with sufficient rotation capacity, resulting in a moment redistribution until other hinges are transforming the member into a mechanism. Because a strengthened hinge (restrained hinge) is not providing the same moment redistribution as a (unstrengthened) plastic hinge, the plasticity theory is no longer valid if all hinges are restrained.

6 Conclusions

Despite the study in previous sections is restricted to two-span beams, these conclusions can be applied for all types of continuous beams. To summarize the conclusions, a distinction is made between the following (strengthening) configurations:

CASE 1	**CASE 2**
Internal reinforcement: According to the linear elastic theory **External reinforcement:** In the spans or at the mid-support Reference is made to: case 1 (section 3.2.2) case 2 (section 3.2.3) Conclusions are given in section 6.1.1	**Internal reinforcement:** Different from the linear elastic theory **External reinforcement:** In the spans or at the mid-support Reference is made to: Chapter 2 Conclusions are given in section 6.2.1
CASE 3	**CASE 4**
Internal reinforcement: According to the linear elastic theory **External reinforcement:** In both the spans and the mid-support Reference is made to: case 3 (section 3.2.5) Chapter 2 Conclusions are given in section 6.1.2	**Internal reinforcement:** Different from the linear elastic theory **External reinforcement:** In both the spans and the mid-support Reference is made to: Appendix C Conclusions are given in section 6.2.2

6.1 Internal reinforcement according to the linear elastic theory

6.1.1 Strengthening of the spans or at the mid-support (CASE 1)

In this configuration the failure load of the two-span beam is increased by strengthening only one critical zone (the spans or the mid-support). In the other zone (the mid-support or the spans respectively), the moment is kept constant by introducing a moment redistribution. Consequently the first plastic hinge is formed in this unstrengthened zone.

By applying a moment redistribution in the design stage, the obtained moment distribution differs from the linear elastic one. It is not allowed to apply the linear elastic theory to these strengthening configurations. The other calculation models which are allowed are:

- the linear elastic theory with limited redistribution
- the non-linear theory
- the plasticity theory

Further, the following remarks can be made:

1/ Concerning the linear elastic theory with limited redistribution, a good agreement is obtained between the assumed redistribution ratio and the obtained redistribution ratio (verified by the non-linear theory).

2/ By using the strengthening technique based on FRP EBR, a smaller elastic and larger plastic redistribution is noticed compared to the Steel EBR strengthening configuration.

6.1.2 Strengthening of both the spans and the mid–support (CASE 3)

The failure load of a two-span beam (with internal reinforcement following the linear elastic theory) can also be increased by applying FRP EBR at both the spans and the mid-support. Two different strategies can be followed:

- the external reinforcement ratios are according to the linear elastic theory
- the external reinforcement ratios are different from the linear elastic theory.

If strengthening is applied according the first option, both the used internal and external reinforcement ratios are according to the linear elastic theory. As a result, no restrained hinges appear in the two-span girder and further a linear elastic moment distribution is obtained. The calculation model which needs to be applied in this configuration is the linear elastic theory.

If strengthening is applied according to the second option, the internal reinforcement ratios are according to the linear elastic theory while the external reinforcement ratios are different from the linear elastic theory. Following section 3.2.5 it is noticed that the moment redistribution, in such a configuration, is forced to follow the linear elastic moment distribution more closely and that the plastic redistribution at the restrained hinges are considerably limited. As a result, the linear elastic theory with limited distribution and the plasticity theory are not valid, as they suppose a certain plastic redistribution. The only valid calculation model for this configuration is the non-linear theory.

6.2 Internal reinforcement different from the linear elastic theory

6.2.1 Strengthening of the spans or the mid-support (CASE 2)

As the internal reinforcement ratio is different from the linear elastic theory, one zone (the span or the mid-support) is provided with a lower reinforcement ratio compared to the linear elastic theory. The other zone (the mid-support or the span respectively) is provided with a higher internal reinforcement ratio compared to the linear elastic theory. The first plastic hinge in this unstrengthened configuration appears in the zone where less reinforcement is placed than required by the linear elastic theory.

By strengthening this member, it is recommended to strengthen the zone with the lower internal reinforcement ratio, so that the critical section with high internal reinforcement ratio can now act as the first plastic hinge, and allowing further moment redistribution.

As can be noticed, the location of the first plastic hinge is moved from the critical section in the lower reinforced zone (unstrengthened configuration) to the critical section in the higher internally reinforced zone (strengthened configuration). For further illustrations of this approach, reference is made to Chapter 2.

If on the other hand, it was opted to strengthen the zone with the higher internal reinforcement ratio, the existing plastic hinge in the unstrengthened beam also acts as the plastic hinge in the strengthened beam. The plastic rotation capacity of this plastic hinge is used to a further extent, in order to obtain a sufficient strengthening ratio. In this case, a considerably higher amount of FRP needs to be used (see Chapter 2).

Due to the application of a moment redistribution in the design stage, the obtained moment distribution differs from the linear elastic moment distribution. Hence it is not allowed to apply the linear elastic theory to these strengthening configurations. Valid calculation models are:

- the linear elastic theory with limited redistribution
- the non-linear theory
- the plasticity theory

6.2.2 Strengthening of both the spans and the mid–support (CASE 4)

As follows from Appendix C and Chapter 2, only restrained hinges are obtained in this strengthening configuration. As the hinges are strengthened with a linear elastic FRP material, redistribution is different from those involved by (unstrengthened) plastic hinges. The linear elastic theory with limited redistribution and the plasticity theory are not valid. The only calculation model left which can be applied in this configuration is the non-linear theory.

6.3 Overview

In Table 6.22, an overview is given of the strengthening strategy and the applicable calculation models of two-span beams.

Table 6.22: overview of strengthening strategy and applicable calculation models

CASE1: **Internal reinforcement:** According to the linear elastic theory **External reinforcement:** In the spans or at the mid-support Strengthening strategy: Strengthening of one zone (mid-support zone or span zone) in order to obtain a plastic hinge at the other zone (span zone or mid-support zone) Applicable calculation models: - the linear elastic theory with limited redistribution - the non-linear theory - the plasticity theory	**CASE 2:** **Internal reinforcement:** Different from the linear elastic theory **External reinforcement:** In the spans or at the mid-support Strengthening strategy: Strengthening the zone with the lower internal reinforcement ratio compared to the linear elastic theory in order to obtain a plastic hinge at the zone with the high internal reinforcement ratio compared to the linear elastic theory Applicable calculation models: - the linear elastic theory with limited redistribution - the non-linear theory - the plasticity theory
CASE 3 **Internal reinforcement:** According to the linear elastic theory **External reinforcement:** In both the spans and the mid-support Strengthening strategy: Use strengthening ratios according to the linear elastic theory in order to obtain a linear elastic moment distribution. With this no redistribution (FRP strengthened hinges) is obtained. Applicable calculation models: - the linear elastic theory - the non-linear theory	**CASE 4** **Internal reinforcement:** Different from the linear elastic theory **External reinforcement:** In both the spans and the mid-support Strengthening strategy: In this case, the combination of a redistribution and only restrained hinges (FRP strengthened hinges) is obtained which is counteracting. Therefore, it is recommended to strengthen the structure according to case 2. If with case 2 the required failure load is not able to be obtained, case 4 can be applied on condition that the non-linear theory is used. Applicable calculation models: - the non-linear theory

References

[1] CEN, *Eurocode 2: EN 1992-1-1: Design of concrete structures - Part 1-1: General rules and rules for buildings*. ed. CEN. 2004.

[2] D.J. Oehlers and R. Seracino, *Design of FRP and Steel Plated RC Structures*. Elsevier. Adelaide, Australia. 2004.

[3] D.J. Oehlers, et al., *Moment redistribution in continuous plated RC flexural members. Part 1: neutral axis depth approach and tests.* Engineering Structures. 2004. Vol. 26 (14): pp. 2197-2207.

[4] I. Liu, et al., *Moment redistribution parametric study of CFRP, GFRP and steel surface plated RC beams and slabs.* Construction and Building Materials. 2006. Vol. 20 (1-2): pp. 59-70.

[5] A.F. Ashour, S.A. El-Refaie and S.W. Garrity, *Flexural strengthening of RC continuous beams using CFRP laminates.* Cement and Concrete Composites. 2004. Vol. 26 (7): pp. 765-775.

[6] L. Taerwe and B. Espion, *Serviceability and the Nonlinear Design of Concrete Structures*. Proceedings of IABSE PERIODICA 2/1989. 1989: pp. 61-76

[7] L. Vasseur, S. Matthys and L. Taerwe, *Load tests on 2-span reinforced concrete beams strengthened with fibre reinforced polymer.* Proceedings of ACIC 07, Claverton Down, Bath, England. University of Bath. 2007: pp. 422-429

[8] L. Vasseur, S. Matthys and L. Taerwe, *Proceedings of the 8th International Symposium on Fiber-reinforced Polymer Reinforcement for Concrete Structures*. ed. Thanasis C. Triantafillou. Patras, Greece. 2007: pp. 701.

[9] D.J. Oehlers, et al., *Moment redistribution in continuous plated RC flexural members. Part 2: Flexural rigidity approach.* Engineering Structures. 2004. Vol. 26 (14): pp. 2209-2218.

[10] D. Vandepitte, *Berekening van constructies*. E. Story-Scientia. Ghent. 1979. Vol. 3: pp. 721.

[11] G. Macchi and E. Siviero, *Deformability of prismatic reinforced concrete members with rectangular cross-section under combined bending and axial load.* Construzione in cemnto armato, studi e Rendiconti. 1974. Vol. 11.

[12] G. Macchi, *Elastic distribution of moments on continuous beams. Flexural mechanics of reinforced concrete*. Proceedings of International Symposium, Miami, Florida. 1964

[13] CUR-rapport-83, *Doorgaande balken van gewapend beton*. Stichting voor onderzoek, voorschriften en kwaliteitseisen op het gebied van beton. 1980. pp. 124.

[14] L. Vasseur, S. Matthys and L. Taerwe, *Analytical study of a 2-span reinforced concrete beam strengthened with fibre reinforced polymer*. Proceedings of IABSE symposium: 'Responding to tomorrow's challenges in structural engineering', Budapest. IABSE Hungarian Group 2006

[15] fib, *fib bulletin 14, Externally bonded FRP reinforcement for RC structures*. International federation for structural concrete, Lausanne. 2001: pp. 138.

Chapter 7
CONCLUSIONS

1 Concluding remarks

1.1 Conclusions on the non-linear behaviour of strengthened continuous beams

Analysing a continuous beam, four different types of analysis can be used (some of which are only valid for the ultimate state):

- linear elastic analysis
- linear elastic analysis with limited redistribution
- non-linear analysis
- plastic analysis

In Chapter 2 the analysis of a two-span beam is given by means of the non-linear analysis. An additional equation is introduced to solve the statically indeterminate system by assuming no rotation of the beam at the mid-support. This additional equation is written in function of the bending stiffness ratio k (= $K_{support}/K_{span}$) and the moment distribution ratio m (=$M_{support}/M_{span}$). Each bending stiffness ratio k corresponds to a certain moment distribution ratio m. To obtain finally the full moment distribution curve, five different stages are assumed during the loading of the two-span beam:

- Stage k_1: $F \leq \min(F_{cr,span};F_{cr,support})$
- Stage k_2: $\min(F_{cr,span};F_{cr,support}) \leq F \leq \max(F_{cr,span};F_{cr,support})$
- Stage k_3: $\max(F_{cr,span};F_{cr,support}) \leq F \leq \min(F_{y,span};F_{y,support})$
- Stage k_4: $\min(F_{y,span};F_{y,support}) \leq F \leq \max(F_{y,span};F_{y,support})$
- Stage k_5: $\max(F_{y,span};F_{y,support}) \leq F \leq \min(F_{u,span};F_{u,support})$

Concerning this non-linear analysis, the following conclusions can be made:

1/ The analytically obtained moment redistribution following from the non-linear analysis shows a good to excellent agreement with the experimentally obtained moment redistribution.

2/ Also the analytically obtained strain distribution according the non-linear theory has a good to excellent agreement with the experimental obtained strain distribution.

3/ In unstrengthened two-span beams, plastic hinges are expected in the zones with low internal reinforcement ratios (compared to the linear elastic reinforcement ratios). By strengthening only these zones with FRP EBR, the possibility exists to move the location of the plastic hinge to the zones with

high internal reinforcement ratios (compared to the linear elastic reinforcement ratios).

4/ On the other hand, if it is opted to strengthen the zone with the high internal reinforcement ratio (compared to the linear elastic reinforcement ratios), the existing plastic hinge in the unstrengthened beam also acts as the plastic hinge in the strengthened beam. The plastic rotation of this plastic hinge is used to a further extent, in order to obtain a sufficient strengthening ratio. No high strengthening ratios can be obtained with this strengthening configuration.

5/ If both the internal and external reinforcement ratios of the two-span beam are calculated according to the linear elastic approach, a linear elastic moment distribution is obtained.

6/ Comparing the experimentally obtained deflection of a strengthened and unstrengthened beam, a significant reduction is observed which is caused by the use of the linear elastic EBR. Furthermore the local rotations at the plastic hinges in the unstrengthened beam are clearly visible, while in the strengthened beam no local rotations are visible, neither at the point loads nor at the mid-supports.

1.2 Conclusions concerning debonding of laminates in statically indeterminate structures

The use of FRP EBR to strengthen reinforced concrete structures always implies the possibility of debonding of the laminates. In order to design a strengthened member, first a full composite action is assumed. In a second stadium, all different debonding mechanisms have to be checked to prevent early debonding of the laminates. The different debonding mechanisms which can appear at the strengthened regions in a continuous beam are similar to the mechanisms which appear in isostatic beams. The following distinction is made between the debonding mechanisms:

- Debonding at flexural cracks
- Debonding at shear cracks
- Debonding by a limited anchorage length
- Debonding by concrete rip-off

By investigating these mechanisms in continuous beams, certain differences between continuous beams and statically determined beams have been observed:

1/ The difference between isostatic beams and continuous beams is the moment line with opposite signs. Whereas the moment in the span is positive, the moment at the mid-support is negative. In contrast to reinforced isostatic beams, this allows to anchor the FRP laminates in compression zones. By extending a laminate into these compression zones, two out of the four different debonding mechanisms will be avoided: debonding by a limited anchorage length and debonding by end shear failure (concrete rip-off).

2/ A second difference between continuous and isostatic beams is the non-linear behaviour. By using reinforcement ratios different from those corresponding to the linear elastic theory, both a moment and shear force redistribution is observed. These redistributions on their turn do influence both the real acting shear force as well as some parameters which are necessary to calculate the debonding load (the anchorage length l_t and the distance between laminate end and point of contraflexure L). As the non-linear behaviour is dependent on the stiffness distribution along the length of the beam or, in other words on the reinforcement/strengthening ratios, also the debonding load will be dependent on the different reinforcement/strengthening ratios along the length of the beam. This dependency can result in earlier or later debonding of the laminates compared to the linear elastic theory. As a result, it is of importance to check all different debonding mechanisms by taken into account the real acting moment distribution.

3/ IC-debonding has been observed at the location of the mid-support of two span-beams. The mid-support acts as a concentrated point-load, for which a combination of high shear forces and high moments can be found. As a result, this configuration is comparable with a 3-point-bending test. As most of the experimentally calibrated debonding models are based on 4-point-bending tests, it is interesting to investigate IC-debonding for 3-point bending configurations and related to this the IC-debonding at the location of the mid-support. In the 3-point-bending test program, it has been observed that fib Bulletin 14 gives good predictions of the intermediate crack debonding load in 3-point-bending tests, on average 9.2 % lower compared to the experimental debonding load. For all beams these predictions correspond to the 'debonding at flexural cracks' model (represented by the envelope line of tensile stresses in the FRP) while the 'debonding at shear cracks' model appeared not to be representative. An alternative model to evaluate intermediate crack debonding is proposed by Oller et al. [1]. This model gives the impression to combine both debonding at shear cracks and at flexural cracks, as it gives a failure envelope for combinations of shear forces and bending moments. However, vertical crack displacement is not explicitly considered in the model. An experimental verification by means of the conducted 3-point-bending-tests, shows that this model is as conservative as the fib Bulletin 14 model (on average 9.6 % lower compared to the real debonding load). It can be concluded that both the 'debonding at flexural cracks' model of fib Bulletin 14 (represented by the envelope line of tensile stresses in the FRP) and the model by Oller give accurate predictions of the debonding load in the case of 3-point-bending tests. Compared to the fib Bulletin 14 model, the model by Oller is less complex to calculate.

4/ Considering IC-debonding at the location of the mid-support of the two span beams, again both predictions by fib Bulletin 14 and by Oller are verified. As is noticed in the 3-point-bending configurations, the model at flexural cracks proposed by fib Bulletin 14 and the model proposed by Oller et al. give similar and accurate predictions. However, too conservative results are obtained for the top laminate in the case of two

span beams. The other model proposed by fib Bulletin 14 (debonding at shear cracks), gives better predictions, but at the unsafe side for both CB3 and CB4.

1.3 Conclusions about the plastic rotation capacity of strengthened cross-sections

For an unstrengthened cross-section, a large plastic rotation capacity is obtained due to the yielding capacity of the internal steel reinforcement. This rotation capacity corresponds to the rather long horizontal branch in the M-χ diagram. In the case of a FRP-strengthened cross-section, the rotation capacity is considerably decreased due to the use of the linear elastic FRP. Indeed, the curvature at ultimate of a FRP-strengthened cross-section (assuming full composite action) is significantly lower than the unstrengthened reference. Moreover, failure of a FRP-strengthened cross-section is often characterized by debonding of the externally bonded laminates, which reduces also the plastic rotation capacity to an important degree. From the experimental results it follows that this early debonding of the FRP laminate can be delayed by wrapping the cross-section with carbon textile. Herewith a higher ultimate moment is obtained and the third branch of the experimental moment-curvature graph is continued, which is of importance for the rotation capacity.

Due to the restraining action of FRP EBR on the rotation, with additional post-yielding rotations related to an increase of the internal moment, no plastic hinge action and related moment redistribution can be achieved in an FRP-strengthened cross-section.

The plastic rotation capacity is dependent on different parameters, among which the reinforcement ratio, the tensile strength of the internal steel reinforcement, the compressive strength of the concrete and the effective depth. Depending on the considered configuration (unstrengthened (see Table 7.1) or strengthened (see Table 7.2)), these parameters are resulting in a favourable or unfavourable influence.

Table 7.1: Influence of different parameters on the rotation capacity and the occurring rotation of an unstrengthened cross-section

Increasing of:			Influence on θ_{pl}
A_{s1}	↗	(tensile reinforcement)	↙
f_y	↗		↙
f_c	↗		↗ (limited)
A_{s2}	↗	(compression reinforcement)	↗ (limited)
d	↗		↗ (limited)

Table 7.2: Influence of different parameters on the rotation capacity and the occurring rotation of an strengthened cross-section

Increasing of:			Influence on θ_{pl}
A_{s1}	↗	(tensile reinforcement - steel)	↗ (limited)
A_f	↗	(tensile reinforcement - FRP)	↗ (limited)
f_y	↗		↙
f_c	↗		↙ (limited)
A_{s2}	↗	(compression reinforcement)	↙ (limited)
d	↗		↙

As can be noticed from Table 7.1 (unstrengthened cross-section) and Table 7.2 (strengthened cross-section), an opposite influence of the parameters comparing unstrengthened and strengthened cross-section is obtained. Only the change of the yielding strength of the internal steel reinforcement (f_{yk}) is resulting in a similar influence for both configurations.

To verify sufficient plastic rotation capacities, a distinction is made between unstrengthened and FRP strengthened cross-sections:

Unstrengthened cross-sections:

1/ By applying the linear elastic approach with limited redistribution, no control of the plastic rotation capacity is needed if the following ductility conditions are fulfilled:

a) based on concrete strength:

$\delta \geq k_1 + k_2 \xi_u$ for $f_{ck} \leq 50$ MPa (7.1)

$\delta \geq k_3 + k_4 \xi_u$ for $f_{ck} > 50$ MPa (7.2)

b) based on ductility of steel:

$\delta \geq 0.7$ for Class B and Class C reinforcement (7.3)

$\delta \geq 0.8$ for Class A reinforcement (7.4)

2/ By applying the non-linear approach, taking into account both the bending stiffnesses K_0, K_1 and K_2 and the critical internal moments M_{cr}, M_y and M_u of all critical cross-sections, no explicit check of the rotation capacity at the plastic hinges is needed as this is already taken into account in the non-linear study.

3/ By applying the non-linear approach, taking only into account the bending stiffnesses K_0 and K_1 and the critical internal moments M_{cr} and M_y (assuming that $K_2 = 0$ and $M_y = M_u$), Eq. 7.5 has to be checked explicitly for all critical cross-sections where a plastic rotation is expected, as sufficient plastic rotation capacity of the plastic hinges is assumed in this calculation model.

$$\theta_d \leq \theta_{pl} \quad (7.5)$$

4/ By applying the plastic approach in order to obtain the bearing capacity of the statically indeterminate structure, no control of the plastic rotation capacity is needed if following ductility conditions are fulfilled:

- the area of tensile reinforcement is limited such that, at any section
  $\xi_u = x_u/d \leq 0.25$ for concrete strength classes ≤ C50/60
  $\xi_u = x_u/d \leq 0.15$ for concrete strength classes ≥ C55/67
- reinforcing steel has either ductility Class B or C
- the ratio of the moments at intermediate supports to the moments in the span should be between 0.5 and 2.

FRP strengthened cross-sections:

As mentioned before, FRP-strengthening is not recommended in cross-sections where plastic hinge formation is needed to involve the required moment redistribution assumed in design. FRP-strengthened post-yielding cross-sections act as a restrained hinge, capable of taking up a significant degree of additional internal moment.

1.4 Conclusions about influence of externally bonded reinforcement on the crack spacing

Analytical models to predict crack spacing have been compared. The best prediction of the crack spacing of a strengthened reinforced concrete beam is obtained by the model based on the crack formation in a mixed reinforced tensile member.

According to a microscopic investigation of the crack pattern underneath the FRP laminate of a continuous beam and DICT-monitoring of an isostatic beam, it has been observed that macro cracks visible at the side-faces of the beam split up into multiple micro cracks under the laminate. This phenomenon is also confirmed by the analytical study which compares the transfer length in the vicinity of embedded steel rebars and the transfer length in the vicinity of an FRP laminate. Both from the experimental and analytical investigations, a smaller crack spacing is observed under the laminate compared to the crack spacing around the steel rebars.

For the beams considered, the crack spacing of these micro cracks appeared to be equal to 27.5 % of the macro crack spacing on the mean (respectively 23 % for the continuous beam and 32 % for the isostatic beam). The depth over which the micro cracks expand, roughly corresponds to the concrete layer between the FRP laminate and the internal steel reinforcement.

By considering the more restricted crack spacing of these micro cracks in further investigations concerning debonding models of the FRP EBR, refined debonding models can be achieved.

1.5 Recommendations for strengthening of continuous beams

In Table 7.3, an overview is given of the strengthening strategy and the applicable calculation models of two-span beams. In this a distinction is made between the two-span beams with internal reinforcement according to the linear elastic theory and two-span beams with internal reinforcement different from the linear elastic theory. Further also a distinction is made concerning the external reinforcement, i.e. FRP EBR applied in one zone (or in the spans or at the support) and FRP EBR applied in both the span zone and the mid-support zone.

This results in the following 4 cases to be distinguished:

- case 1: with internal reinforcement according to the linear elastic theory with external reinforcement applied in the spans or at the mid-support
- case 2: with internal reinforcement different from the linear elastic theory with external reinforcement applied in the spans or at the mid-support
- case 3: with internal reinforcement according to the linear elastic theory with external reinforcement applied in both the spans and at the mid-support
- case 4: with internal reinforcement different the linear elastic theory with external reinforcement applied in both the spans and at the mid-support

Concerning the check of the debonding mechanisms, the moment distribution assumed in the design and the related shear force distribution have to be taken into account. Especially the end spans of a continuous beam need special attention, as in these spans often a shear force distribution different from the linear elastic shear force distribution is obtained.

Table 7.3: overview of strengthening strategy and applicable calculation models

CASE 1	**CASE 2**
Internal reinforcement: According to the linear elastic theory **External reinforcement:** In the spans or at the mid-support Strengthening strategy: Strengthening of one zone (mid-support zone or span zone) in order to obtain a plastic hinge at the other zone (span zone or mid-support zone) Applicable calculation models: - the linear elastic theory with limited redistribution - the non-linear theory - the plasticity theory	**Internal reinforcement:** Different from the linear elastic theory **External reinforcement:** In the spans or at the mid-support Strengthening strategy: Strengthening the zone with the lower internal reinforcement ratio compared to the linear elastic theory in order to obtain a plastic hinge at the zone with the high internal reinforcement ratio compared to the linear elastic theory Applicable calculation models: - the linear elastic theory with limited redistribution - the non-linear theory - the plasticity theory
CASE 3	**CASE 4**
Internal reinforcement: According to the linear elastic theory **External reinforcement:** In both the spans and the mid-support Strengthening strategy: Use strengthening ratios according to the linear elastic theory in order to obtain a linear elastic moment distribution. With this no redistribution (FRP strengthened hinges) is obtained. Applicable calculation models: - the linear elastic theory - the non-linear theory	**Internal reinforcement:** Different from the linear elastic theory **External reinforcement:** In both the spans and the mid-support Strengthening strategy: In this case, the combination of a redistribution and only restrained hinges (FRP strengthened hinges) is obtained which is counteracting. Therefore, it is recommended to strengthen the structure according to case 2. If with case 2 the required failure load is not able to be obtained, case 4 can be applied on condition that the non-linear theory is used. Applicable calculation models: - the non-linear theory

2 Further perspectives

In the framework of this thesis, the theoretically obtained models are based on a two-span beam with one point load in each span (see Fig. 7.1). Also the tests are conducted on two-span beams with the same configuration. The length of one span is taken equal to 5 m (with a = 2 m and b = 3 m).

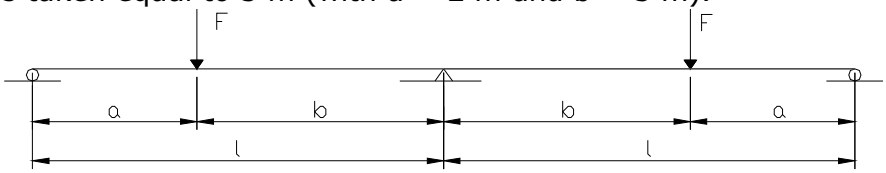

Fig. 7.1: Continuous girder with two spans

In a further research it would be interesting to extend the already obtained models according to the non-linear theory to a configuration with more than two spans.

Concerning the loading configuration, it would be interesting to investigate also a uniformly loaded configuration, as this configuration occurs more frequently in practice.

As mentioned above, debonding of the top laminates is a critical point in the design of strengthened continuous beams. Especially the debonding mechanism induced by crack bridging needs special attention. Concerning the calculation of debonding at flexural cracks, the complex model according to Niedermeier given in [2] or the model according to Oller et al. [1] can be applied. Concerning the calculation of debonding at shear cracks, a model is actually proposed in fib Bulletin 14, which was calibrated by means of 4-point-bending tests [2]. As the combination of shear forces and bending moments is different in 4-point-bending compared to 3-point-bending (similar to the intermediate support of a continuous beam), it would be interesting to further verify and optimize the crack bridging models, taking into account e.g. 3-point bending tests.

Due to the debonding of the laminates, also a limitation of the rotation capacity is obtained in FRP strengthened cross-sections. Therefore, it would be interesting to investigate the plastic rotation capacity of near surface mounted (NSM) FRP reinforcement, as this reinforcement method shows a later debonding. Related to this later debonding, a larger rotation capacity is expected.

Finally, despite the obtained non-linear model is giving good to excellent results, several simplifications have been introduced in this model. In order to refine the model, it would be interesting to introduce the effect of tension-stiffening as well as a more realistic stress-strain model for concrete under compression instead of the bilinear model.

References

[1] E. Oller, *Peeling failure in beams strengthened by plate bonding. A design proposal*. PhD thesis. Departament d'Enginyeria de la construcció, Universitat Politècnica de Catalunya. Barcelona. 2005. pp. 334.

[2] fib, *fib bulletin 14, Externally bonded FRP reinforcement for RC structures*. International federation for structural concrete, Lausanne. 2001: pp. 138.

Appendix A

ANALYTICAL IMPLEMENTATION OF THE NON-LINEAR THEORY FOR A TWO-SPAN BEAM

1 Introduction

To study the non-linear behaviour of a two-span beam strengthened in flexure with FRP EBR and subjected to bending, a calculation programme (using the software MS-Excel) has been developed. This programme makes use of the non-linear model derived in Chapter 2 and calculates the behaviour of a two-span beam loaded with one point load in each span (see Fig. A.1). The cross-section of the beam is rectangular.

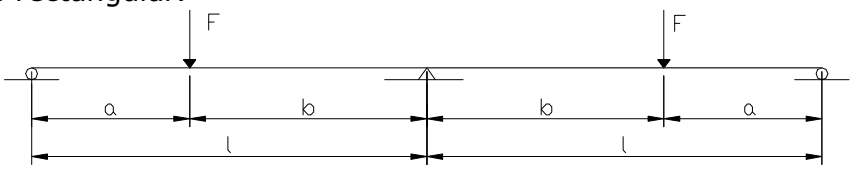

Fig. A.1: Continuous beam with two spans

The moment distribution of such a configuration is shown in Fig. A.2. In this figure, two critical sections (sections with maximum bending moment) can be noticed, i.e. the section at the mid-support and the section under the point load. In the first critical section the bending moment is denoted as $M_{support}$, while in the second critical section the bending moment is denoted as M_{span}. Remark that in the moment distribution graph of Fig. A.2, the dead weight of the beam is not taken into account. Nevertheless, in the calculation program the dead weight is taken into account (see step 1 of section 2.

In the model, all calculations concerning the moment redistribution are referring to these two critical bending moments. The bending moment at another location along the length of the beam is easily obtained from these critical bending moments.

In Fig. A.2, the real stiffness distribution is simplified by assuming two zones with a constant bending stiffness. In the zone covering all positive bending moments the bending stiffness is denoted as $K_{support}$ while in the zone with negative bending moments the bending stiffness is denoted as K_{span}.

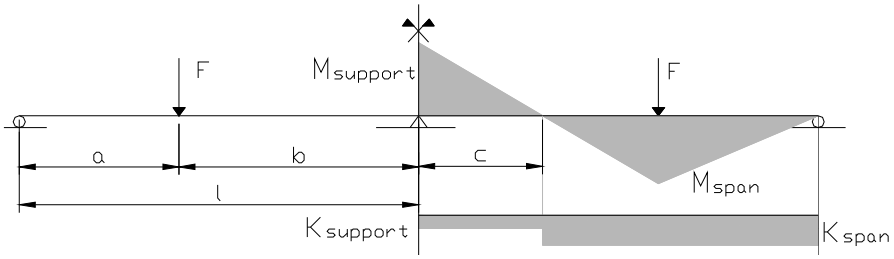

Fig. A.2: Variable bending stiffness model for a 2-span beam

2 Determination of moment redistribution graph

In order to obtain the non-linear moment distribution the following successive steps have to be followed, which are also implemented in the calculation programme, mentioned above.

1/ Initially the M-χ diagrams of both critical cross-sections needs to be determined. This calculation is performed stepwise. Assuming a value as given in Table A.1 and considering the strain compatibility and equilibrium of forces and moments, a corresponding moment and curvature is calculated.

Table A.1: Assumed values in order to obtain the M-χ diagrams

Assumed value		Obtained strain distribution
M	(=M_{cr})	the strain distribution of the uncracked cross-section
ε_s	(= ε_{sy})	the strain distribution at yielding of the internal steel reinforcement
ε_c* or ε_f	(= ε_{cu}) (= ε_{fu})	the strain distribution at ultimate

*: ε_c = concrete strain at extreme compression fibre

From the obtained M-χ diagrams the cracking moment (M_{cr}), yielding moment (M_y) and ultimate moment (M_u) can be obtained. Besides also the different bending stiffnesses can be obtained (see Fig. 1.6 of Chapter 1), among which:

- K_0: Bending stiffness of the uncracked cross-section
- K_1: Bending stiffness of the cracked cross-section until yielding of the internal steel reinforcement
- K_2: Bending stiffness of the cross-section after yielding of the internal steel reinforcement

As the moment redistribution is depending on the bending stiffness and the bending stiffness itself is depending on the applied load level, a subdivision of the loading scheme is made in five different stages (see Table A.2).

Table A.2: Transition loads of the different stages

Stage 1	F_0 [= dead weight situation]	≤ F ≤	F_1 [= min($F_{cr,span}$;$F_{cr,support}$)]
Stage 2	F_1 [= min($F_{cr,span}$;$F_{cr,support}$)]	≤ F ≤	F_2 [= max($F_{cr,span}$;$F_{cr,support}$)]
Stage 3	F_2 [= max($F_{cr,span}$;$F_{cr,support}$)]	≤ F ≤	F_3 [= min($F_{y,span}$;$F_{y,support}$)]
Stage 4	F_3 [= min($F_{y,span}$;$F_{y,support}$)]	≤ F ≤	F_4 [= max($F_{y,span}$;$F_{y,support}$)]
Stage 5	F_4 [= max($F_{y,span}$;$F_{y,support}$)]	≤ F ≤	F_5 [= min($F_{u,span}$;$F_{u,support}$)]

2/ Secondly, the bending stiffness ratios (k) are calculated from the bending stiffnesses K derived in step 1. For every stage mentioned in Table A.2 a typical bending stiffness ratio is obtained (see Eq A.1). Remark that for the determination of the bending stiffness ratios k_2 and k_4 two different formulations are given (denoted by k and k'). Depending on which critical cross-section cracks first and which critical cross-section yields first, one of the two expressions needs to be used. As the determination of the load increase per stage is obtained in a further step, it is not known yet which critical cross-section cracks first and/or yields first. As a consequence it is not possible yet to decide which expression for k_2 and k_4 needs to be used and it is needed to calculate both expressions.

$$
\begin{aligned}
k_1 &= \frac{K_{support,0}}{K_{span,0}} \\
k_2 &= \frac{K_{support,1}}{K_{span,0}} \quad \text{or} \quad k_2' = \frac{K_{support.0}}{K_{span,1}} \\
k_3 &= \frac{K_{support,1}}{K_{span,1}} \\
k_4 &= \frac{K_{support,2}}{K_{span,1}} \quad \text{or} \quad k_4' = \frac{K_{support.1}}{K_{span,2}} \\
k_5 &= \frac{K_{support,2}}{K_{span,2}}
\end{aligned}
\qquad \text{(A.1)}
$$

3/ Once the bending stiffness ratios (k) are known, the corresponding bending moment ratios (m) are calculated by means of Eq. A.2 (obtained in section 2.2.1 in Chapter 2). Again two values for the moment distribution ratio will be obtained in stage 2 (m_2 and m_2' related to k_2 and k_2') and stage 4 (m_4 and m_4' related to k_4 and k_4').

$$(2+3\lambda)m^3 + (3+3\lambda-2k\lambda^2)m^2 - k\lambda(3+4\lambda)m - (1+\lambda)(1+2\lambda)k = 0 \qquad \text{(A.2)}$$

4/ Given the bending moment ratios (m), the increase of the bending moments for stage i at both the span ($\Delta M_{span,i}$) and the support ($\Delta M_{support,i}$) can be calculated (see Fig. A.3). For these calculations Eq. 2.25 until Eq. 2.31 given in Chapter 2 can be used.
Again, depending on which critical cross-section cracks first, yields first and fails first, the Eqs. 2.25 until 2.31 need to be interpreted differently. However, as the determination of the load increase per stage is obtained in a further step, it is not known yet which critical cross-section cracks first, yields first and/or fails first. As a consequence, all possible combinations need to be calculated.
In total 8 different combinations are possible, given below (see combination –a- until –h-). For each combination the used bending moment ratio (m) of stage 2 and 4 is mentioned.

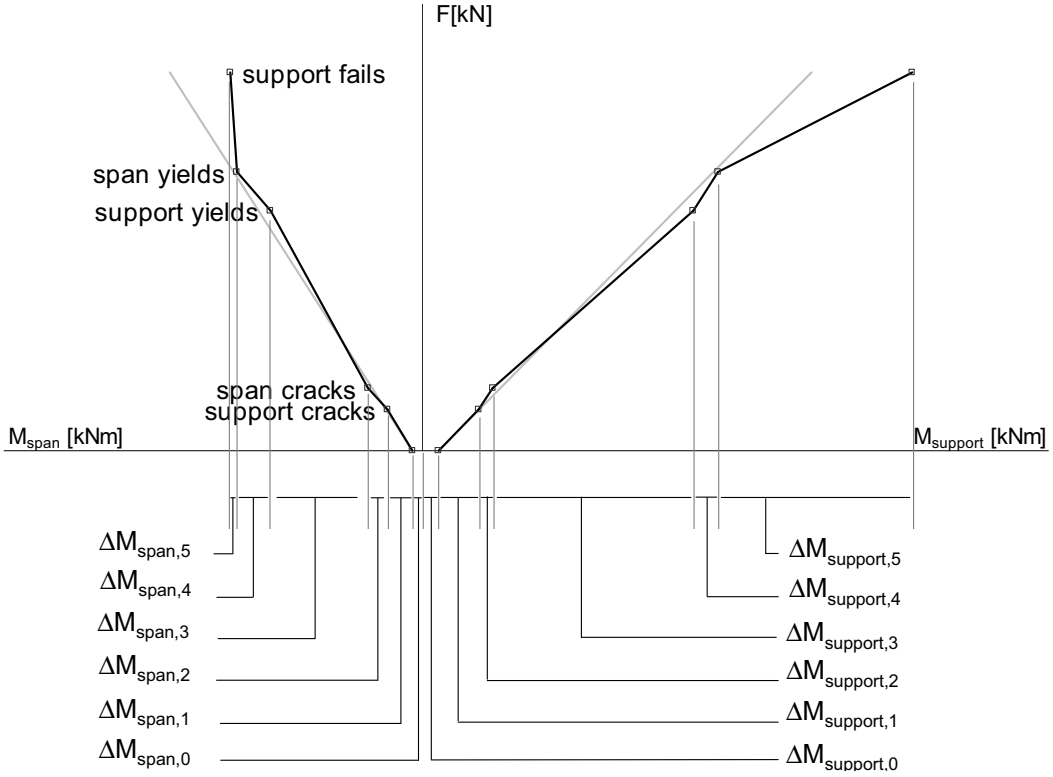

Fig. A.3: Increase of the bending moments at the critical cross-section for all stages

a/ $0 < F_{cr,support} \le F_{cr,span} \le F_{y,support} \le F_{y,span} \le F_{u,support}$ use of $k_2\ (m_2)$ and $k_4\ (m_4)$

b/ $0 < F_{cr,support} \le F_{cr,span} \le F_{y,support} \le F_{y,span} \le F_{u,span}$ use of $k_2\ (m_2)$ and $k_4\ (m_4)$

c/ $0 < F_{cr,support} \le F_{cr,span} \le F_{y,span} \le F_{y,support} \le F_{u,support}$ use of $k_2\ (m_2)$ and $k_4'\ (m_4')$

d/ $0 < F_{cr,support} \le F_{cr,span} \le F_{y,span} \le F_{y,support} \le F_{u,span}$ use of $k_2\ (m_2)$ and $k_4'\ (m_4')$

e/ $0 < F_{cr,span} \le F_{cr,support} \le F_{y,support} \le F_{y,span} \le F_{u,support}$ use of $k_2'\ (m_2')$ and $k_4\ (m_4)$

f/ $0 < F_{cr,span} \le F_{cr,support} \le F_{y,support} \le F_{y,span} \le F_{u,span}$ use of $k_2'\ (m_2')$ and $k_4\ (m_4)$

g/ $0 < F_{cr,span} \le F_{cr,support} \le F_{y,span} \le F_{y,support} \le F_{u,support}$ use of $k_2'\ (m_2')$ and $k_4'\ (m_4')$

h/ $0 < F_{cr,span} \le F_{cr,support} \le F_{y,span} \le F_{y,support} \le F_{u,span}$ use of $k_2'\ (m_2')$ and $k_4'\ (m_4')$

stage 1 stage 2 stage 3 stage 4 stage 5

5/ Once the increases of the bending moments for all stages are known, the acting bending moment at the end of each stage, at the two critical cross-sections can be obtained. Remark that this calculation needs to be determined for all 8 different combinations mentioned above.

6/ Given ΔM at the critical cross-sections, the increase of the load per stage can be calculated following Eq. A.3 (resulting from vertical and moment equilibrium).

$$\Delta F_i = \Delta M_{span,i} \frac{l}{ab} + \Delta M_{support,i} \frac{1}{b} \qquad (A.3)$$

Similar to the bending moments, the total loads at the end of each stage are obtained by cumulating the increase of the load in each stage.

7/ As mentioned in step 4, 8 different combinations are considered. Nevertheless only one out of the 8 combinations is giving the correct non-linear moment distribution (correct sequence of critical loads). This one combination is characterized by only positive load increases for every stage ($\Delta F_i \geq 0$ for i = 1 until 5). All other combinations are characterized by one or more negative load increases ($\Delta F_i < 0$).

8/ Finally, once the bending moments at the two critical sections and the load level at the end of each stage are known, the moment redistribution curve can be drawn by a linear interpolation between the end points of each stage.

Appendix B
OVERVIEW OF 3-POINT-BENDING TESTS

1 Overview of test program

1.1 Test set-up

In the following, an overview is given of the test set-up and test results of rectangular beams (total depth 400 mm, width 198 mm) with 3.6 m span, tested in 3-point-bending (see Fig. B.1). The cross-section of the FRP laminate equals 100 mm (w_f) x 1.0 mm (t_f). the internal reinforcement ratios (ρ_s) and external reinforcement ratios (ρ_f) are given in Table B. 1;

The external reinforcement ratio (ρ_f) equals 0.13 % for all strengthened beams. The laminates are applied over the entire free distance between the supports (length of laminate = 3500 mm).

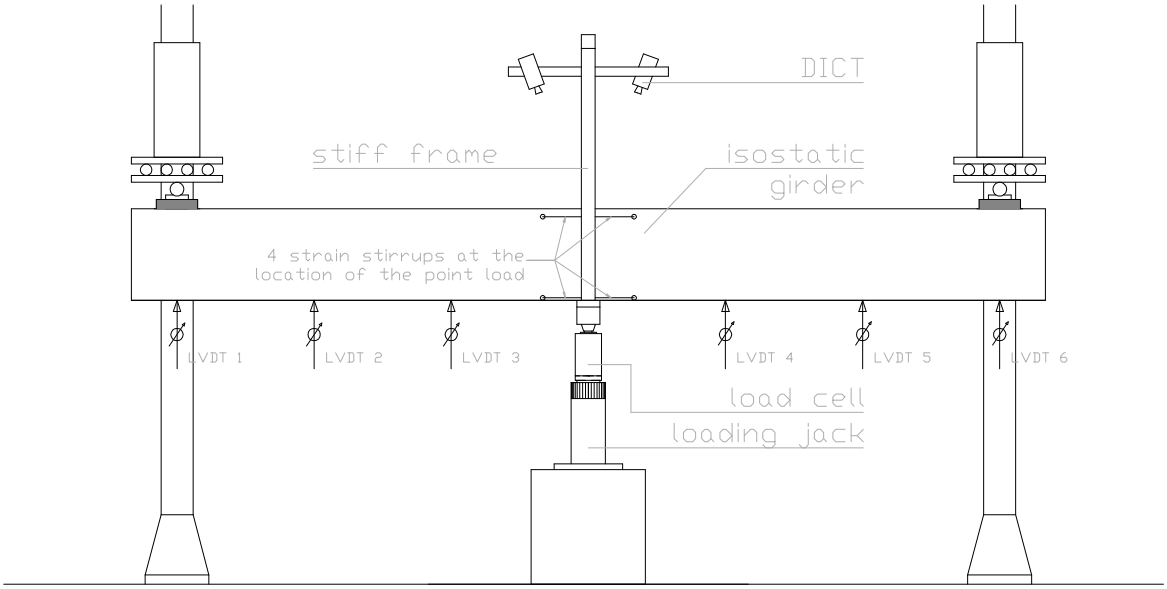

Fig. B.1: three-point-bending test configuration

The material properties of each beam are given in the following sections (see Table B.2 till Table B.7). These values result from standard tensile tests for the steel and FRP reinforcement [1, 2]. To determine the properties of the concrete, standard tests are conducted at the age of 28 days [3, 4].

Table B. 1: Reinforcement ratios used in 3-point-bending tests

	Steel reinforcement ratio ρ_s	FRP reinforcement ratio ρ_f
IB REF.	0.64 %	0.00 %
IB1	0.31 %	0.13 %
IB2	0.64 %	0.13 %
IB3	1.43 %	0.13 %
IB4	0.64 %	0.13 %
IB5	0.64 %	0.13 %

As can be noticed from Fig. B.1 a test set-up has been used, by which the tested beam is loaded by means of an upward oriented load. This test set-up is used to be able to apply a Digital Image Correlation Technique (DICT). By using this technique strain and displacement variations of a limited surface of the beam are recorded by means of two cameras. In order to obtain reliable measurement results, these two cameras have to be kept on a constant distance. This is obtained in this test set-up by the use of an additional stiff frame which is clamped between the loading jack and the beam and on which the DICT-cameras are fixed.

1.2 Measurements

During the tests both manual and electronic measurements were performed, among which (see Fig. B.1):

- Load cells at the location of the load cell: electronical measurement of force
- LVDT (linear Variable Displacement Transducer): electronical measurement of deflection
- Strain stirrups: electronical measurement of strain
- Strain gauges glued on the FRP laminate: electronical measurement of strain
- Manual measurement of crack spacing
- Manual measurement of crack width

For detailed information concerning these measurement techniques, reference is made to section 3.1.3 of Chapter 2.

Electronic measurements are executed by a dedicated data acquisition system (type system 5000) at a sampling rate of 2-4 Hz during the loading stages.

1.3 Loading scheme

At an age of 28 days, the static bending tests on the beams are conducted by means of one hydraulic jack, with a maximum capacity equal to 40 t. At every step of 10 kN, the load is kept constant, in order to execute the manual measurements. At 80 % of the analytically estimated failure load, the beam is loaded continuously until failure.

1.4 Results

In the following sections, for every beam, the following is given:

- reinforcement configuration
- tested material properties of the concrete and the reinforcement
- failure load and failure aspect
- crack pattern of different load stages
- load curvature graph
- concrete compression strain, concrete strain at the level of the internal reinforcement and FRP strain, measured at the mid-span

In these graphs, both experimentally and analytically obtained results are given. The analytical curves are obtained by taking into account the horizontal and moment equilibrium equations and besides by taking into account full composite action. Also a horizontal dashed line is given in these graphs, which indicates the calculated failure load characterized by debonding of the externally bonded reinforcement.

In general it can be concluded that the experimentally obtained results agree very well with the analytically obtained results.

2 IB ref.

2.1 Configuration

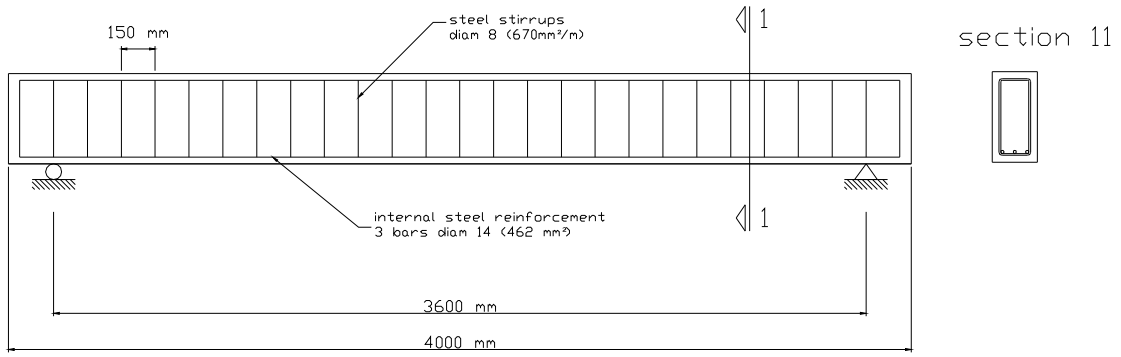

Fig. B.2: Configuration of tested beam IB ref.

Table B.2: Material properties of beam IB ref.

		Concrete	Steel	FRP
Modulus of elasticity	[N/mm²]	35500	211900	-
Mean compressive strength	[N/mm²]	40.5	-	-
Yielding stress	[N/mm²]	-	618	-
Tensile strength	[N/mm²]	2.7	682	-
Ultimate strain	[%]	0.35	6.82	-

2.2 Failure load and failure aspects

The beam failed at 121,5 kN by steel yielding followed by rupture of the steel reinforcement (see Fig. B.3).

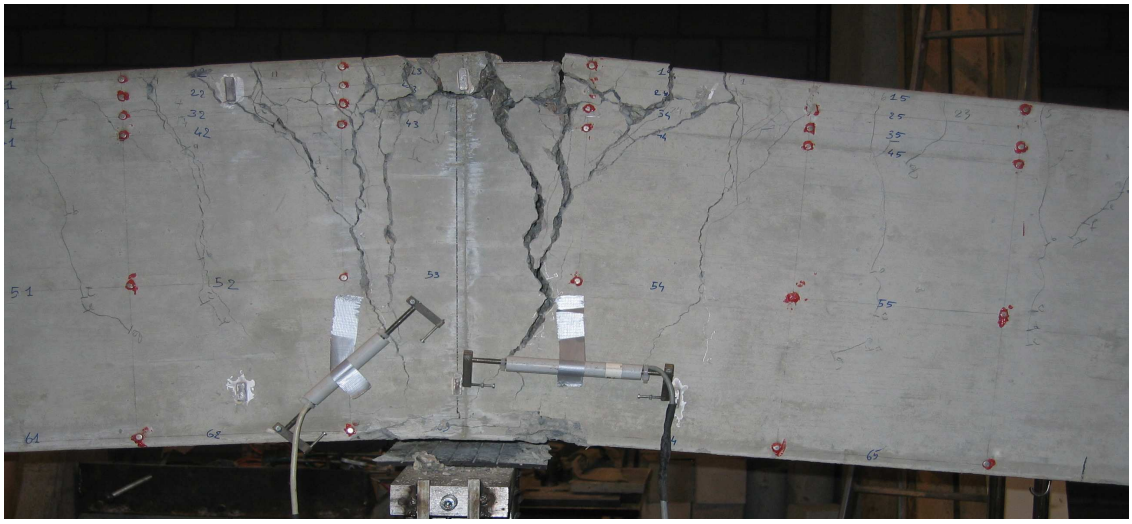

Fig. B.3: View of plastic hinge at IB ref.

2.3 Crack pattern

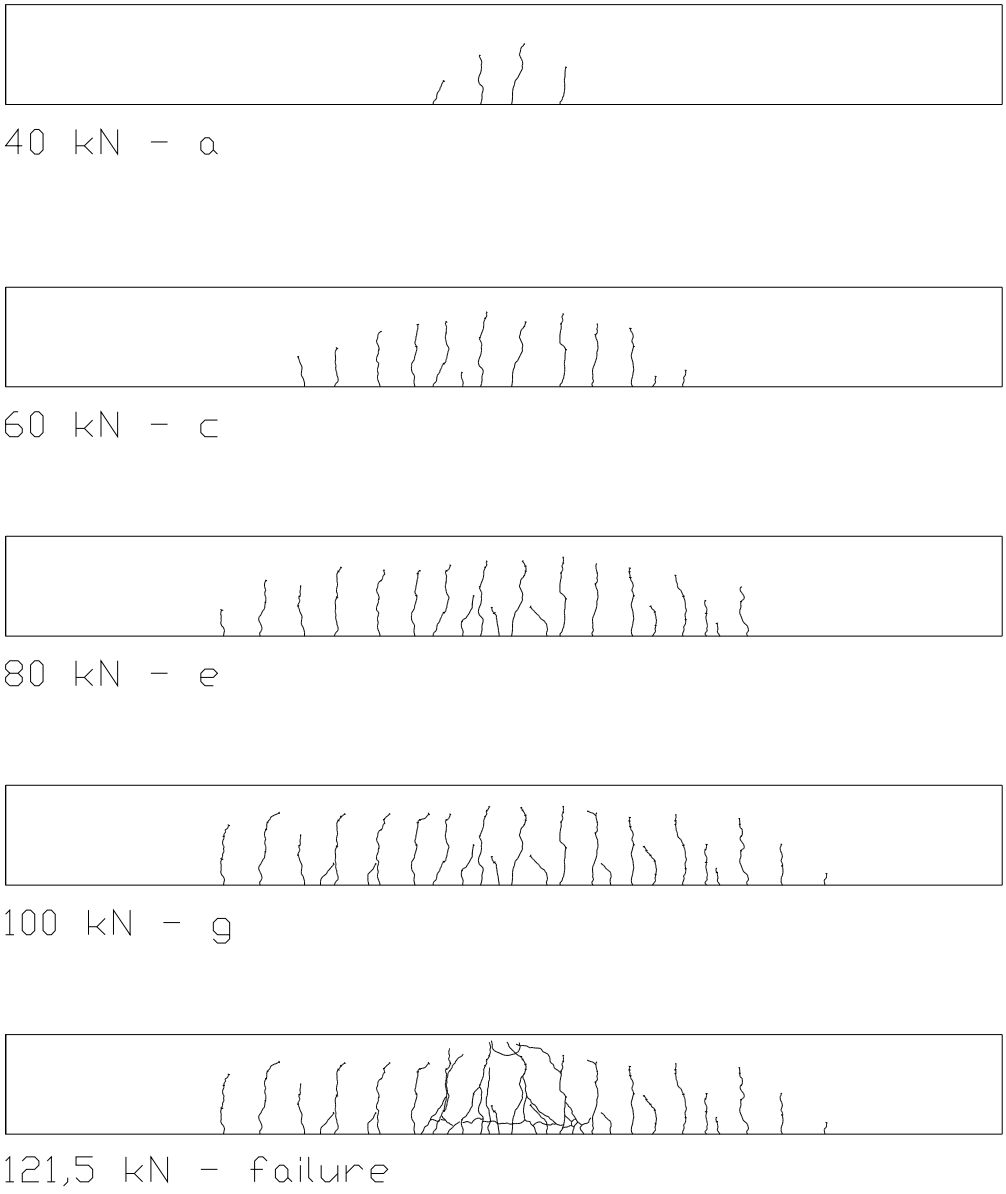

Fig. B.4: Crack pattern of IB ref.

2.4 Load-curvature graph

Due to the large deformations, the electronical strain measurements are recorded only until 110.9 kN.

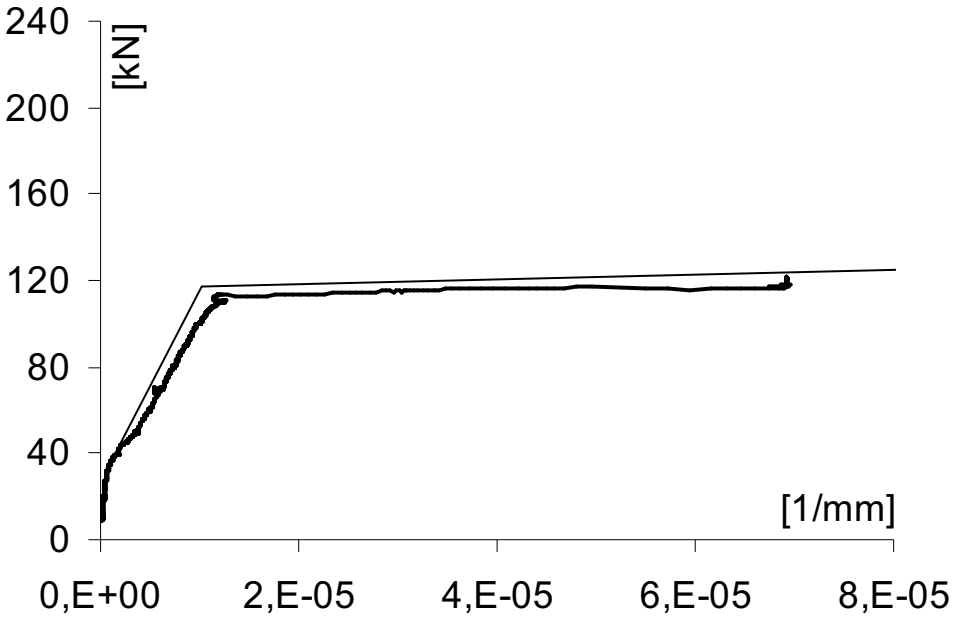

Fig. B.5: Load-curvature graph of IB ref.

2.5 Strain evolution at mid-span

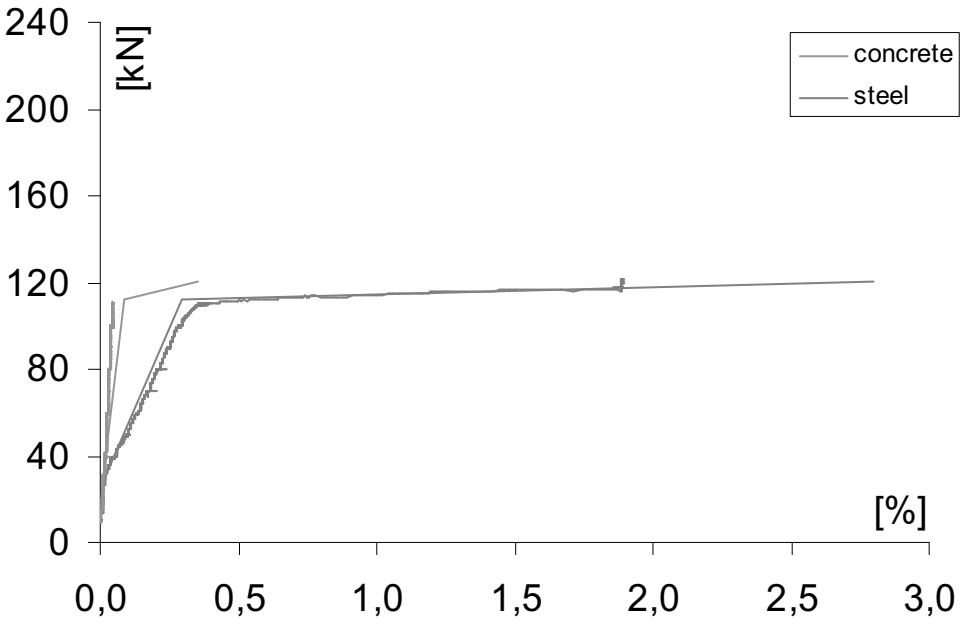

Fig. B.6: strain evolution of concrete and internal steel reinforcement (IB ref.)

3 IB1

3.1 Configuration

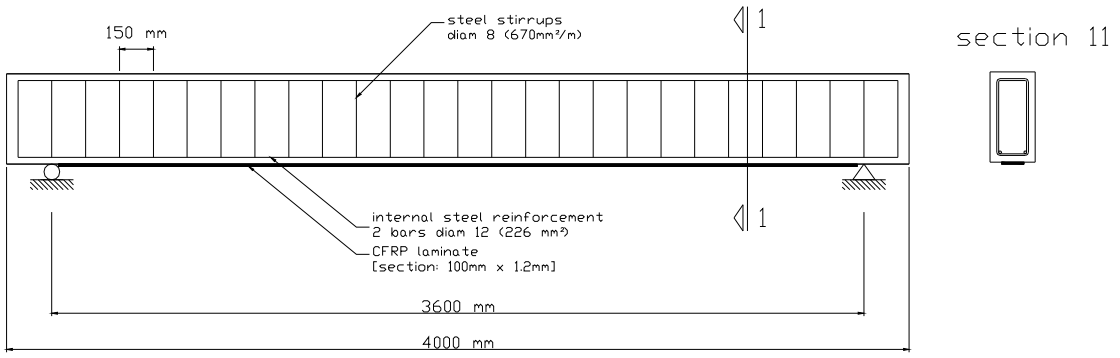

Fig. B.7: Configuration of tested beam IB1

Table B.3: Material properties of beam IB1

		Concrete	Steel	FRP
Modulus of elasticity	[N/mm²]	33900	222800	180000
Mean compression strength	[N/mm²]	39.0	-	-
Yielding stress	[N/mm²]	-	589	-
Tensile strength	[N/mm²]	2.84	674	2981
Ultimate strain	[%]	0.35	9.62	1.65

3.2 Failure load and failure aspects

The beam failed at 100.3 kN by debonding of the external reinforcement (see Fig. B.8).

Fig. B.8: View of debonded laminate of IB1

3.3 Crack pattern

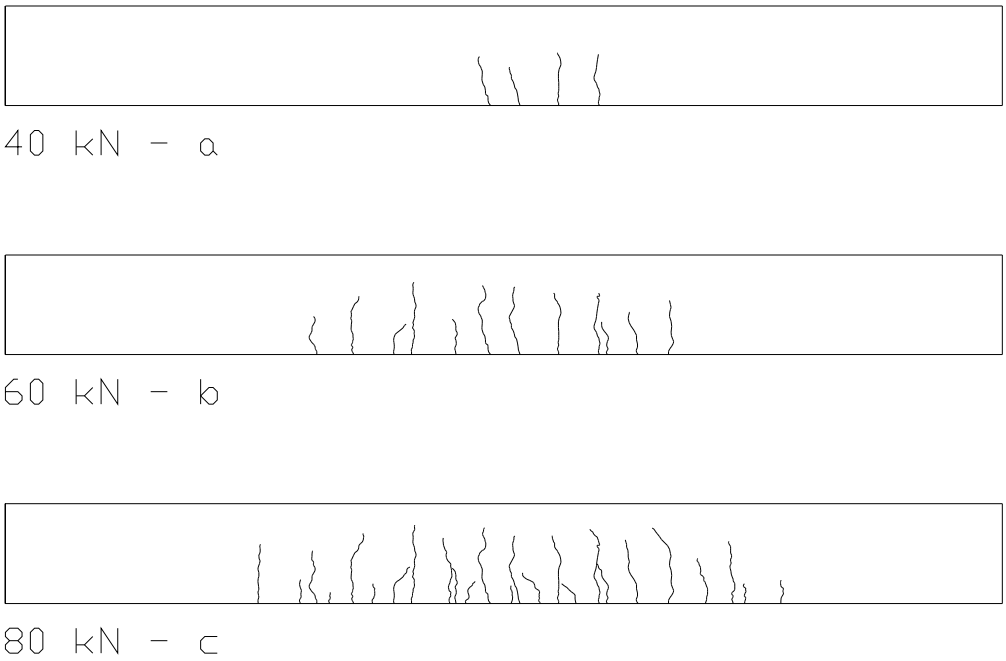

Fig. B.9: Crack pattern of IB1

3.4 Load-curvature graph

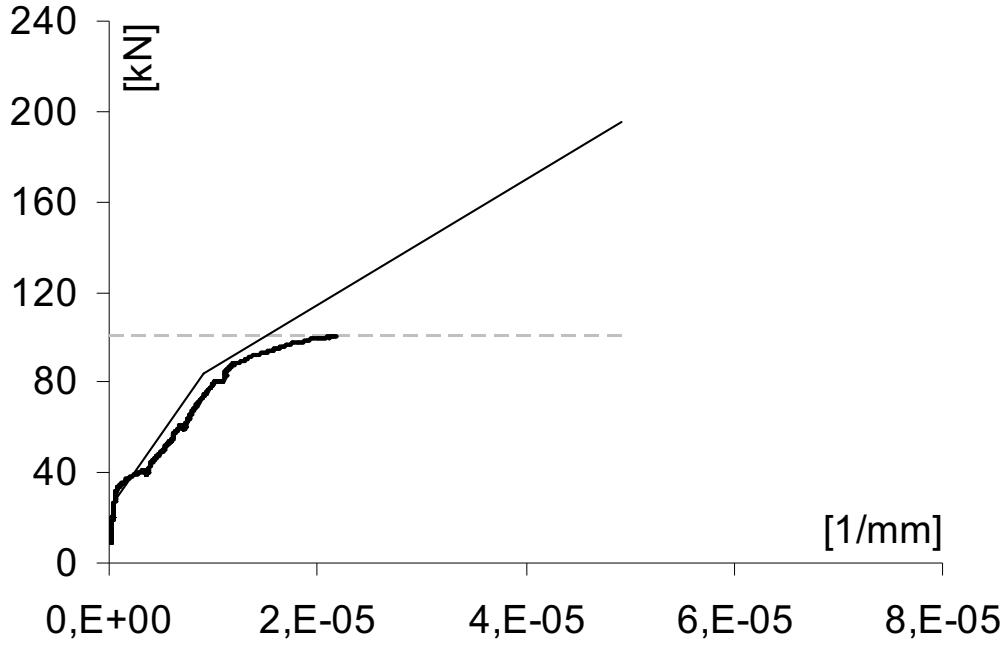

Fig. B.10: Load-curvature graph of IB1

3.5 Strain evolution at mid-span

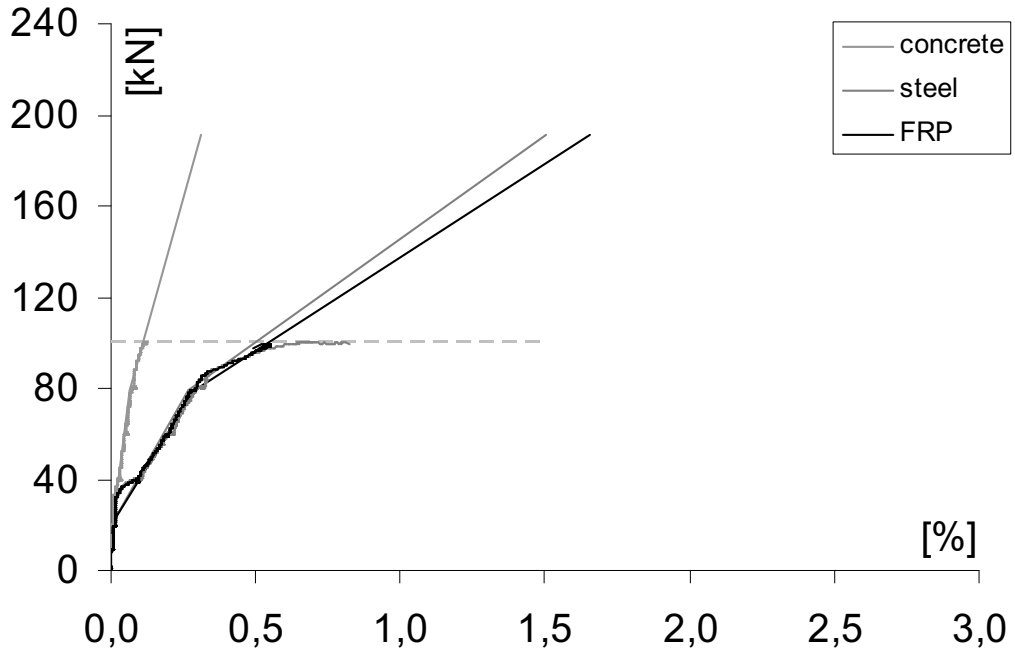

Fig. B.11: strain evolution of concrete, internal steel reinforcement and FRP (IB1)

4 IB2

4.1 Configuration

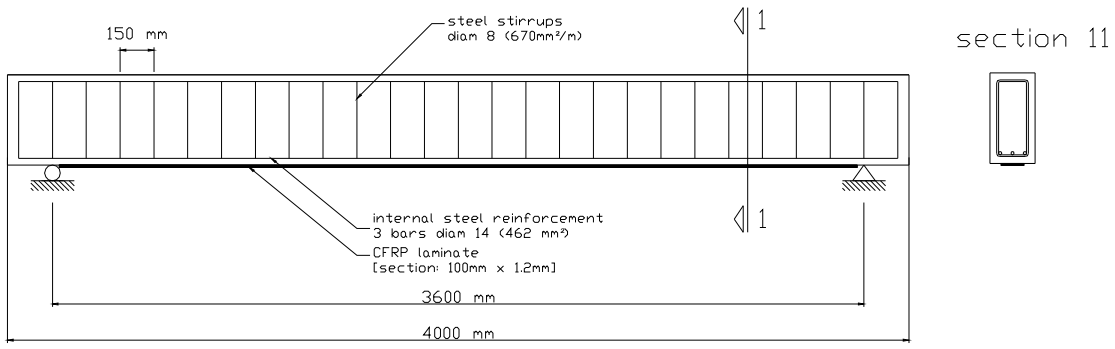

Fig. B.12: Configuration of tested beam IB2

Table B.4: Material properties of beam IB2

		Concrete	Steel	FRP
Modulus of elasticity	[N/mm²]	35500	211900	180000
Mean compression strength	[N/mm²]	40.5	-	-
Yielding stress	[N/mm²]	-	618	-
Tensile strength	[N/mm²]	2.7	682	2981
Ultimate strain	[%]	0.35	6.82	1.65

4.2 Failure load and failure aspects

The beam failed at 153.0 kN by debonding of the external reinforcement (see Fig. B.13).

Fig. B.13: View of debonded laminate of IB2

4.3 Crack pattern

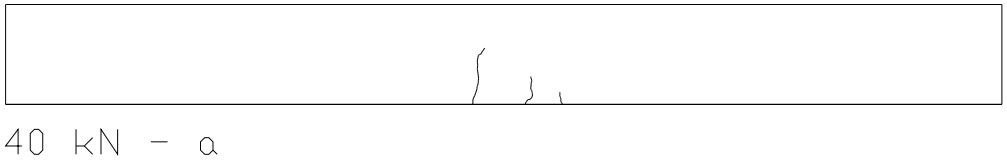

40 kN – a

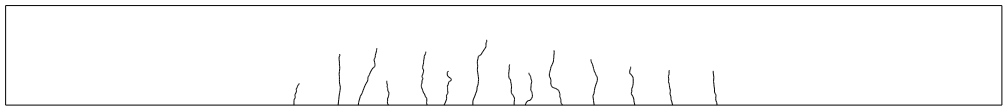

60 kN – b

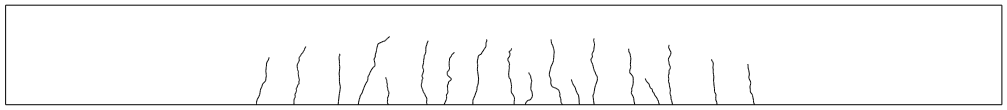

80 kN – c

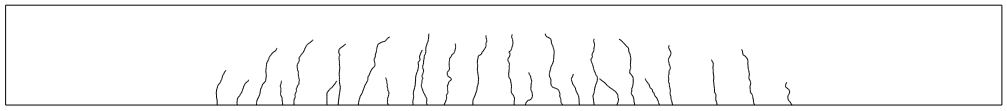

100 kN – d

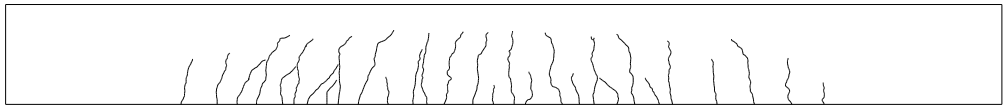

120 kN – e

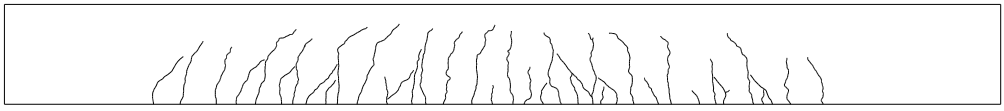

140 kN – f

Fig. B.14: Crack pattern of IB2

4.4 Load-curvature graph

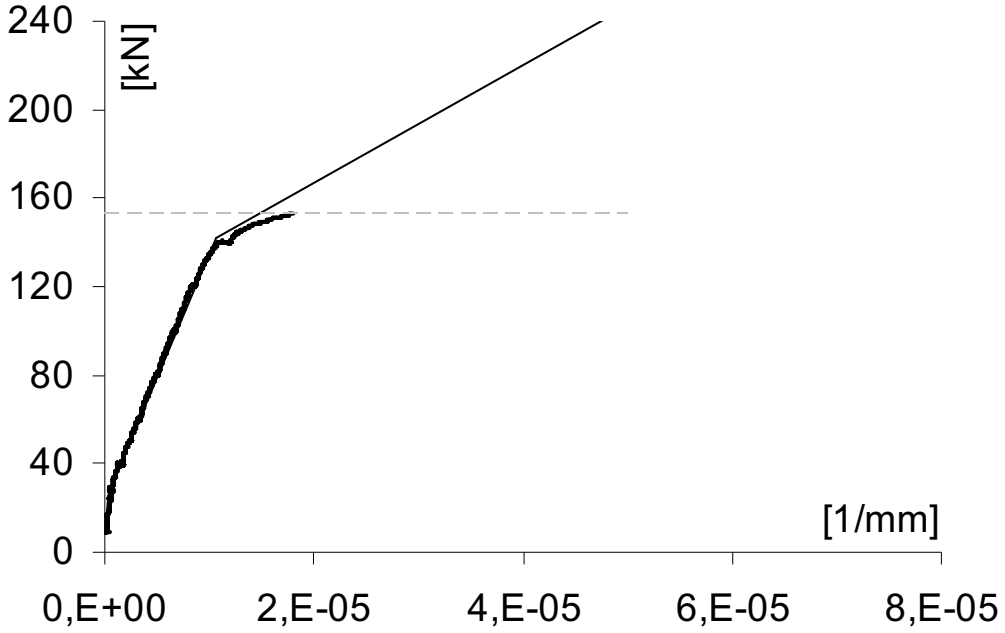

Fig. B.15: Load-curvature graph of IB2

4.5 Strain evolution at mid-span

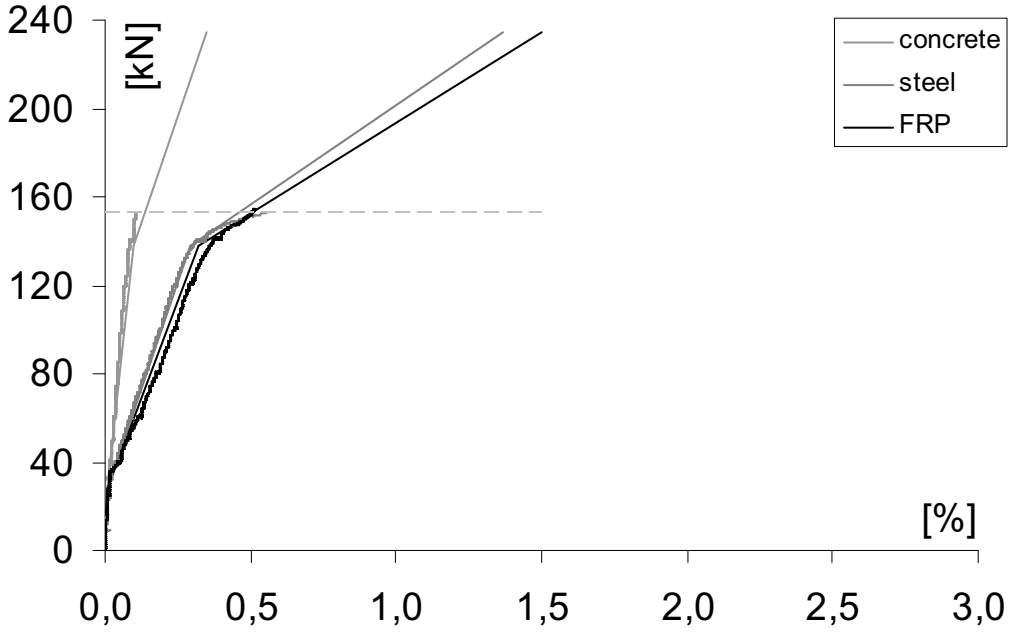

Fig. B.16: strain evolution of concrete, internal steel reinforcement and FRP (IB2)

5 IB3

5.1 Configuration

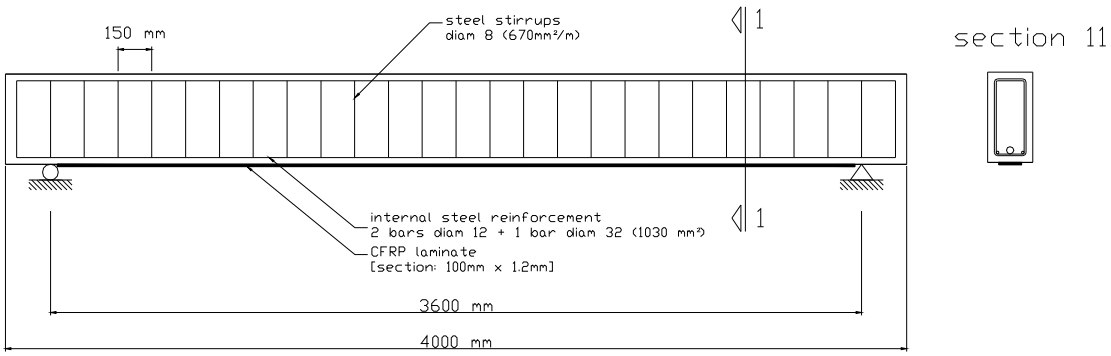

Fig. B.17: Configuration of tested beam IB3

Table B.5: Material properties of beam IB3

		Concrete	Steel	FRP
Modulus of elasticity	[N/mm²]	35600	210000	180000
Mean compression strength	[N/mm²]	38.7	-	-
Yielding stress	[N/mm²]	-	474	-
Tensile strength	[N/mm²]	3.0	703	2981
Ultimate strain	[%]	0.35	11.39	1.65

5.2 Failure load and failure aspects

The beam failed at 218.8 kN by debonding of the external reinforcement (see Fig. B.18).

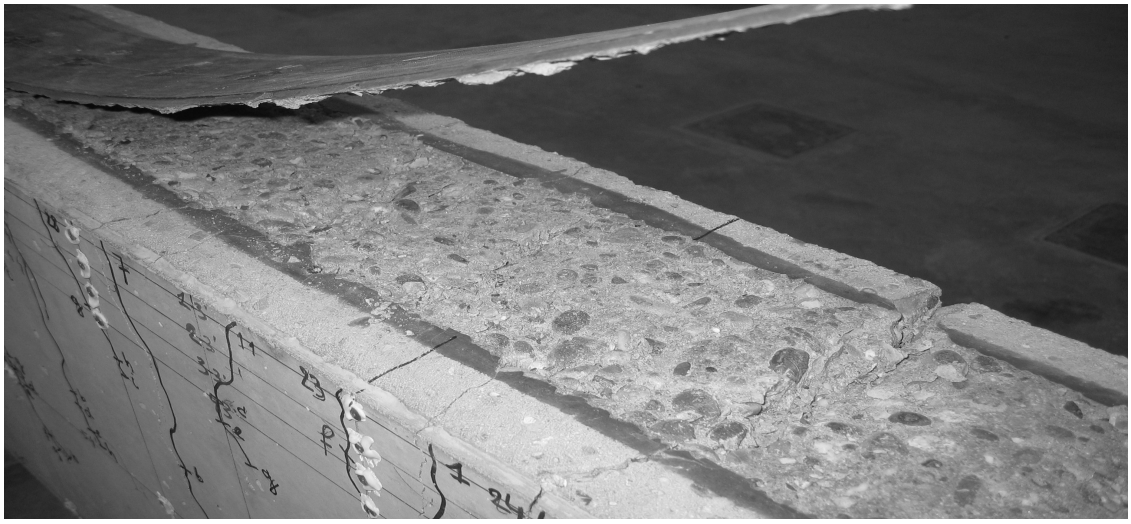

Fig. B.18: View of debonded laminate of IB3

5.3 Crack pattern

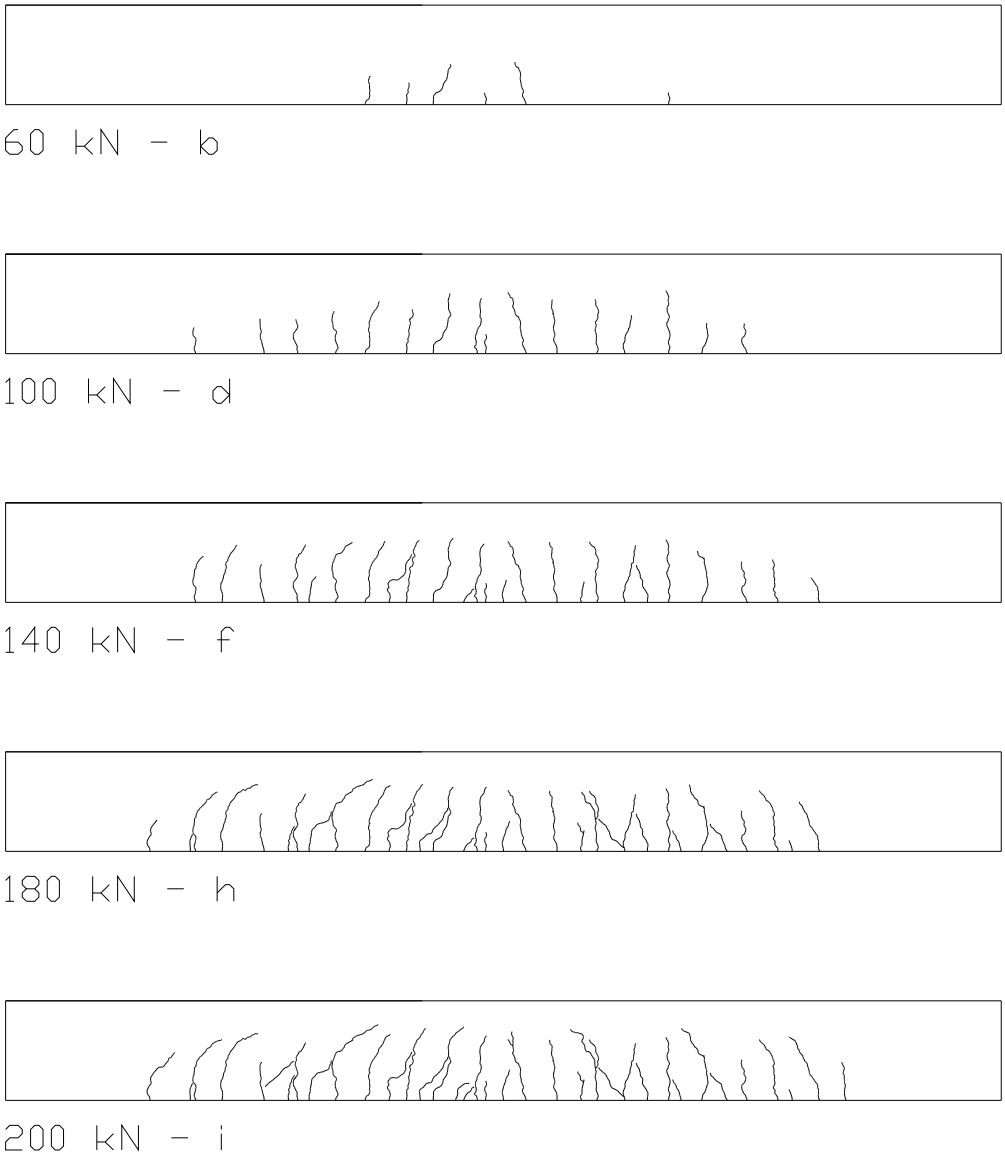

Fig. B.19: Crack pattern of IB3

5.4 Load-curvature graph

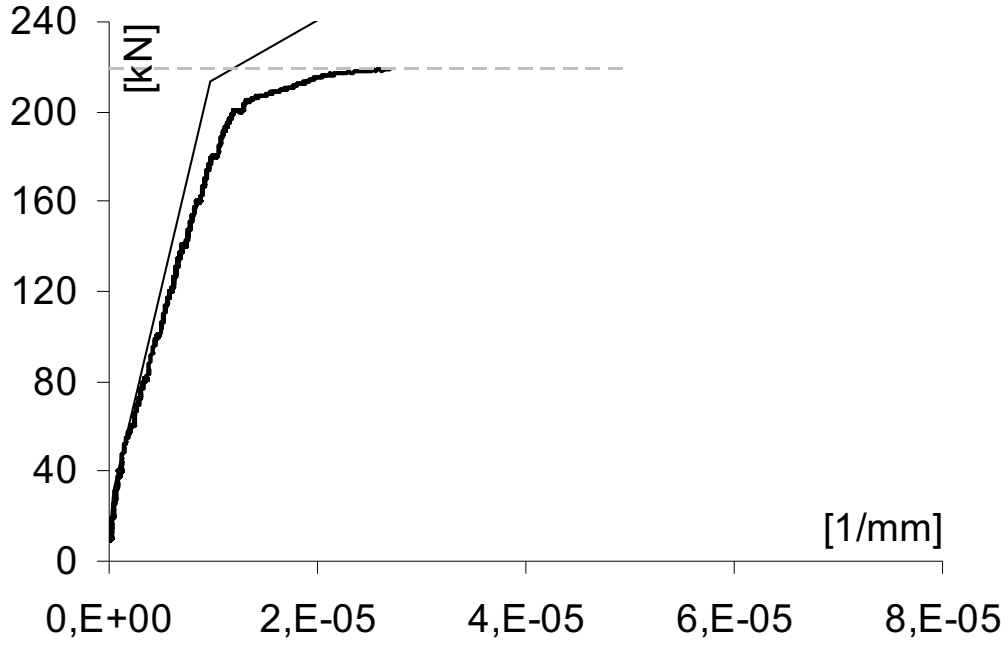

Fig. B.20: Load-curvature graph of IB3

5.5 Strain evolution at mid-span

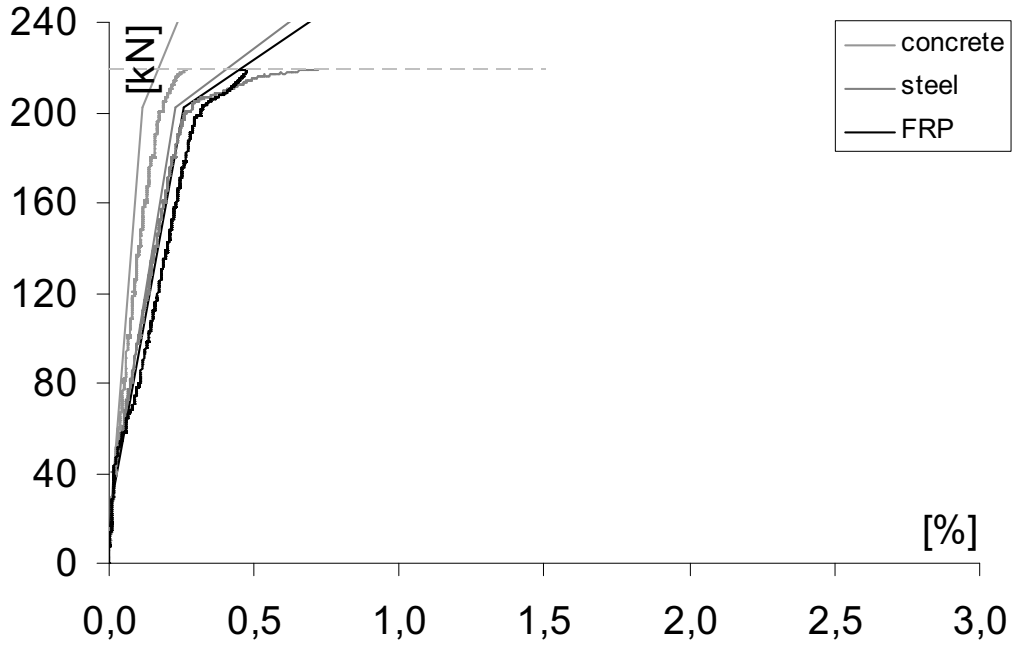

Fig. B.21: strain evolution of concrete, internal steel reinforcement and FRP (IB3)

6 IB4

6.1 Configuration

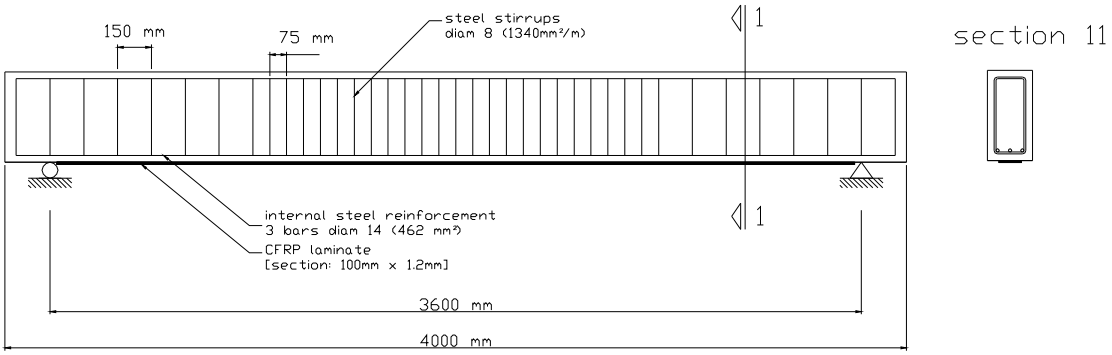

Fig. B.22: Configuration of tested beam IB4

Table B.6: Material properties of beam of IB4

		Concrete	Steel	FRP
Modulus of elasticity	[N/mm²]	33900	211900	180000
Mean compression strength	[N/mm²]	39.0	-	-
Yielding stress	[N/mm²]	-	618	-
Tensile strength	[N/mm²]	2.84	682	2981
Ultimate strain	[%]	0.35	6.82	1.65

6.2 Failure load and failure aspects

The beam failed at 147.6 kN by debonding of the external reinforcement (see Fig. B.23).

Fig. B.23: View of debonded laminate of IB4

6.3 Crack pattern

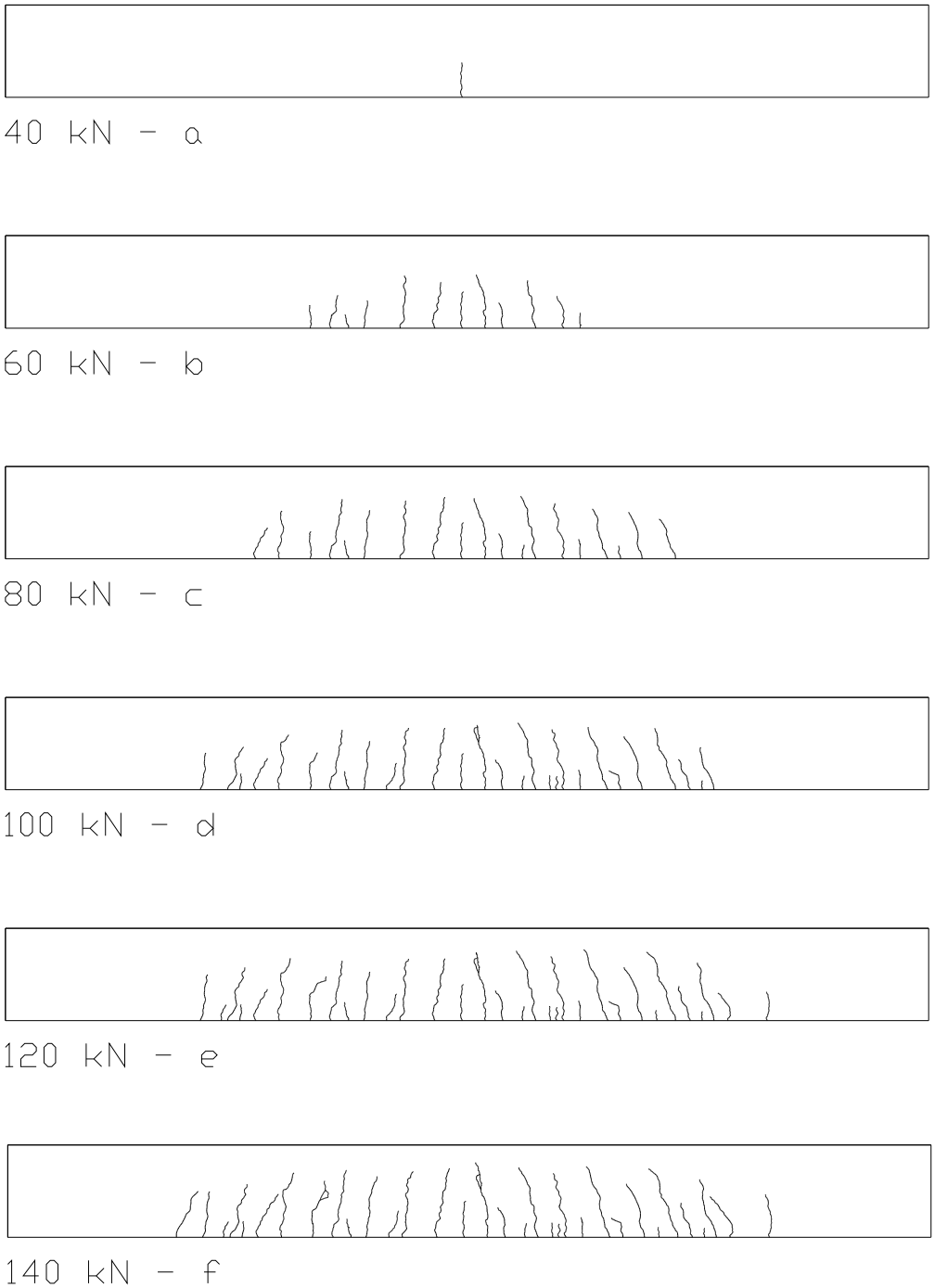

Fig. B.24: Crack pattern of IB4

6.4 Load-curvature graph

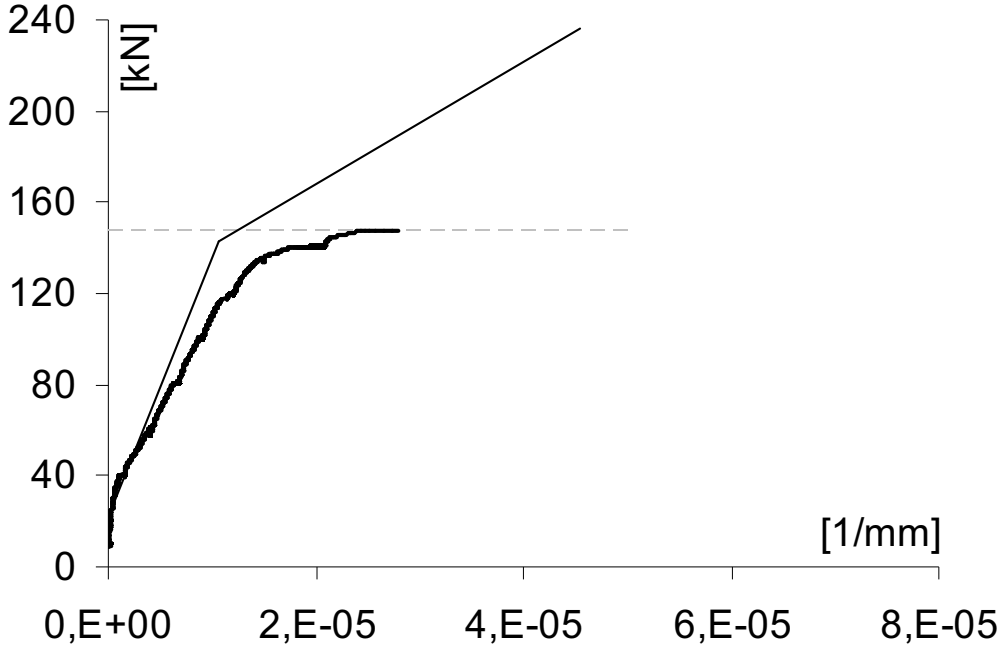

Fig. B.25: Load-curvature graph of IB4

6.5 Strain evolution at mid-span

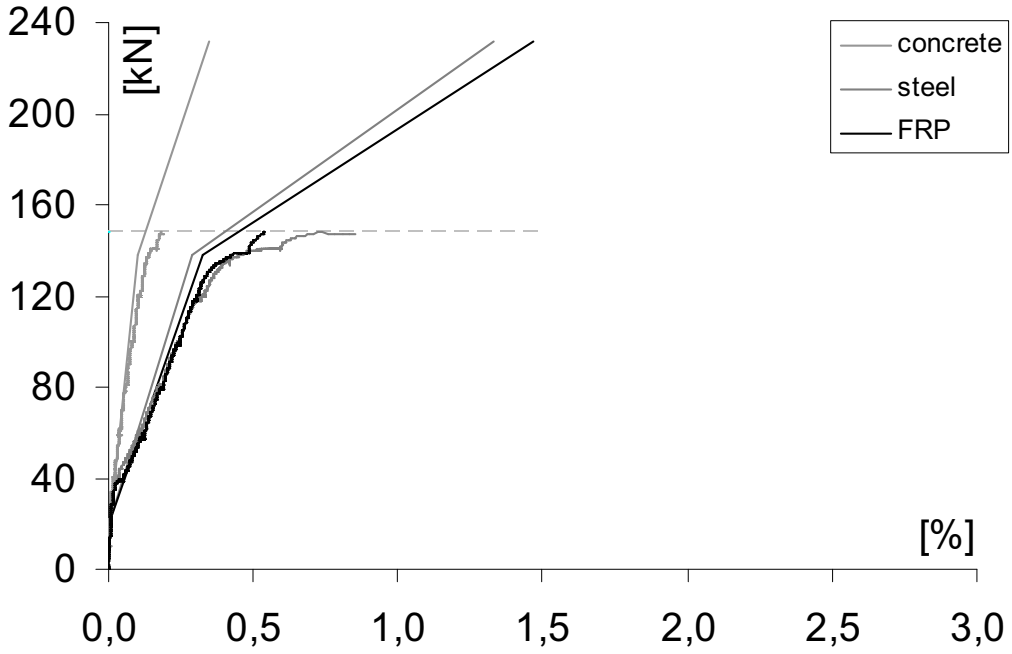

Fig. B.26: strain evolution of concrete, internal steel reinforcement and FRP (IB4)

7 IB5

7.1 Configuration

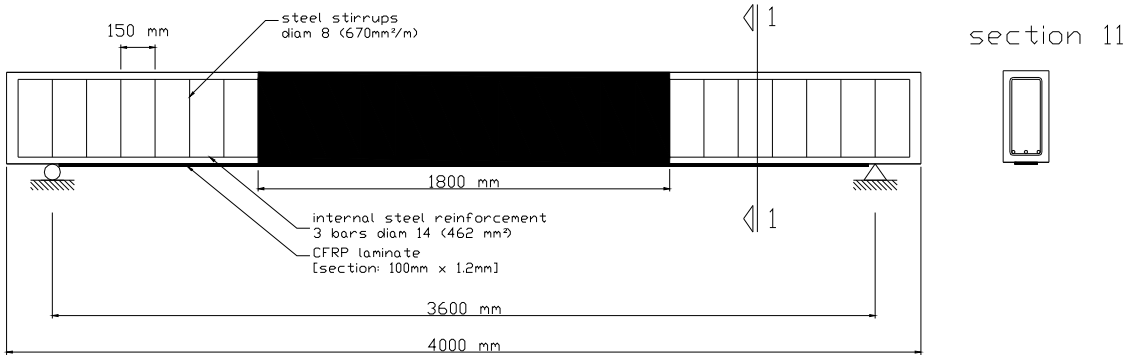

Fig. B.27: Configuration of tested beam IB5

As can be noticed in Fig. B.27, the central zone of the beam is wrapped by means of one layer of carbon textile. The material characteristics are given in Table B.7 (FRP-textile).

Table B.7: Material properties of beam IB5

		Concrete	Steel	FRP	FRP-textile
Modulus of elasticity	[N/mm²]	35600	211900	180000	180000
Mean compression strength	[N/mm²]	38.7	-	-	-
Yielding stress	[N/mm²]	-	618	-	-
Tensile strength	[N/mm²]	3.0	682	2981	3840
Ultimate strain	[%]	0.35	6.82	1.65	1.65

7.2 Failure load and failure aspects

The beam failed at 178.4 kN by debonding of the external reinforcement (see Fig. B.28).

Fig. B.28: View of debonded laminate of IB5

7.3 Crack pattern

Fig. B.29: Visible crack pattern of IB5

7.4 Load-curvature graph

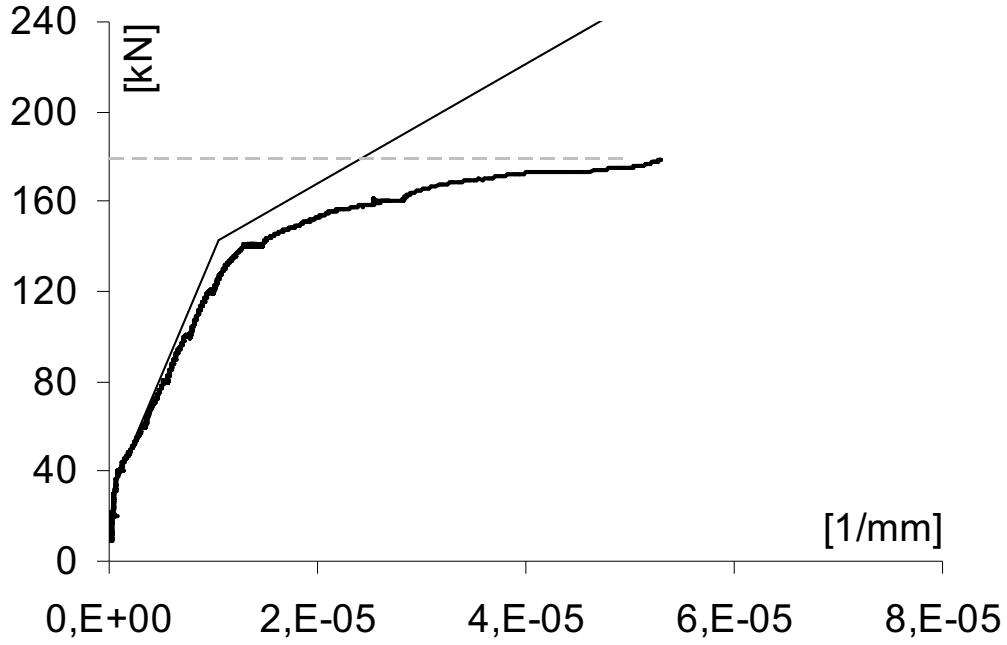

Fig. B.30: Load-curvature graph of IB5

7.5 Strain evolution at mid-span

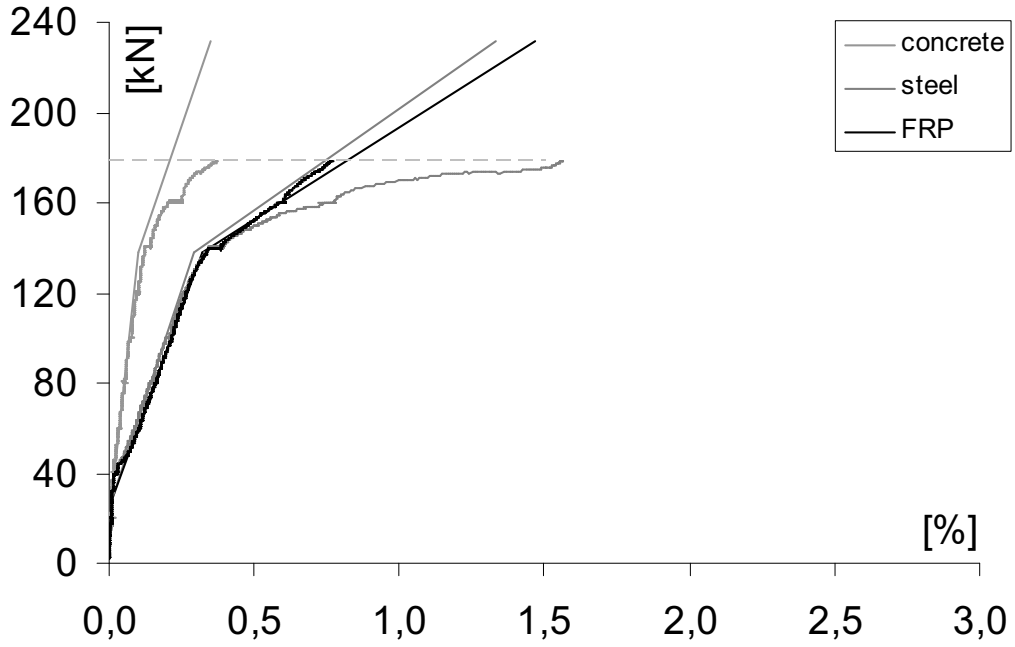

Fig. B.31: strain evolution of concrete, internal steel reinforcement and FRP (IB5)

References

[1] ISO-6892, *Metallic materials - Tensile testing at ambient temperature* 1998.
[2] NBN-EN-ISO-527, *Kunststoffen - Bepaling van de trekeigenschappen - Deel 1 : Algemene principes*. 1996.
[3] NBN-B15-220, *Proeven op beton - Bepaling van de druksterkte*. 1990.
[4] NBN-B15-214, *Proeven op beton - buigproef op betonprisma's*. 1990.

Appendix C

STRENGTHENING OF BOTH THE SPAN AND THE MID-SUPPORT OF A BEAM WITH INTERNAL REINFORCEMENT RATIOS DIFFERENT FROM THE LINEAR ELASTIC DISTRIBUTION

1 Introduction

In this appendix FRP strengthening of both the span and the mid-support of a beam with internal reinforcement ratios different from the linear elastic distribution is investigated. This investigation is supplementary to the study of design recommendations concerning strengthened two-span RC beams with internal reinforcement ratios according to the linear elastic theory, given in Chapter 6.

As configuration for this study a two-span beam is taken loaded with a point load F in each span (see Fig. C.1). As can be noticed this configuration is the same as the configuration used in Chapter 6.

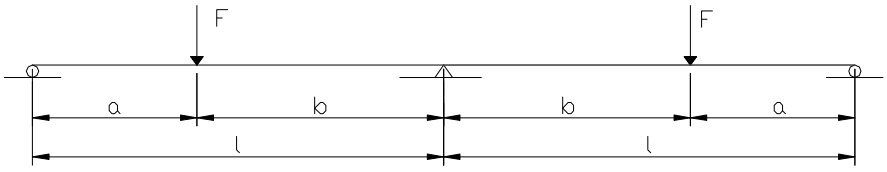

Fig. C.1: Continuous beam with two spans

2 Linear elastic theory with limited redistribution

2.1 Unstrengthened reference beam

In the framework of Appendix C, no predefined unstrengthened reference beam (with non-linear internal reinforcement configuration) is used. For comparison reasons, reference is made to case 1 of Chapter 6 (see section 3.2.2), which starts with un unstrengthened beam with linear elastic moment distribution (see Fig. C.2). For this beam a moment redistribution of 20 % or 30 % is considered (see Fig. C.3), which for the purpose of this calculation relates to a non-linear

reinforcement configuration of both the internal and external reinforcement, as explained in the following section

2.2 Strengthened beam

A higher load bearing capacity of the two-span beam, given in Fig. C.2, is obtained by increasing the bending moment in the spans, keeping a constant moment at the mid-support (plastic hinge). This is illustrated in Fig. C.3, introducing a moment redistribution 20 % or 30 %. In Chapter 6 this is obtained by strengthening only the spans with FRP, in order to resist additional bending moments.

For the purpose of creating a non-linear internal reinforcement configuration, and to strengthen also the mid-support, case 1 of Chapter 6 is still followed (see Fig. C.3), although a certain part of the internal steel reinforcement at the mid-support is replaced by FRP EBR. The amount of FRP EBR is chosen in such a way that the resisting moment of the mid-support with internal steel and external FRP reinforcement is equal to that of the originally steel reinforced mid-support of the beam in Fig. C.2.

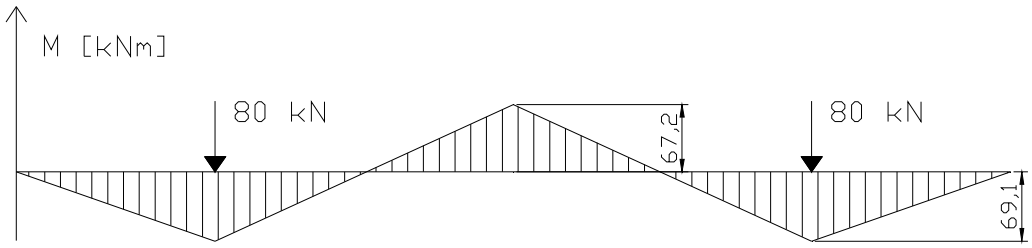

Fig. C.2: Linear elastic moment distribution of unstrengthened two span beam

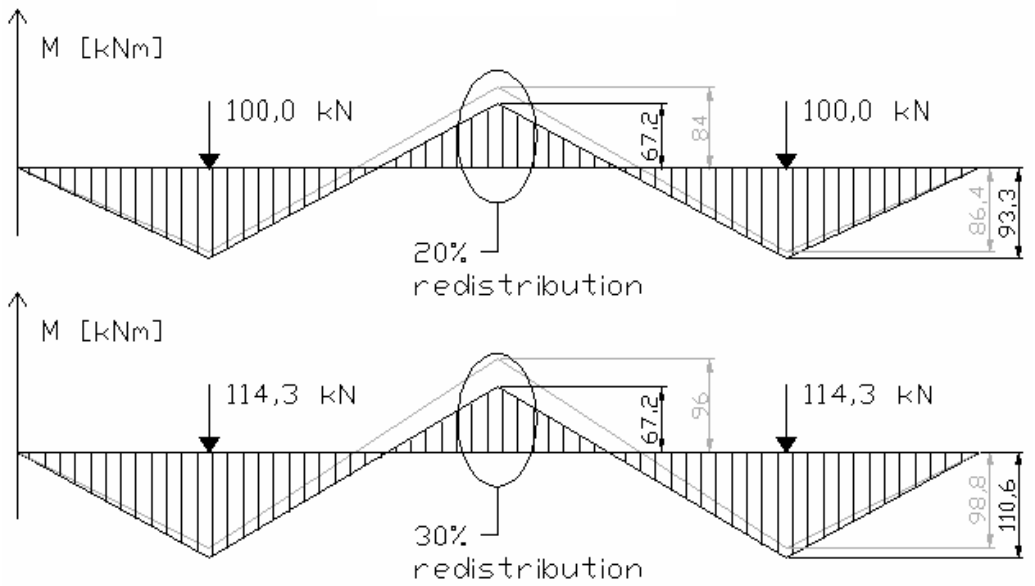

Fig. C.3: Moment redistributions (20% and 30%) at ultimate state

Four different strengthening cases are distinguished:

- Case A: 20 % redistribution (see Fig. C.3) and 20 % of the internal steel reinforcement at the mid-support is replaced by FRP EBR
- Case B: 20 % redistribution (see Fig. C.3) and 40 % of the internal steel reinforcement at the mid-support is replaced by FRP EBR
- Case C: 30 % redistribution (see Fig. C.3) and 20 % of the internal steel reinforcement at the mid-support is replaced by FRP EBR
- Case D: 30 % redistribution (see Fig. C.3) and 40 % of the internal steel reinforcement at the mid-support is replaced by FRP EBR

The mechanical properties used in this analytical study are again identical to the properties used in Chapter 6, see also Table C.1. In Table C.2, both the internal and external reinforcement ratios of all different cases mentioned above are given, calculated according the linear elastic theory with limited redistribution. Besides these four cases, also the reinforcement ratios of the beams, for which no internal reinforcement of the mid-support is replaced by FRP EBR, are given. These beams are indicated with Ref 20 % and Ref 30 % respectively. Both beams were already discussed in case 1 of Chapter 6.

Table C.1: Material properties

	C35/45		S500		CFRP	
Compressive strength	35	N/mm²				
Yielding strength			500	N/mm²		
Tensile strength	3.5	N/mm²	550	N/mm²	2850	N/mm²
Failure strain	0.35	%	12.40	%	1.81	%
E-modulus	32000	N/mm²	200000	N/mm²	175000	N/mm²

Table C.2: Reinforcement ratios of different cases

	$\rho_{f,span}$ [%]	$\rho_{s,span}$ [%]	$\rho_{f,support}$ [%]	$\rho_{s,support}$ [%]
Ref 20 %	0.11	0.50	0.00	0.50
Case A	0.11	0.50	0.06	0.40
Case B	0.11	0.50	0.11	0.30
Ref 30 %	0.19	0.50	0.00	0.50
Case C	0.19	0.50	0.06	0.40
Case D	0.19	0.50	0.11	0.30

A verification of the results obtained with the linear elastic theory with limited redistribution is given in the next section (section 3). Similar as for case 3 of Chapter 6, it is demonstrated that the linear elastic theory with limited redistribution is not applicable if strengthening is applied in both the spans and the mid-support. A discussion on the ductility verification is given in section 4.

3 Non-linear approach

In Fig. C.4 to Fig. C.11, the graphs for the different redistribution ratios are given. The moment redistribution, the redistribution factor, the neutral axis depth of the critical cross-sections and the curvature of the critical cross-sections are given in function of the applied point load.

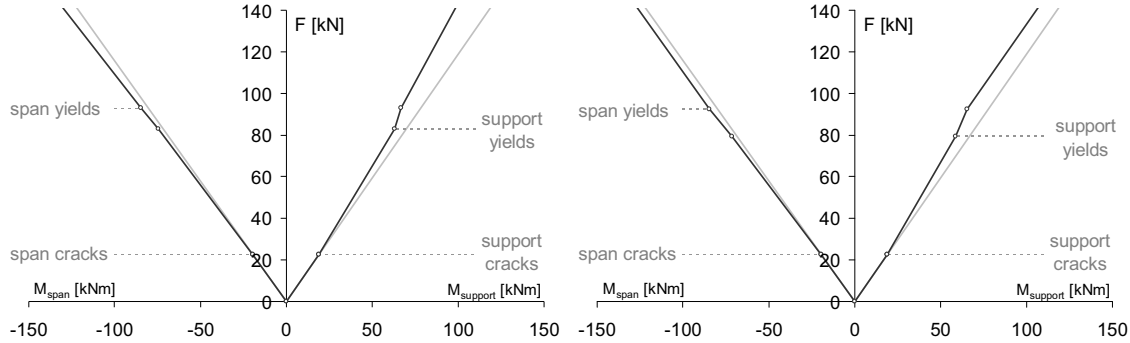

Fig. C.4: 20% redistribution by applying FRP EBR in the span and by replacing 20 % (left figure - Case A) or 40 % (right figure - Case B) of the internal steel reinforcement at the support by FRP EBR

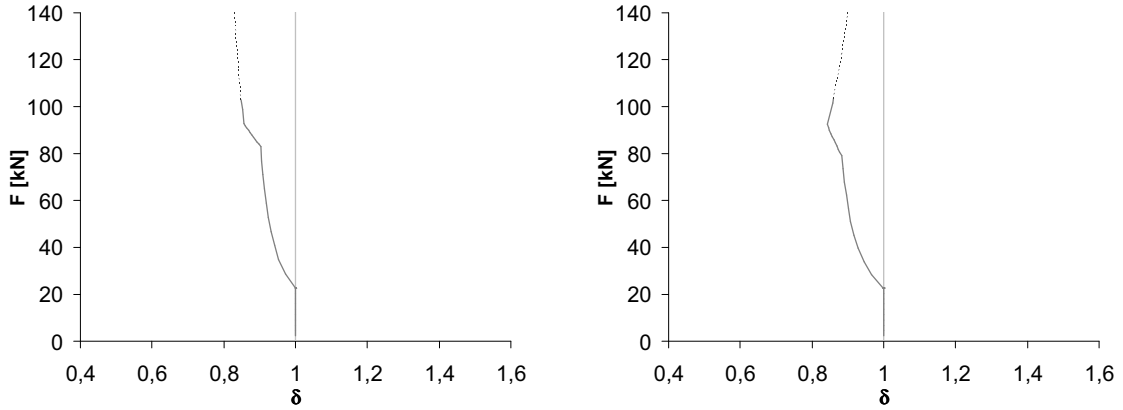

Fig. C.5: Redistribution factor δ for 20 % redistribution (left fig. – 20 % FRP at mid-support – Case A; right fig. – 40 % FRP at mid-support – Case B)

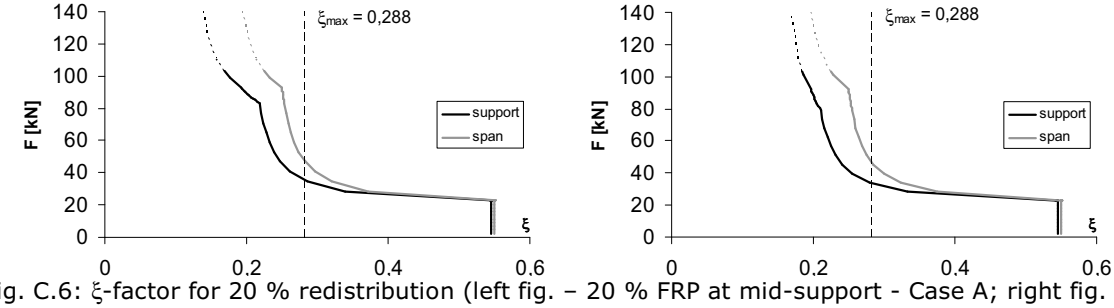

Fig. C.6: ξ-factor for 20 % redistribution (left fig. – 20 % FRP at mid-support - Case A; right fig. – 40 % FRP at mid-support - Case B)

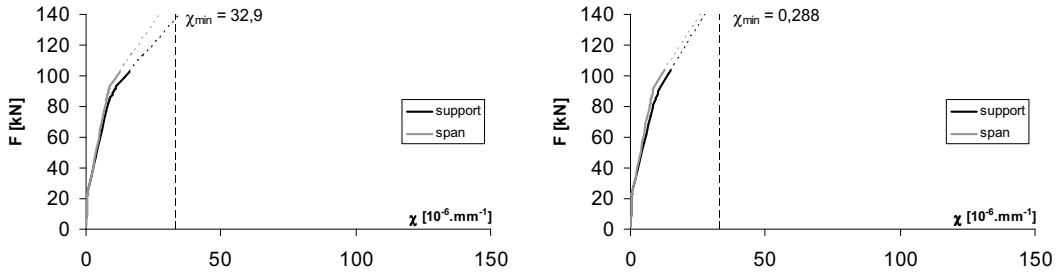

Fig. C.7: Curvature for 20 % redistribution (left fig. – 20 % FRP at mid-support - Case A; right fig. – 40 % FRP at mid-support - Case B)

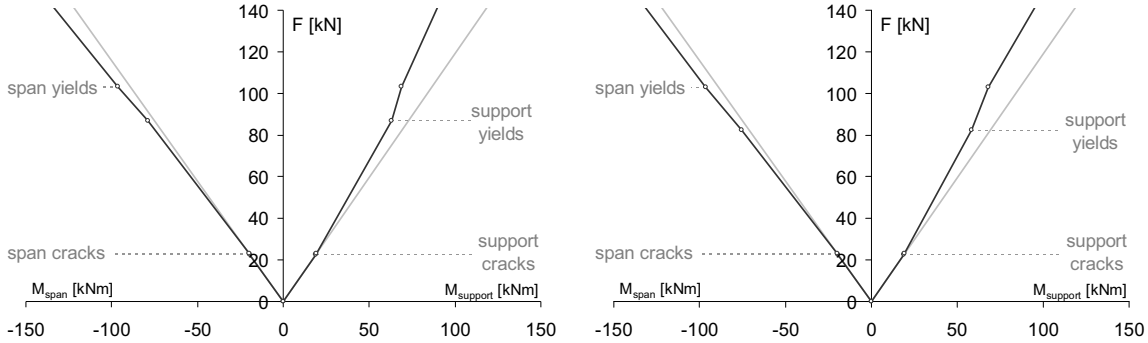

Fig. C.8: 30% redistribution by applying FRP EBR in the span and by replacing or 20 % (left figure - Case C) or 40 % (right figure - Case D) of the internal steel reinforcement at the support by FRP EBR

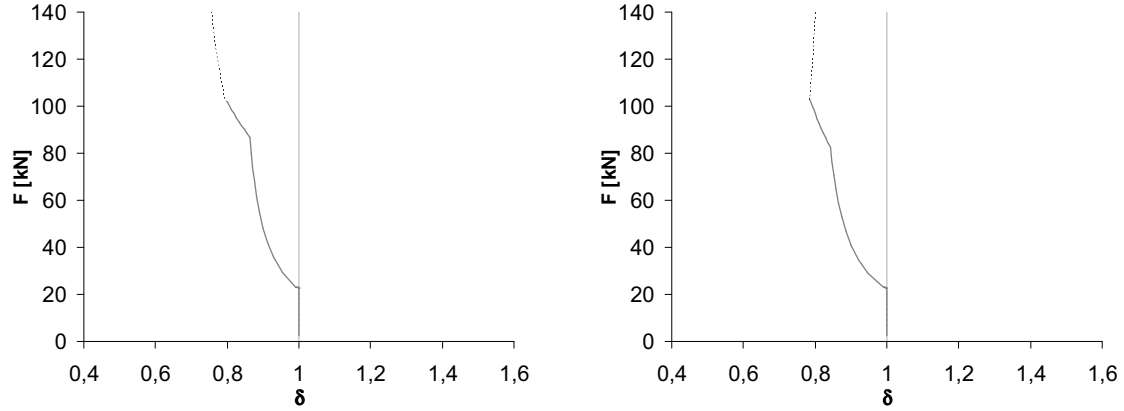

Fig. C.9: Redistribution factor δ for 30 % redistribution (left fig. – 20 % FRP at mid-support - Case C; right fig. – 40 % FRP at mid-support - Case D)

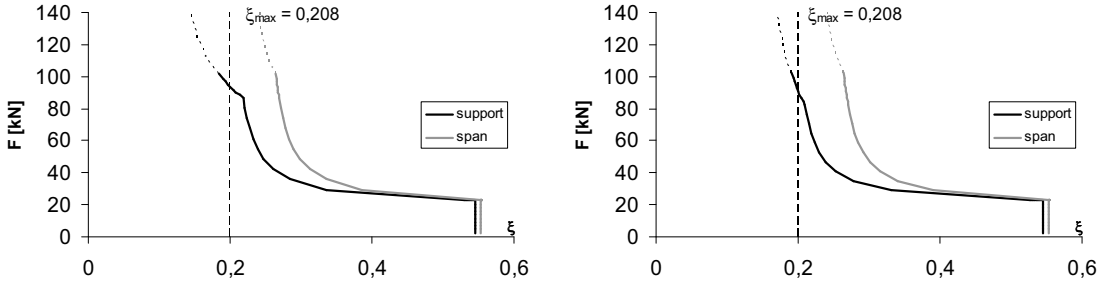

Fig. C.10: ξ-factor for 30 % redistribution (left fig. – 20 % FRP at mid-support - Case C; right fig. – 40 % FRP at mid-support - Case D)

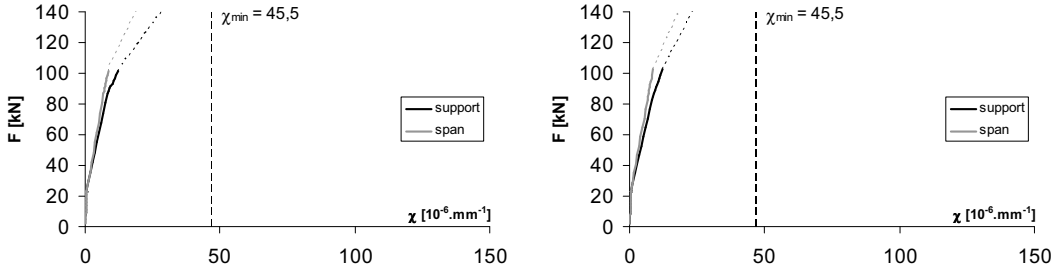

Fig. C.11: Curvature by 30 % of redistribution (left fig. – 20 % FRP at mid-support - Case C; right fig. – 40 % FRP at mid-support - Case D)

The graphs at the left side concern the strengthening configuration, where 20 % of the internal steel reinforcement at the mid-support is replaced by FRP EBR. The graphs at the right side concern the strengthening configuration, where 40 % of the internal steel reinforcement at the mid-support is replaced by FRP EBR.

In Table C.3, the obtained ultimate loads according to the non-linear theory ($F_{u,0.4\%}$: for simplicity, it is assumed that debonding of the FRP EBR laminate occurs at a strain of 0.4 %) and the ultimate loads according to the linear elastic theory with limited redistribution are given. It is noticed that when a part of the steel reinforcement of the expected plastic hinge is replaced by FRP EBR, the required ultimate load according to the linear elastic theory with limited redistribution will not be achieved any more (verified by the non-linear theory). Regarding cases A and B (20 % of redistribution and FRP EBR at the mid-support) a lack of roughly 5 % of the required ultimate load is noticed. Regarding cases C and D (40 % of redistribution and FRP EBR at the mid-support) a lack of roughly 10 % is noticed.

In Table C.3, also the yielding loads of both the span and the mid-support are given. Notice that the yielding load of the critical cross-section in the span remains approximately constant. On the other hand, the yielding load of the mid-support decreases:

- about 4 % by replacing 20 % of the internal steel reinforcement at the mid-support by FRP EBR
- about 8.5 % by replacing 40 % of the internal steel reinforcement at the mid-support by FRP EBR

In the last column of Table C.3, the location where debonding is expected, is given. In the reference beams, this location is situated in the spans. As soon as a small amount of the internal reinforcement at the mid-support is replaced by FRP EBR, debonding is expected at the mid-support. The appearance of the limit strain in the FRP EBR at the mid-support explains the decrease of the ultimate load ($F_{u,0.4\%}$) of these configurations.

Table C.3: Ultimate and yielding loads for different strengthening configurations

Linear el. theory with limited redistribution	Non-linear theory				
	F_u [kN]	$F_{u,0.4\ \%}$ [kN]	$F_{y,span}$ [kN]	$F_{y,support}$ [kN]	'Debonding' expected at
Ref 20 %	100.0	101.3	93.1	86.4	span
Case A	100.0	94.4	92.9	83.0	mid-support
Case B	100.0	95.2	92.4	79.3	mid-support
Ref 30 %	114.3	116.1	103.0	90.4	span
Case C	114.3	101.6	103.3	86.8	mid-support
Case D	114.3	102.7	103.0	82.5	mid-support

In Fig. C.12 and Fig. C.13, a comparison is made of the different moment distribution graphs in function of the different applied amounts of FRP at the mid-support. Notice that also the moment distribution graphs of the beams with designation Ref 20 % and Ref 30 % are given (reference is made to case 1 in Chapter 6).

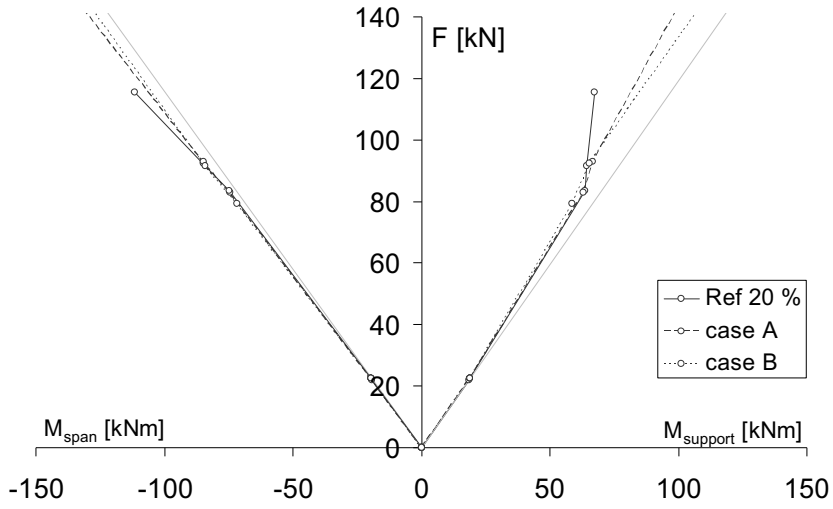

Fig. C.12: Moment distribution graphs for cases A, and B compared to beam Ref 20 %

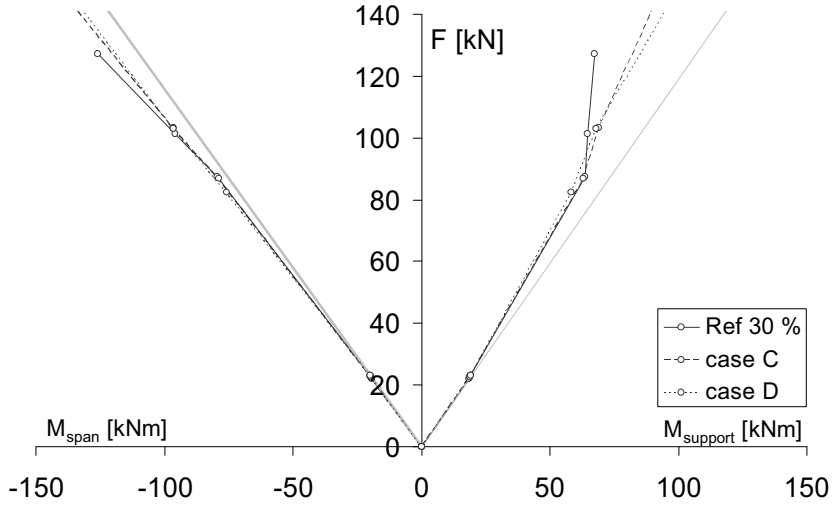

Fig. C.13: Moment distribution graphs of case C and D compared to beam Ref 30 %

Comparing the different redistribution graphs it is remarkable that the configurations with both FRP EBR applied in the spans and at the mid-support is forced to approach the linear elastic moment distribution more closely. As a result, the plastic redistribution reduces considerably. This also can be deduced from Table C.4, in which the total, elastic and plastic redistribution are given for the different strengthening configurations. A considerable reduction of both the total and plastic redistribution is noticed. Especially the reduction of the plastic redistribution is noticeable.

The results of Table C.4 also are visualised in Fig. C.14, where the reduction of the total and plastic redistribution is clearly visible. Remark in these figures also the gap between the obtained redistribution and the redistribution ratio according to the linear elastic theory with limited redistribution. In addition to the results of Table C.4, also replacing 10 % of the internal steel reinforcement by FRP EBR is given in Fig. C.14. Herewith it becomes clear that from the moment a small

amount of FRP EBR is applied at the location of a restrained hinge, the total and plastic redistribution decrease considerably.

Table C.4: Total, elastic and plastic redistribution for different strengthening configurations

Linear el. theory with limited redistribution		Non-linear theory		
		total red. [%]	el.red. [%]	pl. red. [%]
Ref 20 %	20 %	19.6	7.8	11.8
Case A	20 %	15.1	9.7	5.4
Case B	20 %	15.8	11.8	4.0
Ref 30 %	30 %	29.4	11.9	17.5
Case C	30 %	20.0	13.6	6.4
Case D	30 %	21.4	15.8	5.6

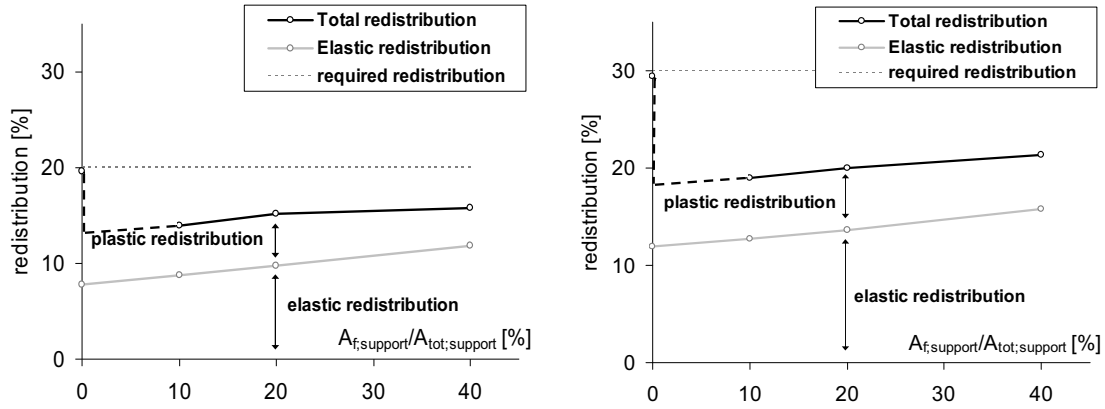

Fig. C.14: Total, elastic and plastic redistribution of the strengthening configurations with 20 % of redistribution (left fig.) and the strengthening configuration with 30 % redistribution (right fig.).

4 Comparison between neutral axis depth (related to ξ-factor) and curvature (χ)

In Fig. C.6 and Fig. C.10, the neutral axis depth is given in function of the applied load. Furthermore, in Fig. C.7 and Fig. C.11, the curvature is given in function of the applied load. The obtained values of the ξ_u-factor and the curvature at failure of the continuous beams are given in Table C.5.

To check the plastic rotation capacity in the linear elastic theory with limited redistribution, the neutral axis depth at failure of the first plastic hinge needs to be checked (see limitations in Table 6.4 in Chapter 6). But, as the first hinges are strengthened with FRP, debonding of the laminate will appear earlier than concrete crushing. Hence no check of the ξ_u-factor can be conducted.

On the other hand, it is possible to check the maximum curvature of the expected restrained hinges. In Table C.5 a large reduction of the curvature at the restrained hinges is noticed. Moreover, if a hinge is strengthened with FRP (restrained hinge in case 3 – 20 % and case 3 - 10 %), the curvature will not exceed the minimum curvature value given in Table 6.5 (Chapter 6).

Table C.5: Minimal neutral axis depth and maximal curvature at the 'failure situation'

	ξ_{span} [-]	χ_{span} [10^{-6} mm^{-1}]	$\xi_{support}$ [-]	$\chi_{support}$ [10^{-6} mm^{-1}]
Ref 20 %	0.225	12.6	0.102	49.9
Case A	0.225	12.6	0.168	16.3
Case B	0.225	12.6	0.185	14.8
Ref 30 %	0.259	13.2	0.093	74.2
Case C	0.264	8.55	0.185	12.3
Case D	0.264	8.71	0.191	12.2

5 Conclusions

The following conclusions concerning moment redistribution can be made for a two span beam with internal reinforcement ratios different from the linear elastic theory, and strengthened with FRP EBR in both the spans and at the mid-support. These conclusions are similar to the conclusions of case 3 in Chapter 6.

- By using FRP EBR at a hinge (= restrained hinge), the moment redistribution is forced to approach the linear elastic moment distribution. As a result, the ultimate moment at the restrained hinges is achieved at a lower (ultimate) load.
- In case a two-span beam with internal reinforcement ratios different from the linear elastic theory is strengthened with FRP EBR in both the spans and the mid-support, restrained hinge(s) are obtained. In this case the required moment redistribution at ultimate according to the linear elastic theory with limited redistribution does not agree with the obtained moment redistribution (verified according to the non-linear theory).
- If a restrained hinge is introduced in a statically indeterminate structure, a considerably restriction of the plastic redistribution is obtained.
- The minimum curvature values given in Table C.5 are not exceeded at the restrained hinges.
- The linear elastic theory with limited redistribution is not a valid design method in case FRP EBR is applied to both the spans and the mid-support.

Lander Vasseur werd geboren te Kortrijk op 13 mei 1981. In 2004 studeerde hij met grote onderscheiding af aan de Universiteit Gent als Burgerlijk Ingenieur, optie Bouwkunde. Sinds september 2004 is Lander werkzaam als doctoraatsbursaal aan het Laboratorium Magnel voor betononderzoek, aan de faculteit Ingenieurswetenschappen aan de Universiteit Gent. Gedurende deze periode werkte hij aan dit proefschrift, stond hij in voor de oefeningen sessies van de vakken 'Voorgespannen Beton', 'Betonconstructies', 'Waarschijnlijkheidsrekening en Statistiek' en 'Statistiek en Gegevensverwerking'. Tevens stond hij ook deels in voor de dienstverlening in het labo en begeleidde hij 5 thesisstudenten bij het uitvoeren van hun masterscriptie. Lander is auteur van verscheidene publicaties en verzorgde diverse voordrachten en postervoorstellingen op nationale en internationale congressen en symposia.

Publications

A1-publications

L. Vasseur, S. Matthys and L. Taerwe, *An analytical study on the bond behaviour between an externally bonded FRP and concrete in the case of continuous beams*. Mechanics of Composite Materials. 2008. Vol. 44 (3 / May, 2008): pp. 269-278.

A4-publications

L. Taerwe, L. Vasseur et al., *Betononderzoek aan de Universiteit anno 2007*. Bouwkroniek. 2007.

P1-publications

L. Vasseur, S. Matthys and L. Taerwe, Debonding mechanisms in continuous RC beams externally strengthened with FRP. Proceedings of FraMCoS, Catania, Italy. A. Carpinteri, et al.: Taylor & Francis/Balkema. 2007. Vol. 2 ('Design, Assessment and retrofitting of RC Structures'): pp. 1101-1110
Journal Article (P1) - Oral presentation

C1-publications

L. Vasseur, S. Matthys and L. Taerwe, *Influence of externally bonded reinforcement on the crack spacing*. Proceedings of CICE2008: 'FRP Composites in Civil Engineering', Zurich, Switzerland. Masoud Motavalli. 2008. Vol. 1: pp. 116
Conference Proceeding (C1) - Oral presentation

L. Vasseur, S. Matthys and L. Taerwe, *Bond behaviour of externally bonded FRP to concrete in the case of 3-point-bending tests*. Proceedings of CCC2008: 'Challenges for Civil Construction', Porto, Portugal. A.Marques. 2008. Vol. 1: pp. 164 – 165
Conference Proceeding (C1) - Oral and poster presentation

L. Vasseur, S. Matthys and L. Taerwe, *2-span reinforced concrete beams strengthened with fibre reinforced polymer*. 8th FirW Doctoral-symposium, Ghent, Belgium. 2007
Conference Proceeding (C1) - Poster presentation

L. Vasseur, S. Matthys and L. Taerwe, *Continuous beams strengthened with externally bonded reinforcement (EBR)*. Symposium - "Mooi bedacht nuttig toegepast"/"De la bonne idée à la réalisation pratique", Brussels, Belgium
Conference Proceeding (C1) - Poster presentation

L. Vasseur, S. Matthys and L. Taerwe, *Debonding mechanisms and moment redistribution of 2 span RC beams*. Proceedings of FRPRCS 8, Patras, Greece. Thanasis C. Triantafillou. 2007
Conference Proceeding (C1) - Oral presentation

L. Vasseur, S. Matthys and L. Taerwe, *Load tests on 2-span reinforced concrete beams strengthened with fibre reinforced polymer*. Proceedings of ACIC 07: 'Advanced Composites in Construction Conference 2007', University of Bath, UK. 2007: pp. 422-429
Conference Proceeding (C1) - Oral presentation (by promoter S. Matthys)

L. Vasseur, S. Matthys and L. Taerwe, *2-span reinforced concrete beams strengthened with fibre reinforced polymer*. Proceedings of 2° Young Researcher's Seminar 'FRP Reinforcement in Construction', Zurich, Switzerland. EN-CORE (The European Network for Composite Reinforcement) in corporation with fib TG 9.3 and EMPA Academy.
Conference Proceeding (C1) - Oral presentation

L. Vasseur, S. Matthys and L. Taerwe, *Analytical study of a 2-span reinforced concrete beam strengthened with fibre reinforced polymer*. Proceedings of IABSE symposium: 'Responding to tomorrow's challenges in structural engineering', Budapest, Hungary. IABSE Hungarian Group 2006
Conference Proceeding (C1) - Oral presentation

L. Vasseur, S. Matthys and L. Taerwe, *2-span reinforced concrete beams strengthened with fibre reinforced polymer*. 6th FirW Doctoral-symposium, Ghent, Belgium. 2005
Conference Proceeding (C1) - Poster presentation

Conferences, Seminars and Task Groups

2008

CICE2008: 'FRP Composites in Civil Engineering', Zurich, Switzerland. 22-24 July 2008. *Influence of externally bonded reinforcement on the crack spacing*. Oral presentation.

CCC2008: 'Challenges for Civil Construction', Porto, Portugal. 16-18 April 2008. *Bond behaviour of externally bonded FRP to concrete in the case of 3-point-bending tests.* Oral and poster presentation.

fib Task Group 9.3: FRP (Fibre Reinforced Polymer) Reinforcement for Concrete Structures. 19th fib TG9.3 Meeting – University of Porto, Portugal 18-19 April 2008.

2007

8th FirW Doctoral-symposium, Ghent, Belgium. 5 December 2007. *2-span reinforced concrete beams strengthened with fibre reinforced polymer.* Poster presentation.

Symposium - "Mooi bedacht nuttig toegepast"/"De la bonne idée à la réalisation pratique", Brussels, Belgium. 28 November 2007. *Continuous beams strengthened with externally bonded reinforcement (EBR).* Poster presentation.

FRPRCS 8: 'Fiber Reinforced Polymer Reinforcement for Concrete Structures', Patras, Greece. 16-18 July 2007. *Debonding mechanisms and moment redistribution of 2 span RC beams.* Oral presentation.

fib Task Group 9.3: FRP (Fibre Reinforced Polymer) Reinforcement for Concrete Structures. 18th fib TG9.3 Meeting – University of Patras, Greece 14-15 July 2007.

FraMCoS-6: '6th International Conference on Fracture Mechanics of Concrete and Concrete Structures', Catania, Italy. 17-22 June 2007. *Debonding mechanisms in continuous RC beams externally strengthened with FRP.* Oral presentation.

ACIC 07: 'Advanced Composites in Construction Conference 2007', University of Bath, UK. 2-4 April 2007. *Load tests on 2-span reinforced concrete beams strengthened with fibre reinforced polymer.* Oral presentation (by promoter S. Matthys).

2° Young Researcher's Seminar 'FRP Reinforcement in Construction', EMPA, Zurich, Switzerland. 18 January 2007. *2-span reinforced concrete beams strengthened with fibre reinforced polymer.* Oral presentation (Winner of the Mirkó Ros Silver Medal Award).

fib Task Group 9.3: FRP (Fibre Reinforced Polymer) Reinforcement for Concrete Structures. 17th fib TG9.3 Meeting – EMPA, Zurich, Switzerland. 19 January 2006.

2006

6th FirW Doctoral-symposium, Ghent, Belgium. 30 November 2006. *2-span reinforced concrete beams strengthened with fibre reinforced polymer*. Poster presentation.

IABSE symposium: 'Responding to tomorrow's challenges in structural engineering', Budapest, Hungary. 13-15 September 2006. *Analytical study of a 2-span reinforced concrete beam strengthened with fibre reinforced polymer.* Oral presentation.

2nd International fib congress, Naples, Italy, 5-8 June 2006

fib Task Group 9.3: FRP (Fibre Reinforced Polymer) Reinforcement for Concrete Structures. 16th fib TG9.3 Meeting – University of Naples, Italy. 3 June 2006.

fib Task Group 9.3: FRP (Fibre Reinforced Polymer) Reinforcement for Concrete Structures. 15th fib TG9.3 Meeting – Limassol, Cyprus. 27-28 January 2006.

2005

CCC2005: 'Composites in Construction', Lyon, France 11-13 July 2005

fib Task Group 9.3: FRP (Fibre Reinforced Polymer) Reinforcement for Concrete Structures. 14th fib TG9.3 Meeting – Claude Bernard Lyon 1 University, Lyon, France. 9-10 July 2005.

fib Task Group 9.3: FRP (Fibre Reinforced Polymer) Reinforcement for Concrete Structures. 13th fib TG9.3 Meeting – Magnel Laboratory for Concrete Research, Ghent University, Belgium. 13-14 January 2005.